A Multicolour Search For Quasars

Paul Simon Mitchell

Presented for the Degree of Doctor of Philosophy

at the University of Edinburgh

1989

This thesis is my own composition, except where specifically indicated in the text.

October, 1989

Contents

List of Figures

List of Tables

Abstract

The Edinburgh Multicolour Survey is a dataset of approximately 1.3 million images covering a contiguous area of 0.1 steradians at high Galactic latitudes. These data are derived from 130 UK Schmidt photographic plates taken in passbands U, B, V, R and I in two strips at declinations –5°and 0°, comprising the standard UKST fields 789–794 and 861–867 respectively. The aim of the survey is to produce a dataset containing accurate *UBVRI* information and morphological classification for every image detected in any waveband in the measured area, enabling the discrimination of intrinsically rare populations of objects with non-stellar colours from the foreground of normal Galactic stars. This thesis is concerned with **(a)** the development of the dataset from its initiation as raw plate material through to the production of the final five-band catalogues, and **(b)** the selection of quasars over a wide range in redshift.

The plate material was scanned with the COSMOS fast-measuring machine at Edinburgh. Care was taken to reduce to a minimum the number of incorrectly measured images, which would badly contaminate candidate lists, and to minimise photometric errors. The presence of two plates for each field/colour enables the rejection of spurious images which was performed after applying a local coordinate transformation between plates. Each set of *UBVRI* plates was taken close together in time to allow the correct measurement of the colours of variable stars and the rejection of images varying significantly in colour between epochs. Three different parameters were used to morphologically classify images over the full range in apparent magnitude. The data were calibrated with CCD sequences providing a total of about 30 measurements per UKST field, and zero-pointed using photoelectric measurements of bright ($B = 15-16$) stars. Systematic calibration errors outside the well-calibrated magnitude range and field-effects due to variations in image structure with position were minimised by new techniques such that the final photometric accuracy of the mean magnitude in each band is 0.02–0.05 magnitudes at about two magnitudes brighter than each plate-limit. The median depths of the final catalogues are $U = 20.7$, $B = 20.8$, $V = 19.6$, $R = 20.0$ and $I = 18.4$. The survey, complete in all but fields 793 and 794, was used (i) to enable the selection of a new low-redshift sample of 69 quasars using a modification of the UVX technique which improves its efficiency, and (ii) as a basis for the selection of bright quasars at the highest redshifts $z \geq 3.4$.

The UVX results compare very favourably with two similar samples, producing a corrected surface density of $0.40 \pm 0.05\,\mathrm{deg}^{-2}$ for quasars with $15 \leq B \leq 18$ and $0.3 \leq z \leq 2.2$; examination of the distribution of objects in colour space provides further confirmation of the sample's completeness. Power spectrum analysis and correlation function analysis produce some evidence for the presence of clustering in the 3-D distribution on scale sizes up to $r \sim 250\,h^{-1}\,\mathrm{Mpc}$; factors capable of producing such a signal spuriously are outlined and the implications of such a result discussed.

For the highest redshift quasars, nearest-neighbour analysis was used to locate objects with non-stellar colours in multicolour space. The full range of survey colours increases sensitivity to $z = 4.1$–4.5 as shown by two approaches: synthesizing quasar colours for a range of spectral type and redshift in a real dataset shows that the efficiency for most quasars with $3.4 \leq z \leq 4.5$ is very high, and the inclusion of genuine quasars into a survey dataset confirms this conclusion. Three such quasars were confirmed spectroscopically with redshifts $z = 3.4$, 3.5 and 3.7 from a candidate list selected with $17 \leq R \leq 18.5$, which imply a corrected surface density of 0.02–$0.08\,\mathrm{deg}^{-2}$ for $3.4 \leq z \leq 4.1$. This is lower but not significantly different from estimates based on visual emission-line surveys, and implies that the luminosity function for bright quasars has the same amplitude as that at $z \simeq 2$. Various simple parameterisations for the evolution of the optical luminosity function are examined in the light of the new result.

Acknowledgements

By far the greatest acknowledgement must go to Lance Miller, who has been an excellent supervisor and friend over my 3+ years in Edinburgh. His unique brand of clear-thinking and extreme lunacy has been ideally suited to a student with "delusions of adequacy".

Academically I am indebted to the UK Schmidt Telescope Unit of the Royal Observatory, Edinburgh, who have provided the main photographic material and facilities on which this work is based, the staff of the COSMOS Unit for scanning the plates, and STARLINK for (some of their) software. Brian Boyle deserves special thanks for assistance in observing, much-needed beers, and letting me win once at snooker. In the same vein, I am grateful to Richard Prestage for his support at Steward Observatory in Arizona. Bob Stobie, Sandy Leggett and Mike Hawkins must also be thanked for saving me from topping myself when faced with 300 CCD images to reduce in 7 days. More generally I am grateful to the staff of the Department of Astronomy and Royal Observatory, and in particular David Emerson for reading the final version with one week to go. I also acknowledge the S.E.R.C. for a studentship and one Panda Seat.

I am indebted to the other students in the department for many things, including laughing at my jokes and calling me lots of new names. I owe much to Ye-Gods-Of-Old-Now-Long-Departed, James "Hen-heid" Dunlop, Andrew Mead, Toby Moore, Neil Heydon-Dumbleton, Phil Puxley etc. I would like to thank in particular Stuart Lumsden for the use of his large red thing, Keith Ballard for falling backwards off many chairs during my time at the observatory, and Steve Torchinsky for his enthusiastic use of my programs and for lending me his *schm.* I also thank Chris Collins for teaching me everything I know about computing and Bob Nichol for not standing on his head with his trousers down, even in *Garbo's.*

I am very grateful to my parents for their support, both emotional and financial, during my time in Edinburgh, and finally Linda.

Part I

Construction Of The Edinburgh Multicolour Survey

This thesis is split into two parts, comprising I: the various elements needed to construct the dataset, and the techniques invoked to combine these elements and reduce photometric errors to a minimum, and II: two results derived from the survey concerning the distribution and evolution of quasars. These results rely heavily on previous achievements in QSO research, and so this account is initiated with a brief discussion of the relevant cosmological background and a review of the main milestones in optical quasar studies, concluding with some general remarks concerning the evolution and distribution of quasars.

Chapter 1

Introduction

Since the discovery of quasars in the 1960's, many different aspects of their spectral form and behaviour have been used to aid selection. Their star-like appearance offers no help in discriminating from galactic foreground stars, but the presence of strong emission lines and a non-thermal continuum shape in addition to their variability, mean that the derivation of optical samples of quasars is possible. The quality and size of these samples has increased greatly as astronomical techniques have improved over the ensuing twenty-five years, especially at lower redshifts, but at the other extreme quasars with redshifts $z > 3.4$ are still rare.

This thesis is partly concerned with the selection of a new large-area low-redshift sample in a traditional manner using broad-waveband photography, but incorporating a modification to the standard method which greatly increases its power. This principle is further extended in the final chapter to cover the whole of the optical wavelength range in a search at the highest end of the redshift range, where the few listed quasars represent the furthest known reaches of the Universe. These two results are used as the basis of discussion concerning the evolution and distribution of quasars on very large scales. By way of introduction, the next section lays down briefly the foundations of cosmology upon which this work relies, and discusses areas of current interest for which the study of quasars is relevant.

1.1 Modern cosmology

1.1.1 General principles

For two hundred years, the Newtonian theory of gravitation held sway as the centre of any cosmological picture. The overriding successes of this description ensured its predominance, providing for the first time a theoretical and verifiable approach to the problems of the dynamics of matter in the Universe. Along with this picture came the assumption of a static Universe of infinite extent. However, certain inconsistencies became apparent upon consideration of this model: "Olber's Paradox" dictates that in an infinite homogeneous Universe, the apparent intensity at the Earth due to a shell of stars $r \rightarrow r + dr$ diverges as $r \rightarrow \infty$, i.e. realistically that the intensity of the night sky should be equal to the average stellar surface brightness. Furthermore, in a finite universe, the model predicts the collapse of all matter by way of self-gravitation.

The appearance of special and general relativity represented a huge leap forward in our understanding of the Universe, and by 1917, Einstein was attempting a more rigorous examination of the cosmological problem. The understanding that consistent geometrical models other than the "flat" Euclidean representation of space existed led Einstein, unaware at the time of the expanding nature of the Universe, to propose a static, finite, positively-curved model as a solution. The necessary inclusion in this picture of a repulsive force represented by Λ, the "cosmological constant", was however unfortunate, and the publication in 1929 by Edwin Hubble of

> "a roughly linear relation between velocities and distances among nebulæ", (Hubble 1929),

resulting in the formulation of "Hubble's Law", $v = H_0 r$ (small z), resolved the situation, and provided a stepping-stone to the modern "standard" view of the Universe. In this picture, the Universe is an isotropic, uniformly expanding (implied by Hubble's law) pressure-less "gas". The expansion implies an earlier stage of high density, culminating in a singularity about $1\text{–}2 \times 10^{10}$ years ago, and the "Big-Bang" model is born.

Two observational facts confirm the standard contemporary understanding of the "Big Bang" model. The isotropy of the Universe was confirmed to a high degree by the discovery in 1965 by Penzias & Wilson of an excess antenna temperature at 7.3 cm, interpreted by Dicke *et al.* (1965) as the "cosmic microwave background" (CMB). It appears that the Universe is immersed in a bath of highly isotropic radiation, characterised by a power spectrum following closely that of black-body radiation. Subsequent measurements all confirm the nature (Planckian at $T \simeq 2.74$K — see Smoot *et al.* 1987 for an amalgamation of recent results) and isotropy (fluctuations $\delta T/T < 10^{-4}$ on scales from $\sim 12''$ to $\sim 90°$— Wilkinson 1988 and Silk 1989 contain useful summaries of recent work), and a simple and generally accepted interpretation is that this represents an adiabatically-cooled relic radiation from a very early phase of the Universe. For the first $10^6 - 10^7$ years after the Big Bang, the energy density of the radiation exceeded that of the matter in the Universe and the history of the Universe was determined by the dynamics of photons: this is termed the *radiation-dominated* era (matter now exceeds radiation in energy density by a factor $\sim 10^3$). Baryonic matter was ionised in the very high temperature and this in turn implies that baryonic matter and radiation were coupled strongly, and the CMB thus represents an "echo" from the time when decoupling occurred, the *recombination time* when temperatures were low enough, about 4000 K, to allow neutral hydrogen to form, and the Universe became relatively transparent to photons, which were previously strongly interacting with free electrons via Thomson scattering.

The abundances of light elements at the present epoch present independent evidence for this picture. Nuclear reactions at the centres of stars provide a well-understood mechanism for generating heavy elements such as C, N, O etc., (the so-called "onion-ring" model), but the amounts of ^{3}He, ^{4}He, D and other light elements are more difficult to manufacture — the more fragile elements are dissociated or combine to form heavier matter very quickly, and ^{4}He itself is not produced in sufficient quantities. It is now understood that the nuclei of neutral elements which formed at recombination, could themselves assemble at a much earlier stage, in particular, for He at $T \sim 10^{10}$ K, in the first seconds after the Big Bang, and from these considerations, abundances in agreement with observational constraints can be derived. These in turn place quite severe

limits on the total baryonic density of the Universe (Yang *et al.* 1984).

The geometry of the Universe is however still not known. The mathematical formulation of the above model lies in the principles of relativity. Special relativity requires that the interval between events must be given by the Minkowski metric:

$$ds^2 = dt^2 - \frac{1}{c^2}(dr^2) \tag{1.1}$$

where dt is the cosmic time interval, dr the proper distance, and c the speed of light. In a massless universe, the propagation of light is governed by this law. However, the presence of matter in our Universe complicates the picture. General relativity sees gravity as a curvature of space-time due to the distribution of mass, derived via an appropriate transformation between accelerated frames of reference. In fact, mathematical analyses of the nature of isotropic curved spaces leads to the conclusion that, for spaces of constant curvature, which can only depend on time, the Robertson-Walker metric is the only choice of metric, expressed as:

$$ds^2 = dt^2 - \frac{R^2(t)}{c^2}\left[\frac{dl^2}{1-kl^2} + l^2(d\theta^2 + \sin^2\theta\, d\phi^2)\right] \tag{1.2}$$

where l, θ, ϕ are dimensionless coordinates, $R(t)$ is the "scale factor" of the universe (such that $R(t)l$ is proper distance), and k is a curvature index. Three values of k are of particular significance, $k = 0$ for Euclidean flat space, and $k = \pm 1$ for positive and negative curvatures respectively. Thus the curvature of the universe depends on the mass content, and even determines its eventual fate — the case $k = 0$ implies that the Universe contains *just* enough mass to halt the expansion at infinity; for $k < 0$ this is not the case and the Universe will expand forever, whereas for $k > 0$ the expansion will reverse and the Universe contract again. A formulation of this problem is the definition of a density parameter, Ω_0, which is a measure of the mean density of the Universe compared to the closure density. Furthermore, general relativity predicts that the deceleration parameter, defined as

$$q_0 = -\frac{\ddot{R}(t_0)R(t_0)}{\dot{R}^2(t_0)} \tag{1.3}$$

is equal to $\Omega_0/2$. This in theory provides an independent way of determining the

geometry. Returning to Hubble's observations, we now understand H_0 as a measure at the present epoch of a "constant" which will in general follow:

$$H(t) = \dot{R}/R \tag{1.4}$$

A fuller discussion of these principles is omitted here, as many excellent texts exist; for further details Weinberg (1973), and Gunn (1979), are particularly helpful.

Much effort has subsequently been expended to determine H_0 and Ω_0, but in practice it is very difficult to decide observationally. Present *observational* evidence appears to favour H_0 in the range $50 - 100$ km s^{-1} Mpc^{-1} (Sandage & Tammann 1988, de Vaucouleurs 1986), and $\Omega_0 \simeq 0.2 - 1.0$ (see Oemler 1989 for a review), and all cosmological models are dependent on these values. Where appropriate, the values adopted are indicated in this thesis, and the convenient definition of $h = H_0/100$ km s^{-1} Mpc^{-1} will often be useful. A key to the confusion that still surrounds different cosmological pictures is that the understanding of current observations and theory produce conflicting results when applied to the value of Ω_0. There remain strong theoretical reasons to prefer a value of $\Omega_0 = 1.0$ exactly: Ω diverges rapidly from 1 in the universal expansion, and any departure from this value in the early Universe would be blown up and lead to an Ω_0 today outside observational constraints.

These then are the basic tools used in the work presented here. This study is concerned almost exclusively with the large-scale properties and evolution of quasars, and all the work herein is dependent on the cosmological interpretation of redshifts. Redshift, defined as $z \equiv (\lambda_o - \lambda_e)/\lambda_e$, can be thought of in terms of a measure of the scale factor of the Universe at the time the radiation measured was emitted, given by

$$R(z) = R(0)/(1+z) \tag{1.5}$$

Thus a measurement of z leads to a distance determination (neglecting random motions superimposed on the Hubble flow), dependent on assumed values of H_0 and Ω_0. Other interpretations of redshift do exist (see e.g. the work of Arp, e.g. Arp 1987), but the prevailing view in support of their cosmological nature is of necessity taken here.

1.1.2 The Universe at high redshift

The uncertainties in the picture described above can lead to very different predictions for the formation of the structure we see presently in the Universe, and specific models of the behaviour of radiation and matter, and the overall composition of the Universe are constrained strongly by the levels of small and large scale inhomogeneities observed at the present epoch. Part of this thesis is concerned with the debate about the level on which the Universe becomes truly isotropic, so some mention of the effect large-scale clustering has on the picture is appropriate here.

The galactic structures seen today are the outcome of the influence of gravitation on initial perturbations in the early Universe. There are three main constraints to any proposal for galaxy formation:

(a) a low value for the cosmic density parameter $\Omega \simeq 0.15$, as predicted from light element abundances at nucleosynthesis and dynamical mass estimates from the study of galaxy clusters, and the need to reconcile this with the theoretically desirable $\Omega = 1$;

(b) the size of CMB fluctuations at the present epoch (Wilkinson 1988);

(c) the scale, amplitude and form of mass fluctuations seen today.

These considerations must be related to the general principles of the expanding Universe we already understand. The variation in behaviour of matter and radiation with cosmic time is generally pictured as follows:

(a) The very early Universe is radiation-dominated, expanding with a scale size $\propto t^{1/2}$. Baryonic matter and radiation are strongly coupled, and hence any mass fluctuations up to the horizon size are quickly smoothed out by "Silk Damping" (Silk 1968) under radiation pressure. Only structures greater than the horizon, and thus not causally connected, survive.

(b) Matter-radiation equality occurs at $z \sim 1500$. The Universe thereafter expands more rapidly as $t^{2/3}$ under matter-domination. However, all electro-magnetically

interacting matter will still be smoothed by photon scattering. Any fluctuations in weakly-interacting species of matter can however now begin to grow.

(c) When recombination occurs, baryonic inhomogeneities are allowed to grow. Photons lose their ability to smooth out matter, lacking a strong non-gravitational interaction with neutral hydrogen. Hence, any fluctuations in the baryonic mass distribution at this point must be reflected in a present CMB anisotropy. As mentioned, the stringent constraints on the CMB present a formidable obstacle to the construction of the galaxies, clusters and superclusters seen today.

The most popular formation models today assume the expansion is adiabatic, such that the ratio of radiation to matter energy densities is everywhere constant at a given epoch; particles are all perturbed in the same manner. The models depend critically on the assumed dominant particle that constitutes the gravitating mass content of the Universe, and this in turn determines the direction of growth in scale size. Broadly speaking, models divide into "top-down" and "bottom-up" categories. Theoretical models generally assume some initial density perturbation spectrum and, assuming a value for Ω_0, follow the non-linear development of structure through N-body simulations etc. Although present computing facilities can only follow a maximum of about 2×10^5 particles, some realistic pictures are still produced (White 1989).

Purely baryonic models, where the dominating massive particles are protons and neutrons, conclude that the only structures that can grow before recombination are outside the horizon scale, due to Silk damping. This leads to a top-down model, and the first structures to form are on the scale of superclusters; these very large and initially smooth structures must then somehow break down into present epoch galaxies. The isotropy of the CMB is a major problem here, fixing the level of fluctuations in the whole mass content of the Universe at recombination to a very low level, which in no formulation can be made to agree with the galaxy-galaxy correlation function and produce the observed Universe. The consequence is that the simplest baryonic models come nowhere near to forming the structure we see today. Another drawback is that in most pictures the galaxy formation starts only very recently ($z \simeq 1-2$), which is clearly inconsistent with the observations of high-redshift quasars.

The realisation that at least 95% of the matter content of the Universe is probably "dark", i.e. that luminous objects do not necessarily trace the mass distribution, has recently provided the opportunity for significant improvements to this view of galaxy formation. Whole sets of models based on one dominating non-baryonic particle species, known to exist or even only postulated, have sprung up, and are based on the principle of a weakly-interacting particle which of consequence can begin to form growing structure as early as the epoch of matter-radiation equality, at the same time producing only very small CMB fluctuations. Baryonic matter meanwhile is kept smooth until recombination, when it can fall into the potential wells of the underlying non-baryonic matter. Mass-light segregation is achieved by *biasing* the efficiency of galaxy formation, such that formation only occurs at $n\sigma$ peaks in the underlying mass distribution, where $n \sim 2.5$ is chosen in the high-peak model of Bardeen *et al.* (1986). The observational evidence for $\Omega_{baryons} \sim 0.2$ from nucleosynthesis can thus be reconciled to a much higher *total* value, and the earlier growth of structure can lead to a more realistic result. Progress is critically dependent on the particle rest mass.

"Hot dark matter" (HDM) models rely upon very light particle species, named because of their consequent high thermal motions at early epochs. Dark matter must not be involved at nucleosynthesis, and must only interact weakly with baryonic matter, and the neutrino is a prime candidate here, which, if massive, only amounts to several eV; in fact $m_\nu = 98h^2\,\mathrm{eV}$ is sufficient for closure (Bond & Szalay 1983). However, the advantage of a *known* particle is probably outweighed by the results for this model. A top-down picture is again appropriate here: all fluctuations within the particle horizon are again smoothed out, and only structures as large as about 20 Mpc survive, which are blown up to larger scales at the present epoch. Discrete galaxies and quasars must condense from these structures at relatively recent times. The effect is a prediction of galaxy clustering which is difficult to reconcile with the findings of observational astronomy.

Weakly-interacting particles of higher rest masses produce a very different picture. Parallel developments in particle physics have produced a wealth of such particles such as the photino and gravitino. These all have sizeable rest masses (several GeV), and

thus are termed "cold dark matter" (CDM). Also included in this category is the axion, which, although possessing a low mass, possess very low thermal motions, being created in a low momentum state, and never reaching thermal equilibrium. The consequence for all these particles is a very small smoothing length, and the formation of small scale structures first, this time producing in general a bottom-up model; in fact structures smaller than galaxies can form and survive at early epochs.

The biased CDM picture is generally considered the most viable today (Frenk 1988), in spite of various problems, and can produce fairly realistic representations of galaxy clustering seen today (current progress is summarised in White 1989). The existence of the constituent particles is at present still speculative, and consistent results for galaxy-galaxy clustering appear to predict too low an amplitude for cluster-cluster correlations when compared to the analyses of Bahcall & Soneira (1983) and Ling *et al.* (1986) of the Abell catalogue. However, there is some doubt as to the validity of the observational result, and this point thus awaits further more verifiable data, although the conflict in predicted and observed amplitudes is large. Further evidence of large-scale bulk motions, and tentative QSO clustering on very large scales also tend to undermine attempts to achieve a consensus.

Before discussing the repercussions of the present research on the above choices of cosmological model, it is necessary to introduce previous efforts in the area of quasar research. The next section will sketch out briefly the development of QSO research, concentrating on work at optical wavelengths, and discussing the advantages and drawbacks of various popular techniques to derive homogeneous samples. Current opinion concerning the 3-D distribution and evolution of quasars will be outlined, and the reasons for the present work argued.

1.2 Quasar surveys

1.2.1 Beginnings and evolving definitions

> "The only explanation found for the spectrum involves a considerable redshift. A redshift $\Delta\lambda/\lambda_0$ of 0.158 allows identification of four emission bands as Balmer lines... The nuclear region would be about 100 times brighter optically than the most luminous galaxies which have been identified with radio sources thus far..." — "**3C 273: A Star-Like Object With Large Red-shift**" Schmidt (1963)

The publication of this article on March 16, 1963 marked the discovery of a new astronomical species with dramatic repercussions for all areas of cosmology. Quasi-stellar objects, and other related active galactic nuclei phenomena, have become a huge field of study, and from the view-point of a quarter of a century later, their contribution to the modern cosmological picture is incalculable.

The above identification of features in the spectrum of the optical counterpart to the radio source 3C 273 (Matthews & Sandage 1963) with, for the time, highly redshifted but still recognisable emission lines, together with the point-like appearance quickly established a precedence for many further "quasi-stellar object" identifications. With these publications came the realisation that the colossal intrinsic luminosities of these objects, coupled with the apparently small spatial dimensions of their emitting cores, could not be easily explained by simple nuclear energy arguments. Parallel to these developments came the first indications that QSOs exhibit significant cosmological evolution (Schmidt 1968, 1970), although at first the small numbers of confirmed objects prohibited any accurate evaluation of the form and behaviour of this evolving function.

The field of QSOs has since followed a familiar path for scientific research. The initial discovery spawned a rapidly expanding field of research, with many schools of interest each centred in a different range of wavelength coverage. The field rapidly diverged, with subdivisions and sub-subdivisions of the early object definitions, attempting to isolate the various intrinsic and global properties of these objects. In more recent years, it has become increasingly fashionable (and generally observationally justified) to attempt some synthesis of these groups back into a single or set of related

phenomena, connected either via evolutionary models, or differences in scale of some astrophysical property intrinsic to each source.

Therefore, in order to circumvent the difficulties inherent in such a highly-evolved object definition, some compromise is necessary: it is sufficient to surrender precision for a generally accepted definition upon which most researchers agree. The term "quasar" can be said to have fully entered into agreed usage in 1970, when, as a footnote to a paper by Schmidt, the *Astrophysical Journal* noted their acceptance of the term as a collective description of the hitherto individually segregated species "QSO" (optically-selected) and "QSS" (radio-selected). Such distinctions have since become blurred, and in this work, in line with usage elsewhere, the terms "quasar" and "QSO" will be used interchangeably.

History then has taught us the lesson that too rigid a definition may lead to a highly diversified field, in itself a great obstacle to any overview of the whole phenomenon: however, for the sake of completeness, to initiate this discussion a loose definition is given here. For the purposes of this discussion, a quasar may be seen as an extragalactic unresolved optical source exhibiting a component of roughly power-law continuum emission, usually underlying a system of broad emission lines, and seen at high redshift. Immediately problems are encountered. A "quasar" at low redshift may allow optical identification of its underlying host galaxy if its intrinsic core luminosity is low enough; conventionally therefore a low luminosity limit of $M_B \lesssim -23$ (e.g. Boyle, Shanks & Peterson 1988b) is usually added to the above definition to make room for Seyfert galaxies, in practice meaning that some "quasars" are resolved. There is clearly some "continuum" in such properties, and many authors have suggested that the underlying similarities are sufficient to unite these objects in a scheme dictated only by the level of core activity (e.g. Hutchings *et al.* 1982, Hutchings, Crampton & Campbell 1984). Furthermore, "blazars" are highly ($> 3\%$) polarized versions of a very similar nature, further divided into BL Lacs, with no (or very faint) emission lines, and OVVs (optically violently variable), highly and rapidly variable in luminosity and polarization. To some extent all quasars probably exhibit both optical variability and polarization, and again there have been attempted unifying schemes (e.g. Orr & Browne 1982).

Table 1.1: The diversity of QSO-orientated research. The bottom table indicates some areas of theoretical research upon which these observations impinge.

Optical observations:

(i)	UVX samples
(ii)	Multicolour techniques
(iii)	Slitless surveys
(iv)	Variability searches
(v)	High resolution spectroscopy (absorption systems & Ly-α forest studies)
(vi)	Emission line analysis
(vii)	Quasar-quasar clustering
(viii)	Quasar-galaxy clustering
(ix)	Quasar-galaxy associations
(x)	Search for gravitational lenses
(xi)	Morphological studies

Theory:

Power source and lifetimes/birth-rates (i) (ii) (iii) (iv) (viii) (xi)
Evolution of quasar comoving density (i) (ii) (iii) (iv) (x)
Homogeneity of the quasar distribution (vii)
Homogeneities of galaxies and clouds at high redshift (v) (viii) (x)
The composition of intervening material (v) (vi) (x)
Quasar environments (v) (vi) (viii) (xi)
Quasars in the general AGN picture (viii) (xi)
The origin of redshift (ix)

Table 1.1 gives a rough guide to the diversity in quasar-related optical observations currently popular, and the wide range of relevant theoretical questions. Clearly this is a vast simplification of the scientific method, with observations actively interacting with, and influencing theory and back again. This thesis is concerned with only categories (i), (ii) and (vii), although all these fields are related in some way.

Observations in other wavebands further qualify the above statements, and radio and X-ray selection are major topics in their own right. The nature and behaviour of quasars cover a vast field of research and attention is restricted here primarily to two areas: their evolution with cosmic time, and the characteristics of their spacial 3-D

distribution. In addition to this, the observations of this thesis are conducted purely at optical wavelengths, and the following summary of techniques will cover only optical searches.

1.2.2 Optical survey techniques

The quasar phenomenon was first discovered through radio emission (Matthews & Sandage 1963), and this continues to be a large influence today. However, it soon became apparent that only a fraction of quasars are "loud" at radio wavelengths (where "loud" is usually defined in radio power as $P_{2.7GHz} > 10^{24}\,\mathrm{W\,Hz^{-1}\,sr^{-1}}$ — see e.g. Peacock, Miller & Longair 1986), and the presence of a large population of "quasi-stellar galaxies" in the optical demonstrated (Sandage 1965). Much attention consequently turned to optical wavelengths (Ryle & Sandage 1964). Such is the power of the techniques described below that the vast majority of quasars known today are optically selected.

Differentiation from the overriding contaminating influence of stars is usually achieved through some combination of the following spectral features:

I blue continuum spectral form when compared to the thermal distribution of stellar black-body emission;

II more general deviations from stellar colours over > 2 wavebands;

III presence of emission and absorption features;

IV discontinuities in the continuum;

V variability.

The method by which selection is achieved is a vital element in the description and assessment of any survey — visual inspection of survey data has in the past been the only option, but the well known biases of subjective judgement and tiring caused by the formidable amounts of work required make any results notoriously hard to discuss. More recently, the advances in automated plate measuring and processing power have

led to more objective selection, with the advantage that selectivity can be assessed *a posteriori*. These improvements are to be unreservedly encouraged (especially at high redshifts) if a final account of quasar evolution is to achieved.

The following categorisation of techniques indicates the extent to which the above quasar characteristics are exploited in the major surveys of the last decade; the following two sections will proceed to discuss the remarkable degree to which these measurements have constrained low-redshift evolution, the continuing level of uncertainty at higher redshifts ($z > 2.5$), and future requirements. This section will conclude with a discussion of the current uncertainties in quasar clustering.

Ultra-violet excess

Ryle & Sandage (1964) first implemented this technique successfully after the discovery of a significance excess of light at blue wavelengths for radio sources 3C48, 3C196 and 3C286 (Matthews & Sandage 1963). This was soon understood in terms of spectral shape, and has become the major technique for lower redshifts, being conceptually simple and relatively straightforward to apply to large datasets, particularly since the advent of automated direct photographic plate measurement. Most investigators use broad-band magnitudes in two band-passes (generally approximating Johnson U and B) and apply as severe a red limit as is possible (generally $(U-B) \lesssim -0.30$ to -0.45) given the sample size (limited by available follow-up spectroscopy and completeness) and photometric errors (determining the contamination from the main stellar locus and sample completeness).

This method of quasar selection, although highly successful, like all methods is subject to some powerful selection effects. The prime advantages of this technique are the easily understood nature of the factors governing spectral shape, and their slow variation with z. The broad-band colours of quasars are to first order a reflection of the continuum shape, and thus powerful as a discriminant up to $z = 2.2$, when the continuum is broken down by the presence of strong Ly-α emission and the subsequent Ly-α forest in the B band. However it has become apparent that other strong emis-

sion lines can have a powerful effect on QSO colours (e.g. Schmidt 1968, Véron 1983, Wampler & Ponz 1985, Peterson 1988), producing significant losses in surveys with bluer UVX limits particularly at $z \sim 0.6 - 0.9$ (MgII and FeII multiplets in B) and $z \sim 1.55 - 1.75$ (CIV in B). The effect of these losses can be quite pronounced for some surveys (e.g. Schmidt & Green 1983).

The first large systematic ultra-violet excess (UVX) survey (Braccesi, Formiggini & Gandolfi 1970) was performed in a 6° x 6° area using a two-colour 14″ x 14″ Palomar 48″ plate. 175 candidates were selected to $b = 19.5$. Formiggini *et al.* (1980) subsequently applied the same technique (this time blinking u, b and v plates) to produce a deeper sample in a subset of the same area. Follow-up spectroscopy produced the AB and BF samples (respectively, 22 quasars in 37.2 deg^2 to $B = 18.25$, and 35 quasars in 1.72 deg^2 to $B = 19.8$ — Marshall *et al.* 1983b, 1984). The largest survey of its kind was meanwhile published, the Bright Quasar Survey (BQS) (Schmidt & Green 1983) derived from the Palomar-Green (PG) survey of blue stellar objects (Green, Schmidt & Liebert 1986) covering 10,714 deg^2 to an average limiting magnitude of $B = 16.16$. Blue objects were selected from 266 double U and B plates taken with Palomar 18″ Schmidt telescope. The final catalogue contained 93 QSOs ($M_B < -23$) out of 1715 objects with $(U - B) < -0.46$. This provided a definitive database for very bright low-redshift quasars, in spite of the many problems inherent in such a large survey at the time; in particular, the survey limit is poorly defined, varying from $B = 15.49$ to 16.67 over the area of the survey, and the relatively blue (and imprecise) UVX cut-off leads to many objects being missed in a not easily quantifiable manner (e.g. see Chapter 4 of this thesis), and completeness (and systematic errors) are hard to define (Wampler & Ponz (1985) indicated that the BQS may be substantially less complete even than the quoted 72% in the redshift range $0.6 < z < 0.8$).

To fill out the Hubble diagram for quasars, providing as firm constraints as possible to any evolution model is the primary reason for the increasing number of quasar samples. In order to fill the gap between BF and AB samples on the one hand, and the BQS on the other, Mitchell, Warnock & Usher (1984) reported the construction of the Medium-Bright Quasar Survey (MBQS) of 32 quasars at $B < 17.65$, again

basing their work on the UVX technique, but with an important modification. In the traditional UVX sample, the successful discrimination between quasars and hot F and G subdwarfs is somewhat diminished by the inclusion of hotter (but rare) main sequence stars, and an extension of the technique to 2-D, using U, B and V provides better separation from the black-body locus (see also Miller & Mitchell 1988). The technique remains one based on blue excess, and so is rendered useless for $z > 2.2$, but generally spectroscopic completeness for quasars can rise from about 40% (Boyle *et al.* 1987) to as high as 80-90% (Miller & Mitchell 1988). The MBQS survey followed this approach in five selected Palomar Schmidt fields: three-colour plates were visual inspected (non-extended sources only) and uncalibrated photometry used to select 3 final candidate classes for follow-up spectroscopy. The loss of quasars in the traditional UVX "holes" at $z \sim 0.75$ and 1.65 is less apparent than for the BQS sample; there is some evidence of losses in candidates at the bright end but this does not affect QSO numbers (Warnock *et al.* 1986). Since the initiation of this survey, the sample has doubled to 61 quasars for $15.6 \leq B \leq 18.2$ (Usher, Mitchell & Warnock 1988, Mitchell & Usher 1988).

The transition to automation has only occurred in the last few years. The faint survey of Boyle *et al.* (1987, 1988a, 1988b) has been fundamental in firmly establishing the evolution of low-z quasars, extending Hubble diagram coverage to faint limits in a quantifiable way. Pure UVX methods ($(U-B) < -0.35$) were applied in seven United Kingdom Schmidt Telescope (UKST) $5^\circ \times 5^\circ$ fields for U and B_J ($\simeq$ Johnson B) plates to a limiting magnitude of $B = 20.9$, producing a sample of 420 confirmed quasars in 34 randomly chosen $0.35\,\mathrm{deg}^2$ areas. Advances in fibre-optic systems in the last few years (here FOCAP on the Anglo-Australian telescope) allowing the simultaneous acquisition of up to 50 objects make spectroscopy of such a large sample a possibility. The relative ease with which a two-colour UVX criterion is applied was again counterbalanced to a small degree by a lack of quasars at $0.6 \lesssim z \lesssim 0.9$, although even here, as the UVX limit was pushed back, incompleteness was demonstrated to be $< 10\%$ (Boyle, Shanks & Peterson 1988b), with no discernible dip at $z \sim 1.65$. The present understanding of low-z evolution discussed in the next section was only possible with these data, and the consequently large apparent magnitude range span from the BQS. The large amount of

work has thus now been done, although amplification of these very important results is still vital for confirmation. The continuing popularity of the UVX method can be readily appreciated by scanning the number of present on-going surveys in recent literature (e.g. *Proceedings of a Workshop on Optical Surveys for Quasars,* Astronomical Society of the Pacific Conference Series, Volume 2).

In conclusion, the UVX technique is an extremely effective way of selecting quasars with $z \lesssim 2.2$; its power can be increased further by the introduction of another longer-wavelength discriminating broad-band measurement. Systematic biases can be introduced through (a) the aforementioned "holes" in two restricted redshift intervals (dependent on $(U-B)$ limit applied), (b) morphological misclassification (dependent on techniques applied, usually only apparent for $z < 0.3$ — Schmidt & Green 1983), (c) QSO variability — plate material separated by time-scales of about a year or more may be subject to some losses, (d) systematic loss of weak-lined objects in follow-up spectroscopy (important only for fainter surveys), and finally (e) other non-UVX $z < 2.2$ quasars — these seem to be rare (Véron 1983), as indications from variability searches confirm (Hawkins & Woltjer 1985, Hawkins 1986).

Multicolour surveys

The increase in UVX selection efficiency with the inclusion of longer wavelength information has recently led to the development of a new technique that provides a way of overcoming the upper redshift limit of the traditional UVX approach, while maintaining the advantages of broad redshift coverage. By extending to longer-wavelength band-passes, further discrimination is afforded against galactic stars, in particular for the redder colours seen in high-z QSOs (see Chapter 6). The aforementioned work of Mitchell, Usher *et al.*, and Koo, Kron *et al.* below, can be seen as a transition into this area, but an important difference requires amplification: a pseudo-multidimensional approach is often employed, whereby objects are selected via different colour-colour diagrams, but these are in effect only projections of the multi-dimensional "hypercube" and hence a projection of the distance from the nearest point in the stellar locus will

in general be a less powerful discriminant than a true measure of this distance. A fully multi-dimensional approach consequently must be developed to extract the full information content of the data, placing each object in multi-dimensional space and measuring distances in quadrature in this space. A by-product of this is a quantifiable selection criteria (in the simplest case, distance from the main sequence locus) which may be used *a posteriori* to check selectivity. The volume of information for such techniques is high (often five band-passes) and the need for a truly multi-dimensional approach, coupled with the rarity of high-redshift quasars, requires quick image analysis, large storage space, and computing power, with the result that developments have until recently been slow. UKST direct plates, and the development of fast plate-measuring machines in Cambridge (the APM) and Edinburgh (COSMOS) have provided British astronomy with the opportunity for great advances in this field.

The principle of triple-colour (U, B, V) selection was first applied systematically in a quasar survey by Usher (1981). Concentrating on field SA57 near the North Galactic Pole, he reselected all 13 known quasars within 44 deg^2 to $B = 20$ from Palomar Schmidt plate derived magnitudes, and discovered 4 previously unknown. This was done by considering separate classifications of objects on a 2-D colour-colour diagram, efficiently selecting quasars as having $(U - V) \leq 0$, and thus providing better discrimination than one dimensional UVX selection, and was soon adopted by other groups (Borra & Lepage 1986).

The work of Koo & Kron and others has concentrated to a large extent upon this level of multicolour selection. Attention has been directed to extremely deep searches in two selected fields: an early search in 0.3 deg^2 of field SA68 (Koo & Kron 1982) led to a sample of 65 quasar candidates to $B \leq 22.5$, selected as unresolved objects on a set of two of each of U, J, F ($\simeq (V + R)/2$) and N ($\simeq I$) 4 m KPNO Mayall plates. Objects were picked out as outliers on 2-dimensional $(U - J)$, $(J - F)$ and $(F - N)$, visually checked, but awaited spectroscopy: in the meantime the ultra-violet nature of most candidates implied $z \lesssim 2.2$. Koo, Kron & Cudworth (1986) presented a more comprehensive attempt, this time in field SA57, with 77 candidates to $B \leq 22.5$ in 0.3 deg^2, selected again by U,J,F and N 2-dimensional analysis, but also examined

for variability over a ten-year baseline and proper motions. CCD spectroscopy was performed on the sample, culminating with Koo & Kron (1988) and the identification of 30 quasars with $0.91 \leq z \leq 3.07$ in $0.29\,\mathrm{deg}^2$ selected from U, J and F colours, complete to $B = 21.1$, and unbiased to $B = 22.6$. Koo, Kron & Cudworth (1986) had indicated that (a) incompleteness was likely to be small up to $z \sim 3.2$, and (b) that most candidates colours indicated them to be of low redshift, and these facts were indeed borne out. The implication of their results will be discussed below, but it is worth mentioning that Kron (1988) intends to extend this work to an F-selected survey using a $(J-F)$, $(F-N)$ diagram, and thus increasing sensitivity to $z \sim 4.5$ for quasars with $F \lesssim 21.5$.

Zamorani, Zitelli & Marano (1986) and Marano, Zamorani & Zitelli (1988) have pursued a very similar method of *U, J, F* multicolour selection in a $J \leq 22.0$ selection covering $0.69\,\mathrm{deg}^2$, while complementing these results with prism and variability selection, providing some interesting results: these will be discussed as appropriate below. Two sets of CCD-calibrated *U, J, F* plates were taken at the European Southern Observatory (ESO) 3.6 m, star-galaxy separated, and objects visually selected as outliers on a two-colour diagram (Marano, Zamorani & Zitelli 1986). 23 quasars were confirmed to a limit of $J = 20.9$. These quasars possessed a fairly smooth redshift distribution in the range $0.6 \leq z \leq 2.8$, but no higher redshifts were measured. In principle the multicolour technique, and certainly the prism technique should remain sensitive to $z \sim 3.3$, and this result confirms that of Koo & Kron (1988) and others, that quasars with $z \gtrsim 3$ are relatively rare, implying that the dramatic increase in space density seen for redshifts up to 2.2 may not continue indefinitely. More stringent constraints on QSO behaviour however proved hard to impose with a technique insensitive to very high redshifts.

The use of large-scale UK Schmidt plates for multicolour selection work was stimulated in 1983 with the discovery of DHM0054-284 with $z = 3.61$ (the second highest then known) from U, B, V and R exposures (Shanks, Fong & Boyle 1983). The APM group at Cambridge (Warren, Hewett *et al.*) have produced the most spectacular results in the field of high-z searches. The basic method is set out in Warren, Hewett &

Irwin (1987b) and Warren, Hewett & Osmer (1988), and consists of a nearest-neighbour search in 4-D colour space, constructed from Schmidt colours *UBVRI*, where nearest-neighbour distance defines the sparsity of colour-space in a straightforward manner. The technique is fully described in this thesis (Chapter 6), where it is applied in a very similar manner — the principle difference is the parameters associated with their search, in particular restricting the analysis to one, and later two UKST Schmidt fields, but extending to relatively fainter limits ($R = 20.0$). Other modifications exist (the APM treatment of digitised data, the level of nearest-neighbour probing, the definition of colour "axes"), but these, although technically important, are secondary to the general rationale. Given the contamination by galaxies and blended images, extensive star-galaxy separation is required, as is the case in the Edinburgh Multicolour Survey, and the reduction of photometric errors to a minimum is a vital component, allowing close probing into the stellar locus without excessive contamination making spectroscopic confirmation of objects unfeasible. Ideally a comprehensive search of all objects in under-dense regions can then be performed, independent of assumptions as to the spectral features at high redshift: in practice this is not always possible, given the limitations in resources, and some colour selection is required. At the time of writing, the latest publication (Warren, Hewett & Osmer 1989) from this group is of 53 confirmed quasars of $z \geq 3.0$ in an effective area of $50\,\mathrm{deg}^2$, comprising two Schmidt fields, the South Galactic Pole ($0^{\mathrm{h}}\,53^{\mathrm{m}}$, $-28°\,03'$) and UKST field 401 ($20^{\mathrm{h}}\,48^{\mathrm{m}}$, $-35°\,00'$). The technique has been demonstrated by simulation of quasar broad-band colours to be most effective at redshifts $z > 3.0$ (the high z limit dependent on the plate material) (see Chapter 6, and also McGraw & Cawson 1988, Cristiani & Vio 1989), and initial work in the APM multicolour survey has concentrated on this regime. The most spectacular results are inevitably the very high-redshift findings, and quasars at z =4.43, 4.07 and 4.01 have so far been reported (Warren *et al.* 1987a, 1987c), all at large distances from the stellar loci (Warren, Hewett & Osmer 1988), indicating the ease with which this method locates such objects.

The biases intrinsic to this technique overlap to some degree those of UVX selection, and any method based on broad-band measurements. By definition, these techniques are only insensitive to any QSO which, through a combination of spectral

components, conspires to coincide in colour space within the stellar locus (e.g. BALs). However, as will become apparent in this work, stars occupy a relatively small "volume" compared to the possibilities for any "reasonable" QSO, and multicolour photometry can be very powerful (see the discussion in Chapter 6). The biases against extended, and variable sources mentioned above are also relevant here, and caution is necessary when considering very low redshifts. As in any technique, the power of selection varies as a function of redshift, but this can be assessed *a posteriori*, as will be seen later. Multicolour photometry does not claim to select every conceivable QSO, but its power rests in its ability to select automatically, and quantifiably, the vast majority of known objects.

The power of multicolour selection has meant that concentration of research in this direction is increasing all the time. Anderson & Schechter (1988) are currently conducting a faint ($m < 22.5$) 4-band (Johnson B and Gunn g, r and i filters) survey in two $0.3\,\mathrm{deg}^2$ fields, using the Palomar 5 m. Instead of the usual photographic approach, they are taking advantage of the accuracy and high efficiencies of CCDs to reach faint magnitudes, using a 2×2 large CCD array (the "Four-Shooter"). McGraw & Cawson (1988) are also using CCDs, in a transit survey at Kitt Peak to $V = 21$ with a two CCD array. Results for both these surveys look promising. Kron (1988) further proposes an extension as faint as $B = 24$ with existing instrumentation, based on specially tailored, narrow-band filters. Information at these magnitudes would be of great significance, not only for intrinsically faint objects, but also for the detection of underlying galaxies in relatively high-redshift QSOs.

Emission-line searches

As soon as the limitations of ultra-violet excess were realised, other methods were sought to overcome the upper redshift limit of $z \simeq 2.2$, which had partly contributed in the past to incorrect assumptions concerning QSO evolution (Schmidt 1972, Sandage 1972). An independent alternative to the relatively recent multicolour technique has been to utilise the unique, strong spectral features of quasars, in particular, the strong,

broad emission lines, although the additional discriminating factors of blue continua and spectral discontinuities are often under emphasised (see e.g. Hazard *et al.* 1986).

The basis of the technique is the dispersion of stellar light simultaneously for all objects in a given area of the sky over an integrating surface, usually a photographic plate; it is often referred to as "slitless spectroscopy". A rough spectrum for each object is produced, allowing easy identification of strong-lined objects. The first suggestion that this technique might be a powerful tool for quasars came from Hoag & Schroeder (1970), who initiated trials on the 1 m at Kitt Peak with the Kodak IIa-O emulsion.

An immediate drawback inevitable in this method is that it does not produce directly magnitude-limited samples but rather is limited by emission-line strength for the faintest objects, which in turn depends on the line detected — the inherent difficulties are discussed fully for instance in Schmidt, Schneider & Gunn (1986a). The depth of a survey is a vital quantity to define, primarily because the number of quasars as a function of apparent magnitude is very steep. The depth is therefore usually related to an approximate continuum magnitude at some wavelength. As with broad-band colour work, the biases of visual inspection have recently led to more automated approaches; the early visual searches however still contributed much, and the technique is still widely used. A discussion of the contribution of "eyeball" techniques is therefore given first.

Up until recently, the Kodak emulsion IIIa-J was almost exclusively chosen for slitless work: the combination of high quantum efficiency, low noise and broad, smooth spectral response towards the blue has proven highly tempting to investigators. The long-wavelength cutoff, set by the red cutoff of IIIa-J response, allows in principle detection of quasars by Ly-α in the range $1.8 < z < 3.4$, and so is very useful in determining the space density of quasars in the transition from the UVX regime to high redshifts. A large amount of IIIa-J work has been conducted with Schmidt telescopes, giving very large field coverage (and relatively bright apparent magnitude depth, usually equivalent to $B \sim 18.5 - 19$). The "Curtis-Schmidt" IIIa-J survey at CTIO of the late 1970's and early 1980's, utilising an objective prism on the Curtis telescope to provide low resolution ($\sim 1500 \text{Å}\,\text{mm}^{-1}$) spectra in a $5^\circ \times 5^\circ$ field, provided the most

important results in the intermediate redshift regime. Initiated by Smith (1975), the survey quickly produced 9 new high-redshift ($2.5 \leq z \leq 3.1$) confirmed QSOs (Smith 1976, Osmer & Smith 1976) and 27 at lower redshifts (Osmer & Smith 1977a). 4 more high-redshift quasars were reported soon afterwards (Osmer & Smith 1977b), demonstrating for the first time the relative abundance of quasars at $z > 2.2$. This led in turn to the conclusion that the space density of quasars did not decline dramatically in the region $1.9 < z < 3.25$ (Osmer & Smith 1977c, 1980), when the finished survey of 108 confirmed QSOs in $340\,\mathrm{deg}^2$, complete to $m_{\lambda 1475} \sim 18.5$ (approximate continuum magnitude) was published. Results from the Michigan-Tololo survey with the same instrument confirmed this conclusion (Lewis, MacAlpine & Weedman 1979, MacAlpine & Feldman 1982): following the analysis of Carswell & Smith (1978), they concluded that behaviour in the range $2.0 \leq z \leq 3.3$ is consistent with constant comoving space density.

Much IIIa-J work has also been conducted using large 4 m telescopes. The Canada-France-Hawaii (CFHT) 3.6 m in particular has produced excellent results in conjunction with a transmission-grating, prism and lens combination (grens), which produces low-resolution spectra with linear dispersion response. 1 hour exposures on IIIa-J plates provide the opportunity for deep quasar identifications over a narrow ($0.8\,\mathrm{deg}^2$) field, complementing well the Schmidt technique. Crampton, Schade & Cowley (1985) produced a list of 439 QSO candidates from such material by visual inspection; Crampton, Cowley & Hartwick (1987) reported the virtual completion of this survey, with a total of 163 confirmed quasars to $B \lesssim 20.5$. Less than 5% of these quasars possessed $z > 2.5$, although the technique should again be sensitive to $z \sim 3.4$. Crampton, Cowley & Hartwick (1988) indicate the extension of this survey to another field containing more than 500 candidates, producing 216 confirmed quasars. The grens set-up at the CFHT remains popular, and has produced many other successful results for $z < 3.3$ (Weedman 1985, Borra, Beauchemin & Edwards 1988, and references therein).

The intriguing results for IIIa-J led to much speculation as to the QSO population at redshifts beyond the red cutoff, and Hoag & Smith (1976) showed that, in spite of its non-uniform response, the redder IIIa-F emulsion could in principle extend sensitivity

to the range $3.7 < z < 4.7$. Within a year they had published results from such a survey, using the Cerro Tololo Inter-American Observatory (CTIO) 4 m telescope in conjunction with a grating-prism ("grism") combination and producing over 70 candidates in the range $17 < B < 22$ from 17 plates covering $5.1\,\mathrm{deg}^2$ (Hoag & Smith 1977). Osmer (1980) summarised the results: 66 quasars were confirmed, 52 of which possessed $z > 1.7$, but significantly none with $z > 3.45$, suggesting a strong decline in space density beyond this redshift. These initial indications were soon qualified by the exhaustive analysis of Carswell & Smith (1978), who showed that the combined effect of a grism blazed in the blue, the non-uniformity of the emulsion response at the long-wavelength end, and the steep quasar luminosity function could artificially produce this result. Their suggestion that a grism blazed at a longer wavelength would provide high-redshift Ly-α sensitivity was quickly picked up, and Osmer (1982) published 13 confirmed emission-line objects from such a survey with the same instrument as before: none were detected with $z > 3.4$, i.e. by Ly-α, and Osmer, arguing from the full redshift range of C IV detections, convincingly showed that this was a highly significant result. This evidence, combined with that of the IIIa-J surveys of the relative abundance of $z \sim 3.2$ objects, was taken as symptomatic of a significant decline at $z \gtrsim 3.5$.

The United Kingdom Schmidt Telescope has also been used to great effect for visual IIIa-J work with an objective prism, providing low-resolution spectra over a very large $6^\circ \times 6^\circ$ field (e.g. Kunth & Sargent 1986, Barbieri & Cristiani 1986). The most important recent results from eyeball surveys in the higher redshift range have however again come from the extension to high-z afforded by the use of IIIa-F: Hazard and collaborators, who, through visual inspection of 17 IIIa-J objective prism plates had earlier published a list of 50 confirmed quasars, again up to $z = 3.3$ (Hazard *et al.* 1986), extended their treatment to higher redshift, producing some spectacular finds. Hazard & McMahon (1985) reported the discovery of two bright quasars at $z = 3.4$ and 3.7 (the second highest measured at the time), and later one of $z = 3.80$ (Hazard, McMahon & Sargent 1986), making a total of 7 bright ($R \leq 18.5$) $z \geq 3.3$ quasars in only two Schmidt fields (although these apparent magnitudes are probably too bright by ~ 0.5 magnitudes — compare quoted surface densities with those of Hazard 1986). The irregular IIIa-F response was compensated for by auxiliary IIIa-J and IIa-D checks

on likely candidates: the non-linearity in dispersion from the prism limited the useful detectable range to $3.3 \leq z \leq 3.9$. These findings seemed to favour an interpretation of a steady decline in space density from lower redshifts, rather than an abrupt cutoff, and the supposed predominance of higher redshift quasars at brighter magnitudes also seemed to indicate a somewhat less steep luminosity function. Although these objects are intrinsically very interesting, and, because bright, very useful for intervening matter studies, no reliable measure of completeness is, or can be, deduced from such studies, and the need for a more automated approach to detection, as was the case for broad-band work, becomes very strong.

In 1986, Schmidt, Schneider & Gunn embarked upon a major search for faint quasars in a novel way, using the high quantum efficiency and smooth response of CCDs to provide a detector for faint dispersed light. A large Texas Instruments red-sensitive CCD was set up to scan 0.91 deg^2 with 34.4 Å pixel^{-1} dispersion ($\sim$2300Å mm^{-1}) from 4800Å to 7100Å, thus being sensitive to Ly-α in the range $2.7 \lesssim z \lesssim 4.9$. An effective limiting magnitude in the range $B = 21 - 22$ was achieved. In an attempt to surmount the problems of ill-defined survey limits, all candidate emission-line objects were chosen *automatically* by an algorithm with accurately-defined parameters — lines were required to exceed a minimum signal-to-noise value of 7 and exhibit equivalent widths above 50Å. 45 candidates were so selected and 27 confirmed as emission-line objects: as in the study of Osmer (1982), none were detected through Ly-α redshift being in the range $0.9 < z < 2.7$. This result was compared to that expected by an extrapolation of the evolution model of Schmidt & Green (1983) for $z \leq 2.2$ (now possible because the survey limit was well-defined), yielding a figure between 32 and 104. The strength of this result lay in its claims to completeness and quantifiable limits, and it again seemed to indicate that the assumed picture of a continuing abundance of quasars at $z > 2.7$ followed by a dramatic redshift cutoff at $z \sim 3.5$, at least at these faint magnitudes, was not correct. In attempt to investigate the successes elsewhere at brighter magnitudes, a change to a transit method was made: Schmidt, Schneider & Gunn (1986b) described the application of their technique in a wider area of 7.84 deg^2 to $B \sim 20$, achieved by tracking the CCD across the sky. This brighter "transit" survey seemed at first to concur with other results, producing no Ly-α detections, but upon moving to the

4-Shooter, nine Ly-α quasars with $3.0 < z < 3.8$ were reported (Schmidt, Schneider & Gunn 1987a). Soon a $z = 4.04$ detection was also noted (Schmidt, Schneider & Gunn 1987b), and the interpretation of results in the earlier surveys remains unclear. The completion of this work has now been reported (Schmidt, Schneider & Gunn 1988) yielding 44 quasars: using simple $< V/V_{max} >$ analysis (see next section) they confirm the well-known sharp increase in space density up to $z \sim 2$, and find much a lower value at $z = 3.3$, indicating a sharply decreasing density there. Comparing their results with those of Boyle, Crampton and Osmer and their collaborators, they point to a peak in comoving density at $z = 2 - 2.5$ followed by sharp decline.

Other on-going projects are involved in automated quasar detection, returning to the use of objective-prism UK Schmidt IIIa-J plates scanned by the fast measuring machines such as COSMOS in Edinburgh (Clowes, Cooke & Beard 1984) and the APM in Cambridge (Hewett *et al.* 1985). Very different approaches are employed. Clowes *et al.*, in a technique termed Automated Quasar Detection (AQD), use COSMOS "mapping mode" scans (see Chapter 2) of IIIa-type objective prism exposures to recognise and extract many thousand spectra per square degree, which are examined in blocks of 8×128 pixels. These are quality-tested, and the local sky background extracted; subsequent analysis can select on emission, absorption or discontinuity features and also colour excess. Clowes (1986) indicated the addition of direct plates information to pinpoint spectra, establish a λ zero-point and star-galaxy separate. Clowes (1987, 1988) subsequently published results from the ROE/ESO large-scale survey of 7 IIIa-J Schmidt plates ($\sim$200 deg^2), compiling a list of "high-probability" Ly-α candidates in the redshift range $1.8 \leq z \leq 2.4$ — the compression of the wavelength scale towards the emulsion cutoff makes emission lines increasingly hard to detect and redshift estimates inaccurate. Clowes (1987) estimated that $\sim$80% of these were candidates were probably quasars, of which 30% had incorrectly assigned redshifts. The technique clearly works well at bright magnitudes, selecting most known quasars, and detecting candidates otherwise missed in visual studies. But at fainter levels, the technique lacks discrimination and the explicit nature of spectral behaviour upon which objects are selected biases strongly towards specific quasar types.

The APM group instead employ a more general approach, mimicking more that of a human being, wherein objects showing *any* significant deviations from a "normal" stellar spectral shape, itself defined by examination of the many thousands of spectra on each plate, are selected. This renders the technique in principle sensitive to all abnormal spectra, not preselecting a particular subset, and also means that careful calibration of the emulsion and the optical system is not required. A detailed description of this technique can be found in Hewett *et al.* (1985); the one-dimensional spectra for each object are extracted by first scanning a direct-plate for coordinate positions, followed by a background correction from 256 x 256 raster scans around each object, and quality checking. Linear and median filtering is then applied to identify continuum and emission/absorption features, and some crude colour selection is possible by binning different wavelength ranges. The real power of this technique lies again in its specified detection limits, which allows a measure of the *detectability* of any particular QSO spectral shape, possible by synthesising a pseudo-APM spectrum via rebinning and noise addition (Foltz *et al.* 1987). An initial test indicated that the procedure worked well with a IIIa-J emulsion when compared to a visually-selected sample up to $z \leq 2.5$, and as faint as $R \simeq 19-20$. A large-scale IIIa-J survey to $B \leq 18.5$, expected eventually to contain about 1000 quasars, was initiated with the above techniques. Foltz *et al.* (1987) contained some first results, reporting 192 quasars in $102\,\mathrm{deg}^2$, and Chaffee *et al.* (1988) have recently noted the increase in this figure to about 700 in $350\,\mathrm{deg}^2$ — the survey is 60% complete. MacAlpine *et al.* (1988) have showed the relative lack of z selection effects of these quasars, particularly for $z < 2.0$ when compared to other samples, and its is hoped that this survey when complete will contribute greatly to our understanding of quasar evolution for $z \leq 3.3$.

In conclusion the slitless technique is a fairly powerful way of selecting quasars in the redshift range $1.8 \leq z \leq 2.5$ and remains somewhat powerful to $z \simeq 3.3$, at least at bright limits — Marano, Zamorani & Zitelli (1988) concluded that prism selection techniques were as powerful as 3-colour selection for $B \lesssim 20.9$, but at fainter levels were significantly less good. Extension to higher redshifts obtained through use of the IIIa-F emulsion has proved successful in locating very high-redshift quasars; however this in turn increases the complexity of the response with z and makes quantification of com-

pleteness hard. The presence of some quite severe redshift selection effects, the lack of sensitivity at very high redshifts and the complex wavelength and redshift dependence of the faint limit also make comparison with samples derived from other techniques difficult. Searches will inevitably be biased towards the stronger-lined objects (Peterson 1988); redshift-dependent changes in emission line strength further complicate the situation (Baldwin 1977). Attempts at automated detection succeed in overcoming to some degree these drawbacks, but redshift estimates from lines in prism spectra can be wrong $\geq$30% of the time (Lewis, MacAlpine & Weedman 1979, Crampton, Cowley & Hartwick 1987). The possibility of "doubling-back" and assessing selectivity is however a significant advantage and appears the best step forward.

Variability

There is not here room to discuss quasar detection by variability in full, partly because the majority of results of primary interest to the present study were produced by colour and slitless surveys. This however is not said to belittle the variability approach, and indeed for some applications it seems a highly powerful method of independent detection, which would not be subject to the same z-dependent selection effects as previous work. This is of vital importance to any evolutionary model, prone as the history of QSO research is to rash judgement.

The violently variable nature of quasars has been known ever since their discovery (Matthews & Sandage 1963), but has not until relatively recently been employed as a common selection technique. The first variability survey was conducted by van den Bergh, Herbst & Pritchet (1973) in an area of 6.2 deg^2 around M31. Using 22 Palomar Schmidt plates taken over a seven year period, 13 variable objects were selected by blinking. Usher (1978) provided a firmer basis for systematic searches by examining variability in 820 quasars, using 10 plates over a total baseline of 23 years; finding a large fraction of such objects variable, he established the feasibility of variability as a means of detection.

The main work in this area has been done by Hawkins, who, using machine-

scanned UK Schmidt data, has attempted selection of quasars subject to the constraints (a) that magnitude difference between two epochs (of $\gtrsim 1\,\mathrm{yr}$) exceeds a certain value ($\sim 0.3^{\mathrm{m}}$), and (b) that magnitude variations on shorter timescales ($\sim$ weeks) should not be significant. The latter constraint is necessary to exclude short-term variable stars. Initial investigations in UKST field 287 (Hawkins 1981, 1983), where images of $18 \leq B \leq 21$ were examined over a 1 year baseline, produced a list of 77 candidate variables; objective prism spectra indicated that the sample consisted, at least at the bright end, of emission-line and/or UV excess objects in the main. Hawkins (1985) used this sample and one in field 401, adding a severe UVX cutoff to exclude all stars, and found no significant surface density fluctuations. The relative successes of the technique were fully discussed in Hawkins (1986), with IIIa-J plates covering the period 1975–1983 to measure variability, two pairs of U and B plates to measure colour, and two objective prism plates. The extended baseline was seen to greatly increase selection power. Restricting the sample to bright magnitudes ($17 \leq B \leq 18.5$), 11 variability candidates were selected and confirmed, and, comparing with the $(U - B) \leq -0.4$ UVX sample of 37 objects, while 10 displayed UV excess, only 7 of these would have been selected in conventional surveys with this limit (2 are however $z > 2.2$). Again, only seven showed unambiguous evidence for emission lines on the objective prism plates; these results seem to indicate that the variability method, although probably only sampling 40–70% of all quasar types, might well be vital for revealing the "blind-spots" of the two major selection techniques. The project is continuing, and evidence seems to indicate time-scales of about 4 years for these variations (Hawkins 1987), meaning that about 35% of all quasars are selected over the longer baseline (another 35% show variability to some extent), whereas 1 year surveys may be sensitive to as little as 2% of all UVX quasars. The completeness of such samples is very high.

The rate of success of the variability technique agrees well with other attempts. Marano, Zamorani & Zitelli (1988) employed variability as an additional discriminant in their multicolour selection, mentioned above. Objects discrepant in two or more different bands over a 1 year period were selected, giving a total of 24 "best" candidates, of which 8 were confirmed quasars. Again, the evidence indicated that a significant fraction of quasars are variable. The smaller success rate *within* the candidate list can

be attributed to the shorter baseline *c.f.* Hawkins. Koo, Kron & Cudworth (1986) also examined variability in their sample, and over a ten-year baseline again found 40% (31 out of 75 objects). The technique is also being extended to fainter magnitudes by Trevese & Kron (1988), who employ an 11-year baseline in a machine-based survey to $B = 22.6$. Results are consistent with the analysis of Koo, Kron & Cudworth in the same field, but few additional candidates were found.

The successes of this technique provide a firm basis for further study. Most probably there is little, if any, redshift-dependent bias present in selected samples, and this provides an independent check on broad-band and prism-selected catalogues. Carefully conducted machine-selected samples are essentially uncontaminated. A significant fraction of known quasars are however missed, and the technique will be biased if any trend between variability and absolute magnitude, colour etc. is present; quasars varying over short time-scales ($\sim$ weeks) will also be excluded. Moreover, time dilation means that slower variations will be seen for more distant objects, possibly making them harder to select. This technique will probably come into its own in surveys based on a combination of techniques, such as that of Marano, Zamorani & Zitelli (1988).

1.3 Theoretical implications of optical quasar research

1.3.1 Low-redshift evolution

The quantity of quasar research detailed above has provided a firm basis for understanding the evolutionary behaviour of the population at low redshifts. The enormous growth in quasar discovery rate due to their UV excess quickly established the rapid increase in comoving density with redshift up to the limit of $z = 2.2$. The *form* however of the evolution proved more elusive. In order to easily parameterize QSO numbers, the **luminosity function** (LF) $\Phi(M, z)$ for quasars is introduced, as the space density as a function of absolute magnitude and redshift. This is most easily conceived in the absolute magnitude vs. space density plane, plotting the luminosity function within a restricted z range, and thus providing a "snapshot" of the quasar population at a given

epoch. The evolution question then consists of assessing the movement of this function in Φ–M space with z. In the simplest picture, necessary initially due to the restricted number of quasars available, the LF retains its shape and moves in either direction. Vertical shifting in the Φ direction, in many ways the simplest case, is termed **pure density evolution** (PDE) and was used early on by Schmidt (1968, 1970, 1972) — this can be understood as tracing the changing density of objects of the same luminosity with epoch, represented by

$$\Phi(M, z) = \Phi(M, 0)\, \rho(z) \tag{1.6}$$

Pure luminosity evolution (PLE) is characterised by movement in the luminosity direction, representing either a fading luminosity of a fixed population of objects, or a more general property of a changing population, and can be given by

$$\Phi(M + \Delta M(z), z) = \Phi(M, 0) \tag{1.7}$$

Schmidt (1968) arrived at his result via his $< V/V_{max} >$ analysis, where the position of a source in space is compared with its maximum possible distance, calculated from knowledge of its intrinsic luminosity and the flux limit of the survey. Significantly higher values than 0.5 indicated strong cosmological evolution when 3CR (the Third Cambridge Radio Catalogue) radio sources were examined. With further analysis of radio and optical identifications Schmidt (1972) claimed consistency with density evolution (with a proposed cutoff at $z = 2.5$), somewhat favouring evolution exponential in look-back time τ such that density $\rho \propto 10^{5\tau}$ over a power law form $\rho \propto (1 + z)^6$. The PLE model was strongly rejected. Furthermore, no evidence was found for a dependence in this evolution on luminosity, although the numbers of quasars, and narrow "window" in luminosity were clearly a great constraint.

The firm conclusions in favour of PDE were not confirmed for radio sources in other studies. Longair (1966) pointed out that differential evolution was required for these objects, the most powerful sources evolving fastest. The major obstruction to deciding between PDE and PLE pictures is that the orientation of movement is not directly evident from quasar counts: Longair & Scheuer (1970) pointed out the difficulty

of discriminating between PLE and PDE without some feature to allow tracing of a particular type of source through its cosmic evolution. The power-law form at the bright end of the LF provides no feature to pin the evolution down, and Mathez (1976, 1978) indicated that the data available to Schmidt could be equally well described by PLE, allowing longer QSO lifetimes. An inconsistency in Schmidt's analysis concerning the treatment of low-luminosity sources led to the implicit assumption of no evolution for these objects, and luminosity evolution was clearly consistent when low-luminosity sources were included. However the situation remained unclear due to the lack of wide coverage in QSO luminosity.

The appearance of the BF UVX-selected samples in the 13^h $+36°$ field placed stronger constraints on the evolution of optically-selected quasars. Braccesi *et al.* (1980) studied a collection of 183 objects spanning $B = 14.5$ to 19.5, combining their results with data from other samples. They indicated the high degree of conformity between different surface density estimates, and showed that the integral number-magnitude relation could be fitted by a steep increase, implying an increase of factor 7.25 per magnitude. They concluded that density evolution appeared to be taking place, noting no flattening in the number-magnitude relation; however, they could not fit these data to a simple single power-law form (as Schmidt) and had to invoke a break in this evolution at $z \sim 1$. This analysis however was highly inadequate, being an assembly of very different samples and containing many unconfirmed candidates; attention was turning more and more to the need for high levels of completeness, uniformity and knowledge of selection effects in quasar samples. The complete and confirmed BF sample of Marshall *et al.* (1983b) to $B = 19.2$, and later $B = 19.8$, when combined with the brighter AB quasars and extrapolated to the fainter levels of Kron & Chiu (1981) and Koo & Kron (1982) rejected the PDE evolutionary picture strongly (Marshall *et al.* 1983a, 1984). These data favoured PLE with a low-luminosity cut-off, naturally dependent on z, restricting the amount of low-luminosity high-redshift quasars and thus matching better a flattening number-magnitude relation. The luminosity function was described well as a power law $L^{-3.5}$, with luminosity evolving as $(1+z)^{3.9}$ or $e^{7.3\tau}$ ($q_0 = 0$). The flattening in faint counts in the data of Koo *et al.* provided the key to rejecting PDE, although full spectroscopic confirmation was not as yet available.

The publication of the Bright Quasar Survey (Schmidt & Green 1983) represented a great advance in our knowledge of bright quasar evolution, and allowed more complex models to be considered. Applying the luminosity dependence of $< V/V_{max} >$ for the sample, it was there concluded that luminosity-dependent density evolution (LDDE) provided an alternative way to describe the data — here the amount of evolution in space density depends upon the luminosity, with the bright end evolving more quickly. Space density at any given intrinsic luminosity varies exponentially with look-back time. Pure luminosity evolution appeared to fit less well when other samples (AB, Hoag & Smith) were considered. However, in a re-examination of the BF and AB samples in the light of these data, Marshall (1985) showed that the evolution was better described by a power law function $(1+z)^{3.5}$, which was then independent of luminosity. Complete confirmed UVX surveys only were used for this analysis, so avoiding complications in interpretation of selection effects. Exponential evolution appeared inconsistent when fitting separately for low and high redshift. Indicating that the shape of the luminosity function was consistent with a power-law over a large luminosity range (while conceding that a break must occur at some faint level), Marshall again concluded that pure luminosity evolution worked best.

In the BF, AB and BQS analyses, the importance of the very faint Koo & Kron samples cannot be over emphasised. However, the uncertainties involved in early candidate work were large, forcing for example Schmidt & Green to adopt different models for different estimates at faint levels. Koo & Kron (1988) provided 30 spectroscopically confirmed QSOs and demonstrated the turn-over in the n(m) relation and its corresponding feature at low luminosities in the LF. They there proposed a combined luminosity and density evolution model, extending to $z \sim 3.5$. Boyle, Shanks & Peterson (1987, 1988b) presented direct evidence for this feature within their own data, which extends to $B = 21.0$, and by tracing its movement with z as the LF evolves, convincingly demonstrated that PLE is an excellent description of its behaviour: for the first time, this appears directly to the eye from plotting the luminosity function binned in redshift. Representing the LF as a smoothed two power-law form, they considered PLE in its exponential and power-law forms, and also consider the combined evolution models, where density evolution is also allowed, as in Koo & Kron

(1988). Again, Marshall's conclusion of the inadequacy of exponential evolution was confirmed, and power-law pure luminosity evolution $(1+z)^{3.2\pm0.1}$ only provided a good fit (some additional evolution in *density* may be required for the very faintest quasars ($M_B < -23$)). This work seems the most reasonable interpretation of the best data available at present, and works extremely well; however, doubts are still being expressed concerning the validity of faint quasar counts, and the situation is far from conclusive.

1.3.2 Evolution at $z > 2.2$

Recent advances in the field of quasar research can give the impression that current efforts are directed solely towards the discovery of ever increasing redshifts. This point of view carries some justification for some investigators, but much more effort has been expended in deriving complete samples, whose selectivity as a function of redshift, apparent magnitude etc., can be determined. This is vital for the accurate determination of space densities. At the same time, the definition of "high redshift" progressively increased as the $z = 4$ barrier was exceeded.

The increasing success of slitless techniques in the late 1970's produced impressive results in a redshift regime previously thought to represent the "edge of the world" (Sandage 1972). Véron (1986) provided a summary of the various IIIa-J and IIIa-F slitless surveys, combining these results and examining the resulting redshift distribution. The sharp fall-off in space density of a factor 5 at $z \simeq 2.4 - 2.5$ is clear, followed by a relatively flat response to $z \simeq 3.8$, where another sharp drop is seen. Véron goes so far as to interpret these results as evidence for a two-component quasar population, with birth epochs at these two redshift epochs.

The relative abundance of $z > 2.2$ quasars was quickly realised as the Curtis-Schmidt survey produced its first results, finding redshifts in excess of 3. These results led to somewhat exaggerated claims as to densities at high redshifts, partly to counterbalance the pessimistic predictions of previous UVX investigators. As more powerful techniques were employed, in particular using the IIIa-F emulsion, sensitive to $z = 4.7$, the residual drop in space density at higher redshifts was well established. The posi-

tion of the actual decline (sometimes loosely termed a "cut-off") was however highly contested: the efforts of Hoag & Smith (1977), Osmer (1980), and later Osmer (1982) seemed to support a value of $z \gtrsim 3.5$, while Schmidt, Schneider & Gunn (1988) favour a sharply decreased density at $z \sim 3.3$, and Koo & Kron (1988) and Marano, Zamorani & Zitelli (1988) find a very small space density for fainter quasars at $z > 3$. Hazard & collaborators further complicate the picture with claims of high densities at $z = 3.8$, although this is harder to quantify. It is now nevertheless well accepted that some decline exists, and a continuing strong positive evolution as seen for low-redshift quasars can be categorically ruled out. The emergent picture does not lend itself to simple interpretation, but whether the complexity of models such as Véron's is required is uncertain.

Much work remains to be done at very high redshifts. For high-redshift work, the regime $3.4 \lesssim z \lesssim 4.5$ is primarily of interest in this thesis, lending itself well to multicolour techniques. The APM group have so far provided by far the most useful contribution to knowledge in this area, producing not only spectacular results, but also estimations of selectivity and completeness. Analysis is still at a preliminary stage, but appears to point to a relatively *flat* luminosity function, a factor 3 or so less in space density than the results at $z = 2.2$ for $z = 3$ and another factor 3 down for $z = 4$. Space density only approaches that at $z = 2.2$ at luminosities in the range $-29 \leq M_B \leq -28$: the slope appears intermediate between that at bright and faint ends of the Boyle *et al.* result. This appears qualitatively to agree well with the fainter counts of Koo & Kron (1988) if the LF is naïvely extrapolated to fainter intrinsic luminosity. These results, results from the brighter study undertaken here, and their implication are discussed in full in Chapter 6, but the indications from Warren, Hewett & Osmer (1988) seemed to be of an excess of brighter ($M_B \leq -28$) quasars; this is backed up somewhat by the successes of Hazard. The consequent need for a brighter, wide-field survey sensitive to $z = 4$ and beyond, and derived in an automated manner is obvious, and it is for this reason that the current work, introduced in the last section of this chapter, was undertaken.

In order to explain the observed decline in quasar numbers, several models have

been introduced, which consider the under-densities measured to be a product of (a) effects intrinsic to the quasar population, e.g. proposed epochs of formation, resulting in attempts to account for evolution over the whole observed redshift range by a single, or combined model, and (b) the influence of external effects on the true quasar densities, e.g. dust-obscuration. All such attempts are hampered by the very small numbers involved, and conclusions have only been tentative. Koo & Kron (1988) attempted to account for their observation of the changing LF shape above $z = 2.5$ by introducing an isolated epoch of constant birth-rate at $15 < z < 3$, and allowing the most luminous quasars to burn out faster, which produces a flattening in the bright end of the LF with z. They found acceptable fits for $z \leq 3.2$, but the authors acknowledge that their model does not reproduce well results at very low and high redshift (see Marshall 1988 and the following discussion), in particular beyond $z = 3.5$, where far too many quasars are predicted. Heisler & Ostriker (1988a) presented a combined PLE and LDDE model which accounts well for QSO numbers at $z < 3$, but again over-estimates by orders of a magnitude at higher redshifts; for this reason, wishing to maintain a single evolutionary form, Heisler & Ostriker (1988b) attempted to explain the lack of high-z quasars, by modeling obscuration by dust in intervening galaxies of constant comoving density. A model in agreement with the results of Koo & Kron however produces far too few quasars $z > 3.5$ when compared with the results of Warren, Hazard and this work.

We are still in the early days of $z > 4$ research, but it is already apparent that to fit a single continuous evolution model from the known LF at $z = 2.2$ is very difficult. First indications seem to indicate a significantly changed LF shape at $z > 3.5$, but this requires confirmation at brighter magnitudes. The multicolour method works extremely well at high redshift and it is hoped that its application when combined with the power of current high-speed photographic digitisation will provide much needed clarification of the situation.

The existence of objects at high redshift introduces problems for many "top-down" models of galaxy formation, in particular neutrino-dominated schemes. Frenk, White & Davies (1983) examined the growth of primordial density fluctuations through N-body simulations in an attempt to model galaxy formation. They found a correlation

function steepening with time for adiabatic fluctuations, and, fitting this to the slope at the present epoch, predicted the collapse of large-scale structures only as late as $z = 2$. The condensation of quasars in these models is highly implausible, even if $z = 4$ objects are considered statistical outliers. Cold dark matter pictures produce these objects more easily; matter condenses from initial subgalactic masses, and quasars can form at an earlier stage as larger galaxies are formed through mergers. Efstathiou & Rees (1988) have investigated the formation of such objects under the $\Omega = 1$ adiabatic CDM model. Examining the onset of "z_{crit}", the redshift at which sufficient mass has accumulated to form luminous quasars as a function of the ratio of quasar to underlying host mass, quasar lifetime, luminosity, and the efficiency of conversion from central rest mass to energy, they conclude that luminous quasars at $z = 4$ are compatible with CDM. Differential evolution should be seen at higher redshifts, with less luminous quasars forming more readily from less massive systems. A steep decline in quasar numbers is predicted at $z \simeq 5$, and thus is within reach observationally. Much uncertainty however remains concerning energy conversion efficiency, speed of formation and the extraction of energy from the vicinity of the central mass.

1.3.3 Quasar clustering

The huge increase in yield in optical quasar surveys in the last 10 years has meant that a new cosmological probe for large scale structure apart from galaxies is now available. The CTIO surveys produced the largest samples of spectroscopically confirmed quasars in the early 1980's, and provided the first real opportunity for the study of the 3-dimensional distribution of quasars. Webster (1982) and Osmer (1981) published analyses of the sample of 108 quasars published in Osmer & Smith (1980), both finding no evidence for clustering on scales as small as $20\,h^{-1}$ Mpc. The warning that "groupings" seen on the sky may not be statistically significant was clear. Webster did however note a highly significant group of 4 quasars within about $75\,h^{-1}$ Mpc(previously mentioned by Arp 1980). Such observations of statistically improbable groupings have since appeared regularly, used either to examine quasar location and formation (e.g. Oort, Arp & de Ruiter 1981, Crampton, Cowley & Hartwick 1988) or as evidence

for associations on galactic scales and nonstandard cosmological interpretations (Arp 1980).

Clustering in quasar populations was first tentatively confirmed by Shaver (1984), studying the large but inhomogeneous sample in the Véron catalogue (Véron-Cetty & Véron 1984), and finding significant clustering on scales $< 5\,h^{-1}$ Mpc. The large UVX catalogue of Boyle *et al.* provided a homogeneous database for further study with large coverage in redshift, and Shanks *et al.* (1987) confirmed the existence of clustering on small scales in a more rigorous way, using correlation function analysis. Later results on a larger sample have confirmed these results (Shanks, Boyle & Peterson 1988, Shanks *et al.* 1989), finding 25 quasar pairs with separations $< 10\,h^{-1}$ Mpc, while expecting 11.1 on a null hypothesis, a 4.2σ result. At the mean redshift of the sample, $z = 1.4$, this is of a higher amplitude than that expected for galaxy-galaxy clustering, while being significantly less than that for rich galaxy clusters (on the assumption that galaxy clusters are stable i.e. not expanding with the Hubble flow). Only very low levels of evolution in the clustering are allowed by the data, in contrast to other studies based on combined datasets (Iovino & Shaver 1988, Kruszewski 1988) where a clear drop in the level of clustering with z is claimed. On a larger scale, $10 \leq r \leq 2000\,h^{-1}$ Mpc, no significant detection of clustering was found, leading to the conclusion of homogeneity at the 10% level. Other recent studies have in general agreed with these conclusions, confirming small-scale clustering, but finding no significant signal on scales $> 15\,h^{-1}$ Mpc, while pointing out an increasing number of "interesting groups" (Crampton, Cowley & Hartwick 1988, Osmer & Hewett 1988). Tentative evidence for large-scale clustering has appeared (Chu & Zhu 1983, Zhou *et al.* 1986) but remains highly uncertain.

The clustering of matter on very large scales is a highly powerful test of any model for galaxy formation and evolution. The study of the distribution of QSOs may seem somewhat derivative in this respect, given the serious doubts concerning the tracing of underlying mass in the Universe, but will continue to attract a high level of attention, presenting as it does the only opportunity (besides the CMB) of mapping the Universe at a significant fraction of its present age and at super-large scales. The significance

of any large-scale structure cannot be over-emphasised. As stressed in Section 1.1, the "standard" high-Ω, cold dark matter picture, as a "bottom-up" model, encounters problems when trying to produce the strong Abell cluster-cluster results of Bahcall & Soneira (1983) etc. CDM in many formulations may also be at odds with recent claims to detect large-scale streaming (e.g. Lynden-Bell *et al.* 1988, Aaronson *et al.* 1989).

Chapter 5 of this thesis examines the 3-D distribution of QSOs from a new UVX sample of large contiguous area coverage, sensitive to clustering on scales in excess of $300\,h^{-1}$ Mpc. Any indication of power on such large scales would have strong implications for all formation models, requiring low values of Ω_0, because the horizon scale at matter-radiation equality, and thus structure scale size, is approximately proportional to $(\Omega_0 h^2)^{-1}$.

1.3.4 The present work

The following chapters will discuss in detail the compilation of a new database of photographic images, from its conception to the derivation of complete samples. The chosen approach is the multicolour method, utilising *UBVRI* wavebands derived for a total of 13 U.K. Schmidt fields, and taking advantage of the remarkable speed and quality of the COSMOS fast-measuring machine at Edinburgh. The end-product will be a complete dataset of about 1.3 million objects, from which a catalogue of morphologically stellar images are selected and calibrated to an accuracy of $0.05^{\rm m}$ in *UBVRI*. Clearly such a dataset provides the opportunity for discrimination of many different astronomical species, but the recent successes and prospects from theoretical modeling of quasar selectivity (see Chapter 6) lend credence to this survey as a highly efficient method for locating quasars: this thesis will therefore treat the survey simply as a source for quasar detection.

Chapter 2 will introduce the basic photographic backbone of this project, comprising *UBVRI* material in all 13 fields. The derivation of each combined dataset is discussed in full, and the very strict controls applied at each stage to ensure high quality data, necessary for high levels of completeness and low levels of contamination in the

final samples. Chapter 3 will concentrate further on the intermediate calibration stage, discussing photoelectric and CCD observations made in each field, their reduction, and their application to the data.

The completed catalogues are used in an attempt to clarify two highly controversial areas outlined above. The efficiency of standard UVX quasar samples is greatly amplified by the addition of information from another longer wavelength, and U, B, R selection is used here to produce a large-field ($35^\circ \times 10^\circ$), intermediate magnitude ($B \leq 18$) sample of 69 $z \leq 2.2$ quasars, providing large-scale information on a scale between that of the MBQS and the AB samples. Chapter 4 will describe the selection and spectroscopy of these objects, and Chapter 5 will examine the 3-dimensional distribution of these quasars, producing surprising results in a controversial area. The full extent of the original material is exploited in Chapter 6, where nearest-neighbour selection is employed in 4-D colour space to isolate high-redshift quasar candidates with $z > 3.4$. The results of a search over several Schmidt fields are discussed, and future prospects reviewed.

Chapter 2

UKST Photographic Material

2.1 Astronomical photography

Since the realisation that the accumulation of photons on a photographic plate leads to the detection of objects far fainter than those observable with the naked eye, great endeavours have been made to utilise photography in astronomy. Dry photographic techniques were developed in the late 19^{th} century, and were increasingly used in astronomy as time progressed, but it was not until 1930 when Bernard Schmidt produced the first version of the Schmidt Camera that wide-field photography became possible. The original design featured an aperture of 35 cm, through which light over a field of 16° was incident on a primary reflector. The field was imaged on a photographic plate in the body of the camera. The principal feature of the camera was a corrector plate at the entrance aperture with a complex profile calculated to reduce large-field effects to a minimum.

Several telescopes have been constructed on this design. The United Kingdom Schmidt Telescope (UKST) is situated at an altitude of 1130 m at Siding Spring, Australia. It is a standard Schmidt telescope, based on the design of the 48″ Schmidt at Mt Palomar, California, with a 1.24 m diameter aperture and a 1.83 m reflecting mirror. Light from the mirror is reflected back up the telescope to a photographic plate held in a curved plate-holder in the focal plane. It provides very large field coverage ($6.4° \times 6.4°$) images on plates of 356 mm square, giving a plate scale of $67.14'' \, mm^{-1}$: an achromatic corrector lens at the aperture ensures that point images are kept to 2″ full width at half maximum in the absence of seeing effects.

The UKST was opened in September 1973 and principally assigned to the task of

obtaining photographs for the ESO/SERC Southern Sky Survey. Since that time, it has participated in many new surveys and extended existing surveys in both baseline and sky area; alongside this task however, it has provided many astronomers with plates for individual projects as is the case here. Between March 1985 and April 1988, this project has received 182 plates from the UKST (including 3 prism plates and 16 plates taken as part of other surveys).

In the intervening period since the development of astronomical photography several new techniques for 2-D direct imaging have appeared, the most spectacular of which was the advent of the charge-coupled device (CCD) which has revolutionised photometry techniques. The advantages of the CCD in this area are obvious: as well as being highly sensitive to incident photons, with quantum efficiencies up to 80%, its response to light is linear up to saturation point. CCD's are now invaluable in astronomical photometry for these reasons, and indeed are of fundamental use in this project (see Chapter 3). In contrast, photographic emulsions present a quite complex response to incident light and are less sensitive; nevertheless, the overriding advantage of high resolution data over a very wide field (most CCD's cover only a few arcminutes square on the sky), coupled with ease of data storage, ensure that the position of astronomical photography is secure for the future.

The advantages of photography however must be accompanied by efficient techniques to extract the full potential from the data. The advent of high-speed plate-measuring machines, in particular the COSMOS machine in Edinburgh in 1978 which was used to scan the UKST plates for this survey, has provided the opportunity for large-area surveys on an unprecedented scale. UKST plates can now be scanned and analysed within about 4 hours, producing a dataset of all images found (above a certain threshold) with information concerning position, intensity, morphology and orientation, which allow the further selection of particular species of object in an automated way.

The next section will deal with the raw photographic material from which the Edinburgh Multicolour Survey was constructed. Section 2.3 will discuss the processes involved in scanning these plates, including a brief description of the COSMOS machine. Sections 2.4 and 2.5 will describe in detail the techniques developed and utilised to

produce a calibrated *UBVRI* dataset for each Schmidt field, free from spurious images, morphologically defined, and finally accurate to within 0.05^{m}.

2.2 Edinburgh Multicolour Survey plates

The Edinburgh Multicolour Survey, as proposed in 1985, was intended as a definitive database of 0.1 steradians (325 deg^2) of the sky in *UBVRI* to apparent magnitude $B \sim 17 - 18$, providing an accurate broad-band classification for every object brighter than the survey limit. Although this thesis is concerned solely with the selection of quasars, in principle the survey provides discrimination for many different species of galactic and extra-galactic objects which exhibit significant deviations from the colours of main sequence stars. These include hot subdwarfs, white dwarfs, cataclysmic variables, and extragalactic H II regions: indeed many such objects have already been detected as a by-product of recent quasar searches. Much work in each of these areas is to be expected now that the survey is substantially complete. The original specifications set out for the survey comprised the provision of two good-quality plates in each waveband, covering 13 Schmidt fields. The inevitable presence of spurious images caused by for example by plate flaws, satellite trails, image break-up around bright stars is a major problem when attempting to separate a small subset of unusual objects from the vastly overriding quantity of "normal" stars, and a large part of this thesis is concerned with their removal. Two plates in each band ensure that the vast majority of such phenomena can be isolated, confirming the genuine nature of objects of extreme colour before spectroscopic confirmation, and additionally reducing measurement errors by a factor $\sqrt{2}$. The plate material for each field was taken largely simultaneously to minimise variability effects on measured colours.

Dark and grey time were requested (I plates are largely unaffected by moonlight) with reasonable seeing ($< 4''$). The depth of U and particularly I plates is clearly the major limitation for exposure times, and integrations of about 90 minutes were necessary reaching $I \simeq 19.5$ and $U \simeq 20.5$. Photographs in other bands required between 20 and 40 minutes integration to reach $m \sim 20.5$. Table 2.1 presents the

Table 2.1: Emulsion/filter combinations used in the Edinburgh Multicolour Survey. Emulsions names specified are Eastman Kodak codes, and all filters are Schott glass broadband filters. Wavelength range is λ in Angstroms at 20% of maximum values, derived from values in the "UKSTU Handbook". The 3200Å blueward cut-off is a characteristic of atmospheric and telescope optical effects.

Waveband Name	Emulsion	Filter	Approximate λ–range
U	III-aJ	UG1	3200–4000
B_J	III-aJ	GG385	3600–5000
V	IIa-D	GG495	5000–6400
OR	IIIa-F	OG590	5900–7000
I	IV-N	RG715	6900–8800

emulsion/filter combinations used in each waveband and their associated codes — all wavebands approximate reasonably well the extended standard Johnson system except B_J, which has a fairly substantial colour term transformation when compared to the photoelectric B band (Blair & Gilmore 1982). The label OR is used to distinguished this passband from the earlier R band which used the RG630 filter[1]. Figure 2.1 presents graphically these broad-band responses as a function of wavelength, normalised to unity at the peak of each response. Note that all IIIa-type emulsions are "hypersensitised" by successive exposure to nitrogen and hydrogen, removing oxygen and water vapour from the emulsion prior to exposure which greatly increases sensitivity (see e.g. *Astronomical Photography* 1984 and Cannon *et al.* 1978 for more details of this and other aspects of plate processing).

Fields were chosen near the celestial equator for easy accessibility from northern and southern hemispheres (vital for subsequent calibration). Burstein & Heiles (1982) indicate that Galactic reddening cannot amount to more than $E_{B-V} = 0.03$ for $|b| > 50°$: with these two criteria, the zone $12^h\,40^m \leq \alpha \leq 14^h\,40^m$ and $-5 \leq \delta \leq 0$ (field centres) was chosen, covering standard UKST field names 861–867 and 789–794. Appendix A

[1]Note that all subsequent references in this thesis to bands *UBVRI* refer to these *photographic* bands except where specifically indicated: CCD and photoelectric calibrations of the survey data were transformed from the standard system via Blair & Gilmore (1982) as described in Chapter 3.

Figure 2.1: UKST *UBVRI* pass-bands.

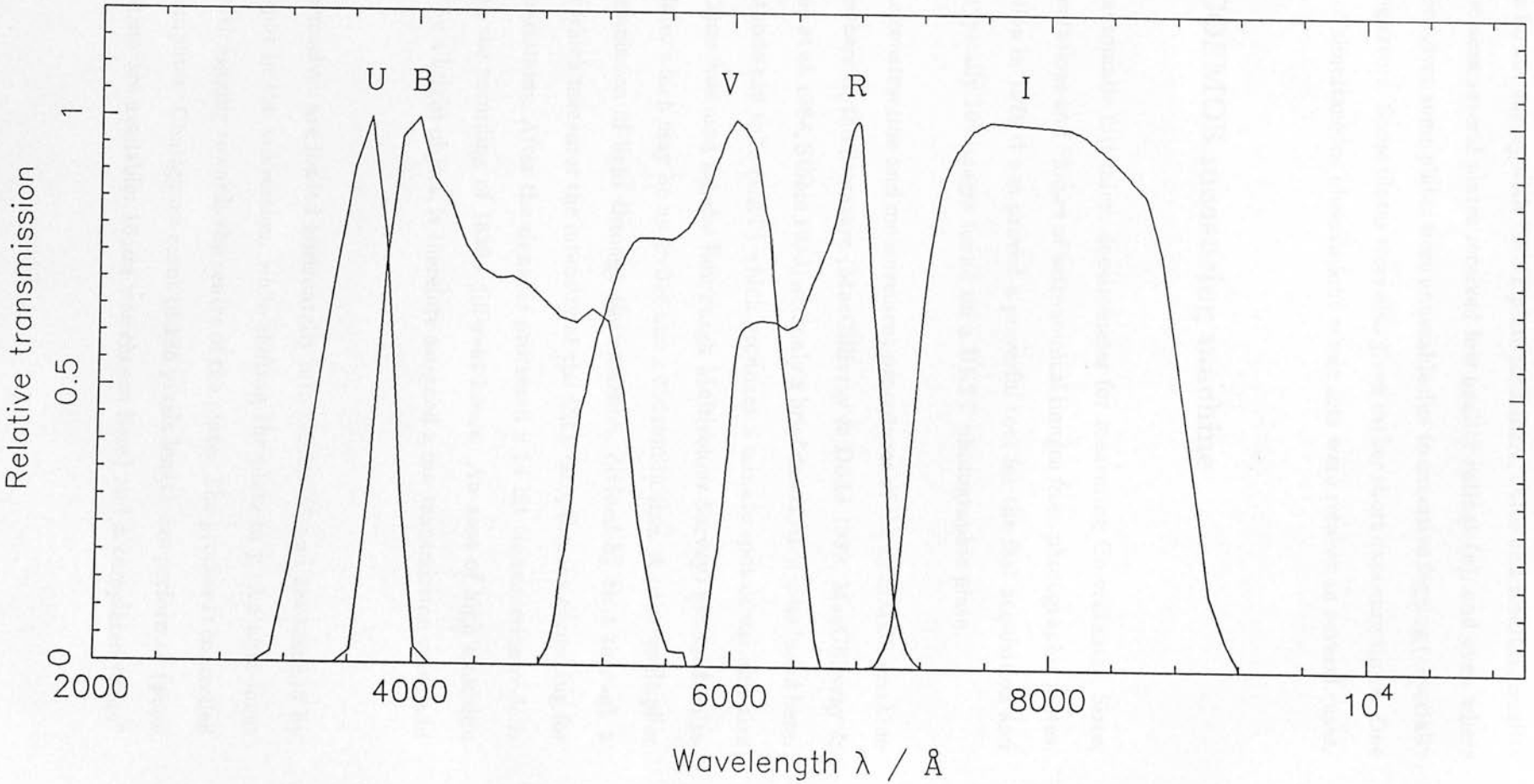

lists plates taken for the survey with UKST plate identifiers, dates and resulting quality grades: as can be seen several plates received low quality ratings (c), and even where higher ratings were given some plates were unuseable due to excessive fogging (especially *I*), and processing errors. Some plates were also given rather short exposure times. Due to the necessity of simultaneous observations whole sets were retaken in several cases.

2.3 The COSMOS measuring machine

COSMOS is an automatic fast micro-densitometer for measuring Co-ordinates, Sizes, Magnitudes, Orientations and Shapes of astronomical images from photographic plates. Since its installation in 1978 it has proved a powerful tool for the fast acquisition and measurement of typically 10^5 images found on a UKST photographic plate.

Details of the construction and measurement procedures of the COSMOS machine can be found elsewhere in the literature (MacGillivray & Dodd 1982, MacGillivray & Stobie 1984, Stobie *et al.* 1984, Stobie 1986) and only a brief description is included here. It comprises a cathode-ray tube (CRT) which produces a minute spot of variable size (12, 16, 32 μm: 32 μm was used for the Edinburgh Multicolour Survey) focussed on to a photographic plate, which may be up to 356 mm x 356 mm in size. A photomultiplier measures the transmission of light through the emulsion, divided by that through a reference channel, which measures the intensity at the CRT face, thereby correcting for any tube output variations. After the signal is processed a 14-bit transmission code is produced, allowing the recording of 16384 different levels. An area of high emulsion density, produced by a bright object, is therefore assigned a low transmission value and vice versa.

The plates themselves are loaded horizontally into COSMOS and are scanned by moving the CRT spot in the x-direction, while shifting the plate in y. An auto-focus mechanism deals with sagging towards the centre of the plate. The process is controlled by a PDP 11/24 computer. Contiguous scans of 128 pixels length are performed (pixel sizes of 8, 16, or 32 μm are available: 16 μm was chosen here) and a completed "lane"

is defined as 128 such linear scans. Lanes are successively covered until the whole measurable area (300 mm x 287 mm = 5.60° x 5.35°) is complete.

A VAX 11/750 is currently used to process this information. Two main modes of operation are available. In mapping mode (MM), every pixel transmission value obtained is output for later off-line analysis: this mode is expensive in terms of disk storage space and in practice is rendered unnecessary for all but very special requirements (e.g. objective prism scanning, in-depth analysis of small areas on plate). Image Analysis Mode (IAM), which incorporates threshold mapping (TM), provides the opportunity for quick and easy access to large numbers of images (the whole process currently takes about 4 hours per plate). In this mode each plate is first "pre-scanned" at low resolution in order to establish a measurement of "sky" background as a function of position (in practice the predominant sources of background variations are optical vignetting and desensitisation across the plate area, which usually far outweigh any contribution from night-sky effects; see e.g. Gilmore 1982). A 2-D grid of background values is determined by filtering these values within small cells ($\sim$1 mm^2) to remove contaminating objects, and finding the median. The plate is then scanned again at higher resolution and pixel values at a fixed percentage above this sky level are recorded as potential images. Clearly a high threshold value, while being desirable as a barrier against noise from the emulsion grain, would lead to loss of faint images and therefore a low threshold (typically 7%) is combined with an "area cut" (5 pixels) for the data here. Thresholded pixels are combined into a single object if connected and all objects covering an area equal to or in excess of the area cut are accepted.

The analysis of connected images can proceed in conjunction with a single scan by simply summing up intensity-weighted and unit-weighted moments up to second order. The zeroth order unit-weighted moment provides the area of each object above the chosen isophote, and the (background-subtracted) intensity-weighted moments gives measurements of the total intensity above sky; first order moments give centroids in x and y, and second-order moments provide information on the elliptical nature of images. Celestial coordinates right ascension (α) and declination (δ) are obtained from catalogued SAO stars (the Smithsonian Astrophysical Observatory Star Catalog of

Table 2.2: COSMOS attribute names and descriptions obtained after image analysis, and used in the Edinburgh Multicolour Survey.

Attribute Name	Description
RA	right ascension (equinox 1950)
DEC	declination (equinox 1950)
XMIN	minimum x coordinate of image (0.1 μm)
XMAX	maximum x coordinate of image (0.1 μm)
YMIN	minimum y coordinate of image (0.1 μm)
YMAX	maximum y coordinate of image (0.1 μm)
AREA	area of image (pixels)
IMAX	maximum intensity
COSMAG	COSMOS isophotal magnitude
ISKY	sky intensity at IXCEN, IYCEN
IXCEN	intensity-weighted x-centroid (0.1 μm)
IYCEN	intensity-weighted y-centroid (0.1 μm)
UMAJAX	unit-weighted semi-major axis (0.1 μm)
UMINAX	unit-weighted semi-minor axis (0.1 μm)
UTHETA	unit-weighted orientation (degrees)
IMAJAX	intensity-weighted semi-major axis (0.1 μm)
IMINAX	intensity-weighted semi-minor axis (0.1 μm)
ITHETA	intensity-weighted orientation (degrees)
CLASS	COSMOS image classification (star-galaxy)
SPARE	user-definable

1966) found on the plate by use of a coordinate transform. Positional information is accurate to a few microns (MacGillivray & Stobie 1984) which in turn leads to (α, δ) coordinate accuracies of $\sim 0.3''$. Table 2.2 shows the COSMOS attributes deposited in each catalogue after the IAM stage.

The machine magnitude is derived from the summed above-threshold intensity within the chosen isophote. This in turn must be obtained through a density-to-intensity transformation which requires a scale of known intensity comparison areas treated in the same way as the images. 16 sensitometer step-wedges are included on the edge of the emulsion for this reason, masked off from the telescope and exposed and processed in the same way as the sky image area. These steps are scanned by

COSMOS, and a density-to-log(intensity) transformation obtained by spline-fitting the relation; the "Baker" density is here defined as:

$$\mathrm{BD} = \log_{10}\left(\frac{T_C - T_D}{T_S - T_D} - 1\right) \tag{2.1}$$

where T_C, T_D and T_S are transmissions of, in turn, an unexposed "clear" area, the machine dark current, and the step-wedge under examination. A look-up table is produced and pixel transmission values converted to intensity.

The machine magnitude m_c (referred to as "COSMAG") is calculated from these intensity values as simply:

$$m_c = -2.5\log_{10}\sum_{pix}(I_{pix} - I_{b/g}) \tag{2.2}$$

where I_{pix} and $I_{b/g}$ are the intensities of the measured pixel and background respectively. This magnitude will clearly produce erroneous results in the case where the sensitivity changes across the plate. This is often the case, even since the advent of nitrogen flushing to remove the "Malin effect" (Dawe, Coyte & Metcalfe 1984), a radial desensitisation caused by differential exposure of the emulsion to humid air in the plate-holder: the telescope optics give rise to a strong vignetting function towards the edges such that only the central $2.7^\circ \times 2.7^\circ$ are unaffected. As was mentioned above, variations in the background level are largely caused by such effects, and dividing by the local sky value presents itself as a simple solution; this can be applied to any dataset by an alternative machine magnitude ("COSMAGCAL") thus:

$$m_c{}' = -2.5\log_{10}\left(\frac{\sum_{pix}(I_{pix} - I_{b/g})}{I_{b/g}/A_{pix}}\right) \tag{2.3}$$

Here A_{pix} is the area of one pixel in square arc seconds. This gives a sky-divided magnitude scale such that a value of zero is equal to the sky brightness in magnitudes/square arc seconds. However the situation remains complex. This correction only applies in the case where images are unsaturated: the CRT spot produces a halo around high density emulsion areas which leaks light into the photomultiplier and this in effect sets an upper limit on measurable density for central pixels of bright images (this occurs at $B_J \gtrsim 19$ for a typical survey plate). Thus "saturated" images contain some pixels

limited to these constant values and these will clearly lead to deviations from a photometric magnitude scale. Furthermore, because background will vary with position, the effective saturation level will be a function of position. The averaging of emulsion density across an image by transmission measurements within a spot of comparable size to the image also complicates the density-to-intensity conversion, causing deviations from the true scale. We can clearly see here a fundamental drawback of photographic data, and the remainder of this chapter will deal in detail with how these effects are overcome, so that a reliable photometric magnitude calibration is obtained.

2.4 Producing five-band datasets in each field

2.4.1 Introduction

This section describes the first steps taken in combining the raw COSMOS datasets for each band into a combined *UBVRI* catalogue, first matching two plates in a single waveband and removing spurious images. The catalogue calibration is briefly described (a full treatment is given in the next chapter) and an extensive morphological classification procedure discussed. The results are again paired between bands and a five-band *UBVRI* catalogue produced.

Some use here was made of procedures written for COSMOS data under the umbrella of the "HAGGIS" database system (Handling and Analysis of Graphical data in a General Interactive System). Although many procedures were available which dealt with data in a similar way to that described at several stages below, in practice they proved to be far too slow[2] for the amount of data involved, and did not satisfy the full requirements in extracting the maximum potential from the COSMOS measurements. Accordingly all of the work presented below is original, and in practice HAGGIS routines were used only for quick visual inspection (e.g. catalogue sizes or attribute list-

[2]Input and output are chiefly to blame for this: all routines access a data description file at each i/o stage, and significant improvements are seen with direct i/o FORTRAN statements: see e.g. Davenhall, A.C. "Timing Tests" (1986, ROE internal note).

ings). A particular exception is the pairing routine, referred to below, which was only modified slightly.

The HAGGIS format was followed for these datasets: the main catalogues consist of direct access files, with one record for each object containing one entry per attribute (see Table 2.2). A data description file (DDF) contains the names, units and description of each of these attributes in turn, so that individual attributes can be accessed by name alone; it also contains COSMOS measuring parameters, such as UKST plate number and spot size. "Index" files are direct access files of record length one and contain pointers to objects in the main catalogue, so that a subset of images can be accessed by a routine without the need to compile a new catalogue — this last step is vital in reducing the amount of disk storage required when performing the many processes involved below.

2.4.2 Pairing COSMOS datasets

The HAGGIS pairing routine finds common objects between two datasets by searching for objects in the secondary within a given tolerance box around primary objects, defined in a two-dimensional coordinate system (in this case right ascension and declination). Several options are available, e.g. all paired objects into a new catalogue, all images, paired and unpaired, into a new catalogue, all paired objects into subsets of the primary and secondary catalogues, all rejected objects into subsets. Multiple matches are dealt with in the following way: in the case where 2 or more secondary objects are found within one tolerance box of a single primary object, the nearest secondary is chosen; when a single secondary object is inside a tolerance box for more than one primary, the nearest primary is chosen. For more complex cases unpredictable results occur. Clearly the definition of primary and secondary catalogues is arbitrary: in practice however most efficient results are achieved by specifying the largest dataset as primary.

2.4.3 Single-band positional transformation and pairing

MacGillivray & Stobie (1984), through a test involving the double scanning of a IIIa-J plate, rotated through 90°, indicate that although the intensity-weighted centroid position for objects 2 magnitudes above the plate limit is accurate to 1.2 μm rms, systematic errors of 2–3 μm are present on scales of several centimetres (these investigations were carried out with the same spot and pixel sizes used in this survey). The effects of differential refraction can cause systematic positional shifts between plates exposed at different airmasses, and more seriously at different wavelengths. Further systematic shifts may be introduced when transforming to celestial coordinates. Therefore it is important first to check and correct for shifts on these scales before attempting to pair between the datasets.

All plates were first trimmed at the edges: it is important to compare plates only over common scan regions, and this is the simplest way to achieve this. Accordingly 1 mm was trimmed from every edge, excepting the lower x-edge which corresponds to the physical plate edge: here 3 mm was removed. If this was not first done, subsequent positional transformations obtained from comparing catalogues in the same field produced excessive errors at the field edges and were in practice unuseable. This process removed only 2% of the measured area. Next index files were created with the top 40,000 brightest images on each single-band plate (this was done by calculating a COSMAG corresponding to this cumulant value and selecting images brighter than this value): these indices were paired together into a dummy catalogue with a tolerance box of 4″ half-width in declination and right ascension (calculated at $\delta \sim 0$). The transformation between cells of side 10′ smoothed over 30′ with pyramid weighting in primary and secondary was determined by comparing positions for these bright objects in these catalogues. A small-angle rotation ($\sin\theta \simeq \theta$, $\cos\theta \simeq 1$) and an (x,y) translation were allowed in the transformation so that a one step solution can be found for each cell. The routine averaged around bins with fewer than 40 objects and exited with a warning if any residual after the transformation greater than 1″ was detected. Under normal operation, half of the full transformation was applied to each catalogue. In no case was any significant rotation detected and typical maximum translations applied were

around 1″.

The transformed right ascensions and declinations were written into the main catalogues. The major pair for the full primary and secondary catalogues was then performed using these transformed values, this time with a tolerance of 3″. Results were written into a new catalogue, named wUUU, where 'w' is the waveband code, and 'UUU' is the UKST field number; only attributes RA, DEC, AREA, IMAX, ISKY, IMAJAX, IMINAX and COSMAG (for primary and secondary) were retained at this stage in order to minimise the substantial storage space required. A check was performed after each pair by re-pairing rejected images in both catalogues as a check for multiple match problems. In no case were any more pairs matched.

At this stage the calibration in each waveband was applied to the one-band catalogues using photoelectric and CCD sequences as fully described in Chapter 3. The process by which the calibrated stars were matched with those in the catalogues, the COSMOS-to-UKST magnitude transformation obtained via the standard UBVRI *measurements and how this was applied to each dataset is described. The result at the end of this process was a catalogue in which COSMOS magnitudes had been replaced by calibrated magnitudes.*

2.4.4 Star-galaxy definition and morphological separation

The subject of this thesis is the derivation of a sample of quasars from the Edinburgh Multicolour Survey, by way of searching for peculiar colours when compared to the main sequence clump. In order to do this, it is important that the vast majority of all possible non-QSO images that may also exhibit extreme colours are excluded before the search is conducted. Discrimination against stars is afforded through photometric analysis alone due to their fixed spectral energy distributions, but calibration of extended images by

stellar photometry produces wildly inaccurate results; furthermore the spectral shape and presence of emission lines, coupled with a variable redshift, of galaxies means that some other method must be sought. Hence as well as aiming to reduce photometric errors as far as possible, it is also important to develop techniques to differentiate quasars from any other real population of objects or class of spurious machine images, in this case using the basic parameter associated with their definition: their quasi-stellar profiles.

Much effort has been made in previous years to devise efficient and quantifiable algorithms for star-galaxy separation. Results in general have varied considerably and depend greatly on the desired result: to some degree a compromise between tolerating significant levels of contamination against high levels of completeness is always made. A typical approach with COSMOS-derived data (MacGillivray & Stobie 1984) uses two separate techniques to cover the whole apparent magnitude range. Brighter than $B_J \lesssim 16$, the parameter $P = A/\pi ab$, where A is image area above threshold, and a and b are (unweighted) semi-major and semi-minor ellipse axes, is a measure of the degree to which the image fills out its traced elliptical profile. For such bright stars diffraction spikes are formed around the images, and hence P is smaller than that for galaxies: the value of $P = 0.9$ is typically used to differentiate between the two populations (stars oscillate below this level due to the competing influences of diffraction spikes with image haloes and ghosts). For fainter images however the diffraction spikes gradually disappear and the saturated core of stellar images dominates. In this region, log(area) versus magnitude is used instead: galaxies possess a higher threshold area for the same summed intensity of point spread functions. This is generally reasonably efficient as faint as $B_J \sim 21 - 21.5$, when image areas are sufficiently small that pixel sizes bring about quantised area values. In an attempt to extend separation to even fainter magnitudes Heydon-Dumbleton, Collins & MacGillivray (1989) make use of a gaussian fit to maximum and threshold intensity parameters, differentiating between stars and galaxies with the width produced by the fit. In this way they achieve >95% completeness to all galaxies, with stellar contamination in the region of 10%.

The situation here is rather different. Although the exclusion of genuine galax-

ies is clearly required, the majority of rejected images will be blends of faint objects (themselves susceptible to highly erroneous colour measurements being resolved in some datasets though not in others), and spurious images caused for example by plate flaws, satellite trails, image break-up around bright stars, which for some reason have escaped the pairing stage. Blends occur where stellar or galactic images from separate pixels are assigned to the same object undifferentiated by a single threshold; the resulting errors in photometry through different levels of discrimination in different bands can generate apparently extreme colours where none exist. These cases are always a problems for any automated survey even at high galactic latitude, and special attention must be paid to their exclusion. It is vital here to exclude *all* such images which would otherwise contaminate candidate lists considerably.

It is important here to mention the likely effects of any morphological selection on a COSMOS dataset when it comes to extracting quasar samples. It is well known that the host galaxies of quasars can be seen photographically (a) at low redshift, and (b) for intrinsically weak core components as compared to the underlying galactic emission. The Bright Quasar Survey (the PG sample) of Schmidt & Green (1983) uses a cut-off in absolute magnitude of $M_B < -23$ (H_0=50 km s^{-1} Mpc^{-1}, $q_0 = 0.5$) to define the UVX quasar population, thus removing Seyfert galaxies. These objects occupy readily visible spiral host galaxies and will be excluded here; however, there will be a further bias here against low-redshift quasars which may also display some slightly extended structure. Figure 5 in Peacock, Miller & Longair (1986) shows Hubble diagrams for various optical and radio-selected quasar samples, and indicates what PG-defined quasar types may be missed — it appears from this figure that an evolving early-type galaxy will be relatively strong compared to the central core at $z < 0.3$. At the higher redshift end, close gravitationally-lensed quasars may also be missed due to merging in the COSMOS datasets leading to high measured ellipticity. Surdej and colleagues suggest that this effect may be common: searching for highly luminous quasars (HLQ's) with $M_B < -29.0$ as candidates for amplification due to lensing through some intermediate object, they have discovered UM673, a quasar at $z = 2.719$ split into two images separated by 2.2″ by a lensing galaxy at $z = 0.493$ (Surdej *et al.* 1987, 1988a) and H1413+117, a 4-image system at $z = 2.55$ (Magain *et al.* 1988). Inspecting 111 HLQ's

by CCD imaging they have found 5 "very good candidates" (Surdej *et al.* 1988b). They claim that features possibly associated with lensing are present in 20% of these cases. In general though there is much doubt as to the extent of the effect at high redshift: other searches do not produce the same results. Visually inspecting CFHT grens plates, Weedman & Djorgovski (1988) found no candidates for lensing with separations $< 4''$ from 200–400 quasars despite two earlier serendipitous finds. No candidates $< 10''$ were subsequently confirmed. If gravitational lensing has a large influence at high redshift, the consequent distortions to the quasar luminosity function, both through extended images and amplification mean that considerable modifications are required to current conclusions. In this investigation the exclusion of non-stellar images is therefore carried out with this proviso.

The attributes associated with intensity assigned to images on photographic plates are only a small subset of the total parameters at our disposal when classifying objects. By far the most useful morphological attributes provided by COSMOS are IMAJAX ($= a$) and IMINAX ($= b$), the intensity-weighted major and minor axes fitted at the IAM stage. The elliptical nature of objects can be defined in terms of the axial ratio ($= b/a$) which is equal to unity for perfectly circular images. Random noise tends to dilute this effect somewhat, and the faintest images become quantised in profile due to the finite pixel size, and so the mean value of this ratio tends from $1 \rightarrow 0$ as area decreases. Figure 2.2(a) shows an axial-ratio/log(area) plot for all objects on the secondary V plate in field 862, a typical plot (the digitisation of area at small values can clearly be seen). In order to establish a suitable parameter to measure the significance of any observed axial ratio as a function of area, the quantity

$$\sigma_A = \frac{(\overline{b/a} - b/a)}{(1 - \overline{b/a})} \tag{2.4}$$

is used, where the denominator is a measure of the noise at this area.

This parameter was evaluated as a function of plate position and image area for all images in each one-band catalogue (a histogram of values can be seen in Figure 2.3) and written into a new catalogue for later use in $20'$ cells applying pyramid-weighted smoothing over adjacent bins. Table 2.3 shows results for this plate for each stage in

Figure 2.2: Illustrations of the morphological separation procedure for field V862:
(a) the distribution of axial ratios as a function of log(area);
(b) the result of a cubic spline fit to the log(area)/magnitude relation;
(c) & (d) residual magnitude versus log(area) relation before and after correction.

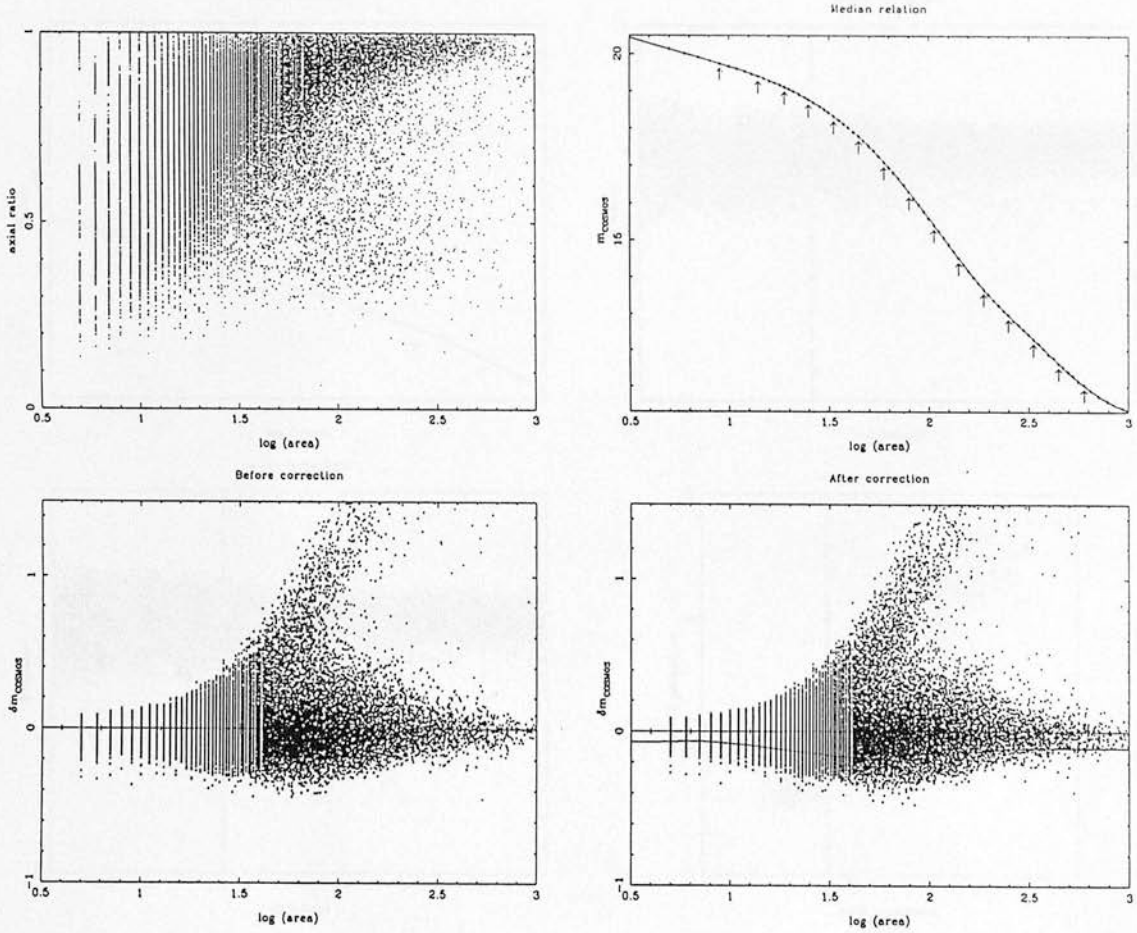

Figure 2.2: Illustrations of the morphological separation procedure for field V862:
(e) the result of a cubic spline fit to the log(imax)/magnitude relation;
(f) & (g) residual magnitude versus log(imax) relation before and after correction;
(h) scatter plot of AREA and IMAX "significance" parameters (see text).

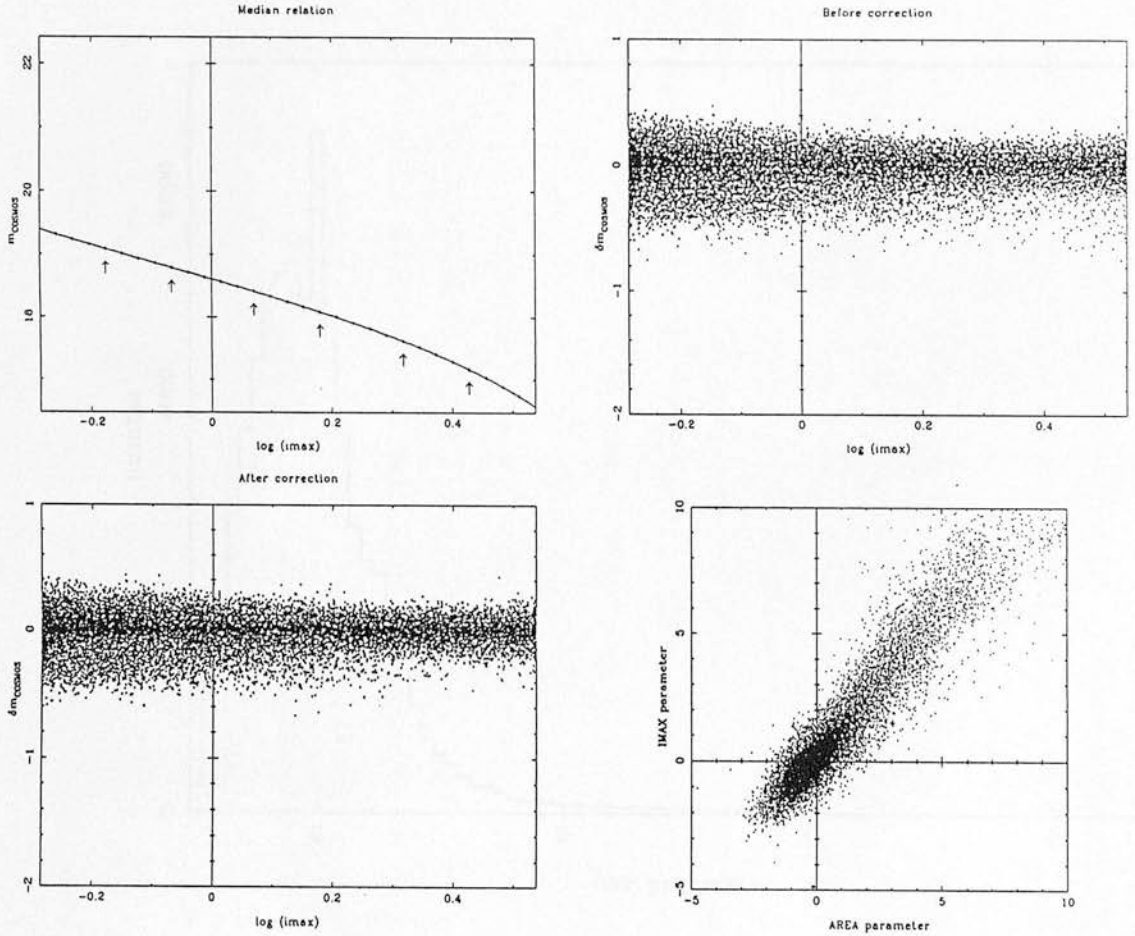

Figure 2.3: Histogram of "axial ratio significance parameter" values, a measure of the deviation from point-source morphology (see text). The profile is clearly asymmetrical, showing a large tail to high values.

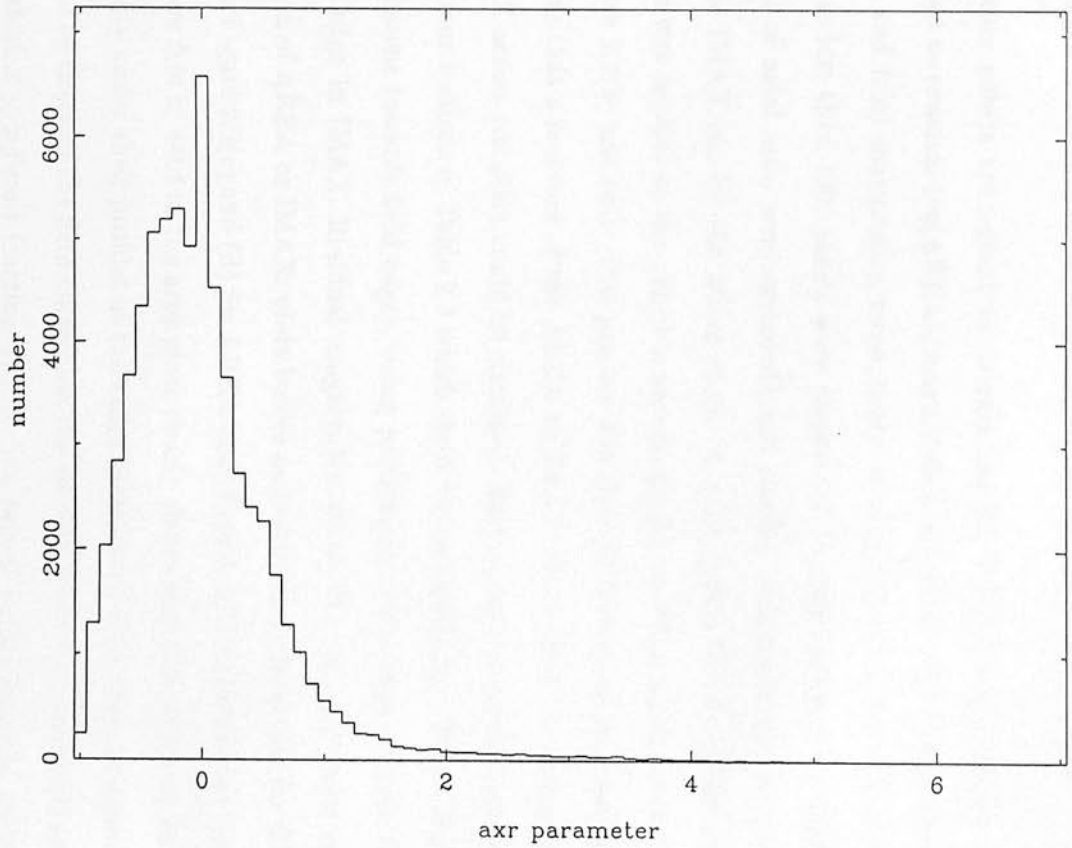

the analysis: the first two sections show axial ratios for two area cuts in cells across the plate (blank entries contain too few objects for analysis). This first stage is sufficient to separate all highly elliptical objects: the distribution is asymmetric with a large tail towards higher values. Figure 2.3 shows that a cut above $\sigma_A = 1.5 - 2$ would be a suitable value to eliminate most elliptical images while including practically all objects within the underlying symmetric distribution which represents circular images.

However further efforts are needed to extract the full information available. A routine was devised to examine log(AREA)/magnitude and log(IMAX)/magnitude relations at bright and faint magnitudes respectively as morphological discriminators. Objects with areas less than 1000 pixels were chosen (all images shown to be highly elliptical in terms of axial ratio were excluded) and median magnitude values found for each AREA or IMAX bin for the whole plate. A cubic spline fitted against calibrated magnitude was applied to this relation automatically inserting knots every five data points (Figure 2.2(b) and (e)). This process was then performed in position bins across the plate, so that a measure of the AREA or IMAX "field-effect" as a function of AREA or IMAX across the plate could be obtained. Results for this analysis can be seen in the latter four sections of Table 2.3 which show deviations in Δm. Field-effects of $\sim 0.2^{\mathrm{m}}$ are apparent towards field edges, being particularly noticeable towards the bottom left-hand edge in IMAX. Residual magnitudes about the spline fit were obtained as a function of AREA or IMAX: plots before and after field-correction for field V862 are shown in Figure 2.2(c) and (d) for AREA and (f) and (g) for IMAX: the large tail of objects above $\Delta m \simeq +0.4$ in the area plots clearly shows how non-stellar objects contain less intensity under their profiles at the same thresholded area when compared to stellar images. The effect of the field-correction can be seen when comparing (f) and (g) which has pushed a significant fraction of low-Δm valued points into the stellar locus. Deviant images as shown by the area/magnitude relation are excluded before progressing to the IMAX calculation. From these distributions, 10 percentile points are calculated (on the negative Δm non-elliptical side) as shown in plot (d), and AREA, IMAX "significance parameters" were defined as a fraction of one 10% deviation from the median value and written to the output catalogue.

Table 2.3: Output from the morphological separation algorithm, as applied to the secondary V plate in field 862. The first two panels show variation in axial ratio with position for two different area cuts, and the remainder show Δm variations derived via examination of the dependence of image area and maximum intensity with calibrated magnitude. The variations in axial parameter for different area cuts are apparent, and some field-effects can be seen, especially in IMAX, which are well corrected by the algorithm (see Figure 2.2 (g)). The catalogue contains 64948 images, and the number of objects passed to each subsequent stage is shown.

---

mean axial ratio, at area = 10

0.66	0.67	0.67	0.68	0.66	0.67	0.69	0.66	0.67	0.68	0.68	0.68	0.68	0.68	0.69	0.70	
0.67	0.67	0.67	0.67	0.68	0.68	0.68	0.69	0.67	0.68	0.68	0.67	0.68	0.69	0.70	0.68	0.66
0.66	0.66	0.66	0.68	0.68	0.69	0.70	0.68	0.67	0.68	0.68	0.68	0.68	0.68	0.67	0.68	
0.67	0.67	0.68	0.66	0.68	0.69	0.68	0.68	0.68	0.68	0.69	0.68	0.68	0.67	0.67	0.69	0.69
0.68	0.69	0.68	0.68	0.68	0.68	0.68	0.67	0.69	0.69	0.68	0.68	0.66	0.68	0.69	0.67	0.69
0.66	0.68	0.70	0.68	0.69	0.70	0.68	0.68	0.68	0.69	0.68	0.67	0.67	0.67	0.68	0.68	0.68
0.67	0.69	0.69	0.70	0.69	0.70	0.72	0.72	0.69	0.66	0.68	0.69	0.69	0.68	0.68	0.68	
0.70	0.69	0.70	0.68	0.69	0.69	0.71	0.72	0.69	0.67	0.68	0.69	0.69	0.69	0.68	0.68	0.68
	0.68	0.69	0.70	0.69	0.69	0.70	0.70	0.69	0.68	0.69	0.68	0.67	0.68	0.68	0.69	
	0.69	0.69	0.70	0.69	0.70	0.69	0.69	0.69	0.67	0.68	0.68	0.67	0.68	0.69	0.68	0.70
0.68	0.69	0.69	0.69	0.70	0.69	0.69	0.70	0.67	0.68	0.68	0.68	0.68	0.69	0.69	0.69	
	0.67	0.70	0.71	0.71	0.70	0.70	0.69	0.69	0.70	0.69	0.69	0.69	0.69	0.68	0.69	
0.64	0.66	0.68	0.69	0.71	0.69	0.69	0.68	0.68	0.69	0.70	0.70	0.70	0.68	0.67	0.68	0.67
	0.65	0.67	0.68	0.69	0.69	0.68	0.68	0.67	0.69	0.70	0.70	0.69	0.69	0.68	0.68	
	0.65	0.66	0.68	0.70	0.70	0.69	0.68	0.69	0.68	0.68	0.68	0.68	0.68	0.68	0.69	
0.65	0.65	0.65	0.69	0.71	0.69	0.68	0.70	0.68	0.66	0.65	0.68	0.68	0.66	0.68	0.67	

mean axial ratio, at area = 100

0.85	0.84	0.83	0.83	0.85	0.87	0.88	0.88	0.85	0.84	0.85	0.86	0.85	0.85	0.85	0.85	
0.84	0.85	0.84	0.83	0.85	0.88	0.89	0.88	0.83	0.83	0.85	0.85	0.85	0.86	0.85	0.86	0.84
0.85	0.86	0.85	0.84	0.85	0.86	0.87	0.86	0.86	0.85	0.86	0.85	0.86	0.85	0.86	0.85	
0.87	0.86	0.85	0.85	0.86	0.85	0.84	0.86	0.87	0.88	0.87	0.87	0.85	0.85	0.85	0.86	0.87
0.87	0.86	0.85	0.86	0.86	0.85	0.84	0.87	0.88	0.88	0.88	0.86	0.84	0.85	0.85	0.86	0.87
0.87	0.85	0.86	0.86	0.85	0.84	0.86	0.87	0.88	0.89	0.88	0.87	0.86	0.84	0.85	0.85	0.85
0.86	0.85	0.85	0.86	0.85	0.86	0.85	0.88	0.88	0.86	0.87	0.87	0.86	0.84	0.86	0.84	
0.84	0.86	0.86	0.84	0.86	0.86	0.88	0.87	0.87	0.87	0.86	0.86	0.85	0.85	0.86	0.87	0.83
	0.87	0.87	0.85	0.85	0.88	0.90	0.89	0.88	0.88	0.87	0.86	0.87	0.87	0.85	0.86	
	0.87	0.87	0.87	0.86	0.89	0.89	0.89	0.88	0.87	0.87	0.88	0.87	0.86	0.86	0.86	0.84
0.87	0.87	0.87	0.88	0.90	0.89	0.88	0.89	0.88	0.86	0.86	0.88	0.86	0.87	0.86	0.86	
	0.88	0.87	0.88	0.89	0.89	0.89	0.88	0.86	0.86	0.87	0.86	0.87	0.87	0.87	0.86	
0.88	0.90	0.88	0.87	0.87	0.88	0.88	0.87	0.86	0.87	0.88	0.87	0.86	0.87	0.86	0.87	0.85
	0.88	0.89	0.87	0.87	0.88	0.86	0.88	0.88	0.88	0.89	0.89	0.87	0.85	0.86	0.86	
	0.88	0.87	0.88	0.88	0.89	0.88	0.85	0.89	0.88	0.89	0.89	0.89	0.87	0.88	0.88	
0.85	0.88	0.88	0.86	0.88	0.88	0.85	0.85	0.88	0.90	0.89	0.88	0.89	0.88	0.87	0.88	

131 images larger than 1000 pixels were flagged

3023 images with small axial ratios were flagged

Table 2.3: (continued)

mag/area field effect at area = 10

-0.07	-0.07	-0.05	-0.01	0.00	0.00	0.03	0.02	0.01	0.01	0.00	0.00	0.00	0.00	-0.01	-0.04	
-0.08	-0.05	-0.03	-0.01	-0.01	0.01	0.01	0.02	0.01	0.01	0.01	0.00	0.00	0.00	0.00	0.00	-0.03
-0.04	-0.04	-0.01	-0.01	0.01	0.01	0.01	0.01	0.01	0.01	0.00	0.00	-0.01	0.01	0.01	0.01	
-0.02	-0.02	-0.01	0.01	0.01	0.02	0.02	0.01	0.00	0.00	-0.01	0.00	0.00	0.00	0.00	0.00	0.00
0.00	0.00	0.00	0.02	0.02	0.01	0.02	0.02	0.01	-0.01	0.00	0.00	0.00	0.00	0.00	-0.01	0.00
0.00	0.01	0.01	0.02	0.02	0.03	0.02	0.02	0.02	0.01	0.00	0.00	0.00	0.00	-0.01	-0.01	0.00
0.00	0.00	0.01	0.02	0.03	0.02	0.02	0.01	0.02	0.01	0.00	0.00	0.00	-0.01	-0.01	-0.01	
0.00	0.00	0.00	0.00	0.02	0.02	0.02	0.01	0.01	0.01	0.00	0.01	-0.01	-0.01	-0.01	-0.01	-0.02
	0.00	0.00	0.00	0.01	0.02	0.01	0.02	0.01	0.01	0.00	0.00	0.00	0.00	-0.01	-0.02	
	0.00	0.01	0.01	0.02	0.01	0.01	0.01	0.01	0.01	0.01	0.01	0.01	0.00	-0.01	-0.01	-0.01
0.01	0.01	0.01	0.01	0.00	0.01	0.00	0.00	0.02	0.01	0.01	0.01	0.00	0.01	0.00	0.00	
	0.02	0.02	0.00	-0.01	0.00	0.00	0.01	0.00	0.01	0.01	0.00	0.00	0.00	0.00	0.00	
0.02	0.03	0.02	0.01	-0.01	-0.01	0.00	0.00	0.00	0.00	0.01	0.01	0.00	0.00	0.00	-0.01	0.00
	0.03	0.02	0.02	0.00	0.00	-0.01	0.00	0.00	0.00	0.00	0.01	0.00	-0.01	-0.01	0.00	
	0.00	0.00	-0.01	0.00	-0.01	-0.01	-0.01	0.00	0.01	0.00	-0.01	-0.01	-0.01	-0.01	-0.03	
-0.05	-0.04	-0.01	-0.02	-0.01	-0.01	-0.02	-0.01	-0.01	0.00	0.00	-0.01	-0.01	-0.01	-0.01	-0.03	

mag/area field effect at area = 100

0.00	0.04	0.00	0.01	-0.01	-0.01	0.02	0.03	0.03	-0.01	0.04	-0.04	-0.03	0.01	0.01	-0.01	
0.02	0.04	0.03	0.01	0.00	-0.01	0.01	0.01	-0.02	0.03	0.00	-0.01	-0.03	-0.02	-0.02	0.02	-0.04
0.05	0.04	0.03	0.02	-0.02	0.00	-0.02	-0.02	0.01	0.01	0.02	0.01	-0.01	-0.05	-0.03	-0.04	
0.01	0.08	0.04	0.00	-0.02	-0.04	0.02	0.00	-0.03	-0.03	-0.01	0.03	0.00	0.00	-0.02	-0.05	-0.02
0.03	0.00	0.01	-0.01	-0.03	-0.01	0.01	0.00	-0.01	-0.02	-0.02	0.01	0.01	0.01	-0.02	0.01	-0.01
0.03	0.01	0.01	0.00	-0.01	-0.02	-0.01	0.00	0.00	-0.01	0.00	-0.01	0.01	0.03	0.03	-0.01	0.04
0.02	0.04	0.02	-0.02	-0.01	-0.03	-0.03	-0.01	-0.01	0.00	-0.03	-0.02	-0.03	-0.02	-0.01	0.01	
0.01	0.03	0.00	-0.04	-0.02	-0.01	-0.02	-0.02	-0.04	-0.05	-0.04	-0.05	-0.04	-0.03	-0.02	-0.01	-0.01
	0.00	-0.01	-0.03	-0.04	-0.02	-0.02	-0.02	-0.03	-0.05	-0.04	-0.03	-0.01	-0.02	-0.03	-0.01	
	0.01	0.00	-0.02	-0.03	-0.02	-0.03	-0.04	-0.02	0.00	-0.02	0.02	0.00	-0.04	-0.02	0.01	-0.01
0.00	0.03	0.02	0.02	-0.01	-0.04	-0.04	-0.04	-0.03	-0.01	0.02	0.00	-0.03	-0.03	-0.02	0.00	
	0.07	0.08	0.02	-0.02	-0.04	-0.04	-0.04	-0.01	-0.03	-0.04	-0.02	-0.03	-0.03	-0.01	0.01	
0.20	0.11	0.08	0.07	0.00	-0.02	-0.01	-0.03	0.01	-0.02	-0.03	-0.04	-0.02	-0.02	0.02	0.00	0.02
	0.18	0.11	0.05	0.00	-0.01	-0.02	-0.01	-0.01	0.01	-0.01	-0.03	-0.03	0.00	-0.02	0.02	
	0.16	0.11	0.03	-0.01	-0.04	-0.01	-0.01	0.00	-0.02	-0.02	-0.04	-0.02	-0.02	-0.02	-0.05	
0.18	0.09	0.06	0.05	-0.02	-0.05	-0.03	0.04	0.00	0.03	-0.04	-0.04	-0.03	-0.02	-0.04	-0.01	

5547 images were flagged as non-stellar

Table 2.3: (continued)

mag/imax field effect at log(imax) = -0.08

-0.04	-0.02	-0.02	-0.03	-0.04	-0.04	-0.07	-0.03	-0.06	-0.04	-0.05	0.00	0.03	0.01	-0.02	-0.01	
-0.03	-0.03	0.00	-0.04	-0.02	-0.04	-0.03	-0.04	-0.03	-0.07	0.01	-0.02	0.00	0.01	0.01	0.03	0.00
-0.01	0.01	-0.03	-0.01	0.01	0.02	-0.06	-0.04	-0.03	0.00	-0.02	0.03	0.01	0.02	0.04	0.04	
0.00	0.00	0.00	-0.03	-0.01	0.01	-0.07	-0.04	0.04	0.00	0.04	0.04	0.02	0.03	0.02	0.00	0.00
-0.01	-0.01	0.00	0.01	-0.03	-0.05	-0.05	-0.02	0.04	0.04	0.05	0.05	0.03	0.02	0.00	-0.03	-0.02
0.01	-0.02	0.01	-0.01	0.02	-0.03	-0.04	-0.01	0.03	0.05	0.03	0.04	0.00	0.00	-0.01	-0.08	-0.03
-0.01	-0.02	-0.02	-0.03	0.00	0.01	0.00	0.03	0.04	0.02	0.03	0.02	0.02	0.00	-0.01	-0.02	
-0.01	0.00	-0.04	-0.04	0.00	0.03	0.04	0.05	0.03	0.01	0.02	0.03	0.03	0.03	0.01	-0.02	0.01
	0.00	0.00	0.05	0.04	0.04	0.02	0.04	0.00	0.01	0.03	0.03	0.03	0.04	0.03	0.00	
	-0.01	0.02	0.04	0.04	0.02	0.05	0.03	-0.01	0.02	0.02	0.01	0.03	0.03	0.01	0.01	-0.03
-0.03	-0.04	-0.03	0.03	0.02	0.01	0.05	0.06	0.01	0.01	0.02	0.03	0.02	0.01	0.00	0.02	
	-0.15	-0.06	-0.02	0.02	0.03	0.05	0.03	0.03	0.05	0.03	0.03	0.00	0.01	0.03	0.03	
-0.28	-0.24	-0.15	-0.03	0.03	0.05	0.05	0.03	0.04	0.04	0.03	0.01	0.01	0.01	0.03	0.00	0.00
	-0.34	-0.20	-0.02	0.03	0.04	0.03	0.02	0.00	0.01	0.02	0.00	0.02	0.03	0.01	-0.01	
	-0.25	-0.14	-0.02	0.03	0.03	0.01	0.01	0.00	0.00	0.00	0.01	0.03	0.04	0.01	0.03	
-0.13	-0.10	-0.07	0.01	0.02	0.01	0.01	0.02	0.03	-0.01	-0.02	0.01	0.04	0.04	0.02	-0.02	

mag/imax field effect at log(imax) = 0.33

0.09	0.05	0.02	0.00	0.00	-0.02	-0.04	-0.07	-0.06	-0.03	-0.04	-0.04	-0.02	-0.02	-0.01	0.03	
0.03	0.04	0.01	0.01	-0.03	-0.01	-0.02	-0.02	-0.02	-0.03	-0.03	-0.03	-0.03	-0.03	0.00	0.00	0.04
0.01	0.02	0.00	-0.01	-0.03	-0.01	0.01	0.00	0.00	0.00	-0.01	-0.02	0.00	-0.01	0.00	0.00	
0.02	-0.01	-0.02	-0.02	-0.01	0.00	0.00	0.01	0.02	0.03	0.00	0.01	0.00	0.00	0.01	0.02	0.01
-0.04	0.00	-0.01	-0.02	-0.01	-0.01	0.00	0.01	0.02	0.02	0.04	0.03	0.01	0.01	0.03	0.01	0.00
-0.02	-0.04	-0.01	-0.01	-0.01	-0.01	0.00	0.00	0.02	0.02	0.04	0.04	0.01	0.03	0.02	0.00	0.00
-0.02	-0.01	-0.02	-0.01	-0.01	0.00	0.00	0.02	0.03	0.03	0.04	0.03	0.03	0.03	0.03	0.03	
-0.02	-0.03	-0.01	0.00	0.00	0.01	0.02	0.03	0.04	0.03	0.01	0.03	0.03	0.04	0.04	0.03	0.02
	-0.02	-0.01	0.00	0.01	0.02	0.03	0.01	0.00	0.01	0.01	0.02	0.03	0.02	0.01	0.00	
	-0.07	-0.04	0.00	0.00	0.02	0.00	0.02	0.02	0.02	0.03	0.01	0.00	-0.01	0.00	0.01	-0.01
-0.12	-0.13	-0.06	-0.03	0.01	0.01	0.02	0.02	0.02	0.02	0.03	0.01	0.01	0.00	-0.03	0.01	
	-0.18	-0.15	-0.04	0.01	0.03	0.03	0.02	0.01	0.01	0.02	0.01	0.00	0.01	0.03	0.01	
-0.33	-0.32	-0.21	-0.07	0.02	0.02	0.04	0.02	0.01	0.02	0.01	0.02	0.02	0.03	0.03	0.02	0.01
	-0.39	-0.26	-0.09	0.00	0.02	0.01	0.02	0.03	0.02	0.03	0.01	0.02	0.02	0.03	0.02	
	-0.30	-0.20	-0.03	-0.01	-0.01	0.01	0.00	0.00	0.04	0.05	0.03	0.02	0.03	0.03	0.02	
-0.05	-0.06	-0.07	-0.02	0.00	-0.01	0.01	0.00	0.00	0.00	0.04	0.04	0.03	0.02	0.03	0.05	

The final plot in Figure 2.2 shows the distribution in significance parameter space (AREA versus IMAX) for all objects, once again for plate V862. A large tail to high values in both these parameters is seen superimposed upon the symmetrical elliptical spread around (0,0) for near-circular images. In practice it was better to iterate the whole process once: the first pass was used to produce an index with highly deviant objects (defined as exceeding unity in σ_A, the axial ratio "significance", or exceeding 3 in AREA or IMAX "significance") excluded which improves the percentile level determination.

The next stage was to actually perform the separation using these three parameters. This was left until single five-band catalogues were produced from the combination of all catalogues in each field.

2.4.5 Five-band positional transformation and final pairing

In order to produce *UBVRI* datasets it was necessary to combine each catalogue into a final dataset. Differential refraction effects can be very large (see e.g. Wallace & Tritton 1979), especially between different wavebands and so again local coordinate transformations are essential. The comments that applied to the one-band pairing are equally relevant here. The brightest 40,000 objects were selected and paired again into a dummy catalogue and the transformation between cells of size $10'$ again obtained. The corresponding transformed coordinates were used to pair the major catalogues; this process was done a total of four times. The major difference between this and the previous case is that once the transformation was obtained, its total value was applied to the secondary band (arbitrarily defined), instead of splitting the derived values between each catalogue. The reason for this was that differential refraction is strongest is the blue. In order to determine as correctly as possible the positions of each object the R plates alone were used to define the final catalogue values (I plates were considerably less deep).

In the case here, positional shifts before transformation of up to $3''$ were detected on some plates (larger than before due to differential refraction effects between different

wavebands). All transformed residuals were $< 1''$, and in most cases much better than this. All final catalogues were paired in the order *R, B, I, V, U*, retaining this time *all* objects for the final dataset so that objects sufficiently peculiar to be absent in any given band (other than *R*) were still present in the final catalogue.

2.5 Deriving a field-corrected stellar dataset

2.5.1 Rejection of elliptical images

At this stage the parameters derived in Section 2.4.4 were used to reject non-stellar images. As mentioned earlier, for the purpose of a quasar search a very strict morphological separation is appropriate and indeed necessary, bearing in mind that most anomalous and erroneously measured images would become prime candidates for non-stellar colours if not rejected here. Because this is the case, all images displaying peculiar profiles by way of ellipticity, thresholded area to magnitude and maximum image intensity to magnitude were rejected as non-stellar. This method not only rejects almost all galaxies but any residual blends and spurious images, and leads to a much higher completeness in the final dataset at the expense of no more than a reduction in effective area searched. This statement goes with the caveat that any objects that might display significantly non-stellar profiles would be preferentially rejected: as has been said, there is no evidence that this would be important for QSOs with $z > 0.3$.

Output such as that produced in Figures 2.2 and 2.3 was inspected to determine the apparent magnitude ranges in each waveband in which each criterion was applicable. Any object exceeding a value of 1.5 in any one of the ten σ_A (axial ratio significance) parameters was first rejected, providing a straightforward and severe elliptical cut. The significance parameters for AREA were used for the bright end of the magnitude scale up to the point at which quantised area effects produce deviations from the known relationship for stars: this was usually about $m = 19$. The IMAX significance parameters by then have become a powerful discriminant: all images are unsaturated at these magnitudes. A *bright* magnitude limit for the IMAX parameters was also sought, and

again was estimated from the previous output as the point at which the δm errors diverge (usually about $m = 17 - 18.5$). In all cases there was a considerable degree of overlap in the magnitude ranges for each parameter. Within this overlap region all images displaying a combined value greater than 3.0 in any band when these parameters were combined in quadrature were rejected; in the single-parameter regions a simple cut at 2.0 in the appropriate parameter value was used. These cuts were applied only on the "extended" side, i.e. very compact objects were not rejected but their numbers were noted as a check for the severity of the "extended cut" — in all cases only ten's of objects were rejected on the compact side, implying that only the extreme wings of the stellar distribution are removed.

2.5.2 Faint calibration corrections

Figure 2.4(a) shows the cumulative log(number) versus magnitude relation for the master U plate in field 862. The plot in general follows the expected relation of a steady increase in counts up until the "plate-limit", defined as the magnitude at which objects drop below the detection threshold of COSMOS, and its sensitivity curve turns over. It is important to define this quantity carefully, as all subsequent treatment of the data will treat magnitudes fainter than this limit as unreliable. The limit is defined as the magnitude at the peak, because the catalogue will be incomplete at any fainter magnitudes — Table 2.4 shows the plate-limits adopted for each field in this way. It is clear from the figure however that significant deviations from the expected relation can be seen at the faint end of the magnitude scale ($U \geq 18.5$) due to calibration errors: even though sharp features in the calibration relation are removed prior to calibration, so that a low-order polynomial with well-defined behaviour is applied (see next Chapter), the lack of accurate CCD photometry at very faint levels can sometimes give rise to smooth but systematic deviations from the photometric magnitude scale when calibration is extrapolated towards the plate limit. The effect of these small calibration errors can be quite appreciable on the N/m relation. In order to obtain the high level of photometric accuracy required in this survey it was occasionally necessary to correct this.

Table 2.4: Table of plate-limits for each UKST field/waveband.

Field	789	790	791	792	861	862	863	864	865	866	867
U	21.1	20.65	21.3	20.0	20.2	21.2	20.2	20.2	20.0	21.0	20.8
B	21.3	20.6	20.85	21.2	20.8	21.0	20.8	20.7	20.6	20.7	20.6
V	20.2	19.25	19.6	19.8	19.35	19.6	19.1	20.1	19.3	18.7	19.6
R	20.2	19.8	20.1	20.3	20.0	20.3	19.7	20.6	20.0	19.3	19.7
I	19.2	18.3	18.4	18.4	19.0	17.9	18.6	18.8	19.0	17.6	18.2

The $\log(N)/m$ relations for well-calibrated plates appear linear up to the plate-limit, and this behaviour was used to correct the few plates displaying systematic deviations. The method chosen was to sort the dataset into 0.025^{m} bins and, extrapolating from the slope at the bright end of the relationship, to force the same slope up to the plate limit. Three points on the magnitude scale were chosen: LPT and UPT, the magnitude range from which the slope is to be calculated, and the plate-limit. The slope was then calculated with a linear least squares fit applied to the $\log(N)/m$ relation, excluding the faintest point which was used to calculate the intercept, so that the slope passed exactly through this transition point. A corresponding "model" was produced, extrapolated up to the survey limit (as estimated from the $\log(N)/m$ plot) which was tied to the real counts at faint magnitudes. A cubic spline fit was produced for this transformation, extrapolating the relationship brighter than LPT by 1 magnitude with a slope of unity in the magnitude transformation to ensure a smooth transition. The correction was then applied to the catalogue via a look-up table with linear extrapolation beyond the plate-limit.

Results for this process, again for the master U plate in field 862, can be seen in Figure 2.4(b) where a $\log(N)/m$ plot after the process is shown. The routine has had an effect where problems arose previously: all deviations from the linear seen in the response before correction have been straightened out successfully. It should also be noted that this field has very little calibration information in this waveband, and few plates were this bad. The effect of this process has been estimated by comparing the final relation for corrected data with data in the same waveband but which followed

Figure 2.4: Cumulative log(number) versus magnitude relations for the master U plate in field 862 before and after straightening.

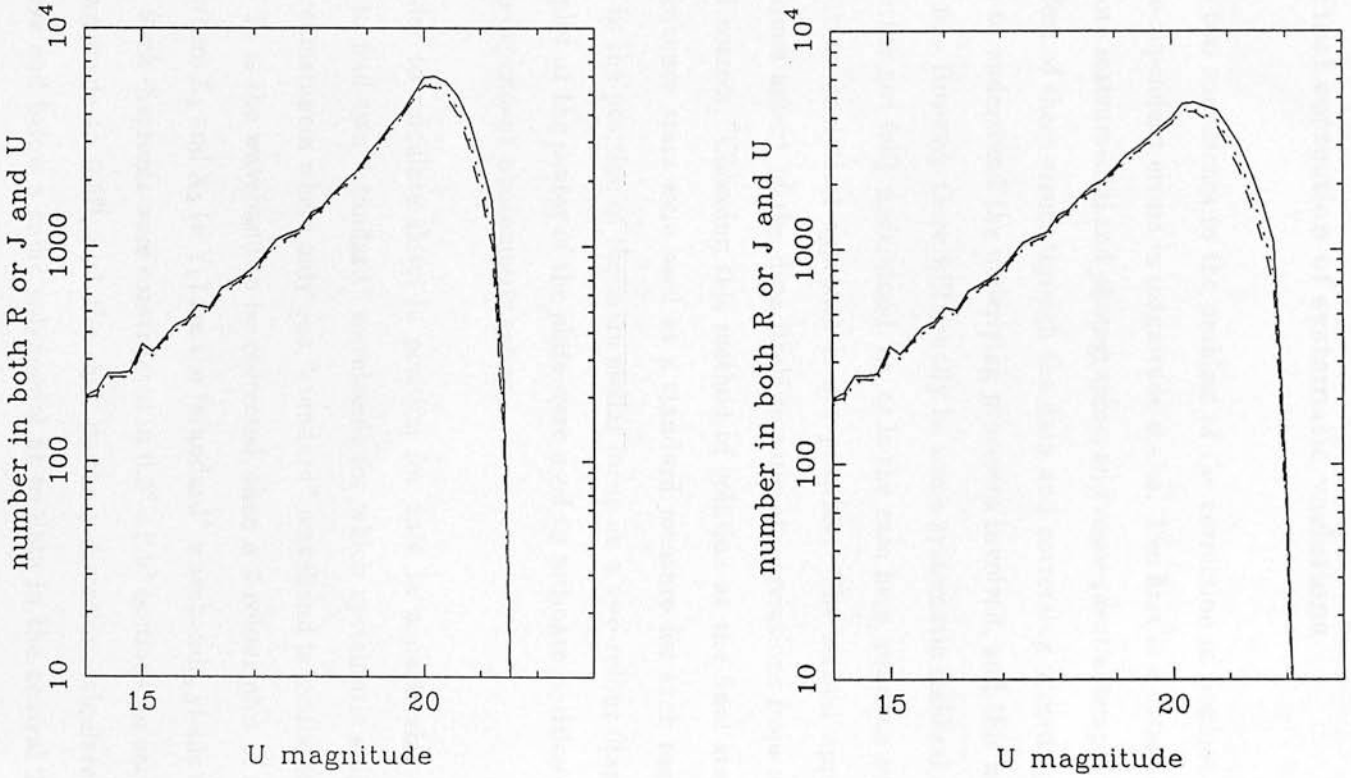

the expected relation. The result of this was that no systematic error should have been introduced to the real $\log(N)/m$ relation amounting to more than 0.15^{m} at the faint end, as estimated from deviations in this curve.

2.5.3 Final correction of systematic variations

There are two approaches to the problem of the correction of position-dependent and magnitude-dependent errors in magnitude scales. The first is a detailed study of their sources, both instrumental and photographic, and consequent attempts to correct, tracing the effect of these errors through the data and correcting accordingly. It is clearly preferable to understand the underlying processes involved, and this has been the approach so far. However there will usually be some systematic residual sources of error that are either not fully understood, or, as is the case here, produce such complicated results that an analytical approach is not possible. The second approach available is to use some aspect of the data itself to estimate deviations from an expected relation and correct. Choosing this method of solution at the final stage, the colours of main sequence stars were used as a standard measure for each region on a plate, and shifts in the position of the main stellar locus on a two-colour diagram, measured against a plot at the center of the plate were used to estimate position-dependent and magnitude-dependent photometric errors.

In order to calculate shifts in position for data in a particular waveband it is necessary to find two "standard" wavebands for which systematic shifts are believed absent (circumstances where only one "standard" waveband is available are dealt with below). If Y_2 is the waveband to be corrected, then a 2-colour plot of $(X_1–X_2)$ versus $(Y_1–Y_2)$, where X_1 and X_2 $(=Y_1)$ are the "standard" wavebands, yields the information necessary. Such diagrams were constructed in $0.5° \times 0.5°$ sections on each plate, binned also in magnitude to 0.5^{m}, and the shift in the y-direction calculated by summing values above and below a cubic polynomial fit to data in the central 2 deg^2 of plate, chosen from primary or secondary plate according to which presented the least field-effects. A NAG routine was used to invert a matrix, deriving the cubic fit between two

given points in colour (on the x-axis) for which the locus was well-defined; this fit was plotted on a 2-colour diagram for checking. The cells calculations were carried out for all objects within the plate-limits in X_1 and X_2, and between a specified bright limit and a faint "truncation point" in Y_2, specified as the plate-limit in Y_2, or, if brighter, the Y_2 limit corresponding to the plate-limit in any other waveband within the colour range for which the shift was calculated. This was necessary to avoid any limit producing a colour-dependent cut-off which could badly bias the results. To elucidate, consider a catalogue with plate-limits as follows: $B \leq 20.6$, $R \leq 19.3$ and $I \leq 18.7$ (field 863). Suppose shifts in I are sought via a $(B-R)/(R-I)$ plot: a truncation point of $I = 18.7$ applied up to $(R-I) = 0.8$ would exceed the R plate-limit, and thus be biased leading to excessive shift calculations in the direction of brighter I. A truncation point of $I = 18.5$ is required to eliminate these effects. In order to avoid erroneous shifts caused by small-number fluctuations, cells were combined in (a) area, stepping sideways in 2-D, and (b) magnitude, adding bins either side until at least 50 objects were obtained. Checking of the accumulated object number was performed after each (symmetrical) adding stage to keep smoothing to a minimum. The data were then shifted accordingly by smoothing around each object in 2-D in area, based on its position within the cell (smoothing length 0.5°), and 1-D in magnitude (smoothing length 0.5^{m}).

Output was produced in the form of shifts applied in 1000^{th}'s of a magnitude, an example of which can be seen in Figure 2.5 for field 864, where corrections in I were calculated using R and B as "standard" wavebands. The first two plots show $(R-I)/(B-R)$ 2-colour plot of this field (master and secondary) with a cubic fit to stars in the central 2 deg^2 on the secondary plate, within the $(B-R)$ range shown $(0.5 \leq (B-R) \leq 1.5)$. The secondary plate was chosen as the standard, being slightly more uniform. The middle plots indicate calculated shifts as a function of I magnitude up to the truncation point of $I = 18.5$, plotted here for the central 2 deg^2 — shifts of up to 0.1^{m} are clearly present. The numbers below each point indicate the number of objects per bin. In all cases a diagnostic second pass was made producing no new shifted dataset, but re-calculating residual shifts, and showing the effects of the previous correction.

Figure 2.5: Stellar locus-shifting routine. The upper plots show $(R-I)/(B-R)$ two-colour plots for field 864 master and secondary (J in diagram indicates the B_J passband) with cubic polynomial fit to the central 2 deg^2 in the region $0.5 \leq (B-R) \leq 1.5$. Calculated shifts as a function of magnitude for the plate centre are shown in the center two plots. The lower panels show a $(R-B)/(R-I)$ two-colour plot for the same field. Note the red-tail parallel to the $(R-I)$ axis, by which the B magnitude-dependent errors are corrected.

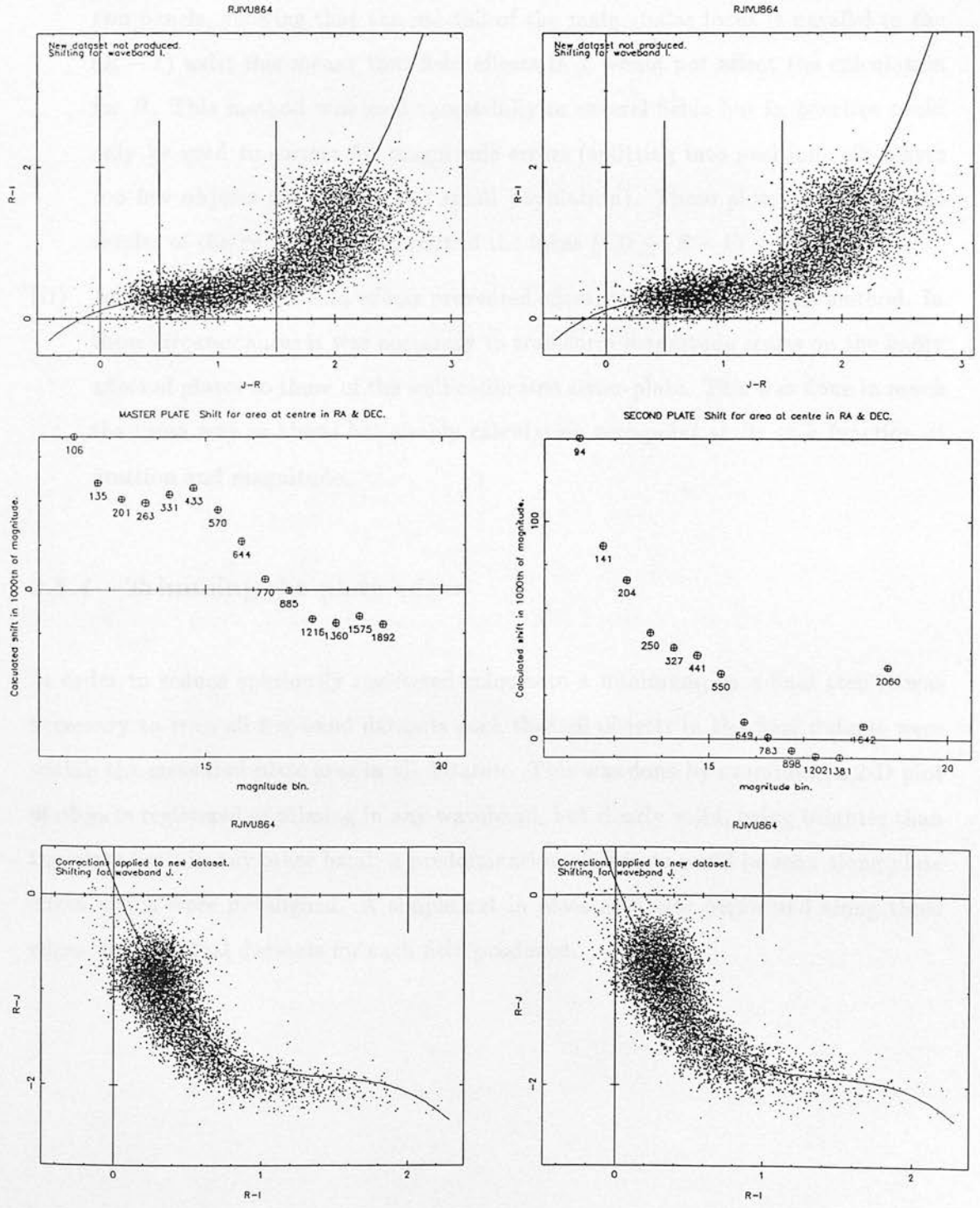

Two modifications to the above method were used in some situations:

(i) In most fields, R and B could be used as "standard" wavebands, being free from severe magnitude-dependent and position-dependent field-effects and deep enough to allow faint enough corrections in the required band. However in some fields (e.g. 864) even B required magnitude corrections. This was however still possible. A $(R-B)/(R-I)$ 2-colour plot of field 864 can be seen in Figure 2.5 in the lower two panels, showing that the red tail of the main stellar locus is parallel to the $(R-I)$ axis; this means that field effects in I would not affect the calculation for B. This method was used successfully in several fields but in practice could only be used to correct for magnitude errors (splitting into position-cells leaves too few objects per bin for this small population). These plots also shows the results of the cubic fit to this part of the locus ($1.0 \leq (R-I) \leq 2.0$).

(ii) In two cases, severe field effects prevented effective correction by this method. In these circumstances it was necessary to transform magnitude scales on the badly affected plates to those of the well-calibrated sister-plate. This was done in much the same way as above but simply calculating zero-point shifts as a function of position and magnitude.

2.5.4 Trimming the plate edges

In order to reduce spuriously registered colours to a minimum, as a final step it was necessary to trim all five-band datasets such that all objects in the final dataset were within the measured plate area in all datasets. This was done by examining a 2-D plot of objects registered as missing in any waveband, but clearly valid, being brighter than the plate limit in any other band: a predomination of objects could be seen along plate edges which were misaligned. A simple cut in plate area was performed along these edges and the final datasets for each field produced.

2.5.5 Photometric accuracies in the final dataset

Part II of this thesis deals with the use this final dataset is put to in a specific area: the selection of quasars, by their non-stellar colours. It has been with this end in mind that the careful reductions and corrections of this and the next chapter have been undertaken, in order to reduce contaminants that may mimic the colours of such objects to a minimum, while not biasing the dataset against quasars in any way. Therefore it is appropriate to examine the derived photometric accuracies of each field dataset in turn at the end of these reductions. This is the final test of any large dataset, and knowledge of the photometric errors gives confidence as to the completeness of any sample subsequently obtained.

In this case we are fortunate in having available two sets of plates for each field, reduced independently, from which rms errors can be estimated. This was estimated by comparing magnitudes from each epoch for all objects, allowing for possible systematic calibration differences by evaluating the result about the mean difference in each band. The final result represents the rms error on this difference, by the following equation

$$\sigma_D^2 = \frac{1}{(N-1)} \sum_i \left((m_1^i - m_2^i) - \Delta m \right)^2 \tag{2.5}$$

where m_1 and m_2 are the measurements for the magnitude of object i on each plate, and Δm is the mean difference between magnitudes on each plate, evaluated as

$$\Delta m = \frac{1}{N} \sum_j (m_1^j - m_2^j) \tag{2.6}$$

σ_D is evaluated as a function of magnitude after an initial rejection of 3σ deviant objects, which represent an additional component to the expected gaussian error distribution, caused by any remaining spurious images. At all later stages the mean magnitude from both plates was used, and it is convenient to express the errors in terms of this mean magnitude. If σ_M is this error then $\sigma_M = \sigma_D/2$: this quantity is presented here in Figures 2.6 (a)–(k). The error curves all trace the same behaviour, increasing gradually with magnitude until within about 2 magnitudes of the plate limit, where they diverge more rapidly. In some cases field effects at bright ($m \lesssim 16$) magnitudes are still present,

Figure 2.6: (a) Rms error on the mean magnitude in each passband, calculated from the master and secondary plate values, as a function of magnitude. The error is calculated about the mean zero-point difference in each waveband, to allow for systematic calibration differences.
This plot: field 789.

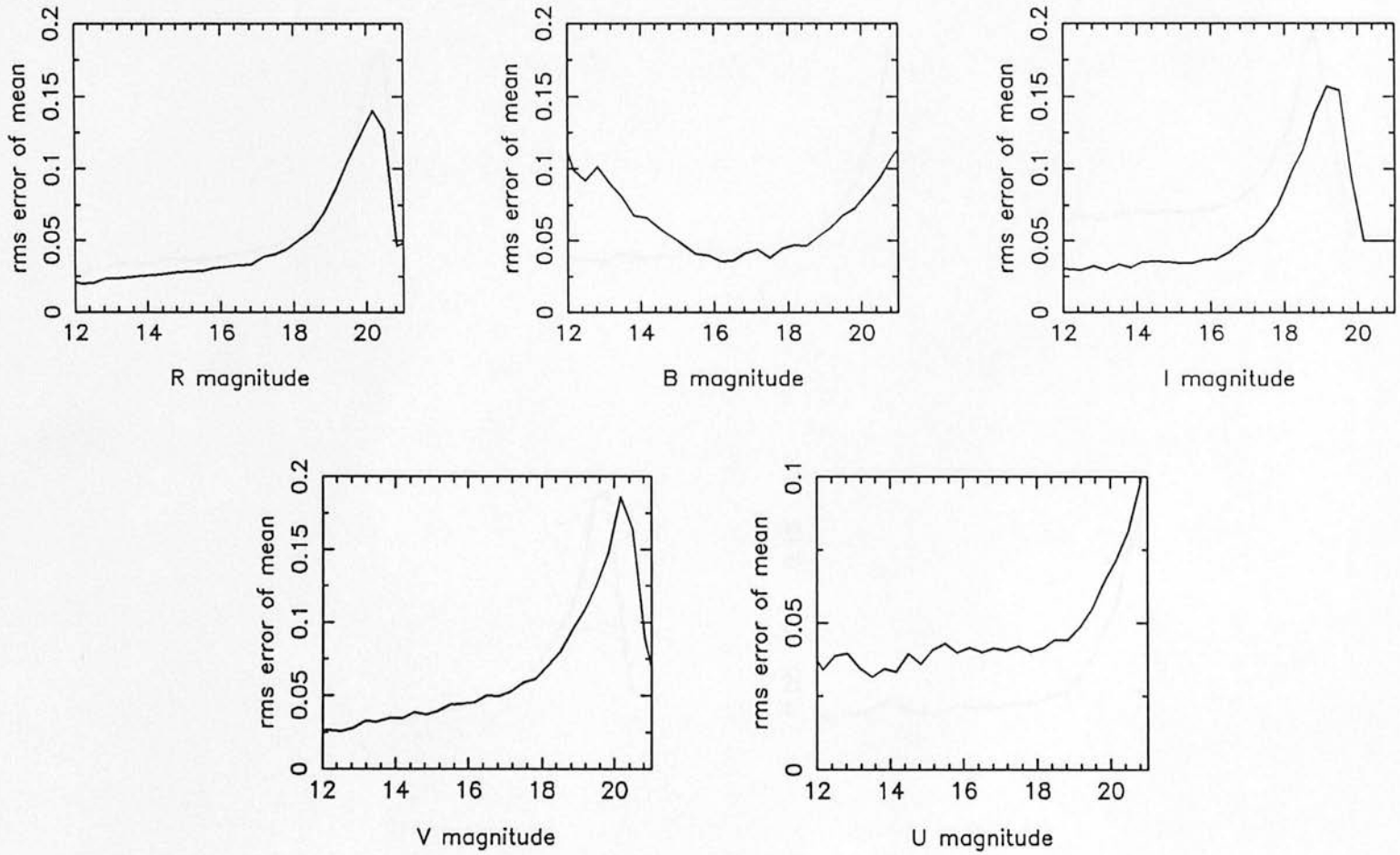

Figure 2.6: (b) Field 790.

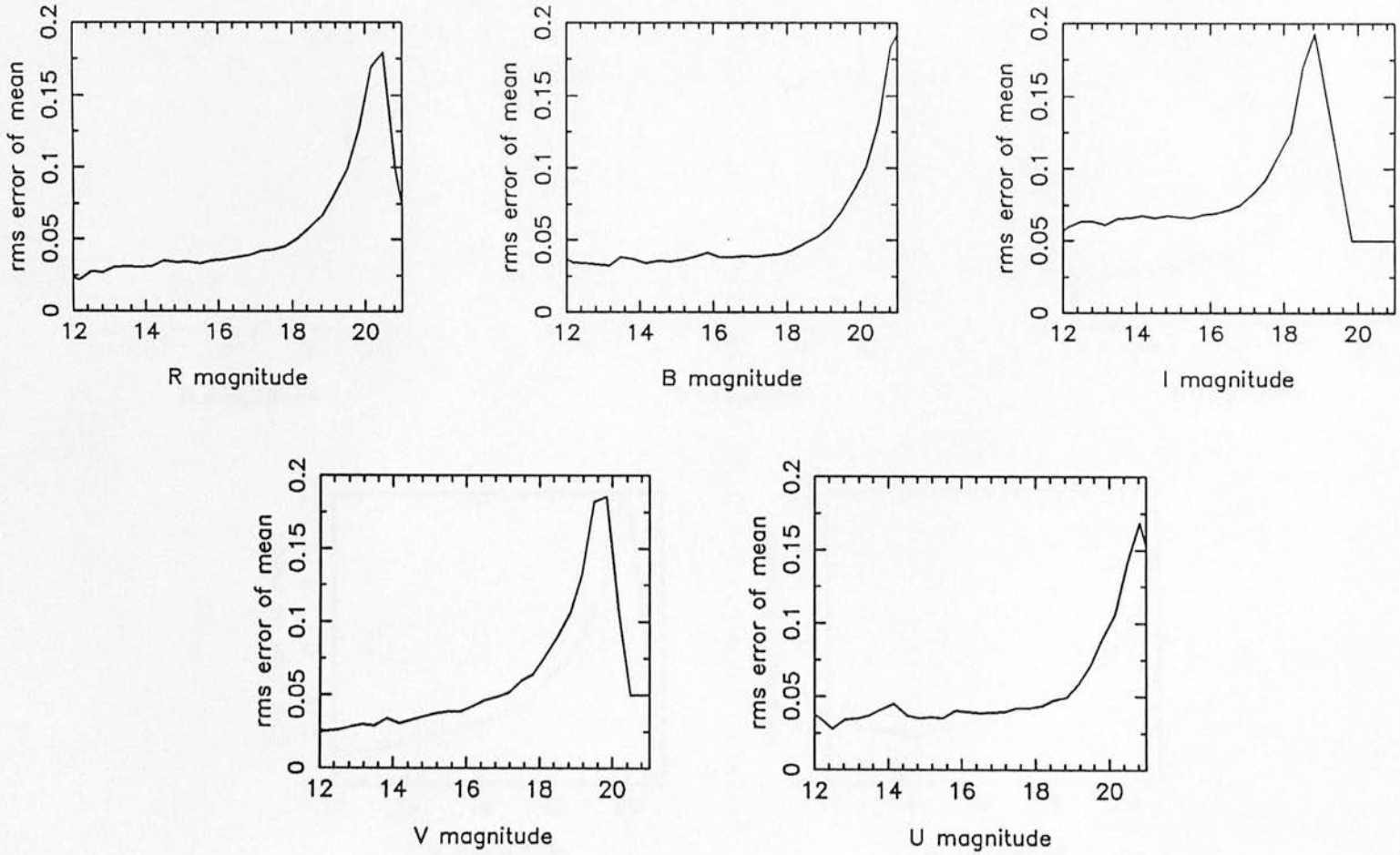

Figure 2.6: (c) Field 791.

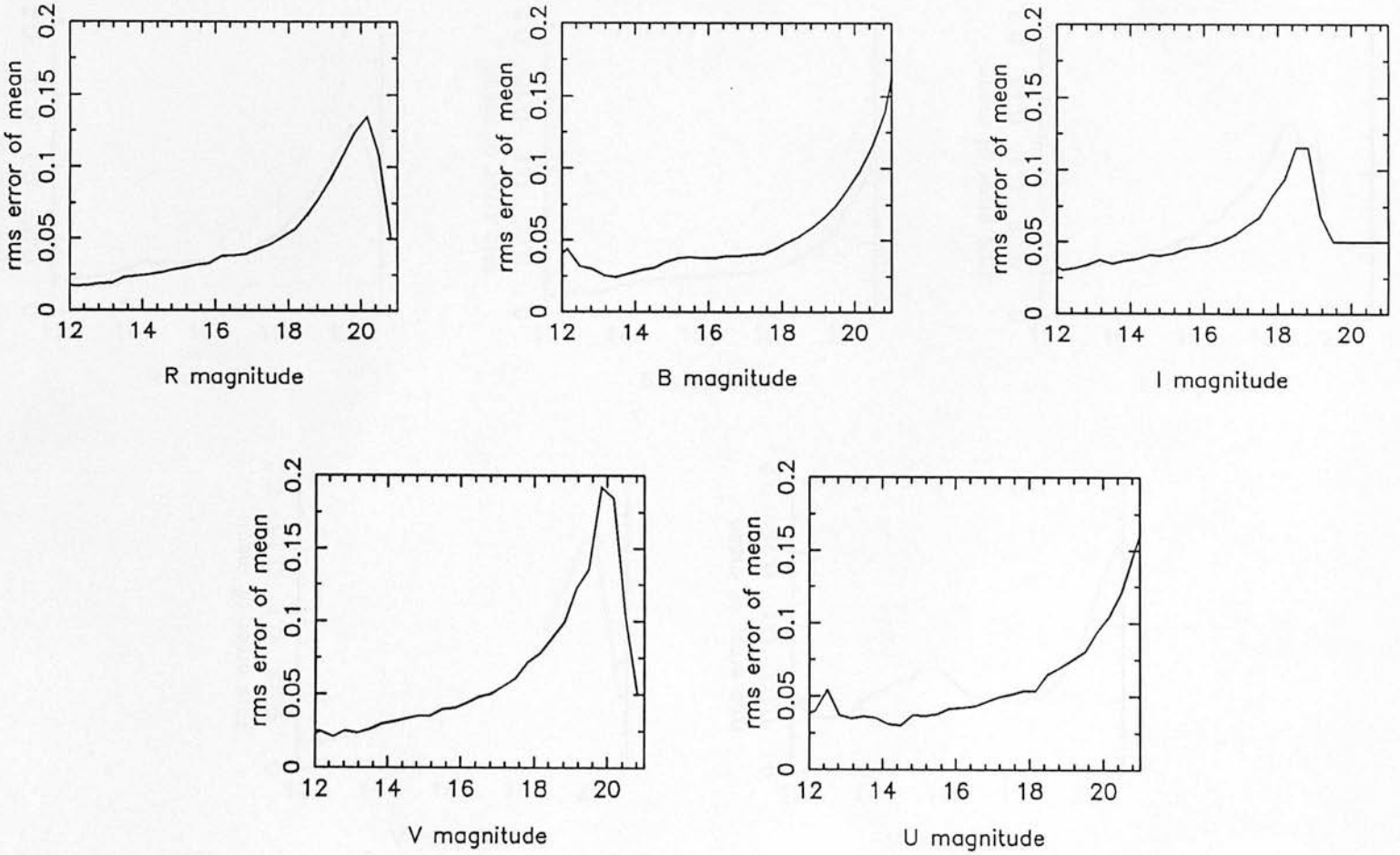

Figure 2.6: (d) Field 792.

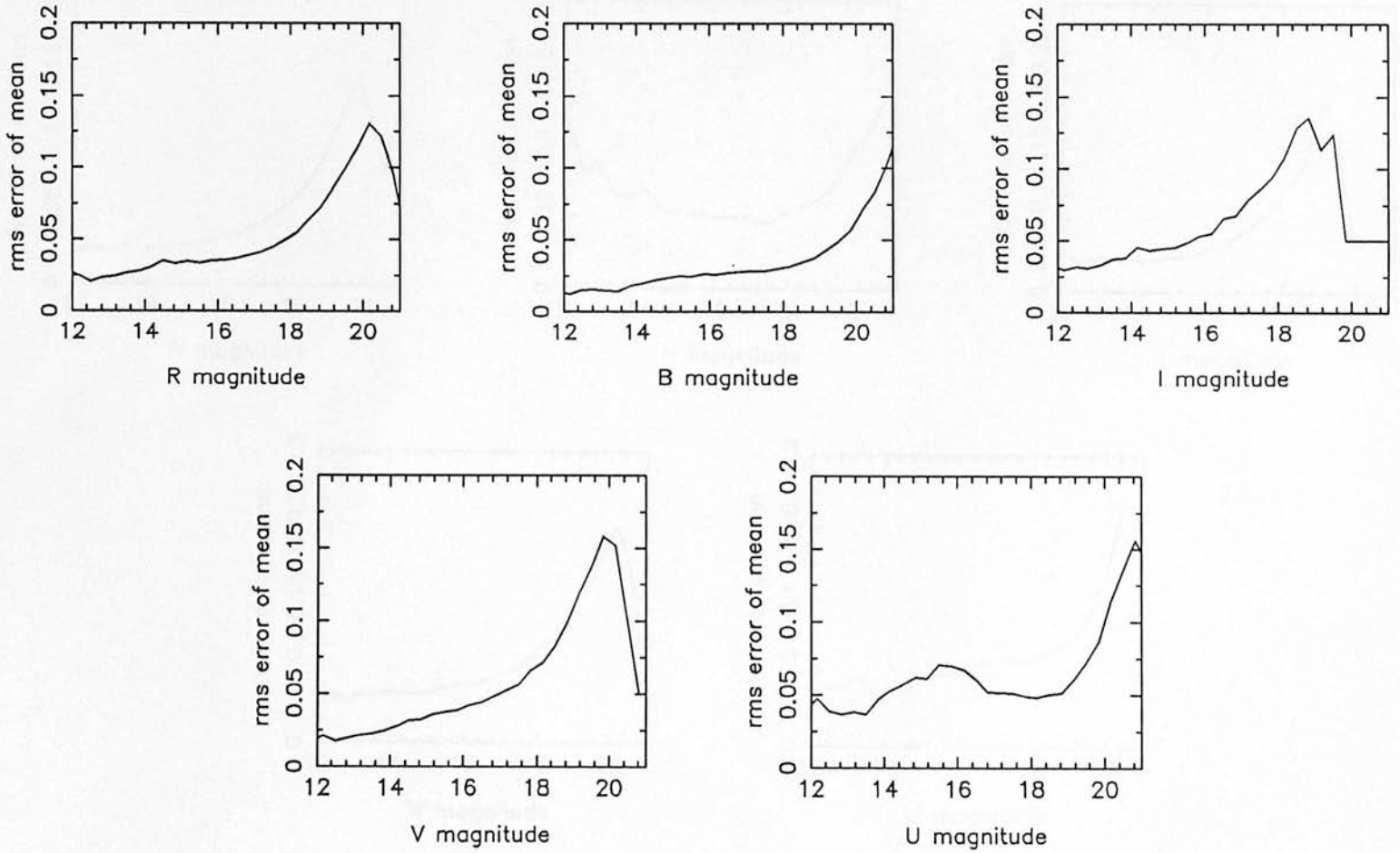

Figure 2.6: (e) Field 861.

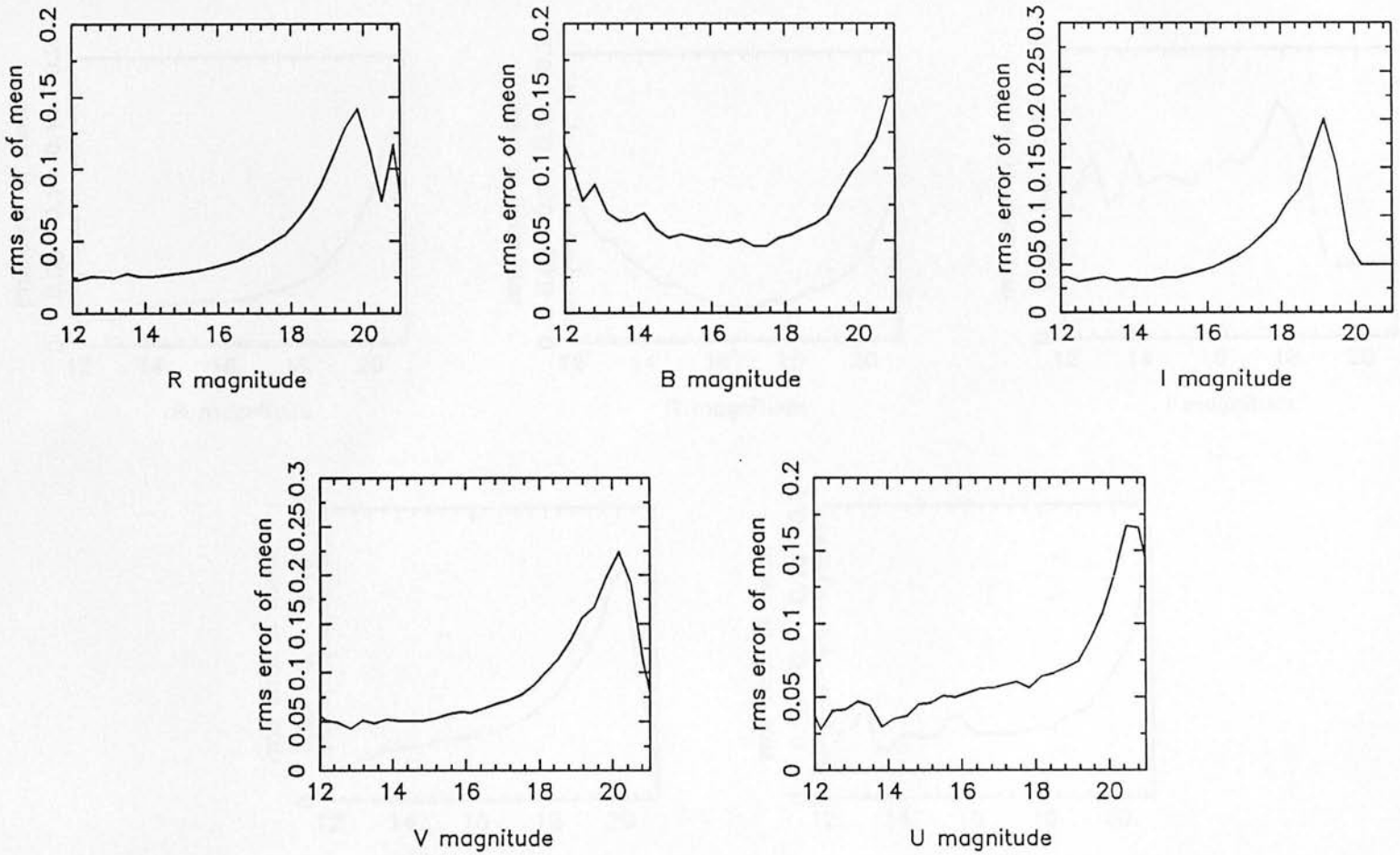

Figure 2.6: (f) Field 862.

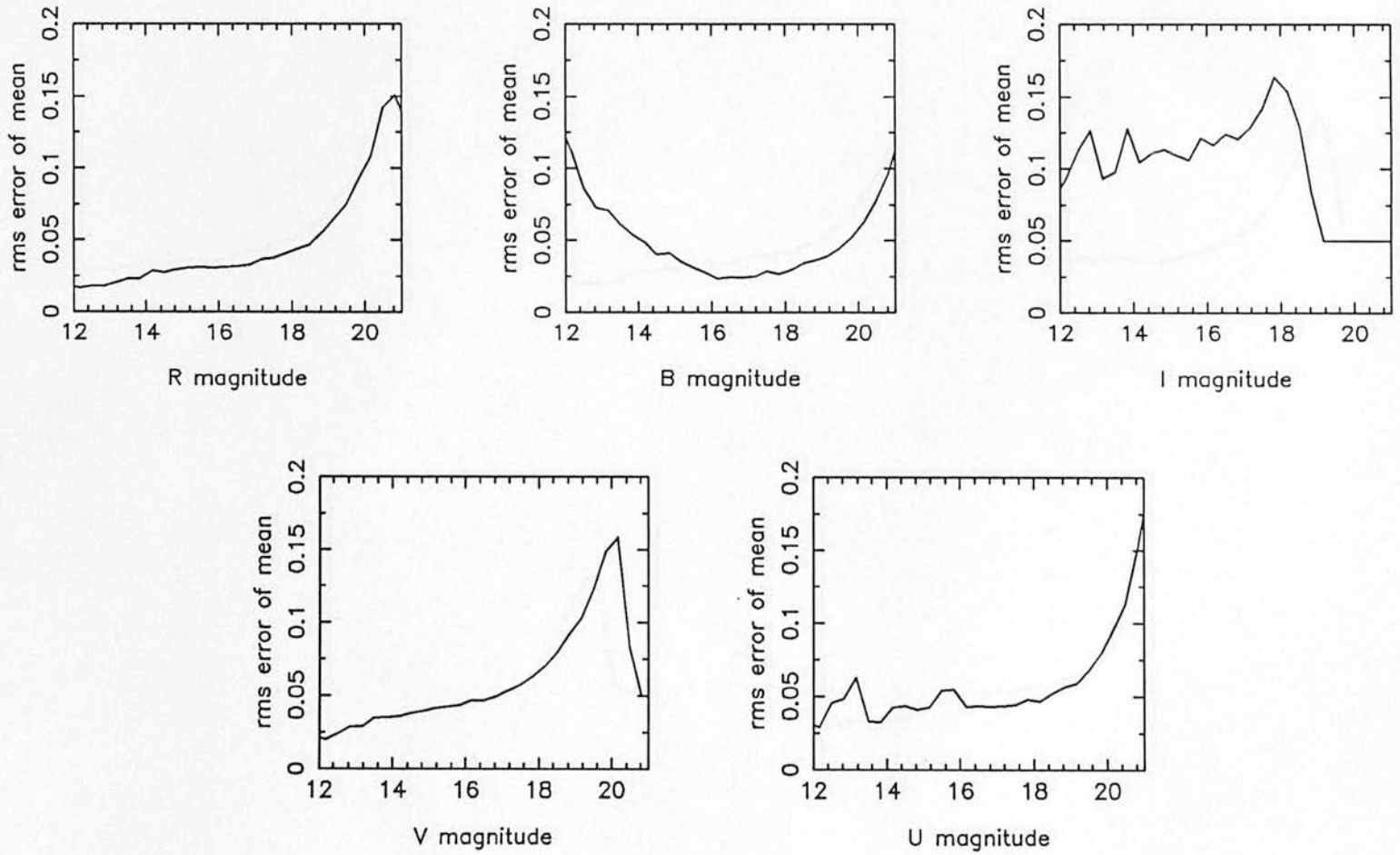

Figure 2.6: (g) Field 863.

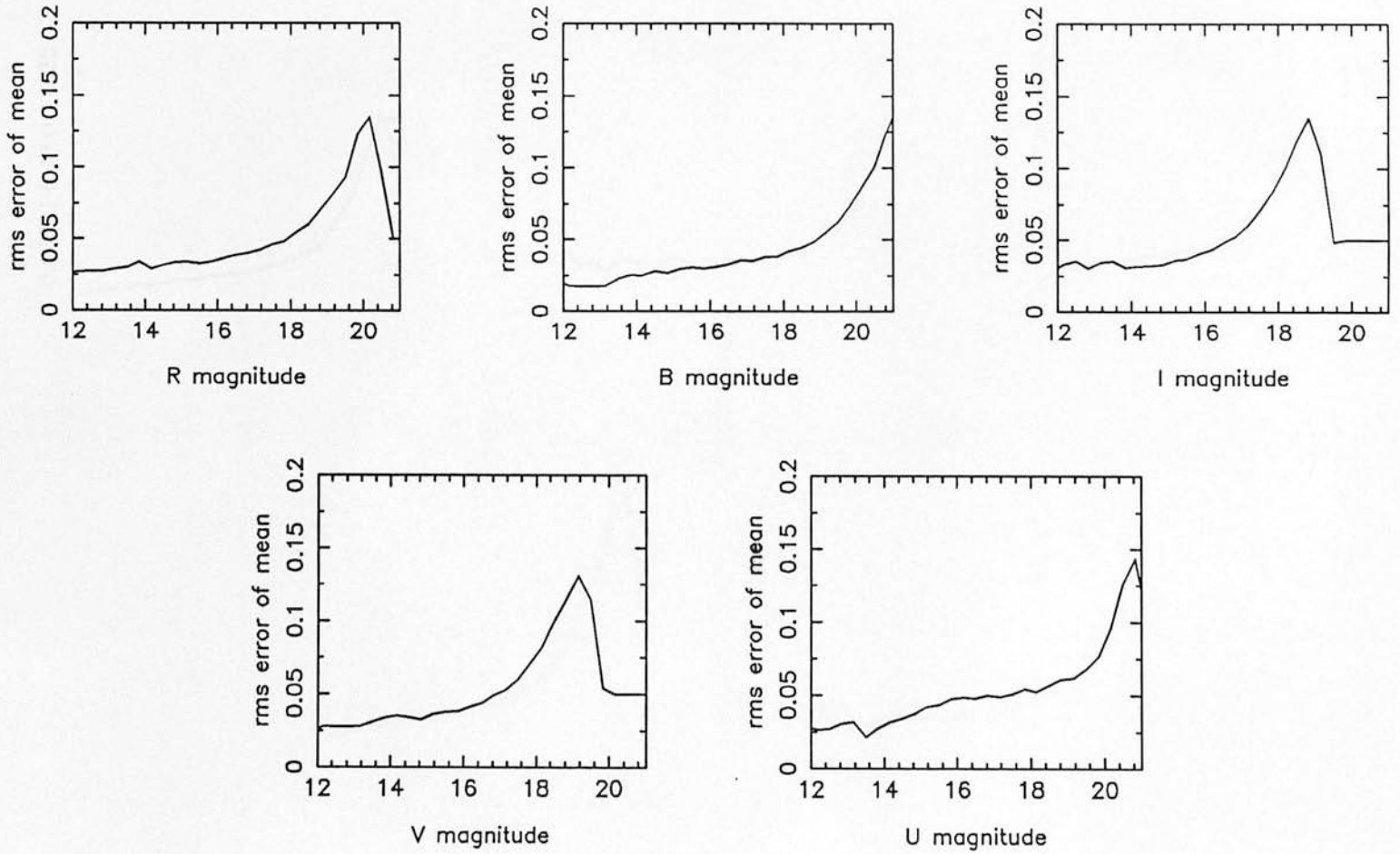

Figure 2.6: (h) Field 864.

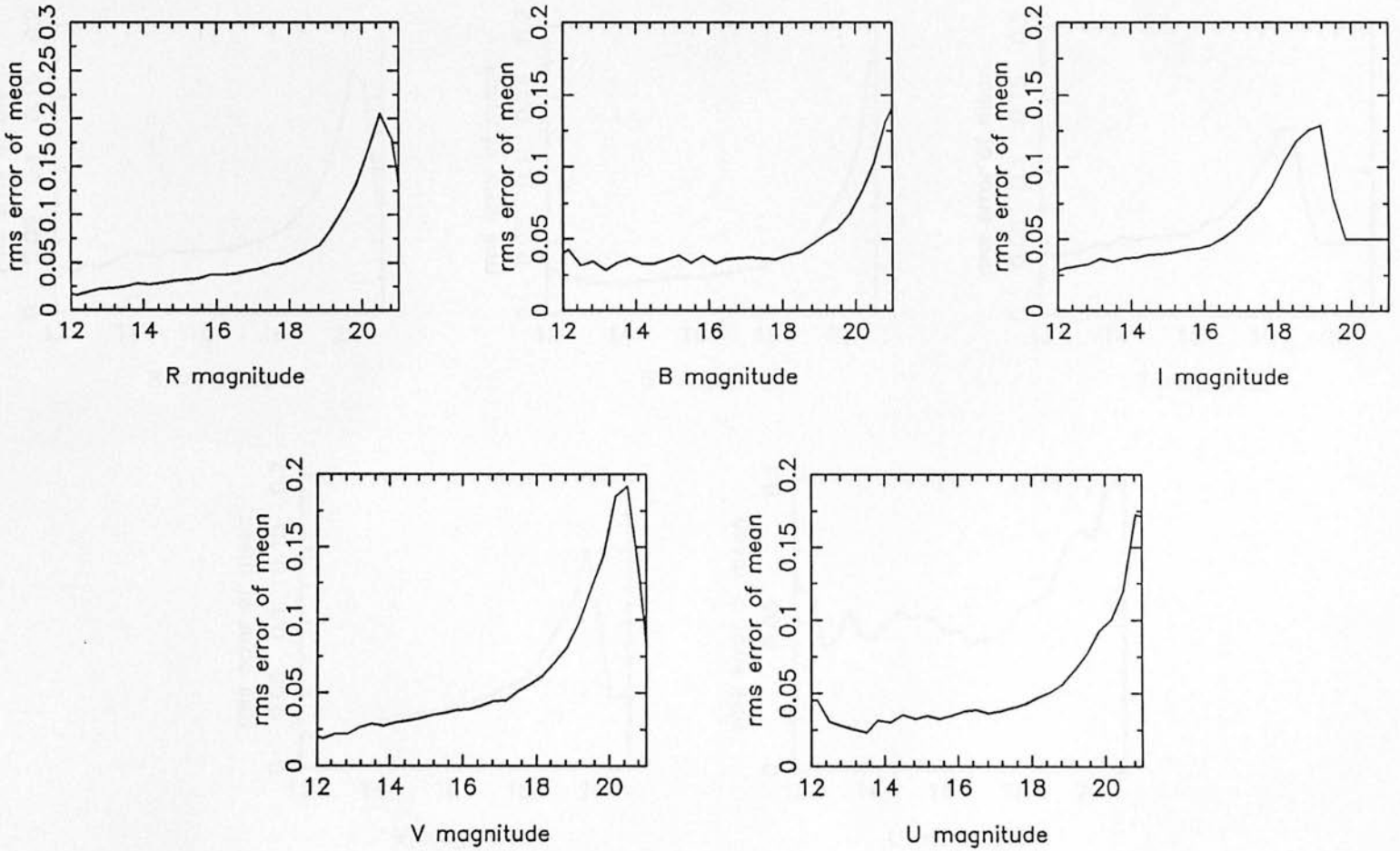

Figure 2.6: (i) Field 865.

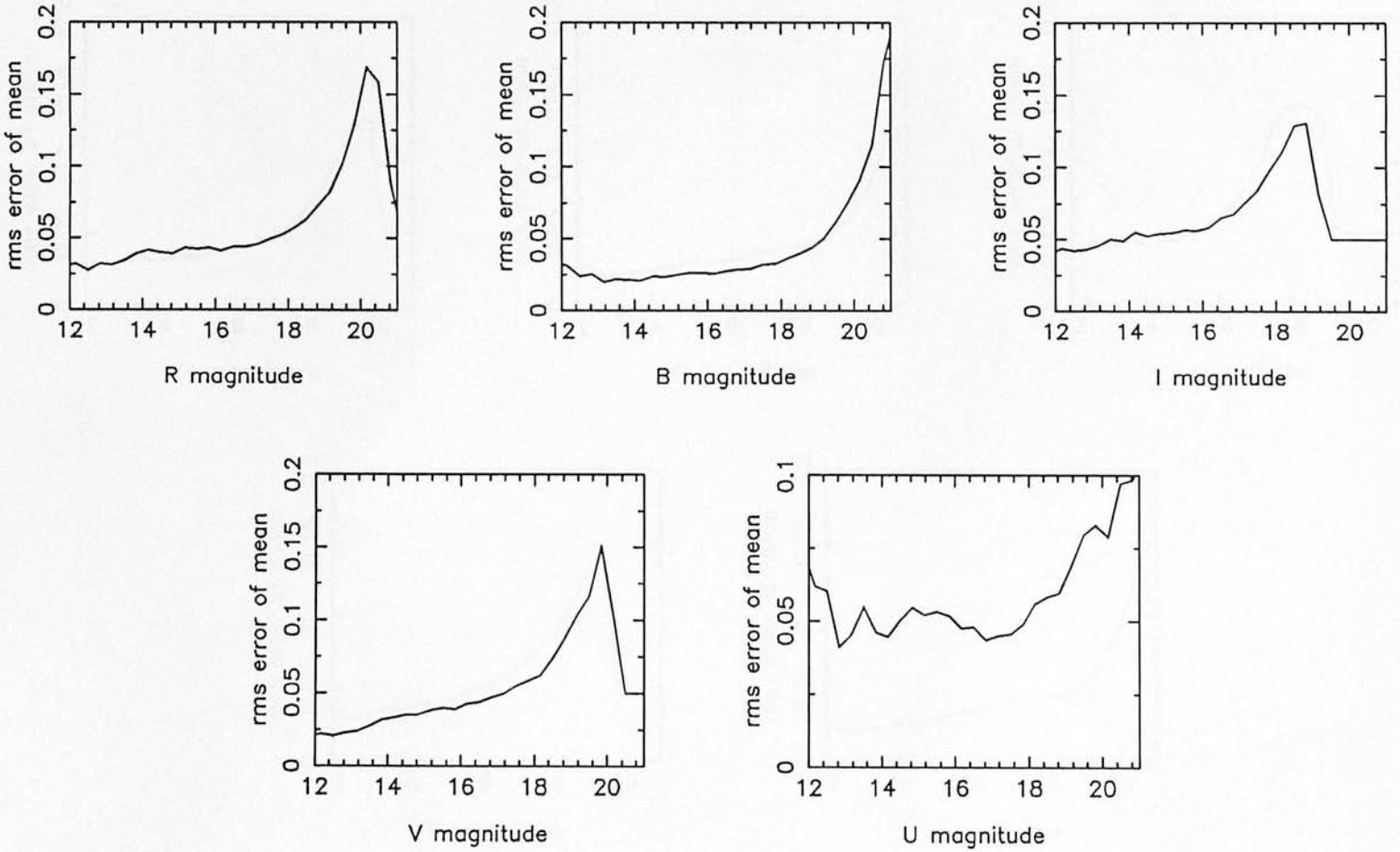

Figure 2.6: (j) Field 866.

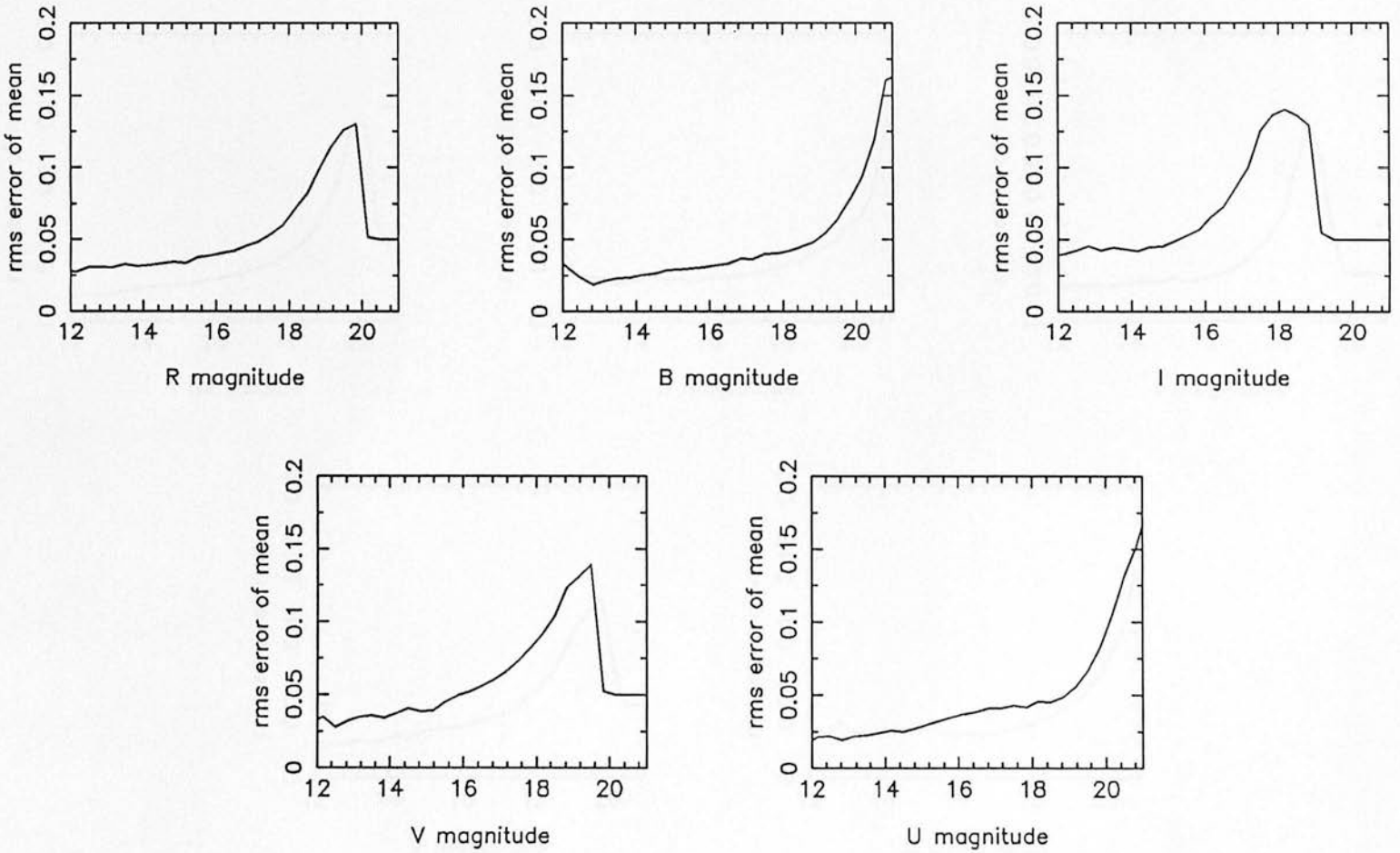

Figure 2.6: (k) Field 867.

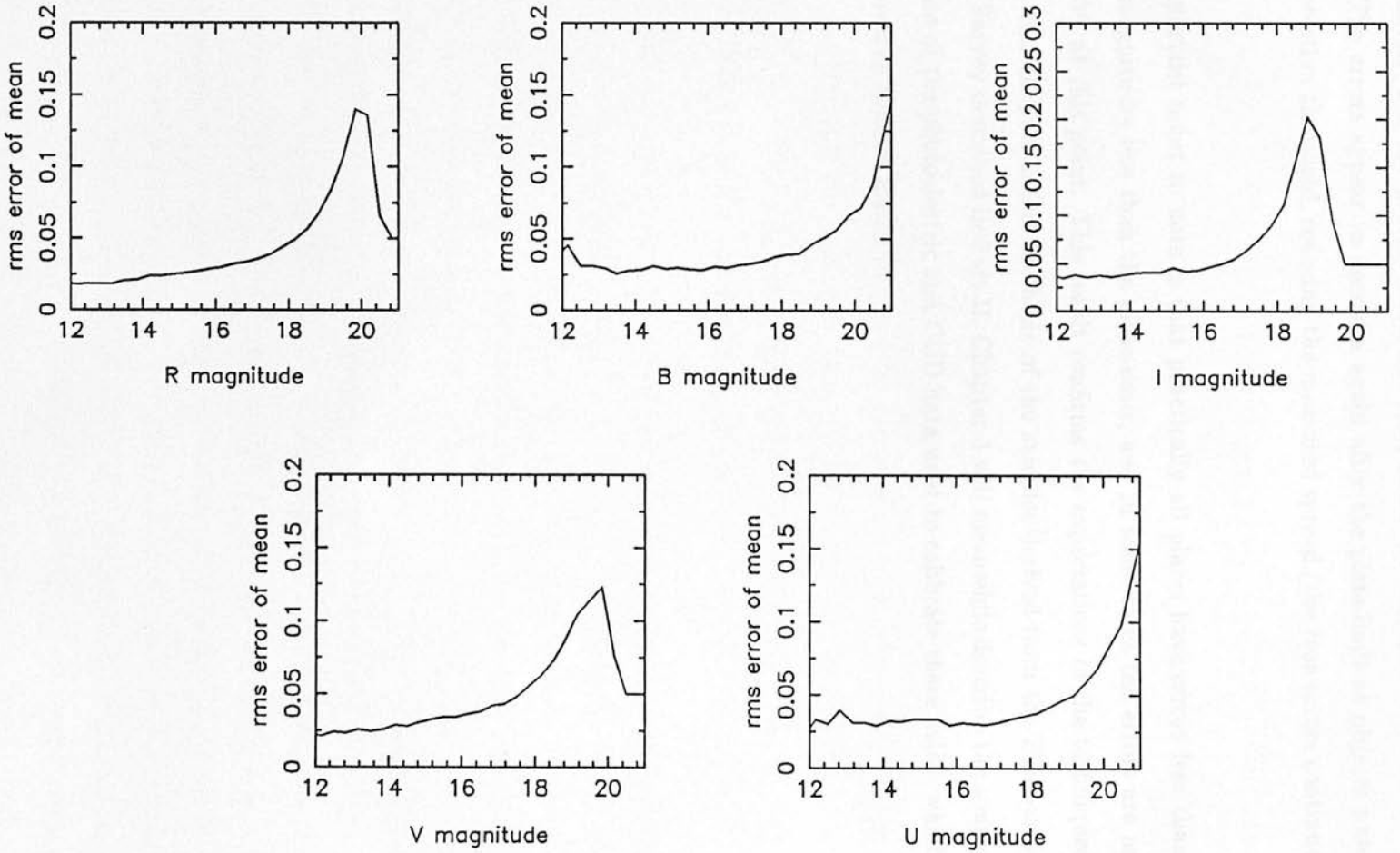

which would adversely affect any bright survey sample and require different techniques for their removal. For the present work however, these are unimportant as will be seen later. The errors appear to decrease again after the plate-limit as objects pass below the detection threshold, reducing the measured spread (the true errors continue to diverge).

The important point to note is that practically all plates have errors less than 0.05^{m} at 2 magnitudes less than the plate-limit, and in some cases the errors are as small as 0.03^{m} at this point. This result confirms the expectations of the techniques described in this chapter and is the basis of the samples derived from the Edinburgh Multicolour Survey described in Part II. Chapter 3 will meanwhile describe the source and treatment of the photoelectric and CCD data used to calibrate these fields, which was passed over in Section 2.4.3.

Chapter 3

Survey Photometry

3.1 Introduction

Chapter 2 has indicated the need for an accurately measured photometric scale in order to calibrate linearly the machine-derived magnitudes. The minimum necessary requirements for this is a sequence of calibrated stars in each field, covering a large range in apparent magnitude, and accurate to better than 0.05^{m}. In practice, several sequences scattered across each field are preferable, to tie down any photographic field effects.

Modern astronomical photometry has two main methods in operation at present. The principles of photoelectric photometry have been well understood since 1911 and the invention of the *photoelectric cell* which, because of its linear response to incident radiation in terms of the number of photoelectrons released, soon became a vital tool for standard astronomical measurements. This was furthered in 1930 with the invention of the *photomultiplier*, providing noiseless amplification of the electron current, and has remained popular ever since. In a typical set-up, light from a small diaphragm is focussed through a set of chosen filters and a Fabry lens on to a constant position on the face of a photomultiplier tube, producing a cascade of some 10^{6} secondary electrons at the last dynode for every photoelectron emitted at the cathode. The current at the anode is amplified through external electronics, converted into voltage pulses and counted electronically with a pulse discriminator. Sky-level determination is achieved through repositioning to some "empty" portion of sky nearby. The system itself and observing conditions may be calibrated by the observation of standard stars throughout each observing night.

A modern alternative to photoelectric techniques has become available in the last decade or so. The limitation of the former method is largely the time taken for each observation: by contrast, any 2-dimensional imaging technique can accumulate data for several stars during each exposure and information concerning image profile can improve the relative accuracy of measurement through 2-D spatial weighting. Charge-coupled devices (CCD's) were developed in the 1960's and provide the opportunity for 2-D imaging with very high quantum efficiencies. They consist of arrays of charge storage capacitors inter-connected such that charge can be transferred from one cell to the next with high transfer efficiencies. Each capacitor acts as an electron well, and arrays of around 500 x 500 cells provide spatial resolutions of fractions of an arcsecond. After a given period of exposure of the CCD to incident light, read-out is performed by means of successive "clocking out" of rows and columns in turn to the output amplifier.

Both techniques were employed in the calibration of the Edinburgh Multicolour Survey, as described below, and were used to produce more than 1200 CCD frames and a total of 7 nights photoelectric data. The acquisition and analysis of these data will be discussed in later sections. Some photometry already exists in fields contained in the survey, and these sources are first discussed below.

3.1.1 Existing photometry

UKST field 867 ($14^h\,30^m \lesssim \alpha \lesssim 14^h\,50^m$, $-2^\circ\,30' \lesssim \delta \lesssim 2^\circ\,30'$) has been well calibrated with photoelectric standards to $V < 16$ and corresponding CCD sequences to $V < 22$ as part of a galactic structure study constructed from photographic material from the UK Schmidt in Australia and the 2.5m Du Pont telescope of Las Campañas Observatory, Chile. 25 stars were observed in B, V, R and I with four different photoelectric systems in 867 (Stobie, Gilmore & Reid 1985), and these were supplemented by 27 stars within the measured area from CCD sequences in fields F867-5, -8 and -11, observed on the ESO-Danish 1.5m telescope at La Silla, Chile, and measured in B, V and I (Stobie, Sagar & Gilmore 1985).

Field 861 contained stars with CCD photometry measured by B.J. Boyle (private

communication) at the Anglo-Australian telescope in 1985, in bands U, B, V and R of which 7 were useful here. Field 863 was examined by R.M. Prestage in 1985 at the Steward Observatory 60″ telescope of the University of Arizona with the Catalina Photometer, an existing two-aperture photometer which he refurbished and for which automated software is now available, making the collection and storage of large amounts of data relatively simple. On a preliminary run, he observed 6 stars in U, B, V, R and I.

In order to extend the existing photometry to the whole survey area, extensive photometry was required. The intention was to establish sequences as deep as $B \lesssim 21$, zero-pointed in good conditions by use of the CCD as an absolute photometer, otherwise used to establish relative magnitude sequences, zero-pointed by the Steward data. Further observing time for photoelectric photometry was granted at Steward Observatory in 1986, again with the Catalina photometer, and CCD photometry at various sites. These are listed here, followed by abbreviations by which they will be referred in later sections: the Isaac Newton 2.5m Telescope [INT], La Palma; the University of Hawaii 88″ [UH88]; the University of Arizona 90″, Kitt Peak [UA90]; the ESO-Danish 1.5m, La Silla [ESO-D]). Section 3.2 will describe the acquisition and reduction of the CCD data, and Section 3.3 will discuss the photoelectric photometry. The application of these data to each COSMOS dataset will be covered in Section 3.4.

3.2 CCD photometry of selected regions

The availability of the COSMOS dataset for each field meant that it was possible to select areas containing stars with a suitable range in magnitude for the CCD observations in an automated way. A search was therefore performed for each field, and regions selected which satisfied specific criteria for each observing run (dependent on the size and orientation of the CCD chip on the sky for each instrumental set-up). The basic criterion used was that at least one bright photoelectric ($B < 16$) star appeared in the projected CCD area, with a specified minimum number of intermediate ($B < 18$) and fainter ($B < 20$) stars in the same field. Selected fields were compared, and ones with

the best coverage chosen automatically. From the selected areas generated, some quick visual checking was performed, and five areas chosen, as indicated in Appendix B. The following section will describe the various observing runs, strategies followed, and the resulting data obtained.

3.2.1 Observations and preliminary reductions

Table 3.1 presents details of the CCD photometry observing runs in 1986. The entries are ordered by date, and telescope, instrumentation and observers are given. A list of fields observed, and wavebands in which data were obtained follows.

As can be seen in this table, data in U are somewhat lacking: the basic problem of little CCD sensitivity in the blue, even after chip thinning, is compounded by the appalling state of some existing U filters: the only available filter for the ESO-D run was much too small, rendering useless about 30% of the chip. Severe vignetting problems were encountered also on the INT U data, and the sensitivity of the UA90 system in U was very poor, thus requiring very long integration times. These problems will be discussed in the next section, where individual aspects of each set of data are described. In general the weather conditions were very good, though not photometric; although photometric standards were observed on various runs, they were not eventually used.

The manipulation and analysis of the data was performed within the context of the Starlink "FIGARO" reductions package. Each of the instrumental/telescope systems posed different problems for reduction, and needed to be dealt with in a unique manner. However, there are several general processes that are involved in all direct CCD image reductions, and these are set out first below.

Before read-out of a CCD, the signal in each pixel is given a certain offset before conversion to a digital value. This is in general slightly variable both with temperature, and with position across the chip. In order to measure the variation in bias structure with position, it is customary to obtain zero (or negligible) integration time exposures, except where previous knowledge of the system makes such a check unnecessary. In

Table 3.1: CCD observations in 1986. Listed are the sites, dates, instrumentation, observers and UKST / CCD fields measured. Derived instrumental magnitudes can be found in Appendix B for all fields except those marked by a dagger, which are not reduced at the time of writing.

Field	Bands	Field	Bands	Field	Bands	Field	Bands
Isaac Newton 2.5m, La Palma: 16/17 May 1986 Instrumentation: RCA1 CCD 512 x 350 Observers: I.N. Reid							
793nf	UBV	794np†	UBV	865sp	UB	867cf	UBV
Isaac Newton 2.5m, La Palma: 27/28 – 31/1 March/April 1986 Instrumentation: RCA1 CCD 512 x 320 Observers: R.D. Cannon, W.K. Griffiths							
789cp	UBVRI	790cp	UBVRI	791c	UBVRI	793c†	UBVRI
861sc	UBVRI	862c	UBVRI	864c	UBVRI	865cf	UBVRI
ESO-Danish 1.5m, La Silla: 3/4 – 6/7 April 1986 Instrumentation: RCA CCD 512 x 337 Observers: P.S. Mitchell, L. Miller							
789s	BVRI	790nf	BVRI	792c	UBVRI	794c†	UBVRI
861sf	BVRI	861sc	UBVRI	863c	UBVRI	863np	BVRI
866cf	UBVRI	867s	UBVRI	867cf	R		

Table 3.1: (continued) CCD observations 1986.

Field	Bands	Field	Bands	Field	Bands	Field	Bands
University of Arizona, Steward Observatory 90″ Instrumentation: RCA CCD 512 x 340 Observers: P.S. Mitchell, R.M. Prestage							
793sp†	BVRI	794nf†	BVRI	794c†	UBVRI	861sp	UBVRI
863sp	BVRI	863sf	UBVRI	863nf	UBVRI	867np	BVRI
867cp	BVRI						
University of Hawaii 88″: 14/15 – 17/18 April 1986 Instrumentation: TI CCD 500 x 500 Observers: S.J. Lilly, L. Miller							
789np	VRI	789cf	UBVRI	791nf	UBVRI	792sf	VRI
793nf	VRI	794np	RI	794sp	VRI	862sp	UBVRI
863sf†	RI	864sf	UBVRI	865sp	VRI	866sp	UBVRI
867cf†	RI	867nf†	VRI				

practice, this "bias-frame" usually displays very little variation, and is not required. To take into account the systematic variations in bias level with time, the CCD's also have an "over-scan" region, at the side or top (or both) of the chip, which is not exposed to light, but clocked out at read-out time with the active area. The mean bias level at the time of exposure can be estimated from this, and subtracted from all bins.

Although CCD systems are cooled to the order of 150°K, there is still a small dark current contribution. This usually varies negligible across the chip surface, and is of such a low level, that the subtraction of a "dark frame", a lengthy integration with shutter closed which is subsequently scaled for each exposure time, is unnecessary.

Note that if the dark current is therefore ignored, its level (but not structure) will be removed in the case of a photometry routine which subtracts the local sky values before summing objects pixels.

The sensitivity of any CCD/telescope system will vary with pixel position and with wavelength. Large-scale variations in sensitivity across the chip are apparent in most cases, and small-scale pixel-to-pixel variations, in particular "cold columns" caused by charge transfer problems as the pixels clock out vertically, and "hot-spots" of non-linear response or excessive dark current, are also usually present. It is therefore vital to obtain "flat-field" frames, ideally consisting of exposures from a uniformly emitting source, in each waveband. Each data image is then divided by this frame. In order to retain the original peak pixel values in all objects, so that any saturation effects may be identified, it is important to normalise the flat-field frame to unity before division.

Three different approaches are usually possible when measuring the flat-field: (a) dome exposures, where a grossly out-of-focus white surface is evenly illuminated by some incandescent light or by a small amount of sunlight; (b) twilight exposures upon the sky in the evening or morning of observing; (c) flat-fields obtained during the night: here a 'blank' section of sky is used. Options (a) and (b) preserve valuable time in the night; however, the colour of dome lamps is very different to that of the night sky, and the resulting frames are not always a perfect match to the data. The twilight sky is a *better* match, but often still not perfect, and the difficulty in timing exposures correctly in the rapidly changing light is a disadvantage. Options (b) and (c) also may be affected by sky emission lines, which can produce severe fringing (see later comments) in long exposures. Finally, the removal of faint stars from "empty" sky exposures is often a problem.

In some cases, the read-out process can create charge losses when the CCD "wells" are near to empty. In the case of low sky background, this can cause severely distorted images. To correct for this, many systems provide a "pre-flash" facility, where the chip is exposed to a short burst of light before or during exposure, in order to partially fill up the CCD wells. A "pre-flash image" must then also be subtracted from each frame.

The final situation to which some of the data presented here are exposed is that of interference "fringing". The sensitivity layer of the chip is only a few microns thick, and because of slight non-uniformities in this thickness, light from night-sky emission lines can caused Fabry-Perot effects, which manifest themselves as fringes on long exposures, particularly in the red, following lines of constructive and destructive interference as the surface thickness varies. This in theory can simply be subtracted from the images, but in practice, these fringes are difficult to map, and their presence on flat-field exposures complicates the situation. In many cases, they must simply be tolerated as a systematic variation of a few percent.

3.2.2 Aperture photometry of the reduced frames

The next stage in the reductions was the photometry itself, and the derivation of instrumental magnitudes. Two main types of photometry are appropriate here, aperture photometry, where object pixel values are simply summed (with weighting if desired), and profile fitting, where the area under a curve fitted to the stellar profile is calculated. The first approach was used here; a substantial revision of existing code however was required, and brief details of the method are appropriate here. The basic difference lies in the weighting of aperture sums: in order to maximise signal-to-noise in an image, it is necessary to weight pixels according to their position from the object centroid, with a function derived from the image profile (the same weighting function must of course be used for all objects in a given sequence). Accordingly, it was necessary to estimate a good approximation to the seeing profile for point sources. The following form was found to fit the general profile well:

$$GW(r) = \exp\left(-\frac{1}{2}\left(\frac{r}{\sigma}\right)^{\gamma}\right) \tag{3.1}$$

which is a modified Gaussian, where σ and γ are free parameters, which are estimated from several stellar profiles on each frame. In general, values of $\gamma \simeq 1.8$ provide acceptable fits, with σ being matched according to projected pixel size and the seeing.

Reduced frames were examined and approximate object positions for all but the faintest point-like objects marked. A routine for locating the centroid of these images was used and positions in fractions of a pixel derived. At the same time, appropriate σ and γ values were chosen interactively from image profiles (a limitation here is the assumption of radial symmetry — trailed images would be given less accurate weighting; however errors in this profile match only serve to increase somewhat the measurement error, and do not systematically affect relative photometry). Pixel values were then summed within five different object apertures and the mode of the sky distribution calculated from a concentric circular aperture around the object, with aperture sizes chosen according to various aspects of the data, e.g. projected pixel size and seeing (contamination by surrounding objects was dealt with to some extent by an iterative high pixel rejection technique, although all images were examined visually before reduction). Instrumental magnitudes for each aperture were obtained. Checks on the reliability of each result included the examination of a sky histogram, and the opportunity to check that derived magnitudes converged at the final aperture size chosen.

Random errors for each magnitude derived were calculated from contributions from (a) the weighted Poisson shot error for total (electron) counts in object pixels, (b) the weighted Poisson error for sky counts from the calculated sky error, and (c) the readout noise contribution for object pixels. In practice, these values were found to be lower limits on the true error.

Various situations can give rise to systematic errors and every attempt was made to identify these. These included flagging objects specifically where: (a) apertures extended beyond the CCD edges; (b) apertures extended into the bias strip; (c) pixels exceeded the quoted maximum value in the linear regime (hot spots and genuine saturation); (d) pixels fell below a stated minimum level (cold columns); (e) there were too few sky pixels (limit 20). Unfortunately, no reliable automated way was found to allow the tying together of incremental exposures and different sequences, and a large fraction of time was spent simply doing this.

These reductions were carried out principally by myself over the period between these observations and the spectroscopic observing runs described in later chapters;

however, mention should be made here of the help given in the final stages by R.S. Stobie in particular, and also S.K. Leggett and M.R.S. Hawkins.

3.2.3 Specific comments on individual reductions

A list of the idiosyncracies and limitations of each dataset is given below. These extensive comments are not made as a criticism of the quality of the data: as will be seen, the results obtained were on the whole very good, and most calibrations problems were intrinsic to the COSMOS, rather than the photometric data. Detailed mention is given for each dataset as an indication of the care taken in the treatment of the data.

3.2.3.1 ESO-Danish 1.5m observations

These observations were conducted over the period from the night of the 4^{th} to 7^{th} April 1986 at La Silla, Chile, by myself and Lance Miller, using the RCA CID53612 chip, *B* and *V* Johnson filters, Gunn *GR* and *GI* filters, and a very poor 1-inch *U* filter, which, in a 2-inch holder, gave rise to very bad vignetting effects (the Johnson *U* filter was unuseable due to a severe red leak). The chip has a full area of 350×520 30 μm pixels, with a projected pixel size of 0.47″, read-out noise of 85 e^-, and a gain of 17.8 e^-/ADU. The chip is cosmetically quite poor, with many hot-spots and cold columns, which were avoided for data reduction. The weather was very good, with seeing in the range 1.2″ – 2.2″.

According to the manual, no dark frame was necessary for this data: the level is extremely low ($\sim$ 0.002 ADU/s/pixel) and thus was not subtracted. However deep frames exhibited some increase in level towards the bottom left-hand corner, the final read-out point, probably attributable to dark current — consequently stars in this corner were avoided in subsequent procedures.

The bias level varied little during the night and was subtracted as a simple constant calculated from the bias strip. There was some "spill-over" of charge from the active

area, such that columns 320–334 declined smoothly from a high value to a more realistic bias count of about 180 ADU. Plotting this decline led to the conclusion that a value calculated from columns 335 and 336 gave the best results, and could only be over-estimating the zero-level by $\sim$ 0.2 ADU. This was confirmed in that some reduced frames contained on average slightly negative sky values: subsequent sky subtraction however dealt with this properly.

Flat-fields were obtained from twilight exposures inside the dome, and averaged for each night. As already noted, the poor *U* filter gave rise to quite bad vignetting, particularly at the top and bottom of the image. In theory, this could simply be corrected as a sensitivity variation by the flat-field, but in practice, large gradients were still apparent. The variation in position of the filter as it fell into place was diagnosed as the problem, so that a slight shift in position could cause significant errors because of the very steep gradient of the sensitivity curve. However, simply applying a shift to the flat-field position, thus correcting for large-scale variations, also shifted the small-scale components, which are a facet of the chip itself. A partial solution was found by median filtering the flat-field frame (a box of 25x25 pixels was used for each median calculation), effectively creating a map of the large-scale structure. The flat-field was then divided by this map, and the small-scale structure isolated, which was used to correct the image frames in the usual manner. The vignetting was removed by translating the median-filtered flat-field with respect to each series of image frames a few pixels in the X and Y directions, until satisfactory results were achieved. This method was found to work well: however, it was important to exclude stars where surrounding sky displayed some residual gradient, and this further reduces the data available in this band.

A manual pre-flash was in operation at the time of observing, consisting of a 0.6 ms flash during a pause in integration, amounting to about 180 ADU. This successfully overcame the charge transfer problems producing undistorted images. The pre-flash images displayed significant structure and were an important step in the reductions.

All fields were exposed for short, intermediate and long integration times to span the gap between low signal-to-noise and saturation (non-linear at $\sim$10,000 for all objects

over the whole magnitude range). Average long integration times necessary were as follows: U: 1800s, B, V and R: 300s, I: 600s. Clearly the U photometry was by far the most difficult and was in practice not pursued excessively at the expense of other data.

Having reduced the frames, the photometry was fairly straightforward, though time-consuming. Objects were given a range in apertures up to a diameter of 25 pixels, with sky values evaluated in a surrounding annulus of 25–30 pixels diameter. All object magnitudes converged at these distances and sky histograms verified to be symmetrical.

3.2.3.2 INT 2.5m observations

Two sets of observations were carried out at the Observatorio del Roque de los Muchachos del Institutio de Astrofisica de Canarias, La Palma, the first on the period of 27th to 31st March, by R.D. Cannon & W.K. Griffiths in *UBVRI* (hereafter INT1) and the second on the night of the 16th May by I.N. Reid, using filters U, B and V (INT2). In each case, the RCA1 chip was used, with an active area of 500×320 pixels, a gain of $4\,e^-$/ADU, read-out noise of $55\,e^-$, and a pixel size of 0.735″. Standard U, B and V filters were employed, and Cousins R and I.

No dark frame was used in either case, and bias reduction was simple in both cases: although some charge leaked into the first few bias strip columns, columns 340 to 345 were clear of these effects, and so were used as level indicators. Bias frames showed very little structure and were scaled accordingly (an averaged frame was used for INT1 data).

Flat-fields were obtained both from twilight sky and illuminated dome methods; in practice the dome flats were found to fit the data better in many cases. The U flat-field was again badly vignetted and appeared to shift in position occasionally. The same method as above was applied where necessary.

Fringe-like structure was apparent on close inspection of the redder flat-field frames,

whose origin is unknown, and indeed is not expected on dome flat-fields: however there may have been some external light entering the dome at the time of observations. Very deep image frames also exhibited this structure to a slight degree, but no way was found of removing it without introducing further uncertainties. It was decided to treat them as a genuine part of the flat-field, i.e. as a multiplicative, rather than an additive effect. The variations were at the 1–2% level on the flat-field frames and flat-field division did not visually deteriorate any of the deeper data, improving the uniformity in most cases.

Photometry was then performed on all frames, again using 25 pixel diameter apertures and the results combined to produce sequences over a large range in apparent magnitude. The data for run INT2 were however difficult to tie together in some instances (only two incremental exposures were used, e.g. 300s and 5s), and the restrictive dynamic range of the system left few stars between the signal-to-noise limit and saturation. In some instances, faint and bright sequences in the same field could not be tied together with any certainty, and were left to "float" independently.

3.2.3.3 University of Arizona 90″ Observations

These observations were carried out on the nights of the 16th and 17th April 1986 by R.M. Prestage and myself with the Steward Observatory 90″ telescope at Kitt Peak, using a similar RCA CCD thinned for blue response. The characteristics of the system were: 55 e^- readout noise, a gain of 4.98 e^- per ADU, and a pixel size of 0.30″, which, combined with the seeing, gave very large stellar images on the chip. The weather was reasonable, though not photometric, with seeing estimates of 2–3″. Broad-band Johnson filters were used. U data were again very difficult to obtain, and required long integrations.

Bias subtraction was performed again by the scaling of an averaged bias exposure (with very little structure) with a value derived from the overscan region. The dark frames were not used, adding only about 2 ADU to the longest U exposures, and displaying little variation.

Some low-level (<2%) fringing effects were seen on the flat-fields, which again had to be allowed for in the absence of fringe-frames. In this case, no such effects were seen in the deepest image frames, and the problem became how to remove them entirely. Median-filtering could not help here, as the "structure" of the variations was intermediate between large and pixel-to-pixel scales. An attempt was made to produce a correct flat-field, using software devised by A.R.G. Mead, where many long-exposure sky-limited image frames can be "stacked" together, scaled, and the median value for each pixel derived (highly deviant values, such as those caused by the presence of stars are iteratively removed) thus mapping the variations. This was partially successful, and was employed when an improvement in genuine noise above the "fringing noise" could be achieved, i.e. stacking 7 V images of approximately 1000 ADU mean sky values each gives rise to an random noise level of $\sqrt{35000}/35000\,e^-$, or 0.5%, which is clearly smaller than the 2% fringing error.

Very large apertures were required for the large stellar images on these data: object apertures of $\sim$ 35 pixels converged, and 35–40 pixel diameter annuli were used for the sky. For some data the sky was nevertheless hard to estimate because so much of the chip was covered by images.

3.2.3.4 University of Hawaii 88″ Observations

The nights of the 15th to 18th April 1986 were allocated for CCD photometry at the Institute for Astronomy (IFA). L. Miller and S.J. Lilly obtained data in *UBVRI* with a thinned backside-illuminated Texas Instruments (TI) chip of dimensions 500x500. The gain was $3\,e^-$/ADU, with readout noise of $25\,e^-$ rms. The projected pixel size was quoted as 0.41″ (later measures of the projected pixel size modify this figure a little). An alternative blue-sensitive focal reducer with a smaller pixel scale was adopted on the final night for U, B & V exposures, and charge from individual pixels are added on the chip prior to readout as a single charge packet so that data were obtained in a 2x2 format.

An averaged, scaled bias frame was again used, and no dark frame required — the

dark current only contributed ~1 ADU per minute exposure. Flat-fields were obtained from a choice of dome lamps and corrected the image frames very well for both formats. Aperture photometry was again carried out as above, with an object aperture of 25 pixels diameter. The projected sky area covered by the chip however was small, and many offset exposures were required, displaced in position to fainter areas of each bright sequence. The tying together of large sequences was consequently very hard.

Results for all CCD data can be found in Appendix B, listed by field number, and showing celestial positions and results in each waveband. The next step, the tying up of CCD measurements with objects in the various HAGGIS catalogues, is left until after a discussion of the acquisition and reduction of the photoelectric data.

3.3 Photoelectric photometry

3.3.1 Observations

Observing time was allocated from 6^{th} to 14^{th} May 1986 on the Steward Observatory 60″ telescope, one of the Catalina group of telescopes on Mt Lemmon, Tucson, Arizona. The observers on the run were myself and R.M. Prestage, who rebuilt the Catalina photometer, a single-aperture device made substantially automatic by the recent development of an operating system. This was used in conjunction with available photometer *UBVRI* filters, close to the standard system.

Observing conditions were variable: nights 6 and 11 were lost totally with heavy cloud, while nights 10, 12 and 13 were completely clear and exhibited good seeing. Nights 7, 8, 9 and 14 appeared almost totally clear, although conditions during the day were variable and the consistency of the data during the night occasionally showed evidence of variations, as described below.

The operating system allowed the definition of procedures for each object, in terms

of filter order, integration time etc. Sky values for each filter were measured by applying a "wobble" to an adjacent position on the sky, checking for stars in the eyepiece, and integrating. Because all observations must be identified with a unique airmass, defined by the mean time of observation, filters were symmetrically ordered for each sky observation around the midpoint. A comparable number of standard stars were taken throughout each night compared to program objects (~20), in order to properly constrain the atmospheric behaviour throughout the night, and to properly determine colour transformations.

3.3.2 Reductions

The majority of the reductions were performed using a modification of a program by P.B. Stetson, called "PEPHOT"; the method is well described elsewhere, and so will not be thoroughly revised here, but a sketch of the philosophy behind the method is included below. Some of the initial sorting of data, and preliminary reductions were performed in collaboration with R.M. Prestage at the University of Arizona.

In the traditional approach, the conversion from instrumental magnitudes to a standard photometric system such as *UBVRI* is achieved through two sets of "standard" star observations: (a) "extinction" stars, observed over a large airmass range, to measure atmospheric absorption for each band as a function of hour angle; and (b) once this has been corrected, regular observations of stars with documented photometric indices, to enable the transformation from instrumental to standard systems. In the approach taken here, these two transformations are combined in one set of equations (as suggested by Harris, Fitzgerald & Reed 1981); the terms considered here are set out below:

$$v = V + A_{11} + A_{12}(B-V) + A_{13}(B-V)^2 + A_{14}X + A_{15}(B-V)X + A_{16}t + A_{17}t^2 - A_{18}\,\partial V/\partial\tau \quad (3.2)$$

$$b-v = A_{21} + A_{22}(B-V) + A_{23}(B-V)^2 + A_{24}X + A_{25}(B-V)X \quad (3.3)$$

$$u-b = A_{31} + A_{32}(U-B) + A_{33}(U-B)^2 + A_{34}X + A_{35}(U-B)X \quad (3.4)$$

$$v-r = A_{41} + A_{42}(V-R) + A_{43}(V-R)^2 + A_{44}X + A_{45}(V-R)X \quad (3.5)$$

$$r-i = A_{51} + A_{52}(R-I) + A_{53}(R-I)^2 + A_{54}X + A_{55}(R-I)X \quad (3.6)$$

Note that not all these terms were necessary or even desirable (see below). Here, the instrumental and photometric systems are defined by lower and upper case letters respectively. Allowance is made for a zero-point shift between systems, first- and second-order colour terms, and a linear and colour-dependent airmass (X) term (coefficients 1 to 5). Higher terms than this in colour are not expected (the instrumental system matches the photometric fairly closely) and higher terms in atmospheric absorption are only required at very high airmasses (all measurements here were made with $X < 2.2$). Additional terms for time(t)-dependence, and dead-time(τ)-dependence are included in the first equation (these terms are assumed to cancel for colours). Dead-time is a measure of the effective resolution time of the detector, an allowance for coincidence counting, whose behaviour is commonly expressed in the form:

$$N_{true} = N_{obs}(1 + \tau N_{obs}) \quad (3.7)$$

where the N's refer to counting rates. τ may show some variation from the canonical value quoted for the instrument, and the coefficient A_{18} in the above transformation is included so that such a variation can be fitted as a free parameter, where $\partial V/\partial\tau$, the derivative of the V magnitude with respect to τ, is calculated from raw counts. However, τ must be corrected explicitly once A_{18} ($= \delta\tau$) has been calculated, and this term removed from the transformation equations, so that *all* instrumental indices are coincidence-corrected with an accurate dead-time estimate.

The procedure calculates coincidence-corrected counting rates in each filter from the system dead-time value, resulting instrumental magnitudes, and the Poisson measurement noise errors on these figures. For the standard stars (hereafter "standard"

refers specifically to those stars whose photometric indices are known, in contrast to "extinction" stars, which may not have this information available) the mean error is calculated from (a) the Poisson shot noise for the observation, (b) the mean error associated with the documented measurement, and (c) a "nightly mean error", which is a measure of the photometric quality of the night, assumed the same for all observations, and comprising low-level sources of error not already accounted for such as scintillation and instrumental effects. A weighted least squares fit is performed for each index with initial guesses for (c) in each index, and the transformation equations inverted to give values for the photometric indices of each extinction star and standard star. Residuals are in turn calculated for the standards, and the "nightly mean error" adjusted on comparison with the expected rms residuals: iteration is performed until the nightly error ceases to change, becomes $\leq 0.0003^{\mathrm{m}}$, or $\geq 1^{\mathrm{m}}$ (presumably the result of some faulty standard star measurement). Upon completion a list of standard star residuals are produced for checking. Any deviant objects ($> 2\sigma$) are flagged and may be removed at this stage, and the fit re-done.

If the results are satisfactory, the equations are again transformed and photometric indices for the program objects obtained. Standard errors on these values are computed from the Poisson shot noise and the "nightly mean error".

The raw data from the instrument were obtained in text-file form, with one entry for each integration. Details given were the mean UT of the observation, the object name, the filter in place, the integration time, "star" or "sky" observation information, followed by the total count. The entries were checked for consistency and combined into single start and sky counts and integration times for each filter, while also being labelled as "standard" or "program" objects. A further stage was necessary to collect these data into a form suitable for the reductions package, to include standard star photometric indices with errors and object positions, and to derive local sidereal times at mean observation time. A FORTRAN routine to perform the latter calculation can be found in Henden & Kaitchuck (1982), which covers most areas of photoelectric photometry and its reduction.

The first stage of the reductions was to remove erroneous standard star measure-

ments. Simple first-order terms only were allowed in the transformation equations (terms 1, 2 and 4 in equations 3.2–3.6) so that highly deviant measurements did not produce unrealistic fits. A handful of standard star values were removed in this process, their measurements presumably caused by star-sky confusion during observing, the presence of faint stars in the "wobbled" sky position, and filter mix-up. This first stage also highlighted the variation in photometric quality from night to night: nights 10, 12 and 13 were well fitted with extremely low "nightly mean errors", from $.005^{m}$ to $.03^{m}$, even with these very simple equations. Nights 7 and 14 were nearly as good, with maximum values of $.06^{m}$. Assuming for a moment the terms used here were the dominant ones, nights 8 and 9 were clearly hindered by less photometric conditions at some interval during the night: the range in errors fitted was 0.02^{m}–0.4^{m}. In order to investigate whether higher-order terms (such as time-dependence, terms 6 and 7) were required to better account for this behaviour and further improve the quality of the data all round, or whether certain stretches of data were unuseable, more complex fits were attempted. However, as higher-order terms are introduced, the possibility of unrealistic fits also arises. In some cases, this was exhibited as large coefficient values for higher-order terms, only detectable by direct plotting of the data; in other cases, the bad data are sufficient to "twist" the transformation so that it can be multi-valued, resulting in a non-converging or oscillating nightly mean error. The approach taken here was to proceed with caution, adding in terms as necessary and examining graphically those terms with significant contributions to the transformations.

It is necessary to note here the way in which multiple observations of the same star were processed. Where count rates exceed a few hundred or so, the Poisson distribution is nearly symmetric so simple averages of count rates are correct. However this is hard to apply to the observations in general because each observation is made through a different airmass, and with different integration times etc., and this confuses the weighting. Consequently weighted averaging of derived magnitudes, for which these effects have been removed, is performed here. The error distribution of derived magnitudes does *not* follow the same symmetric distribution as count rate, and for faint

stars the averaging leads to systematic errors[1]. However, the program objects here are sufficiently bright that the largest effect possible here is $\sim 0.00006^{m}$.

The main conclusions of this process for each night are listed here:

(a) Nights 10, 12 and 13 produced very consistent results for simple and complex fits, and the indications were that terms in (colour)^2, t and t^2 were unnecessary. Plots of ΔV (standard star residual in V) and Δ(colour) against colour and local sidereal time confirmed these conclusions.

(b) Nights 7 and 14, thought to be subject to more adverse conditions, nevertheless reduced very well, and again terms 3, 6 and 7 proved unnecessary. It was however necessary to remove several program stars (and standards) from the end of night 14, which was hampered somewhat by instrumental problems towards dawn: the uncertainties in derived magnitudes (see Table 3.2 below) are consequently slightly higher.

(c) Nights 8 and 9 exhibited a trend in ΔV with local sidereal time (though not in Δ(colour)), in the form of quite a sharp increase in $(v - V)$, and an increase in the spread of residuals throughout the night. This was attributed to thin cirrus present in the evenings and mornings of observations. The sharp decline of these effects towards the middle of each night however was very noticeable, and the removal of standard and program stars from either end produced better results for V magnitudes, while retaining these areas produced values for colours consistent with their resultant errors (still quite large). It was decided to retain these data for the few objects for whom alternative nights' data were not obtained until more zero-pointing was available, while treating them with some suspicion.

In general, the transformations applied were characterised by the following features:

(a) The dead-time correction term (term 8) varied to some degree for different nights,

[1] To see this, consider for example a measurement whose true counting rate measured over a long period is 1000 counts per second for sky and 1100 for star+sky. Two observations are made $\pm 1\sigma$ from the true value, giving an inferred star counting rate of 100 ± 46; averaging the derived magnitudes would give an estimate $[2.5\log(54/100) + 2.5\log(146/100)]/2 = 0.13$ magnitudes too faint.

but always remained close to 1 standard error: clearly little correction was required.

(b) Pure colour transformation terms (terms 1, 2) agreed fairly well from night to night, and the non-linear colour terms (term 3) were insignificant.

(c) The pure extinction and colour-dependent terms (term 4, 5) were fairly strong, and varied between nights as expected.

(d) No time-dependent effects (other than those resulting from cloud considered above) were seen.

In summary, only terms 1, 2, 4, 5 and 8 were found to be significant in equations 3.2–3.6. Table 3.2 contains final estimates of the nightly mean error for each night and mean values of the resultant standard error in each index. The results of the reduction process are presented in Appendix C, along the derived 1985 results (reduced at the University of Arizona in 1985); the entries are ordered by field number, and include positional information, nights from which the data were taken and derived photometric indices.

3.3.3 Reliability checks on the data

The multiple measuring of various stars on different nights provided an opportunity to check the reliability of the results. Matching observations were paired (comparisons were only made with data from nights 7, 10, 12, 13, 14) for each photometric index, errors added in quadrature, and deviations as factors of σ calculated. For all but the two "poor" nights, all deviations were within $\pm 1.5\sigma$, and approximately distributed around zero, demonstrating the internal consistency of these measurements. Night 8 exhibited a larger spread, as expected, of $< 2\sigma$, but again symmetrically. Night 9 was considerably worse, displaying deviations from reliable measures of $\lesssim 3\sigma$ — clearly these data must be used with great care, and should only be utilised in the absence of other information.

As noted, data from nights 8 and 9 are included in the Appendix, but it should

Table 3.2: Final nightly mean errors in instrumental indices (1) and resultant combined errors in each photometric index (2) for each night which are derived from the nightly errors and Poisson shot noise. For nights 8 and 9, the quoted errors are for "cloud-less" and "full" standard star datasets for V and colours respectively, as described in the text.

Night#		V	$B-V$	$U-B$	$V-R$	$R-I$
7	nightly errors (1):	0.013	0.011	0.025	0.008	0.008
	combined error (2):	0.016	0.020	0.045	0.017	0.017
8	nightly errors (1):	0.091	0.024	0.031	0.032	0.026
	combined error (2):	0.091	0.030	0.040	0.023	0.027
9	nightly errors (1):	0.101	0.063	0.035	0.062	0.039
	combined error (2):	0.101	0.060	0.031	0.099	0.026
10	nightly errors (1):	0.018	0.009	0.023	0.006	0.004
	combined error (2):	0.020	0.014	0.034	0.011	0.011
12	nightly errors (1):	0.014	0.013	0.032	0.009	0.008
	combined error (2):	0.016	0.020	0.040	0.012	0.013
13	nightly errors (1):	0.023	0.010	0.037	0.006	0.007
	combined error (2):	0.024	0.014	0.044	0.010	0.010
14	nightly errors (1):	0.058	0.017	0.015	0.011	0.018
	combined error (2):	0.058	0.017	0.019	0.014	0.019

be remembered that this was only necessary for five of the measured stars: where data were available from another night, it was discarded here. Furthermore, subsequent chapters in this thesis indicate that fields 793 and 794, for which only two "good-night" program objects exist, were not reduced further. The presence of five good measurements in field 863 added to six measurements from the 1985 photoelectric run ensured good enough calibration to exclude information from a twelfth star measured on night 9. Field 864 also possesses four "good" measurements, to which the star from night 8 was added; the two remaining "doubtful" stars, in field 791c, were retained, and although the zero-point of this field must await confirmation, the presence of another measured star ensures that the scale cannot be wildly erroneous.

In conclusion, 31 stars have been measured photoelectrically in the 11 Schmidt fields reduced at later stages in this thesis, corrected for atmospheric absorption, and transformed to the standard *UBVRI* system, with resulting standard errors of about 0.01–0.04 in each photometric index. Information from three more stars has also been included, although obtained under less good conditions and with larger associated random (and possibly systematic) errors; these measurements can only affect the zero-point of one field in the survey (791).

3.4 Calibrating the photographic magnitudes

In the last chapter many aspects of COSMOS data reduction were discussed, and techniques to reduce errors in *UBVRI* magnitudes and discriminate between spurious and genuine images were considered. The vital step of transforming from machine-derived non-linear COSMOS magnitudes into some standard system was however only briefly mentioned, and it is this procedure which must be examined in some detail here. We must step back and discuss how, having obtained accurate and zero-pointed magnitudes for objects in each dataset, this information is used to effect the transformation and to what degree this is successful. The mechanics of how objects on a CCD are identified with images on a photographic plate, how the transformations are derived in each waveband, and how this calibration is applied to the dataset are conceptually fairly straightforward but in practice quite time-consuming.

As discussed in the last chapter, after assigning pixels to particular images in the Image Analysis Software, COSMOS determines summed isophotal intensities for each image at a threshold a given percentage above the local sky background: the purpose of this is to establish a realistic intensity scale in the presence of background effects, such as vignetting and sensitivity changes across the plate. 16 sensitometer wedge steps with known density ratios on the edge of each plate, exposed and processed in parallel with the sky image, are used to derive a density-intensity look-up table which in turn is applied to the data.

The summed intensities are used as a magnitude estimator for each image; however various aspects of the emulsion response to light and of the measuring process ensure that this is not a linear function of true apparent magnitude for stellar images. At faint magnitudes, the relation is well fitted by a slope of near unity, but at brighter magnitudes the slope decreases as the core of each image becomes saturated. For the brightest objects, the very high density on the emulsion means that the halo contributes significantly to estimated image magnitudes and the slope steepens again. These anomalies require that photoelectric and CCD measurements across the whole magnitude range must be obtained to properly calibrate the data. It is for these reasons that the preceding measurements were made, and the rest of this chapter describes their application to the COSMOS datasets.

3.4.1 Identification of measured stars in the COSMOS dataset

Right ascension (α) and declination (δ) values (equinox 1950) were obtained for the photoelectrically measured stars at the time of selection from the COSMOS dataset. CCD positions were derived from these values. A knowledge of right ascension and declination values for one position on a CCD image, combined with an accurate measure of the projected pixel scale is sufficient to determine (α, δ) values for any other position. In practice however, some rotation of the instrument with respect to the coordinate axes is usually observed, and two measured positions are necessary to determine this. The selection of suitable CCD fields meant that many frames for each run contained at least two bright stars whose positions were already known, and rotations could be calculated. These were checked for several nights, and showed no variation throughout any run on a single telescope, and hence, once calculated, could be used throughout with confidence. Rotations on the sky never exceeded 1.5°. The pixel size for the University of Hawaii 90″ images was initially uncertain, but was readily determined from frames containing two known stars.

These objects were then paired with the COSMOS datasets in each passband (this procedure is described more fully in Chapter 2) with a tolerance box of 3″ half-

width in declination and right ascension (calculated at $\delta \sim 0$): COSMOS positions are locally accurate to within $\sim 0.2''$ for UKST plates, depending on the number of positional standards defined in the transformation from (X, Y) to (α, δ). This was done separately for master and secondary plates. Practically all objects were uniquely identified with images in the COSMOS dataset, the few losses being accounted for by blends between COSMOS images, both spurious and real, which were rejected by morphological criterion at an earlier stage, or by extremes in colour for some very faint objects which were therefore not detected above the threshold on certain plates.

3.4.2 Initial straightening of the COSMOS magnitude scale

Spline-fitting is usually required to define the magnitude transformation because of the non-linear relationship between COSMOS magnitude and true apparent magnitude. However measurements used to define this fit rarely span the whole magnitude range of interest and are poorly defined at the faint end. The flexibility of spline-fitting has the disadvantage that sharp features in the calibration relation can cause an extrapolation beyond well-defined limits with unpredictable and unrealistic results; in the extreme this relation may flatten or steepen excessively, or even become multi-valued. This is also true for higher-order polynomials, and so some method must be found to "straighten" the machine-derived magnitude scale so that its general behaviour matches that of the photometric system. A low-order polynomial with simple behaviour at extrapolated ends can then be applied upon comparison to calibrated stellar sequences.

The chosen solution is to force the number-magnitude relation on to that derived in a fit to observations, prior to calibration. Bahcall & Soneira (1980) proposed a two-component (disk and spheroid) model of the galaxy, based on local observations of the stellar luminosity function and scale heights. Measurements of the distribution of light in other galaxies were used to fit a global form for B and V, and in Appendix B *op. cit.* a simple fit to the results, given in terms of differential and integrated star counts and accurate to 15%, was presented. This is valid for $b^{\rm II} \geq 20°$, and $4 \leq m \leq 30$ in each band. These expressions were employed to model expected stellar counts for each

plate, and galactic coordinates of $b^{II} = 57.7$, $l^{II} = 327$ used as representative of the survey. The measurement of a photoelectric star in each field was used to tie down the relation in each band (assumed similar in all bands). The stellar counts were then placed in bins of 0.1^m, and a spline fit applied to the relation, ignoring bins containing less than 100 objects (bright end) or magnitudes exceeding the plate-limit (set at −1 in machine-derived magnitude, 1 magnitude above sky background) for the faint end; a check that image counts were still rising up to this limit was also performed. Beyond the defined limits of each plot, straight lines extrapolations were used. Up to five knots were found necessary to follow the curve. COSMOS magnitudes were then successively corrected for each plate so that they followed this derived relation.

3.4.3 Calibration

Having successfully paired the straightened COSMOS datasets with the calibration stars, a cubic polynomial fit was applied to the magnitude transformation. This is of much lower order than usually required because of the preceding step. In order to do this, colour equations were applied to photometric magnitudes to convert to the photographic system[2], taken from Blair & Gilmore (1982). Strictly a colour transformation should first be applied to each set of CCD observations to convert to the photoelectric system but this was not possible here — the lack of photometric conditions on any observing run meant that no transformation terms could be derived from standard star measurements, and documented transformations were not available except for the ESO system, which showed only very small terms in all wavebands. Consequently it was decided to ignore these transformations: this would only in any case result in a small random spread on the calibration curve. In the case where substantial sensitivity changes are seen across the plate, it is important to attempt a correction for this at this stage using the sky level as a measure of the change, although further attempts to suppress field effects were made as described earlier. An optional tying of the calibrated magnitude scale to local sky background was therefore allowed, in the form of

[2]Note that all references to *UBVRI* magnitudes in subsequent chapters refer to magnitudes in this, the photographic system.

$$m = m + 2.5\log(sky/\overline{sky}) \tag{3.8}$$

where $\overline{sky}$ is the mean sky value over standard stars (for consistency standard star values were *multiplied* by the same factor prior to fitting).

In order to fit a transformation relation between magnitudes for the data here, the zero-point for each waveband was sought only through the photoelectric data: CCD calibrations were allowed to "float" freely. If X represents standard calibrated magnitudes, and Y the corresponding COSMOS estimates, then cubic polynomials were sought to fit

$$Y = aX^2 + bX + c \tag{3.9}$$

c was not constrained to be consistent between datasets and so is represented as a set c_i where i denotes each CCD and photoelectric dataset — the c_i for the photoelectric data were selected for the final solution. The corresponding least squares solution is in the form of a set of equations represented by a matrix of order (number of datasets)+2 as follows:

$$\begin{pmatrix} \sum\sum X^4 & \sum\sum X^3 & \sum X_{i=1}^2 & \sum X_{i=2}^2 & \cdots \\ \sum\sum X^3 & \sum\sum X^2 & \sum X_{i=1} & \sum X_{i=2} & \cdots \\ \sum X_{i=1}^2 & \sum X_{i=1} & N_{i=1} & - & - \\ \sum X_{i=2}^2 & \sum X_{i=2} & - & N_{i=2} & - \\ \vdots & \vdots & - & - & \ddots \end{pmatrix} \begin{pmatrix} a \\ b \\ c_{i=1} \\ c_{i=2} \\ \vdots \end{pmatrix} = \begin{pmatrix} \sum\sum YX^2 \\ \sum\sum YX \\ \sum Y_{i=1} \\ \sum Y_{i=2} \\ \vdots \end{pmatrix}$$

In these equations single summation signs denote summations over all points in each dataset, and double summations are over all points in all datasets. The second (column) matrix contains the coefficients (a, b, c_i) for the cubic fit, and N_i is the number of stars in each dataset. The coefficients were determined by inverting the main matrix and a look-up transformation table was created (the bright and faint end were linearly extrapolated). All objects were calibrated, and residuals calculated: highly deviant points, most usually due to errors in the COSMOS magnitudes, were removed and the fit redone. After final calibration, hard-copy plots of residuals versus sky values and versus colour were produced as a check against correlations. The above method ensured

that all information available was used in determining the *shape* of the magnitude transformation: the zero-point derived from the photoelectric data alone was used for the final result.

An example of the calibration transformation applied to the "straightened" COSMOS magnitude scale can be seen in Figure 3.1, here for the R plates in field 862. The first two panels show "straightened" COSMAG versus photometric magnitudes for (a) master and (b) secondary plates. Different symbols are used for datasets from different sources: open circles denote photoelectric data, asterisks denote CCD data from the Cannon/Griffiths run at the Isaac Newton Telescope, La Palma, and vertical crosses denote University of Hawaii 80″ data. As noted above, the latter two were allowed to "float" in the horizontal direction, being tied down photoelectrically. The resulting transformation curve is well covered by data over the range $12 \leq R \leq 19.5$, and the shape defined by the CCD sequences is well constrained. The linearising of the COSMOS magnitude scale with the Galactic model has worked well, although some trend is still apparent, which is traced well by the cubic fit. The lower two panels indicate that here, as elsewhere, no correlations with sky background can be seen for these residual magnitudes.

3.4.4 Summary

This chapter has discussed the techniques used to calibrate a very large dataset with a relatively small number of measured points, and completes the description of the preparation of the data and the production of calibrated corrected *UBVRI* datasets for 11 of the 13 survey fields. This account of the calibration of the single-band catalogues brings to a close the description of all the elements necessary to bring about this result. In order to draw together and clarify this description, a brief summary of the process for one Schmidt field is given below:

- All 10 plates were scanned, thresholded and analysed by the COSMOS machine, producing a dataset of images with parameters for position, area, isophotal magnitude, shape and orientation.

Figure 3.1: An example of calibration results. The first two plots show the calibration relation between "straightened" COSMOS magnitude and the photometric scale for master and secondary plates in field 862 (R band). Open circles denote photoelectric points, asterisks CCD points from La Palma and crosses University of Hawaii 80″ data. The fit to these relations is a cubic. The lower panels show no correlation in residual magnitude with sky background.

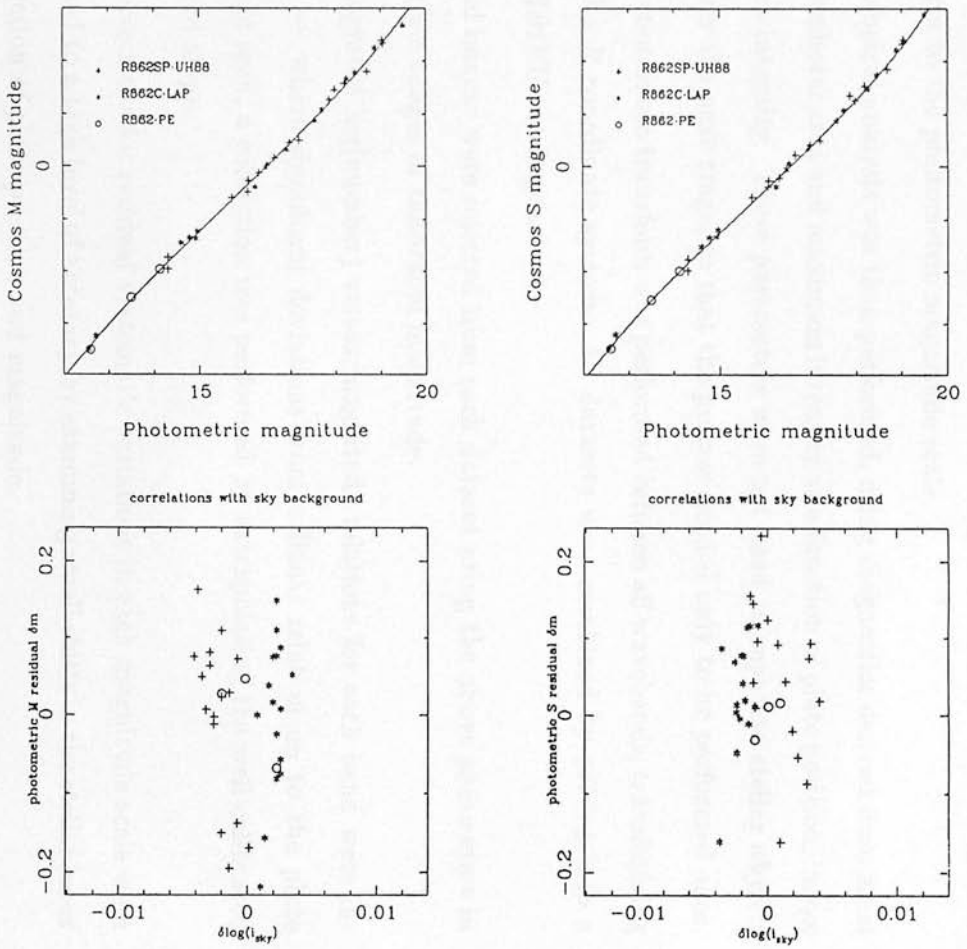

- A local coordinate transformation was performed between each pair of single-band plates by binning the brightest 40,000 images.
- All images found in common between these plates within a tolerance box of 3″, measured in transformed coordinates were identified and five single-band datasets produced.
- The CCD and photoelectrically measured stars described in this chapter were located within this dataset; after "straightening" the machine-derived magnitude scale, removing sharp calibration features, a cubic polynomial was applied to transform to the photometric magnitude scale.
- Morphological analysis was then performed, using diagnostics derived from axial ratio, isophotal area and maximum intensity as a function of plate position, image area and intensity. These parameters were not used to separate stellar objects until after the next stage, so that the process needed only to be performed once.
- A local coordinate transform was performed *between* all wavebands, transforming on to the R coordinate system. All datasets were combined by pairing into a single $RBIVU$ catalogue.
- Elliptical images were rejected from each dataset using the above parameters in appropriate ranges of calibrated magnitude.
- The integrated log(number) versus magnitude relations for each band were inspected — where significant deviations from a linear relation up to the plate limit were seen, a correction was performed by extrapolating the well-calibrated bright end slope.
- Final corrections for residual systematic variations in each magnitude scale were performed to a high level of accuracy by examining small shifts in the stellar locus as a function of plate position and magnitude.
- The final five-band dataset was produced. The accuracy in this dataset as a function of magnitude was estimated from comparing magnitudes from each original COSMOS dataset.

The success of these procedures is demonstrated by the final accuracies achieved; as demonstrated at the close of Chapter 2, each final dataset possesses derived mean

magnitudes accurate to an rms error of $\leq 0.05^{m}$ to within 2 magnitudes of the plate-limit in all wavebands. Thus we are now in possession of a highly accurately calibrated stellar dataset over a large area. In Part II, attention will be turned to two topics for which the survey is immediately appropriate — the selection of low and very high-redshift quasars.

Part II

The Distribution And Evolution Of QSOs

The next three chapters in this thesis deal with the application of the Edinburgh Multicolour Survey to a particular topic: the examination of the space distribution and evolution of quasars. The dataset produced in Part I lends itself to the selection of particular classes of objects that exhibit non-stellar colours and my aim in this thesis has been to concentrate effort in one particular area, namely QSOs. As such, Chapter 4 will deal with the selection of low redshift QSOs using the ultra-violet excess selection technique, employing principally the use of three of the five wavebands available. Chapter 5 will go on to study the 3-D distribution of these objects. Chapter 6 will proceed to the selection of quasars of a higher redshift, in which the full range of the survey colours is required.

Chapter 4

Low-Redshift QSOs: the UVX Sample

4.1 Introduction

Having described in detail the construction of the Edinburgh Multicolour Survey from raw plate material and its reduction to a dataset of approximately 1.3 million stellar images calibrated in U, B, V, R & I to typical accuracies of 0.05^{m} in each waveband, attention must now be turned to the selection of samples of particular classes of objects. Chapter 1 gives a review of major work in the selection of optical quasar samples, and the possession of broad-band optical information lends itself immediately to the most common of these methods: selection by ultraviolet excess (UVX). This technique for the selection of low-redshift ($z < 2.2$) samples of quasars was first implemented by Ryle & Sandage (1964) after the discovery of excess ultraviolet radiation in the radio sources 3C48, 3C196 and 3C286 (Matthews & Sandage 1963) and has been widely used in subsequent years (e.g. Braccesi *et al.* 1980, Schmidt & Green 1983, Boyle *et al.* 1987, Koo, Kron & Cudworth 1986). These studies have been most successful in providing us with a description of the low-redshift luminosity function and its evolution. The UVX technique consists of looking for stellar-like images which exhibit an excess of light at the blue end of the spectrum with respect to the population of galactic stars in general: this excess is mainly due to the blue continuum in quasar spectra when compared with the thermal distribution of stellar light. At redshifts in excess of $z \simeq 2.2$ this technique breaks down due to the presence of Lyman-α in the B band (e.g. Marano, Zamorani & Zitelli 1986); however up to this redshift $> 95\%$ of quasars exhibit ultraviolet excess at the level $(U - B) < -0.40$ (Véron 1983).

Clearly a machine-derived survey such as that presented in this thesis is highly

suitable for such a technique: a simple $(U - B)$ cut can be applied automatically to a clearly-defined flux-limited sample, producing a candidate list with quantifiable selection criteria in a straightforward manner. The candidates selected must then of course be examined spectroscopically in order to reject contaminating objects and to establish the redshifts of the QSOs. As will be seen, this method is capable of providing 10–30 candidates per UK Schmidt field bluer than $(U - B) \sim -0.28$ to a limiting magnitude of $B = 18$. As indicated first by Usher (1981) the inclusion of another waveband, most usefully R, can provide further discrimination *between* UVX objects and indeed turns out to be very successful at distinguishing between quasars and white dwarfs (Koo & Kron 1982). The Edinburgh Multicolour Survey is therefore ideal for such a study, and information in U, B and R wavebands will be used for selection.

The total area surveyed here will be shown to be $\simeq 250\,\mathrm{deg}^2$. Apart from the PG survey (Schmidt & Green 1983) which covered 10616 deg^2 to a limiting magnitude of $B \simeq 16.16$, the present survey is the largest area colour-selected complete sample of QSOs to date. A comparable sample was obtained by Mitchell, Warnock & Usher (1984) over $108.6\,\mathrm{deg}^2$, where 32 quasars were identified with $B < 17.65$; Marshall *et al.* (1983, 1984) also constructed a complete sample of $37.20\,\mathrm{deg}^2$ at $B < 18.25$ from the AB survey (Braccesi, Formiggini & Gandolfi 1970). All other such surveys cover areas less than $10\,\mathrm{deg}^2$. The Edinburgh Multicolour Survey fills a gap between these samples, providing QSOs over a large area of sky and a large redshift range at $B \leq 18$; the worth of studying these new areas of parameter space will become apparent in the discussion which follows.

In this chapter I will describe the application of the UVX technique to the Edinburgh Multicolour Survey. The next section will discuss the initial selection of candidates in each field and the results of spectroscopy on the sample and Section 4.3 will examine the completeness of the sample and compare this work with other UVX results. Chapter 5 will discuss the possible cosmological results obtainable from such a sample.

4.2 Construction of the sample

4.2.1 UVX selection

The UVX sample was constructed from 10 fields selected in $15.0 < B < 18.0$ from the Edinburgh Multicolour Survey as indicated in Table 4.1(a). Fields 793 and 794 remain uncalibrated at the time of writing; field 864 was found to have excessive residual field effects early on in the plate reductions and insufficient time was available after better techniques were devised (see Chapter 2).

It is instructive to begin by considering the distribution of stellar objects in a particular form of colour space, the $(U-B)$, $(B-R)$ plane. A typical colour-colour diagrams for these indices is presented in Figure 4.1, here for field 867. This diagram is composed of images classed as stellar within the magnitude range $15.0 < B < 18.0$ and it is clear that main sequence stars lie tightly packed around a locus, having a typical full-width at half maximum density about this line of 0.15^{m} caused by random photometric errors in the COSMOS datasets and intrinsic variations within the population. The distribution of galactic stars can be roughly traced as follows: at $(U-B) > 1$, K and M stars dominate; moving to bluer $(U-B)$ and $(B-R)$ values the main sequence remains well defined until type F stars and a few stars can be seen to follow the main sequence track to bluer values. The few stars seen at $(U-B) \sim 0.25$ and $(B-R) \sim 0.2$ are horizontal branch stars, being relatively faint in apparent magnitude and at such high galactic latitudes. The colours of main sequence stars are represented in Figure 4.2 with typical $(U-B)$ and $(B-R)$ values from Johnson (1966). To even more extreme values of $(U-B)$ off the end of the clearly defined main sequence at $(U-B) \lesssim -0.3$ a significant population of objects with redder $(B-R)$ values can be seen. The inclusion of R-band information is here discriminating between black-body stellar spectra and the relatively more substantial long-wavelength emission due to the power-law continua of quasars. These then are the constituents of the UVX candidate lists and will be selected via a simple $(U-B)$ cut, the $(B-R)$ index providing further discrimination at the telescope.

Table 4.1: (a) Schmidt fields used in the UVX survey and $(U-B)$ limits applied. The 8^{th} column shows shifts in $(U-B)$ calculated with respect to field 789.

Field name	α_{min}	α_{max}	δ_{min}	δ_{max}	Central $\alpha(1950)$	Central $\delta(1950)$	$U-B$ shift	$U-B$ limit
789	12.470	12.816	-7.72	-2.58	12 38 34.80	−05 06 36.0	0.00	−0.25
790	12.804	13.148	-7.70	-2.55	12 58 33.60	−05 07 30.0	+0.07	−0.23
791	13.138	13.482	-7.70	-2.55	13 18 36.00	−05 07 30.0	+0.27	−0.18
792	13.471	13.816	-7.70	-2.55	13 38 36.60	−05 07 30.0	+0.27	−0.18
861	12.472	12.815	-2.70	2.45	12 38 36.60	−00 07 30.0	+0.20	−0.25
862	12.805	13.148	-2.70	2.45	12 58 35.40	−00 07 30.0	+0.20	−0.15
863	13.139	13.482	-2.70	2.45	13 18 37.80	−00 07 30.0	+0.12	−0.28
865	13.805	14.148	-2.70	2.45	13 58 35.40	−00 07 30.0	+0.13	−0.41
866	14.139	14.482	-2.70	2.45	14 18 37.80	−00 07 30.0	+0.10	−0.25
867	14.471	14.815	-2.70	2.45	14 38 33.00	−00 07 30.0	−0.05	−0.50

Table 4.1: (b) Number of objects in reduced catalogues & effective areas after galaxy exclusion.

Field	789	790	791	792	861	862	863	865	866	867
$15 < B < 18$	14691	15833	15132	16991	12180	12870	14152	13450	18901	21528
# extended	5660	5004	4755	5878	3998	4701	4793	3713	6235	6870
% remaining	61.5	68.4	68.6	65.4	67.2	63.5	66.1	72.4	67.0	68.1

Figure 4.1: $(U-B)$ / $(B-R)$ two-colour plot for Schmidt survey field 867. The plot only shows objects present in all wavebands, and indicate various zones where quasars and contaminants may lie.

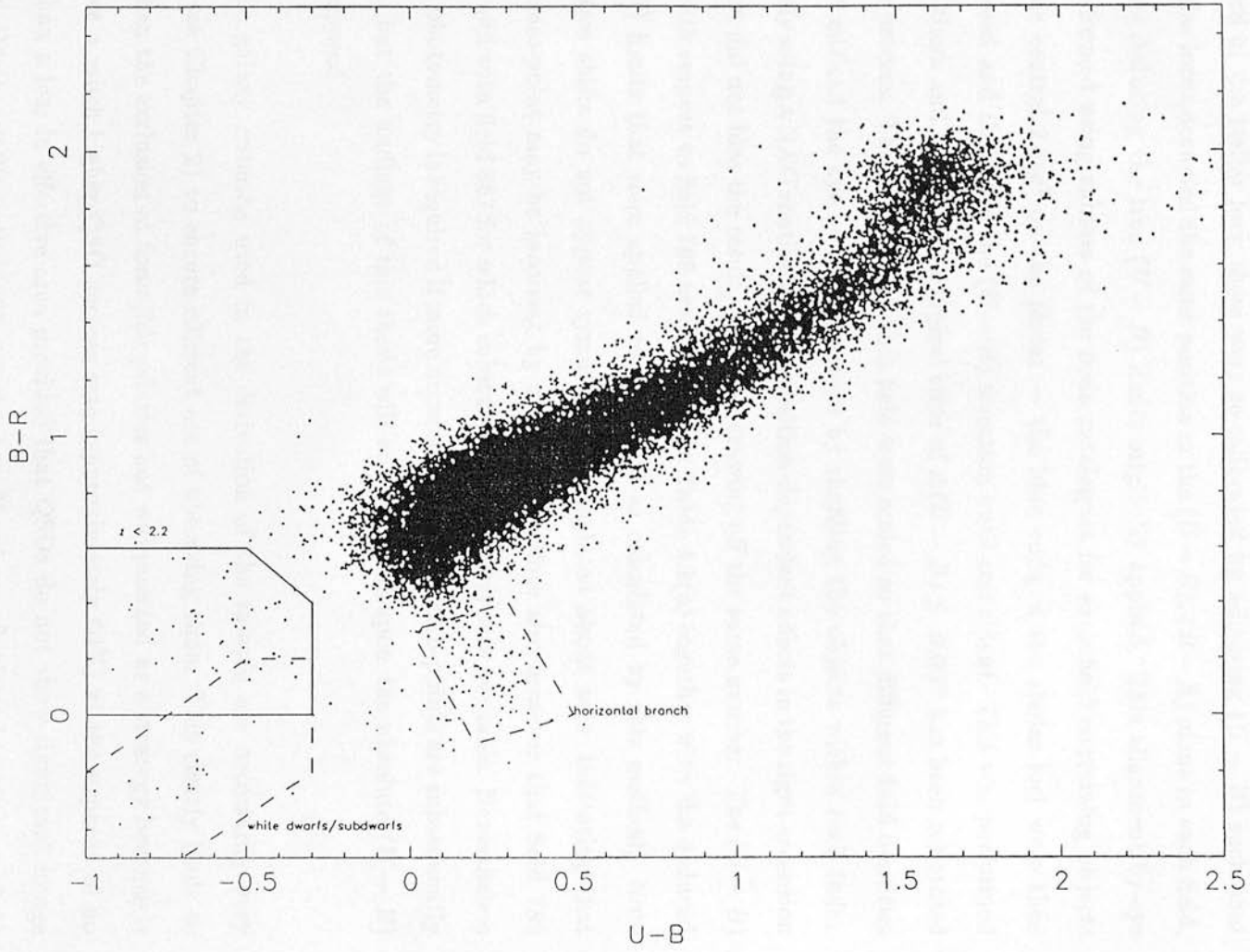

Chapter 3 has indicated the use of photoelectric calibration to derive zero-points for each magnitude scale in each field; however many wavebands possessed as few as two photoelectric measurements. In order to ensure uniformity in the sample therefore, $(U-B)$ limits were chosen by eye for each field individually at a similar distance blueward of the stellar loci; these were re-calibrated by adjusting $(U-B)$ such that the stellar locus occupied the same position in the $(U-B)$, $(B-R)$ plane in each field, and thus deducing the true $(U-B)$ limits originally applied. This alignment-by-eye was performed using subsets of the main catalogues for each field containing objects from the central $2\,\mathrm{deg}^2$ on the plates — the blue ends of the stellar loci were then superposed and shifted in the $(U-B)$ direction until coincident. This was performed several times and compared: a typical error of $\Delta(U-B) \lesssim 0.05^{\mathrm{m}}$ has been estimated for this process. The numbers for each field were scaled so that different field densities did not mislead the eye — this was done by shuffling the objects within each index randomly using a NAG routine (so that position-dependent effects in the right ascension direction did not bias the result) and then drawing off the same number. The $(U-B)$ shifts with respect to field 789 are indicated in Table 4.1(a) together with the deduced $(U-B)$ limits that were applied to each field as calculated by this method. Note that these shifts do not appear symmetrically displaced about zero, indicating that the U zero-point may be incorrect by up to 0.1^{m}. Note also however that field 789 agrees well with field 867 for which substantial photometry was available. Nevertheless further photometry is required if more accurate magnitude zero-points are subsequently needed, but the findings of this thesis will not be based upon the absolute $(U-B)$ limit imposed.

The galaxy criterion used in the derivation of the sample are necessarily very strict (see Chapter 2) to ensure efficient use of observing time. This clearly leads to more than the exclusion of *bona-fide* galaxies but was pursued as a strategy because it produces a much higher QSO success rate (approximately 60%) at the expense of no more than a loss in effective area provided that QSOs do not show significant image extents: this possibility will be discussed later. Numbers of rejected images per field and a calculation of effective area are given in Table 4.1(b).

Figure 4.2: Theoretical $(U-B)$ and $(B-R)$ stellar colours from Johnson (1966). The location of low-redshift quasars is marked.

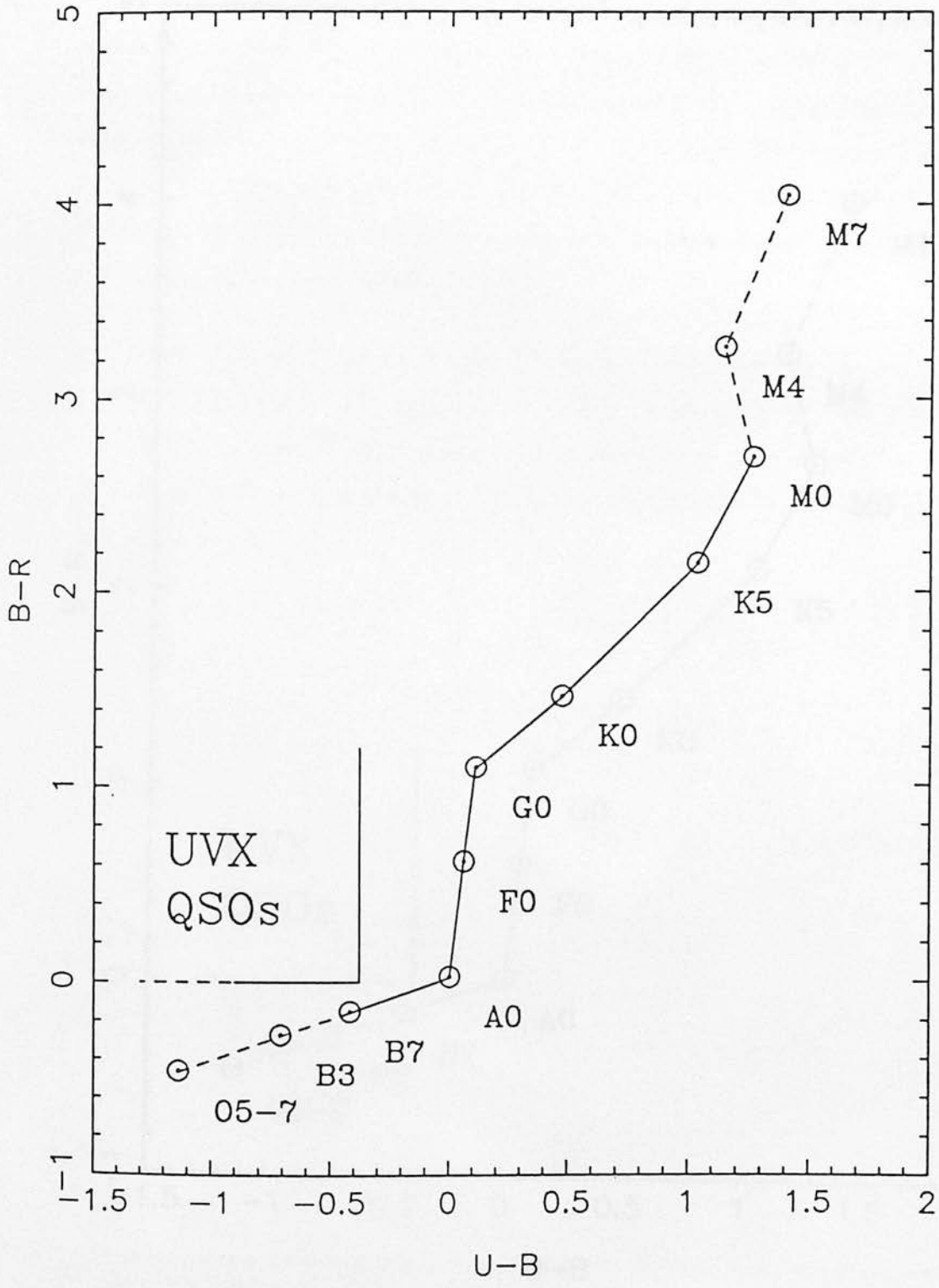

Figure 4.1: Theoretical $(U-B)$ and $(B-R)$ stellar colours from Johnson (1966). The location of low-redshift quasars is marked.

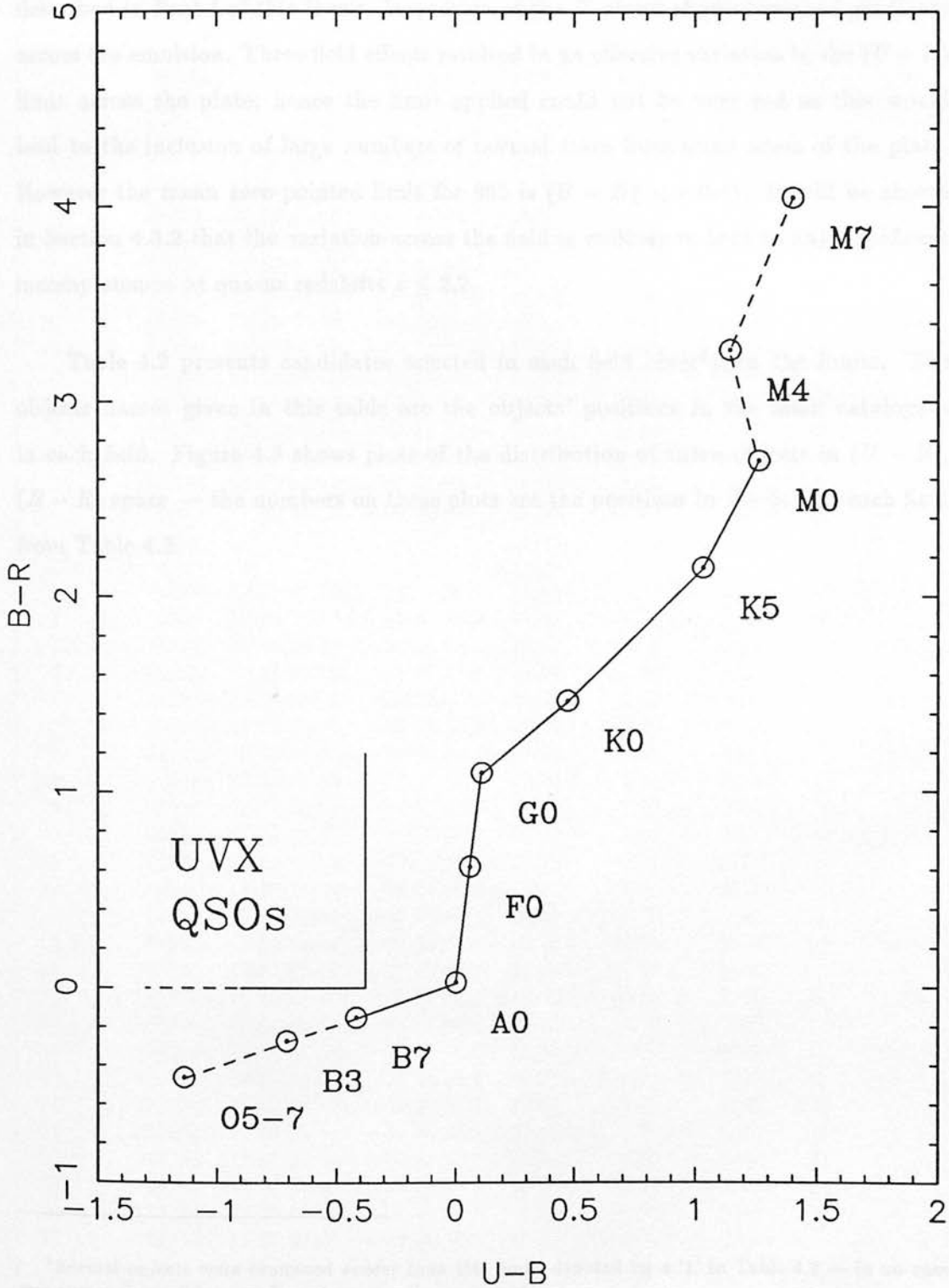

The data for field 865 requires special consideration: $(U - B)$ versus $(B - R)$ plots such as that already seen showed a "swollen" stellar locus for this field, caused by residual field effects in the U data not amenable to full removal by the processes described in Part I of this thesis. Inspection of the U plates showed marked gradients across the emulsion. These field effects resulted in an effective variation in the $(U - B)$ limit across the plate; hence the limit applied could not be very red as this would lead to the inclusion of large numbers of normal stars from some areas of the plate. However the mean zero-pointed limit for 865 is $(U - B) < -0.41$. It will be shown in Section 4.3.2 that the variation across the field is unlikely to lead to any significant incompleteness at quasar redshifts $z \leq 2.2$.

Table 4.2 presents candidates selected in each field bluer[1] than the limits. The objects names given in this table are the objects' positions in the main catalogues in each field. Figure 4.3 shows plots of the distribution of these objects in $(U - B)$, $(B - R)$ space — the numbers on these plots are the positions in the list for each field from Table 4.2.

[1] Several objects were examined *redder* than this limit, denoted by a '1' in Table 4.2 — in no case was any such candidate confirmed as an emission-line object.

Table 4.2: Candidate list for the UVX selection. Each field is listed with magnitudes and colours of candidates. Identifications are given as indicated in the text. See notes at end of table.

#	Obj name	α(1950)	δ(1950)	B	$U-B$	$B-R$	ID	z
Field 789								
1	9023	12 29 36.08	−05 01 53.9	17.39	-0.67	0.33	Q	1.078
2	29630	12 33 02.82	−05 19 06.2	16.38	-0.56	-0.32		
3	31702	12 33 22.57	−07 18 34.4	17.05	-0.66	-0.39		
[1]4	33050	12 33 45.06	−04 28 06.3	17.31	-0.12	-0.16	S	
5	34032	12 33 52.83	−05 03 55.8	17.45	-0.44	-0.06	B	
6	37124	12 34 14.63	−06 59 50.6	16.61	-1.00	-0.39		
7	51598	12 36 47.53	−04 02 39.0	17.20	-0.50	-0.07	B	
8	52031	12 36 48.47	−06 32 28.4	17.70	-0.91	-0.32		
9	66185	12 39 04.99	−07 16 40.3	16.92	-0.53	0.01	B	
10	67128	12 39 10.13	−07 26 28.5	17.41	-0.72	0.68	Q	1.169
11	83588	12 42 04.57	−03 36 25.6	16.48	-0.28	-0.14	S	
12	90488	12 43 06.38	−05 43 33.1	17.28	-0.87	-0.22		
13	102432	12 45 00.44	−03 33 47.4	16.07	-0.46	0.11	Q	0.379
[1]14	113609	12 46 51.31	−05 58 42.4	15.18	-0.20	0.34	B	
15	114470	12 47 04.19	−05 50 26.3	17.37	-1.28	-0.58		
16	115896	12 47 19.14	−03 47 22.4	17.90	-0.53	0.30	S	
17	124063	12 48 44.25	−04 48 44.5	17.28	-0.39	0.73	Q	1.410
Field 790								
[3]1	1534	12 48 17.19	−02 41 55.6	16.63	-0.26	0.75	F	
2	2569	12 48 28.53	−03 34 19.3	17.57	-0.52	0.03	S?	
3	3692	12 48 39.55	−04 46 39.5	17.57	-0.25	-0.01		
4	10760	12 49 55.13	−02 45 11.9	15.31	-1.22	-0.53		
5	14890	12 50 28.72	−04 39 42.3	16.66	-0.54	-0.21		
6	18406	12 51 07.96	−03 12 26.3	17.99	-0.24	-0.13		
7	34832	12 53 35.35	−06 03 15.3	17.52	-0.33	-0.01		
8	40544	12 54 31.43	−05 36 15.9	17.74	-0.71	-0.24		
9	43385	12 55 02.74	−04 35 57.7	17.19	-0.72	0.61	B	
10	63702	12 58 15.98	−04 15 50.6	17.95	-0.45	0.39	QBAL	1.738
11	72057	12 59 40.98	−02 29 10.8	17.73	-0.41	-0.19		
12	76163	13 00 11.69	−04 57 40.5	17.63	-0.98	-0.35		
[3]13	77680	13 00 38.22	−03 07 16.4	16.94	-0.42	0.31	S	
14	79629	13 00 56.84	−03 38 43.0	17.95	-0.60	0.45	Q	0.390
15	96283	13 03 28.31	−05 42 28.0	17.28	-1.03	-0.26		
16	101146	13 04 18.78	−06 14 02.2	17.44	-0.46	0.45	Q	1.563
17	101764	13 04 26.34	−04 18 49.6	17.68	-0.76	-0.11		
18	105028	13 04 53.54	−05 31 25.8	17.12	-0.95	-0.25		
[1]19	119332	13 07 09.56	−05 14 38.2	16.27	-0.22	1.40	S	
20	121234	13 07 29.78	−05 19 29.8	17.89	-0.48	1.15	S	
21	121902	13 07 36.47	−03 26 47.1	15.00	-0.26	0.27	B	
22	123228	13 07 45.44	−05 22 24.1	15.08	-0.35	0.62	B	
23	124917	13 08 06.29	−03 39 17.9	17.68	-0.65	-0.34		
24	126124	13 08 14.02	−04 41 04.9	17.62	-0.35	-0.05		
25	126712	13 08 22.90	−02 35 33.1	16.37	-0.24	0.33		

Table 4.2: continued

#	Obj name	$\alpha(1950)$	$\delta(1950)$	B	$U-B$	$B-R$	ID	z
Field 791								
1	8323	13 09 26.06	−04 42 16.7	17.31	-0.64	-0.05		
[1]2	10757	13 09 42.76	−07 11 11.7	17.38	-0.13	0.53	S	
3	13098	13 10 11.89	−04 58 49.8	17.91	-0.35	0.48	F	
4	16646	13 10 53.19	−03 37 26.4	16.34	-0.66	-0.04		
5	40849	13 14 42.07	−06 43 39.6	16.03	-0.57	-0.03		
6	42252	13 15 02.37	−04 29 44.8	16.93	-0.38	0.02		
7	43060	13 15 14.04	−04 10 14.0	17.78	-0.43	0.37	Q	0.469
8	50545	13 16 26.89	−05 41 44.8	17.52	-0.66	-0.14		
9	51162	13 16 34.37	−03 57 28.5	17.58	-0.46	0.11	B	
10	53576	13 16 48.35	−07 34 43.2	16.51	-0.58	-0.03		
11	55770	13 17 26.14	−04 19 20.7	17.78	-0.65	0.55	B	
12	57171	13 17 33.19	−07 05 08.3	17.73	-0.87	0.06		
13	83449	13 21 38.64	−05 49 00.8	16.83	-0.42	0.58	Q	0.732
14	93656	13 23 21.80	−03 07 55.4	17.79	-1.09	-0.43		
15	95450	13 23 40.18	−02 48 24.1	17.41	-0.40	0.52	Q	2.125
16	100689	13 24 24.98	−05 37 30.6	17.96	-0.21	0.32	B	
17	105622	13 25 10.64	−06 03 24.1	16.95	-0.97	-0.02		
18	110270	13 25 55.56	−05 28 10.3	16.60	-0.45	0.65	B	
19	114975	13 26 40.91	−03 43 23.0	15.64	-0.78	-0.13		
20	116238	13 26 52.47	−05 16 06.6	15.59	-0.39	0.28	Q	0.580
21	127984	13 28 43.70	−05 35 26.1	16.28	-0.93	-0.40		
22	130741	13 29 09.38	−06 15 18.4	17.59	-0.42	0.35	Q	0.718
Field 792								
1	46251	13 35 47.21	−03 32 06.2	16.59	-0.80	-0.25		
2	54919	13 37 13.46	−02 34 48.0	16.27	-0.28	0.56	B	
3	57869	13 37 32.48	−03 24 43.7	17.59	-0.52	0.04	B	
4	61242	13 38 06.62	−05 36 31.6	17.73	-0:44	-0.10		
5	77523	13 40 41.22	−05 30 30.9	16.70	-1.31	-0.23		
6	78300	13 40 50.08	−04 38 41.4	16.64	-1.33	-0.16		
7	84710	13 41 49.20	−03 31 51.1	15.18	-0.27	0.73	S	
8	84730	13 41 54.40	−03 37 40.9	17.74	-0.77	0.03	S	
9	89273	13 42 29.64	−06 17 52.9	16.97	-0.93	-0.43		
10	94027	13 43 14.41	−05 38 21.8	17.50	-0.71	0.23	Q	2.047
11	100799	13 44 23.11	−04 19 26.1	17.02	-0.82	0.38	Q	1.922
12	110940	13 45 55.01	−03 17 27.7	17.73	-0.80	0.46	Q	1.947
13	111328	13 45 47.73	−05 10 19.0	16.91	-0.71	0.48	Q	1.386
14	113578	13 46 11.03	−06 32 26.6	16.36	-0.82	-0.27		
15	113928	13 46 19.86	−03 06 48.6	17.69	-0.68	0.38	Q	2.090
16	117178	13 46 43.82	−04 13 22.8	17.62	-0.55	-0.44		
17	117604	13 46 45.91	−06 20 03.9	17.63	-0.74	-0.44		
18	120399	13 47 18.53	−04 51 20.8	16.81	-1.26	-0.60		
19	126514	13 48 09.45	−05 43 41.0	15.77	-0.33	0.78	B	

Table 4.2: continued

#	Obj name	α(1950)	δ(1950)	B	$U-B$	$B-R$	ID	z
Field 861								
1	30	12 28 09.60	+02 11 40.5	16.00	-0.30	1.15		
[2]2	934	12 28 17.10	−01 30 30.8	17.94	-0.60	0.46	Q	0.71
3	1129	12 28 25.23	+02 19 06.0	16.11	-0.55	1.18		
[2]4	6809	12 29 26.00	−02 07 33.2	17.82	-0.43	1.08	Q	1.01
5	7744	12 29 46.71	+02 12 31.7	17.60	-0.43	0.92		
6	11843	12 30 30.20	−00 15 02.3	17.68	-0.68	0.66	B	
7	41101	12 36 37.98	+01 28 42.4	17.74	-0.55	0.74	Q	1.258
8	55035	12 39 23.07	−02 31 05.6	17.81	-0.43	0.67	Q	1.233
9	69475	12 42 22.14	−01 23 09.8	17.98	-0.42	0.43	Q	0.489
10	72740	12 43 05.23	+01 32 40.9	16.49	-0.80	-0.05		
11	81785	12 44 58.71	+01 32 24.6	16.14	-0.50	0.48	S	
12	92368	12 47 06.24	+01 49 21.9	17.70	-0.31	1.43	S	
13	94143	12 47 17.96	+00 48 34.0	17.25	-1.17	-0.27		
[1]14	96332	12 47 46.81	+02 18 33.5	16.55	-0.20	0.95	S	
15	97289	12 47 53.58	+00 36 08.7	17.99	-0.28	0.21	B	
Field 862								
1	4978	12 48 47.76	−02 21 20.9	17.85	-0.24	0.22		
2	7776	12 49 17.13	−02 07 17.8	17.04	-0.22	0.48	Q	1.184
[1]3	9306	12 49 34.82	−00 13 15.2	16.14	-0.15	0.92	B	
4	10337	12 49 40.35	−00 34 41.5	17.49	-0.49	-0.06		
5	11507	12 49 56.58	−02 18 01.6	17.83	-0.29	0.26	F	
6	11898	12 50 01.01	+00 45 28.0	16.80	-0.16	0.46	B	
7	13291	12 50 11.57	−01 41 08.0	17.90	-0.52	-0.10		
8	21141	12 51 35.05	+01 59 39.6	15.31	-0.98	-0.54		
9	26630	12 52 23.78	−02 02 23.2	16.71	-0.29	-0.15		
10	28789	12 52 46.44	+02 00 26.5	15.48	-0.58	0.19	Q	0.345
11	32033	12 53 16.44	−00 02 17.4	17.93	-0.49	0.09	Q	0.721
12	35769	12 53 54.53	+00 48 12.4	17.82	-0.70	0.17	Q	0.833
13	35979	12 53 51.74	−00 25 15.6	16.92	-0.28	0.68	S	
14	39557	12 54 29.46	+00 40 48.0	17.79	-0.71	0.42	Q	1.267
15	40932	12 54 40.45	−01 34 41.3	17.16	-0.46	0.10	F	
16	41398	12 54 46.01	+01 06 31.0	17.76	-0.48	0.51	Q	1.510
17	47671	12 55 40.94	−01 43 07.9	17.95	-0.47	0.33	Q	0.410
18	56036	12 57 07.93	−00 23 19.2	17.06	-0.67	0.15	B	
19	58155	12 57 18.20	−01 40 57.9	17.95	-0.48	0.18	Q	0.448
20	64684	12 58 25.74	+01 13 20.0	16.38	-1.02	-0.34		
21	65650	12 58 37.09	+01 23 47.8	16.48	-0.33	-0.07		
22	75424	13 00 13.67	+01 44 44.6	16.84	-0.55	-0.24		
23	95745	13 03 21.04	+02 05 32.0	17.29	-0.54	0.30	Q	0.736
24	110315	13 05 42.51	+02 30 10.2	17.38	-0.45	0.41	Q	0.773
25	111083	13 05 40.82	−01 43 04.6	16.96	-1.18	-0.38		
26	111639	13 05 47.22	+00 29 29.9	16.40	-0.64	-0.19		
27	113359	13 06 09.30	+01 50 43.9	17.34	-0.39	0.31	B	
28	117165	13 06 32.35	−02 13 17.5	17.90	-0.39	0.50	Q	0.835
29	125132	13 07 59.00	+02 14 28.1	15.73	-0.19	0.48	S	
30	126546	13 08 01.03	+00 19 50.8	17.65	-0.47	0.28	Q	1.311
31	130553	13 08 46.41	+00 42 33.8	17.72	-0.31	0.75	S	

Table 4.2: continued

#	Obj name	$\alpha(1950)$	$\delta(1950)$	B	$U-B$	$B-R$	ID	z
Field 863								
[1]1	9703	13 10 00.38	−01 04 11.2	17.28	-0.23	0.67	S	
2	18292	13 11 53.55	+02 17 06.9	16.94	-0.80	0.76	Q	0.306
3	18415	13 11 52.09	+01 27 44.7	15.46	-0.43	-0.16	B	
4	27650	13 13 35.36	−01 38 15.2	17.74	-0.61	0.53	Q	0.406
5	28858	13 13 57.04	+01 07 13.8	17.99	-0.44	0.01	Q	2.398
6	33386	13 14 51.02	+00 18 24.3	15.85	-1.25	-0.25	S	
7	34727	13 15 12.47	+01 20 37.1	16.74	-0.84	-0.22	S	
8	36898	13 15 37.47	+01 27 26.9	17.94	-0.41	0.47	Q	1.630
9	39441	13 16 06.49	+00 23 20.6	17.97	-0.48	0.61	Q	0.490
[1]10	40837	13 16 23.15	+01 51 46.0	17.33	-0.25	0.90		
11	42799	13 16 41.94	−00 58 20.1	16.25	-0.39	-0.06		
12	44634	13 17 07.88	+02 03 52.7	17.52	-0.76	-0.01		
13	45934	13 17 15.85	−01 42 20.3	17.35	-0.46	0.61	Q	0.225
14	48149	13 17 46.28	−00 18 45.5	17.78	-0.70	0.61	Q	0.350
15	50498	13 18 11.10	+00 34 37.3	17.28	-0.72	0.07		
16	57230	13 19 38.99	+01 46 15.2	17.45	-0.29	1.03	NELG	
17	73436	13 22 44.89	−01 21 13.6	16.96	-0.52	0.20	B	
18	89696	13 26 10.58	+02 06 47.6	17.34	-0.67	0.65	Q	1.430
19	89697	13 26 13.13	+02 06 41.8	15.27	-0.34	-0.02	B	
20	93275	13 26 50.52	−00 41 14.5	16.24	-0.77	-0.14		
21	94910	13 27 02.72	−01 18 58.6	17.27	-0.30	0.48	B	
22	100232	13 28 07.10	−00 01 44.6	15.81	-0.98	-0.34		
Field 865								
1	4761	13 48 55.12	+01 18 27.5	17.79	-1.06	0.76	Q	1.094
2	6937	13 49 16.61	+00 07 08.8	17.31	-1.20	0.76	Q	1.435
3	10935	13 49 46.46	−01 03 59.1	15.72	-0.62	0.93		
4	20729	13 51 21.60	−02 41 47.8	17.57	-1.50	-0.34		
5	23114	13 51 51.33	+00 00 44.4	17.24	-0.95	0.62	Q	1.501
6	26029	13 52 16.09	−00 37 08.4	17.82	-0.72	0.83	B	
7	30428	13 52 58.79	+00 26 04.5	16.13	-0.93	0.10		
[1]8	36781	13 54 05.64	+01 48 07.3	17.35	-0.59	1.78	S	
9	39763	13 54 34.22	+01 19 31.4	17.75	-0.90	0.48	F	
10	42275	13 54 53.83	−02 33 02.6	17.34	-1.06	0.41	Q	0.559
11	47081	13 55 51.57	+02 28 18.0	16.72	-0.85	0.75	Q	0.955
12	64663	13 58 36.94	+00 01 24.3	17.17	-0.64	0.53	Q	1.845
13	65845	13 58 44.22	−01 05 57.2	17.23	-1.15	-0.25		
14	73174	13 59 59.13	+00 20 20.7	16.74	-1.02	-0.18		
15	78901	14 00 54.22	+00 35 42.1	17.18	-1.06	-0.30		
16	96980	14 03 45.66	−01 05 14.9	15.77	-0.89	-0.02		
17	103583	14 04 49.73	+00 52 55.1	18.00	-0.65	0.45	B	
[1]18	117077	14 06 48.92	−01 10 21.1	17.98	-0.47	0.32	F	
19	121364	14 07 20.88	−02 31 55.0	17.90	-0.75	0.82	Q	1.263
20	122903	14 07 47.22	+00 33 01.5	15.51	-0.85	-0.39		

Table 4.2: continued

#	Obj name	α(1950)	δ(1950)	B	$U-B$	$B-R$	ID	z
Field 866								
1	7635	14 09 48.52	+01 01 21.4	16.90	-0.59	0.52	Q	1.635
2	14599	14 11 22.58	−00 12 45.1	17.61	-0.29	0.14		
[3]3	16843	14 11 52.14	−00 59 57.5	17.92	-0.38	0.08	S	
4	19392	14 12 25.02	+01 36 05.5	17.86	-0.28	0.21	B	
5	20683	14 12 32.60	−02 40 35.4	16.86	-0.73	-0.21		
6	21762	14 12 54.76	−00 12 38.4	17.26	-0.46	0.70	Q	1.148
7	22238	14 13 03.58	+01 31 12.6	16.84	-1.01	-0.45		
8	22960	14 13 18.31	+01 36 36.8	17.52	-0.58	0.21	Q	1.246
9	23019	14 13 16.58	+01 07 50.8	17.53	-0.38	0.50	Q	1.042
10	23850	14 13 26.45	+00 21 54.7	16.23	-0.36	-0.03	B	
11	34534	14 15 41.58	−01 54 27.8	17.70	-0.32	0.01		
12	34636	14 15 37.07	−02 30 39.1	16.75	-1.15	-0.41		
[3]13	35311	14 15 50.97	−02 19 46.7	17.07	-0.34	0.62	S	
14	48541	14 18 46.52	−00 47 13.6	16.94	-0.84	-0.26		
15	59916	14 21 07.41	+02 03 22.3	17.04	-0.76	-0.43		
[3]16	60145	14 21 05.91	+00 23 56.2	17.83	-0.93	0.09	S	
17	63491	14 21 41.99	−01 30 01.5	16.50	-0.35	-0.07	B	
18	63880	14 21 57.34	+01 08 32.2	17.79	-0.71	0.35	Q	1.060
19	71381	14 23 16.51	−01 19 47.6	16.34	-1.01	-0.45		
20	72011	14 23 26.21	−00 13 31.1	17.67	-0.58	0.38	Q	1.078
21	72625	14 23 41.58	+00 55 27.8	17.59	-0.53	0.20	Q	0.890
22	76735	14 24 24.63	−00 07 29.6	16.27	-0.52	0.03	Q	0.632
23	79937	14 25 03.62	+00 12 35.0	17.81	-0.92	-0.56		
24	79958	14 25 00.01	+00 02 43.4	17.59	-0.55	0.14	Q	1.548
25	80540	14 25 08.56	+01 56 19.2	15.76	-0.92	-0.66		
26	93010	14 27 24.49	+00 16 38.4	15.28	-0.71	-0.11		
27	93579	14 27 38.15	+01 46 40.1	16.35	-0.40	-0.63		
[1]28	94831	14 27 40.51	−00 46 19.9	16.91	-0.21	1.21	S	
29	96052	14 28 08.46	+02 02 55.9	17.49	-0.58	0.05	Q	2.107
Field 867								
1	3762	14 28 41.00	+00 18 00.5	17.71	-1.04	-0.50		
2	6483	14 29 07.36	+01 53 08.5	17.88	-0.86	-0.22		
3	7023	14 29 07.31	−01 00 17.4	16.87	-0.82	-0.08		
4	7552	14 29 16.58	+01 27 44.6	17.98	-0.89	0.20		
5	7914	14 29 18.97	−00 15 11.0	17.51	-1.31	-0.59		
6	8804	14 29 26.02	+00 15 29.7	17.69	-0.82	-0.31		
7	11444	14 29 57.86	+01 37 47.8	17.54	-0.85	0.15	Q	1.530
8	13433	14 30 16.66	+01 59 27.5	17.27	-0.70	-0.12		
9	13917	14 30 09.99	−00 46 04.3	17.24	-0.98	0.18	Q	1.020
10	14509	14 30 25.26	+01 32 08.6	17.33	-1.24	-0.49		
11	17327	14 30 42.81	−02 34 26.5	16.68	-0.71	-0.43		
12	32419	14 33 07.64	+02 23 48.8	17.79	-0.80	0.12	Q	2.130
13	38091	14 33 50.73	−00 16 03.9	17.56	-0.53	0.62		

Table 4.2: continued

#	Obj name	α(1950)	δ(1950)	B	$U-B$	$B-R$	ID	z
Field 867 continued								
14	38722	14 34 00.40	+01 51 14.1	17.80	-1.04	-0.56		
15	47076	14 35 18.78	+01 05 52.2	17.39	-0.81	-0.33		
16	47588	14 35 13.31	−01 34 13.7	15.83	-0.90	0.54	Q	1.310
17	48077	14 35 28.19	+01 20 35.0	17.46	-0.98	-0.32		
18	57077	14 36 49.38	+01 53 56.1	17.29	-0.75	-0.26		
19	57180	14 36 44.72	+01 15 44.8	16.27	-0.79	-0.40		
20	60587	14 37 13.09	−00 53 14.9	16.54	-1.15	-0.10	B	
21	69092	14 38 35.59	+01 23 08.8	16.80	-1.05	-0.37		
22	79529	14 40 18.01	+01 49 37.9	17.86	-0.78	0.33	Q	1.170
23	80895	14 40 25.72	−00 24 42.0	17.82	-0.85	0.31	Q	1.820
24	82284	14 40 38.41	−02 34 40.4	17.07	-0.57	0.33	Q	0.675
[1]25	94144	14 42 40.75	+01 13 49.5	16.95	-0.36	-0.33	S	
26	109285	14 45 05.80	+02 22 12.2	17.98	-0.97	-0.29		
27	111176	14 45 08.84	−02 31 38.2	17.60	-0.81	0.16	Q	1.730
28	116100	14 46 05.69	+02 18 54.2	17.75	-0.50	0.33	Q	0.668
29	118922	14 46 23.72	−02 20 01.6	16.87	-0.54	0.00	B	
30	125196	14 47 28.98	+00 28 51.8	17.88	-0.72	0.27	Q	0.946
31	11895	14 29 54.71	−00 53 04.6	17.50	-0.97	0.16	Q	2.075
32	17853	14 30 47.03	−00 41 36.0	15.85	-0.91	0.39	Q	1.112
33	86006	14 41 27.19	+01 42 36.9	16.77	-0.53	0.77	Q	0.296

Field 863 attributes are for 1987 study.

Labels:
1 : objects where $U-B > \mathrm{UVX}_{lim}$;
2 : quasar confirmed by P.C. Hewett (see text);
3 : identification by B.J. Boyle.

4.2.2 Observing strategy

Spectroscopy of the candidate sample was performed at the Isaac Newton telescope at the Observatorio del Roque de los Muchachos del Institutio de Astrofisica de Canarias, La Palma on 28–29 May 1987 and 17–22 May 1988 with the RGO Spectrograph and the IPCS detector. Briefly, the IPCS is a blue-sensitive photon-counting device which stores individual photon events in a 2D image of about 10^6 elements, with zero readout noise and a negligible dark count. Each photoelectron produced when an optical image is focussed at the photocathode of the high-gain 4-stage EMI image intensifier leads to

Figure 4.3: $(U-B)/(B-R)$ plots for candidates in each field. $(U-B)$ is on the x-axis, $(B-R)$ on the y-axis. Left hand plots show candidate numbers as given in Table 4.2, right hand indicates spectroscopic ID's as specified in the text. UVX limits are shown (note that the inner regions of the stellar locus have already been removed on some plots).

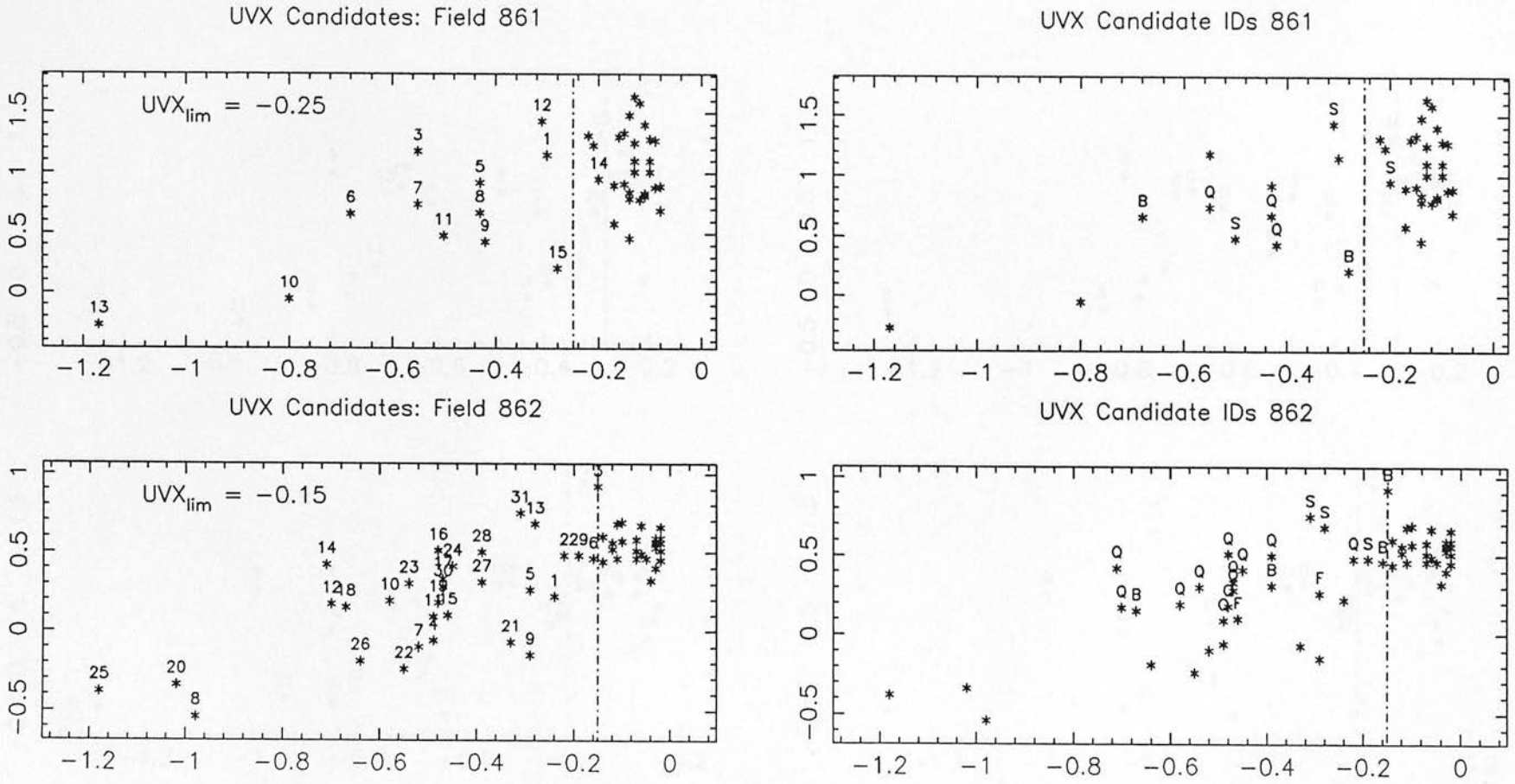

Figure 4.3: continued

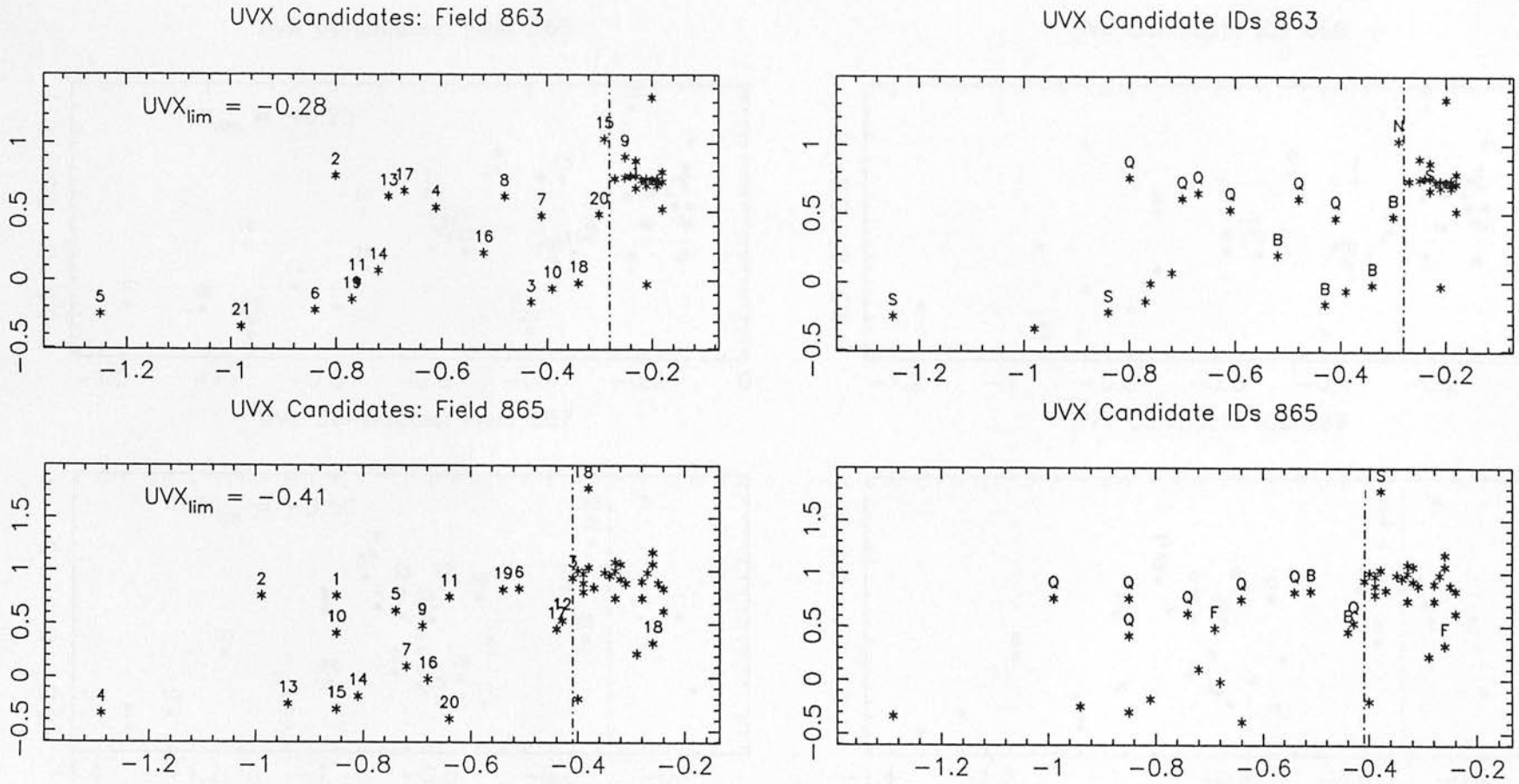

Figure 4.3: continued

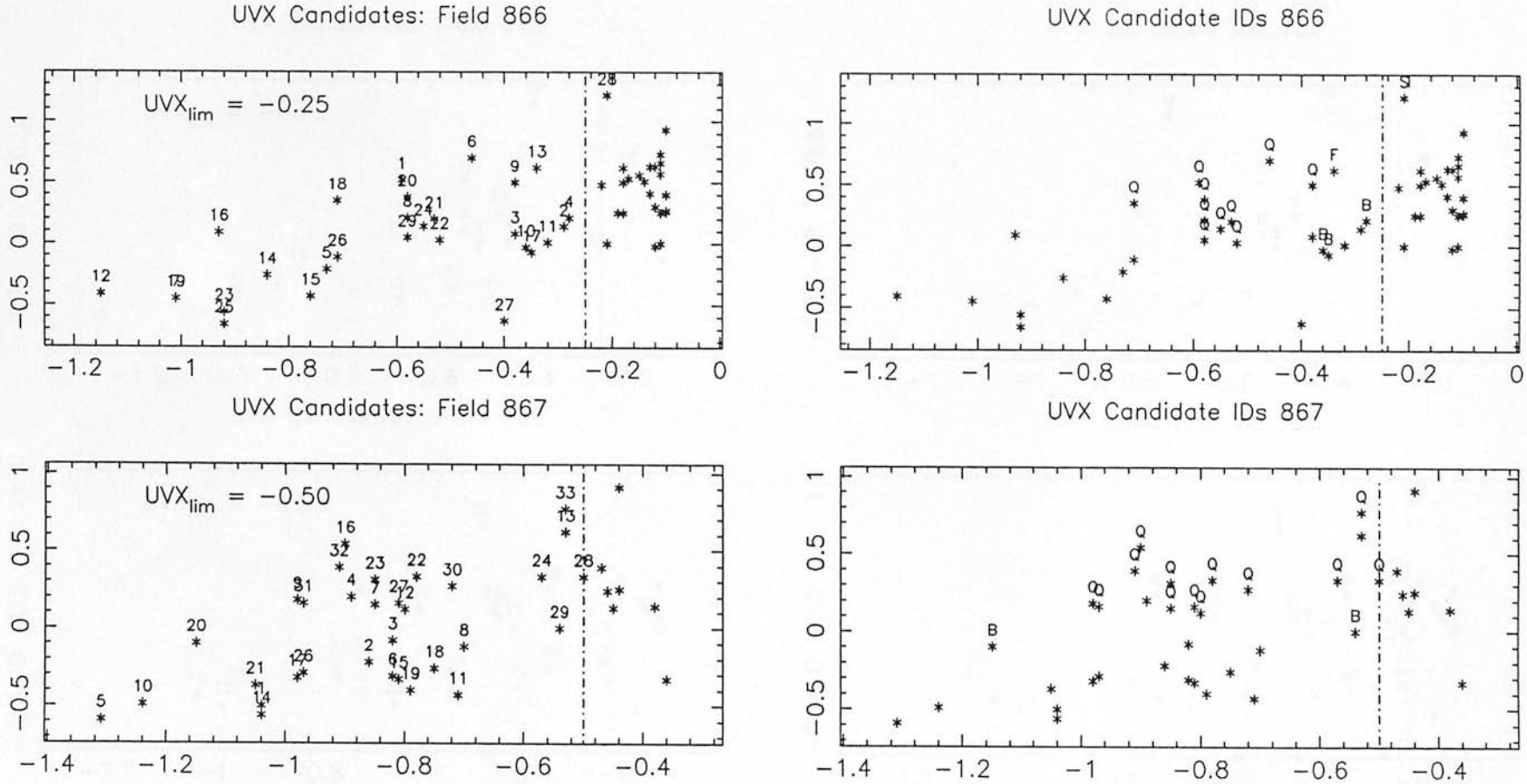

Figure 4.3: continued

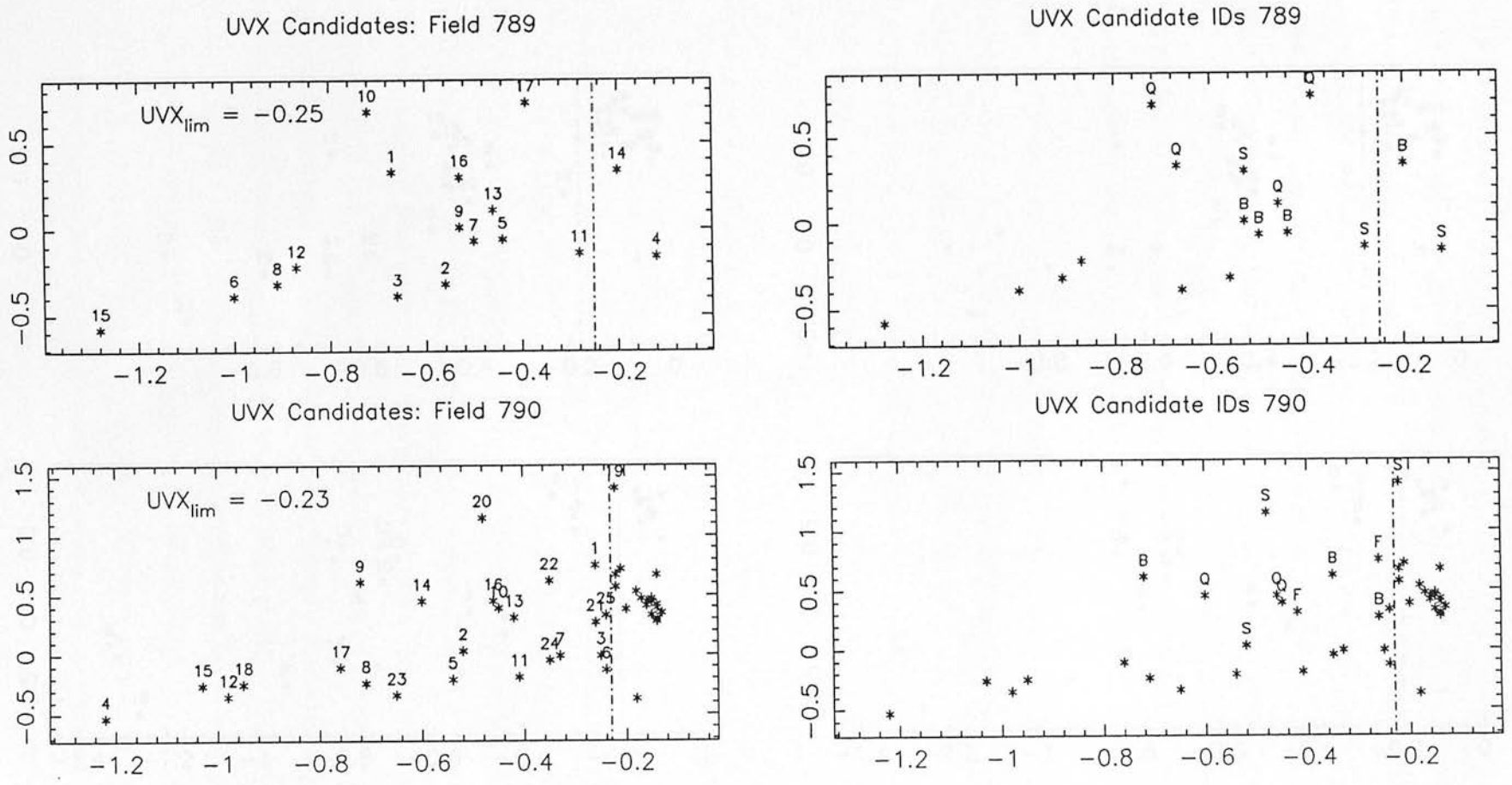

Figure 4.3: continued

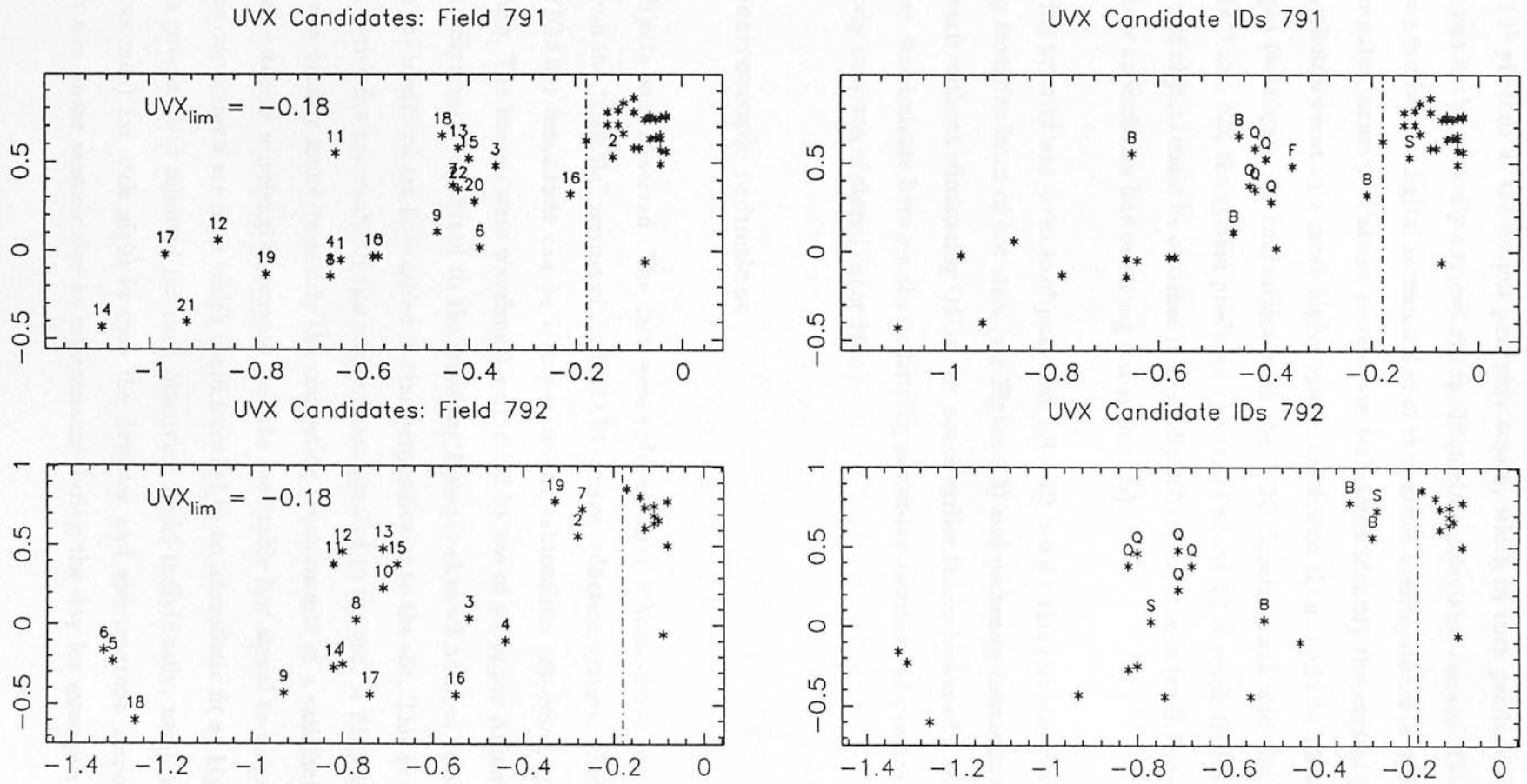

on average 10^8 photons at the output phosphor screen, which in turn produce about 7×10^5 electrons in the optically-coupled Philips Plumbicon television camera. Continuous scanning produces a digital accumulation of the photon events, stored in 512K of external computer memory. Pattern recognition techniques identify the central position of each photon event to a much higher spatial resolution than would be obtained with analogue techniques. In conjunction with the RGO Spectrograph and the configurations in Table 4.3, the system produced spectra of about 12 Å resolution where identification of objects could be obtained in typically 300–1000 seconds (sufficient time to clearly show an emission line or strong stellar feature).

Observing priority was given to objects with $(B-R) > 0.0$: this criterion favours objects away from the locus of hot stars (see Figure 4.3) and decreases contamination by white dwarfs without eliminating QSOs. As noted earlier the inclusion of a redder waveband can discriminate between the underlying power-law continua of quasars and the black-body continua of stars (Usher 1981).

4.2.3 Spectroscopic reductions

In all 134 objects were observed. The data were reduced using a home-made package developed from the "callable" version of the FIGARO image reduction system, whereby individual FIGARO commands can be incorporated as subroutines providing speed and ease of use. The images were wavelength-calibrated by use of a Copper-Argon arc spectrum: a polynomial was fitted to the wavelength-versus-channel number relation derived from the identified arc-lines added in bins perpendicular to the slit. This fit was then used to derive fits automatically for each column parallel to the slit. A fifth-order polynomial was usually found to satisfy the competing requirements of a satisfactory fit to the real detector wavelength response and the inevitable low signal-to-noise on some extreme one-column arc-lines which could have led to an unrealistic fit at higher orders. This process was followed for each observing night individually, using long arcs (>360 seconds) for each night in case the detector and spectrograph response changed in a non-linear manner due to maintenance during the day for example. In

order to account for linear shifts *during* the night (due to temperature changes, EHT changes etc.) short arcs (usually 60 seconds) were performed at regular intervals: the wavelength scales for images were then derived from the long arc fits together with interpolated linear shifts from suitable surrounding arcs (which were always $\leq$ 1.5Å within one night's observing).

Before the reduction to 1D spectra another step was necessary. The Plumbicon TV tube electron optics produce "s-distortion" in the shape of spectra. This can largely be eliminated at the telescope by adjusting the clocking of each TV scanning row in the electronics to counteract the effect. However differential refraction at high hour angles produces a similar distortion in shape; these two effects can be removed by fitting a polynomial (usually third order is sufficient) to the spectra and re-binning to straighten the spectra. The object spectra were then extracted with sky spectra either side and sky-subtracted spectra obtained. These were flux-calibrated using standard stars whose spectra were taken at the beginning and ends of nights, in order to correct for instrumental response and atmospheric features. In an attempt to eliminate second-order diffraction effects which occur at $\lambda \simeq$ 6900Å, a blue-blocking filter WG360 was used to obtained the true red-end of these spectra. This was scaled over the range 5800Å to 6400Å to the blue-end "no-filter" spectra and added. True flux-calibrated values available in FIGARO or derived from the literature for standard stars HZ43 and GD140 (Oke 1974) and Kopff 27 (Stone 1977) were then used to calibrate the data.

The results of the spectroscopy are included in Table 4.2. ID's are given in column 8 which comprise the UKST field number and a label within each catalogue. 69 new QSOs were identified whose redshifts are indicated in column 9 with ID's 'Q'. Other objects are classified in the following way: 'NELG' narrow emission line galaxy, 'F' featureless spectra (including possibly BL Lac objects), 'C' carbon star, 'B' stars with Balmer absorption (this would include horizontal branch stars, white dwarfs etc.), 'S' other main sequence star (further spectral classification not available at present). These ID's are also marked on Figure 4.3. Notice should be drawn in particular to object 790:63702 which exhibits strong broad line absorption (c.f. for instance object 0856+172 in Hazard *et al.* 1984, to which it is practically identical).

An interactive trial-and-error routine was developed for redshift evaluation whereby an identification of a feature as a QSO emission line enabled a redshift calculation and a consequent indication of the positions of other strong lines for verification (Ly-α was excluded from the redshift determination because of the familiar blueward "forest" absorption which together with blending of the N V line on the redward side gives an excessive redshift estimate — see Wilkes (1986). Multiple attempts indicated that this process produced redshifts accurate to $\simeq \pm 0.005$. The QSO spectra are shown in Figure 4.4 with fitted line ID's. Table 4.4 shows the principal lines identified in each QSO for spectra which were not immediately obvious. Problems occurred when only one strong line was seen: usually this was identified as a QSO in the redshift range $0.6 \gtrsim z \gtrsim 1.0$ where the only strong line in the observed wavelength range is Mg II with C III] and Hβ at extreme values of λ. There is the possibility of ambiguity between QSOs with redshift $z \simeq 0.4$ and QSOs with redshift $z \simeq 1.1$ (see for example the redshift revisions of Green, Schmidt & Liebert 1986 to the original PG catalogue). Knowledge of other more subtle QSO features was used in these cases. For example, the continuum around Mg II often rises an appreciable amount due to multiplet Fe II emission (see Wills, Netzer & Wills (1985) for an Fe II emission study). Inspection of the continuum shape together with recognisable features in this emission in most cases provided adequate evidence for Mg II, coupled with comparison with more detailed analyses of Mg II profiles (in particular the apparent "sharp drop" at $\sim \lambda 2650$, an effect of Fe II $\lambda 2500$ emission seen in Grandi (1981) and Wills, Netzer & Wills (1985) was commonly visible). Other features included a sometimes asymmetrical C III] line, caused by Al III $\lambda 1858$ and Si III] $\lambda 1892$ emission (Wilkes 1986). Table 4.4, column 3 contains a rough indication of the estimated probability of correct ID for these more difficult QSOs, where '3' indicates certainty, '2' high probability, and '1' indicates cases of less certainty. Only 5 quasars remain in the last category.

4.2.4 Final tailoring of the sample

In any statistical study involving the properties of a selected sample, it is vital to understand and quantify the limits of validity of the various selection criteria. This

Table 4.3: IPCS/RGO Spectrograph set-up.

Dates of Obs.	Spectr. grating	Camera	Slit widths used / μm	/arcsec	Comparison lamp	Flux standards	IPCS format lines × x-sections	Approx. λ range /Å	Mean dispersion /Å channel^{-1}
28–29 May 1987	R150V	500	180	1.00″	Cu-Ar	HZ43 GD140 Kopff27	2044 × 20	3320 → 7260	1.92
			220	1.20″					
			250	1.35″					
			305	1.65″					
17–22 May 1988	R150V	500	230	1.25″	Cu-Ar	HZ43 GD140 Kopff27	1020 × 50	3330 → 7230	3.80
			250	1.35″					
			270	1.46″					
			305	1.65″					

Figure 4.4: Spectra of identified redshifts in the survey. The wavelength axis is in Angstroms, and the y-axis represents relative flux. The object names are those given in Table 4.2, prefixed by field number. The redshifts are given, along with principal line positions at this redshift.

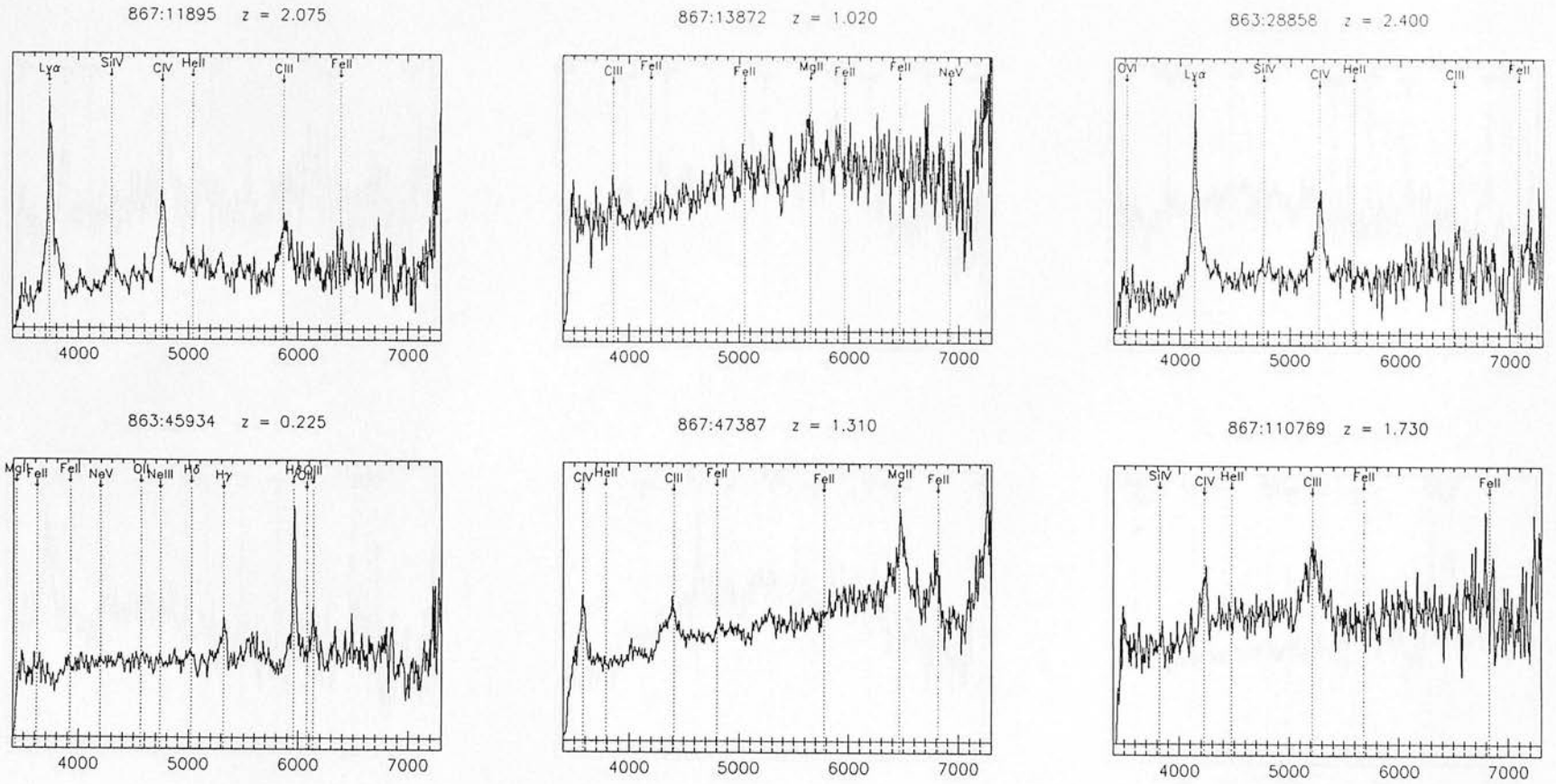

Figure 4.4: continued

867:11407 z = 1.530

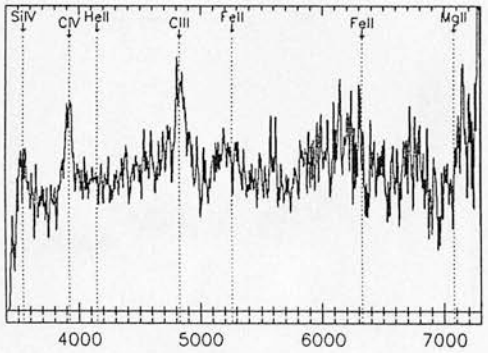

867:17853 z = 1.112

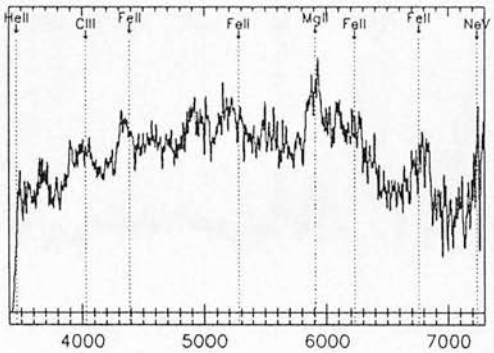

863:27650 z = 0.406

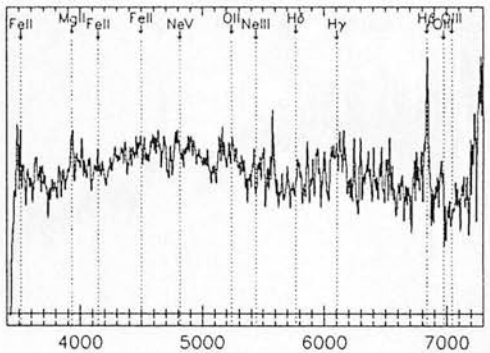

863:48149 z = 0.350

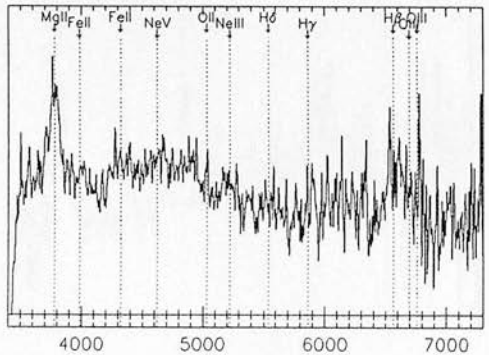

867:81976 z = 0.675

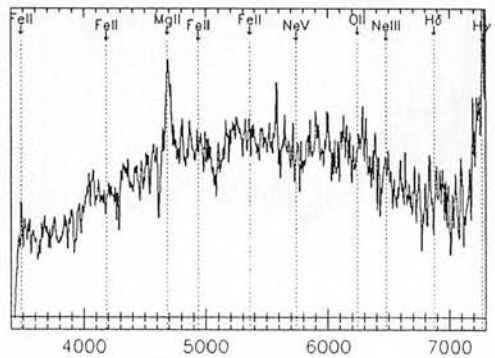

863:18292 z = 0.306

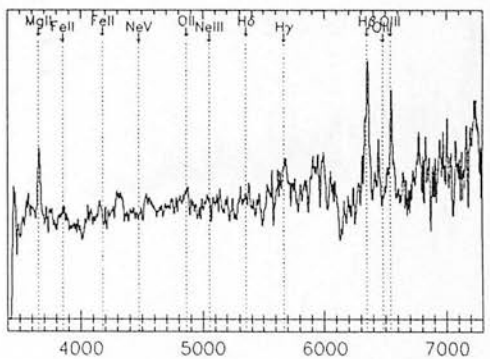

Figure 4.4: continued

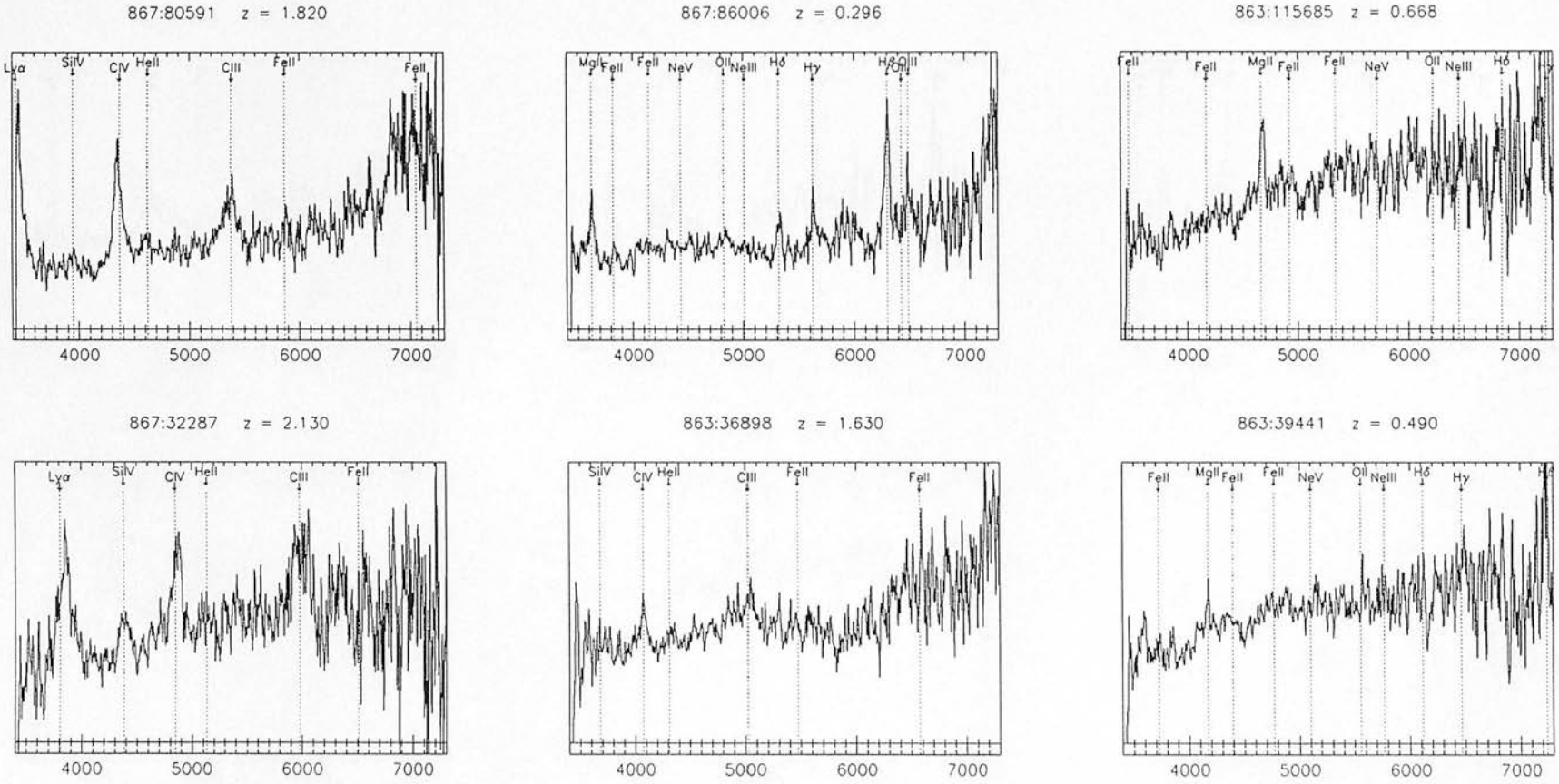

Figure 4.4: continued

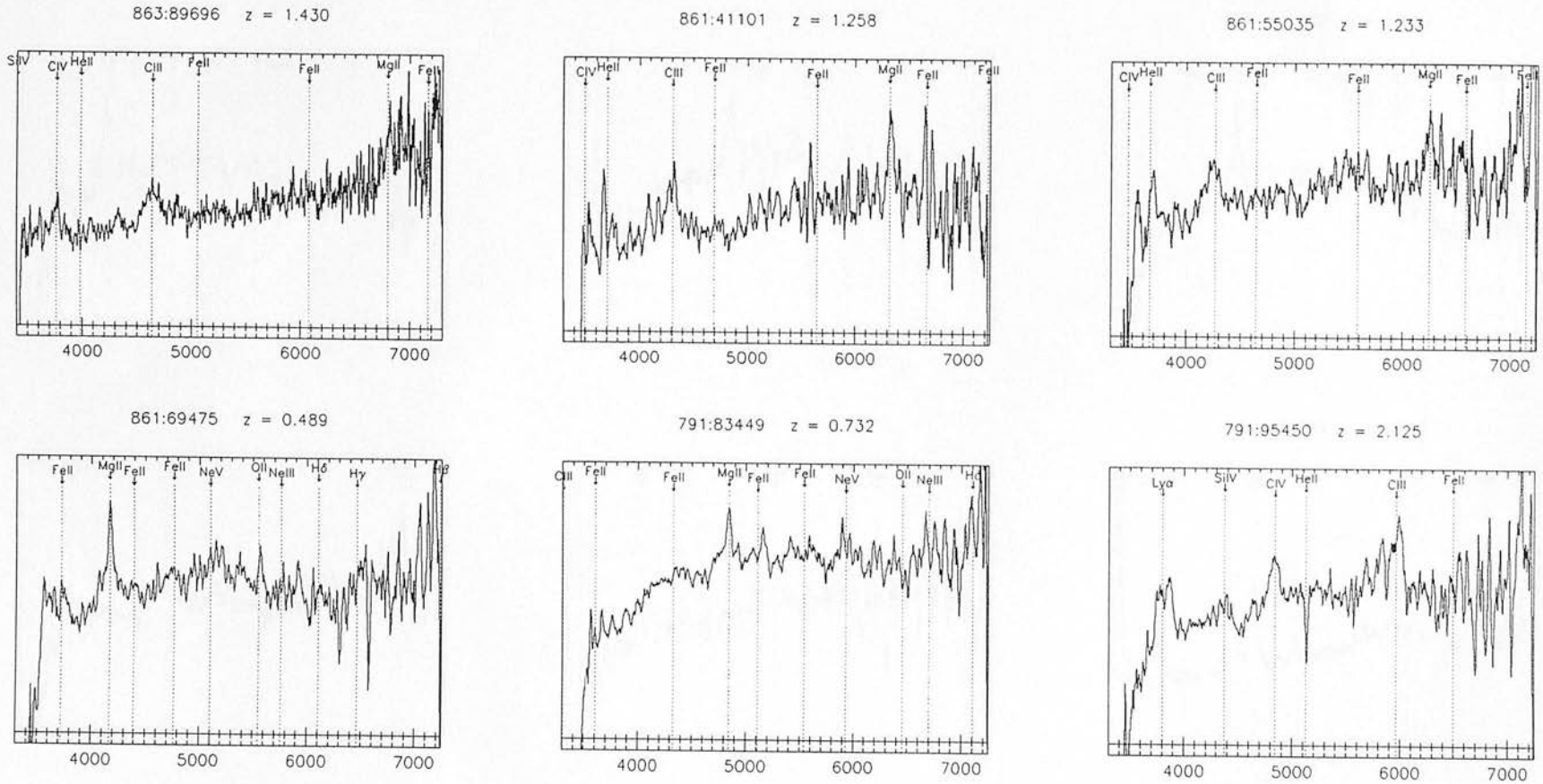

Figure 4.4: continued

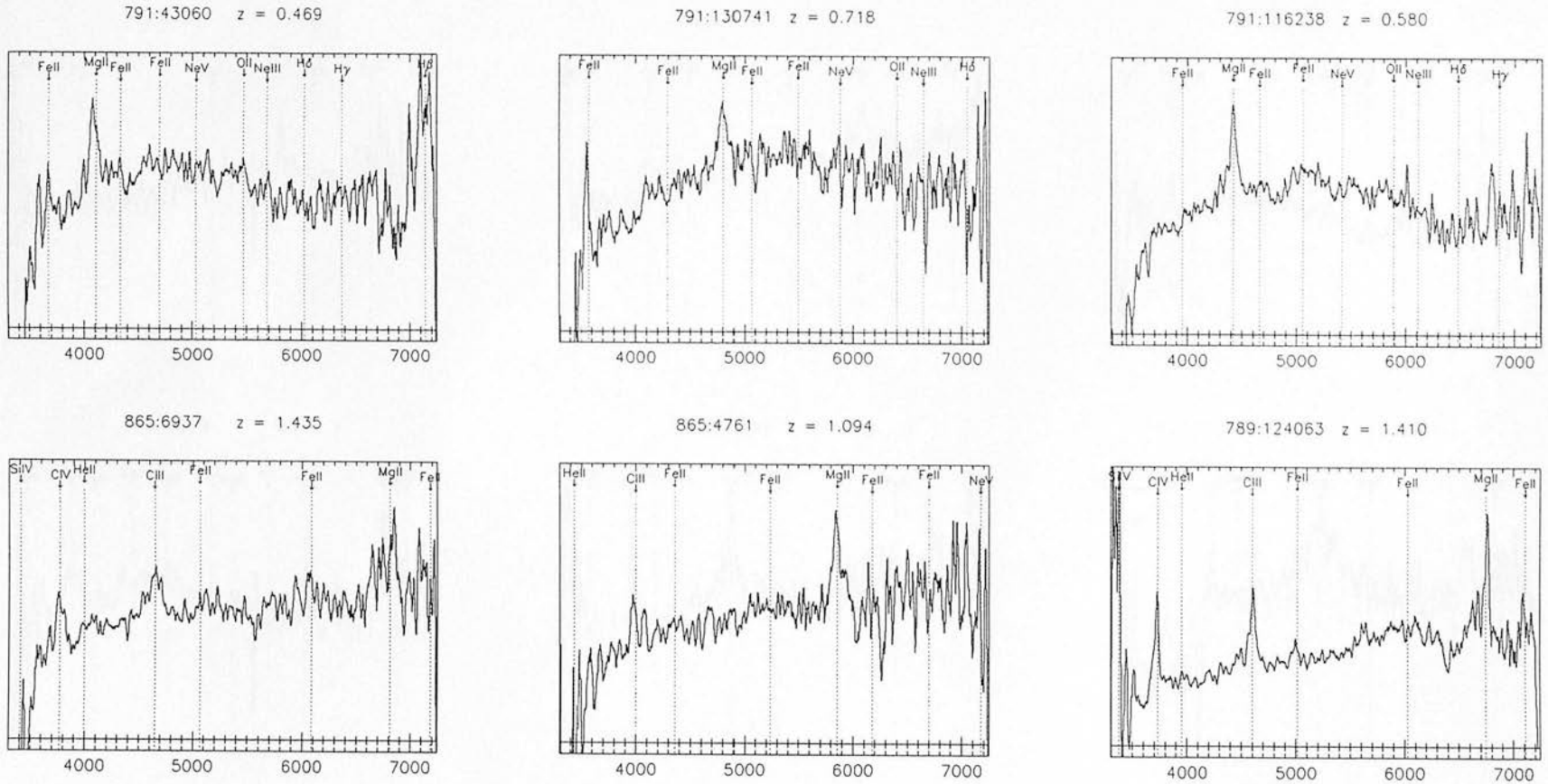

Figure 4.4: continued

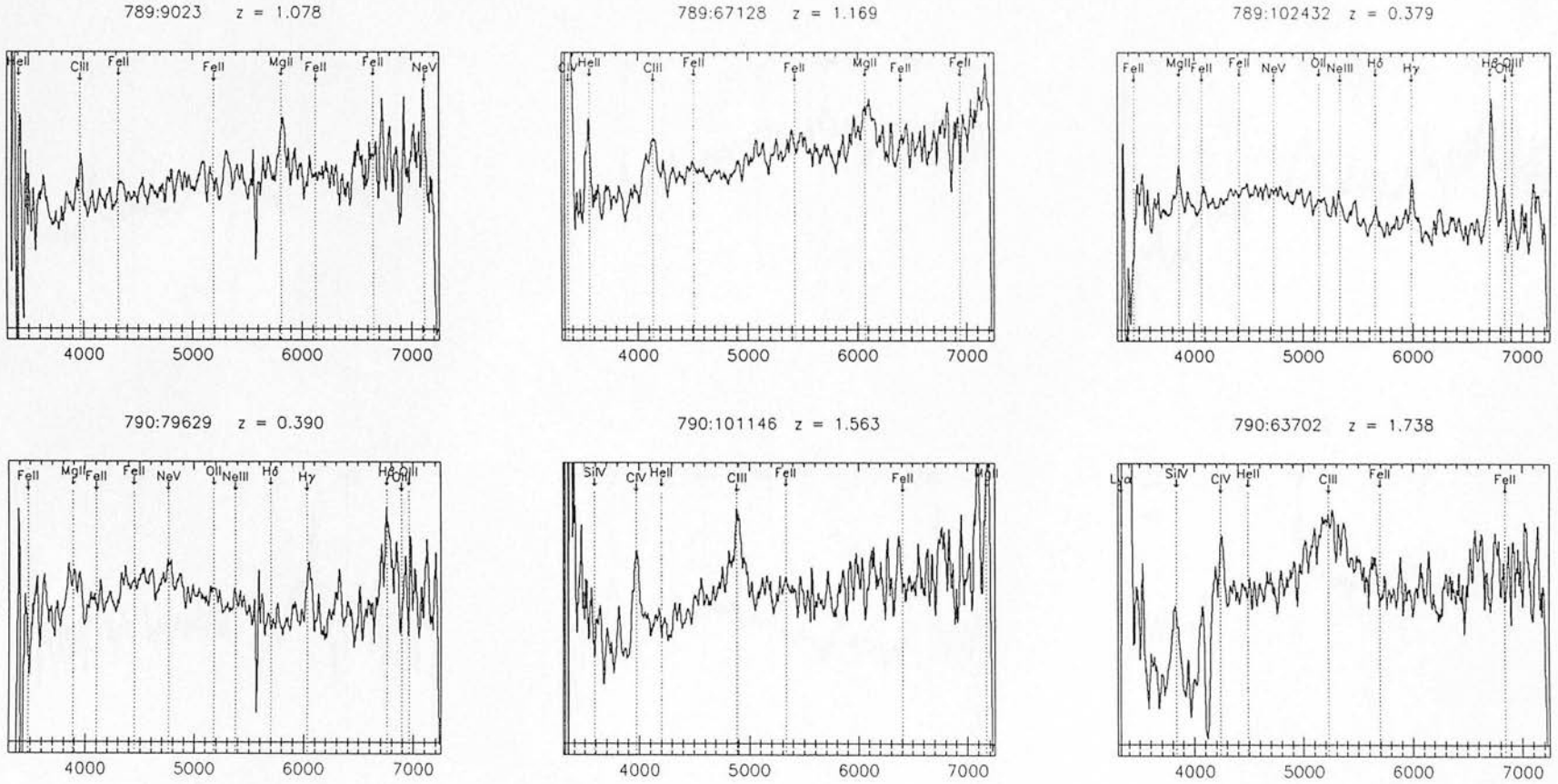

Figure 4.4: continued

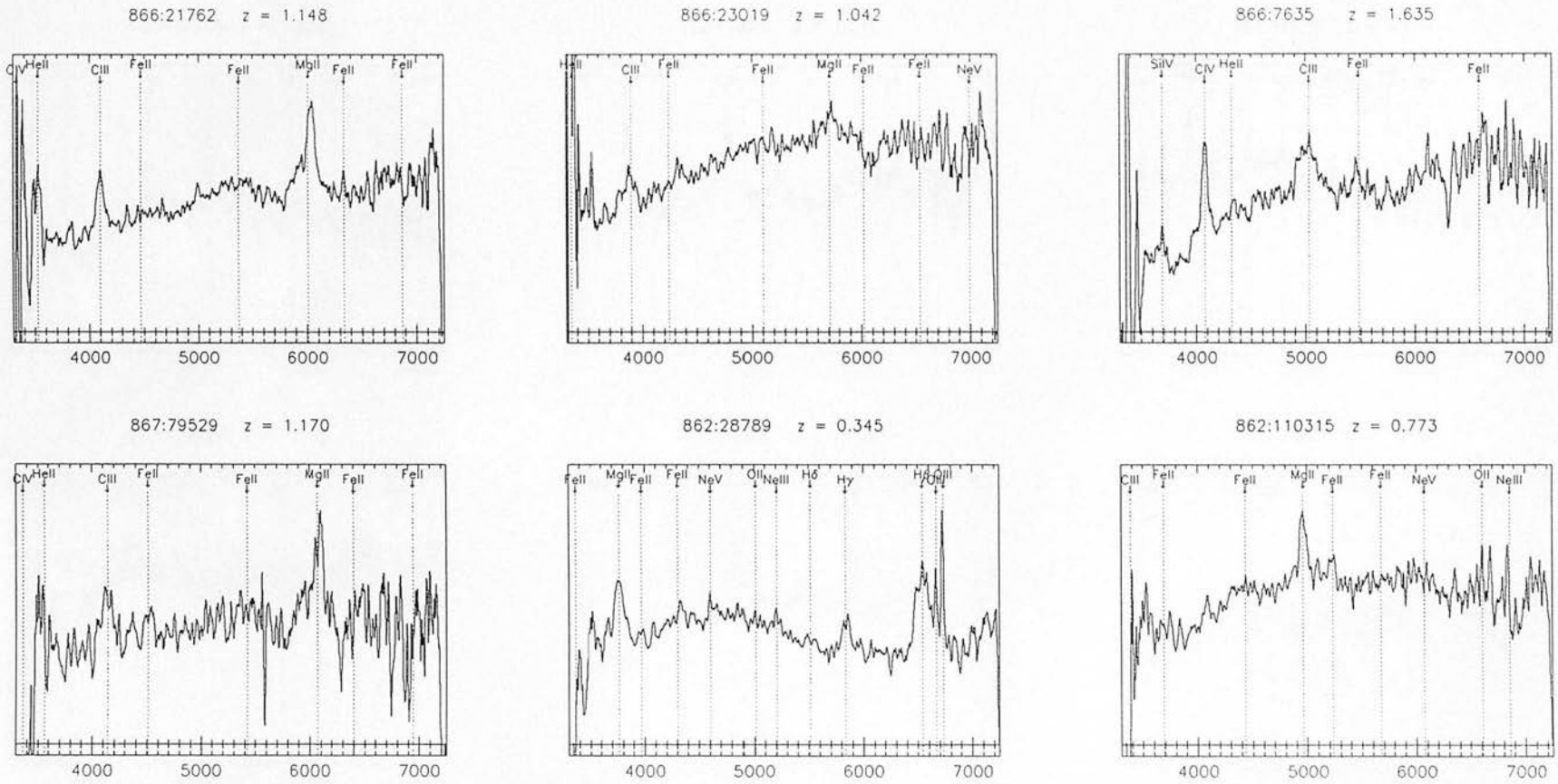

Figure 4.4: continued

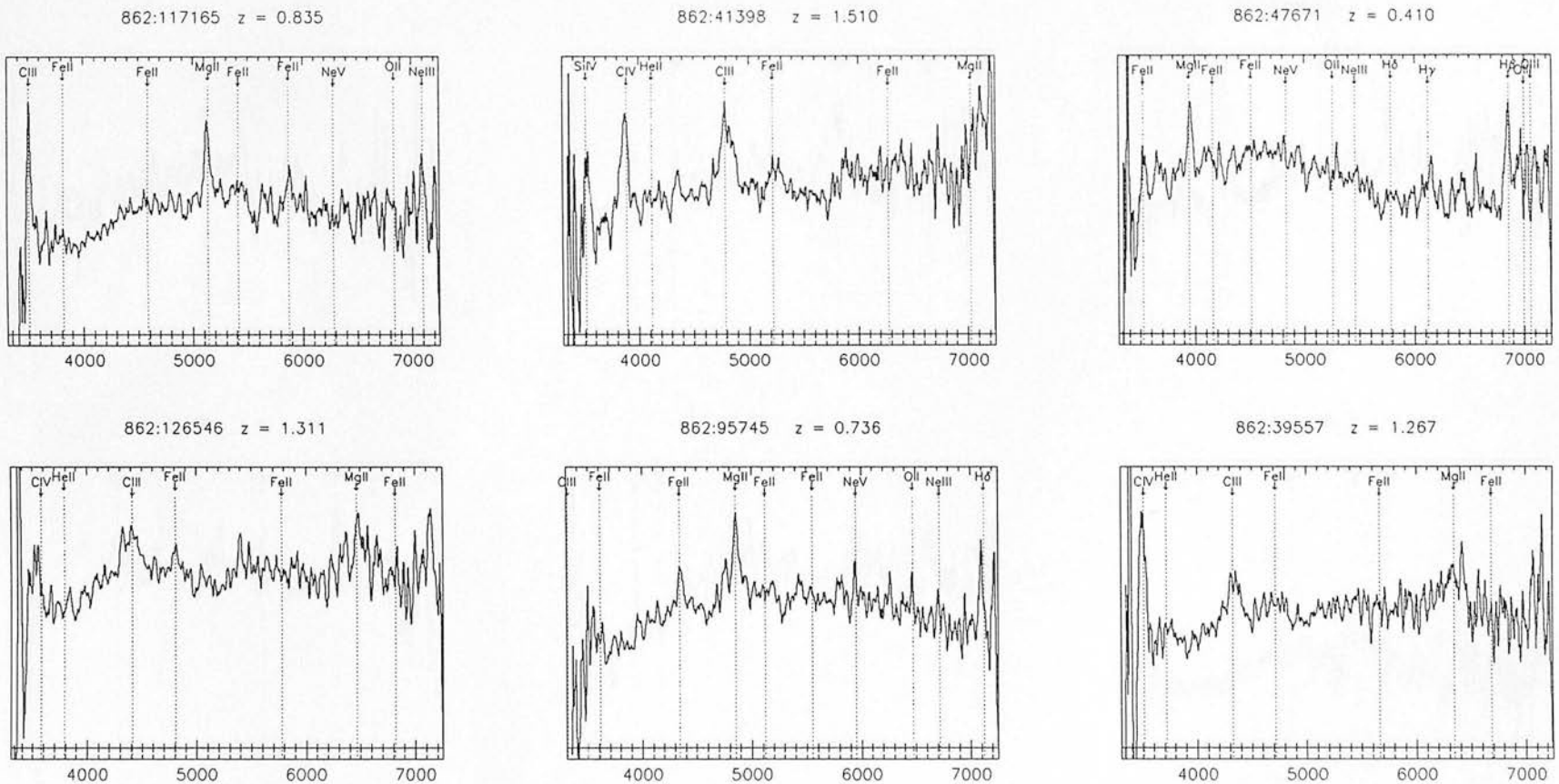

Figure 4.4: continued

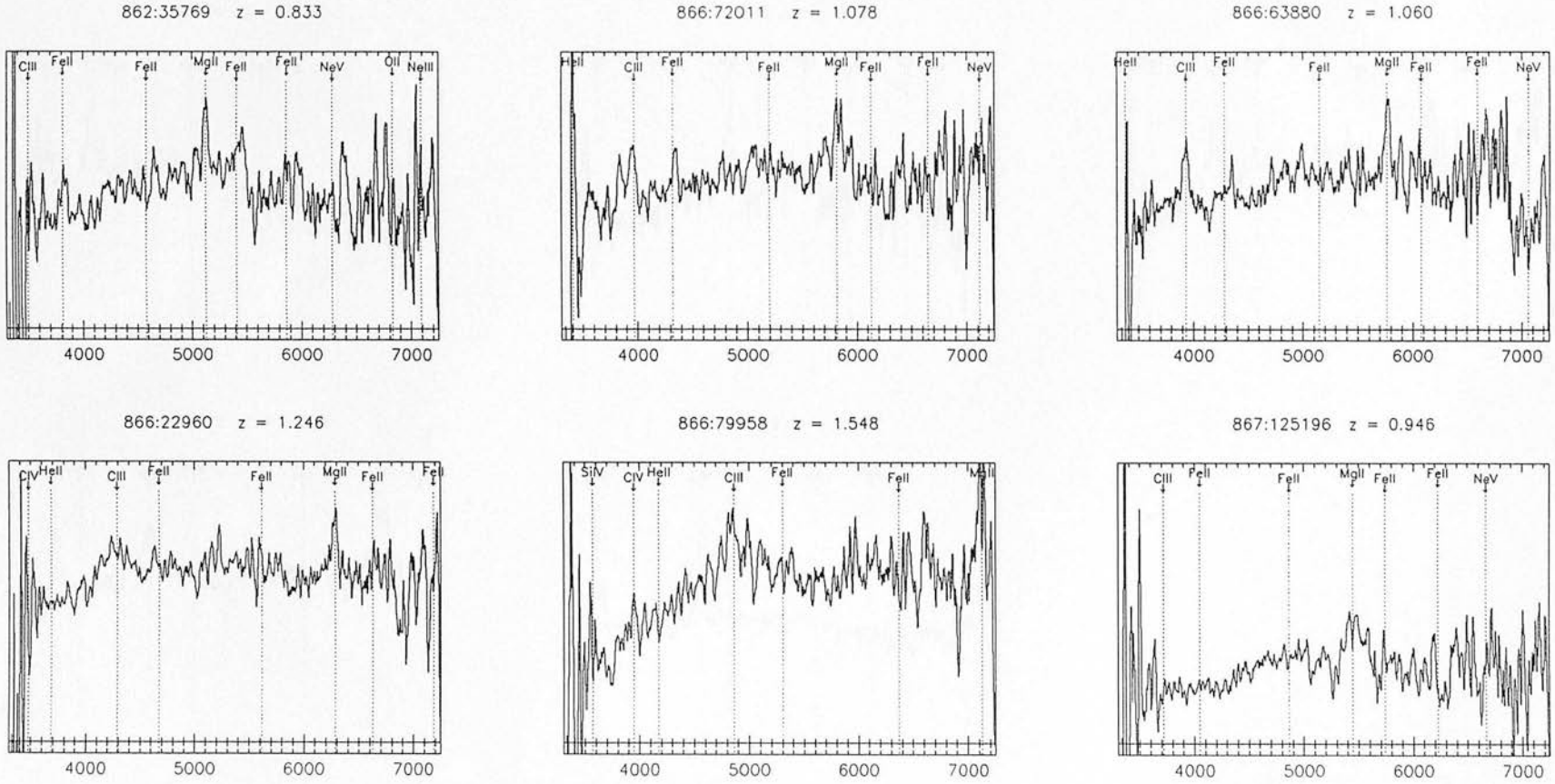

Figure 4.4: continued

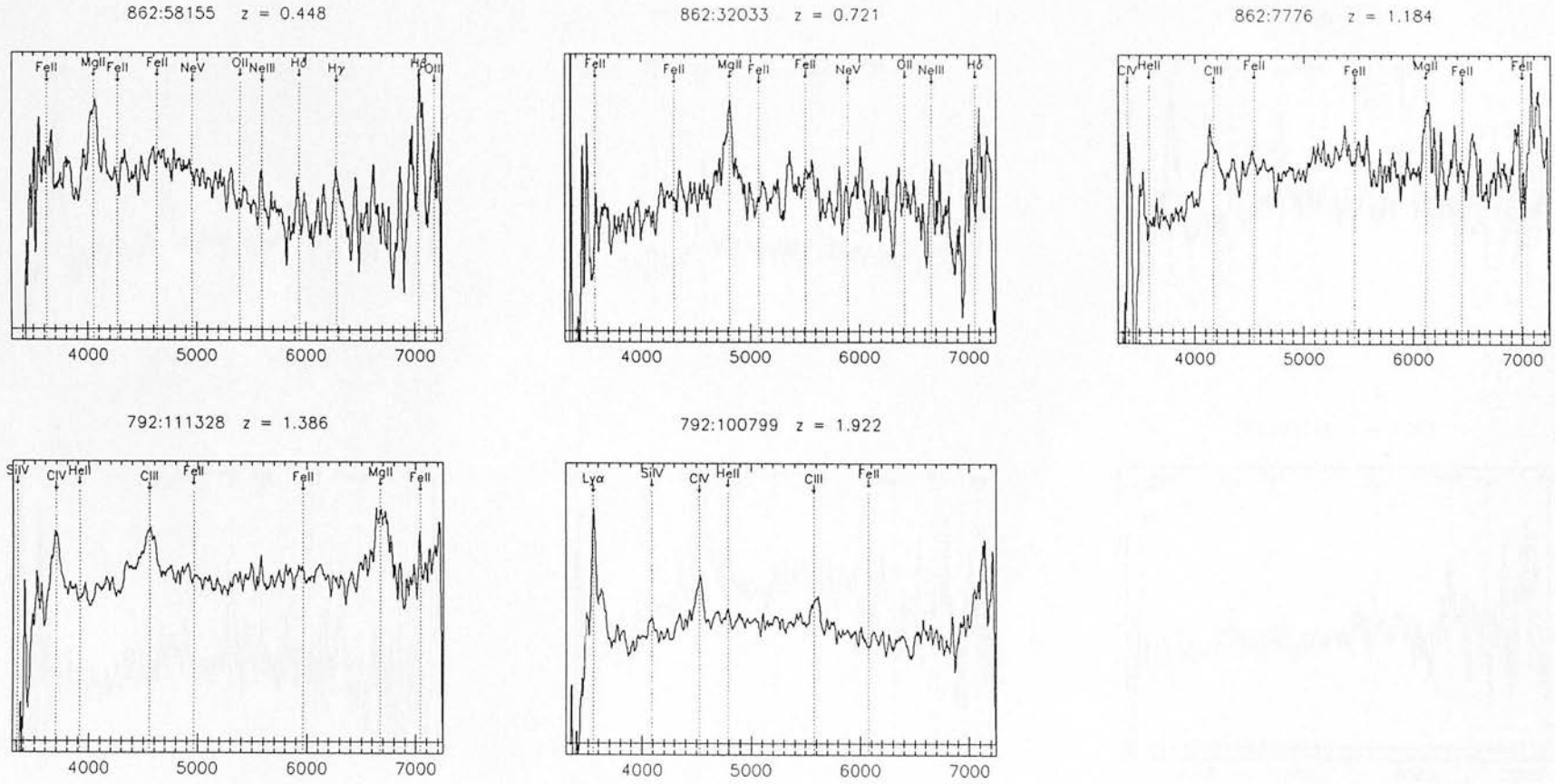

Figure 4.4: continued

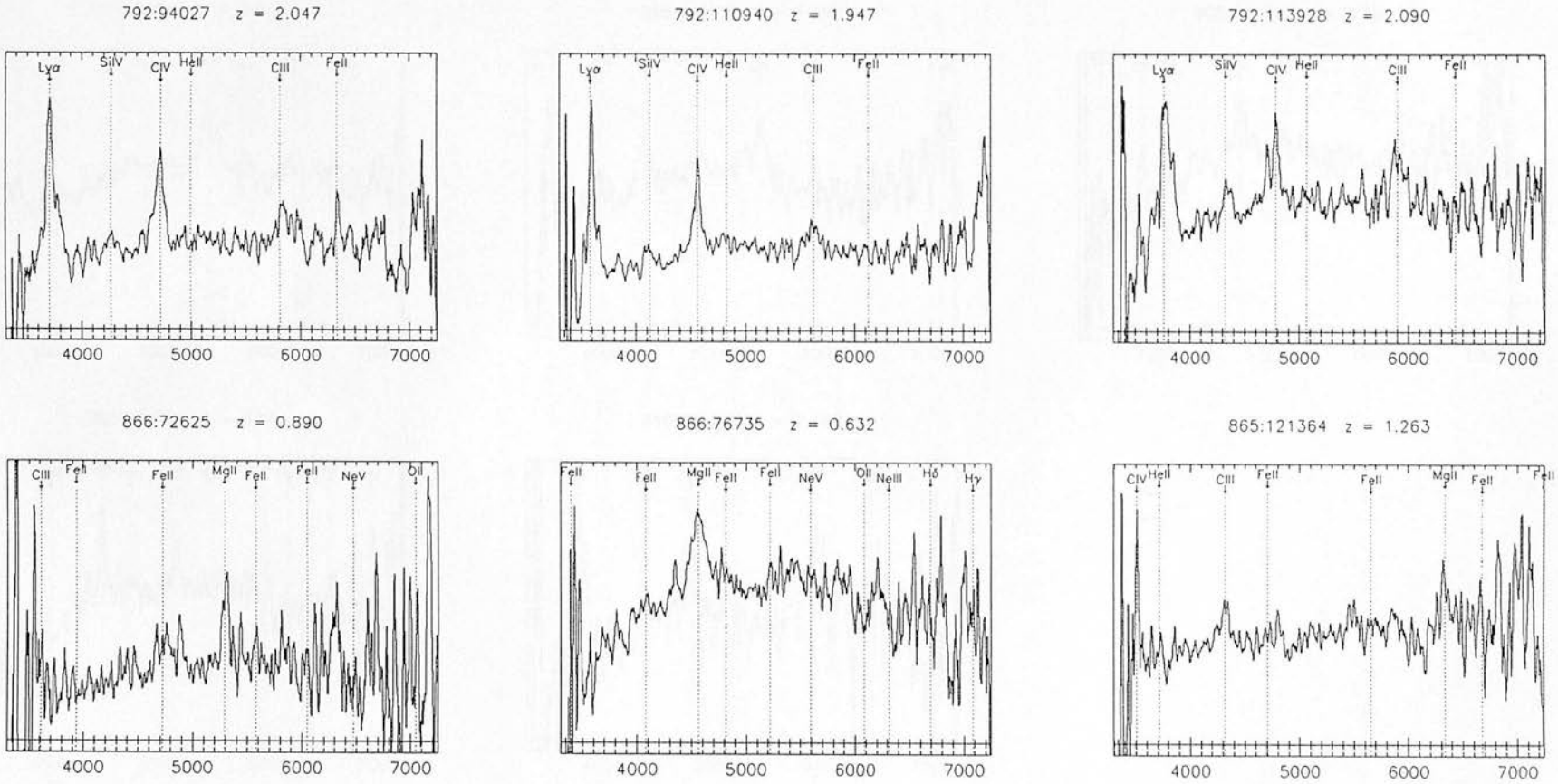

Figure 4.4: continued

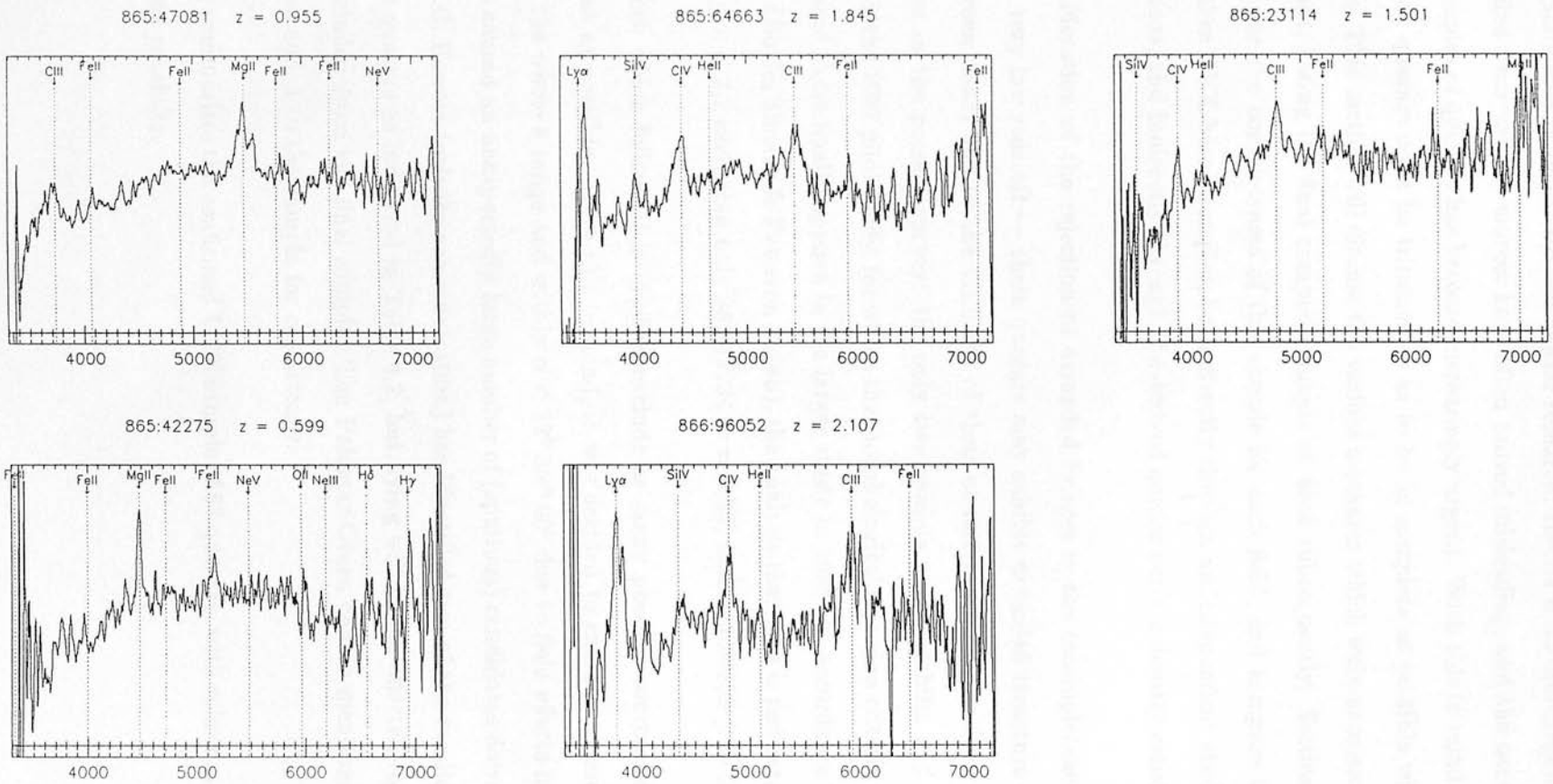

has been especially true in recent optical quasar research: results from inhomogeneous samples compiled from various sources have often proved misleading, and the need for "complete" samples of quasars has become increasingly urgent. With this in mind, the list of confirmed quasars must be trimmed so as to be as complete as possible within specified limits. This section will discuss the various measures which were necessary to bring this about, listing the final complete sample as used subsequently. Section 4.3 will then examine the completeness of this sample for each field, and compare these results with other UVX-based samples, both directly through an independent study in the same sky area, and indirectly through the derived quasar surface density estimate.

One consideration of the rejection of extended images is the incompleteness of the sample at very low redshift — these quasars may exhibit extended structure (e.g. Schmidt & Green 1983) due to the visibility of their underlying host galaxies. This may be evident in the present survey: the only two quasars with redshifts $z \leq 0.30$ were selected in the 1987 pilot study, for which the morphological rejection criteria were relaxed compared those finally applied in the larger study in 1988. In accordance with other samples (Boyle, Shanks & Peterson 1988b), the analysis therefore is restricted to the range $0.3 < z < 2.2$ excluding only 863:45934 ($z = 0.23$) and 863:28858 ($z = 2.4$).

In the work which follows it is vital to exclude as many possible sources of observational bias as possible. With this in mind, it was decided to exclude an area of field 861 over the whole δ range and within $\alpha < 12^{\rm h}\,35^{\rm m}\,00^{\rm s}$ due to field effects in the U data, which caused an unexpectedly large number of (spurious) candidates down the plate edge. P.C. Hewett (private communication) has identified two of the candidates in field 861 as quasars as indicated in Table 4.2, but, lying within the affected region, these were excluded from the final sample. The Palomar-Green quasar mentioned in Section 4.3 was added to the sample for consistency.

Table 4.5 summarises the confirmed UVX sample of 69 quasars, with colour indices for *UBVRI* and redshifts.

Table 4.4: List of principal features used in redshift evaluation in cases of difficulty. Emission lines are listed, and where necessary, use of the continuum shape is noted. Column 3 indicates estimated probability of correct ID (see text).

Object	Features	Prob (1-3)
789:9023	C III] Mg II	2
791:116238	Mg II & cont^m	2
791:130741	Mg II & cont^m	2
791:43060	Mg II Hβ & cont^m	3
791:83449	Mg II & cont^m	2
861:41101	(C IV) C III] Mg II	3
861:55035	C III] Mg II	3
861:69475	Mg II (Hγ) & cont^m	2
862:110315	Mg II & cont^m	2
862:117165	C III] Mg II	3
862:126546	(C IV) C III] Mg II Fe II	3
862:32033	Mg II & cont^m	2
862:35769	Mg II Fe II	1
862:58155	Mg II Hγ Hβ & cont^m	3
862:7776	C III] Mg II Fe II & cont^m	3
862:95745	Mg II Fe II & cont^m	2
863:36898	C IV C III] & cont^m	3
863:39441	Mg II	1
863:48149	Mg II Hβ ([O III]$_{5007}$)	3
865:121364	C III] Mg II	2
865:42275	Mg II Fe II & cont^m	2
865:4761	(C III]) Mg II	2
866:22960	C III] Mg II Fe II	2
866:23019	C III] Mg II	2
866:63880	C III] Mg II	2
866:72011	C III] Fe II Mg II	2
866:72625	Fe II Mg II & cont^m	1
866:76735	Mg II & cont^m	2
866:79958	C III] (Mg II)	2
867:115685	Mg II & cont^m	1
867:125196	Mg II & cont^m	1
867:13872	C III] Mg II	2
867:17853	C III] Mg II Fe II	3
867:27650	(Mg II) Hγ Hβ	2
867:81976	Mg II & cont^m	2

Table 4.5: The final UVX catalogue of 69 quasars. All objects listed for $0.3 \leq z \leq 2.2$ with magnitudes and colours. Object 862:32033 was missing in I.

#	Obj name	B	$U-B$	$B-V$	$V-R$	$R-I$	z
1	789:9023	17.39	-0.67	-0.01	0.34	0.31	1.08
2	789:67128	17.41	-0.72	0.35	0.33	0.34	1.17
3	789:102432	16.07	-0.46	-0.05	0.16	0.25	0.38
4	789:124063	17.28	-0.39	0.30	0.44	0.27	1.41
5	790:63702	17.95	-0.45	0.44	-0.05	0.38	1.74
6	790:79629	17.95	-0.60	0.18	0.27	0.23	0.39
7	790:101146	17.44	-0.46	0.28	0.17	0.41	1.56
8	791:43060	17.78	-0.43	0.04	0.33	0.18	0.47
9	791:83449	16.83	-0.42	0.32	0.26	0.34	0.73
10	791:95450	17.41	-0.40	0.26	0.26	0.33	2.13
11	791:116238	15.59	-0.39	0.10	0.18	0.16	0.58
12	791:130741	17.59	-0.42	0.25	0.10	0.32	0.72
13	792:94027	17.50	-0.71	0.01	0.23	0.32	2.05
14	792:100799	17.02	-0.82	0.14	0.24	0.41	1.92
15	792:110940	17.73	-0.80	0.05	0.42	0.48	1.95
16	792:111328	16.91	-0.71	0.26	0.21	0.20	1.39
17	792:113928	17.69	-0.68	0.06	0.32	0.52	2.09
18	861:41101	17.74	-0.55	0.26	0.48	0.00	1.26
19	861:55035	17.81	-0.43	0.41	0.26	0.10	1.23
20	861:69475	17.98	-0.42	0.08	0.36	0.22	0.49
21	862:7776	17.04	-0.22	0.35	0.12	0.35	1.18
22	862:28789	15.48	-0.58	-0.05	0.25	0.36	0.35
23	862:32033	17.93	-0.49	0.09	0.00		0.72
24	862:35769	17.82	-0.70	0.14	0.03	0.32	0.83
25	862:39557	17.79	-0.71	0.25	0.18	0.32	1.27
26	862:41398	17.76	-0.48	0.15	0.36	0.51	1.51
27	862:47671	17.95	-0.47	0.09	0.23	0.14	0.41
28	862:58155	17.95	-0.48	-0.05	0.23	0.32	0.45
29	862:95745	17.29	-0.54	0.20	0.10	0.35	0.74
30	862:110315	17.38	-0.45	0.31	0.10	0.43	0.77
31	862:117165	17.90	-0.39	0.30	0.19	0.40	0.84
32	862:126546	17.65	-0.47	0.09	0.19	0.46	1.31
33	863:18292	16.94	-0.80	0.20	0.56	0.24	0.31
34	863:27650	17.74	-0.61	0.07	0.46	0.12	0.41
35	863:36898	17.94	-0.41	0.04	0.43	0.28	1.63
36	863:39441	17.97	-0.48	0.24	0.37	0.08	0.49
37	863:48149	17.78	-0.70	-0.02	0.63	0.10	0.35
38	863:89696	17.34	-0.67	0.08	0.58	0.23	1.43
39	865:4761	17.79	-1.06	0.42	0.34	0.16	1.09
40	865:6937	17.31	-1.20	0.33	0.43	0.38	1.44
41	865:23114	17.24	-0.95	0.29	0.33	0.26	1.50
42	865:42275	17.34	-1.06	0.37	0.04	0.24	0.56
43	865:47081	16.72	-0.85	0.46	0.29	0.08	0.96
44	865:64663	17.17	-0.64	0.12	0.41	0.29	1.85
45	865:121364	17.90	-0.75	0.30	0.52	0.17	1.26

Table 4.5: continued

#	Obj name	B	$U-B$	$B-V$	$V-R$	$R-I$	z
46	866:7635	16.90	-0.59	0.18	0.35	0.48	1.64
47	866:21762	17.26	-0.46	0.46	0.24	0.32	1.15
48	866:22960	17.52	-0.58	0.01	0.20	0.07	1.25
49	866:23019	17.53	-0.38	0.42	0.08	0.32	1.04
50	866:63880	17.79	-0.71	0.17	0.17	-0.14	1.06
51	866:72011	17.67	-0.58	0.35	0.03	0.24	1.08
52	866:72625	17.59	-0.53	0.06	0.15	0.09	0.89
53	866:76735	16.27	-0.52	-0.07	0.10	0.32	0.63
54	866:79958	17.59	-0.55	0.14	0.01	0.36	1.55
55	866:96052	17.49	-0.58	-0.20	0.25	0.43	2.11
56	867:11444	17.54	-0.85	-0.10	0.25	0.26	1.53
57	867:13917	17.24	-0.98	0.05	0.13	0.21	1.02
58	867:32419	17.79	-0.80	-0.05	0.17	0.20	2.13
59	867:47588	15.83	-0.90	0.18	0.36	0.25	1.31
60	867:79529	17.86	-0.78	0.16	0.18	-0.06	1.17
61	867:80895	17.82	-0.85	0.11	0.20	0.40	1.82
62	867:82284	17.07	-0.57	0.20	0.13	0.35	0.68
63	867:111176	17.60	-0.81	0.05	0.10	0.43	1.73
64	867:116100	17.75	-0.50	0.05	0.27	0.34	0.67
65	867:125196	17.88	-0.72	-0.08	0.35	-0.13	0.95
66	867:11895	17.67	-0.97	-0.01	0.17	0.60	2.08
67	867:17853	16.24	-0.91	0.24	0.16	0.20	1.11
68	867:86006	17.54	-0.53	-0.02	0.79	0.29	0.30
69	PG QSO	16.03					1.12

4.3 Analysis of survey reliability

The UVX method, while based on continuum shape is nevertheless strongly influenced by the presence of emission lines within the band-passes. There has been much discussion of the "holes" in sensitivity in UVX-derived samples at $z \simeq 0.75$ and $z \simeq 1.65$ due to Mg II and C IV respectively in the B band, causing reddening of the observed quasar $(U-B)$ colours. Significant variations in completeness as a function of redshift are therefore seen in some surveys (Wampler & Ponz 1985, Peterson 1988). Inconsistently applied $(U-B)$ limits, morphological misclassification and errors in limiting magnitudes also seriously impair sample completeness. It is therefore advisable to examine carefully the results of any selection, both directly and wherever possible through comparison with other surveys.

Table 4.6: Estimated overall completeness per field.

Field	N1	N2	N3	Completeness
789	6	6	4	100%
790	7	7	3	100%
791	10	8	5	80%
792	7	7	5	100%
861	9	7	5	78%
862	14	14	11	100%
863	8	7	6	88%
865	17	11	7	65%
866	12	10	10	83%
867	21	14	13	67%

Assumes all QSOs within $(U-B) < -0.38$ and $(B-R) > 0.0$;
N1 : number of candidates in box
N2 : number observed within box
N3 : number of confirmed QSOs in box

4.3.1 Completeness considerations

The sample of 69 quasars described in the previous section was derived from a dataset of about 150,000 objects — clearly a formidable task without the introduction of strict selection criteria to reduce candidates to an accessible number for spectroscopic confirmation. This section will consider the consequences of the two most powerful effects *vis.* (a) $(U-B)$ selection, and (b) $(B-R)$ observational priority.

Table 4.6 estimates the overall completeness in each field, assuming all quasars lie within the region $(U-B) < -0.38$ and $(B-R) > 0.0$ (this assumption is tested below) — this is the fraction of objects *observed* within this "box". As mentioned in Section 4.2.1, due to field effects the effective $(U-B)_{lim}$ in field 865 varied across the plate. The effect of this was to force an overall bluer $(U-B)$ limit which in principle might lead to a deficit of quasars in the redder range $0.5 \lesssim z \lesssim 0.9$. However this has been tested by deriving the effective $(U-B)$ shift in bins across the plate (by

superposition of stellar loci as described in Section 4.2.1). From QSO colours within the rest of the sample it is concluded that 85% of quasars in this redshift range were within observational limits and could therefore have been detected. A mean value of $(U-B) = -0.41$ for the plate gives the completeness estimate indicated.

(a) $(U-B)$ selection

Figure 4.5(a) presents the survey in the $(U-B)$ versus z plane: this follows well the Véron (1983) relation. There is a "gap" in $(U-B)$ for all UVX quasars (bar one) between $(U-B) \simeq -0.25$ (a typical UVX limit applied in the selection of this sample) and -0.38 even in the well-known "difficult" range $0.6 < z < 0.9$ (Wampler & Ponz 1985) where the presence in Mg II and Fe II multiplets in the B passband reddens the colour. It must be emphasised that the survey has UVX limits of $(U-B) \geq -0.28$ in all but two fields: the "gap" is physical (as has been previously demonstrated e.g. Véron 1983).

Figure 4.6(a) shows a histogram of $(U-B)_{limit} - (U-B)_{object}$ for each field and therefore gives a measure of the typical proximity of selected objects to the UVX limit in each field. 94% of these quasars are at least $0.1^{\rm m}$ bluer than their limit as seen from Figure 4.6(b) over the whole survey. On excluding fields 867 and 865 this increases to 98.5%. Hence the assumption in Table 4.6 that practically all quasars $z \leq 2.2$ lie blueward of $(U-B) = -0.38$ is confirmed.

(b) $(B-R)$ selection

Figure 4.5(b) shows the $(B-R)$ versus z distribution. A slight trend blueward is apparent in the range $0.5 \lesssim z \lesssim 1.0$ (again Mg II in B). In order to demonstrate that the observing strategy of $(B-R) \gtrsim 0.0$ leads to no significant incompleteness, a histogram of candidates and results is plotted in Figure 4.7. All candidates are plotted with a broken line, all those observed with a solid line, and the "filled-in" region shows confirmed QSOs. As expected from Figure 4.3, the two separate populations are very

Figure 4.5: (a) $(U-B)$ and (b) $(B-R)$ versus z relation for quasars in the sample.

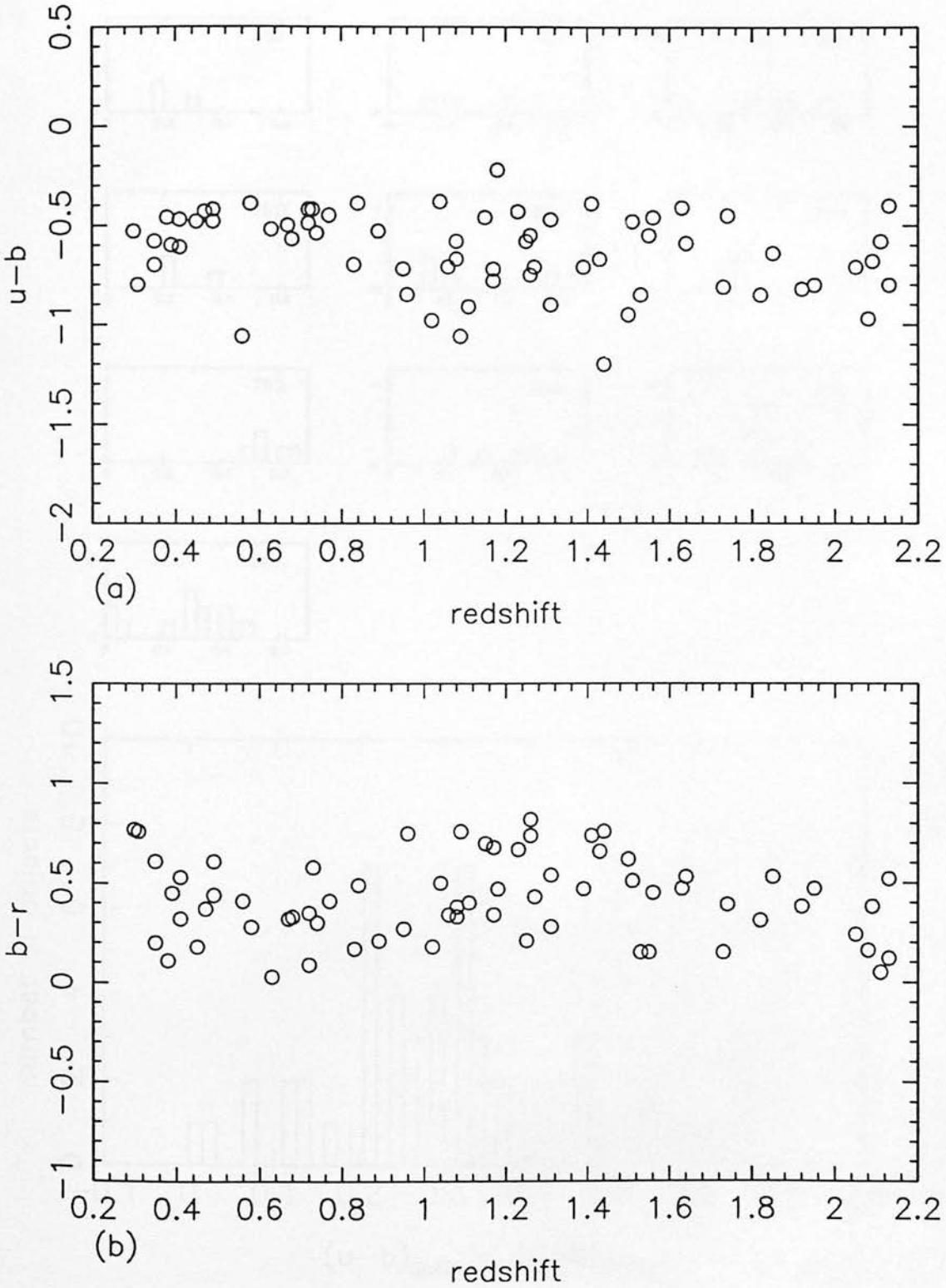

Figure 4.6: (a) Histograms of object $(U-B)$ offsets from limits applied in each field. $(U-B)$ is on the x-axis. (b) For whole survey.

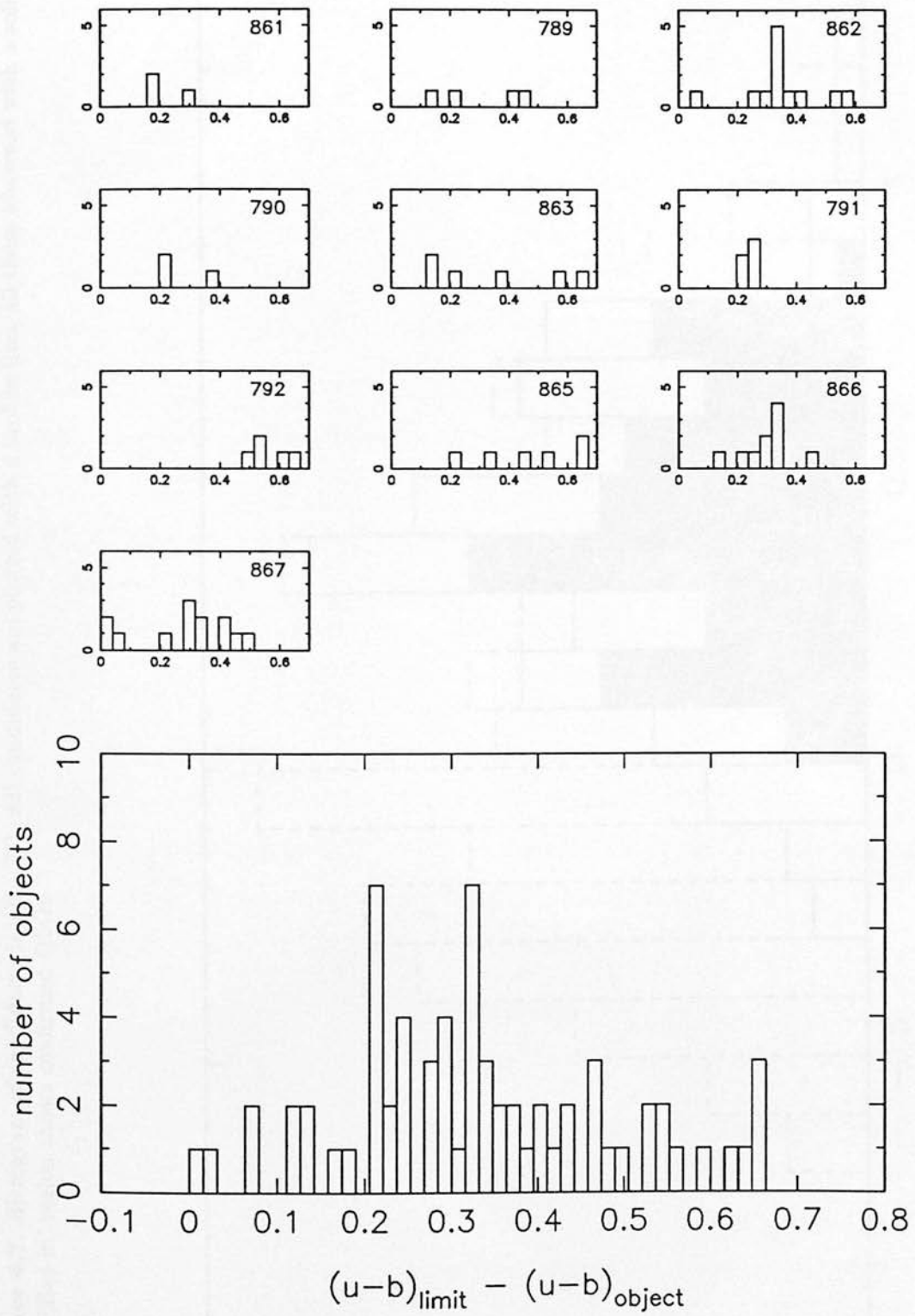

Figure 4.7: Histogram of candidates in $(B-R)$. All candidates are plotted with a broken line, all those observed with a solid line, and the 'filled-in' region shows confirmed QSOs.

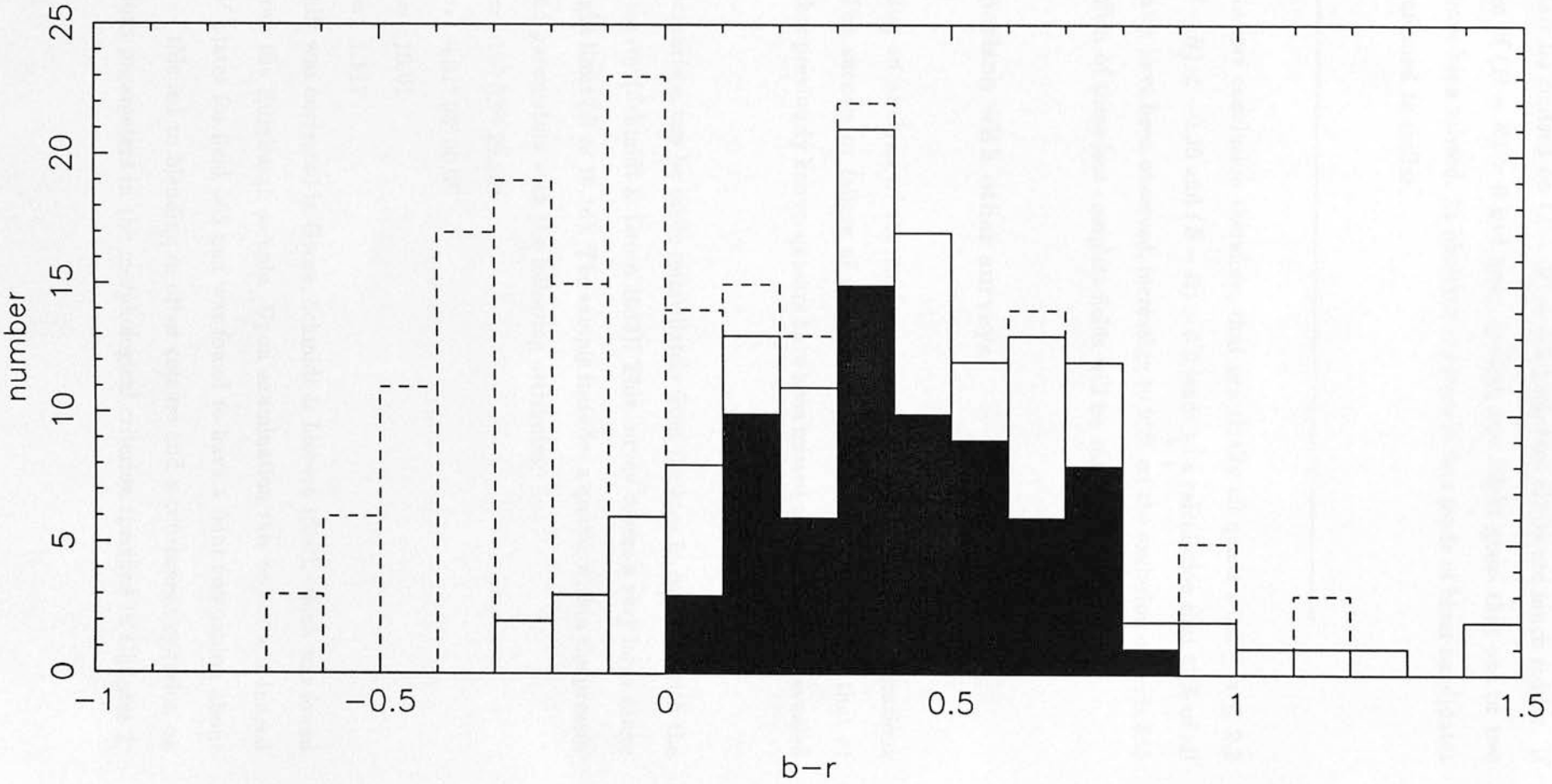

obvious: hot stars lie centred on $(B-R) \sim -0.2$ whereas QSOs are much redder. If a strict criterion of $(B-R) > 0$ had been applied, one might guess that one or two quasars might have been missed. 11 observations were in fact made of bluer candidates and all were confirmed as stellar.

The *a posteriori* conclusion therefore, that practically all quasars $0.3 \leq z \leq 2.2$ have colours $(U-B) < -0.38$ and $(B-R) > 0.0$ leads to a calculation that 82% of all suitable candidates have been observed, increasing to 90% on the exclusion of fields 865 and 867. The effect of these less-complete fields will be considered.

4.3.2 Comparison with other surveys

Before attempting an analysis of the confirmed sample some further considerations are required. The success or failure of this survey must be compared with that of others, i.e. whether previously known quasars have been missed or inadequacies revealed elsewhere.

A direct comparison can be made immediately from the area in common with the Palomar-Green survey (Schmidt & Green 1983). This survey covers a very large range of the sky to bright limit ($B \simeq 16.16$). The sample includes a quasar within the present survey region and parameters with the following attributes:

$$\begin{aligned} \alpha(1950) &= 13^{\mathrm{h}}\,52^{\mathrm{m}}\,25.80^{\mathrm{s}} \\ \delta(1950) &= +01^{\circ}\,06'\,50.0'' \\ B &= 16.01 \\ z &= 1.117 \end{aligned}$$

(where the redshift was corrected in Green, Schmidt & Liebert 1986), which was found to be missing from the Edinburgh sample. Upon examination this object was indeed located on the V plates for field 865 and was found to have a faint companion about $8''$ to the north — this led to blending in other colours and a consequent rejection on the basis of various parameters in the morphological criterion specified in Chapter 2.

Five quasars were confirmed here which should have been detected in the Schmidt & Green survey according to their B_{lim} values. These were objects:

Field	Obj num	B_J	PG field	PG B_{lim}
789	102432	16.07	226	16.18
791	116238	15.59	234	15.99
862	28789	15.48	230	16.28
867	47588	15.83	245	16.09
867	17583	15.85	245	16.09

in Table 4.2. All quasars other than 116238 are bluer than the quoted PG $(U-B)$ limit of -0.46 (102432 is on the limit) and therefore should have been found. The Palomar-Green sample has often been criticised for its lack of completeness and this appears to be borne out here, having detected *none* of the quasars within the Edinburgh region.

It is instructive to compare surface densities between the Edinburgh sample and other recent UVX surveys of comparable limiting magnitude. Before direct comparison can be carried out, an effective surface density must be calculated for the present sample. This was derived directly from Table 4.1(a) and 4.1(b) (subtracting the area removed from field 861), the fraction of the total area scanned being calculated from the fraction of images classed as "stellar". This resulted in an effective area of 171.6 deg^2. In order to compare results directly surface densities in the following UVX samples have been re-calculated for quasars in the range $0.3 \leq z \leq 2.2$.

The Medium Bright Quasar Survey (MBQS) is complete to $B < 17.25$ over 108.6 deg^2 and to $B < 17.65$ over 87.30 deg^2 and contains 32 quasars (Mitchell, Warnock & Usher 1984). Recent reports (Mitchell & Usher 1988) that this figure has increased to 61 quasars subsequently, but no further redshift information is available at present. The 37.2 deg^2 AB sample of Braccesi, Formiggini & Gandolfi (1970) has been fully confirmed to $B < 18.25$ by Marshall *et al.* (1983), producing a list of 32 quasars. Figure 4.8 shows the results of a comparison between all three surveys, presented as the integrated surface density. Each survey is plotted in decreasing bins of 0.4 in redshift from the

survey limit. The Edinburgh survey magnitudes have been corrected to the standard B magnitude via the Schmidt colour equation in Blair & Gilmore (1982). Note that the error bars plotted are simply derived from $\sqrt{N}$ Poisson statistics and that, like all integrated counts, the points are not independent. The MBQS points (filled boxes) appear to lie generally at higher surface densities than the AB points (filled triangles), and this has been attributed to the increased power of the three-colour selection technique (Mitchell, Warnock & Usher 1984). The Edinburgh points (open circles) agree well with the MBQS points, and clearly show no deficit in quasar numbers; the first AB point is again low (this point contains only 3 quasars, partly a result of the exclusion of $z < 0.3$ objects), but the $B < 18.25$ point follows the general trend well. Note also the small error bars on the Edinburgh point at $B = 18.05$, containing 67 objects and defining the integrated surface density here better than before. No consideration has been made for the fact that one or two candidates remain unobserved in various fields (see Table 4.6). We can conclude from these comparisons that the Edinburgh Survey suffers no serious defects in completeness when compared to other UVX selections.

In summary a UVX catalogue of 69 quasars has been constructed of large angular size ($35° \times 40°$), with a median redshift of 1.14. Because of the large area surveyed coupled with the the smoothness of the UVX selection function over the whole redshift range $0.3 \leq z \leq 2.2$, this survey is able to address the question of the large-scale distribution of quasars in a new light. The following chapter will approach this problem in a variety of ways.

Figure 4.8: Integrated surface density comparison for three UVX surveys. The analysis is restricted to the range $0.3 \leq z \leq 2.2$. Filled boxes are results for the MBQS survey, filled triangles the AB sample, and open circles show results for the Edinburgh Survey. Note that the data points are not independent.

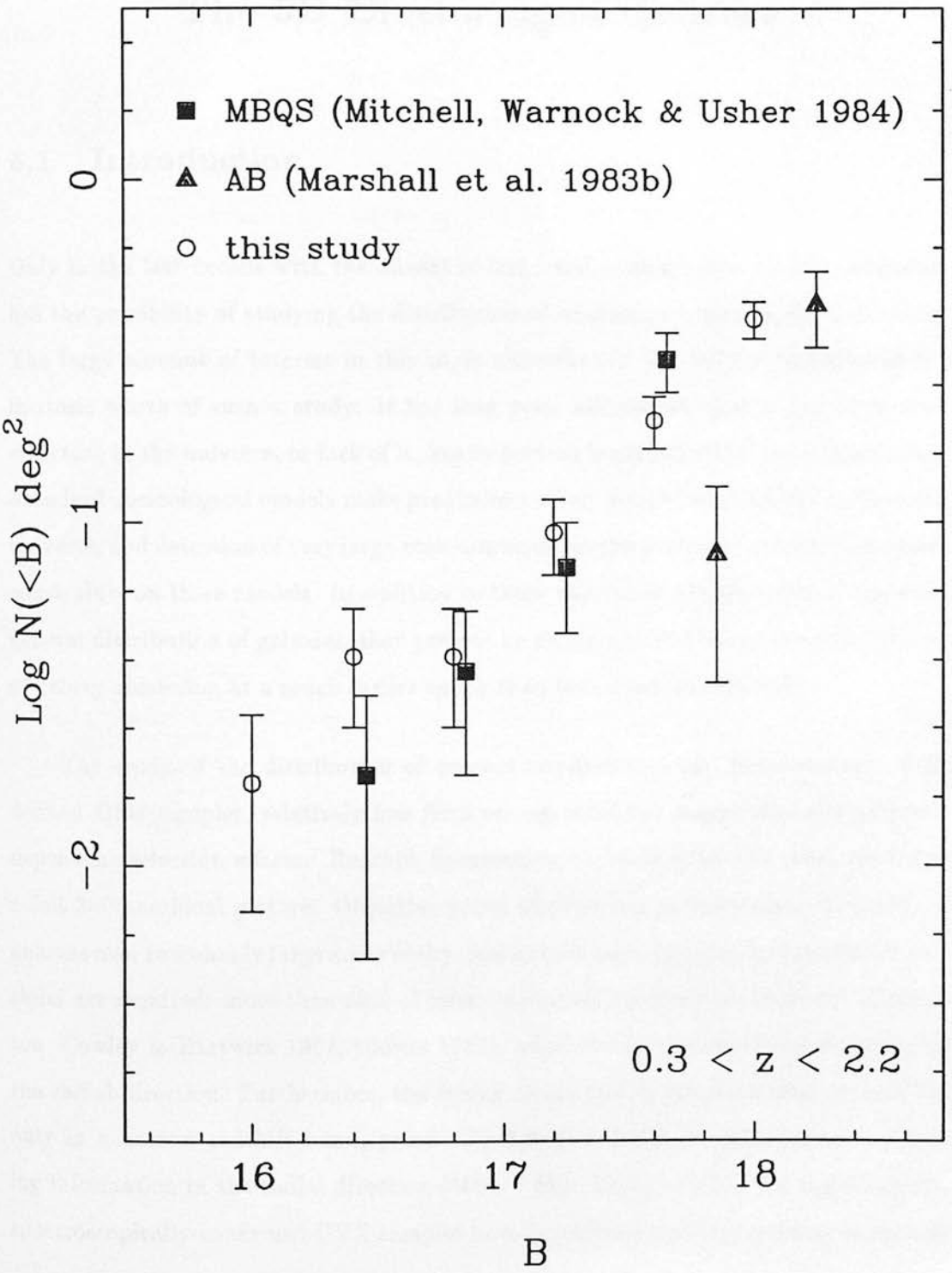

Chapter 5

The 3D Clustering of Quasars

5.1 Introduction

Only in the last decade with the advent of large and homogeneous optical catalogues has the possibility of studying the distribution of quasars in a meaningful way arisen. The large amount of interest in this topic since then is not only a reflection of the intrinsic worth of such a study: it has long been acknowledged that any large-scale structure in the universe, or lack of it, has important implications in many other areas. Standard cosmological models make predictions about density fluctuations in the early universe, and detection of very large-scale clustering at the present epoch imposes severe constraints on these models. In addition to these comments, if these objects trace the general distribution of galaxies, they present an opportunity to study the development of galaxy clustering at a much earlier epoch than that accessible directly.

The study of the distribution of quasars requires first and foremost large well-defined QSO samples, relatively free from strong redshift-, magnitude- and position-dependent selection effects. Redshift information for each quasar is vital, providing a full 3-dimensional picture. Objective prism surveys can produce many hundreds of quasars over reasonably large areas of sky, and so have been popular, but confirmed redshifts are required: more than 30% of prism-estimated redshifts are incorrect (Crampton, Cowley & Hartwick 1987, Clowes 1987), which tends to smooth out structure in the radial direction. Furthermore, the strong sensitivity of prism-selected quasars lies only in a narrow redshift band, principally $1.8 \leq z \leq 2.5$ for IIIa-J studies, limiting information in the radial direction ($380\,h^{-1}$ Mpc for $q_0 = 0.5$). For these reasons, spectroscopically-confirmed UVX samples have become increasingly popular as sources

for this study. The Edinburgh Multicolour Survey provides a unique opportunity to study this topic, covering a large contiguous area of the sky and yet possessing a smooth selectivity function over a large range in redshift.

5.1.1 The growth of structure

Present structure seen in the Universe is thought to have its origins in initially very small primordial fluctuations. The way in which these perturbations in the mass grow is however not well understood, and different initial conditions can lead to highly dissimilar predictions at the present epoch. Mass in the universe is thought to be predominantly in the form of "hot" or "cold" dark matter, depending on the species of dominant particle postulated, and the predicted scale of mass fluctuations currently seen depends upon the choice of particle. A useful technique for predicting the outcome of such models is through "N-body" simulations which follow the behaviour of the initial "particles" to the present epoch. These and other tests, show that a model consisting of cold dark matter (CDM) in a flat universe ($\Omega_0 = 1$) explains well the galaxy-galaxy clustering properties seen up to scales of $\sim 10\,h^{-1}$ Mpc (see e.g. White 1989).

Recent observational results however on larger scales qualify greatly this success. The enhanced superclustering of rich Abell clusters (Ling, Frenk & Barrow 1986, Bahcall & Soneira 1983) point to inhomogeneities on scales of $\lesssim 50\,h^{-1}$ Mpc; other observations indicate apparent bulk motion ("streaming velocities") in our neighbourhood on scales out to $\sim 50\,h^{-1}$ Mpc relative to the microwave background (Collins, Joseph & Robertson 1986; Lynden-Bell *et al.* 1988); and there are recent indications that the cosmic microwave background itself exhibits anisotropy on an angular scale of $8° - 10°$ (Davies *et al.* 1987). The cumulative effect of these observations undermines general acceptance of the "standard" flat CDM scheme: as a "bottom-up" model of galaxy formation, any large-scale clustering present in the distribution of quasars would further undermine the general picture.

5.1.2 Previous results

The Curtis-Schmidt objective-prism survey initiated by Smith (1976) provided astronomers with the largest complete optical sample of quasars to date with large sky coverage, and quickly spawned several very different approaches to the analysis of the 3-D distribution of quasars therein. The most controversial claims came from Arp (1980) who examined the confirmed sample of Osmer & Smith (1980), a sample of 108 quasars obtained by objective prism techniques in 15 Schmidt areas at declination –40°. Offering only subjective, visual evidence, Arp stated that the survey showed spatial groupings on scales appropriate to galaxies at a lower redshift, thereby calling into doubt the cosmological nature of redshift. In response to these claims two more analytical approaches were taken. Webster (1982) adopted the method of Fourier power spectrum analysis in an attempt to identify the signal of any clustering in a verifiable manner. The analysis, in agreement with the treatment of Osmer (1981) (who used a variety of techniques including correlation function analysis), concluded that no significant clustering was detected, in particular in the range $375\,h^{-1}$ Mpc $> \lambda > 22.5\,h^{-1}$ Mpc[1] for the 3-D analysis in the range $1.8 \leq z \leq 3.3$, although he did note an interesting group of 4 quasars at $z = 0.37$, with a size of about $75\,h^{-1}$ Mpc. Oort, Arp & de Ruiter (1981) in their statistical examination of the same catalogue reported a handful of other "possible" associations on a similarly large scale, in support of the idea of quasar location in superclusters.

The first claims for detection of significant clustering came from Shaver (1984) who employed over 2000 quasars from the catalogue of Véron-Cetty & Véron (1984), to compare distributions in projected linear distance between quasar pairs for small and large redshift and position differences, in the hope of isolating physical association from other effects. He reported a detection of positive clustering on a scale size $< 5\,h^{-1}$ Mpc with significance in the region $2.3 - 4.9\sigma$. The sample used however was inhomogeneous; nevertheless, by 1987 Shanks *et al.* had confirmed this result with the large UVX catalogue of Boyle *et al.* (1987). Using two-point correlation function

[1] h is Hubble's constant in units of 100 km s^{-1} Mpc^{-1}.

analysis on their homogeneous sample of 172 quasars, they were able to confirm 3σ clustering on a comoving scale $< 10\,h^{-1}$ Mpc, with an amplitude somewhere between that of the galaxy-galaxy correlation function and that of rich Abell clusters. This result has been confirmed recently with an amalgamation of three samples (Iovino & Shaver 1988) although the compilation includes the data of Boyle *et al.* and hence is not completely independent. Evidence for evolution in the clustering with redshift is also presented, in agreement with the findings of Kruszewski (1988) with a compilation of 15 surveys. However, Shanks *et al.* also claimed to have shown the correlation function to be consistent with zero on scales $10 < r \leq 100\,h^{-1}$ Mpc implying the quasar distribution to be more homogeneous than that of rich clusters at these separations.

There have been tentative suggestions of quasar clustering on larger scales in recent years, but so far the results have been at best ambiguous. In 1983, Chu & Zhu, using correlation function analysis and nearest-neighbour testing, claimed that weak clustering was present at the $50\,h^{-1}$ Mpc scale in one $25\,\mathrm{deg}^2$ region from a survey of Savage & Bolton (1979) but *absent* in another. Zhou *et al.* (1986) again claimed evidence for weak clustering on a scale $\sim 50\,h^{-1}$ Mpc from a variety of samples. But until the present time, there has been no convincing case for super-large scale clustering.

The UVX sample of Chapter 4 is an ideal source for searching for large-scale clustering because of the large contiguous sky area covered. Because the subject is still so controversial, it is above all vital to employ a quantifiable and reproducible technique for the examination of quasar distributions. Previous work has been consistently hampered by subjective judgements and unverifiable statements. The new sample provides a firm basis for such a study, and with these in mind the following sections analyse the clustering properties of the new sample.

5.2 Preliminary inspection of the data

To initiate the study of the 3-D distribution within the confirmed UVX sample, a preliminary examination of the data is given first. The distribution of confirmed quasars

Figure 5.1: Distribution of identified quasars on the sky. All other candidates are represented as asterisks. The fields are distorted as shown.

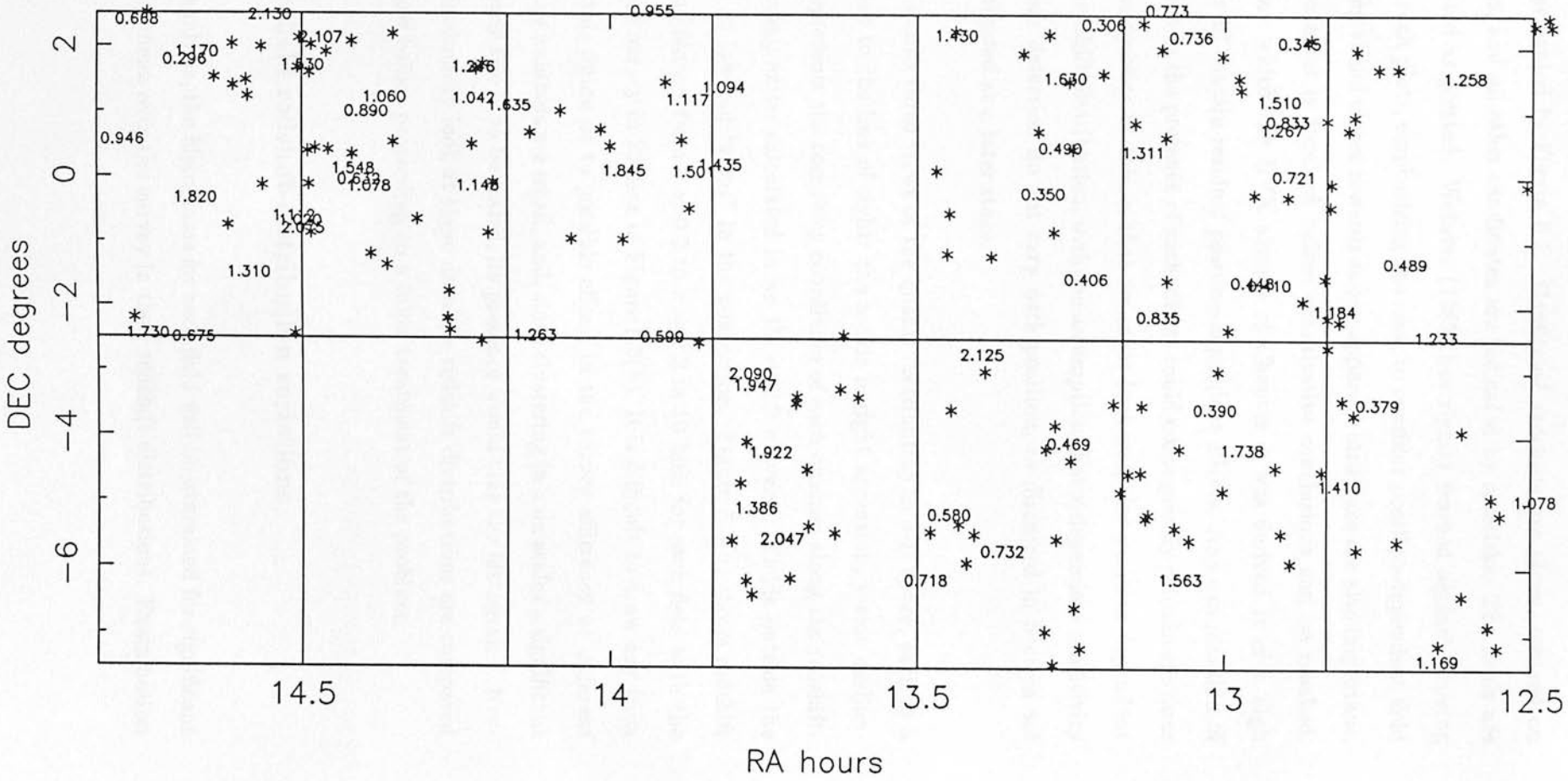

on the sky is represented in Figure 5.1. Confirmed redshifts are given, centred on detected positions, and all other candidates are indicated by asterisks. The fields are necessarily distorted as plotted. Webster (1982) has rightly warned against drawing conclusions from such plots, emphasising the need to consider position-dependent field effects fully. Strong visual biases towards seeing apparent structure are also important, and a proper treatment is required before quantitative conclusions can be reached. The database from which the UVX sample of Chapter 4 was derived is of a high quality, but may still contain residual position-dependent effects. Any examination of the 2-D distribution in the presence of such effects could consequently contain spurious clustering. A consequence of this is that we must look only for position-dependent variations in the redshift distribution, with the assumption that z-dependent sensitivity variations in quasar detection do not vary with position, as discussed in Section 4.3 and further investigated at a later stage.

Figure 5.2 contains three views of the quasar distribution in 3-D space, each at a different inclination to the line of sight: the x-axis is right ascension, y-axis declination, and z-axis represents the comoving coordinate of each quasars along the redshift-direction in comoving units, calculated in an $\Omega_0 = 0.2$ universe. Fields outside the survey are shown as lowered "steps" in the z-direction. Figure 5.3(a) shows redshift number histograms binned from $z = 0.2$ to $z = 2.2$ in 10 bins for each field with the total over the whole survey in 20 bins in Figure 5.3(b). It is difficult to draw any from conclusions from this figure as to possible effects in the survey efficiency at different redshifts; clearly the numbers are small, and, since clustering in z on scales a significant fraction of the survey size is to be tested, its presence would bias the histograms. Nevertheless as an introductory look at these data the redshift distributions are compared between fields below before proceeding to a fuller treatment of the problem.

5.2.1 Field-to-field redshift-distribution variations

As a preliminary analysis, the histograms for each field will be examined for significant deviations from the mean over the survey in their redshift distributions. Examination

Figure 5.2: 3-D representation of the quasar distribution. The x-axis is RA, the y-axis DEC, and the z-axis represents the comoving coordinate of each quasars along the redshift-direction in comoving units, calculated in an $\Omega_0 = 0.2$ universe. The views are respectively at 20°, 45° and 60° inclination to the line of sight. Fields outside the survey are plotted as lowered "steps".

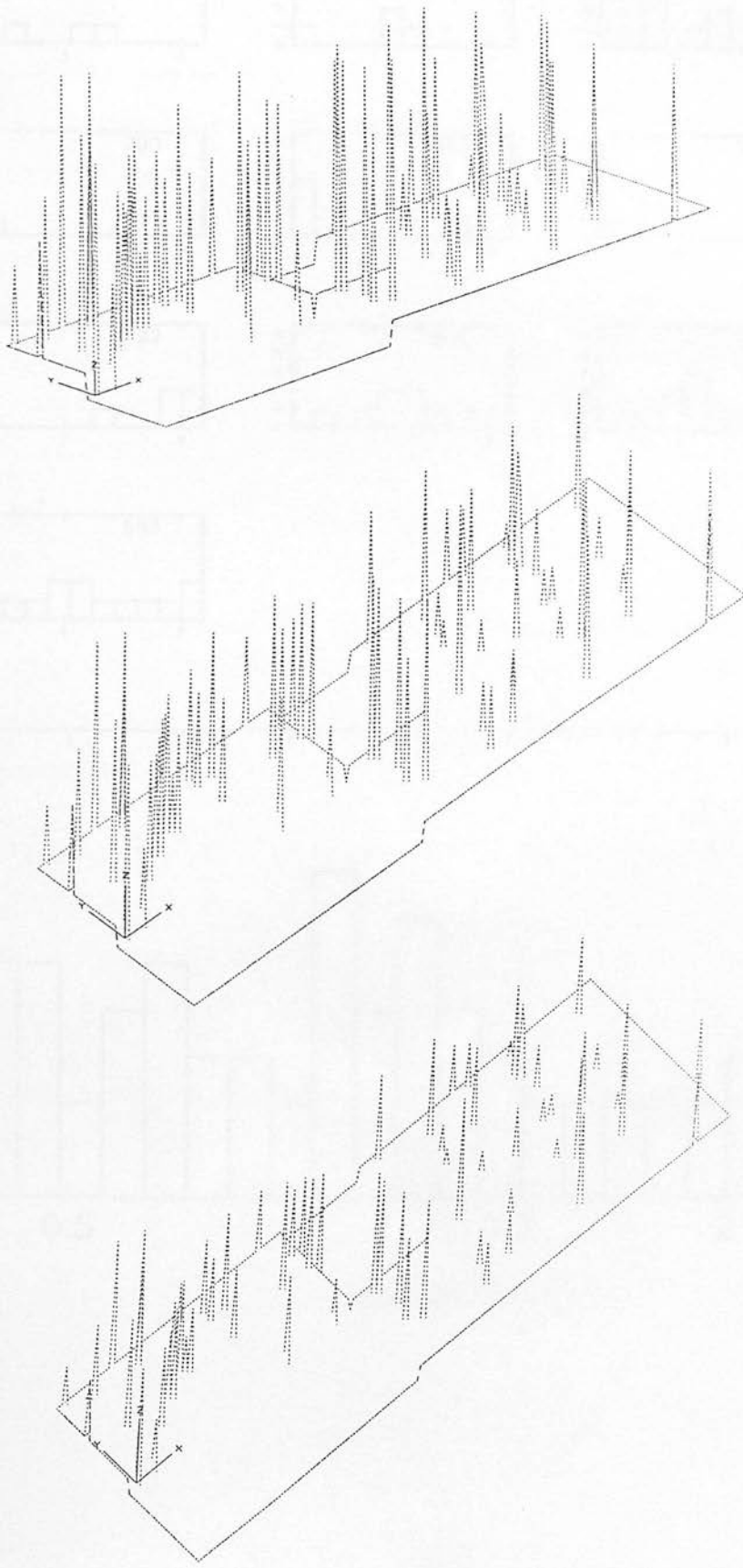

Figure 5.3: Redshift-number histograms for (a) each field and (b) the whole survey. The x-axis is redshift.

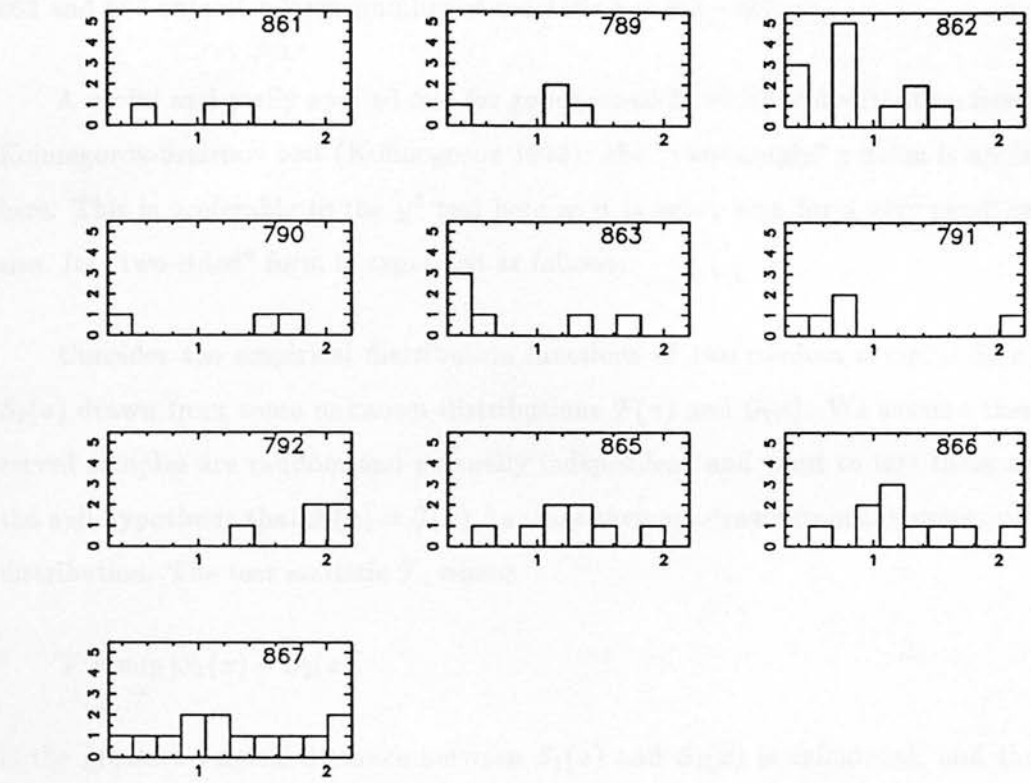

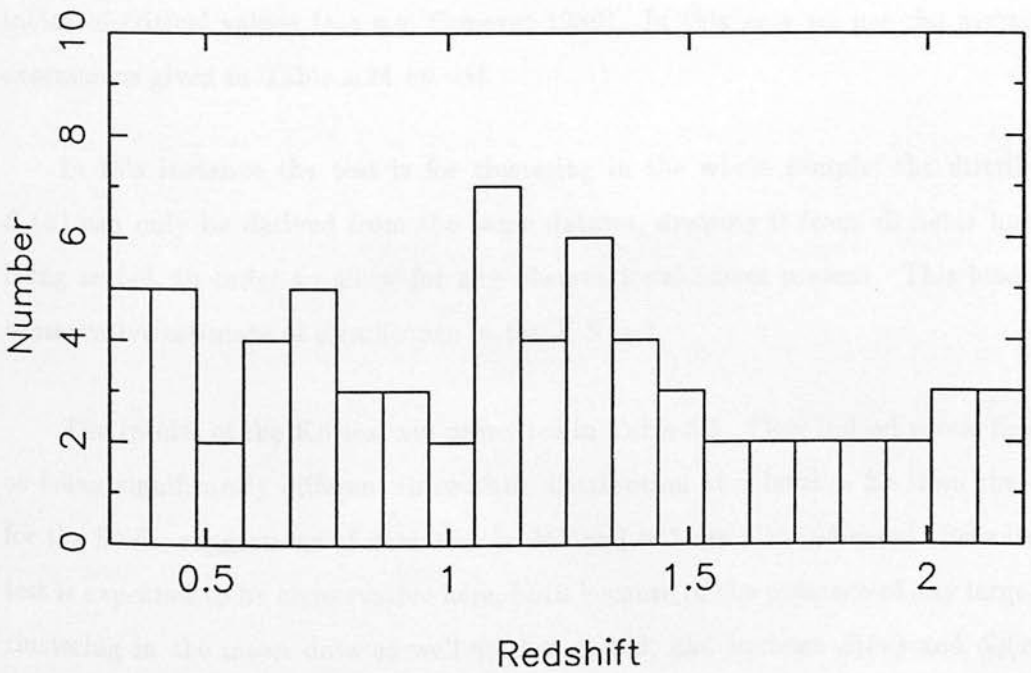

of Figure 5.3(a) tentatively points in particular to fields 792 and 862, 863 in this respect: Figure 5.1 shows indeed that in 792 out of 10 prime candidates fairly well spread across the field, 4 quasars were confirmed within $2.44\,\mathrm{deg}^2$, 3 of which have $z = 2.00 \pm 0.09$; 862 and 863 exhibit a large number of redshifts $z \simeq 0.3 - 0.7$.

A useful and easily applied test for goodness-of-fit which is distribution free is the Kolmogorov-Smirnov test (Kolmogorov 1933): the "two-sample" version is applicable here. This is preferable to the χ^2 test here as it is exact even for a very small sample size. Its "two-sided" form is expressed as follows:

Consider the empirical distribution functions of two random samples $\mathcal{S}_1(x)$ and $\mathcal{S}_2(x)$ drawn from some unknown distributions $\mathcal{F}(x)$ and $\mathcal{G}(x)$. We assume these observed samples are random and mutually independent and want to test them against the null hypothesis that $\mathcal{F}(x) = \mathcal{G}(x)$, i.e. that they are drawn from the same unknown distribution. The test statistic $\mathcal{T}$, where

$$\mathcal{T} = \sup_x |\mathcal{S}_1(x) - \mathcal{S}_2(x)| \tag{5.1}$$

is the greatest vertical distance between $\mathcal{S}_1(x)$ and $\mathcal{S}_2(x)$ is calculated, and the test rejects the fit at a level of significance α if $\mathcal{T}$ exceeds the $1 - \alpha$ quantile as given in tables of critical values (see e.g. Conover 1980). In this case we use the asymptotic expressions given in Table A21 *op. cit.*

In this instance the test is for clustering in the whole sample; the distribution $\mathcal{S}_2(x)$ can only be derived from the same dataset, drawing it from all fields but that being tested, in order to allow for any observational biases present. This leads to a conservative estimate of significance in the K-S test.

The results of the KS test are presented in Table 5.1. They indeed reveal field 792 as being significantly different in redshift distribution at a level $> 2\sigma$ from the mean for the fields; suggestions of deviation in 862 and 863 are also indicated. Because this test is expected to be conservative here, both because of the presence of any large-scale clustering in the mean data as well as that tested, and because $\mathcal{S}_1(x)$ and $\mathcal{S}_2(x)$ are

Table 5.1: KS test results for the redshift distribution in each Schmidt field.

Field	$\mathcal{T}$	z'	n1	n2	$\mathcal{T}_{95}$	$\mathcal{T}_{99}$	$\widehat{\alpha}$
861	0.42	1.260	3	65	.720		> 0.05
789	0.33	1.410	4	64	.629		> 0.05
862	0.40	0.840	12	56	.388	.484	$0.01 \rightarrow 0.05$
790	0.47	1.550	3	65	.720		> 0.05
863	0.55	0.490	6	62	.522	.650	$0.01 \rightarrow 0.05$
791	0.55	0.740	5	63	.569		> 0.05
792	0.74	1.850	5	63	.569	.706	< 0.01
865	0.28	0.950	8	60	.459		> 0.05
866	0.28	0.840	10	58	.418		> 0.05
867	0.25	0.640	12	56	.388		> 0.05

z' : redshift at $\mathcal{T}$;
n1 : number in field;
n2 : number in rest of fields;
$\mathcal{T}_{95}$: 5% quantiles of KS statistic;
$\mathcal{T}_{99}$: 1% quantiles of KS statistic;
$\widehat{\alpha}$: critical level

discrete (Noether 1967), it seems advisable to probe the (α, δ, z) distribution in the survey in greater detail.

5.3 Fourier power spectrum analysis

A powerful test for detecting spatial clustering in a distribution of points within a sample volume of space, and determining its significance, is Fourier power spectrum analysis. The aim is to evaluate certain quantities which are functions of the Cartesian coordinates of the system by obtaining a 3-D spatial Fourier transform of the distribution. These are then compared with those derived from the distribution of points expected on some hypothesis, for example, the "null hypothesis", that the points are uniformly and independently distributed at random in the volume. An evaluation of the probability distribution for the null hypothesis leads to an assessment of the consistency of the actual and hypothetical distributions.

5.3.1 Theory

Power spectrum analysis (PSA) as a means of investigating astronomical clustering has been described in detail by Webster (1976a) in the context of the clustering of radio sources in the 4C, GB and MC_I radio catalogues (Webster 1976b). The following treatment follows closely his approach.

Consider m points distributed in a 3-D volume with a Cartesian coordinate system defined such that the position of each point is $\boldsymbol{r}_j$, $(j = 1, 2, \ldots, m)$. A function to represent this distribution may be constructed from a δ function at each point:

$$f(\boldsymbol{r}) = \sum_{j=1}^{m} \delta(\boldsymbol{r} - \boldsymbol{r}_j) \tag{5.2}$$

which, under the Fourier transform, may be expressed as a sum of waves with propagation vector $\boldsymbol{k}$ in the Fourier series expansion:

$$f(\boldsymbol{r}) = \sum_{k=1}^{\infty} (c_k \cos(\boldsymbol{k}\cdot\boldsymbol{r}) + s_k \sin(\boldsymbol{k}\cdot\boldsymbol{r})) \tag{5.3}$$

where c_k and s_k are the Fourier coefficients for wavelengths of scale size $\lambda_k = 2\pi/|\boldsymbol{k}|$, and thus contain all clustering information on this scale. Fourier theory shows that they can be evaluated thus:

$$c_k = \int_{-\infty}^{+\infty} f(\boldsymbol{r}) \cos(\boldsymbol{k}\cdot\boldsymbol{r})\, d\boldsymbol{r} \tag{5.4a}$$

$$s_k = \int_{-\infty}^{+\infty} f(\boldsymbol{r}) \sin(\boldsymbol{k}\cdot\boldsymbol{r})\, d\boldsymbol{r} \tag{5.4b}$$

With the distribution of points in equation (4.1), they become:

$$c_k = \sum_{j=1}^{m} \cos(\boldsymbol{k}\cdot\boldsymbol{r}_j) \tag{5.5a}$$

$$s_k = \sum_{j=1}^{m} \sin(\boldsymbol{k}\cdot\boldsymbol{r}_j) \tag{5.5b}$$

The power spectrum statistics, I_k, are now defined such that:

$$I_k \equiv \frac{2}{m}(c_k^2 + s_k^2)$$

$$= \frac{2}{m}\left(\sum_{j=1}^{m}\cos(\boldsymbol{k}\cdot\boldsymbol{r})\right)^2 + \frac{2}{m}\left(\sum_{j=1}^{m}\sin(\boldsymbol{k}\cdot\boldsymbol{r})\right)^2$$

$$= \frac{2}{m}\left(\sum_{j=1}^{m}\cos(k_x x + k_y y + k_z z)\right)^2 + \frac{2}{m}\left(\sum_{j=1}^{m}\sin(k_x x + k_y y + k_z z)\right)^2 \qquad (5.6)$$

which represents the amplitude of power of scale size $\lambda_k = 2\pi/|\boldsymbol{k}|$ in the distribution. Webster (1976a) has shown that, in the asymptotic limit as $m \to \infty$, the I_k for the null hypothesis of no clustering are distributed as χ^2 with 2 degrees of freedom.

So, in principle I_k could be evaluated from equation (5.6) for the observed data, within the framework of an assumed cosmological model (where $q_0 = 0.5$, $\Omega_0 = 1$); values of q_0 other than that for a flat universe require more complex transforms. The result could then be compared to that expected for a random, uniform distribution, revealing any excess power in the data at each particular scale size.

5.3.2 PSA applied to the UVX survey

The procedure described in the last section cannot be followed exactly here for various reasons:

- the surveyed zone occupies an incompletely filled cone in 3-D;
- the space density of even non-clustered quasars is non-uniform due to both the cosmological distribution (evolution), and observational selection effects (any trend in sensitivity to detection with redshift);
- artificial variations may exist in the quasar surface density between and possibly within fields due to zero-point shifts in B, and residual field-effects.

The method adopted here was to determine the 3-D spatial Fourier transform expected for the observed dataset if it were *intrinsically* unclustered but still subject to the observational selection effects. This was done by Monte Carlo simulations, assigning random redshifts drawn from the observed redshift values to the 69 observed quasar coordinates. Many simulations were performed to guarantee uniformity. This ensured the preservation of any observational bias in z as well as any 2-D bias on the sky that could result from residual plate field effects. In this way the typical Fourier transform expected for unclustered but observationally biased data was obtained, with the pessimistic assumption that any clustering in the plane of the sky or redshift direction is entirely spurious.

One advantage of this technique over those such as the correlation function (see Section 5.4) is that the Fourier coefficients preserve the phase information of any power. For each wavenumber, the excess power is calculated from the amplitude of the *vector* subtraction of observed and mean Fourier components (determined from the Monte-Carlo simulations). It is also possible to exclude Fourier contributions close to, and perpendicular to, the plane of the sky, thus removing position-dependent and redshift-dependent observational selection effects — both the actual and simulated data have similar distributions and no extra information is gained.

A rectangular cartesian coordinate system was defined using the following transformations:

$$X = s(z)\ \cos(\delta)\ \sin(15\{\alpha - \bar{\alpha}\}) \tag{5.7a}$$

$$Y = s(z)\ \sin(\delta) \tag{5.7b}$$

$$Z = s(z)\ \cos(\delta)\ \cos(15\{\alpha - \bar{\alpha}\}) \qquad \bar{\alpha} = (\alpha_{max} - \alpha_{min})\ /\ 2 \tag{5.7c}$$

where s is the comoving coordinate given by the standard formulae:

$$s(z) = \frac{zq_0 + (q_0 - 1)[-1 + (2q_0 z + 1)^{1/2}]}{(1+z)q_0^2} \qquad q_0 \neq 0 \tag{5.8}$$

which reduces here to

$$s(z) = 2(1 - (1+z)^{-1/2}) \tag{5.9}$$

α and δ are respectively the right ascension and declination of the objects; the new coordinate z-axis points in the direction of $\alpha = \bar{\alpha}$ and $\delta = 0$, the x-axis is defined in the $\delta = 0$ plane and the y-axis in the $\alpha = \bar{\alpha}$ plane. The analysis proceeded in three stages:

1. The observed data (α, δ, z) coordinates were transformed using equation 5.7 above. These were scaled such that the maximum distance range in X, Y or Z was set equal to 2π.
2. The redshift values were shuffled randomly and (X, Y, Z) coordinates again calculated for many iterations.
3. The range of wavenumbers required in each Fourier component were calculated; then, working through each component in turn, and explicitly excluding those close to and perpendicular to the plane of the sky as discussed above, the relevant wavenumber was calculated. The mean sine and cosine components of the random dataset were obtained (equation 5.6) and the amplitude of the *resultant* vector after subtraction of the mean vector for both the observed and simulated datasets was computed. This was performed for each Fourier component. 1, 2 and 3 σ errors on the random dataset were calculated as 68, 95 and 99.7 percentiles of the random distribution from the Monte-Carlo simulations, and hence the significance of power in the observed dataset was deduced. Following Webster (1982) the effectiveness of the statistic was increased by finding the mean power of all components in bins of component wavenumber.

5.3.3 Results of the PSA analysis

The results of the PSA are presented in Figure 5.4. 10,000 iterations were performed for $\lambda > 250\,h^{-1}$ Mpc and 1000 for $\lambda < 250\,h^{-1}$ Mpc. Points indicate the amplitude, Q, of the power spectrum, derived in bins of constant wavenumber interval and plotted as a function of wavelength. The solid line shows the values expected in the absence of clustering, and the other lines trace the envelopes of the 68, 95 and 99.7 percent confi-

dence regions (corresponding to the 1, 2 and 3 sigma regions of the normal distribution) expected in the absence of clustering. The median value tends to unity for small wavelengths, as expected for uniformly-distributed random data, and falls below unity at large wavelengths, as the simulated datasets are all constrained to have the same large-scale distributions. The residual power spectrum of the actual data shows a significant (p <0.1%) excess at wavelengths $\lambda \gtrsim 500\,h^{-1}$ Mpc, falls to unity at $\lambda \sim 250\,h^{-1}$ Mpc and below unity at $\lambda \sim 120\,h^{-1}$ Mpc (note however that the data points shown are not independent). Adding in the components in the plane of the sky and along the redshift axis lowers the amplitude of the residual power spectrum without altering the statistical significance of the excess. The interpretation of the excess power at large scales is that there appear to exist structures with sizes up to $250\,h^{-1}$ Mpc: on the simplest representation of the mass distribution as a "top-hat" function of radius r, the power spectrum in reciprocal wavelength $\bar{k}$-space is a sinc^2 function $[\sin 2\pi\bar{k}r/\pi\bar{k}]^2$ which falls to zero at $\bar{k} = 1/2r$ i.e. $\lambda = 2r$. This result has been obtained with the conservative assumption that any clustering in the angular and redshift distributions is due to observational selection, so that the true amplitude of the power spectrum will have been underestimated.

5.4 Correlation function analysis

In order to provide compatibility with previous results, it is instructive to derive the spatial two-point correlation function for the sample. This statistic, developed largely by Peebles, is used widely in investigations of astronomical clustering, both in its 2-D form (galaxy clustering studies) and its 3-D form where redshift information is available, as is the case here. The technique is to measure the excess number of real data pairs over those derived from a uniform random distribution as a function of separation.

5.4.1 Theory

For any distribution, the two-point correlation function, ξ, is defined by

Figure 5.4: Power spectrum analysis results. The amplitude, Q, is shown in bins of constant wavenumber interval. Points indicate the derived values, the solid line the values expected in the absence of clustering, and the other lines trace the envelopes of the 68, 95 and 99.7 percent confidence regions (corresponding to the 1, 2 & 3 sigma regions of the normal distribution) expected in the absence of clustering.

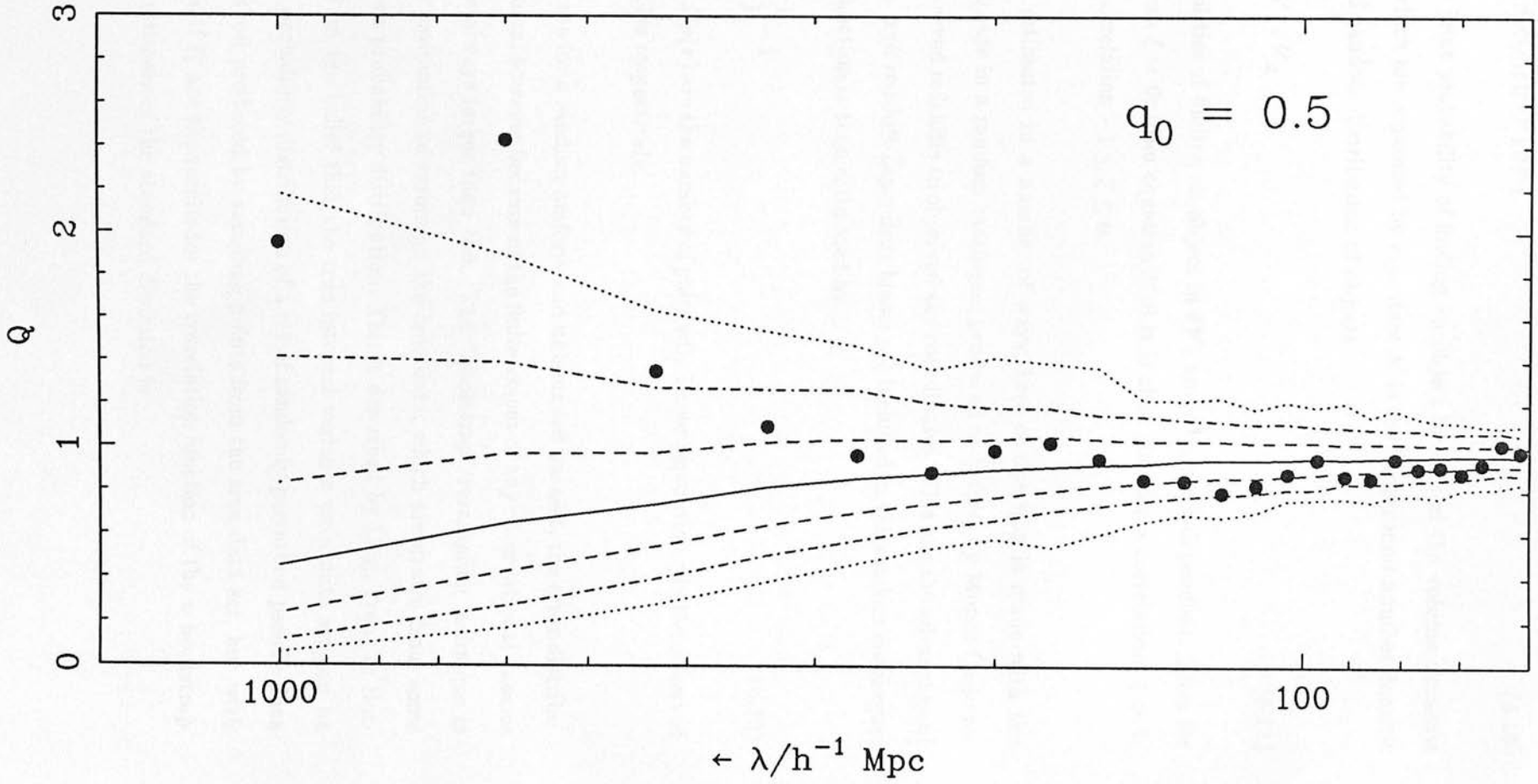

$$\delta P = \mathcal{N}^2[1 + \xi(r_{12})]\,\delta V_1\,\delta V_2 \tag{5.10}$$

where δP is the joint probability of finding an object in each of the volume elements δV_1 and δV_2, which are separated by r_{12}. Here $\mathcal{N}$ is the background number density. In a uniform and random distribution of objects

$$\delta P = \mathcal{N}^2\,\delta V_1\,\delta V_2 \tag{5.11}$$

since the probabilities of finding an object in δV_1 and δV_2 are independent. Thus for the null hypothesis $\xi = 0$; from equation 5.10 it is clear that for a correlation, $\xi > 0$, and for an anti-correlation $-1 \leq \xi \leq 0$.

$\xi(r)$ can be estimated in a number of ways; here comparison is made with the distribution of objects in a random catalogue, produced as before, by Monte-Carlo re-assignment of observed redshifts to observed sky coordinates. This has the advantage of ensuring position- and redshift-dependent biases are included in the random catalogue. The correlation function is then estimated by

$$\xi(r) = \frac{N_O(r)}{N_R(r)} - 1 \tag{5.12}$$

where $N_O(r)$ and $N_R(r)$ are the number of pairs with linear separation r in the observed and random samples respectively.

In the ideal case for a random uniform and unbounded dataset, the error distribution of ξ is Poissonian; however because of the finite extent of any observational dataset realistic errors are always larger than this. The "bootstrap" resampling technique is often used for the estimation of errors on the true data, which are drawn from some underlying unknown probability distribution. This is described by Ling, Frenk & Barrow (1986), based on the belief that the true internal variance on a data set can be obtained from the probability distribution of a set of randomly perturbed pseudo data sets — in this method produced by sampling points from the true data set, but with replacement. Thus, if $\xi_i^\star$ are the results for the correlation function of the n bootstrap samples, then the estimate of the standard deviation is

$$\sigma_{b-s} = \left(\frac{\sum_{i=1}^{n} [\xi_i^\star - \xi^\dagger]^2}{(n-1)} \right)^{1/2} \tag{5.13}$$

where

$$\xi^\dagger = \sum_{i=1}^{n} \frac{\xi_i^\star}{n} \tag{5.14}$$

which is the mean value of $\xi^\star$ for the n pseudo data sets. This result will be used below to derive errors on the data points, and in an attempt to estimate the zero-crossing point of the correlation function.

5.4.2 Correlation function analysis applied to the survey

In order to apply the analysis to the UVX sample, it is necessary to calculate the comoving distance between all pairs of quasars. This is done by using equation 5.8, the conversion from redshift to dimensionless comoving coordinates. Following Shanks *et al.* (1987), the coordinate system is shifted from observer to one of the QSOs and the magnitude of the vector to the other QSO in this coordinate system is calculated. We use Weinberg's transformation (Weinberg 1973, eqn.[14.2.1]):

$$\boldsymbol{X'}_2 = \boldsymbol{X}_2 + \boldsymbol{a}\{(1 - k\boldsymbol{X}_2^2)^{1/2} - [1 - (1 - k\boldsymbol{a}^2)^{1/2}] \times (\boldsymbol{X}_2 \cdot \boldsymbol{a}/\boldsymbol{a}^2)\} \tag{5.15}$$

where $k = (2q_0 - 1)$, $\boldsymbol{a}$ is the coordinate system translation vector (as measured from the *new* origin), and $\boldsymbol{X}_2$ and $\boldsymbol{X'}_2$ are the coordinates of QSO_2 as measured in observer's and QSO_1's coordinate systems respectively. In the observer's system, if QSO_1 is at comoving distance s_1 and QSO_2 at s_2, an angle of θ away on the sky, then the (x, y, z) coordinates can be represented by $(0, 0, s_1)$ and $(s_2 \sin\theta, 0, s_2 \cos\theta)$ respectively, giving

$$\begin{aligned} \boldsymbol{X'}_2 &= (s_2 \sin\theta, 0, s_2 \cos\theta) + (0, 0, -s_1) \times \Phi \\ &= s_2^2 + s_1^2(\Phi) + 2 s_1 s_2 \cos\theta(\Phi) \end{aligned} \tag{5.16}$$

where

$$\Phi = \{(1 - ks_2^2)^{1/2} + [1 - (1 - ks_1^2)^{1/2}][(s_2/s_1)\cos\theta]\} \quad (5.17)$$

As expected, for $q_0 = 0.5$ this reduces to the cosine rule. The magnitude of $\boldsymbol{X}_2$ is then the comoving distance between QSO_1 and QSO_2.

The analysis proceeded as follows:

1. Comoving distances were calculated between all pairs in the actual dataset and number of pairs in distance bins derived.
2. The cumulative distribution in redshift was derived and smoothed over a z interval of 0.1; a Monte-Carlo simulation was then performed by generating a random cumulative value and assigning a redshift value for each observed quasar position. In the derivation of the cumulative redshift count, redshifts from two previous UVX surveys were added, its purpose being to attain a better smoothed relation while retaining any UVX z-selection effects. These surveys were (a) the AB survey of Braccesi, Formiggini & Gandolfi (1970), and, (b) the MBQS survey of Mitchell, Warnock & Usher (1984). In practice the addition of these datasets did not alter the results. Comoving distances were then calculated again for each of these simulations, binned, and averaged over all simulations. Standard errors on the null hypothesis were also calculated.
3. The "boot-strap" resampling method (Ling, Frenk & Barrow 1986) described above was applied to the data by randomly reassigning redshifts to the observed positions *with replacement* and deriving standard errors from these simulations.
4. The three steps were combined using equation 5.12 for $\xi(r)$.

5.4.3 Results of the analysis

The results of the analysis are presented in Figure 5.5(a,b) for $\Omega_0 = 1$ and $\Omega_0 = 0.2$ respectively. Filled dots are the $\xi(r)$ values as a function of separation. Errors on these points are the boot-strap errors at the 68% confidence level, represented by the dashed envelope, and the shaded region represents the 68% confidence region expected

Figure 5.5: Correlation function analysis results:
(a) Results for $\Omega_0 = 1$
ξ is shown as a function of separation. The shaded region indicates the 68 percent confidence region expected in the absence of clustering obtained from 1000 Monte-Carlo simulations. The dashed envelope indicates the extent of the 68 percent confidence region for the actual correlation function derived by bootstrap resampling.

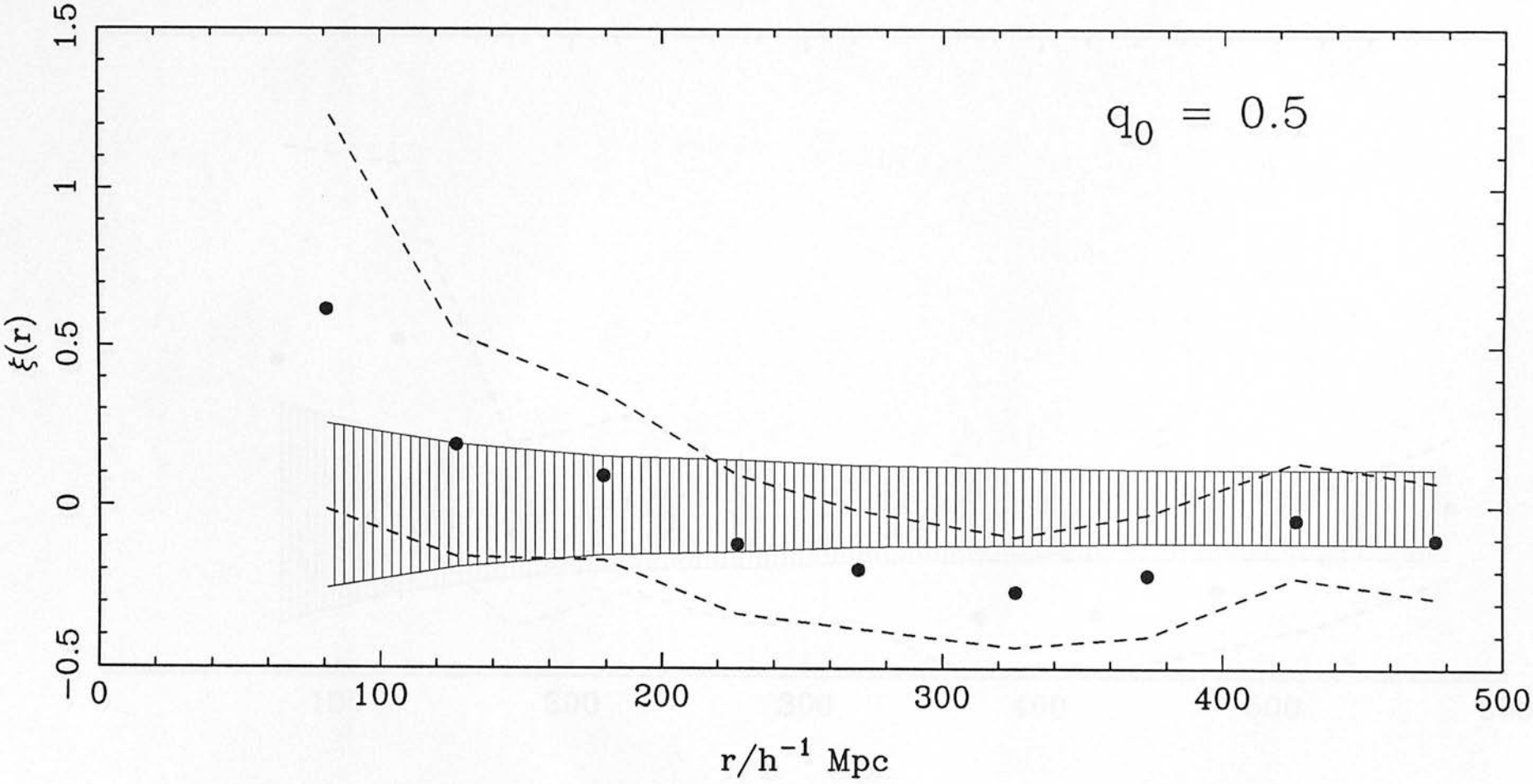

Figure 5.5: (b) Correlation function analysis results for $\Omega_0 = 0.2$

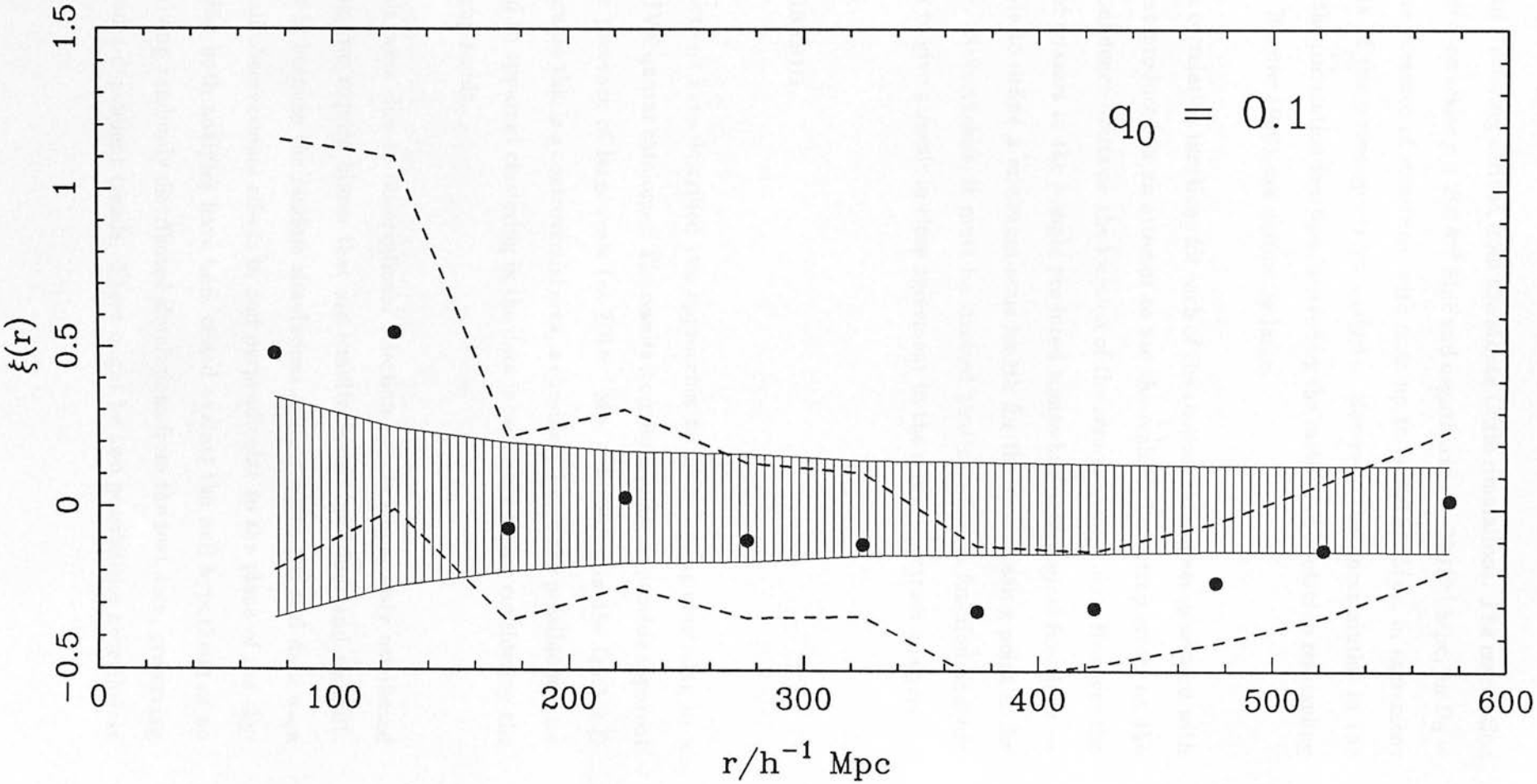

in the absence of clustering derived from the Monte-Carlo simulations. The correlation function is positive on scales $r \lesssim 200\,h^{-1}$ Mpc and negative at $r \sim 300\,h^{-1}$ Mpc, for $\Omega_0 = 1$, indicating the presence of structures with sizes up to $\sim 300\,h^{-1}$ Mpc, in agreement with the results of the power-spectrum analysis. However, the uncertainties in the precise form of the correlation function, derived by the method of bootstrap resampling (Ling, Frenk & Barrow 1986), are extremely large.

Simulation correlation functions for each of the random catalogues generated with replacement were produced in an attempt to use the realistic bootstrap errors on the data to place confidence limits on the location of the zero-crossing point. However the small number of quasars in the sample produced somewhat pathological functions — it was impossible to define a minimum scale length for the zero-crossing point to 3σ with these data. Nevertheless, it must be stressed that correlation function analysis has been shown to give a result in close agreement to the power spectrum analysis.

5.5 Discussion

The previous sections have described two approaches to investigating clustering in a new large-area UVX quasar catalogue. The results from both analyses provide apparent evidence for the presence of large-scale ($\sim 250\,h^{-1}$ Mpc) clustering in the QSO 3-D distribution. Because this is a controversial area, a consideration of any possible sources which might lead to apparent clustering in the data is necessary before considering the implications of any result.

If this result were due to observational selection effects erroneously attributed to real clustering, we require biases that are simultaneously position- and redshift-dependent. This is because the random simulations against which the real data were tested included all observational effects in and perpendicular to the plane of the sky: as described earlier both analyses have been tested against the null hypothesis of no clustering by deriving randomly distributed simulations from the real data, preserving any positional and z-dependent trends. There might be two possibilities nevertheless

where such biases may be present in the data.

Firstly, the effectiveness of the rejection of extended images might vary with position, possibly introducing apparent clustering at low redshifts by excluding low-redshift quasars preferentially as a function of α and δ. This is unlikely to be significant here for three reasons:

1. the clustering signal is not only due to quasars with low redshifts (this has been tested restricting the z range for analysis);
2. at $z \sim 0.4$ the angular scale of the clustering extends over several Schmidt fields (see Figure 5.1), indicating that the presence of low-redshift quasars is at least not confined to a single field;
3. the fraction of objects which are rejected as being extended does not vary significantly between fields (see Table 4.1(b)).

Secondly, the $(U-B)$ and $(B-R)$ colours of quasars vary systematically with redshift (Figure 4.5(a,b)), so that the variations in the colour limits with position could introduce variable incompleteness. This is also unlikely to be significant, because the quality of the data from which the survey was derived has allowed deeper probing than is usual towards the main sequence locus in colour space as indicated in Chapter 4. In particular,

1. as we have seen 94% of the quasars are at least 0.1 magnitudes bluer than their respective $(U-B)$ limits, implying high completeness even in the difficult redshift ranges centered on $z = 0.75$ and $z = 1.65$ where QSOs on average redden;
2. similar confidence has been demonstrated in the case of $(B-R)$ completeness, again implying few losses in the range $0.5 \lesssim z \lesssim 1.0$ where MgII enters the B band.

As expected Figure 4.5 indicates that there only appears to be a trend towards the quasars having significantly deviant colours in these indices for $0.5 \lesssim z \lesssim 0.9$, whereas the clustering is not only due to signal at these redshifts. Furthermore, since the $(U-B)$ limits are sufficiently blue to cause potentially significant incompleteness in this redshift

range in fields 865 and 867, the PSA analysis has been repeated without these fields. The results have shown that even with these fields excluded, a significant (3σ) result is still obtained.

Aside from observational biases, what other effects may mimic the presence of true clustering in such an analysis? In principle cosmological obscuration might produce an apparent signal on large scales, but only by reducing the numbers of quasars with redshifts greater than the redshift of the obscuring matter. This hypothesis however does not seem compatible with the observed distribution of objects on the sky. The above sources of possible bias therefore do not offer any immediate reasons for suspecting the result to be spuriously generated by observational effects. Clearly further observations are required to confirm this conclusion.

Having outlined possible sources of bias that may influence these results, it is appropriate to conclude with a brief discussion of the implications if later investigations substantiate these first indications. It is first pertinent to ask why this result might not have been found previously. The most extensive study of clustering in samples selected by ultraviolet excess (Shanks *et al.* 1987) only used information on scales much smaller than the angular scale of the clustering so that for $r \gtrsim 120\,h^{-1}$ Mpc the amplitude of the correlation function is determined almost entirely by distances between quasar pairs along the redshift axis. Further, the distribution of quasars is biased to high redshifts, with 50 percent of them lying within a range of comoving radial distance of only $440\,h^{-1}$ Mpc ($\Omega_0 = 1$). Because of this weighting to high redshifts the correlation function at large separations is extremely insensitive to the presence of even strong clusters at $z < 1$: the random errors at large separations are much larger than Poissonian, although the correlation function and its uncertainties are correctly estimated at smaller separations. Hence the results from that survey may not be inconsistent with those presented here. Larger-area surveys have been made using objective prisms, but such surveys have resulted in a restricted redshift range, with most of the quasars found in the range $1.8 < z < 2.5$. If clustering in the plane of the sky is excluded as being dominated by observational selection effects, then the maximum wavelength that can be investigated in those samples is $\lambda \sim 250\,h^{-1}$ Mpc

(Webster 1982), whereas significant power is only detected here at $\lambda \sim 400\,h^{-1}$ Mpc.

If this result were to be accepted at face value it would favour cosmological models with a low density, since predicted scale-sizes vary approximately as $(\Omega_0 h^2)^{-1}$ (e.g. Silk & Vittorio 1987; Blumenthal, Dekel & Primack 1988). It is however vital to qualify the results described in this chapter with the proviso that there are reasons to doubt whether quasars trace the mass in the universe; again the amplitude of the mass fluctuations would have to be smaller than the amplitude of the quasar number fluctuations to avoid exceeding the observational limits of the CMB. Nevertheless if these first indications of large-scale structure in the distribution of quasars are substantiated, this result is complementary to other recent observational studies mentioned in the introduction which call into question the "standard" flat CDM picture. Before far-reaching conclusions can be drawn this work must be further examined by extending the study. The techniques for the processing further plate material are all existant, so production of a larger area survey is entirely feasible. Further calibration will of course be required for this and the reduction of any sources of uncertainty that may lead to apparent clustering is now also essential. The techniques for the reduction of systematic errors in calibration and the removal of field effects described in earlier chapters have produced good results, but clearly any increase in sample homogeneity is to be welcomed.

Chapter 6

A Search for High-Redshift QSOs

6.1 Introduction

The previous chapter dealt with the selection of low-redshift quasars via a modified ultra-violet excess criterion. Due to the successes of the UVX selection technique in the last decade, many thousands of $z \lesssim 2.2$ quasars have now been catalogued. This is in addition to contributions made by the other widely used selection technique, that of slitless spectroscopy. The UVX technique relies mainly on the power-law continuum shape of quasars, as opposed to the black-body continua of stars, as a discriminator — emission lines are only important in as much as they influence the broad-band colours. Slitless spectroscopy however aims to select quasars on the basis of sharper spectral features such as emission lines. The result is that the latter technique is not subject to the same high-redshift limit ($z \simeq 2.2$ when Ly-α enters the B band); sensitivity continues until Ly-α exceeds the emulsion limit. This fact has meant that slitless techniques remain popular for higher-redshift searches.

Colour selection however is not rendered useless above $z = 2.2$. The inclusion of information from a band other than U and B provided excellent discrimination between very blue stars and quasars in the previous chapter. In the same way, it has been demonstrated in recent years that using the full range of optical bands *UBVRI* can provide adequate discrimination in theory for quasars up to and beyond $z = 5$, and in practice, this has led to considerable success. The recent work by Paul Hewett, Steve Warren and collaborators (e.g. Warren *et al.* 1987a, Warren, Hewett & Irwin 1987b, Warren, Hewett & Osmer 1987c, 1988, 1989) has produced a total of 4 quasars presently known beyond $z = 4$.

Broad-band colour selection has many attractive features. Small changes in redshift do not in general dramatically affect the sensitivity of the technique, as is the case in line-orientated work. The smoothness of UVX redshift-number histograms in comparison to those produced by prism-selected surveys clearly demonstrates this: the complex selection function for the latter technique makes quantitative conclusions about number densities at different epochs very hard. These problems are further compounded by the presence of observer biases in "eyeball" searches of photographic plates making any estimation of space density and completeness notoriously difficult. The concentration on automated procedures is an attempt to reduce these uncertainties; in particular, in this study, the spectral colours of known high-redshift quasars are re-examined within the present datasets, and the efficiency of selection is measured. The above comments are not made to invalidate the considerable contributions of prism work — indeed a combination of the two methods seems to be the best step forward.

The technique presented here relies on a clear distinction between quasars and the main sequence in colour space, as they move with redshift; clearly this is a presupposition that must be tested, and Section 6.2 will address the problem theoretically, attempting to examine the sensitivities to different quasar spectral types, and how this progresses with redshift. Later sections will discuss the technique applied to the Edinburgh Multicolour Survey and analyse results of the search.

6.1.1 Previous work

The luminosity function, $\Phi(M_B, z)$, (LF), for a population of objects is defined as the space density as a function of absolute magnitude and redshift. Its form for low-redshift quasars has been well determined in recent years, mainly due to the increasing efficiency of the UVX technique and new spectroscopic methods. The catalogue of Boyle *et al.* (latest version Boyle, Shanks & Peterson 1988b) using $(U-B)$ colour selection in 34 0.35 deg^2 areas on 7 COSMOS Schmidt fields down to $B < 20.9$ contains 420 confirmed QSOs, an increase of $2\frac{1}{2}$ times that in the previous study (Boyle *et al.* 1987), due to the speed of the fibre-optic system FOCAP at the Anglo-Australian Telescope.

Boyle, Shanks & Peterson (1988b) subsequently showed that a smoothed two power law luminosity function is consistent with these and other data, and that, except for the very low-luminosity objects ($M_B > -23$), the progression with redshift is best represented by pure luminosity evolution (PLE), i.e. that of a systematic evolution in the luminosity coordinate with z, with an unchanged LF both in shape and density. In the simplest picture, this can be seen as the dimming of single QSOs as they age, with no change in their space density.

Although at present, the above result appears to satisfy the data available, alternative forms have been proposed in the past. The simple picture of pure density evolution (PDE), where the LF again maintains its shape with z, but is modified only in the density direction, was employed in early days (e.g. Schmidt 1970, 1972) as an expression of the observation that the newly-discovered quasi-stellar objects apparently exhibited a marked increase in co-moving space-density with redshift (Schmidt 1968). Mathez (1976, 1978) however showed that Schmidt's data could be equally compatible with a pure luminosity evolution scheme, indicating that the supposed disagreement was due to the exclusion of low-luminosity objects from Schmidt's theoretical predictions at fainter magnitudes, while including them in a brighter observational dataset.

Schmidt & Green (1983) reported the completion of a very large scale UVX selection ($\sim$ 10,714 deg^2) to a bright limiting magnitude ($B \sim 16.16$), producing the Bright Quasar Survey (BQS) of 114 objects. From these data, they showed the inconsistency of the pure density evolution model, and replaced it with a form of luminosity-dependent density evolution (LDDE), where the space density of QSOs is a function of cosmic time and of intrinsic luminosity (with more luminous quasars evolving at a higher rate). At the same time, Marshall and others applied various forms of evolution to data from the UVX Braccesi Faint (BF) (Formiggini *et al.* 1980) sample of 35 quasars in 1.72 deg^2 to $B < 19.8$, and the AB sample (Braccesi, Formiggini & Gandolfi 1970) of 22 quasars in 37.2 deg^2 to $B < 18.25$, confirmed by Marshall *et al.* (1983b, 1984). In Marshall *et al.* (1983a) the pure density evolution model was again strongly rejected as producing far too many faint quasars, in favour of pure luminosity evolution. Marshall (1985) went further in excluding the LDDE model of Schmidt & Green, while reconciling the data

with the PLE model.

Although these other forms seem at the moment to be redundant for quasars with $z < 2.2$, the PLE picture is clearly not appropriate at higher redshifts. As Section 6.4 will demonstrate, a straight extrapolation of the "Boyle model" to $z \gtrsim 3.5$ predicts a massive excess number of QSOs over that observed. This phenomenon has in the past been referred to as a redshift "cutoff", a term which leads to much confusion: the term was used by Schmidt in earlier days to account for the apparent lack of QSOs with $z > 2.5$ (now understood as a facet of the UVX technique); in practice, this usually is now meant to signify not an immediate decrease to zero in space density, but a fall-off beyond a certain redshift. For the reasons described in the following section, the survey presented here is sensitive to quasars in the z-regime $z > 3.4$, and at these redshifts, the behaviour is still uncertain.

In the past much effort has been put into visual emission-line searches at these redshifts. The "Curtis-Schmidt" survey (Smith 1975, 1976; Osmer & Smith 1976, 1977a, 1977b, 1977c) was successful in finding many high-redshift quasars with a slitless spectra visual search of IIIaJ photographic plates. The response of IIIaJ however limits the redshift range accessible to $z < 3.1$. The proposal that IIIaF emulsion, which, because of the continued emulsion response up to $\lambda \sim 6800$Å, in principle enables detection of QSOs to $z \sim 4.7$ through Ly-α emission, could be used in emission-line searches beyond $z = 3.5$ has led to many approaches. A visual grating-prism (grism) search by Hoag & Smith (1977) with IIIaF emulsion located no quasars with $z > 3.5$ in 5.1 deg^2, but was later shown to be strongly insensitive above this redshift by Carswell & Smith (1978), due to the steep power-law luminosity function when combined with the use of a grism blazed in the blue. Osmer (1982) therefore performed a red-blazed grating prism search of 5.1 deg^2, sensitive to quasars with $3.7 < z < 4.7$; still no detection was made by Ly-α emission. A maximum redshift of $z = 3.36$ was recorded by Osmer, and a space density decrease established at $z > 3.5$, suggesting a cutoff, in the sense of a sharp turn-down in density, following that proposed by Schmidt some twelve years earlier. This could be the result of a genuine "birth epoch" of quasars, or alternatively the blocking effect of intergalactic material at some high redshift. The

reliability of this result has since been contested: Mathez & Nottale (1982) claimed that the supposed depth of the survey was not so great as claimed, and found PLE to again adequately describe the evolution. Savage & Peterson (1983) also drew notice to the similarity between the Osmer redshift distribution and the shape of the sensitivity response with z.

Koo & Kron, and co-workers have meanwhile been pursuing the multicolour approach at the faintest magnitudes. In selected area 57, a total of 77 quasar candidates were selected in 0.3 deg^2 down to $B < 22.5$ (Koo, Kron & Cudworth 1986). Stellar-size images were separated from other contaminants with information from wavebands essentially equal to U, B, and $(V + R)/2$, although still on the basis of single two-colour diagrams. However, the colours of candidates found indicated that most were probably at $z < 2.5$, as indeed preliminary spectroscopy seemed to show. The same result had previously been suggested by similar data in Koo & Kron (1982). Koo & Kron (1988) established this result: 30 quasars were spectroscopically confirmed and results indicated that the success at high redshift was limited; $z = 3.12$ was the highest redshift obtained. When combining their data with brighter samples, they saw the smooth turn-over in slope of the LF, with the "break" luminosity increasing with redshift. No evidence of a high-redshift cutoff was seen, although clearly the scope of their conclusions was limited at high redshift.

The above results have given rise to a change in approach in recent years — since deeper samples appear to be obtaining little more in terms of high-z detections, surveying larger sky areas to a brighter limit seems appropriate. Hazard and collaborators have identified several high-z objects through the visual searching of the larger area UK Schmidt prism IIIaJ and IIIaF plates (Hazard & McMahon 1985, Hazard, McMahon & Sargent 1986, Webb *et al.* 1988) the most spectacular of which was the discovery of Q0000-2619 with $z = 4.11$ (Webb *et al.* 1988). The successes have been taken as evidence against a cutoff, instead indicating a steady decline in comoving density from $z \sim 2$. The discovery of six quasars with $z \geq 3.3$ on two Schmidt plates has given rise to the claim that, when compared with surface densities at $z \simeq 2.25$, for similar QSOs in the range $3.5 < z < 3.8$ for $R < 18$:

> "...our incomplete observations imply a strong increase in the co-moving density of the brightest QSOs with increasing redshift."

In order to reconcile their result with the much lower reported surface densities for deeper surveys, Hazard *et al.* found evidence for:

> "...a transition from the steep QSO luminosity function found at lower redshifts to one that is relatively flat above $z = 3.5$ or perhaps even one where the number of QSOs per magnitude interval decreases at lower luminosities."

It is difficult to know how to approach these results: although it cannot be denied that Hazard and co-workers have had much success in locating these bright objects, no indication is given as to the number of fields searched, and how many of these revealed no such candidates. It is not clear whether the surface densities derived are statistically justified. More importantly, it now appears that the quoted surface densities may be too bright by $\sim 0.5^{\rm m}$ — Hazard (1986) refers to surface densities at $R = 18.5$. For these reasons, it is clear that spectacular detections of high-z quasars are not enough: it is vital that better estimates of completeness and sensitivity are available, and machine measured and selected data appear the most obvious choice.

The main two automated studies until the present time have been that of the APM group (Warren *et al.* 1987a, Warren, Hewett & Irwin 1987b, Warren, Hewett & Osmer 1987c, 1988, 1989) and that of Schmidt, Schneider & Gunn (1986a, 1986b, 1987a, 1987b). The latest available data from the APM group (Hewett, private communication) consists of 24 quasars with $4.5 < z < 3.0$ to $R < 20$ in $\sim 30{\rm deg}^2$; these results complement our survey at brighter magnitudes and in a larger sky area. The APM data, although at present uncertain, appear to show a luminosity function somewhat flatter than that of Boyle *et al.*, with a progressively decreasing comoving space density at faint luminosities. At the brighter end, $M_B \lesssim -27.5$ ($q_0 = 0.5$, $H_0 = 50$), they conclude that the space density may exceed that of Boyle *et al.*, although the small numbers involved make any conclusion tentative.

Schmidt, Schneider & Gunn used a scanning CCD and grating technique, the data from which was then examined for emission lines with an automated search algorithm.

These results have been less clear — in an initial examination of 0.9 deg^2 to a limiting magnitude in the range B =20–22, although claiming sensitivity in the range $2 < z < 5$, they found no quasars with $z > 2.66$ (1986a); upon brightening the limit to $B \sim 19$ and increasing the area covered to ~ 8 deg^2, the highest redshift was again $z = 2.77$. They considered this to indicate a luminosity-dependent redshift cutoff (i.e. an abrupt decline in space density) at $z \sim 3$, following on from the proposal of Osmer (1982), although at lower z. However, a subsequent investigation by Schmidt, Schneider and Gunn in 14 deg^2 (1987a) led to the discovery of 9 quasars in the range $3.0 < z < 3.8$, a result which does

> "...not strongly support the sharp decline in quasar density at a redshift close to three proposed by the surveys described in Papers I and II."

The discovery of PC 0910+5625 with $z = 4.04$ in October (1987b) in the same survey and the more recent detection of a $z = 4.7$ quasar (as yet unpublished) further complicates the situation, and a more complete treatment of this survey is required before quantitative conclusions can be reached.

The situation therefore still seems uncertain; the data available are still insufficient at present, and any number of evolutionary schemes can be envisaged. Nevertheless, the physical implications of the idealised models considered are clear. In the very simple picture of a high-redshift LF of the same essential shape as that at low-redshift, simply shifted in the luminosity direction (necessarily changing sign at some intermediate z), the observed properties most simply imply the birth of long-lived QSOs at a high redshift dimming or brightening uniformly with cosmic time; an alternative explanation could be a population of shorter-lived quasars displaying these same properties globally. In the case of density evolution, shorter lifetimes coupled with a genuinely changing birth-rate seem appropriate, which in turn bring into question the assumption that the LF would necessarily maintains its shape over the 1–2 Gyrs between $z = 2$ and $z = 5$, an assumption which is necessary in the simple treatment given here. For the LF to change in shape, it is necessary to consider the more complex models of LDDE (c.f. Schmidt & Green 1983), or even combined luminosity evolution and LDDE of Heisler & Ostriker (1988a).

6.1.2 Introduction to the nearest-neighbour technique

It is necessary to introduce the selection technique before further discussion. The multicolour approach is grounded in the belief that in multi-dimensional colour space such as *UBVRI*, discrimination between galactic stars and most types of object normally referred to as quasars is possible. Any method, then, that isolates objects away from the main stellar clump can be considered. Many mathematical approaches to the problem have been developed, tailored to particular forms of clustering; however, one of the simplest approaches was used here. The distance from the object in question to its n^{th} nearest neighbour (where n is chosen to suit the size of the main dataset and the size of distinct target groups) in five-waveband colour space is a good indication of its level of isolation. The choice of n was influenced by (a) the likelihood of substantial groups of objects away from the stellar locus (small values of n could generate too small resulting distances in the case of a small association of objects away from the main stellar locus), and (b) the sparsity of parts of the main locus (large n would cause the selection of progressively more stars from the red end). A value of n between 10 and 100 appeared a suitable compromise: there is no clustering outside the main stellar locus in the survey.

By way of introduction, Appendix D shows four projections of the data in each Schmidt field. Each plot contains about 20,000 objects, consisting of all images *found in all wavebands* with $17 \leq R \leq 18.5$. The data clearly still varies in quality from field to field but the locus for stars is considerably tighter than was seen at earlier stages. Very few points can be seen away from the main stellar locus and it is this quality which is vital for nearest-neighbour searching.

The simulations in the next section were an attempt to copy as accurately as possible conditions in the real data, a major limitation of which is the varying depth of each photographic exposure. As has been shown in Figure 2.4, the number of objects detected by COSMOS increases with apparent magnitude, then abruptly falls as objects pass beyond the detection threshold: the magnitude at which this occurs is termed the plate-limit. Objects of genuinely extreme colour may therefore be unrecorded in one or more wavebands, the only information available being that its magnitude is fainter than

the relevant plate-limit. The procedure adopted for such an object will be described in full later, but is introduced here for use in the next section. In order to optimise the information available, a trial magnitude is calculated such as to minimise the Euclidean distance of the object from the stellar locus in multi-dimensional colour space subject to the constraints of its measured magnitudes. This trial magnitude is adopted if brighter than the plate-limit for the missing waveband, otherwise the plate-limit itself is chosen. This technique ensures that the object is assigned colours as close as possible to the normal colours of stars, thus adopting a "worst-case" estimate of its abnormality.

6.2 Theoretical quasar colour predictions

There are two possible approaches to evaluating the effectiveness of nearest-neighbour multicolour searches. A straightforward method is to use known quasar colours. These can be added to a stellar database and a nearest-neighbour search performed. Positions in the resulting nearest-neighbour list then indicate the extent of penetration into the stellar locus required for a given level of completeness. However, there are various basic observational reasons why the scope of this method is limited here:

- The majority of known quasars in the region $2.2 \leq z \leq 4.5$ are prism-selected — thus any examination would tend to be biased towards strong-lined objects. Insensitivity towards weak-lined objects in certain redshift regimes is indeed a possibility as will be indicated.
- Very few examples of quasars exist above $z \simeq 3.8$ making quantitative analysis of success beyond this redshift very hard.

Another approach to the problem is to simulate quasar spectra at different redshifts. The basic spectral characteristics used can then be varied within observational limits, in an attempt to mimic the spectra of all known quasars. The U, B, V, R and I magnitudes for each model quasar can be obtained, and appended to an observed five-waveband dataset. Again a nearest-neighbour analysis yields the sensitivity of the selection to particular models. One drawback of this method is our ignorance of the rel-

ative numbers of each quasar spectral type, preventing actual completeness estimates. However, it can still provide information on what particular classes may be missed.

In order to assess the successes of the technique to be employed, the following study combines the two approaches.

6.2.1 Simulated quasar spectra

The aim here is to mimic the broad-band optical colours of quasars. Only features that affect these values will be considered below. The basic redshift-independent components of the model considered are as follows:

- A basic power law continuum is constructed, with

$$F_\lambda(\lambda) = K_1 \lambda^\alpha \tag{6.1}$$

where α is the spectral index. This is related to the more usual index in

$$F_\nu(\nu) = K_2 \nu^{-\alpha_\nu} \tag{6.2}$$

by $\alpha = \alpha_\nu - 2$. The continuum is normalised to unity at C IV λ1549, and derived for $\lambda = 1$ to 10,000Å.

- Emission lines are added as listed in Table 6.1(a). Relative line strengths are taken from the studies of Baldwin (1975, 1977), Wilkes (1986), Puetter *et al.* (1981), Grandi (1981, 1982), Kwan & Krolik (1981) and Neugebauer *et al.* (1979) as indicated. The normalisation is taken from observational C IV equivalent widths. A gaussian line broadening is applied to these lines with widths of 4500 km s^{-1} for allowed and semi-forbidden lines, and 1000 km s^{-1} for the oxygen forbidden lines (see e.g. Wilkes 1986). Fe II multiplets are included, and widths are estimated from published spectra and from the studies of Grandi (1981, 1982), again with a gaussian spread for simplicity, as shown in Table 6.1(b).

- The residual underlying "blue bump", an apparent further rise in the continuum centred at around 3000Å (see e.g. Grandi 1982) is modelled again by a gaussian function, with a rest-frame equivalent width of 200Å.

- A small amount of interstellar dust reddening is added, from the galactic dust model of Seaton (1979), a simple analytical fit to UV observations (Table 2 *op. cit.* is extrapolated to longer wavelengths). The amount of reddening is parameterised by $E_{B-V} = A_B - A_V$, the extinction in magnitudes in the B and V bands. Extinction A_λ is then calculated by:

$$X(\lambda) = A_\lambda / E_{B-V} \tag{6.3}$$

where $X(\lambda)$ is the Seaton expression, giving a resulting drop in flux of $10^{-0.4(A_\lambda)}$. The amount of reddening chosen is $E_{B-V} = 0.02$ (Grandi 1982 discusses justifications for such a value). Note that the line ratios for Ly-α and the Balmer lines are unreddened and hence must be added before reddening.

In addition to these features, several redshift-dependent features must be considered:

- Lyman discontinuity absorption shortward of 912Å, the ionisation threshold of ground-level hydrogen, is modelled by assuming an intervening absorbing cloud density increasing as $(1+z)^{2.17}$ (this value derived by Murdoch *et al.* 1985, from Lyman forest studies). The photoionisation cross-section for ground-level hydrogen follows closely

$$\sigma(\lambda) \propto \lambda^{2.8} \tag{6.4}$$

(see e.g. Davidson & Netzer 1979) up to the Lyman limit; the integrated effect of clouds between the observer and quasar give a resultant absorption coefficient as a function of the redshift of the quasar and the rest-frame wavelength. The absolute level of this absorption is a variable, D_{disc}, determined within observational limits from published spectra, defined for simplicity as a relative fractional drop in continuum level at 900Å from that extrapolated from the continuum longward of Ly-α. Limits on this value are taken from many published high-redshift spectra, and estimated for a $z \sim 3$ quasar. The drop in flux is then:

$$F_\lambda'(\lambda) = F_\lambda(\lambda) \exp\left[\log_e(1 - D_{disc})\, X_{disc}(\lambda)\right] \qquad \lambda \leq 912\text{Å} \tag{6.5}$$

where

$$X_{disc}(\lambda) = \left(\frac{1+z}{1+z_d}\right)^{(2.17+1)} \left(\frac{(\lambda/912)^{(2.8)} - (\lambda/912)^{(2.17+1)}}{(\lambda_d/912)^{(2.8)} - (\lambda_d/912)^{(2.17+1)}}\right) \tag{6.6}$$

Table 6.1: (a) Emission lines used in QSO model. The main references from which relative line strengths were obtained are shown.

Emission line	Rest λ	Relative strength	References
Ly-α	1216	1.00	Kwan & Krolik 1981
Ly-β	1025	0.07	Puetter *et al.* 1981
Hα	6563	0.50	Puetter *et al.* 1981
Hβ	4861	0.17	Puetter *et al.* 1981
Hγ	4340	0.07	Puetter *et al.* 1981
Hδ	4101	0.03	Puetter *et al.* 1981
C III	977	0.05	Kwan & Krolik 1981; Grandi 1982
O VI	1034	0.17	Kwan & Krolik 1981; Wilkes 1986
N V	1240	0.23	Kwan & Krolik 1981; Grandi 1982, Wilkes 1986
Si II	1264	0.10	Wilkes 1986
O I	1304	0.08	Wilkes 1986
Si IV	1397	0.04	Grandi 1982
O IV	1402	0.03	Grandi 1982
C IV	1549	0.31	Wilkes 1986
He II	1640	0.02	Grandi 1982
O III]	1663	0.07	Grandi 1982
C III]	1909	0.13	Grandi 1982
C II]	2326	0.03	Wilkes 1986
Mg II	2798	0.13	Grandi 1982
He I	5876	0.03	Kwan & Krolik 1981
[O III]	4959	0.03	Neugebauer *et al.* 1979
[O III]	5007	0.08	Neugebauer *et al.* 1979

Table 6.1: (b) FeII multiplets used in the model, which were crudely modelled by gaussian functions with σ determined from Grandi (1981) and real quasar spectra. The blue bump is modelled similarly.

Emission line	Rest λ	Relative strength	Gaussian σ	References
FeII	2100	0.04	50	Grandi 1981
FeII	2500	0.13	150	Grandi 1981
FeII	2950	0.03	34	Grandi 1981
FeII	3200	0.05	47	Grandi 1981
FeII	4570	0.05	41	Grandi 1981
FeII	5250	0.05	46	Grandi 1981
Blue bump	3000	2.00	619	Grandi 1981,1982

Table 6.2: Variable parameters in the simulations. Shown are minimum and maximum values, and estimates of values for the typical QSO. Prime sources for these figures are referenced.

Feature	Min → Mean → Max	References
α, the spectral index	-2.3 → -1.2 → 0.5	Richstone & Schmidt 1980
$EW_{C\,IV}$, the rest equivalent width of C IV (Å)	00 → 30 → 50	Wilkes 1986
D_α, the fractional continuum drop at 1100Å	.11 → .29 → .41	Oke & Korycansky 1982; general overview of spectra
D_{disc}, the fractional continuum drop at 900Å	.00 → .30 → 1.0	Oke & Korycansky 1982; general overview of spectra

z_d is the redshift for which D_{disc} is calculated, (here $z_d = 3$), and λ_d is the wavelength where this is estimated ($\lambda_d = 900$Å). The formula then gives the drop in flux for a quasar at redshift z, at wavelength λ in its rest frame.

- Absorption by Ly-β and Ly-α consecutively is then incorporated shortward of the emission wavelengths using the same intervening cloud model. The resultant drop in flux is given by:

$$F_\lambda'(\lambda) = F_\lambda(\lambda) \exp\left[\log_e(1 - D_{\alpha,\beta})\, X_{\alpha,\beta}(\lambda)\right] \qquad \lambda \leq \lambda_{\alpha,\beta} \quad (6.7)$$

where

$$X_{\alpha,\beta}(\lambda) = \left(\frac{\lambda}{\lambda_d}\left(\frac{1+z}{1+z_d}\right)\right)^{2.17} \quad (6.8)$$

Here $\lambda_{\alpha,\beta}$ is the emission wavelength of the relevant forest (1216Å and 1025Å), and $D_{\alpha,\beta}$ are defined similarly to D_{disc} as the fractional drops, relevant to extrapolated continuum, at λ_d (= 1000Å and 1100Å respectively), specifically due only to Ly-β and Ly-α absorption, again set observationally for a $z = z_d$ (= 3) quasar. In practice, D_α and D_β are set for *both* forests as one variable, with the relative absorption level determined by Oke & Korycansky (1982), who examined the region in detail, and concluded that the fractional drops in the $\lambda \leq$ Ly-β and Ly-$\beta \leq \lambda \leq$ Ly-α regions respectively are 0.39 and 0.29. This allows a rough estimation of the relative absorption strengths between forests, by

$$\frac{\log_e(1-0.39)}{\log_e(1-0.29)} = \frac{\log_e(1-D_\beta)}{\log_e(1-D_\alpha)} + \left(\frac{1000}{1100}\right)^{2.17} \quad (6.9)$$

The parameters, then, that are independently variable in this model are listed in Table 6.2 with an indication of the ranges seen in observed quasars. Figure 6.1 contains examples of quasar spectra produced by this technique, where minimum, mean and maximum values are given consecutively to a particular parameter. In the order they are presented, $EW_{C\,IV}$, α and the short wavelength absorption parameters are varied, and the last three examples are the "standard" quasar for different λ ranges. It is clear that a great many different types of quasar are represented by the full range of models.

The next step is to calculate broad-band colours. Standard band-passes values in 10Å steps for U, B, V and I were used with the $R59F$ (the Schmidt "OR" band)

Figure 6.1: Examples of simulated quasar spectra. In the top row, the rest-frame equivalent width of C IV (and thus all line strengths) is varied through its values in Table 6.2. The next two rows show the effects of variations in the continuum slope and short wavelength absorption parameters, and the last three diagrams are the "standard" quasar at $z = 4.5$, shown for different wavelength ranges.

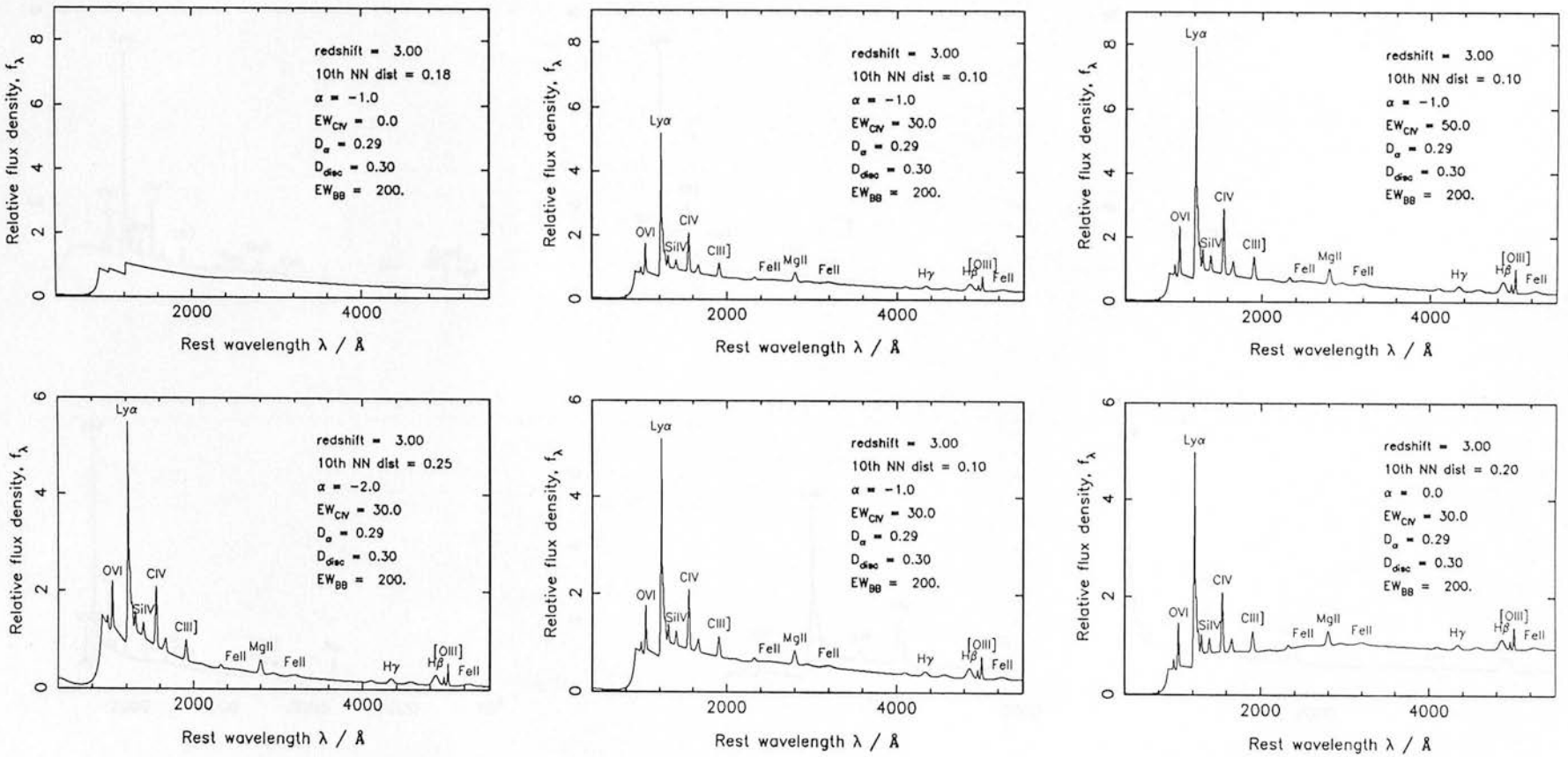

Figure 6.1: continued

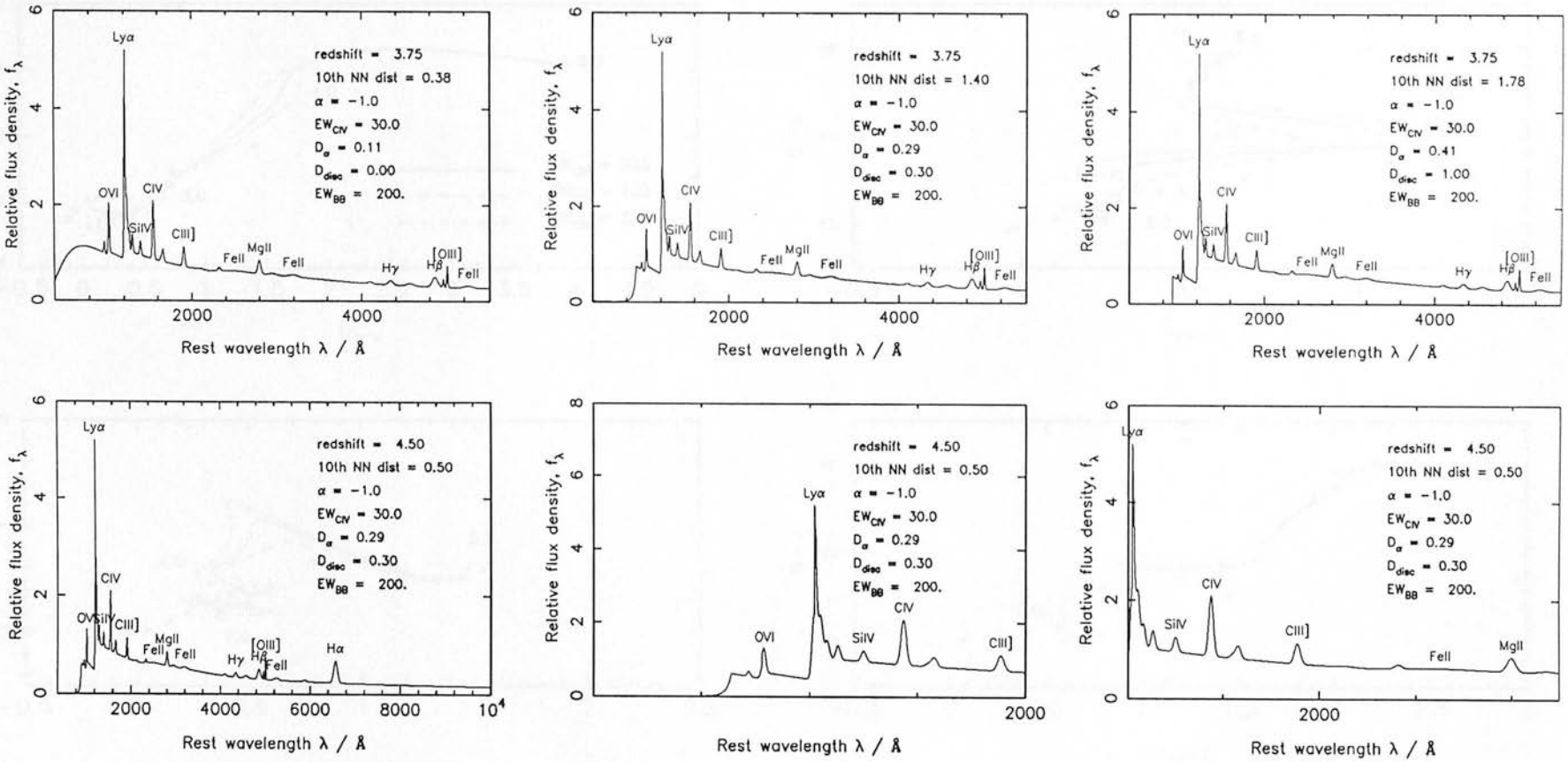

Figure 6.2: Loci of simulated quasars for $2 \leq z \leq 5$ in various representations of colour space. The different loci are for different line strength values, as indicated. Also marked are *UBVRI* colours for the main sequence (Johnson 1966). Note that although quasars and stars overlap in 2D space, when all colours are accounted for, the loci are distinct for these models.

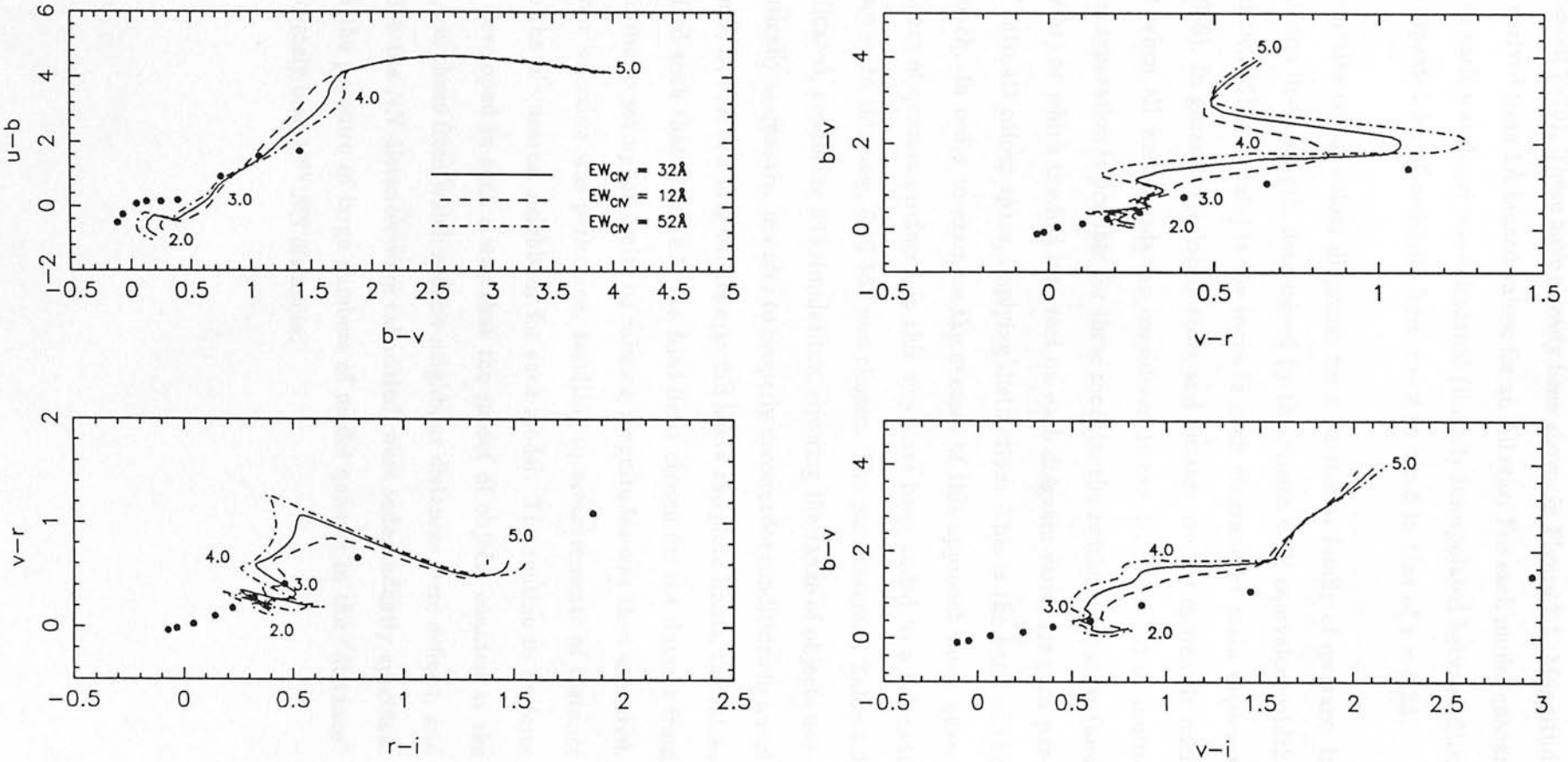

response from (Bessell 1979). These have already been shown in Figure 2.1. Magnitude zero-points were derived from 1Å binned values for an A0 star. For each model quasar, the relative flux in each waveband was calculated (linearly interpolated between filter values); this was repeated for all redshifts from $z = 2$ to $z = 5$ in bins of $z = 0.25$.

Figure 6.2 contains colour-colour diagrams for a particular family of quasars: in this case, the emission line strength, determined by the chosen C IV equivalent width, is varied. Also shown (filled points) is the locus in each diagram for main sequence stars (Johnson 1966). In general, the loci of stars and quasars are not distinct in each 2D diagram, but when all wave-bands are considered it can be seen that in multi-dimensional space, separation is possible for these models: the redshift of quasar (and spectral type of star) at which the loci intersect on each diagram varies for each particular "window" into 4D colour space, implying distinction. This is the basis of the multicolour approach. In order to examine the success of this approach more quantitatively, the colours of quasars produced in this way have been added to a Schmidt multicolour dataset — in this case, field 863 was chosen. The parameters in Table 6.2 were varied as indicated, producing 243 simulations, covering the range of objects usually designated optically as quasars. In order to properly account for conditions in a real dataset, where the U, B, V, R or I magnitudes may fall below the plate-limits, the values for each were shifted such that $R = 18.5$, the faint limit chosen for the dataset from field 863. The routine to set upper limits on missing magnitudes was then executed. A nearest-neighbour selection was performed, resulting in measurements of distance in colour-space to the n^{th} nearest neighbour for each model. The routine to perform the selection was developed in such a way that the subset of objects counted as the "main catalogue", i.e. those from which nearest-neighbour distances were defined, and the subset for which the NN distances were calculated, were independently specified. This was vital, as the presence of large numbers of model quasars in the "distance" catalogue would severely bias 10^{th} NN distances.

6.2.2 Initial nearest-neighbour results

Figure 6.3(a) shows the nearest-neighbour (hereafter *NN*) distances for field 863, where 10^{th} and 100^{th} *NN* distances are plotted together. Only the few objects at large *NN* distances are plotted ($D_{NN} > 0.1^{\text{m}}$). The figure indicates the similarity between results for each choice of nearest-neighbour statistic, showing that 10^{th} nearest-neighbour discriminates sufficiently for all objects for this field. It appears that there is no clustering beyond the main sequence locus amounting to more than 10 members.

The majority of extreme objects present in the data have been identified as horizontal branch (HB) stars (filled points in the figure). These present a contamination problem, particularly to a survey at the bright magnitude limits used here, where there are still significant numbers at these apparent magnitudes. Furthermore, they cannot simply be removed by colour selection, as they genuinely occupy the same colour-space positions as some spectral types of quasars, particularly at $z \lesssim 3$. As will be demonstrated, they do degrade the ability of the *NN* method at these redshifts: however, their easily recognisable spectra suggest that a simple and efficient way to deal with the problem is by previous objective-prism discrimination.

In order to evaluate how realistically the above models represent observed quasars, the results of the simulations were compared with a sample of prism-selected quasar, whose *UBVRI* colours were known. These quasars possessed $2.2 \leq z \leq 3.5$ and were selected at $B \leq 18.5^{\text{m}}$ (P.C. Hewett, private communication). Figure 6.3(b) shows the *NN* positions of these objects when added to the dataset above (filled dots). They are on the whole highly distinct from the main sequence locus — indeed, if we adopt $D_{NN} \geq 0.25^{\text{m}}$ as a reasonable limit for spectroscopic observations, 13 out of 17 quasars would be easily found (the removal of the HB stars would increase efficiency further). In order to determine what spectral types are in the remaining 20%, we must turn to the simulations.

Figure 6.3: Nearest-neighbour distances for field 863. The top diagram shows horizontal-branch stars as filled dots, and the bottom shows the position of prism-selected quasars when added to the dataset.

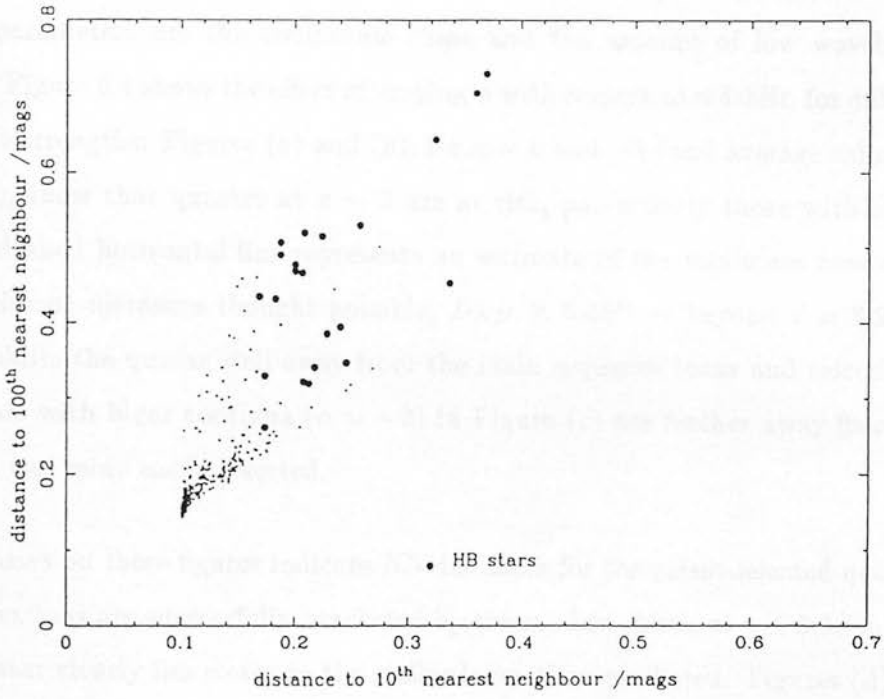

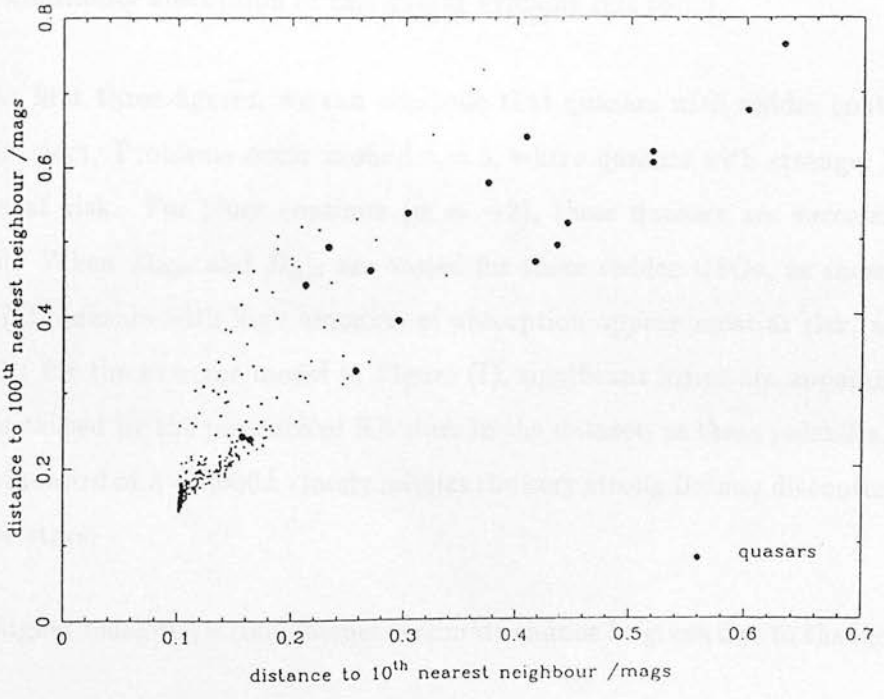

6.2.3 Results of the simulations

The effects of varying the parameters in Table 6.2 are correlated, hence it is necessary to consider combinations for different parameter values. Results show that the most important parameters are the continuum slope and the amount of low wavelength absorption. Figure 6.4 shows the effect of varying α with respect to redshift, for different emission line strengths: Figures (a) and (b), for $\alpha = 0$ and -1 (and average values for $D_{\alpha,\beta}$, D_{disc}), show that quasars at $z \sim 3$ are at risk, particularly those with strong lines. The dashed horizontal line represents an estimate of the minimum reasonable nearest-neighbour distances thought possible, $D_{NN} \geq 0.18^{\mathrm{m}}$ — beyond $z = 3.2$, the absorption shifts the quasar well away from the main sequence locus and selection is easy. Quasars with bluer continua ($\alpha = -2$) in Figure (c) are further away from the stellar locus and more easily selected.

The crosses on these figures indicate *NN* distances for the prism-selected quasars. These observations are successfully bracketed by the models shown at $z \lesssim 3.3$, but the $z = 3.67$ quasar clearly lies closer to the stellar locus than predicted. Figures (d), (e) and (f) show the effects of varying the short-wavelength absorption parameters; the position of the $z = 3.67$ quasar is well represented by Figure (d), and the small amount of Lyman discontinuity absorption in this quasar explains this result.

From the first three figures, we can conclude that quasars with redder continua are harder to select. Problems occur around $z = 3$, where quasars with stronger lines appear to be at risk. For bluer continua ($\alpha = -2$), these quasars are successfully discriminated. When D_{disc} and $D_{\alpha,\beta}$ are varied for these redder QSOs, as shown in (d), (e) and (f), quasars with high amounts of absorption appear most at risk, again around $z = 3$: for the extreme model in Figure (f), significant losses are apparent at $z < 3$. This is caused by the presence of HB stars in the dataset; at these redshifts, the strong drop blueward of $\lambda \sim 4000$Å closely mimics the very strong Balmer discontinuity found in these stars.

For the higher redshifts, a completeness estimate cannot be given due to the lack of

Figure 6.4: Nearest-neighbour distances as a function of redshift with positions of prism-selected quasars. (a), (b) and (c) show quasars with red, typical and blue slopes.

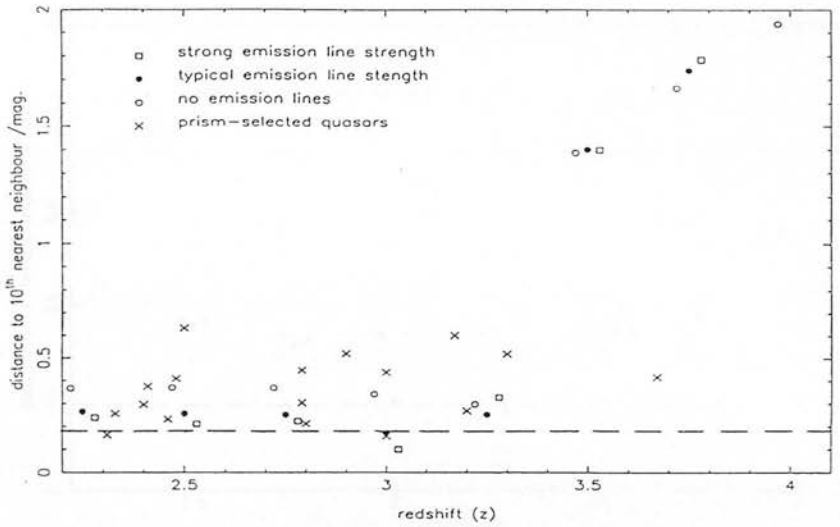

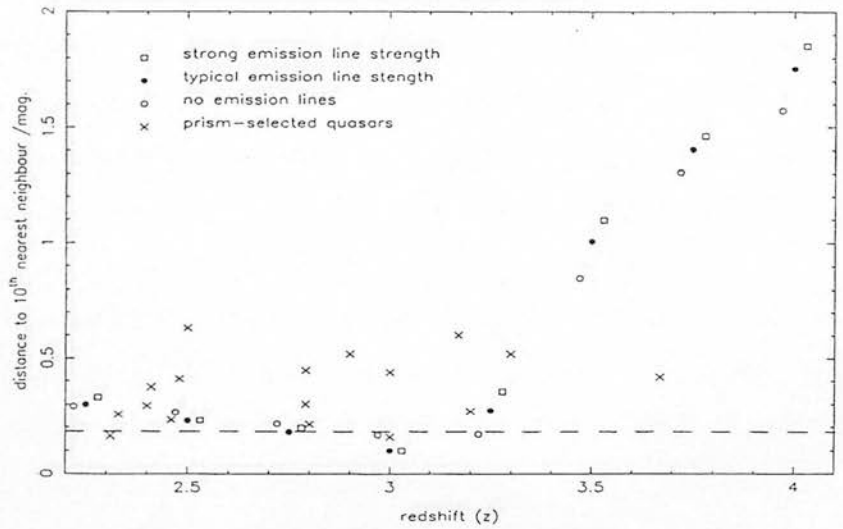

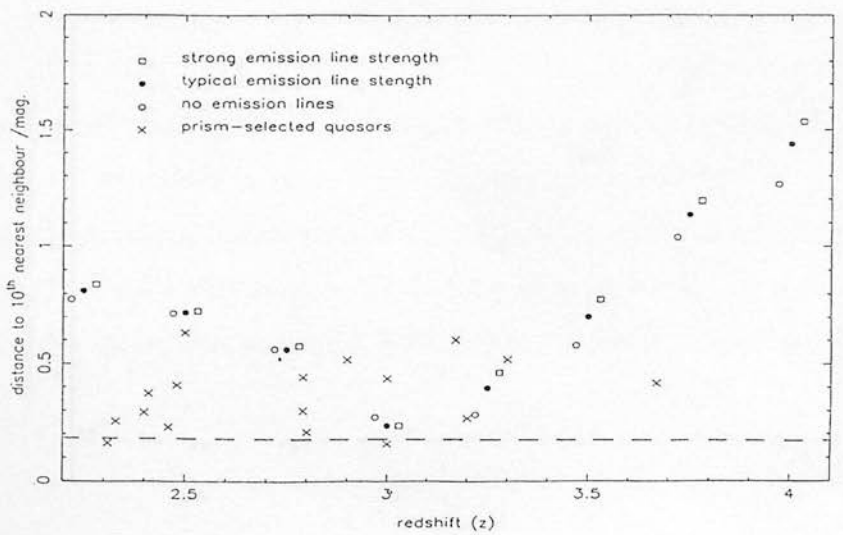

Figure 6.4: (d), (e) and (f) show positions for models with low, average and high short-wavelength absorption values.

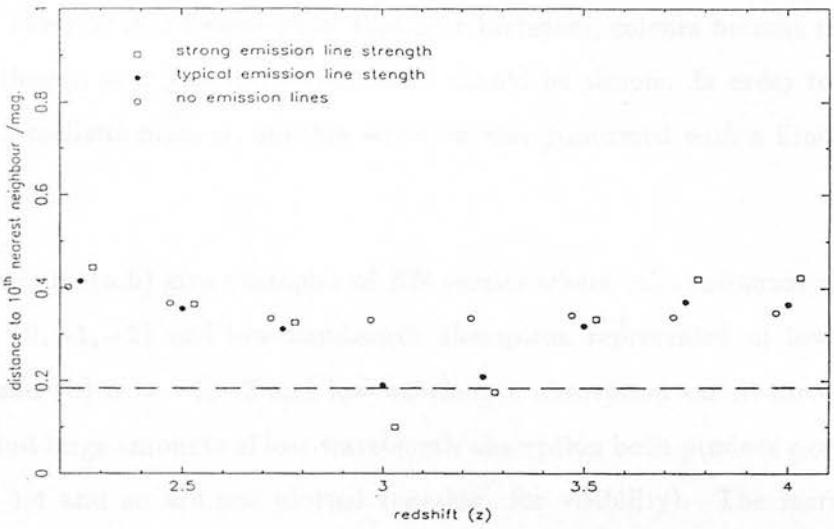

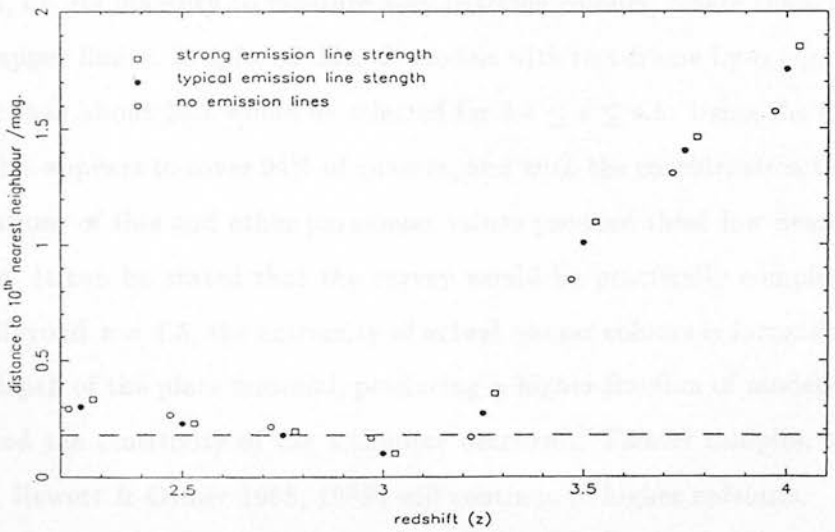

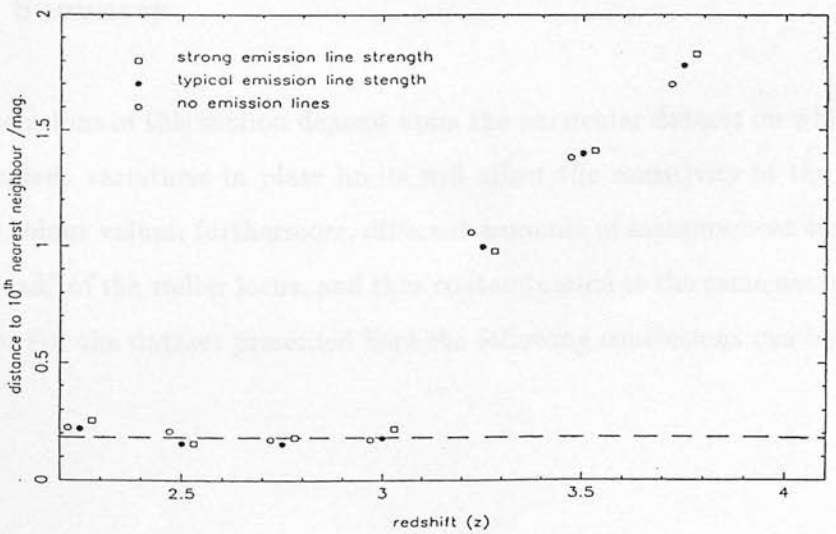

enough prism-selected quasars measured in *UBVRI*. However, the models which have successfully reproduced the intermediate redshift colours can be used to indicate likely results. The previous figures show that as z increases, colours become more extreme, and, in theory, at $z \geq 3.3$, discrimination should be simple. In order to examine the data in a realistic manner, another selection was performed with a limit of $R = 18.5$ imposed.

Figure 6.5(a,b) give examples of *NN* results where (a) continuum slope is varied through $(0, -1, -2)$ and low-wavelength absorption represented at low and average values, and (b) $\alpha = -1, -2$ and low-wavelength absorption varied through all values ($\alpha = 0$ and large amounts of low-wavelength absorption both produce extremes colours at $z > 3.4$ and so are not plotted together, for visibility). The increase in D_{NN} with z is not as obvious as expected, and this is due to the limitations of the plate material, i.e. its inability to measure very extreme colours, where these values are set only at upper limits. In spite of this, all models with rest-frame Ly-α equivalent widths stronger than about 25Å would be selected for $3.4 \leq z \leq 4.5$. Using the data of Wilkes (1986) this appears to cover 94% of quasars, and with the consideration that only a few combinations of this and other parameter values produce these low nearest-neighbour distances, it can be stated that the survey would be practically complete at $D_{NN} \geq 0.18^{\mathrm{m}}$. Beyond $z = 4.5$, the extremity of actual quasar colours is increasingly modified by the depth of the plate material, producing a higher fraction of models with smaller D_{NN}, and the sensitivity of the technique decreases. Fainter samples, however, (e.g. Warren, Hewett & Osmer 1988, 1989) will continue to higher redshifts.

6.2.4 Summary

The conclusions of this section depend upon the particular dataset on which the search is conducted; variations in plate limits will affect the sensitivity of the technique at extreme colour values; furthermore, different amounts of measurement error determine the "spread" of the stellar locus, and thus contamination to the same nearest-neighbour distance. For the dataset presented here the following conclusions can be drawn.

Figure 6.5: Nearest-neighbour distances as a function of redshift for the higher z region. See text for notes.

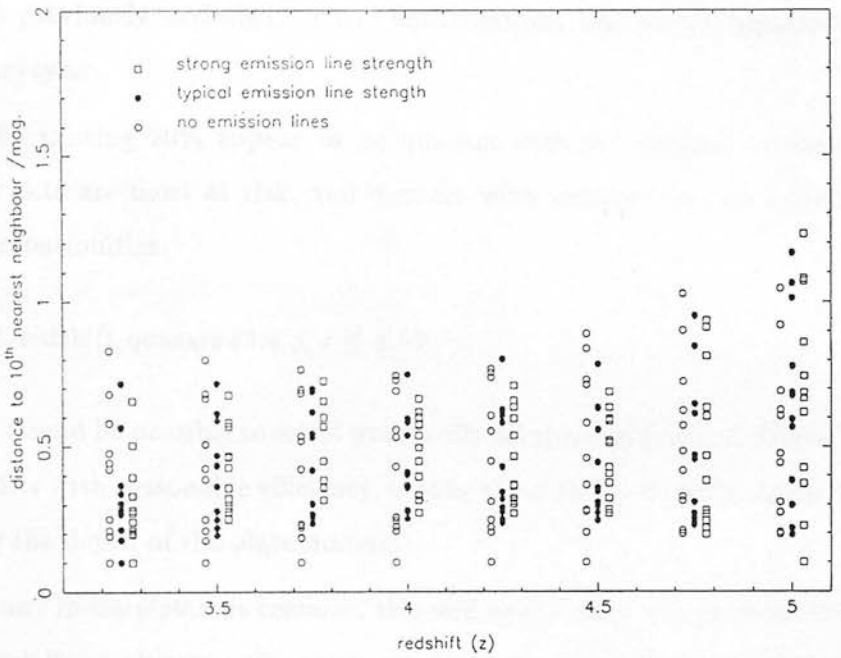

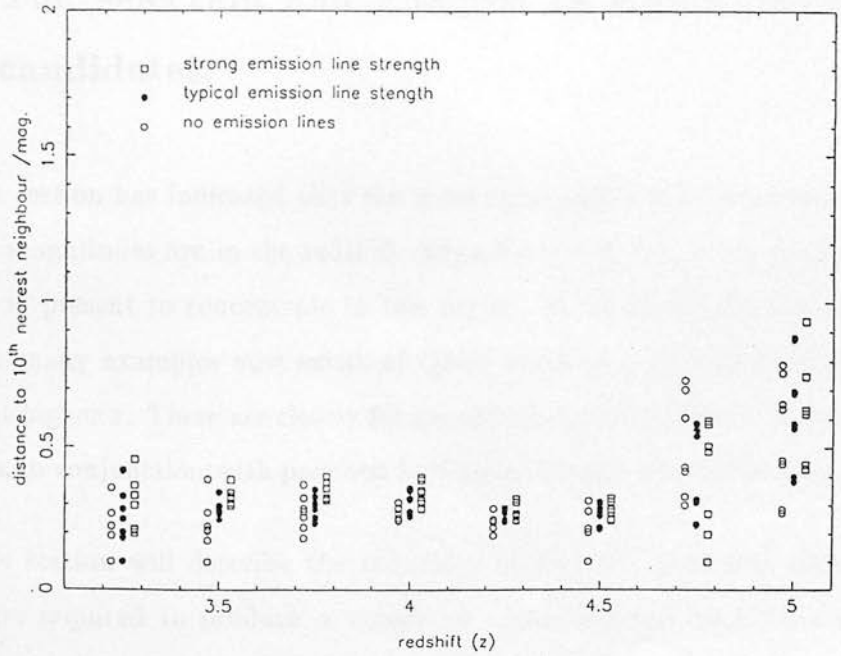

For intermediate redshift quasars ($2.2 \leq z \leq 3.4$):

1. Around 80% completeness can be achieved for a comparable dataset to the one represented here, which will increase significantly if horizontal branch stars can be previously excluded. This contamination will be less significant for fainter surveys.
2. The missing 20% appear to be quasars with red continua, where strong-lined objects are most at risk, and quasars with extreme Lyman forests and Lyman discontinuities.

For high-redshift quasars ($3.4 \leq z \leq 4.5$):

1. It should be possible to select practically all spectral types of quasars at these redshifts with reasonable efficiency, within the constraint of the upper limit imposed by the depth of the plate material.
2. If any incompleteness remains, this will apply only to a small percentage of very weak-lined objects. To what extent these spectral types occur in practice is uncertain.

6.3 The selection and analysis of high-redshift quasar candidates.

The last section has indicated that the most successful multicolour searches at intermediate magnitudes are in the redshift range $3.4 \leq z \leq 4.5$ — for this reason, it was decided at present to concentrate in this region, which is also the region of greatest interest: many examples now exists of QSOs below $z = 3.4$, but relatively little is known at higher z. There are clearly future opportunities to extend this study to lower redshifts, in conjunction with previous horizontal-branch star discrimination.

This section will describe the reduction of each Schmidt field dataset through the stages required to produce a sample of colour-selected candidates as free from

contamination by spurious "junk" images as possible. The data are considered here to be in the state referred to at the end of Chapter 3. A brief revision of the processes involved is given here.

For each Schmidt field, the 10 UKSTU plates have been scanned by COSMOS, mapped onto each other in small cells to determine a positional transformation, paired in each colour for the rejection of spurious images caused by photographic flaws, and calibrated in each band with the use CCD and photoelectric photometry. An attempt has been made to correct for background-dependent field effects in the magnitudes derived (both sensitivity variations in the emulsion, and background "fogging"). The five resulting datasets for each waveband have been again paired and a single *UBVRI* catalogue obtained. Residual effects have been explicitly removed from this catalogue by imposing magnitude-dependent corrections derived from shifts in the stellar locus colour-space position.

Star-galaxy separation has been performed as described in Chapter 3, here designed such that all but highly stellar images are rejected. Strips along the edges of each dataset in X and Y have been inspected for large quantities of images with spurious colours, caused by lack of identical spatial overlap in scanned plate material for each waveband, and trimmed.

6.3.1 Removal of residual defects and the density search

Subsequent stages in the evolution of the datasets are described here. These involve the elimination of any object which demonstrates non-stellar colour but whose magnitudes are shown to be erroneously assigned for a variety of reasons, detailed below. It is unfortunately inevitable that objects with erroneous magnitude values will still be present at the time of candidate selection, and the purpose of these efforts is to reduce these to a minimum. Remaining doubtful objects can be inspected by eye, as was done here, but this method is arduous and time-consuming, and was only allowed as a final check.

Situations which may lead to spurious colours are:

- False images: plate defects, such as scratches, electrostatic marks, processing faults, and shadows caused by dust on the filter, may be mistaken for genuine objects and assigned COSMOS parameters. In spite of prior evacuation, residual dust can collect on plates during scanning; break-up of diffraction spikes around very bright stars and satellite trails can also generate false images. This class of objects will largely be eliminated at the stage of pairing plates in the same waveband.
- Flaws obscuring real images: the above-mentioned effects, together with holes and desensitised spots in the emulsion, may lead to the loss of images on some plates. Again this will mainly disappear at the earlier pairing stage; however, bright star break-up can occur on both plates in one band.
- Blending of close images: multiple objects may be blended by COSMOS on one plate, such that they are considered one object. The subsequent multicolour pairing may lead to (a) the elimination of information from one or more waveband for the un-paired object, (b) loss of waveband information for both objects (false position generated), or (c) loss of both objects at the star-galaxy separation stage (i.e. COSMOS records one highly elliptical object). This is by far the most significant effect at this stage.

The result of these effects is that, with such a large initial number of objects, every step which significantly reduces the contamination level without preferentially eliminating valid candidates is to be welcomed. The techniques referred to below are preceded by labels by which they will be known throughout this chapter.

• 'BADCOLOUR': elimination of objects with highly-deviant colours

All *UBVRI* catalogues were inspected for significant colour variations between each set of five plates for each epoch. In this way, bad data can be identified whilst variable objects (possibly QSOs over timescales of weeks/months), which vary only in magni-

tude, and not colour, are still regarded as valid. Information on which plate belongs to which epoch is required. The RMS deviation for the data in each waveband is estimated by comparing magnitudes from each epoch for all objects, allowing for possible systematic calibration differences, by evaluating the result about the mean difference in each band. Then the difference between both epoch magnitude values is calculated for each object, subtracting both the mean difference in the other valid wavebands (to allow for variable objects) and the mean difference for all objects in this waveband (to allow for systematic calibration errors). This is compared with the error on the result, and if it exceeds twice this value (i.e. $> 2\sigma$), then this object is rejected.

The 'BADCOLOUR' technique was employed twice in each Schmidt field: the estimation of the RMS for magnitude deviations was improved after the rejection of outstanding bad data, and a more sensitive cut possible on the second pass. A subset of the data was then produced with $17.0 \leq R \leq 18.5$, (a decision based on available observing time versus candidate numbers, and the depth of plate material in other bands) which constituted the basis of the candidate lists.

• **'UPPERLIMITS': setting of limits for missing magnitudes**

As described in Section 6.1, a major limitation of the photographic dataset is the existence of plate-limits. Chapter 2 has shown that this is not a hard limit fainter than which all objects are invisible: COSMOS ceases to recognises images in a progressive manner so that stellar counts tail off with increasing magnitude. In this case plate-limits are estimated for each plate in the survey from the observed turning point of the number-magnitude relation; Table 2.4 shows the adopted values for plates in this survey. Plate-limits are a fundamental problem for the nearest-neighbour technique: the colours of high redshift quasars mean that many faint candidates detected on the R plate will be "missing" in other colours. However, to reduce the number of dimensions at this stage is to throw away vital information, namely that the magnitude *is* fainter than the limit. In order to optimise the information available, the plate-limits were used as constraints, and the missing magnitudes varied until the object was brought as

close as possible to the stellar clump. For many such objects this process showed that, even in the worst case, the object was indeed located outside the stellar locus.

A subset of the catalogues, $16.5 \leq R \leq 17.5$, was used to define the stellar locus (no significant shifts in locus position from $R = 16.5$ to $R = 18.5$ were apparent in any field), where a further requirement of greater than 10 neighbours within 0.1^{m} was necessary for membership. Each object was then examined with respect to each locus object, and the minimum distance adopted as the nearest locus point.

In general, if there are N wavebands where waveband n is undefined, where $m_i, i = 1 \ldots N$ represent the object magnitudes and where l_i are the values for each object in the locus, then a trial magnitude, m_n is adopted such that

$$m_n - l_n = \frac{1}{(N-1)} \sum_{i=1}^{N, i \neq m} (m_i - l_i) \tag{6.10}$$

This expression minimises the simple Euclidean distance between the object and locus point in 5-D (in fact only filled in 4 dimensions — we are only interested in *colour* but 5-D is computationally easier). This trial magnitude is adopted if allowed by the constraint of the limit on m_n, otherwise the limit itself is used. In the case where more than one magnitude was undefined, the most deviant point was set first, with the above expression applied only to valid magnitudes. The routine then proceeded to set the next most deviant point, using this information, and so on. In this way, all undefined points were set.

• **'DENSITY': the nearest-neighbour search**

At this stage, the actual nearest-neighbour search was executed. Distances from target objects to each other valid object were calculated from:

$$\begin{aligned} D^2_{NN} &= (U_{main} - U_{targ})^2 + (B_{main} - B_{targ})^2 \\ &+ (V_{main} - V_{targ})^2 + (R_{main} - R_{targ})^2 \\ &+ (I_{main} - I_{targ})^2 \end{aligned} \tag{6.11}$$

Distances greater than 3^{m}, and less than 0.1^{m} were excluded from the search to speed up the process. Numbers of neighbours as a function of distance were calculated, and distance to the n^{th} nearest-neighbour obtained for each object. The result was the subset of target objects re-ordered in *NN* distance where $D_{NN} \geq 0.1^{m}$. The initial choice of 10^{th} nearest neighbour was reassessed for each field individually, and in the case of fields with a higher proportion of remaining spurious images, i.e. with a large number of objects away from the main stellar locus, 100^{th} neighbour distance was adopted.

• **'MATRIXCOLOUR': colour selection of candidates**

Colour selection to the low-density candidates was applied at this stage. Ideally all sparsely-populated regions of colour-space could be examined spectroscopically, such that quasars at any redshift with non-stellar colours are selected; in practice, however, limited telescope time makes some selection by colour necessary, in addition to the stringent defect rejection and star-galaxy separation already applied. In practice, different colour criterion were applied to the candidates at different stages during the subsequent spectroscopic runs, loosely based on a sample of 11 high-redshift quasars (P.C. Hewett, private communication) with redshifts in the range $3.42 \leq z \leq 4.43$; as stated earlier, a decision was made to concentrate on this redshift range. Later sections will discuss the development of these criteria in detail, and select a definitive set of criteria such that all data is treated in uniform manner. Note that all cases where magnitude information is missing must be examined carefully when selecting in colour — if the limits imply that the object could possess the colour indices acceptable by the criteria, then this object cannot be rejected.

• **'NEAREST': automatic elimination of very close objects**

A major problem of machine-measured photographic data is that of spatially discriminating close, faint images. This has been stressed throughout this thesis, and can cause a variety of effects, many of which are considerable problems when searching for

intrinsically rare objects. Images may be blended in some wavebands while remaining resolved in others, thus generating spurious colours when combined into a multicolour dataset. Various classes of such phenomena have been excluded up to this stage, but all candidate objects missing information in any waveband must be visually checked, and such a list must be reduced as much as possible. With this in mind it was found necessary to exclude all candidates pairs missing waveband information with averaged (α, δ) values indicating a proximity of less than one arc minute between them. Note that this exclusion of very close pairs, although powerful in reducing observing lists to a more manageable size, introduces a bias against any such real images that happen to be in "missing" lists. In particular close gravitationally-lensed quasars may possibly be excluded at this stage — this bias has been discussed in Section 2.4 and may be of significance if lensing effects prove more common than is presently believed.

• **'MISSING': eyeball checks of objects missing waveband information**

Objects fainter than the limit in any waveband in the top 500 objects from the 'DENSITY' search were analysed by 'NEAREST' as described above, with the intention of visually inspecting the remaining likely candidates. Typical numbers rejected at these two stages are shown in Table 6.3, for field 790. More than half the top 500 are missing information in at least one band: clearly these objects must be carefully considered.

The visual search was performed with some trepidation: the automated and quantifiable nature is a vital ingredient of this survey. No object was removed from observing lists unless its unusual colours were identified with certainty as associated with some erroneous effect. It is vital when inspecting the plates to consider the plate-limits for each Schmidt field, and to compare with surrounding objects of known magnitude (in some cases a small finding chart with derived magnitudes marked was useful). Criteria for removing objects were adopted for each waveband as follows:

Missing in U

Very hard to eliminate by visual inspection. The very strong absorption shortward of Ly-α for high-redshift quasars (due to a large amount of intervening absorption

Table 6.3: Results of 'MISSING' and 'NEAREST' routines on a typical catalogue. The data shown are for field 790, where the top 500 objects from the nearest-neighbour search are analysed. Note that the sample is selected in R, and notice also that over half of the objects are missing information in at least one band.

Waveband	Plate limit	# obj missing	# obj passed by 'NEAREST'
U	20.65	160	152
B	20.60	103	91
V	19.25	47	35
R	19.80	0	0
I	18.30	55	49

No. of objects present in all bands = 217/500

material) produces $(U-R)$ colours of greater than 2 in most measured $z > 3.4$ quasars (the $z = 3.67$ quasar of Section 6.2 is a notable exception). The steep increase of space density with apparent magnitude expected therefore ensures that high-redshift candidates would largely be genuinely missing in this band, with plate-limits for U on average only extending to 20.5^{m}. Only objects with clearly erroneous measurements were removed.

Missing in B

Absorption is still very strong in this band for $z > 3.4$, giving B magnitudes on fainter than R by 1 magnitude or more. However, the depth of the plate material in this band (plates extend as faint as $B = 20.6$ to $B = 21.3$) ensures that most genuine quasars would be visible to $R = 18.5$.

Missing in V

Colours in $(V-R)$ are usually slightly positive (~ 0.4); the great variation in depth of V plates however means that each field must be considered individually. Field 866, for instance is very poor in V, and so rejection is very hard. By contrast, field 789 exceeds expected maximum V values by over a magnitude.

Missing in I

The I band covers the power-law region of quasars at these redshifts, so in general

Table 6.4: Initial parameters for colour selection of low-density objects. The basic criteria for each run are given; a blank entry implies no upper or lower limit.

Colour	AAT	CTIO	ESO
$U-B$	$-1.0 \rightarrow$	$-0.4 \rightarrow$	$-1.3 \rightarrow$
$B-V$	$+0.5 \rightarrow$	$\rightarrow$	$-1.0 \rightarrow$
$V-R$	$\rightarrow +0.8$	$\rightarrow$	$\rightarrow +0.9$
$R-I$	$-0.5 \rightarrow +1.0$	$-1.0 \rightarrow +1.0$	$-0.7 \rightarrow +0.7$
$B-R$	$+0.8 \rightarrow$	$\rightarrow$	$-1.0 \rightarrow$
$V-I$	$\rightarrow$	$\rightarrow$	$-1.0 \rightarrow +1.5$

$(R-I)$ is variable but not as extreme. Nevertheless, the I plates in the survey rarely extend beyond $I = 18.5$ (field 866 again displays a very poor limit of $I = 17.6$), and so visual elimination is adopted with great caution.

We are now at the stage where final candidate lists can be compiled for spectroscopic observations. Alternative strategies were pursued for different runs, leading to various levels of completeness in different colour space regimes for each field. Candidates selected are listed in full in Appendix E, with colours and R magnitudes, and nearest neighbour distances, where a bullet next to the object name indicates that an observation was performed. All objects still missing any waveband information in these lists were those chosen as still valid after visual inspection. The criterion of Table 6.4 represent the waveband colour-selection values for each spectroscopic run. Fields 864 and 865 were examined under different criterion at CTIO, and field 867 was observed to different levels on each run. Field 789 was given exhaustive treatment at ESO, again under alternative criterion, as indicated in the Table and Appendix. The interplay of different colour indices values is complex when attempting to consider what constitutes a "good" candidate for a high-redshift quasar, and some candidates with less extreme nearest-neighbour distances but a more favourable overall spectral "shape" were chosen in preference to objects higher up each list. This further complicates any estimation of sample completeness, and so a new and uniform colour selection criterion will be imposed to all datasets in the next section.

6.3.2 The derivation of uniform selection criteria

In order to evaluate the sensitivity over all fields, it is necessary to impose a uniform set of criteria in all cases. Some of these will simply be for the exclusion of clearly erroneously recorded objects, i.e. extreme colour indices not seen in nature, whose effect is to push these objects to the top of nearest-neighbour lists — and additional criteria are specifically designed to further reduce observational lists, by choosing colour regimes where high-redshift quasars are known to lie, specifically, from the aforementioned $z > 3.4$ quasar list of Hewett.

$\boxed{(U-B) \geq -1.0}$: a minute fraction of real stars are excluded here: such extreme blueness is not expected for any quasars $z > 2.2$, and the effect of this limit is to restrict greatly the amount of objects missing B information that could still feasibly be genuine, and therefore require visual inspection;

$\boxed{(R-I) \geq -0.5}$: again very few genuine stars are excluded; removal of images with non-physical colours, including many missing I objects;

$\boxed{(V-R) \leq 0.8}$: the purpose here is to reduce needless inspection of the many missing V objects; at $R = 18.5$, objects redder than this limit in many fields will be missing in V. This criterion removes many genuine red stars also, but at $3.4 \leq z \leq 4.5$, all listed quasars are sufficiently blue to remain below this limit.

The region in (U, B, R) space where UVX quasars are known to lie ($U - B < -0.4$, $B - R < 0.8$) (see e.g. Figure 4.3) was also excluded.

To these three basic selection functions were added three genuine high-redshift constraints:

$\boxed{(B-V) \geq 0.5}$: a genuine high-z constraint designed to reduce galactic contamination: Ly-α is well past the B passband for $z > 3.4$;

$\boxed{(R-I) \leq 1.0}$: a genuine high-z constraint that excludes very red stars : no high-redshift quasars with $z < 4.5$ have features in I capable of producing such red indices;

In addition to these two constraints, a sharp dependence on $(V - I)$ is seen for $z \geq 3.4$

quasars such that all such objects known to lie above $(V - I) = 0$ and below a line from $(B - V = 0.5,\ V - I = 0.9)$ to $(B - V = 2.5,\ V - I = 1.4)$. This limit was the final constraint applied to the data.

It is important to note here that no claim is being made as to the completeness for all quasars at these redshifts: it is conceivable that certain combinations of extreme spectral features could conspire to produce quasars outside the selected areas, as is the case in all forms of QSO detection. Indeed, the simulations of Section 6.2 show that some quasars with $z > 4.1$ may be missed through application of the $(V - R)$ and $(V - I)$ criterion above. Nevertheless, it should be noted that *all known* quasars (with available colour information) with $3.4 \leq z \leq 4.5$ lie within the region defined.

6.3.3 Observing strategies

Spectroscopic observations of candidates were performed at the Cerro Tololo Inter-American Observatory (CTIO) 4 metre telescope in Chile, the Anglo-Australian (AAT) 3.9 metre at Siding Spring, Australia, and the European Southern Observatory (ESO) 3.6 metre at La Silla, Chile, on 6–8 March 1988, 22–25 April 1988 and 9–10 May 1988 respectively.

The combination of the Ritchey-Chretien (RC) Spectrograph, the Air Schmidt Camera (a field-flattened camera of 229mm focal length) with preflashed GEC#9 CCD (front-illuminated and thus red-sensitive), and 250Å/mm grating at CTIO provided identifications for most objects within 600 seconds integration; however, although grey-time, the proximity of the moon hampered observations, and in a few cases, positive identifications were impossible. 58 objects in all were observed. Seeing varied between 1.6″ and 2.0″.

The AAT data was obtained from two instruments, the Image Photon Counting System (IPCS) and the Faint Object Red Spectrograph (FORS) with GEC#16 CCD. These were used with the RGO Spectrograph, 25cm camera and grating 250B, and a dichroic mirror to direct blue light to the IPCS and red to FORS for simultaneous

observations, coming into effect at $\lambda \sim 5400$Å such that only 10% of the light is entering the IPCS at $\lambda = 7000$Å. The IPCS and RGO Spectrograph have been referred to in Chapter 4; FORS is a fixed format spectrograph with grism dispersion and a spatial resolution of 1″/pixel. An average of 450 seconds integrating provided enough signal-to-noise in each instrument for adequate identifications for practically all candidates, and 135 objects in all were observed with an average seeing estimate of 1.5″.

The ESO Faint Object Spectrograph and Camera (EFOSC) was used in single object mode for the May run. Together with a 230Å/mm grating and a low resolution 512×320 thinned, back-illuminated RCA chip #3, spectra for 32 objects in the range 3500Å $\lesssim \lambda \lesssim$ 7000Å were obtained on the one night weather permitted, in an average of 300 seconds, with seeing of approximately 1.6–1.8″.

6.3.4 Reductions

The spectroscopic data were reduced using the FIGARO reductions system. Objects positively identified as stars at the time of observing were omitted.

The CTIO CCD was preflashed for 0.6ms for each exposure (a contribution of $\sim$ 65 ADU) to reduce charge transfer problems and hence an averaged preflash-only frame was subtracted from all images along with the averaged bias of approximately 200 ADU, scaled using the overscan region for each frame. Each image was also divided by an averaged quartz-continuum flat field frame, to allow for sensitivity variations across the chip. This process, along with bad feature correction was performed semi-automatically during the run on a SUN workstation. Frames were then rotated such that increasing wavelength lay along the x-axis (this is necessary for FIGARO). The data were then wavelength-calibrated using He-Ar arcs throughout each night; a long arc at the start of each night was used for an absolute fit, giving an RMS of 0.35Å on a 2^{nd} order polynomial for the 17 lines available. A mean dispersion of 5.7Å/channel is obtained for spectra over the range 4600Å $\lesssim \lambda \lesssim$ 7800Å. The southern standard LTT2415 (Baldwin & Stone 1984) was used for approximate flux calibration of the data for each night, and also for the removal of red night-sky absorption features, by dividing by a smoothed

polynomial through the continuum. All spectra were subsequently smoothed.

The AAT data were reduced separately for each instrument. Cu-Ar "chimney" arcs were obtained and used for wavelength calibration for each night. The IPCS was well calibrated with a 6^{th} order fit to 43 lines, giving an RMS error of 0.6Å over all lines, and a mean dispersion of 2.2Å/channel; its wavelength "window" remained somewhat sensitive down to $\lambda \simeq 3200$Å. FORS was best represented by a linear wavelength-to-channel relationship, fitted to 19 lines, up to 9800Å, (linearity is assumed slightly redward of this line), with an RMS error of 0.85Å. Response continues well beyond 10,000Å, with a mean dispersion of 10Å per channel. Individual shorter arcs were used to calculate any linear shifts during the nights. The CCD exhibited no noticeable dark current, and averaged bias frames for each night were scaled using the overscan region, and subtracted.

Objects were extracted and sky-subtracted with surrounding regions. It was necessary to correct IPCS data for residual "s-distortion" by polynomial fitting, and in some cases this was also useful to account for differential refraction of images at high zenith distances (for all runs). Standard calibrations of GD190, L745-46A and L930-80 (Oke 1974) were used to correct for instrumental response; CD-277696, as a smooth-spectrum standard, was used to remove red night-sky absorption in FORS for each night, which was again achieved by dividing the sky-subtracted spectra by a polynomial fitted to the continuum and all known object features. All spectra were smoothed. Final calibrated spectra were joined, attempting to estimate scaling between instruments by the small λ overlap in response (5500Å $\lesssim \lambda \lesssim$ 5700Å); however, the IPCS response is falling rapidly in this region, with the dichroic directing nearly all light to FORS. This makes it difficult to scale correctly, especially where the "break" falls in an unpredictable region (blueward of Ly-α for quasars with $z \geq 3.6$), and estimates may be wrong by as much as 25%.

The ESO data were again processed in much the same way. The data were bias-subtracted ($\sim$ 200 ADU) and flat-fielded (with a halogen lamp) using averaged frames, and subsequently rotated. He-Ar arcs were used, with a 3^{rd} order fit to 22 lines giving an RMS error of 0.9Å for 3500Å $\lesssim \lambda \lesssim$ 7000Å. Spectra of standards L745-46A and

L930-80 (Oke 1974) were used for flux calibration and the spectra smoothed.

Results of the above are shown, ordered by date of observations, in Table 6.5 and Figure 6.6. All observed objects are given in the table, listed by field name and pointer number. Positions are also given. All object without comment were identified as stellar, and further categorisation is available for many objects. Quasars are noted, as are non-QSO extragalactic objects, where a very rough indication of their nature is noted, (e.g. Seyfert versus compact emission-line galaxy depending on the level of ionisation), and their main features indicated. However, all non-QSO categorisation should be regarded as preliminary. Objects with insufficient signal-to-noise to positively indicate their nature are marked "low S/N". The three $z > 3.4$ quasars are shown in greater detail in Figure 6.7.

Table 6.5: (a) CTIO high-redshift spectroscopic results. Objects are listed as field/pointer in Schmidt catalogue. 'Balmer' indicates the presence of strong Balmer absorption, (white dwarfs, HB stars etc.,), 'red star' indicates M or K class, and unmarked objects indicate confirmed stars where no further classification is available at present. Objects which exhibited no strong emission features and where clearly not QSOs are marked 'feature-less', and 'low S/N' indicates objects whose integrated flux was insufficient for identification. 'CELG' indicates compact emission line galaxy, and 'SEYF' Seyfert galaxies (rough guide only based on amount of ionisation).

Field	object	α(1950)	δ(1950)	ID
867	16194	14 42 29.90	−01 16 01.3	feature-less
867	1211	14 29 29.88	+02 01 54.1	red star?
865	14377	14 05 07.18	−01 14 45.0	red star
867	14761	14 41 13.36	−02 38 18.9	
867	16796	14 43 09.31	+02 21 14.7	red star
867	4644	14 32 42.81	−01 11 54.6	feature-less (line? MgII?)
867	176	14 28 27.16	+00 48 26.3	low S/N
867	17169	14 43 21.72	+02 11 57.0	
867	1825	14 29 56.40	−02 38 01.9	low S/N
864	1042	13 29 47.20	+01 07 56.5	red, feature-less
864	13954	13 45 57.94	+01 56 52.1	feature-less
864	2779	13 31 49.67	−00 18 44.9	feature-less (line? MgII?)
864	14890	13 47 03.80	+02 20 56.0	red star
864	16265	13 48 48.21	+00 31 37.0	QSO $z \simeq 1.55$ CIII, MgII
864	2231	13 31 05.05	−02 46 14.7	red star
864	12404	13 43 54.88	+00 23 46.8	CELG? $z \simeq 0.52$
864	337	13 28 35.71	−02 31 28.9	feature-less (line?)
864	14766	13 46 57.27	+01 48 17.2	low S/N
864	14553	13 46 43.18	+01 27 17.2	feature-less
864	1475	13 30 21.15	+01 08 14.0	QSO z=3.506 Ly-α, SiIV, CIV
864	343	13 28 45.12	+02 18 36.5	
864	2599	13 31 42.90	+02 21 15.6	feature-less
864	2126	13 31 02.82	+01 46 13.8	feature-less
867	1003	14 29 10.38	−01 52 09.5	feature-less
867	16167	14 42 28.80	−00 15 54.6	feature-less
867	1991	14 30 15.14	+02 25 36.8	feature-less
867	21614	14 46 57.83	−00 30 04.9	feature-less
864	3248	13 32 23.18	−00 18 39.8	feature-less
864	12315	13 43 45.90	−00 39 10.3	star (Balmer)
864	673	13 29 18.11	+02 26 31.6	feature-less

Table 6.5: (a) continued.

Field	object	α(1950)	δ(1950)	ID
864	3667	13 33 04.16	+01 46 19.7	
864	7057	13 37 22.82	+01 48 42.1	
865	4352	13 53 48.65	+02 17 55.0	red star
865	2274	13 51 23.54	+01 51 21.5	
865	12129	14 02 38.13	−00 31 10.6	
865	3242	13 52 26.55	+01 32 47.6	
865	10200	14 00 31.50	+00 58 52.2	
865	15681	14 06 37.91	+02 08 30.9	
865	7542	13 57 13.60	−02 31 31.4	
865	2164	13 51 17.96	+01 17 24.5	
865	4368	13 53 50.98	+01 51 32.1	
865	6747	13 56 32.71	+02 12 20.4	
865	2491	13 51 27.76	−01 16 16.6	star (Balmer)
865	16756	14 07 40.86	−00 57 44.9	
867	13790	14 40 27.94	−00 31 19.7	CELG z=0.328 O II, Ne III, Hγ, Hβ, [O III]
867	225	14 28 27.29	−00 52 40.5	
867	17173	14 43 19.65	+01 56 53.5	
867	8559	14 36 01.25	−02 34 32.0	
867	316	14 28 37.38	+01 16 25.0	
867	274	14 28 19.54	−02 36 24.8	
867	2446	14 30 30.46	−01 35 50.7	
867	12401	14 39 29.29	+01 51 21.8	
867	12605	14 39 37.30	+01 48 36.0	feature-less
867	958	14 29 11.65	−00 36 45.0	
867	1505	14 29 37.16	−02 27 41.6	
867	23402	14 48 35.69	+01 56 30.7	feature-less
867	4045	14 32 13.18	+01 39 12.6	
864	10982	13 42 02.05	−02 34 53.7	low S/N

Table 6.5: (b) AAT high-redshift spectroscopic results. See notes for Table (a).

Field	object	α(1950)	δ(1950)	ID
789	9342	12 43 43.77	−06 06 33.6	red star
789	1208	12 30 27.88	−03 35 05.1	
789	4552	12 36 02.33	−04 08 33.9	
861	7104	12 40 44.47	+01 43 42.6	
861	11511	12 47 59.38	−00 22 05.5	red star
861	9244	12 44 22.10	−01 40 15.3	red star
861	12020	12 48 43.63	−01 58 07.6	
790	1144	12 50 04.82	−02 39 01.4	
790	8876	13 00 14.97	−03 00 54.3	
790	5328	12 55 28.86	−06 53 18.4	
862	7190	13 01 31.02	−00 44 47.3	
862	8933	13 04 33.33	+01 37 18.7	
862	4153	12 56 32.77	+00 34 37.1	
862	10975	13 07 35.26	−01 12 19.5	
790	14482	13 07 36.47	−04 28 54.4	
791	2394	13 11 55.96	−03 23 01.9	
791	7619	13 18 51.86	−05 31 43.0	red star
791	2779	13 12 15.55	−06 29 11.7	
791	2143			
791	3140	13 13 01.29	−03 04 28.7	
791	9687	13 21 39.56	−04 22 18.9	red star
791	2795	13 12 17.82	−07 18 29.8	low S/N
792	7083	13 39 07.72	−04 42 36.0	red star
792	11152	13 45 07.48	−04 33 02.9	
792	4517	13 35 24.33	−05 36 36.2	
863	5703	13 16 56.66	−00 47 31.8	
789	3617	12 34 28.20	−05 07 55.4	
789	9957	12 44 45.99	−04 24 10.5	
789	455	12 28 56.69	−07 04 45.1	
789	5265	12 37 05.77	−06 42 54.1	
789	3946	12 35 12.85	−02 38 35.9	
861	6533	12 39 40.51	+00 49 54.7	
861	7168	12 40 50.66	−01 29 32.9	
861	10464	12 46 20.48	−01 52 29.0	
861	5727	12 38 09.78	−02 22 50.6	

Table 6.5: (b) continued.

Field	object	α(1950)	δ(1950)	ID
861	2997	12 33 42.32	+01 12 56.4	
861	5942	12 38 34.76	+00 39 23.9	QSO z=1.357 (Si IV), C IV, C III, Mg II
861	4832	12 36 43.59	+02 03 22.6	QSO z=2.119 Ly-α, Si IV, C IV, C III, Mg II
790	8286	12 59 20.77	−07 08 21.2	SEYF z=0.270 Hβ, [O III], Hα
790	7290	12 58 04.79	−03 28 03.7	
790	2187	12 51 23.07	−05 53 19.8	
790	4308	12 54 09.59	−06 08 22.9	
862	9079	13 04 39.27	−01 36 02.8	
862	763	12 50 11.10	+02 09 13.4	
862	5485	12 58 51.19	+01 49 15.9	
862	6706	13 00 41.06	+00 26 02.1	
863	4431	13 15 12.50	+02 21 31.2	
863	12571	13 27 17.01	+02 15 59.7	
863	11850	13 26 13.14	+02 03 22.7	star (binary?)
863	12762	13 27 22.00	−00 50 37.5	
863	6987	13 18 47.36	−02 16 48.3	
863	11097	13 24 59.00	−02 16 59.5	
863	5774	13 17 13.74	+01 23 17.0	
863	4752	13 15 41.91	+00 22 32.0	
863	6788	13 18 45.72	+02 05 20.4	
863	7648	13 19 57.28	+00 04 15.0	SEYF z=0.174 Hβ, [O III], Hα
791	1931	13 10 58.80	−07 03 44.7	
791	11077	13 23 34.23	−06 39 31.8	
791	6827	13 17 54.07	−05 07 51.9	QSO z=3.704 Ly lim, Ly-α, Si IV, C IV, C III
791	2258	13 11 25.78	−07 14 54.5	
792	4380	13 35 21.32	−04 18 44.6	
792	10919	13 44 46.47	−03 10 04.9	
792	11056	13 44 55.81	−04 18 36.7	
792	3823	13 34 32.79	−02 51 16.6	
866	9899	14 19 43.23	−01 22 54.4	
866	18098	14 28 51.71	+02 21 51.7	
866	15813	14 26 25.34	+01 45 28.6	
866	518	14 08 55.25	−01 50 18.4	
861	754	12 29 55.57	+00 28 59.1	
861	3000	12 33 46.79	+01 01 27.1	

Table 6.5: (b) continued.

Field	object	α(1950)	δ(1950)	ID
861	10383	12 46 05.15	−02 28 03.5	
861	10911	12 47 01.07	+00 13 17.5	
861	12042	12 48 52.41	+01 29 10.2	
861	1992	12 32 05.26	−00 00 33.0	
789	2122	12 32 02.95	−03 48 27.4	low S/N
789	7732	12 41 03.21	−07 13 39.4	
789	413	12 28 58.27	−04 50 37.0	
789	3259	12 33 52.68	−02 58 17.5	
789	720	12 29 19.23	−07 31 25.2	
789	2604	12 32 50.50	−03 37 31.3	
789	7433	12 40 35.51	−06 05 06.9	
789	3881	12 34 56.12	−03 37 04.6	
789	9936	12 44 46.42	−03 14 50.4	
789	4610	12 36 01.46	−07 00 51.8	
862	11682	13 08 48.58	+00 43 52.0	
862	51	12 48 32.46	+01 22 02.0	
862	11707	13 08 50.68	−01 24 26.2	
862	46	12 48 27.97	+02 11 35.5	
862	9837	13 05 56.85	−00 54 32.8	
862	5337	12 58 28.62	−00 12 01.2	
862	8001	13 02 56.81	−01 04 18.6	
790	1726	12 50 44.24	−03 19 36.5	SEYF z=0.380 Hβ, [O III], Hα
790	8259	12 59 19.52	−05 53 13.8	
790	91	12 48 32.72	−02 35 17.6	
790	9680	13 01 07.40	−05 20 32.1	
790	3149	12 52 49.33	−03 15 42.5	
790	7888	12 58 50.27	−03 45 50.2	
790	14064	13 06 58.22	−07 35 08.2	
790	7528	12 58 23.13	−03 34 43.1	
790	14021	13 06 59.86	−05 19 14.7	
790	4945	12 55 04.03	−05 15 24.2	
790	490	12 48 50.81	−07 32 44.5	red star
863	3656	13 13 59.15	−02 29 37.1	SEYF z=0.579 Hβ, [O III]
863	7213	13 19 19.30	+00 55 57.2	
863	8251	13 20 48.04	+00 31 22.9	

Table 6.5: (b) continued.

Field	object	α(1950)	δ(1950)	ID
863	7154	13 19 10.47	−00 39 12.5	
863	2005	13 11 28.32	−00 29 18.5	
863	12529	13 27 06.53	−00 54 54.2	
863	12974	13 27 40.93	−01 04 09.7	
863	6024	13 17 32.34	−00 18 20.3	
863	2992	13 13 02.80	−00 19 06.1	
863	4898	13 15 49.69	−01 42 03.6	
863	12428	13 27 01.19	−01 26 14.9	
791	3237	13 12 55.52	−07 06 57.6	
791	14648	13 28 03.49	−06 14 56.6	
791	8896	13 20 36.51	−03 56 59.4	
791	375	13 08 57.54	−03 42 28.5	
792	9273	13 42 18.35	−05 01 41.3	
792	9615	13 42 44.27	−05 37 53.7	
792	5987	13 37 32.50	−03 30 41.2	
792	6665	13 38 33.94	−05 39 50.3	
792	565	13 29 15.76	−05 21 41.1	
792	6239	13 37 54.75	−04 34 29.9	
866	4404	14 13 33.49	−00 22 32.3	
866	13582	14 23 54.54	+02 26 48.2	
866	16552	14 27 11.51	+00 36 35.4	
866	16048	14 26 28.10	−01 31 57.5	QSO z=3.415 Ly lim, Ly-α, Si IV, C IV, C III
866	13388	14 23 33.17	−00 20 27.8	
861	3380	12 34 23.12	+00 47 35.4	CELG z=0.179 Hβ (weak), [O III], Hα
867	17172	14 43 26.93	+01 58 42.8	
867	6160			
867	2081			
867	10380			
867	23318	14 48 20.50	−00 54 03.2	
867	16198	14 42 24.98	−01 30 45.2	

Table 6.5: (c) ESO high-redshift spectroscopic results. See notes for Table (a).

Field	object	α(1950)	δ(1950)	ID
789	9269	12 43 28.79	−07 14 23.8	QSO z=1.290 C III, Mg II
789	3295	12 33 51.21	−05 36 12.3	QSO z=1.416 C III, Mg II
789	6684	12 39 27.64	−05 45 19.4	red star
789	105	12 28 17.67	−06 05 25.5	red star
789	8359	12 42 11.11	−05 41 43.8	red star
789	9195	12 43 34.88	−03 36 51.1	red star
789	4754	12 36 18.96	−04 08 14.5	
789	9277	12 43 28.70	−07 32 18.4	
789	1204	12 30 32.23	−02 51 11.0	
789	10074	12 44 58.16	−05 09 54.4	
789	201	12 28 28.28	−07 03 19.5	
789	8912	12 43 06.67	−03 22 49.0	
789	8800	12 42 44.23	−07 22 19.2	CELG z=0.235 O II, Hβ, [O III]
789	4225	12 35 25.98	−06 40 24.6	star (Balmer)
789	8037	12 41 38.70	−03 58 16.2	star (Balmer)
789	8200	12 42 00.93	−03 11 47.4	QSO z=0.821 Mg II (one line ID)
789	12492	12 48 55.86	−06 49 30.3	
789	7453	12 40 38.54	−07 06 33.8	
789	11701	12 47 39.63	−03 31 03.5	star (Balmer)
789	10594	12 45 52.55	−04 45 39.1	
789	3189	12 33 45.06	−04 28 06.3	star (Balmer)
789	12161	12 48 28.58	−03 34 21.6	QSO z=0.481 Mg II, strong Fe II emission, Hγ
789	2294	12 32 04.35	−07 31 09.8	
789	3303	12 33 50.43	−05 53 29.1	QSO? z=0.475 Mg II (one line ID)
792	10556	13 44 07.47	−05 28 16.2	
792	10297	13 43 51.50	−03 02 58.8	
792	8605	13 41 23.83	−03 35 10.8	red star
867	19814	14 45 28.82	−01 19 40.8	star (Balmer)
867	9261	14 36 42.31	−02 04 45.8	low S/N
867	18229	14 44 03.40	−02 30 22.5	star (Balmer)
867	21540	14 47 02.16	+01 37 18.9	feature-less
867	23182	14 48 17.95	−02 16 00.9	star (Balmer)

Figure 6.6: Reduced spectra from the high-redshift survey. Shown are all emission line objects found, all objects of unsure identity, and examples of contaminants. The wavelength axis is in Angstroms, and the y-axis represents relative flux. The object names are those given in Table 6.5, prefixed by field number. Where relevant, the redshifts are given, along with principal line positions at this redshift. (a) CTIO observations (March 1988).

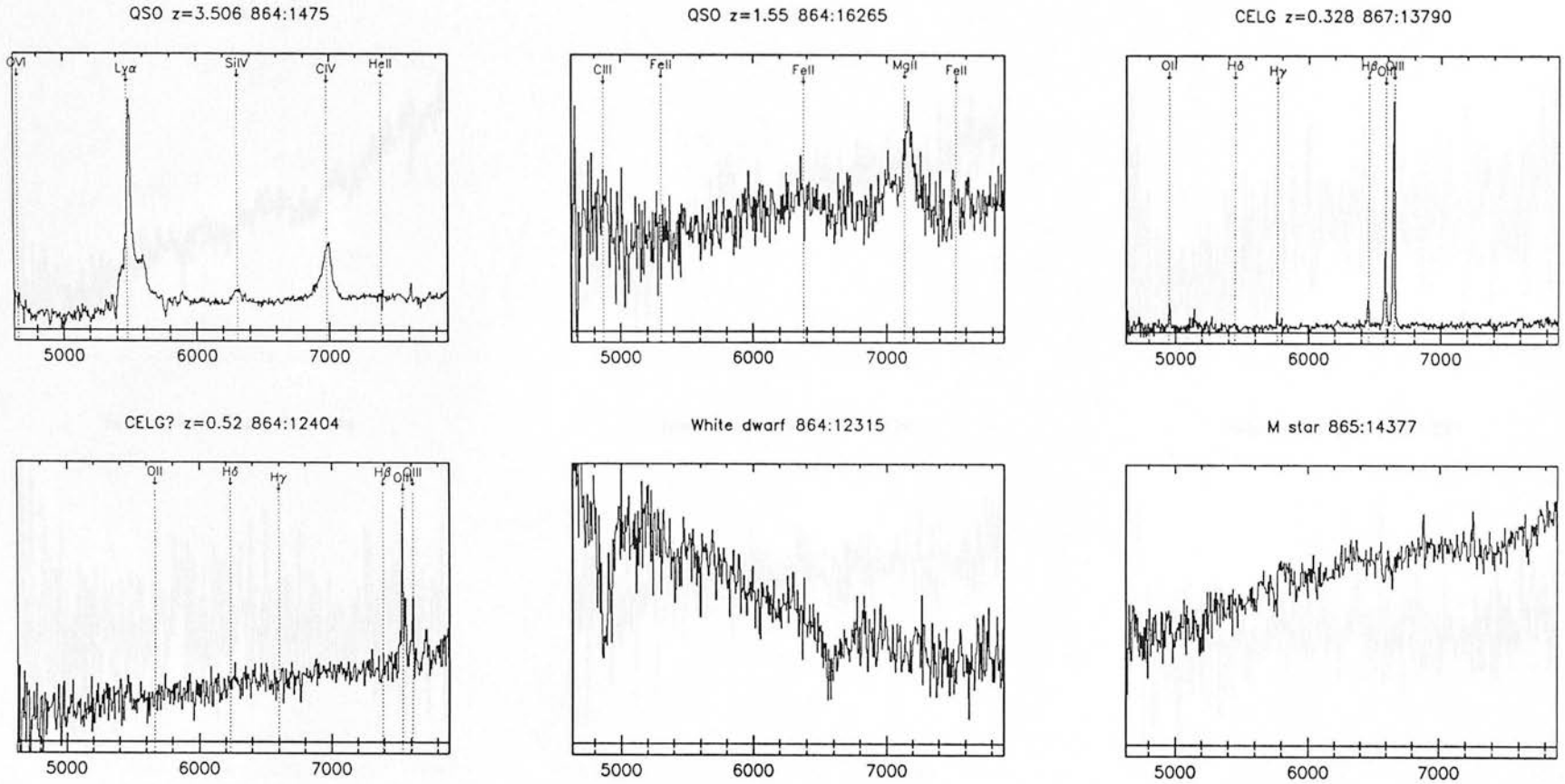

Figure 6.6: (a) continued

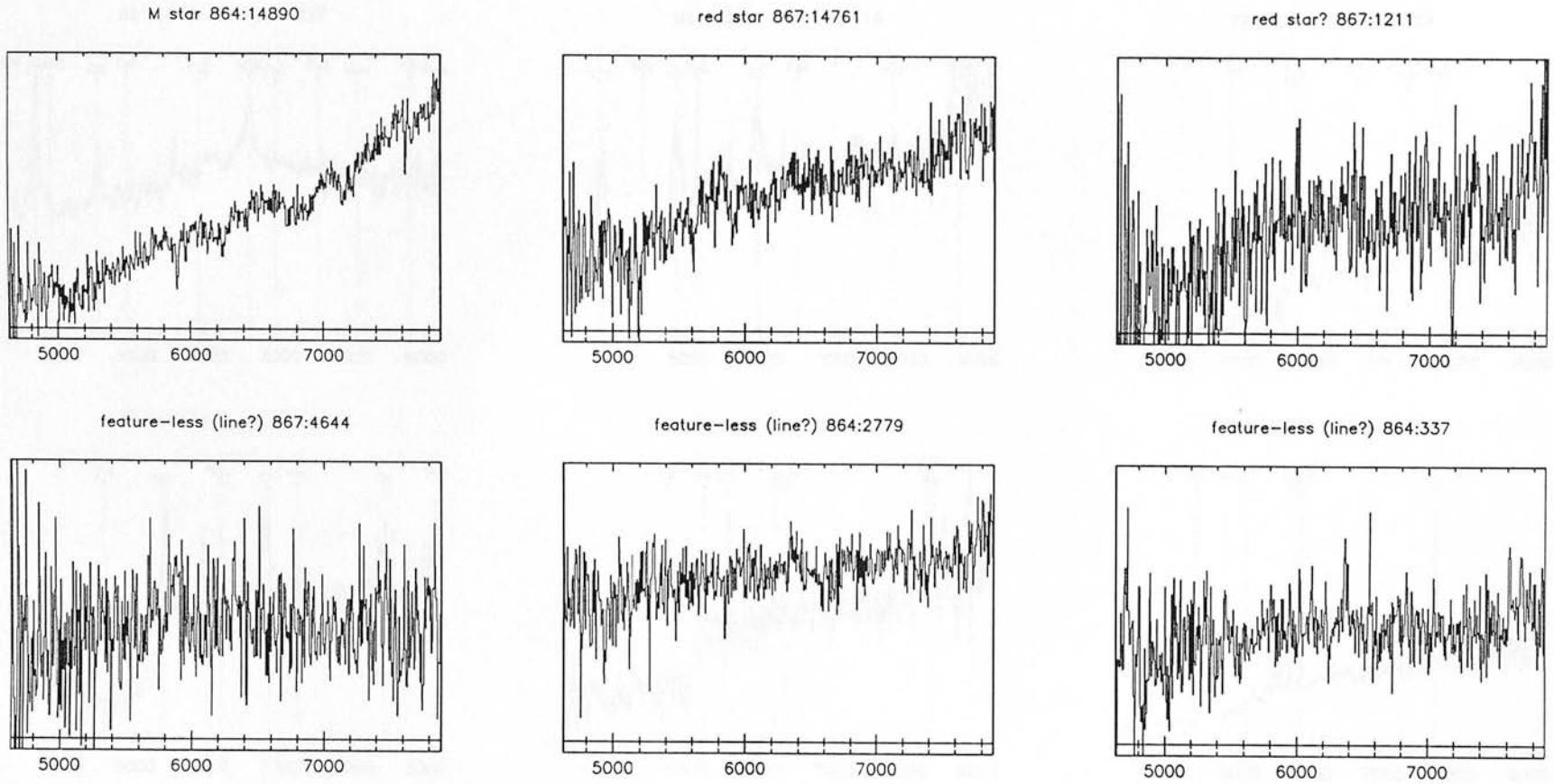

Figure 6.6: (b) AAT observations (April 1988). Note that flux levels around the "merged" region between the IPCS and FORS (5200Å $\lesssim \lambda \lesssim$ 6000Å) may be prone to low signal-to-noise and scaling problems.

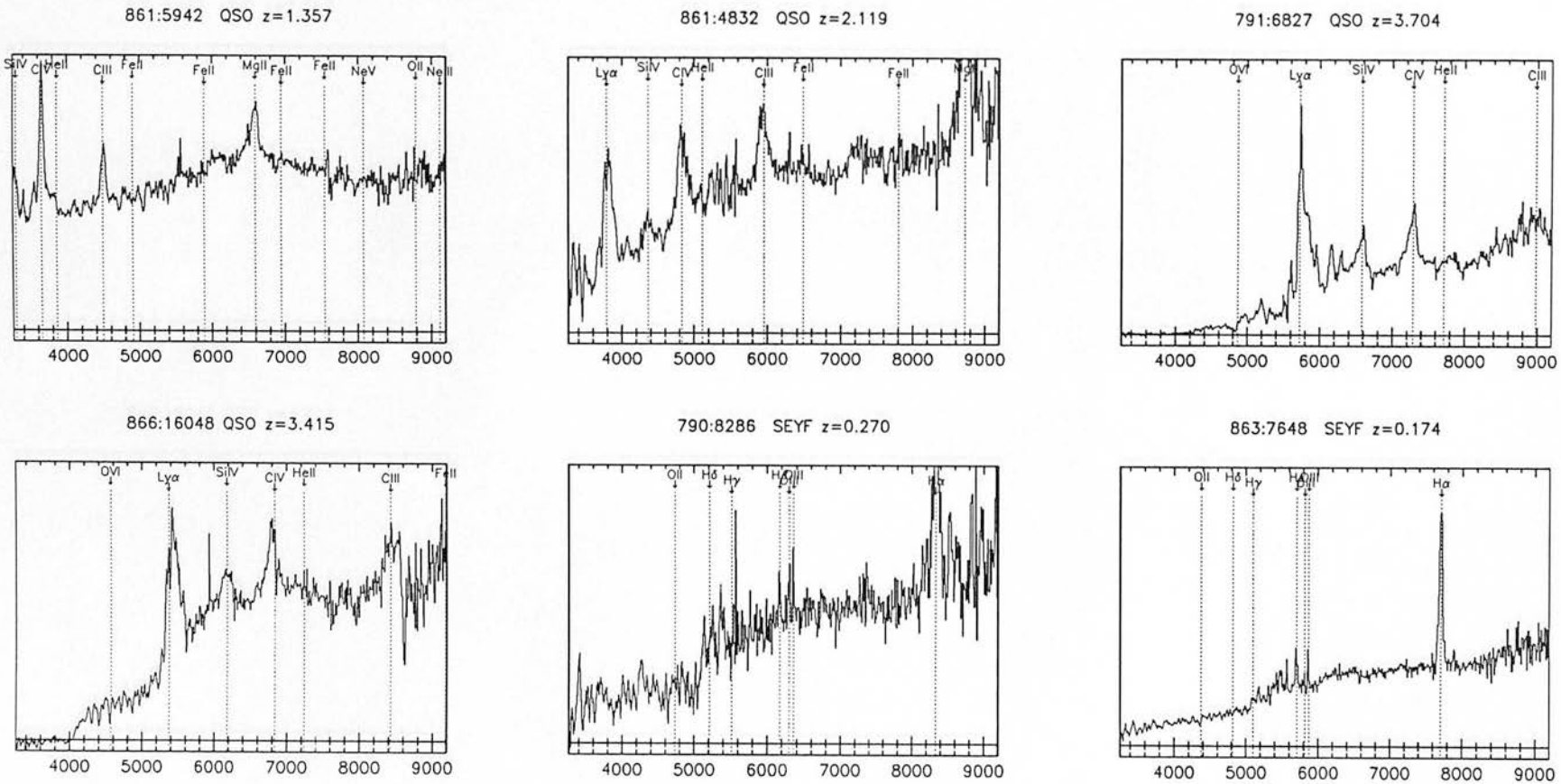

Figure 6.6: (b) continued

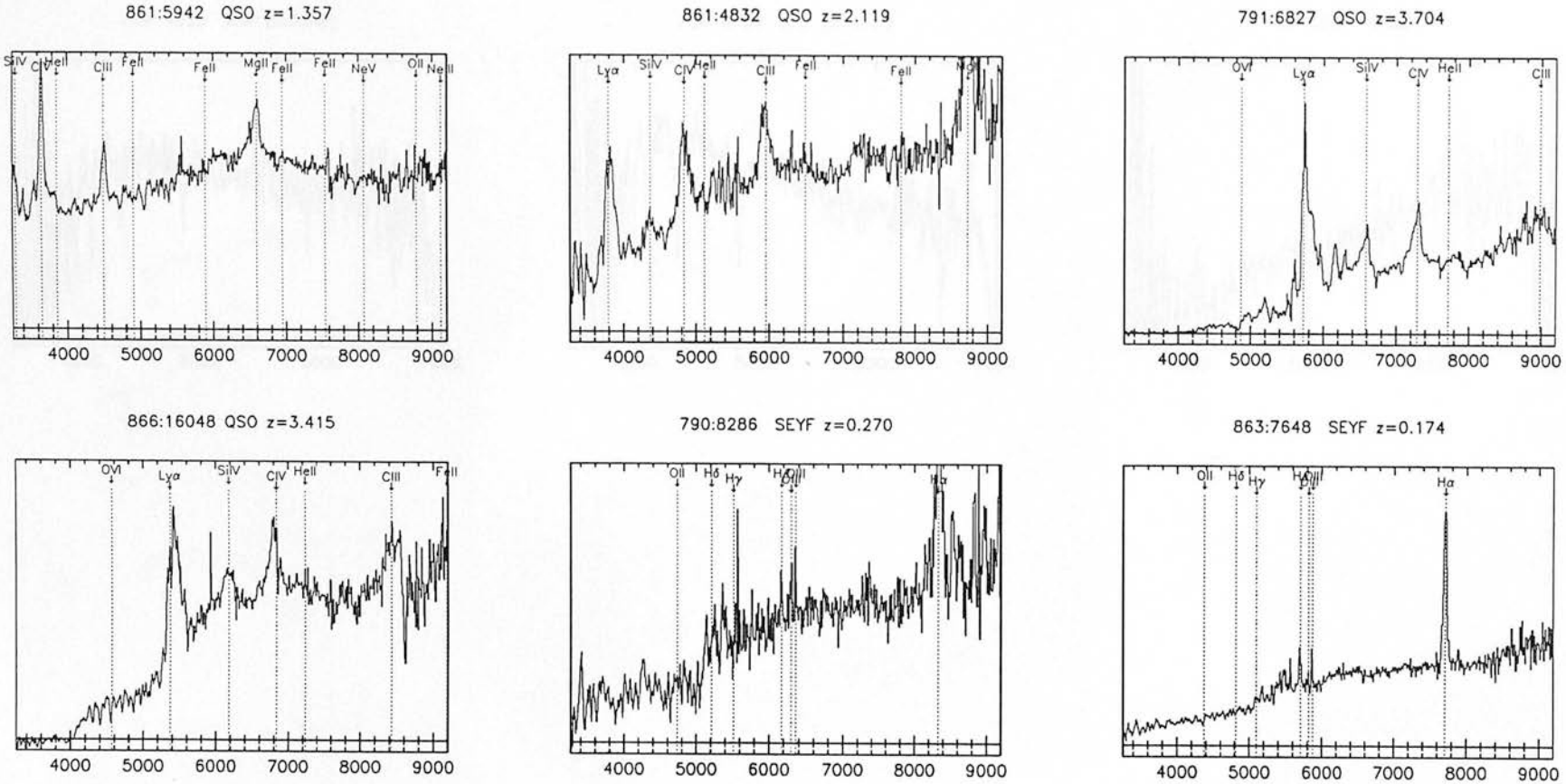

Figure 6.6: (c) ESO observations (May 1988).

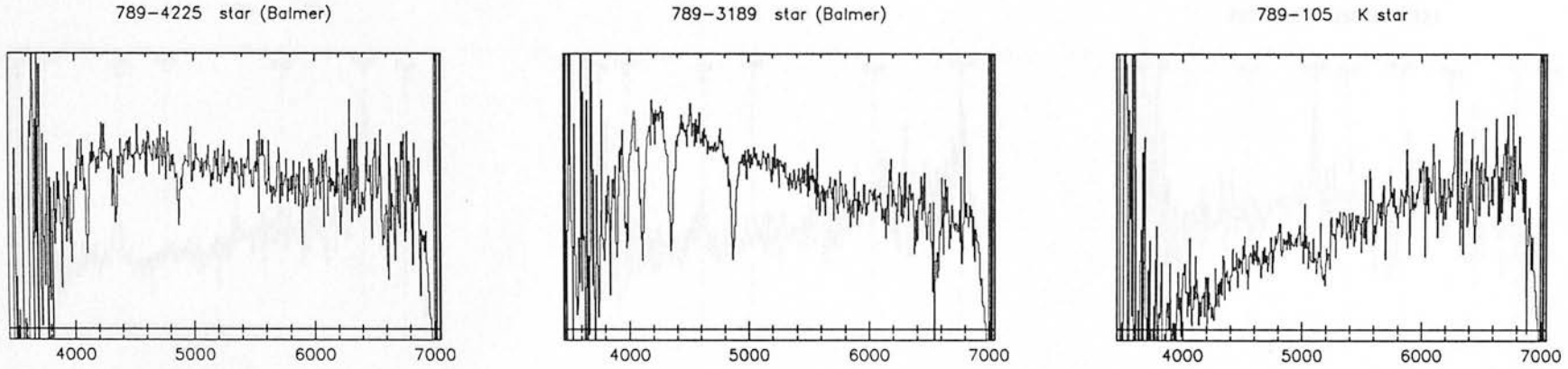

Figure 6.6: (c) continued

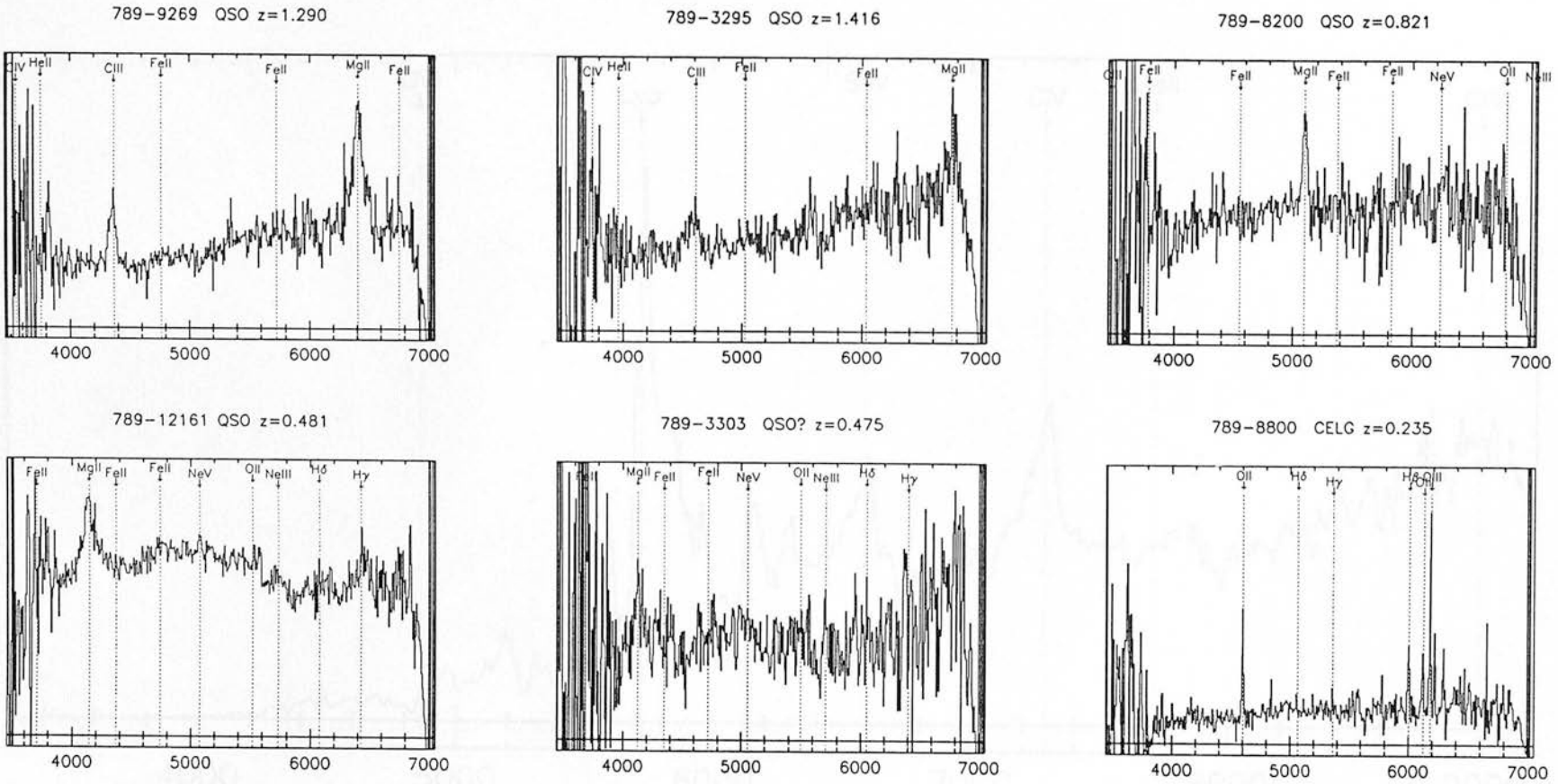

Figure 6.7: Spectra of $z > 3.0$ quasars found in the survey. Positions of common strong emission features are marked.

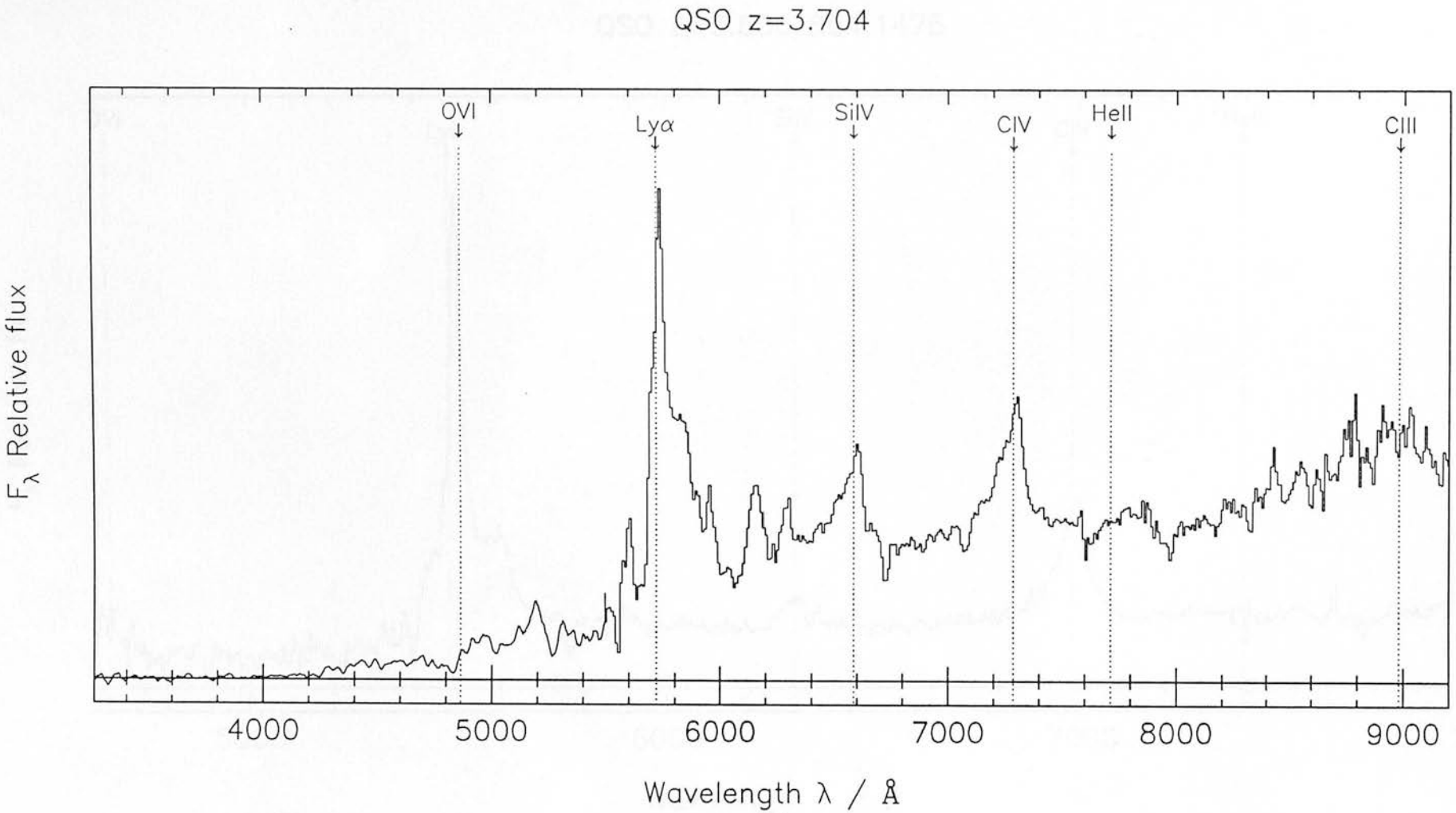

Figure 6.7: continued

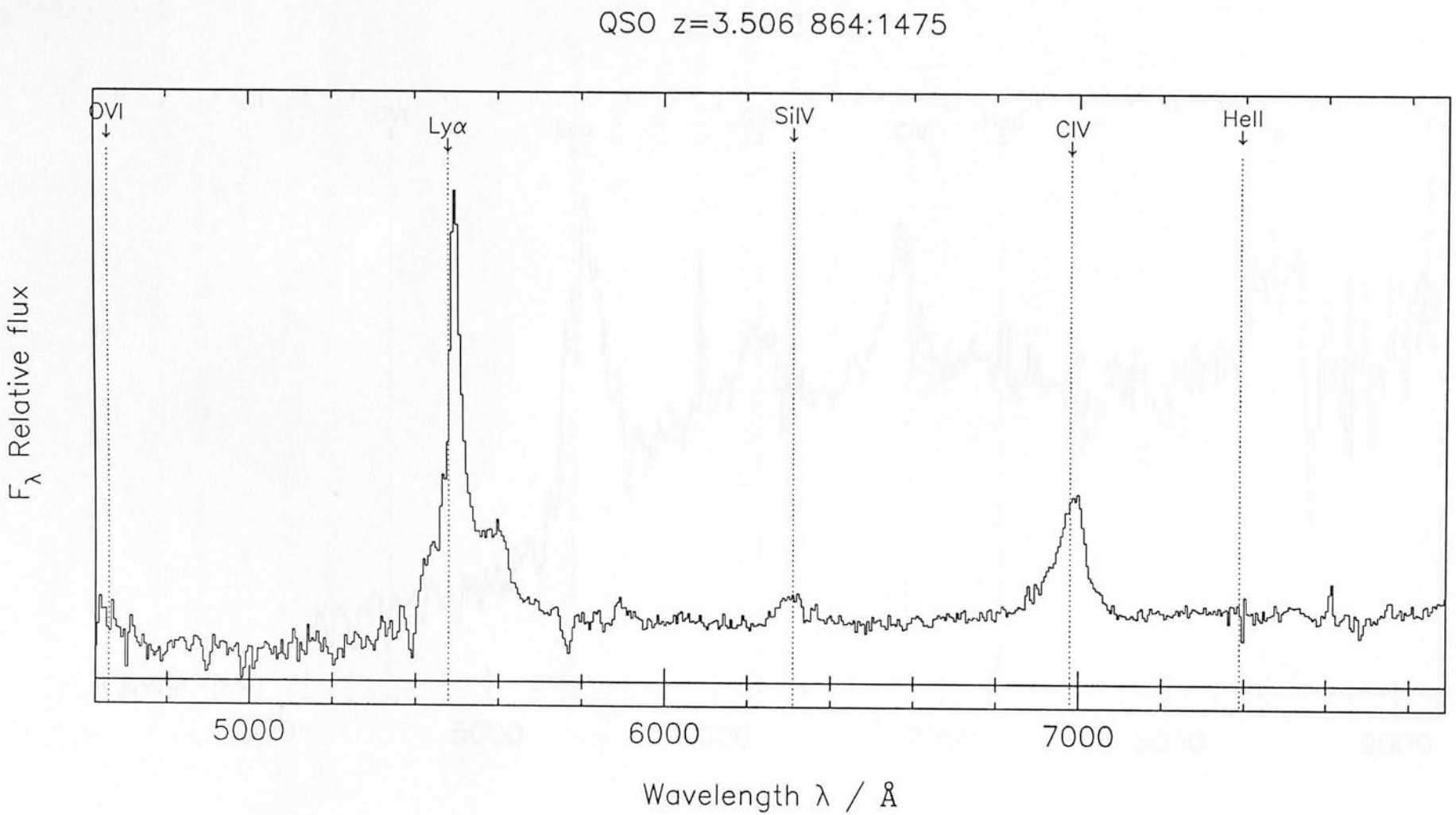

Figure 6.7: continued

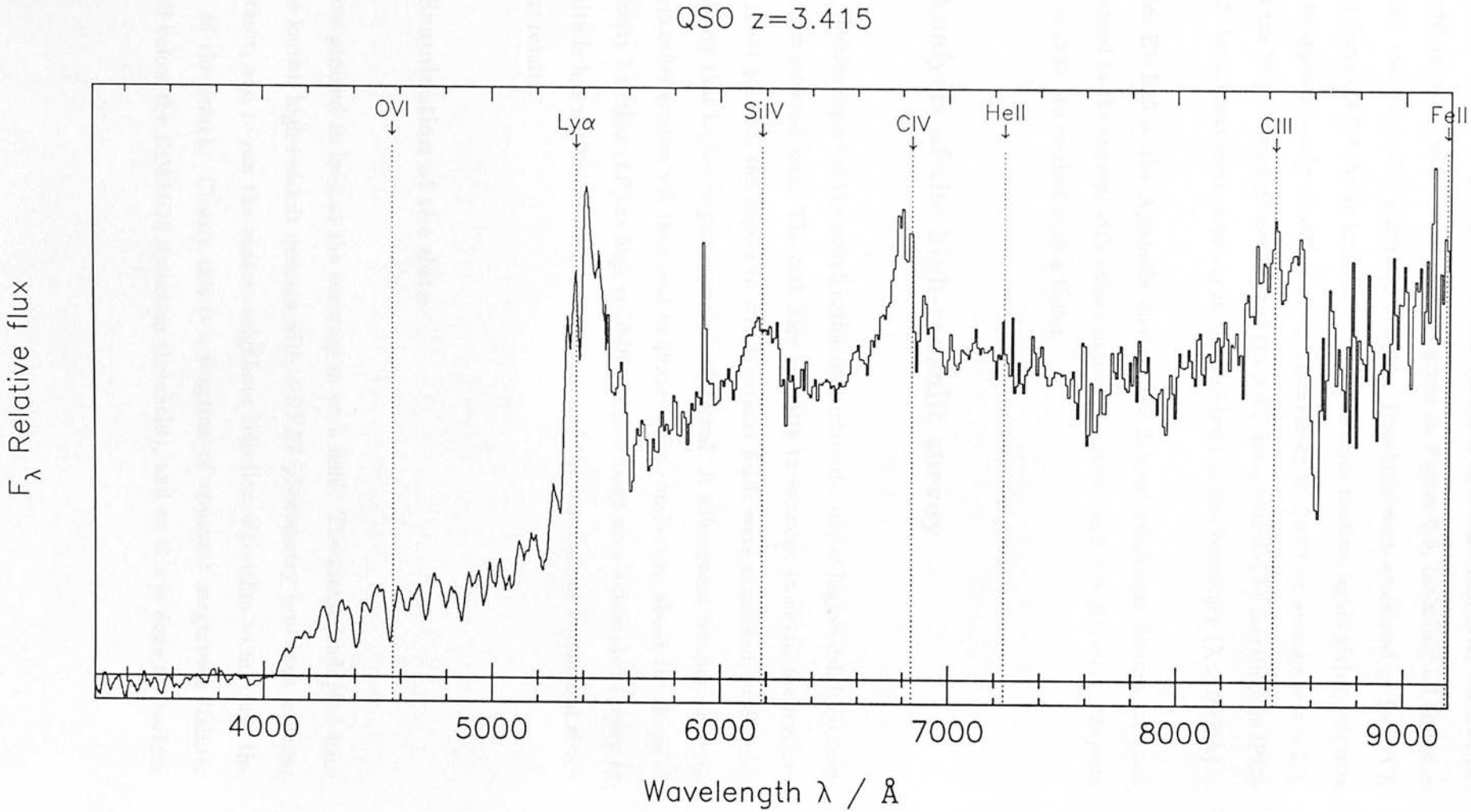

As noted above, every object whose nature was still uncertain after observation was reduced fully. A selection of these is given in Figure 6.6, including all emission line objects, and objects of uncertain identity. Redshifts were evaluated as for UVX QSOs (see Section 4.2.3) by an interactive trial-and-error routine, again giving redshifts accurate to approximately ± 0.005 at $z \sim 1.5$ increasing to ± 0.01 on average at $z \sim 3.5$. Note that the long wavelength coverage of the AAT data, afforded by merging the IPCS and FORS data, leads to uncertainty in the flux level at the boundary ($\lambda \simeq 5000$Å).

Tables E1–E13 in the Appendix contain the nearest-neighbour listings for each field examined in the survey, with colour indices, positions and *NN* distances. Objects observed in 1988 are marked with a bullet.

6.4 Analysis of the high-redshift survey

The most obvious aspect of the search is the low surface density of high-redshift quasars present in the selected area. The task here is firstly to examine in detail the regimes in colour space probed, the degree to which various fields were examined, evaluating the probability that high-z objects remain undetected. A subsequent comparison with results from other studies will then lead to quantitative conclusions about the shape of the luminosity function (LF) at high redshift. Such a large area automated survey at this magnitude has not before been undertaken, and the conclusions herein add much to previous results.

6.4.1 Examination of the data

We can now proceed to look at the coverage in each field. The method adopted here is to place known high-redshift quasars with *UBVRI* photometry into each existing UKST dataset, and re-run the nearest-neighbour selection algorithm to measure the selectivity of the search. Clearly this is a function of apparent magnitude (fainter quasars fall below the COSMOS detection threshold), and so this is done for various

Table 6.6: Details of the three $z > 3.4$ quasars found in the nearest-neighbour search. The colour indices given are for the *UBVRI* Schmidt photographic system as defined in Chapter 2. Limits are derived from the plate-limits for each field.

Name	R	$U-B$	$B-V$	$V-R$	$R-I$	$B-R$	$V-I$	z
1317−0507	17.68	>1.63	1.56	0.43	0.45	1.99	0.88	3.70
1330+0108	18.17	>0.99	1.02	0.03	0.36	1.04	0.39	3.51
1426−0131	17.43	1.96	0.64	0.41	0.08	1.05	0.49	3.42

R values, keeping the known colours fixed. P.C. Hewett (private communication) has supplied a list of 11 colour-selected $z > 3.4$ quasars, to which the three quasars found here are added (the colours of the three quasars found here are given in Table 6.6). These were placed in each dataset with varying R magnitude from $R = 17.0$ to 18.5, and selected *a posteriori* in an identical manner to the real data. The UPPERLIMITS process described above was used to impose limits on the data where (a) information was genuinely missing in the lists in any waveband, and (b) where a derived magnitude value pushed the QSO below the survey plate-limit for the field in question. In situation (b) the survey limit was used as a constraint as usual; in situation (a), in the case of a deeper plate in our survey, ignorance of the true magnitude required the "worst" case to be adopted, i.e. the least restrictive limit; where the limit then pointed away from the locus, the UPPERLIMITS process would push the object as near as possible.

Completeness in each field for these 14 quasars was estimated by examining the fraction lying more extreme than a chosen 100^{th} nearest neighbour limit. The fraction of candidate objects which were observed above the same limit was used to determine the total level of completeness, as a function of NN (the nearest neighbour distance) and the R magnitude of the quasars. Results for this process are given in Figure 6.8, where the thick line indicates the fraction of candidates actually observed and thinner lines show results for objects with the colours of the 14 QSOs, and R magnitudes set to the values shown. As the NN threshold is increased, completeness increases, as expected, due to higher levels of observational completeness, reaching a maximum at $NN \simeq 0.25$

to 0.35. Increasing the threshold further leads to a decrease in completeness, due to a genuine exclusion of some of the quasars more deeply embedded in the main stellar locus. The curves also become more digitised at high NN due to the small numbers of very extreme candidates.

Clearly the fields vary considerably in the quality of the data, and the degree to which they have been examined spectroscopically. Bright plate-limits, particularly in U and I, force some faint quasars out of visibility and hence allow the limiting process to assign as faint a magnitude as desired, leading to loss in completeness at $R \geq 18.25$ for some fields. Table 6.7 gives estimates of the maximum completeness in all fields, and the NN distance where this occurred. The average completeness over the whole survey of eleven plates is 48.1% for $R = 18.50$ and 67.8% for $R = 17.00$. Therefore, from a detection of three quasars, an actual population of $\sim$5 quasars (60%) seems a reasonable estimate, with 6 quasars in the worst possible case (50%). Consideration of the amount of objects excluded in each field due to elimination of blended and elliptical images and the rejection of erroneous colour values leads to an effective area of 144.87 square degrees. The final corrected surface density for quasars in the range $3.4 \leq z \leq 4.1$ therefore is in the region 0.02–0.08 deg^{-2} assuming a 68% confidence region from Poisson statistics.

It should be noted that Warren, Hewett & Osmer (1988) use a nearest-neighbour weighted by apparent magnitude, leading to higher observing priority for brighter objects. This may explain apparent discrepancies here between the two surveys for certain objects: although in general objects were not examined individually, it was apparent that the two objects most likely to be hidden in the Edinburgh dataset were also the brightest in the APM catalogue, and therefore more easily selected there given their fainter plate limits. A brighter magnitude also leads to stronger limits on extreme colours as imposed by the plate material, and, because the zero-point of the magnitude is varied in the simulation, the enhanced chance of detection is not seen here.

Imposing the above uniform set of colour criteria also allows an estimation of the position of the three confirmed quasars in the Edinburgh sample in colour-space,

Figure 6.8: Estimated completeness levels for each Schmidt field as a function of nearest-neighbour distance. Completeness is calculated from the position of 14 high-redshift quasars simulated in the dataset with apparent magnitudes R=17–18.5 with respect to real observations made here.

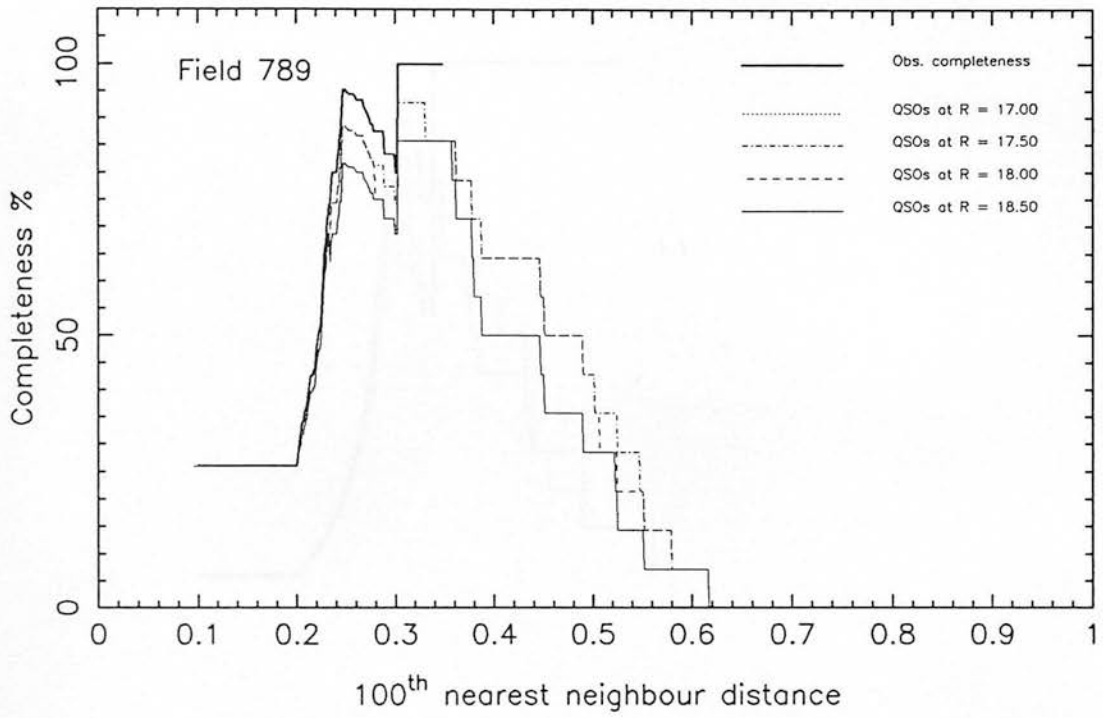

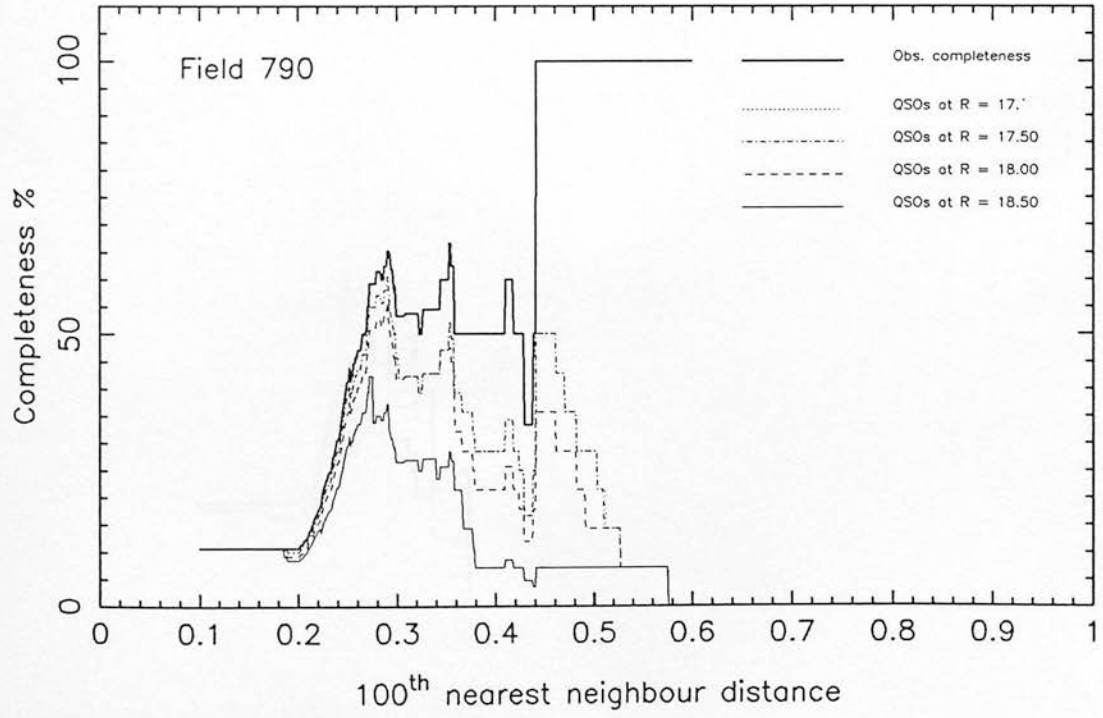

Figure 6.8: continued

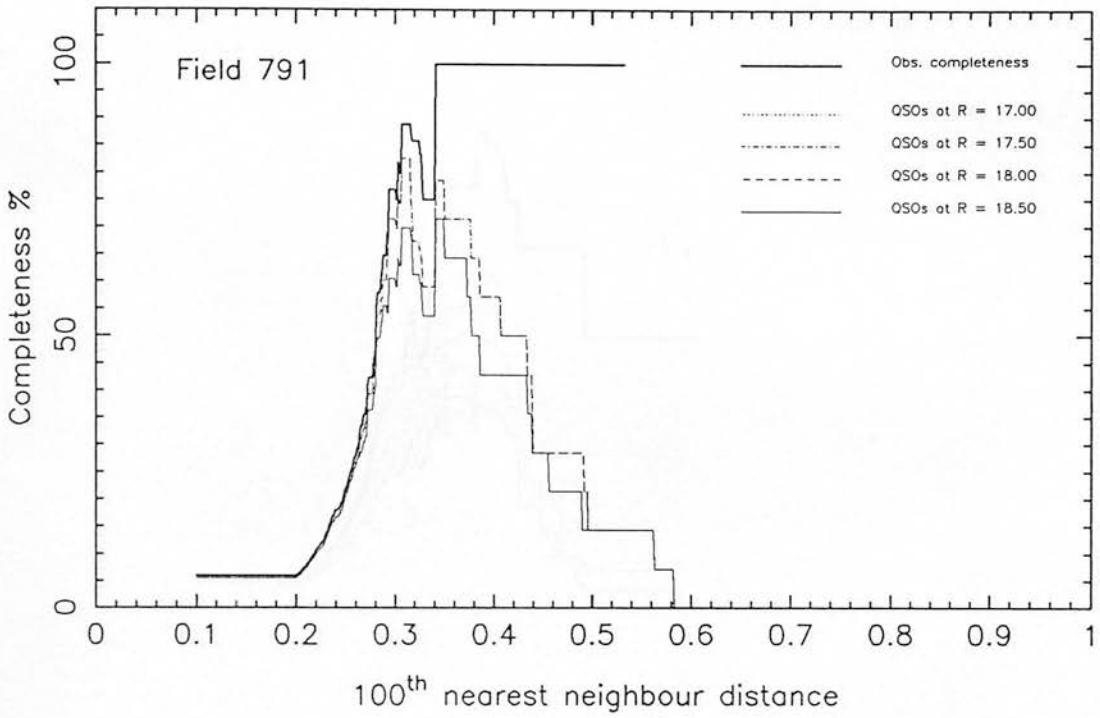

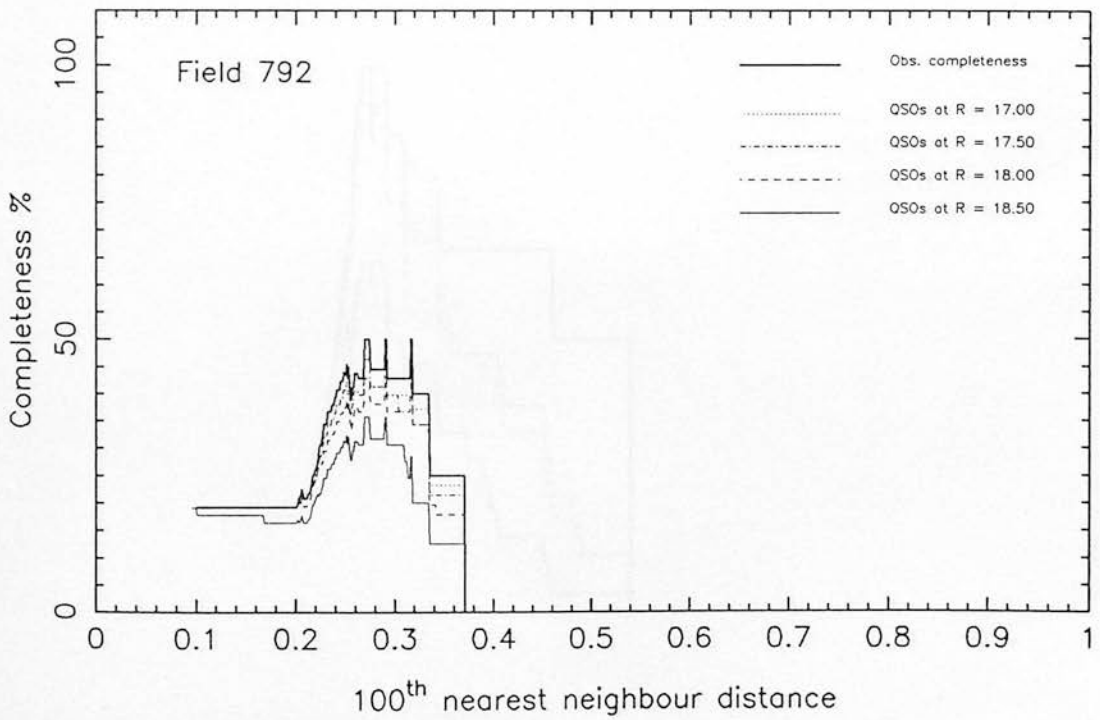

Figure 6.8: continued

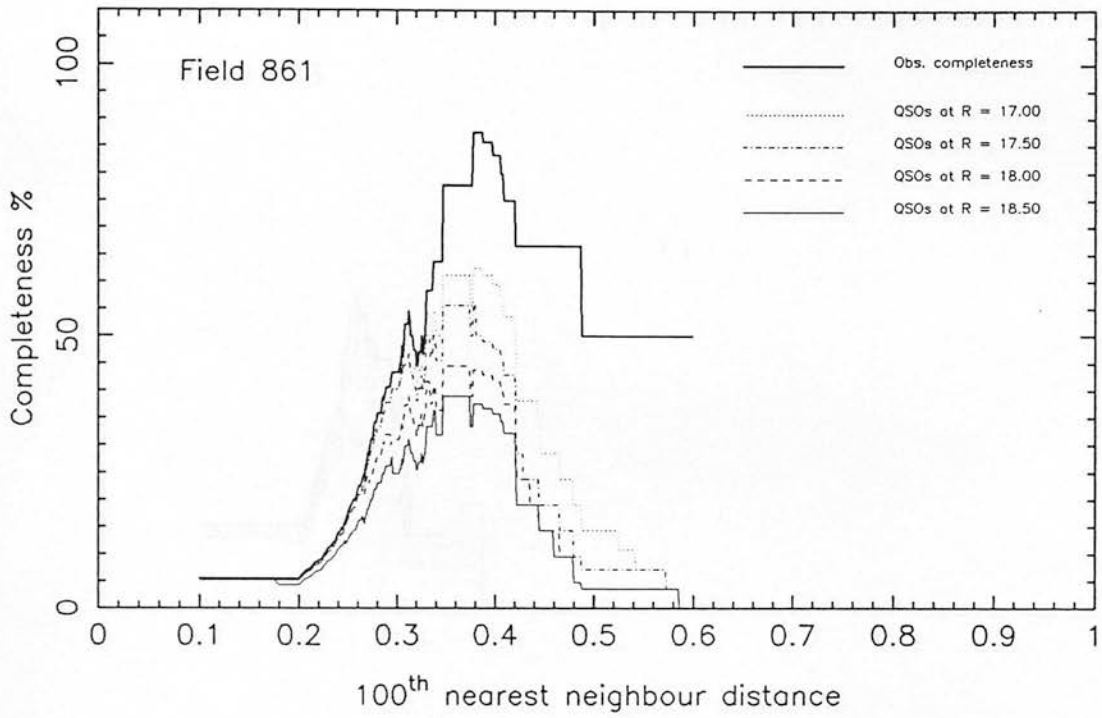

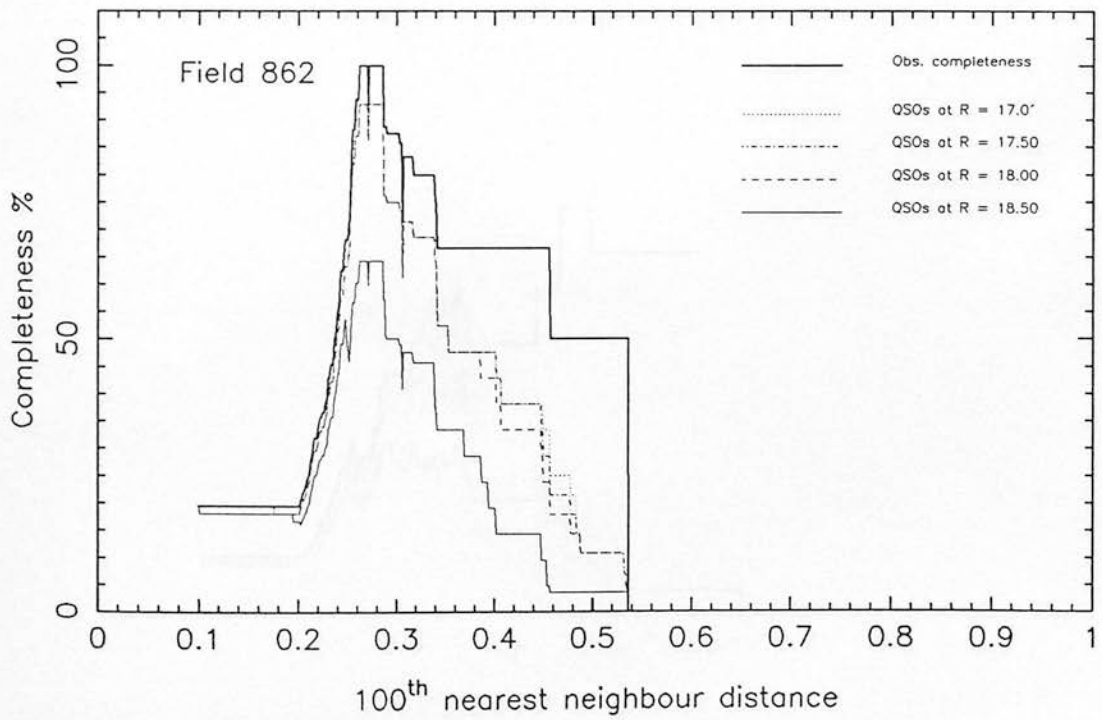

Figure 6.8: continued

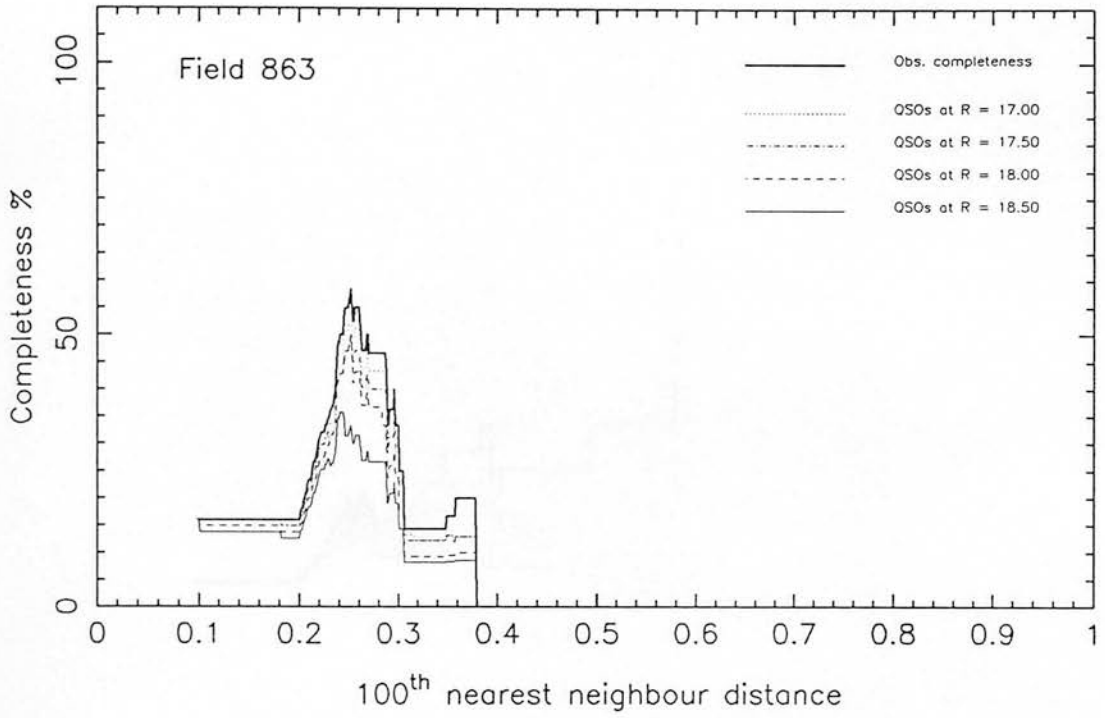

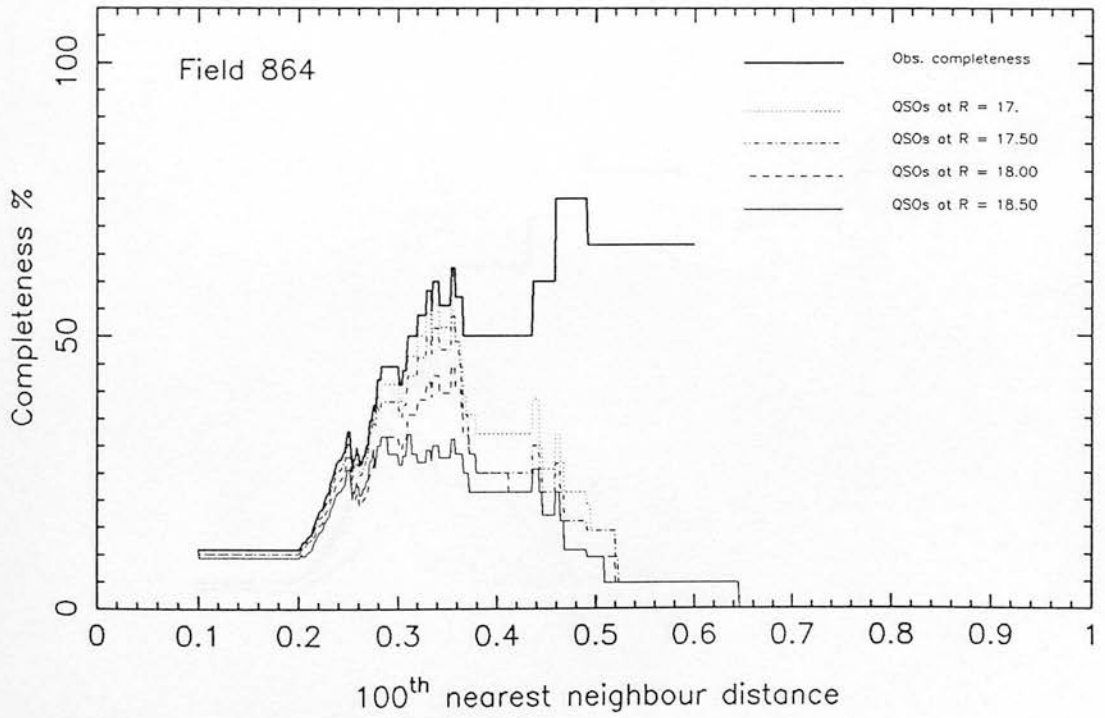

Figure 6.8: continued

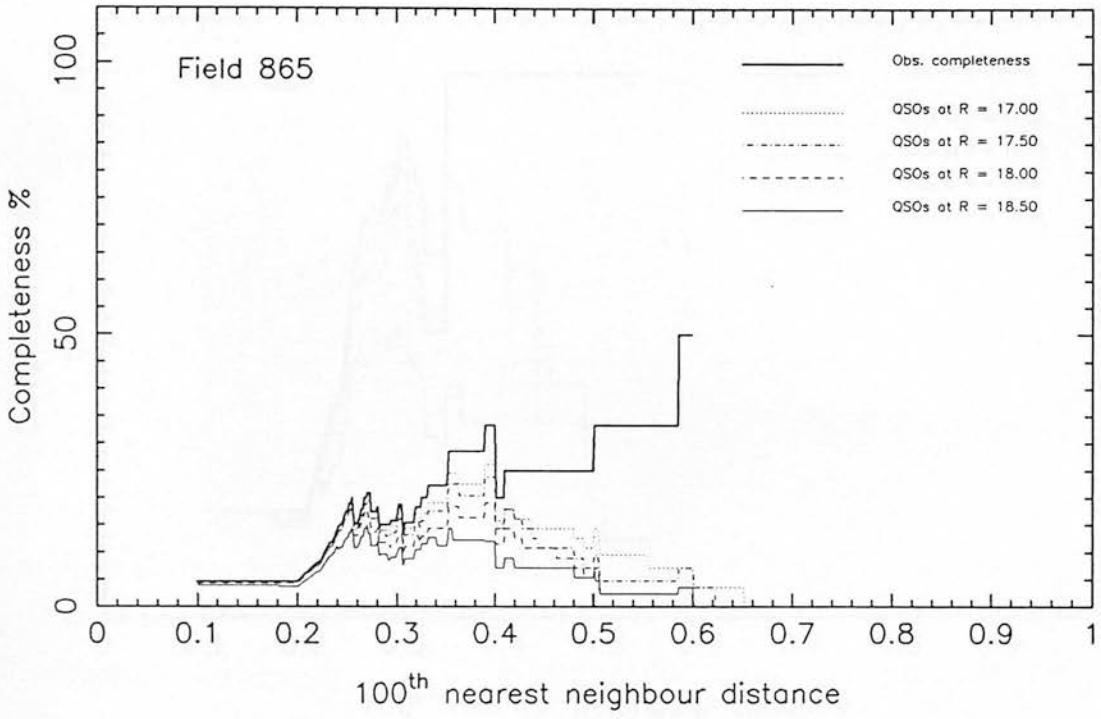

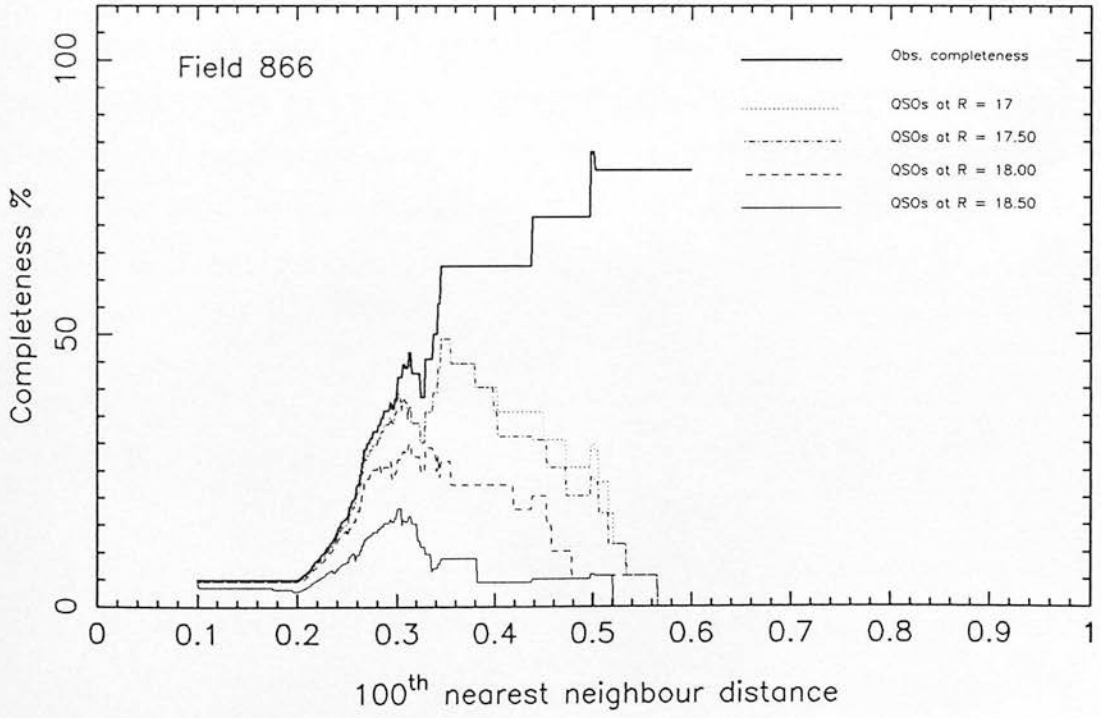

Figure 6.8: continued

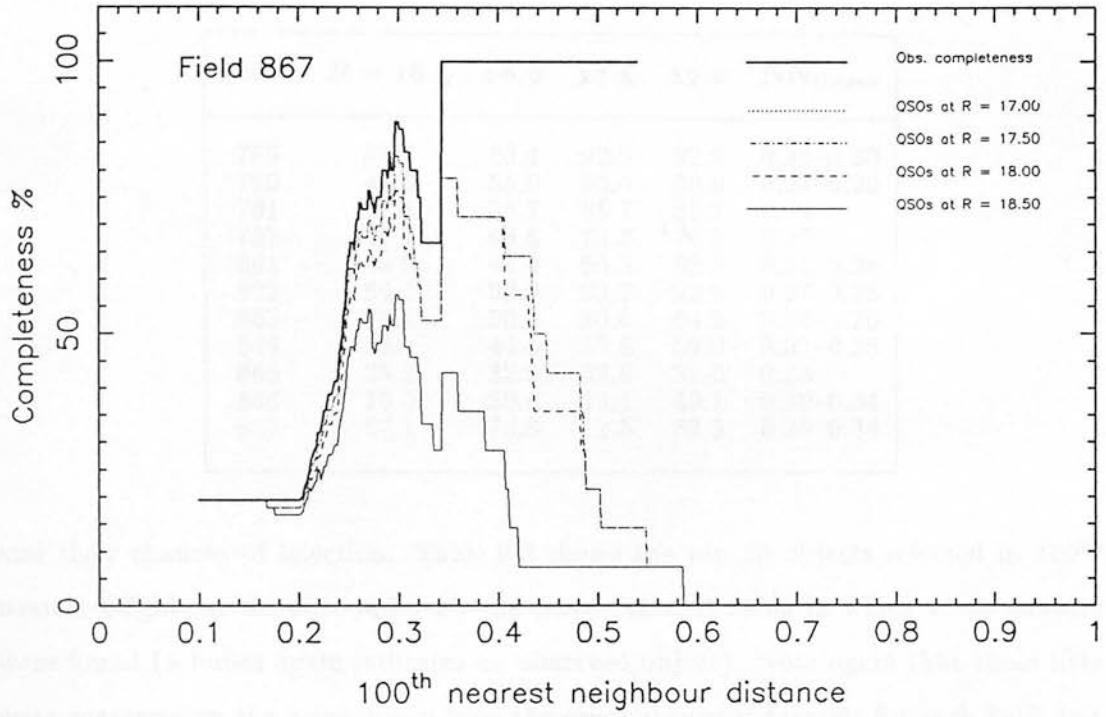

Table 6.7: Listed completeness levels for above quasars in each field. The R magnitude is the value assigned for each quasar, and NN_{thresh} is the nearest neighbour distance for the maximum completeness value.

Field	$R = 18.5$	18.0	17.5	17.0	NN_{thresh}
789	85.7	88.4	92.9	92.9	0.25–0.30
790	42.3	55.9	60.6	60.6	0.27–0.29
791	72.5	85.7	85.7	85.7	0.29
792	57.1	68.6	74.3	74.3	0.27
861	38.9	44.4	56.3	62.5	0.31–0.38
862	64.3	92.9	92.9	92.9	0.27–0.28
863	35.7	50.0	50.0	54.2	0.24–0.25
864	32.1	44.6	53.6	58.0	0.31–0.35
865	25.1	32.6	32.6	32.6	0.25
866	18.0	30.0	49.1	49.1	0.30–0.34
867	57.1	78.6	82.5	82.5	0.30–0.34

and their chances of selection. Table 6.8 shows the top 10 objects selected in 100^{th} nearest-neighbour distance order for the three Schmidt fields in which these quasars were found (a bullet again indicates an observed object). Note again that these lists were generated in the normal way from the original survey datasets for each field, but differ from the lists in Appendix E only in that they were selected according to the above criteria. All three quasars lie very close to the start of the lists, indicating the ease with which they were selected; 791:6827 and 864:1475 are the 8^{th} most "extreme" object in their respective datasets and 866:16048 is the 6^{th}. Indeed 866:16048 was the most sparsely-placed object present on all five plate-pairs for that field. In most cases the fields were examined fairly completely to a much lower NN distance but no further quasars were found.

6.4.2 The luminosity function

The shape of the luminosity function for low-redshift QSOs as determined by the UVX work of Boyle *et al.* (Boyle, Shanks & Peterson 1988b, see also Chapter 4) is represented by a smoothed two power-law function

Table 6.8: Re-selected nearest-neighbour lists for the fields containing high-redshift quasars. The top 10 objects, selected in 100^{th} *NN* distance order are given for each Schmidt field. Observed objects are marked with a bullet, and the three high-redshift quasars are underlined.

#	Obs?	Object	*R*	*U-B*	*B-V*	*V-R*	*R-I*	*B-R*	*V-I*	D_{100}
Field 791:										
1	•	2394	18.36			0.52	0.47		0.99	0.533
2	•	7619	18.50		2.03	0.54	0.66	2.56	1.15	0.419
3	•	2779	18.33		1.71	0.64	0.48	2.36	1.12	0.385
4		2795	18.39	0.55	0.57	0.46	-0.17	1.03	0.30	0.340
5	•	9687	18.03	2.08	1.41	0.37	0.42	1.78	0.79	0.327
6	•	1931	17.82	2.31	1.26	0.37	0.58	1.63	0.95	0.326
7	•	2258	17.72	2.06	0.78	0.50	0.46	1.28	0.96	0.324
8	•	6827	17.68		1.56	0.43	0.45	1.99	0.88	0.316
9	•	3237	17.82	2.26	1.11	0.54	0.39	1.66	0.93	0.315
10		514	18.42	1.66	0.96	0.21	0.80	1.16	1.01	0.306
⋮										
Field 864:										
1	•	3248	18.22	-0.26	1.67	0.69	0.12	2.37	0.82	0.849
2		3128	18.13	-0.43	1.51	0.57	-0.09	2.08	0.48	0.796
3	•	2779	18.38	-0.32	1.27	0.71	-0.22	1.99	0.50	0.719
4	•	2231	18.20			0.64	0.33		0.97	0.490
5		12700	18.44	0.99	0.64	0.58		1.21		0.459
6		99	17.18		0.57	0.37	0.48	0.94	0.85	0.435
7	•	2599	18.27		1.27	0.24	0.22	1.51	0.46	0.365
8	•	1475	18.17		1.02	0.03	0.36	1.04	0.39	0.358
9		1461	18.30	-0.40	0.55	0.57	0.22	1.12	0.79	0.354
10	•	343	17.96		0.81	0.21	0.18	1.02	0.39	0.341
⋮										
Field 866:										
1	•	4404	17.92			0.55				1.214
2	•	13582	18.31			0.26				1.069
3	•	518	17.06		0.78	0.29	0.43	1.07	0.72	0.796
4	•	16552	18.28			0.53				0.702
5		12	18.34							0.641
6	•	16048	17.43	1.96	0.64	0.41	0.08	1.05	0.50	0.502
7		14908	17.75	1.27	0.54	0.08	0.09	0.61	0.17	0.498
8		11414	18.33				0.54			0.437
9		11458	17.88	1.91	1.08	0.61		1.68		0.344
10		12763	17.96	2.01	0.95	0.44	0.37	1.40	0.81	0.341
⋮										

Table 6.9: Best-fit values for the LF of Boyle, Shanks & Peterson 1988b, for UVX ($0.3 \leq z \leq 2.2$) quasars ($M_B > -23$).

q_0	N_{qso}	β_1	β_2	M_B^0	k_L
0.5	567	−3.79	−1.44	−22.42	3.15
0.0	581	−3.84	−1.61	−23.10	3.34

$$\Phi(L,z) = \Phi^\star \left[\left(\frac{L}{L^\star(z)} \right)^{-(\beta_1+1)} + \left(\frac{L}{L^\star(z)} \right)^{-(\beta_2+1)} \right]^{-1} \tag{6.12}$$

where L is the luminosity coordinate corresponding to M_B, the absolute B magnitude, and β_1 and β_2 represent the values of the slope determined by whether L is greater or less than the "break" luminosity $L^\star(z)$. The evolution with redshift is found to be well represented for all but the lowest luminosity objects ($M_B > -23$) by pure luminosity evolution (PLE), in the sense that the break luminosity increases with increasing z (some additional density evolution may be required for $M_B > -23$). This evolution is represented $(1+z)$ power-law thus:

$$L^\star(z) = L_0(1+z)^{k_L} \tag{6.13}$$

(corresponding to $M^\star(z)$ in absolute magnitude) where L_0 is the break for $z = 0$, corresponding to M_B^0, representing uniform dimming of quasars as they approach the present epoch.

Best-fit values for the four parameters β_1, β_2, L_0 and k_L were evaluated for an amalgamation of low-redshift surveys (the AAT survey (Boyle, Shanks & Peterson 1988b), the PG survey (Schmidt & Green 1983), the MBQS (Mitchell, Warnock & Usher 1984), the AB and BF surveys (Marshall *et al.* 1983b, 1984), the CFHT survey (Crampton, Cowley & Hartwick 1987, 1988), and a subset of the UVX survey of Chapter 4, this thesis). Resulting values are given in Table 6.9. The value of the normalisation constant $\Phi^\star$ can be calculated from the number densities of the PG survey (with an estimated completeness of 84% — Green, Schmidt & Liebert 1986), representing the low luminosity end of the LF in which we are interested here.

The relative ease with which UVX quasars are selected is in contrast to the complicated selection effects at higher redshifts, but the recent work of Steve Warren and Paul Hewett (e.g. Warren, Hewett & Osmer 1987c, 1988, 1989) in conjunction with UKST plate material scanned on the Automatic Plate Measuring machine (APM) has demonstrated that significant amounts of high-redshift quasars can be detected by the multicolour approach. The emission-line work of Schmidt, Schneider and Gunn (1986a, 1986b, 1987a, 1987b) using a grism and red-sensitive CCD approach has also resulted in high-redshift detections, and Hazard, McMahon & Sargent (1986) have claimed surface densities of $\sim$0.1 deg^{-2} for $3.3 < z < 3.8$ quasars with $R < 18$, from visual inspection of UKST IIIaF low-dispersion objective prism plates. As noted earlier, Hazard (1986) indicates that this surface density may be estimated at too bright an apparent magnitude.

In order to examine these claims and constrain better the luminosity function at bright magnitudes, the z-regime to which this survey is sensitive must first be estimated. As indicated earlier, the range $3.4 < z < 4.5$ has been chosen from Section 6.2.3, where it was shown that below $z = 3.4$ horizontal branch stars display very similar colours and compromise the nearest-neighbour distances. Above $z = 4.5$, quasars possess extreme colours, but the limits imposed by the depth of the plate material increasingly reduce completeness. This conclusion is consistent with results of the inclusion of known high-z quasars in the dataset: Hewett quasars below this redshift range quickly disappeared into the stellar locus. Section 6.3.2 has further noted that the necessarily strict $(V-R)$ and $(V-I)$ selection criteria imposed may lead to losses for quasars with $z > 4.1$ as Ly-α leaves the V band. This further restriction will be used in the analysis below.

Absolute B magnitudes, M_B, can be derived from the apparent magnitude, R, under an assumed cosmology (H_0, q_0), an assumed continuum spectral index α (the value $\alpha = -0.5$ is adopted here from Richstone & Schmidt 1980), and z. At these redshifts such values of spectral index are clearly not valid for the region of QSO spectra observed in the B band, but absolute B magnitude will be calculated from apparent R magnitude (where such a description is still correct) as below. Hayes & Latham (1975) measure α Lyræ 0.39 magnitudes brighter in f_ν at $\lambda = 6440$Å, the effective wavelength

Table 6.10: Absolute B magnitudes for the three survey quasars, for different q_0.

Field: object	z	R	B	$M_B(q_0 = 0.5)$	$M_B(q_0 = 0.0)$
791:6827	3.704	17.68	19.67	−28.31	−29.90
864:1475	3.506	18.17	19.21	−27.71	−29.24
866:16048	3.415	17.43	18.48	−28.40	−29.68

of the R passband (see UK Schmidt Handbook) than at $\lambda = 4500$Å (the B band). This implies that

$$B = R + 2.5\alpha \log\left(\frac{4500}{6440}\right) + .39 \tag{6.14}$$

The conversion between B and M_B is given by

$$M_B = B - 5\log A(z) + 2.5(1+\alpha)\log(1+z) - 25 \tag{6.15}$$

where $A(z)$ is the luminosity distance. The third term on the left hand side represents the "K-correction", composed of the effect both of (i) compression of the bandwidth $\delta\lambda$ with increasing z, and (ii) the actual form of the spectra, such that a different region is measured by the passband for different z. No account is taken of the effect of emission lines in the R passband. The resulting values for the three quasars found here are shown in Table 6.10.

The form of the LF parameterised above by Boyle *et al.* can be used to estimate the number N_q of quasars found in the range z_1 to z_2 for any survey of Ω steradians coverage, within an apparent magnitude range R_1 to R_2 by

$$N_q = (\Omega/4)\int_{z_1}^{z_2}\int_{M_B(z,R_1)}^{M_B(z,R_2)} \Phi(M_B, z)\, dM_B\, \frac{dV}{dz}\, dz \tag{6.16}$$

where dV/dz is the comoving volume element per steradian:

$$\frac{dV}{dz} = A^2(z)\frac{c\, dz}{H_0(1+z)(2q_0 z + 1)^{\frac{1}{2}}} \tag{6.17}$$

A trivial approach to analysing the results at high redshift must be dealt with first. Extrapolating the results of Boyle *et al.* to $3.4 < z < 4.1$ in an effective area of 144.87

deg^2 down to $R = 18.5$ would give an expected 200 to 350 quasars in our survey. This result is borne out at fainter magnitudes by the Warren *et al.* SGP survey, which would be expected to detect over 1000 quasars in the range $3 < z < 5$ to a limiting magnitude of $R = 20$. The straightforward extrapolation of luminosity evolution is clearly ruled out.

The results of the survey presented here must first be compared with the results of Hazard *et al.*, where the detection of six quasars on two Schmidt plates has been claimed to indicate a strong increase in comoving densities with increasing redshift. The six quasars upon which these claims are based have absolute R magnitudes in the range $-30 < M_R < -28$, exactly matched by the sensitivity of the Edinburgh Multicolour Survey, making a comparison straightforward. A model is chosen ('Model 0') in which the luminosity evolution of the LF is "frozen" at $z = 2.25$ in its state as parameterised by Boyle, Shanks & Peterson (1988b). The reason for Hazard's claim is immediately apparent — this model predicts 0.070 quasars per square degree in this luminosity range, a factor of nearly 1.5 (q_0=0.5) smaller than the estimate of Hazard, McMahon & Sargent (1986). However, predicted numbers for our survey (given in Table 6.11) imply that even this model is inconsistent with our results for objects selected by the multicolour approach for $q_0 = 0.5$, where 4.2 times too high a number is calculated (estimating 60% completeness in the dataset and that sensitivity is limited to the range $3.4 \leq z \leq 4.1$); for $q_0 = 0$ a factor 1.6 too high is found (this is however consistent at the 68% confidence level calculated assuming Poisson statistics). At fainter magnitudes e.g. $R = 20$ for the APM survey, this model predicts far too many QSOs (surface densities too high by factors of about 7 and 12 for $q_0 = 0$ and 0.5 respectively). In order to reconcile this model with our results, a redshift of $z = 1.95$ must be adopted ($q_0 = 0.5$) to obtain 5 detections for $3.4 \leq z \leq 3.71$; with this value, over 5 more QSOs are expected for $3.71 < z \leq 4.5$ and 4 for $3.71 < z \leq 4.1$ when in fact none were found. The inclusion of existing quasars has shown that the technique remains sensitive at these redshifts.

Clearly the results from these two samples differ considerably and appear irreconcilable. In order to determine the extent to which the surface densities found for

$3.4 < z < 3.8$ (the overlap range) are consistent with being drawn from some unknown Poissonian distribution, and assuming no surface density fluctuations between the areas of sky surveyed, a maximum likelihood method is adopted. The most likely value of λ_{12} (the mean of the parent distribution) is calculated from maximising the likelihood, represented by the joint probability $\mathcal{L}$, for finding N_1 and N_2 quasars in surface areas A_1, A_2 deg^2 when drawn from the same mean surface density; i.e. $\lambda_{12} = \frac{N_1+N_2}{A_1+A_2}$, here 0.049 deg^{-2}. The probability of obtaining that $\mathcal{L}$ is then determined by summing the probabilities for all other smaller $\mathcal{L}$'s (i.e. the fraction of lower $\mathcal{L}$'s, weighted by their likelihood, in the probability distribution). The result is that the samples have a probability $P \leq 35\%$ of being consistent on the assumption that $R = 18.5$ is the true limit for the Hazard *et al.* data. This result is clearly an upper limit, depending on the variation of the true parent mean surface density from 0.049 deg^2, but indicates that the apparently very different results agree surprisingly well. The lack of sensitivity of the Hazard *et al.* technique to $z > 3.8$, where the multicolour technique remains sensitive, but nevertheless makes no detections, is the reason why the new data differentiates more substantially between simple model choices.

In order to examine the implications from the result presented here, the small number detected clearly limits the approaches available. It is impossible to construct a luminosity function from these data; the way ahead appears to be to see whether various simple pictures for the evolution can be ruled out.

Dunlop (1987) proposed alternative forms for the evolution of the luminosity function, in connection with the radio source population at high redshift. The existence of redshift cutoffs were confirmed in both flat- and steep-spectrum sources from the Parkes Selected Regions; when these were combined with brighter samples, the evolution of the luminosity function was found to be well described by pure luminosity evolution, with the sign of the evolution changing beyond $z \sim 2$ (hereafter referred to as "Model I"). An alternative model was proposed in which the continuing luminosity evolution for $z > 2$ is modified by negative density evolution ("Model II"), a model similar to that applied by Koo (1983) to account for the lack of faint high-redshift quasars in SA57 and SA68. In applying these forms to results from the APM survey, parameters for

this decline in each case were fitted for $z > 2$ to the known surface density (24 QSOs $3 < z < 5$ for $R \leq 20$ in 30 deg^2). This procedure was followed here, with the LF parameters from Boyle, Shanks & Peterson (1988b) giving the form at $z = 2$, i.e. for $(z > 2)$

$$\text{Model I :} \qquad M^\star(z) = M^\star_{(z=2)} + (-0.25)\mathcal{P}_I(z-2) \tag{6.18}$$

where $\mathcal{P}_I = -0.255$ for $q_0 = 0.5$ and $\mathcal{P}_I = -0.160$ for $q_0 = 0$; and

$$\text{Model II :} \qquad \Phi^\star(z) = \Phi^\star 10^{\mathcal{P}_{II}(z-2)} \tag{6.19}$$

where $\mathcal{P}_{II} = -1.02$ for $q_0 = 0.5$ and $\mathcal{P}_{II} = -1.10$ for $q_0 = 0$ were found to fit the data. The last equation for $\Phi^\star$ represents negative density evolution in the normalisation constant while the positive luminosity evolution in Φ continues unabated.

Dunlop showed that both forms of evolution produce consistent redshift distributions when compared to that found by the APM group. He pointed out the very different predictions at brighter limiting magnitudes, as will be seen here, but was unable to discriminate further between them.

Table 6.11 contains resulting predictions from these models for this study. As expected, the negative density evolution model predicts a higher surface density at brighter luminosities than the negative luminosity evolution model. For $q_0 = 0.5$ and 0, Model II is consistent with the data at the 68% confidence level (Poissonian errors) for a 60% or 50% complete dataset. Model I (negative luminosity evolution) is not consistent with the detection of 3 QSOs at the 99% level for either q_0, with either completeness estimate. Figures 6.9 (a) & (b) illustrate these results. The solid lines show the results for the model of Boyle, Shanks & Peterson (1988b) with an extrapolation to $3.4 < z < 4.1$; broken lines indicate the predictions for each model. The thick short lines in the first diagram for $q_0 = 0.5$ reproduce the provisional luminosity function of Warren, Hewett & Osmer (1988) for $z = 3$ and $z = 4$; the point representing the Edinburgh Multicolour Survey data does not seem to support a straightforward extrapolation of this LF to higher luminosities.

Figure 6.9: Luminosity functions as predicted by models 0, I and II with the Edinburgh Multicolour Survey point. The solid lines represent a simple extrapolation of the UVX-based model of Boyle Shanks & Peterson (1988b), dotted lines show results for the three models, and the point indicates the result from the Edinburgh survey with 68% confidence limits. The first plot also shows the higher-redshift luminosity functions from Warren, Hewett & Osmer (1988).

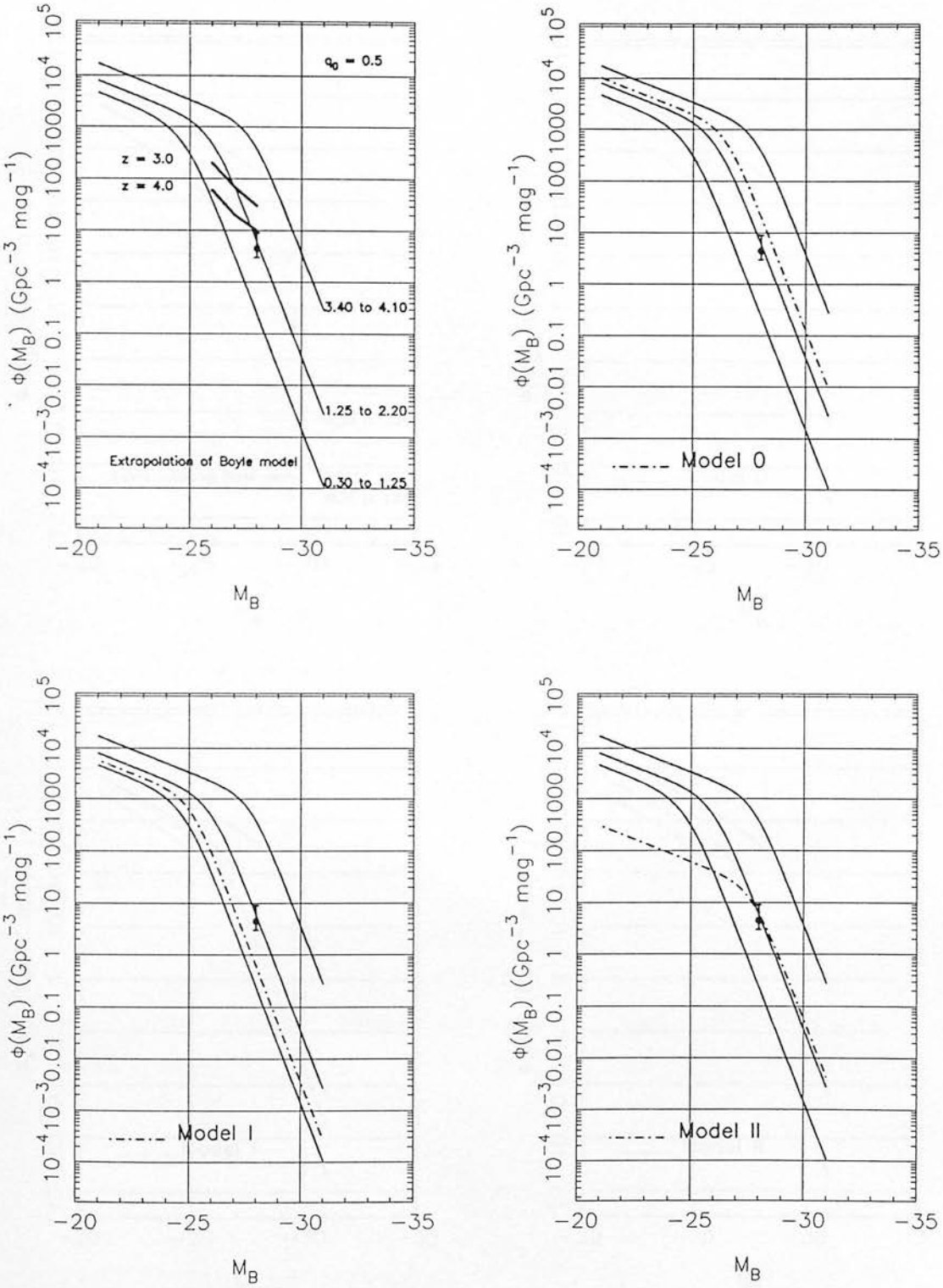

Figure 6.9: continued

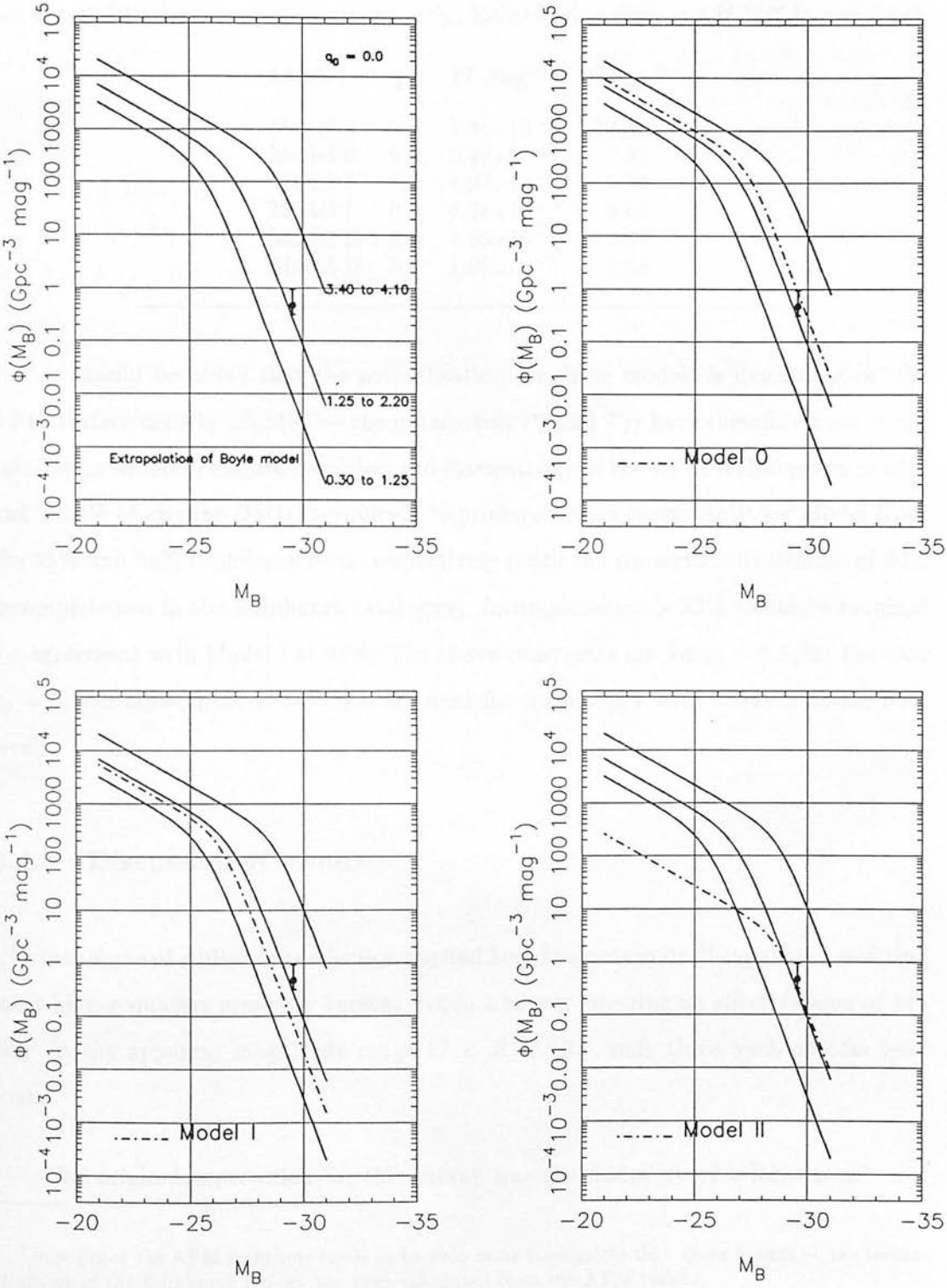

Table 6.11: Surface densities predicted for the luminosity function of Boyle, Shanks & Peterson (1988b), for different evolutionary models (see text). The last column gives values for a survey of 144.87 deg^2 in the range $17 < R < 18.5$ for quasars with $3.4 < z < 4.1$ (the corrected number for the Edinburgh survey is 5 if 60% incomplete).

Model	q_0	N deg^{-2}	N_{total}
Model 0	0.5	1.44×10^{-1}	20.86
Model 0	0.0	5.43×10^{-2}	7.87
Model I	0.5	4.97×10^{-3}	0.72
Model I	0.0	4.58×10^{-3}	0.66
Model II	0.5	4.05×10^{-2}	5.87
Model II	0.0	1.99×10^{-2}	2.88

It should be noted that the normalisation for these models is dependent on the APM surface density adopted — the parameters $\mathcal{P}_I$ and $\mathcal{P}_{II}$ have therefore been recalculated for different surface densities, and insensitivity of the APM technique to $> 38\%$ and $> 21\%$ of existing QSOs is required[1] to produce inconsistent results for Model II, at the 95% and 68% confidence levels respectively (with the conservative estimate of 60% incompleteness in the Edinburgh catalogue). Incompleteness $> 33\%$ would be required for agreement with Model I at 95%. The above comments are for $q_0 = 0.5$; for the case $q_0 = 0$, incompleteness of $> 41\%$ is required for consistency with Model I at the 95% level.

6.4.3 Discussion of results

The technique of multicolour selection applied here has proven itself capable of selecting most high-z quasars presently known. Yet in a survey covering an effective area of 145 deg^2 in the apparent magnitude range $17 < R < 18.5$, only three such objects were found.

The original expectation for this survey was the discovery of a large number of

[1] In practice the APM technique needs to be even more incomplete than these figures — the incompleteness of the Edinburgh Survey has been calculated from the APM results.

high-z quasars. Preliminary results from Hazard, McMahon & Sargent (1986) seemed to indicate that in excess of 25 high-z quasars might be found. Later communications with the APM group reduced the expectations to somewhat smaller values. In order to explain the actual very low surface density measured, the previous examination has followed two very simple evolutionary pictures, chosen because of their small numbers of free parameters, and because they delineate quite well the basic choices available, i.e. continued (though sign-changing) evolution of quasar luminosity versus additional negative density evolution.

The work presented here complements that of the APM group. Their data are still subject to uncertainties, particularly at the intrinsically bright end, but it is interesting that the slope they trace appears to agree with the simple approach of Model II, where the absolute magnitude range probed crosses the "break luminosity" at these redshifts, producing a slope of intermediate value between those at the bright and faint ends of the UVX model, unlike Model I, where the negative luminosity evolution has pushed the break to fainter luminosities.

The presence of "some indication of an excess of bright $M_B \leq -28.0$ high-redshift quasars" of Warren, Hewett & Osmer (1988), admittedly based on "only a handful of objects", finds no confirmation here. If the slope of their luminosity function is accurate, then the indications are that it does not continue to brighter magnitudes: quasars suffers an additional decline in space density. In the simple picture of an evolving two power-law function, it seems that the range in luminosities probed by the two surveys spans the "break"; thus, at luminosities represented by the Edinburgh data-point the Model II slope turns down in agreement with the observations.

Model II produces an apparently "flatter" luminosity function at high redshifts, in general agreement with the suggestions of Hazard, McMahon & Sargent (1986), when compared with results for deeper searches, due to the progression of the "break" point to brighter luminosities. Model I, in contrast leaves the intrinsic slope over the range of luminosities in question unchanged leading to relatively lower predicted densities in such surveys. In order to produce the even flatter LF's postulated by Hazard, it would be necessary to consider more complicated evolutionary pictures such as luminosity-

dependent density evolution (e.g. as discussed at lower redshift by Schmidt & Green 1983) — the increase in free parameters makes testing such a model unfeasible here, and it has been necessary to consider only simple evolutionary forms of the same basic LF shape.

Does the tendency towards lower redshifts detected here lend any credence to the idea of a redshift cutoff? The APM survey does not seem to support belief in any absolute cutoff, and although the number found at the brighter apparent magnitudes sampled here is very small, this again is understandable when examined quantitatively. The small decline in sensitivity as z increases may in some part affect the result as discussed earlier, but this factor is small. The previous tests have indeed shown that the survey remains substantially sensitive well beyond $z = 3.7$. When the redshift distributions for Model II are considered the result appears reasonable: for $3.4 \leq z \leq 3.8$, the model predicts 4.4 quasars for $q_0 = 0.5$; in the whole range $3.8 \leq z \leq 4.5$ only 2.5 more quasars are calculated (100% completeness in the dataset). A continued strong decline in space density within a specified luminosity range seems evident, as in the APM result. There are also strong reasons to avoid concluding the presence of a cutoff: this has been proposed at various times in the past to explain null detections beyond a given redshift, and subsequently superseded as detection techniques improve.

It should be emphasised that the toy models considered here have no direct theoretical basis. The models considered have, of necessity, only one free evolutionary parameter; furthermore, the evolutionary form is highly simplified. Further simple situations could have been considered (such as LF "freezing" at $z \sim 2.5$ coupled with negative density evolution), but were not pursued — results would largely follow the trends in Models I and II, namely that the LF shape at $M_B \simeq -28$ (the "cross-over" luminosity between the APM survey and the Edinburgh Multicolour Survey) is the chief factor in determining the result. The steep power-law form at this magnitude for Model I (and thus all simple models where the break luminosity remains fainter than this value) seems to preclude the (relatively) high surface density measured. The situation is analogous to that in the 1970s for quasars at lower redshift, where the lack of a well-filled redshift-magnitude diagram restricted the number of free parameters

available, so that Mathez (1976) for example could only consider either pure density evolution or luminosity evolution as competing schemes. Nevertheless, the implications of the result presented here are that a genuine decrease in the comoving space density of QSOs with $3.4 \leq z \leq 4.1$ may be required compared with that for $z \sim 2.2$ — a systematic evolution in luminosity is not sufficient to match the surface densities for bright and fainter quasars simultaneously, as it appears to be for $0.3 < z < 2.2$ QSOs. The dramatic claims of a changed LF shape by Hazard, McMahon & Sargent (1986) do not however appear justified: the lack of information as to how many plates were searched, and how many of these resulted in no detections may have produced excessive surface density estimates.

The model of pure luminosity evolution is conceptually straightforward for $z \leq 2.2$, most simply representing a uniform dimming of long-lived quasars. Its extension in Model I to higher redshifts is however harder to imagine — here the sign of the evolution changes, and an initial phase of luminosity increase is hard to conceive for single objects. If this model were shown to represent the real situation in a reasonably straightforward sense, the implications are that the luminosity behaviour is representative more of the evolution of the *properties* of more shorter-lived objects, dependent for instance on environmental changes. The form of Model II is perhaps somewhat easier to understand. The uniform dimming of quasars seen at lower redshifts is extrapolated backwards to earlier epochs, accompanied by a change in birth-rate at $z \sim 2.5$: this model again implies shorter QSO lifetimes. However such abrupt changes in evolutionary form would be hard to explain.

It is certainly very difficult to produce a single model to describe equally well the behaviour at both ends of the redshift scale. Comprehensive attempts in the past have only been made for $z \lesssim 3.5$. Koo (1983) in a preliminary study of field SA57 stated that a model which preserves the LF shape but combines luminosity and density evolution such that at higher redshift, fewer but brighter quasars were seen, was consistent with faint counts. This conclusion was qualified in Koo (1985), where evidence for the density decrease implied in the previous account was shown to be less compelling, and PLE successfully fitted to $z \lesssim 2.5$. The lack of spectroscopic confirmations above $z \sim 2.7$

however meant that a cutoff at higher z was still considered a possible interpretation. On completion of the survey, and backed up by counts in field SA68, Koo & Kron (1988) proposed a further scheme based on an isolated epoch of formation with a constant QSO birth-rate, outside of which no more QSOs are born. Here the more luminous quasars burn out faster; QSOs do not however evolve in luminosity. The physical result of this is that the bright end of the two power-law LF flattens with increasing redshift, and that the amplitude itself should decrease at cosmic times prior to the end of the formation epoch. In applying this model to their faint survey, adding data from other established surveys, and extrapolating to $z = 3.5$, they found successful fits for $q_0 = 0$ and 0.5. However at higher redshift these models are clearly inadequate, predicting excessive surface densities, as is recognised by the authors (see Marshall 1988 and the following discussion). Heisler & Ostriker (1988a) combined LDDE and luminosity evolution to represent the behaviour of quasars from a variety of surveys, and indeed showed that the combined model fitted the data better than each individual form. However, the models again fail badly at $z > 3$, when compared to the actual counts from the surveys of Koo & Kron, Osmer etc. in predicting far too many quasars. They conclude that the redshift cutoff of Osmer (1982) may still be the only way to describe the observations:

> "This inconsistency cannot be resolved and leads one to consider that the density of quasars at all redshifts may not be describable by a single equation."

The present models are indeed not "single equation"s, but rather an abrupt transition from one evolutionary state to another. However, they do not involve a redshift cutoff (Model II has negative density evolution), and they do predict correctly the observed densities where the single model fails. In the case of Koo & Kron, for instance, using the compiled data in Heisler & Ostriker (1988a), which predicts a ratio 0.081 for the number of quasars $3 \leq z \leq 4$ compared to that $2 \leq z \leq 3$ (see Table 5 in this paper[2]), Model II ($q_0 = 0.5$, $B \lesssim 22.5$) here predicts a ratio of 0.093, clearly in excellent agreement (Model I again predicts an excessive ratio of 0.35). This is in sharp contrast to the over-densities by factors $\sim$10 in the single model.

[2]Note that the figures for $N(3-4)/N(2-3)$ in Heisler & Ostriker (1988a) are incorrectly placed in column 2.

As a modification to this result, Heisler & Ostriker (1988b) present a model with dust-obscuration to explain the paucity of high-z detections. The combination LE and LDDE model of (1988a) is re-fitted with an expression for optical depth as a function of redshift taken from an analytic fit to the Galaxy's UV extinction curve from Seaton (1979), extrapolated in a linear manner at both ends. This is applied to dust in intervening galaxies with constant comoving number density. They again find that the combination model works best, giving a large, though supposedly justifiable χ^2. The predictions are in better agreement with the Koo & Kron results, although still over-estimating by factors of 2 or so. However, it is apparent that this model still fails at higher redshift (and brighter magnitudes), predicting only about 0.5 QSOs for 150 deg^2 (100% complete). When tested with Hazard's results, the prospects worsen.

There appears to be no reason to attempt to fit models for the LF where the slope between faint (Koo & Kron) luminosities and those studied here is as high at that seen at the faint end of the UVX LF; rather a slope intermediate in value between that and the bright-end slope seems appropriate. The comoving density for faint magnitudes *must* decrease by factors of $\sim$50 or more while maintaining similar comoving densities per unit absolute magnitude at $z \sim 4$ to those at $z \sim 2$. This has been the problem inherent in previous models, which cannot predict such a change in LF form via a single evolutionary expression.

What happens to the luminosity function for $z \simeq 4$ at even brighter luminosities than those sampled here? Does the LF continue in the relatively sudden decline suggested by these data, in accordance with Model II, or does the extrapolated APM slope continue? These questions could be answered by pursuing the current approach in currently unexamined fields within the survey, and increasing survey area and/or apparent magnitude depth (clearly limited by the plate material). More quasars are needed in this important luminosity range in order to quantify exactly what is going on. What has become clear from these investigations is the need for well-calibrated data — when searching for such rare objects, any small fraction of spurious images outside the stellar locus can increase observational candidate lists to an unworkable number. The need for very strict morphological separation and the rejection of very

close images is also obviously a drawback, biasing as it does against close pairs, but has been necessary to get as close into the stellar locus as has been achieved, making possible the quoted levels of completeness. Further improvements in calibration would therefore be welcomed in order that these restrictions may be relaxed somewhat. The process of calibration in this thesis has been conducted in a thorough manner and at these levels the limitations of the photographic material are already apparent. The advantages of other media for the acquisition of data such as CCD's is obvious and these are indeed becoming popular for such searches (see e.g. Anderson & Schechter 1988) but the lack of very large field coverage means that photographic-based techniques will probably remain popular for some time yet.

References

Aaronson, M., Bothun, G.D., Dawe, J.A., Dickens, R.J., Han Ming Sheng, Hall, P.J., Huchra, J., Lucey, J.R., Mould, J.R., Murray, J.D., Schommer, R.A. & Wright, A.E., 1988. *Ap. J.*, preprint.

Anderson, S.F. & Schechter, P.L. 1988. *Proceedings of a Workshop on Optical Surveys for Quasars, eds. Osmer, P.S., Porter, A.C., Green, R.F. & Foltz, C.B.,* **Astronomical Society of the Pacific Conference Series**, 125.

Arp, H. 1980. *Astrophys. J.*, **239**, 463.

Arp, H. 1987. *Observational Cosmology, IAU Symp. No. 124, eds. Hewitt, A., Burbidge, G. & Fang, L.Z.,* **479**, Reidel, Dordrecht, Holland.

Bahcall, J.N. & Soneira, R.M. 1980. *Astrophys. J. Suppl.*, **44**, 73.

Bahcall, N.A. & Soneira, R.M. 1983. *Astrophys. J.*, **270**, 20.

Baldwin, J.A. 1975. *Astrophys. J.*, **201**, 26.

Baldwin, J.A. 1977. *Astrophys. J.*, **214**, 679.

Baldwin, J.A. 1977. *Active Galactic Nuclei, eds. Hazard, C. & Mitton, S.,* **51**, Cambridge University Press.

Baldwin, J.A. & Stone, R.P.S. 1984. *Mon. Not. R. astr. Soc.*, **206**, 241.

Bessell, M.S. *VRI Photometry III*, Mt. Stromlo & Siding Spring Obs. Preprint.

Blair, M. & Gilmore, G. 1982. *Pub. A.S.P.*, **94**, 742.

Blumenthal, G.R., Dekel, A. & Primack, J.R. 1988. *Astrophys. J.*, **326**, 539.

Bond, J.R. & Szalay, A.S., 1983. *Astrophys. J.*, **277**, 243.

Borra, E.F. & Lepage, R. 1986. *Astron. J.*, **92**, 203.

Boyle, B.J., Fong, R., Shanks T. & Peterson, B.A. 1987. *Mon. Not. R. astr. Soc.*, **227**, 717.

Boyle, B.J., Shanks, T. & Peterson, B.A. 1988a. *Proceedings of a Workshop on Optical Surveys for Quasars, eds. Osmer, P.S., Porter, A.C., Green, R.F. & Foltz, C.B.,* **Astronomical Society of the Pacific Conference Series**, 1.

Boyle, B.J., Shanks, T. & Peterson, B.A. 1988b. *Mon. Not. R. astr. Soc.*, **235**, 935.

Braccesi, A., Formiggini, L. & Gandolfi, E., 1970. *Astr. Astrophys.*, **5**, 264.

Braccesi, A., Zitelli, V., Bonoli, F. & Formiggini, L., 1980. *Astr. Astrophys.*, **85**, 80.

Burstein, D. & Heiles, C. 1982. *Astron. J.*, **87**, 1165.

Cannon, R.D., Hawarden, T.G., Sim, M.E. & Tritton, S.B. 1978. *The U.K. 1.2m Schmidt Telescope and the Southern Sky Survey; II – Photographic Techniques,* **Occ. Rep. R. Obs. Edin.**, No. 4.

Carswell, R.F. & Smith, M.G. 1978. *Mon. Not. R. astr. Soc.*, **185**, 381.

Chaffee, F.H., Foltz, C.B., Frye, B., Hewett, P.C., MacAlpine, G.M., Turnshek, D.A., Weymann, R.J. & Anderson, S.F. 1988. *Pub. A.S.P.*, **100**, 1217.

Chu, Y.Q. & Zhu, X.F. 1983. *Astrophys. J.*, **267**, 4.

Clowes, R.G. 1986. *Mon. Not. R. astr. Soc.*, **218**, 139.

Clowes, R.G. 1987. *Mon. Not. R. astr. Soc.*, **227**, 921.

Clowes, R.G., Cooke, J.A. & Beard, S.M. 1984. *Mon. Not. R. astr. Soc.*, **207**, 99.

de Vaucouleurs, G.H., 1986. *Galaxy Distances and Deviations from the Hubble Flow, eds. Madore, B.F. & Tully, R.B.,* **55**, Reidel, Dordrecht, Holland.

Collins, C.A., Joseph, R.D. & Robertson, N.A. 1986. *Nature*, **320**, 506.

Conover, W.A. 1980. *Practical Nonparametric Statistics*, Wiley, New York.

Crampton, D., Schade, D. & Cowley, A.P. 1985. *Astron. J.*, **90**, 987.

Crampton, D., Cowley, A.P. & Hartwick, F.D.A. 1987. *Astrophys. J.*, **314**, 129.

Crampton, D., Cowley, A.P. & Hartwick, F.D.A. 1988. *Proceedings of a Workshop on Optical Surveys for Quasars, eds. Osmer, P.S., Porter, A.C., Green, R.F. & Foltz, C.B.,* **Astronomical Society of the Pacific Conference Series**, 254.

Cristiani, S. & Vio, R. 1989. *Astronomy & Astrophysics*, preprint.

Davidson, K. & Netzer H. 1979. *Rev. Mod. Phys.*, **51**, 715.

Davies, R.D., Lasenby, A.N., Watson, R.A., Daintree, E.J., Hopkins, J., Beckman, J., Sanchez-Almeida, J. & Rebolo, R. 1987. *Nature,* **326**, 462.

Dawe, J.A., Coyte, E. & Metcalfe, N. 1984. *Astronomical Photography, eds. Sim, M.E. & Ishida, K., Occ. Rep. R. Obs. Edin,* **14**, 59.

Dicke, R.H., Peebles, P.J.E., Roll, P.G. & Wilkinson, D.T. 1965. *Astrophys. J.*, **142**, 414.

Dunlop, J.S. 1987. *Ph.D. Thesis*, University of Edinburgh.

Efstathiou, G. & Rees, M.J. 1988. *Mon. Not. R. astr. Soc.*, **230**, 5P.

Foltz, C.B., Chaffee, F.H., Jr., Hewett, P.C., MacAlpine, G.M., Turnshek, D.A., Weymann, R.J. & Anderson, S.F. 1987. *Astron. J.*, **94**, 1423.

Formiggini, L., Zitelli, V., Bonoli, F. & Braccesi, A. 1980. *Astr. Astrophys. Suppl. Ser.*, **39**, 129.

Frenk, C.S. 1988. *Large Scale Structures of the Universe, IAU Symp. No. 130, eds. Audouze, J., Pelletan, M. & Szalay, A.*, **259**, Kluwer, Dordrecht, Holland..

Frenk, C.S., White, S.D.M. & Davis, M. 1983. *Astrophys. J.*, **271**, 417.

Gilmore, G. 1982. *A Workshop On Astronomical Measuring Machines, eds. Stobie, R.S. & McInnes, B., Occ. Rep. R. Obs. Edin,* **10**, 259.

Grandi, S.A. 1981. *Astrophys. J.*, **251**, 451.

Grandi, S.A. 1982. *Astrophys. J.*, **255**, 25.

Green, R.F., Schmidt, M. & Liebert, J. 1986. *Astrophys. J. Suppl.*, **61**, 305.

Gunn, J.E. 1979. *Observational Cosmology, Proc. 8th Saas-Fee Course, eds. Maeder, Martinet & Tammann,* **3**, Geneva Observatory.

Harris, W.E., Fitzgerald, M.P. & Reed, B.C. 1981. *Pub. A.S.P.*, **93**, 507.

Hawkins, M.R.S. 1981. *Nature,* **293**, 116.

Hawkins, M.R.S. 1983. *Mon. Not. R. astr. Soc.*, **202**, 517.

Hawkins, M.R.S. 1985. *Mon. Not. R. astr. Soc.*, **216**, 589.

Hawkins, M.R.S. 1986. *Mon. Not. R. astr. Soc.*, **219**, 417.

Hawkins, M.R.S. 1987. *Observational Cosmology, IAU Symp. No. 124, eds. Hewitt, A., Burbidge, G. & Fang, L.Z.*, **691**, Reidel, Dordrecht, Holland.

Hayes, D.S. & Latham, D.W. 1975. *Astrophys. J.*, **197**, 593.

Hazard, C., Morton, D.C., Terlevich, R. & McMahon, R. 1984. *Astrophys. J.*, **282**, 33.

Hazard, C. & McMahon, R. 1985. *Nature,* **314**, 238.

Hazard, C. 1986. *in A Workshop on Modern Instrumentation and its Influence on Astronomy at Herstmonceux*

Hazard, C., McMahon, R. & Sargent, W.L.W. 1986. *Nature,* **322**, 39.

Hazard, C., Morton, D.C., McMahon, R., Sargent, W.L.W. & Terlevich, R. 1986. *Mon. Not. R. astr. Soc.*, **223**, 87.

Heisler, J. & Ostriker, J.P. 1988a. *Astrophys. J.*, **325**, 103.

Heisler, J. & Ostriker, J.P. 1988b. *Astrophys. J.*, **332**, 543.

Henden, A.A. & Kaitchuck, R.H. 1982. *Astronomical Photometry*, Van Nostrand.

Hewett, P.C., Irwin, M.J., Bunclark, P., Bridgeland, M.T., Kibblewhite, E.J., He, X.T.

& Smith, M.G. 1985. *Mon. Not. R. astr. Soc.*, **213**, 971.
Heydon-Dumbleton, N.H., Collins, C.A. & MacGillivray, H.T. 1989. *Mon. Not. R. astr. Soc.*, **238**, 379.
Hoag, A.A. 1976. *Pub. A.S.P.*, **88**, 860.
Hoag, A.A. & Schroeder, D.J. 1970. *Pub. A.S.P.*, **82**, 1141.
Hoag, A.A. & Smith, M.G. 1977. *Astrophys. J.*, **217**, 362.
Hutchings, J.B., Crampton, D., Campbell, B., Gower, A.C. & Morris, S.C. 1982. *Astrophys. J.*, **262**, 48.
Hutchings, J.B., Crampton, D. & Campbell, B. 1984. *Astrophys. J.*, **280**, 41.
Hubble, E. 1929. *Proc. N. A. S.*, **15**, 168.
Iovino, A. & Shaver, P.A. 1988. *Astrophys. J.*, **330**, L13.
Johnson, H.L. 1966. *Ann. Rev. Astron. Astrophys.*, **4**, 193.
Kolmogorov, A.N. 1933. *Giornale dell' Istituto Italiano degli Attuari*, **4**, 83.
Koo, D.C. 1983. *Proc. 24th Liège Ap. Colloquium, Quasars and Gravitational Lenses, ed. J.P. Swings*, **Liège: Institut d'Astrophysique**, 240.
Koo, D.C. & Kron, R.G. 1982. *Astr. Astrophys.*, **105**, 107.
Koo, D.C., Kron R.G. & Cudworth K.M. 1986. *Pub. A.S.P.*, **98**, 285.
Koo, D.C. & Kron, R.G. 1988. *Astrophys. J.*, **325**, 92.
Kron, R.G. 1988. *Proceedings of a Workshop on Optical Surveys for Quasars, eds. Osmer, P.S., Porter, A.C., Green, R.F. & Foltz, C.B.*, **Astronomical Society of the Pacific Conference Series**, 36.
Kron, R.G. & Chiu, L.T.G. 1981. *Pub. A.S.P.*, **93**, 397.
Kruszewski, A. 1988. *Acta. Astron.*, **38**, 155.
Kwan, J. & Krolik J.H. 1981. *Astrophys. J.*, **250**, 478.
Lewis, D.W., MacAlpine, G.M. & Weedman, D.W. 1979. *Astrophys. J.*, **233**, 787.
Ling, E.N., Frenk, C.S. & Barrow, J.D., 1986. *Mon. Not. R. astr. Soc.*, **223**, 21P.
Longair, M.S. & Scheuer, P.A.G. 1970. *Mon. Not. R. astr. Soc.*, **151**, 45.
Lynden-Bell, D., Faber, S.M., Burstein, D., Davies, R.L., Dressler, A., Terlevich, R.J. & Wegner, G., 1988. *Astrophys. J.*, **326**, 19.
Lynds, R. & Wills, D. 1970. *Nature*, **226**, 532.
MacAlpine, G.M. & Feldman, F.R. 1982. *Astrophys. J.*, **261**, 412.
MacGillivray, H.T. & Dodd, R.J. 1982. *A Workshop On Astronomical Measuring Machines, eds. Stobie, R.S. & McInnes, B., Occ. Rep. R. Obs. Edin*, **10**, 195.
MacGillivray, H.T. & Stobie, R.S. 1984. *Vistas Astr.*, **27**, 433.
McGraw, J.T. & Cawson, G.M. 1988. *Proceedings of a Workshop on Optical Surveys for Quasars, eds. Osmer, P.S., Porter, A.C., Green, R.F. & Foltz, C.B.*, **Astronomical Society of the Pacific Conference Series**, 163.
Magain, P., Surdej, J., Swings, J.-P., Borgeest, U., Kayser, R., Kühr, H., Refsdal, T.J.-L, Remy, M. 1987. *Nature*, **334**, 325.
Marano, B., Zamorani, G. & Zitelli, V. 1986. *Structure & Evolution of Active Galactic Nuclei, Trieste, Italy, eds. Giuricin, G., Mardirossian, F., Mezzetti, M. & Ramella, M.*, **Reidel, Dordrecht, Holland**, 339.
Marano, B., Zamorani, G. & Zitelli, V. 1988. *Mon. Not. R. astr. Soc.*, **232**, 111.
Marshall, H.L., Avni, Y., Tananbaum, H. & Zamorani, G., 1983a. *Astrophys. J.*, **269**, 35.
Marshall, H.L., Tananbaum, H., Zamorani, G., Huchra, J.P., Braccesi, A., & Zitelli, V. 1983b. *Astrophys. J.*, **269**, 42.

Marshall, H.L., Avni, Y., Braccesi, A., Huchra, J.P., Tananbaum, H., Zamorani, G., & Zitelli, V. 1984. *Astrophys. J.*, **283**, 50.
Marshall, H.L. 1985. *Astrophys. J.*, **299**, 109.
Marshall, H.L. 1988. *Proceedings of a Workshop on Optical Surveys for Quasars, eds. Osmer, P.S., Porter, A.C., Green, R.F. & Foltz, C.B.*, **Astronomical Society of the Pacific Conference Series**, 11.
Mathez, G. 1976. *Astr. Astrophys.*, **53**, 15.
Mathez, G. 1978. *Astr. Astrophys.*, **68**, 17.
Mathez, G. & Nottale, L. 1982. *Astr. Astrophys.*, **113**, 336.
Matthews, T.A. & Sandage, A. 1963. *Astrophys. J.*, **138**, 30.
Miller, L. & Mitchell, P.S. 1988. *Proceedings of a Workshop on Optical Surveys for Quasars, eds. Osmer, P.S., Porter, A.C., Green, R.F. & Foltz, C.B.*, **Astronomical Society of the Pacific Conference Series**, 114.
Mitchell, K.J., Warnock, A. III & Usher, P.D. 1984. *Astrophys. J.*, **287**, L3.
Mitchell, K.J. & Usher, P.D. 1988. *Proceedings of a Workshop on Optical Surveys for Quasars, eds. Osmer, P.S., Porter, A.C., Green, R.F. & Foltz, C.B.*, **Astronomical Society of the Pacific Conference Series**, 56.
Murdoch, H.S., Hunstead, R.W., Pettini, M. & Blades, J.C. 1985. *Quasars, IAU Symp. No. 119., eds. Swarup, G. & Kapahi, V.K.*, **Reidel, Dordrecht, Holland**, 569.
Neugebauer, G., Oke, J.B., Becklin, E.E. & Matthews K. 1979. *Astrophys. J.*, **230**, 79.
Noether, G.E. 1967. *Elements of Nonparametric Statistics*, Wiley, New York.
Oemler, A. 1989. *The Minnesota Lectures on Clusters of Galaxies and Large-Scale Structure, ed. Dickey, J.M.*, **Astronomical Society of the Pacific Conference Series**, 5.
Oke, J.B. 1974. *Astrophys. J. Suppl.*, **27**, 21.
Oke, J.B. & Korycansky D.G. 1982. *Astrophys. J.*, **255**, 11.
Oort, J.H., Arp, H. & de Ruiter, H. 1981. *Astr. Astrophys.*, **95**, 7.
Orr, M.J.L. & Browne, I.W.A. 1982. *Mon. Not. R. astr. Soc.*, **200**, 1067.
Osmer, P.S. 1981. *Astrophys. J.*, **247**, 762.
Osmer, P.S. 1982. *Astrophys. J.*, **253**, 28.
Osmer, P.S. & Smith, M.G. 1976. *Astrophys. J.*, **210**, 267.
Osmer, P.S. & Smith, M.G. 1977a. *Astrophys. J.*, **213**, 607.
Osmer, P.S. & Smith, M.G. 1977b. *Astrophys. J.*, **215**, L47.
Osmer, P.S. & Smith, M.G. 1977c. *Astrophys. J.*, **217**, L73.
Osmer, P.S. & Smith, M.G. 1980. *Astrophys. J. Suppl.*, **42**, 333.
Peacock, J.A. 1986. *Mon. Not. R. astr. Soc.*, **223**, 113.
Peacock, J.A., Miller, L. & Longair, M.S. 1986. *Mon. Not. R. astr. Soc.*, **218**, 265.
Penzias, A.A. & Wilson R.W. 1965. *Astrophys. J.*, **142**, 419.
Peterson, B.A. 1988. *Proceedings of a Workshop on Optical Surveys for Quasars, eds. Osmer, P.S., Porter, A.C., Green, R.F. & Foltz, C.B.*, **Astronomical Society of the Pacific Conference Series**, 23.
Puetter, R.C., Smith, H.E., Willner, S.P. & Pipher, J.L. 1981. *Astrophys. J.*, **243**, 345.
Richstone, D.O. & Schmidt, M. 1980. *Astrophys. J.*, **235**, 361.
Ryle, M. & Sandage, A. 1964. *Astrophys. J.*, **139**, 419.
Sandage, A. 1965. *Astrophys. J.*, **141**, 1560.
Sandage, A. 1972. *Astrophys. J.*, **178**, 25.
Sandage, A. & Tammann, G.A., 1988. *Astrophys. J.*, **328**, 1.

Savage, A. & Bolton, J.G. 1979. *Mon. Not. R. astr. Soc.*, **188**, 599.
Savage, A. & Peterson, B.A. 1983. *Early Evolution of the Universe & Its Present Structure IAU Symp. No. 104, eds. Abell, G.O. & Chincarini G.*, **Reidel, Dordrecht, Holland**, 57.
Schmidt, M. 1963. *Nature*, **197**, 1040.
Schmidt, M. 1968. *Astrophys. J.*, **151**, 393.
Schmidt, M. 1970. *Astrophys. J.*, **162**, 371.
Schmidt, M. 1972. *Astrophys. J.*, **176**, 273.
Schmidt, M. & Green, R.F. 1983. *Astrophys. J.*, **269**, 352.
Schmidt, M., Schneider, D.P. & Gunn, J.E. 1986a. *Astrophys. J.*, **306**, 411.
Schmidt, M., Schneider, D.P. & Gunn, J.E. 1986b. *Astrophys. J.*, **310**, 518.
Schmidt, M., Schneider, D.P. & Gunn, J.E. 1987a. *Astrophys. J.*, **316**, L1.
Schmidt, M., Schneider, D.P. & Gunn, J.E. 1987b. *Astrophys. J.*, **321**, L7.
Schmidt, M., Schneider, D.P. & Gunn, J.E. 1988. *Proceedings of a Workshop on Optical Surveys for Quasars, eds. Osmer, P.S., Porter, A.C., Green, R.F. & Foltz, C.B.*, **Astronomical Society of the Pacific Conference Series**, 87.
Seaton, M.J. 1979. *Mon. Not. R. astr. Soc.*, **187**, 73P.
Shanks, T., Fong, R. & Boyle, B.J. 1983. *Nature*, **303**, 156.
Shanks, T., Fong, R., Boyle, B.J. & Peterson, B.A. 1987. *Mon. Not. R. astr. Soc.*, **227**, 739.
Shanks, T., Boyle, B.J. & Peterson, B.A. 1988. *Proceedings of a Workshop on Optical Surveys for Quasars, eds. Osmer, P.S., Porter, A.C., Green, R.F. & Foltz, C.B.*, **Astronomical Society of the Pacific Conference Series**, 244.
Shanks, T., Fong, R. Boyle, B.J. & Peterson, B.A. 1989. *The Epoch of Galaxy Formation, eds. Frenk, C.S., Ellis, R.S., Shanks, T.S., Heavens, A.F. & Peacock, J.A.*, **Kluwer**, 141.
Shaver, P.A. 1984. *Astr. Astrophys.*, **136**, L9.
Shuder, J.M. & MacAlpine, G.M. 1979. *Astrophys. J.*, **230**, 348.
Silk, J., 1968. *Astrophys. J.*, **151**, 459.
Silk, J. 1989. *The Minnesota Lectures on Clusters of Galaxies and Large-Scale Structure, ed. Dickey, J.M.*, **Astronomical Society of the Pacific Conference Series**, 5.
Silk, J. & Vittorio, N. 1987. *Astrophys. J.*, **317**, 564.
Smith, M.G. 1975. *Astrophys. J.*, **202**, 591.
Smith, M.G. 1976. *Astrophys. J.*, **206**, L125.
Smoot, G.F., Bensadoun, M., Bersanelli, M., De Amici, G., Kogut, A., Levin, S. & Witebsky, C., 1987. *Astrophys. J.*, **317**, L45.
Stobie, R.S., Okamura, A.C., Davenhall, A.C. & MacGillivray, H.T. 1984. *Astronomical Photography, eds. Sim, M.E. & Ishida, K., Occ. Rep. R. Obs. Edin*, **14**, 219.
Stobie, R.S., Gilmore, G. & Reid, N. 1985. *Astron. Astrophys. Suppl. Ser.*, **60**, 495.
Stobie, R.S., Sagar, R. & Gilmore, G. 1985. *Astron. Astrophys. Suppl. Ser.*, **60**, 503.
Stobie, R.S. 1986. *Pattern Recognition Letters*, **4**, 317.
Stone, R.P.S. 1977. *Astrophys. J.*, **218**, 767.
Surdej, J. Magain, P., Swings, J.-P., Borgeest, U., Courvoisier, T.J.-L., Kayser, R., Kellermann, K.I., Kühr, H. & Refsdal, S. 1987. *Nature*, **329**, 695.
Surdej, J., Magain, P., Swings, J.-P., Borgeest, U., Courvoisier, T.J.-L, Kayser, R., Kellermann, K.I., Kühr, H., Refsdal, S. 1988a. *Astr. Astrophys.*, **198**, 49.

Surdej, J., Swings, J.-P., Magain, P., Borgeest, U., Kayser, R., Refsdal, S., Courvoisier, T.J.-L., Kellermann, K.I. & Kühr, H. 1988b. *Proceedings of a Workshop on Optical Surveys for Quasars, eds. Osmer, P.S., Porter, A.C., Green, R.F. & Foltz, C.B.*, **Astronomical Society of the Pacific Conference Series**, 182.

Usher, P.D. 1978. *Astrophys. J.*, **222**, 40.

Usher, P.D. 1981. *Astrophys. J. Suppl.*, **46**, 117.

Usher, P.D., Mitchell, K.J. & Warnock, A. III 1988. *Astrophys. J. Suppl.*, **66**, 1.

van den Bergh, S., Herbst, E. & Pritchet, C. 1973. *Astron. J.*, **78**, 375.

Véron, P. 1983. *Proc. 24$^{\text{th}}$ Liège Ap. Colloquium, Quasars and Gravitational Lenses, ed. J.P. Swings*, **Liège: Institut d'Astrophysique**, 210.

Véron, P. 1986. *Astr. Astrophys.*, **170**, 37.

Véron-Cetty M.P. & Véron P. 1984. *ESO Scientific Report*, No. 1.

Wallace, P.T. & Tritton, K.P. 1979. *Mon. Not. R. astr. Soc.*, **189**, 115.

Wampler E.J. & Ponz D. 1985. *Astrophys. J.*, **298**, 448.

Warnock, A. III, Usher, P.D., Mitchell, K.J. & Howell, S.B. 1986. *Mon. Not. R. astr. Soc.*, **218**, 445.

Warren, S.J., Hewett, P.C., Irwin, M.J., McMahon, R.G., Bridgeland, M.T., Bunclark, P.S. & Kibblewhite, E.J. 1987a. *Nature*, **325**, 131.

Warren, S.J., Hewett, P.C. & Irwin, M.J. 1987b. *Observational Cosmology IAU Symp. No. 124, eds. Hewett, A. & Burbidge, G.*, **Reidel, Dordrecht, Holland**, 661.

Warren, S.J., Hewett, P.C., Osmer, P.S. & Irwin M.J. 1987c. *Nature*, **330**, 453.

Warren, S.J., Hewett, P.C. & Osmer, P.S. 1988. *Proceedings of a Workshop on Optical Surveys for Quasars, eds. Osmer, P.S., Porter, A.C., Green, R.F. & Foltz, C.B.*, **Astronomical Society of the Pacific Conference Series**, 96.

Warren, S.J., Hewett, P.C. & Osmer, P.S. 1989. *The Epoch of Galaxy Formation, eds. Frenk, C.S., Ellis, R.S., Shanks, T.S., Heavens, A.F. & Peacock, J.A.*, **Kluwer**, 135.

Webb, J.K., Parnell, H.C., Carswell, R.F., McMahon, R.G., Irwin, M.J., Hazard, C., Ferlet, R. & Vidal-Madjar, A. 1988. *Messenger No. 51*, 15.

Webster, A. 1976a. *Mon. Not. R. astr. Soc.*, **175**, 61.

Webster, A. 1976b. *Mon. Not. R. astr. Soc.*, **175**, 71.

Webster, A. 1982. *Mon. Not. R. astr. Soc.*, **199**, 683.

Weedman, D.W. 1985. *Astrophys. J. Suppl.*, **57**, 523.

Weedman, D.W. & Djorgovski, S. 1988. *Proceedings of a Workshop on Optical Surveys for Quasars, eds. Osmer, P.S., Porter, A.C., Green, R.F. & Foltz, C.B.*, **Astronomical Society of the Pacific Conference Series**, 226.

Weinberg, S. 1972. *Gravitation & Cosmology*, Wiley, New York.

White S.D.M. 1989. *The Minnesota Lectures on Clusters of Galaxies and Large-Scale Structure, ed. Dickey, J.M.*, **Astronomical Society of the Pacific Conference Series**, 5.

Wilkes, B.J. 1986. *Mon. Not. R. astr. Soc.*, **218**, 331.

Wilkinson, D.T., 1988. *Large Scale Structures of the Universe, IAU Symp. No. 130, eds. Audouze, J., Pelletan, M. & Szalay, A.*, **7**, Kluwer, Dordrecht, Holland..

Wills, B.J., Netzer, H. & Wills, D. 1985. *Astrophys. J.*, **288**, 94.

Yang, J., Turner, M.S., Steigman, G., Schramm, D.N. & Olive, K.A., 1984. *Astrophys. J.*, **281**, 493.

Zamorani, G., Zitelli, V. & Marano, B. 1986. *IAU Symposium No. 119., eds. Swarup,*

G. & Kapahi, V.K., **Reidel, Dordrecht, Holland**, 33.
Zhou, Y., Fang, D., Deng, Z. & He, X. 1986. *Astrophys. J.*, **311**, 588.

Appendix A

UKST plates taken for the Edinburgh Multicolour Survey

The tables on the following pages contain information concerning the survey plates. Entries are listed according to field number (789–867), and underlined plate names indicate plates used in compiling the catalogues referred to in this thesis; the tables contain the following information listed by column:

(1) UKST 7-digit plate number, prefixed by the filter/emulsion combination code (U/J/V/OR/I);

(2) UKST field number;

(3) Right ascension of the field centre (equinox 1950);

(4) Declination of the field centre (equinox 1950);

(5) UT date of exposure;

(6) Eastman-Kodak emulsion name;

(7) Schott glass broad-band filter code;

(8) Exposure time in minutes;

(9) Quality grade of plate; the first letter indicates the overall quality (a=best): see UKST documentation for explanations of other symbols;

(10) Survey code: an indication where a plate is taken as part of a major sky survey: 'ER' denotes the deep IIIa-F $0 \leq \delta \leq 15$ UKST Equatorial Survey (an extension of the Southern Sky Survey), and 'I' denotes the deep IV-N $0 \leq \delta \leq -90$ Near-Infrared Sky Survey.

Table A1: UKST plate numbers, centres and parameters used in the survey — see notes at the start of the Appendix.

Plate Number	Field No.	α(1950) of centre	δ(1950)	Date Taken	Emulsion	Filter	Exposure Time	Grade	Survey Code
U10701	789	12 40.0	−0500	86-02-05	IIIaJ	UG1	120.0	bI	
J10702	789	12 40.0	−0500	86-02-05	IIIaJ	GG 395	25.0	a	
OR10703	789	12 40.0	−0500	86-02-05	IIIaF	OG 590	40.0	a	
I10709	789	12 40.0	−0500	86-02-06	IVN	RG 715	90.0	BI4	I
I10710	789	12 40.0	−0500	86-02-06	IVN	RG 715	90.0	BI3	I
V10711	789	12 40.0	−0500	86-02-06	IIaD	GG 495	20.0	bI	
U10716	789	12 40.0	−0500	86-02-07	IIIaJ	UG1	120.0	bI	
OR10717	789	12 40.0	−0500	86-02-07	IIIaF	OG 590	35.0	bIF	
J10720	789	12 40.0	−0500	86-02-08	IIIaJ	GG 395	30.0	a	
V10721	789	12 40.0	−0500	86-02-08	IIaD	GG 495	25.0	aI	
U12347	789	12 40.0	−0500	88-01-17	IIIaJ	UG1	140.0	aE	
V12374	789	12 40.0	−0500	88-01-26	IIaD	GG 495	45.0	bI	
OR12378	789	12 40.0	−0500	88-01-27	IIIaF	OG 590	100.0	BIE3	ER
J12384	789	12 40.0	−0500	88-01-28	IIIaJ	GG 395	35.0	a	
I12394	789	12 40.0	−0500	88-02-10	IVN	RG 715	90.0	bIT	
I12395	789	12 40.0	−0500	88-02-10	IVN	RG 715	90.0	aI	
V12401	789	12 40.0	−0500	88-02-11	IIaD	GG 495	45.0	a	
OR12409	789	12 40.0	−0500	88-02-17	IIIaF	OG 590	100.0	bIE	
J12421	789	12 40.0	−0500	88-02-20	IIIaJ	GG 395	40.0	a	
U12425	789	12 40.0	−0500	88-02-21	IIIaJ	UG1	180.0	a	
U11782	790	13 00.0	−0500	87-04-06	IIIaJ	UG1	165.0	bI	
J11821	790	13 00.0	−0500	87-04-23	IIIaJ	GG 395	35.0	a	
V11822	790	13 00.0	−0500	87-04-23	IIaD	GG 495	30.0	aI	
OR11823	790	13 00.0	−0500	87-04-23	IIIaF	OG 590	70.0	a	
U11831	790	13 00.0	−0500	87-04-24	IIIaJ	UG1	113.1	aE	
V11834	790	13 00.0	−0500	87-04-25	IIaD	GG 495	30.0	a	
J11835	790	13 00.0	−0500	87-04-25	IIIaJ	GG 395	35.0	a	
OR11841	790	13 00.0	−0500	87-04-26	IIIaF	OG 590	45.0	aE	
I11871	790	13 00.0	−0500	87-05-05	IVN	RG 715	90.0	bID	
I11872	790	13 00.0	−0500	87-05-05	IVN	RG 715	90.0	bIF	
I11874	791	13 20.0	−0500	87-05-08	IVN	RG 715	75.0	bID	
I11875	791	13 20.0	−0500	87-05-08	IVN	RG 715	90.0	bD	
V11888	791	13 20.0	−0500	87-05-20	IIaD	GG 495	30.0	a	
U11889	791	13 20.0	−0500	87-05-20	IIIaJ	UG1	120.0	a	
J11890	791	13 20.0	−0500	87-05-20	IIIaJ	GG 395	30.0	aT	
OR11891	791	13 20.0	−0500	87-05-20	IIIaF	OG 590	55.0	a	
V11893	791	13 20.0	−0500	87-05-21	IIaD	GG 495	30.0	a	
J11894	791	13 20.0	−0500	87-05-21	IIIaJ	GG 395	30.0	cT	
J11900	791	13 20.0	−0500	87-05-22	IIIaJ	GG 395	30.0	bI	
OR11901	791	13 20.0	−0500	87-05-22	IIIaF	OG 590	45.0	a	
U11905	791	13 20.0	−0500	87-05-23	IIIaJ	UG1	165.0	bT	
U11916	791	13 20.0	−0500	87-05-25	IIIaJ	UG1	165.0	a	
I11941	791	13 20.0	−0500	87-06-03	IVN	RG 715	90.0	aI	
I11942	791	13 20.0	−0500	87-06-03	IVN	RG 715	90.0	aI	

Table A1: (continued)

Plate Number	Field No.	α(1950) of centre	δ(1950)	Date Taken	Emulsion	Filter	Exposure Time	Grade	Survey Code
I11077	792	13 40.0	−0500	86-04-29	IVN	RG 715	90.0	BIE3	I
V11085	792	13 40.0	−0500	86-05-02	IIaD	GG 495	30.0	aI	
J11088	792	13 40.0	−0500	86-05-03	IIIaJ	GG 395	27.0	a	
U11098	792	13 40.0	−0500	86-05-09	IIIaJ	UG1	120.0	a	
J11102	792	13 40.0	−0500	86-05-10	IIIaJ	GG 395	27.0	a	
V11103	792	13 40.0	−0500	86-05-10	IIaD	GG 495	30.0	a	
U11107	792	13 40.0	−0500	86-05-11	IIIaJ	UG1	90.0	a	
OR11108	792	13 40.0	−0500	86-05-11	IIIaF	OG 590	60.0	BIF3	ER
OR11113	792	13 40.0	−0500	86-05-14	IIIaF	OG 590	60.0	BIE4	ER
I11118	792	13 40.0	−0500	86-05-26	IVN	RG 715	60.0	bF	
I11121	792	13 40.0	−0500	86-05-27	IVN	RG 715	90.0	bE	
OR11127	793	14 00.0	−0500	86-06-01	IIIaF	OG 590	70.0	BIUF4	ER
U11128	793	14 00.0	−0500	86-06-01	IIIaJ	UG1	120.0	a	
J11129	793	14 00.0	−0500	86-06-01	IIIaJ	GG 395	27.0	bI	
J11136	793	14 00.0	−0500	86-06-02	IIIaJ	GG 395	20.0	a	
V11137	793	14 00.0	−0500	86-06-02	IIaD	GG 495	30.0	a	
OR11138	793	14 00.0	−0500	86-06-02	IIIaF	OG 590	35.0	aE	
U11139	793	14 00.0	−0500	86-06-02	IIIaJ	UG1	100.0	aE	
I11180	793	14 00.0	−0500	86-06-13	IVN	RG 715	90.0	A1	I
I11189	793	14 00.0	−0500	86-06-16	IVN	RG 715	90.0	aE	
V11126	793	14 00.0	−0500	86-06-01	IIaD	GG 495	30.0	a	
OR11244	794	14 20.0	−0500	86-07-26	IIIaF	OG 590	30.0	aI	
V11245	794	14 20.0	−0500	86-07-26	IIaD	GG 495	30.0	bI	
J11246	794	14 20.0	−0500	86-07-26	IIIaJ	GG 395	20.0	aI	
U11247	794	14 20.0	−0500	86-07-26	IIIaJ	UG1	90.0	bI	
U11256	794	14 20.0	−0500	86-07-29	IIIaJ	UG1	90.0	a	
OR11257	794	14 20.0	−0500	86-07-30	IIIaF	OG 590	60.0	bI	
V11258	794	14 20.0	−0500	86-07-30	IIaD	GG 495	30.0	bI	
J11260	794	14 20.0	−0500	86-07-31	IIIaJ	GG 395	20.0	a	
I11273	794	14 20.0	−0500	86-08-08	IVN	RG 715	89.0	bI	
I11279	794	14 20.0	−0500	86-08-10	IVN	RG 715	90.0	cIT	
I11284	794	14 20.0	−0500	86-08-12	IVN	RG 715	90.0	cD	
OR11709	794	14 20.0	−0500	87-03-11	IIIaF	OG 590	65.0	aT	
J11718	794	14 20.0	−0500	87-03-12	IIIaJ	GG 395	40.0	a	
U12017	794	14 20.0	−0500	87-07-20	IIIaJ	UG1	150.0	cT	
U12024	794	14 20.0	−0500	87-07-23	IIIaJ	UG1	31.5	cU	
J12028	794	14 20.0	−0500	87-07-24	IIIaJ	GG 395	25.0	a	
U12050	794	14 20.0	−0500	87-07-31	IIIaJ	UG1	170.0	bTE	
I12402	794	14 20.0	−0500	88-02-11	IVN	RG 715	90.0	aI	
OR12413	794	14 20.0	−0500	88-02-18	IIIaF	OG 590	100.0	a	
V12422	794	14 20.0	−0500	88-02-20	IIaD	GG 495	45.0	aI	
J12426	794	14 20.0	−0500	88-02-21	IIIaJ	GG 395	40.0	a	
U12438	794	14 20.0	−0500	88-02-24	IIIaJ	UG1	150.0	a	
I 9985	861	12 40.0	0000	85-03-12	IVN	RG 715	90.0	a	
J10000	861	12 40.0	0000	85-03-14	IIIaJ	GG 395	20.0	bIE	
OR10001	861	12 40.0	0000	85-03-14	IIIaF	OG 590	30.0	aI	

Table A1: (continued)

Plate Number	Field No.	α(1950) of centre	δ(1950)	Date Taken	Emulsion	Filter	Exposure Time	Grade	Survey Code
V10006	861	12 40.0	0000	85-03-16	IIaD	GG 495	40.0	a	
U10011	861	12 40.0	0000	85-03-17	IIIaJ	UG1	87.0	aT	
J10021	861	12 40.0	0000	85-03-21	IIIaJ	GG 395	20.0	a	
OR10022	861	12 40.0	0000	85-03-21	IIIaF	OG 590	30.0	a	
U10023	861	12 40.0	0000	85-03-21	IIIaJ	UG1	90.0	a	
V10038	861	12 40.0	0000	85-03-28	IIaD	GG 495	40.0	bE	
I10046	861	12 40.0	0000	85-03-30	IVN	RG 715	90.0	bIE	
OR11635	861	12 40.0	0000	87-02-06	IIIaF	OG 590	110.0	bIT	
UJ12533P	861	12 40.0	0000	88-04-15	IIIaJ	WG 305	90.0	A1 1E	P1
U10827	862	13 00.0	0000	86-03-10	IIIaJ	UG1	90.0	a	
OR10828	862	13 00.0	0000	86-03-10	IIIaF	OG 590	65.0	bI	
J10836	862	13 00.0	0000	86-03-11	IIIaJ	GG 395	20.0	a	
V10837	862	13 00.0	0000	86-03-11	IIaD	GG 495	30.0	a	
I10847	862	13 00.0	0000	86-03-12	IVN	RG 715	90.0	a	
OR10855	862	13 00.0	0000	86-03-13	IIIaF	OG 590	70.0	AI3	ER
V10856	862	13 00.0	0000	86-03-13	IIaD	GG 495	30.0	a	
J10857	862	13 00.0	0000	86-03-13	IIIaJ	GG 395	30.0	a	
I10863	862	13 00.0	0000	86-03-14	IVN	RG 715	90.0	AEI2	I
U10864	862	13 00.0	0000	86-03-14	IIIaJ	UG1	90.0	a	
OR11921	862	13 00.0	0000	87-05-26	IIIaF	OG 590	75.0	bI	
I10956	863	13 20.0	0000	86-04-01	IVN	RG 715	90.0	BI3	I
OR10963	863	13 20.0	0000	86-04-02	IIIaF	OG 590	80.0	BI3	ER
I10964	863	13 20.0	0000	86-04-02	IVN	RG 715	90.0	BEI2	I
U10972	863	13 20.0	0000	86-04-03	IIIaJ	UG1	90.0	a	
V11003	863	13 20.0	0000	86-04-08	IIaD	GG 495	30.0	a	
OR11025	863	13 20.0	0000	86-04-13	IIIaF	OG 590	70.0	BIF3	ER
J11026	863	13 20.0	0000	86-04-13	IIIaJ	GG 395	30.0	bI	
U11030	863	13 20.0	0000	86-04-14	IIIaJ	UG1	110.0	a	
J11048	863	13 20.0	0000	86-04-16	IIIaJ	GG 395	27.0	a	
V11054	863	13 20.0	0000	86-04-18	IIaD	GG 495	30.0	bI	
UJ11759P	863	13 20.0	0000	87-04-02	IIIaJ	WG 305	65.0	AP1 1N	P1
U10094	864	13 40.0	0000	85-04-13	IIIaJ	UG1	90.0	aI	
J10135	864	13 40.0	0000	85-05-09	IIIaJ	GG 395	20.0	bIF	
I10141	864	13 40.0	0000	85-05-10	IVN	RG 715	90.0	aT	
OR10150	864	13 40.0	0000	85-05-11	IIIaF	OG 590	45.0	aT	
V10159	864	13 40.0	0000	85-05-12	IIaD	GG 495	28.2	a	
U10162	864	13 40.0	0000	85-05-13	IIIaJ	UG1	90.0	bIT	
J10164	864	13 40.0	0000	85-05-14	IIIaJ	GG 395	20.0	aT	
V10173	864	13 40.0	0000	85-05-15	IIaD	GG 495	40.0	a	
OR10174	864	13 40.0	0000	85-05-15	IIIaF	OG 590	45.0	aI	
I10211	864	13 40.0	0000	85-05-27	IVN	RG 715	90.0	aT	
I11204	865	14 00.0	0000	86-06-26	IVN	RG 715	90.0	aU	
V11208	865	14 00.0	0000	86-06-29	IIaD	GG 495	30.0	bI	
J11209	865	14 00.0	0000	86-06-29	IIIaJ	GG 395	20.0	a	
OR11210	865	14 00.0	0000	86-06-29	IIIaF	OG 590	60.0	bI	

Table A1: (continued)

Plate Number	Field No.	α(1950) of centre	δ(1950)	Date Taken	Emulsion	Filter	Exposure Time	Grade	Survey Code
U11216	865	14 00.0	0000	86-07-06	IIIaJ	UG1	90.0	aI	
OR11223	865	14 00.0	0000	86-07-12	IIIaF	OG 590	30.0	a	
V11224	865	14 00.0	0000	86-07-12	IIaD	GG 495	30.0	a	
J11225	865	14 00.0	0000	86-07-12	IIIaJ	GG 395	20.0	bI	
U11226	865	14 00.0	0000	86-07-12	IIIaJ	UG1	90.0	bI	
I11234	865	14 00.0	0000	86-07-13	IVN	RG 715	90.0	bE	
U11923	865	14 00.0	0000	87-05-28	IIIaJ	UG1	180.0	bI	
V11976	865	14 00.0	0000	87-07-01	IIaD	GG 495	45.0	aI	
J11977	865	14 00.0	0000	87-07-01	IIIaJ	GG 395	35.0	bI	
I11996	865	14 00.0	0000	87-07-14	IVN	RG 715	120.0	aID	
OR11998	865	14 00.0	0000	87-07-15	IIIaF	OG 590	110.0	bID	
U12001	865	14 00.0	0000	87-07-16	IIIaJ	UG1	110.0	aT	
U10314	866	14 20.0	0000	85-07-11	IIIaJ	UG1	90.0	a	
J10315	866	14 20.0	0000	85-07-11	IIIaJ	GG 395	20.0	a	
OR10330	866	14 20.0	0000	85-07-19	IIIaF	OG 590	35.0	aP	
V10331	866	14 20.0	0000	85-07-19	IIaD	GG 495	40.0	a	
U10337	866	14 20.0	0000	85-07-20	IIIaJ	UG1	90.0	aT	
J10338	866	14 20.0	0000	85-07-20	IIIaJ	GG 395	20.0	aT	
V10344	866	14 20.0	0000	85-07-21	IIaD	GG 495	40.0	bHU	
OR10347	866	14 20.0	0000	85-07-23	IIIaF	OG 590	45.0	bIT	
I10350	866	14 20.0	0000	85-07-24	IVN	RG 715	90.0	bI	
I10393	866	14 20.0	0000	85-08-20	IVN	RG 715	90.0	cF	
I10910	866	14 20.0	0000	86-03-21	IVN	RG 715	90.0	AI2	I
I11190	866	14 20.0	0000	86-06-16	IVN	RG 715	90.0	aI	
J11702	866	14 20.0	0000	87-03-10	IIIaJ	GG 395	40.0	a	
U11928	866	14 20.0	0000	87-05-30	IIIaJ	UG1	160.0	c	
R11933	866	14 20.0	0000	87-05-31	IIIaF	RG 630	90.0	aUX	
J11951	866	14 20.0	0000	87-06-16	IIIaJ	GG 395	26.5	cT	
V11952	866	14 20.0	0000	87-06-16	IIaD	GG 495	45.0	cT	
I11953	866	14 20.0	0000	87-06-16	IVN	RG 715	85.0	bIF	
I12463	866	14 20.0	0000	88-03-12	IVN	RG 715	90.0	aI	
J12477	866	14 20.0	0000	88-03-15	IIIaJ	GG 395	40.0	a	
V12487	866	14 20.0	0000	88-03-17	IIaD	GG 495	45.0	aI	
OR12521	866	14 20.0	0000	88-04-13	IIIaF	OG 590	100.0	AI3	ER
U12551	866	14 20.0	0000	88-04-20	IIIaJ	UG1	180.0	a	
OR10223	867	14 40.0	0000	85-06-07	IIIaF	OG 590	30.0	bI	
I10224	867	14 40.0	0000	85-06-07	IVN	RG 715	90.0	bIT	
U10252	867	14 40.0	0000	85-06-13	IIIaJ	UG1	100.0	a	
J10266	867	14 40.0	0000	85-06-16	IIIaJ	GG 395	25.0	aT	
V10267	867	14 40.0	0000	85-06-16	IIaD	GG 495	40.0	bI	
J10273	867	14 40.0	0000	85-06-17	IIIaJ	GG 395	20.0	bHE	
U10276	867	14 40.0	0000	85-06-18	IIIaJ	UG1	90.0	aE	
V10280	867	14 40.0	0000	85-06-22	IIaD	GG 495	40.0	bI	
OR10281	867	14 40.0	0000	85-06-22	IIIaF	OG 590	45.0	bI	
J10282	867	14 40.0	0000	85-06-23	IIIaJ	GG 395	25.0	a	
I10290	867	14 40.0	0000	85-06-24	IVN	RG 715	86.0	aT	
UJ11760P	867	14 40.0	0000	87-04-02	IIIaJ	WG 305	65.0	AI2 1N	P1

Appendix B

CCD Photometry Results

The following tables list all CCD observations made for the Edinburgh Multicolour Survey. Each field is labelled as **UUUdr**, where **UUU** is the UKST field number, **d** an indication of position in declination ('n', 'c', 's' for north, centre and south), and **r** for right ascension ('p', 'f' for preceding (low RA) and following (high RA), blank for central). Each field is listed in turn, with right ascension and declination (epoch 1950) coordinates for each object, and results for each waveband *UBVRI*, where appropriate. A key to abbreviations is given at the end of the appendix. Further details for each observing run can be found in Chapter 3.

Table B1: CCD photometry results for the $\delta = -5$ strip.

α(1950)	δ(1950)	U	B	V	R	I
789np	**University of Hawaii 88″ LM, SJL 1986**					
12 37 12.9	−03 40 20			−13.18	−16.23	−15.16
12 37 11.0	−03 40 25			−12.85	−16.02	−15.24
12 37 04.1	−03 40 54			−10.94	−14.18	
12 37 06.9	−03 41 12			−14.36	−17.72	
12 37 07.5	−03 42 03					−13.88
12 37 13.6	−03 41 25				−13.79	−13.16
12 37 10.2	−03 41 51				−12.85	−12.12
12 37 07.5	−03 42 03				−13.25	
12 37 12.0	−03 43 08				−13.54	−13.04
12 37 04.6	−03 41 31				−11.82	−11.00
12 37 07.9	−03 41 27				−10.39	−9.85
12 37 06.9	−03 41 48				−11.26	−10.54
12 37 12.6	−03 41 29				−11.51	−11.00
12 37 12.7	−03 42 44				−10.50	−9.82
12 37 13.6	−03 43 07				−10.69	−10.08
12 37 08.2	−03 44 17				−11.01	−10.33
12 37 07.8	−03 44 52				−11.10	−10.49
12 37 14.8	−03 44 29				−10.50	−10.08
12 37 15.2	−03 44 33				−11.59	−10.63
789cf	**University of Hawaii 88″ LM, SJL 1986**					
12 39 11.8	−05 09 58				−10.86	
12 39 09.0	−05 11 12				−10.67	
12 39 07.2	−05 11 49				−9.77	
12 39 18.3	−05 12 33				−11.21	−13.17
12 39 10.6	−05 09 44	−12.21	−14.47	−13.45	−8.46	
12 39 13.5	−05 11 12				−9.32	
12 39 16.9	−05 11 00				−10.37	

Table B1: (continued) CCD photometry results.

α(1950)	δ(1950)	U	B	V	R	I
12 39 17.7	−05 11 53				−7.88	
12 39 07.2	−05 12 33	−13.27	−16.59		−13.36	−14.25
12 39 08.2	−05 12 57				−9.02	−10.95
12 39 07.8	−05 13 22					−9.14
12 39 16.6	−05 13 07					−9.32
12 39 07.2	−05 11 05	−11.09	−13.48	−12.45		
12 39 16.1	−05 07 21	−11.13	−14.14	−13.38		
12 39 13.9	−05 06 54	−10.03	−12.23	−11.23		
12 39 19.7	−05 09 49	−10.90	−13.13	−12.21		
12 39 18.7	−05 06 11		−10.60	−10.25		
12 39 10.0	−05 08 04		−9.10	−8.89		
12 39 08.4	−05 07 14		−9.00	−8.62		
789cp	**Isaac Newton Telescope RSS, RDC, WKG 1986**					
12 33 31.2	−05 08 40	−13.34	−15.87	−16.65	−16.94	
12 33 38.1	−05 09 52	−10.25	−13.76	−14.85	−15.34	−15.18
12 33 38.1	−05 09 38		−8.22	−9.44	−10.91	−10.05
12 33 33.7	−05 09 18	−8.48	−11.98	−12.91	−13.42	−13.24
12 33 31.7	−05 10 42	−9.79	−12.63	−13.53	−13.98	−13.83
12 33 41.9	−05 09 45			−12.27	−12.91	−12.69
12 33 22.1	−05 11 13			−8.23	−9.09	−8.92
12 33 23.7	−05 09 44	−9.25	−12.06	−12.74	−13.11	−12.87
12 33 21.9	−05 08 46			−8.21	−9.27	−9.27
12 33 24.6	−05 08 15	−7.46	−9.90	−10.43	−10.73	−10.19
12 33 29.7	−05 09 26			−8.44	−9.15	−8.97
12 33 29.2	−05 08 31			−8.40	−9.46	−10.37
12 33 30.9	−05 11 06			−8.29	−8.71	−8.63
12 33 36.1	−05 11 09				−8.92	−9.06
12 33 40.5	−05 11 08		−7.95	−9.18	−10.07	−10.09

Table B1: (continued) CCD photometry results.

α(1950)	δ(1950)	U	B	V	R	I
12 33 41.7	−05 08 19				−8.52	
12 33 39.6	−05 10 16					−9.15
789s	**ESO-Danish 1.5m PSM, LM 1986**					
12 45 46.3	−06 13 07		−13.97	−14.84	−14.48	−14.49
12 45 46.7	−06 11 08		−12.71	−13.67	−13.36	−13.42
12 45 43.0	−06 12 36		−11.60	−12.87	−12.67	−12.81
12 45 46.5	−06 11 34		−10.30	−11.73	−11.70	−11.93
12 45 41.2	−06 12 13		−10.22	−11.35	−11.12	−11.29
12 45 45.8	−06 14 02		−9.83	−11.08	−10.94	−11.11
12 45 43.8	−06 13 49		−8.94	−9.98	−9.72	−9.83
12 45 45.1	−06 12 19		−8.33	−9.62	−9.49	−9.69
12 45 40.7	−06 10 52		−7.91	−8.99	−8.76	−8.88
12 45 42.3	−06 11 27		−6.68	−8.60	−9.22	−10.33
12 45 42.5	−06 12 18		−7.88	−9.13	−8.99	−9.49
12 45 43.9	−06 11 43		−7.14	−8.21	−7.92	−8.07
12 45 45.2	−06 12 06		−6.32	−7.28	−6.90	−7.01
12 45 45.7	−06 12 33			−6.76	−6.46	−6.52
12 45 40.4	−06 13 43			−6.91	−7.23	−7.88
12 45 41.8	−06 12 36			−6.86	−7.31	−8.10
12 45 40.1	−06 14 07			−6.47	−6.29	
12 45 47.6	−06 13 10					−7.07
790nf	**ESO-Danish 1.5m PSM, LM 1986**					
13 02 14.2	−03 32 35		−14.82	−15.09	−14.76	−14.61
13 02 09.6	−03 30 52		−13.03	−13.97	−13.63	−13.54
13 02 14.2	−03 33 38		−9.40	−10.73	−10.79	−10.80
13 02 12.6	−03 33 35		−9.50	−10.48	−10.25	−10.14
13 02 13.6	−03 32 53		−10.50	−11.50	−11.25	−11.16

Table B1: (continued) CCD photometry results.

α(1950)	δ(1950)	U	B	V	R	I
13 02 08.8	−03 32 03		−8.70	−9.83	−9.72	−9.70
13 02 07.9	−03 30 24		−6.61	−8.02	−7.95	
13 02 12.1	−03 30 25		−8.42	−9.29	−8.95	−8.87
13 02 14.1	−03 30 58		−6.72	−8.28	−8.48	−8.75
13 02 15.0	−03 32 22		−7.52	−8.61	−8.41	−8.49
13 02 15.4	−03 32 03			−7.52	−7.92	−8.57
13 02 15.3	−03 31 49			−7.13	−7.59	−8.45
790cp	**Isaac Newton Telescope RSS, RDC, WKG 1986**					
12 57 06.0	−05 40 39	−10.46				
12 57 04.2	−05 40 52	−10.12	−12.54	−12.78		−13.06
12 56 51.4	−05 39 51	−9.94	−12.17	−12.29		−12.50
12 56 51.5	−05 40 33	−8.65	−10.94	−11.08	−11.80	−11.30
12 56 48.9	−05 40 23		−9.22	−9.63	−10.57	−10.27
12 56 57.3	−05 39 47	−7.51	−9.90	−10.12	−10.87	−10.51
12 57 02.9	−05 39 36	−6.69	−9.65	−9.97	−10.78	−10.47
12 57 10.5	−05 39 46		−9.95	−9.96	−10.55	−10.07
12 56 58.3	−05 40 25		−8.17	−8.39	−9.19	−8.84
12 56 55.9	−05 40 35		−8.38	−8.55	−9.29	−8.86
12 56 55.0	−05 40 37			−7.51	−8.49	−8.29
12 56 49.7	−05 40 53		−7.88	−8.40	−9.31	−9.03
12 56 47.3	−05 41 55				−7.99	−7.75
12 56 48.1	−05 41 46				−8.19	−8.35
12 56 49.0	−05 42 13				−7.95	−8.32
12 56 57.7	−05 42 43					
12 57 03.9	−05 42 24				−7.83	−8.36
12 57 04.8	−05 42 33				−7.46	
12 57 05.5	−05 43 15				−7.93	
12 57 10.1	−05 42 57					
12 57 03.2	−05 41 13				−7.88	−9.33

Table B1: (continued) CCD photometry results.

α(1950)	δ(1950)	U	B	V	R	I
791nf	**University of Hawaii 88″ LM, SJL 1986**					
13 25 06.1	−03 54 58	−8.88	−11.38	−11.88	−13.42	−12.55
13 25 07.4	−03 55 12	−13.52	−14.78	−14.89	−16.10	−14.80
13 25 10.6	−03 55 10	−11.63	−12.90	−13.05	−14.04	−13.01
13 25 10.3	−03 54 05					−9.37
13 25 01.1	−03 54 30				−10.71	
13 25 06.2	−03 54 30	−8.19	−10.30	−10.61	−12.01	−10.96
13 25 09.4	−03 54 56	−10.00	−11.35	−11.51	−12.63	−11.56
13 25 11.9	−03 54 47					−9.27
13 25 03.4	−03 55 20				−10.32	−9.39
13 25 06.4	−03 55 16					−10.27
13 25 11.0	−03 51 47	−11.77			−14.16	−12.99
13 25 09.9	−03 51 16				−13.54	−12.44
13 25 05.1	−03 51 38	−10.69	−11.87	−12.08	−13.36	−12.02
13 25 08.9	−03 52 23	−10.48	−11.65	−11.76	−13.00	−11.82
13 25 09.6	−03 51 34				−10.45	−10.27
13 25 07.2	−03 52 10	−8.30	−9.83	−10.18	−11.58	−10.43
13 25 01.0	−03 52 48				−10.70	−9.39
13 25 03.6	−03 52 42				−9.14	−7.91
13 25 06.7	−03 53 00	−9.85	−11.66	−11.93	−13.32	−12.19
13 25 13.0	−03 52 11				−9.37	
13 25 11.8	−03 53 08	−10.22	−11.28	−11.36	−12.46	−11.32
13 25 03.5	−03 53 17				−10.75	−9.69
13 25 05.6	−03 53 23				−8.74	−8.40
13 25 06.0	−03 53 30	−7.85	−8.54	−8.78	−10.20	−8.97
13 25 03.2	−03 53 39				−9.36	−8.47
13 25 00.5	−03 54 03				−11.88	−10.71
13 25 10.7	−03 54 10	−9.60	−10.64	−10.68	−11.78	−10.76

Table B1: (continued) CCD photometry results.

α(1950)	δ(1950)	U	B	V	R	I
791c	**Isaac Newton Telescope RSS, RDC, WKG 1986**					
13 20 06.2	−04 47 51	−10.69	−13.98	−14.01	−14.47	−14.02
13 20 04.3	−04 45 18	−10.83	−13.75	−13.69	−14.02	−13.51
13 20 10.1	−04 46 09	−10.02	−12.99	−13.11	−13.66	−13.27
13 19 53.4	−04 47 54		−11.53	−11.63	−12.18	−11.66
13 19 57.2	−04 46 34	−8.87	−10.98	−11.27	−11.88	−11.65
13 19 57.9	−04 46 02	−7.17	−11.61	−11.58	−11.90	−11.51
13 20 02.5	−04 47 22	−8.69	−11.61	−11.58	−11.90	−11.51
13 20 09.3	−04 48 57		−10.88	−11.36		−11.99
13 20 15.4	−04 47 54		−8.31	−8.96	−9.94	−10.63
13 20 13.4	−04 47 25		−9.17	−9.32	−9.85	−9.53
13 20 11.2	−04 46 36		−9.46	−9.45	−9.82	−9.39
13 20 06.8	−04 47 17		−7.46	−8.13	−9.00	−9.16
13 20 04.8	−04 46 54	−6.49	−9.31	−9.39	−9.81	−9.53
13 20 06.1	−04 45 33			−7.36	−8.42	−8.97
13 20 01.8	−04 47 56		−7.72	−8.02	−8.63	−8.35
13 19 59.9	−04 47 02		−7.66		−7.98	−7.50
13 19 55.4	−04 45 55			−7.28	−7.94	−7.80
13 19 59.3	−04 48 58				−7.23	−7.68
13 19 53.0	−04 48 25		−8.70	−9.51	−10.49	−11.27
13 19 51.5	−04 47 51				−7.29	−7.28
792c	**ESO-Danish 1.5m PSM, LM 1986**					
13 40 40.7	−04 42 47	−12.78	−12.67	−13.62	−13.22	−13.23
13 40 33.9	−04 44 08		−11.39	−12.55	−12.26	−12.36
13 40 32.9	−04 43 10	−9.57	−9.25	−10.30	−9.93	−10.06
13 40 35.7	−04 45 06		−9.34	−10.34	−10.00	−10.04
13 40 40.6	−04 43 32	−8.49	−9.63	−10.03	−9.80	−9.89

Table B1: (continued) CCD photometry results.

α(1950)	δ(1950)	U	B	V	R	I
13 40 36.9	−04 43 58	−7.43	−7.53	−8.69	−8.49	−8.64
13 40 39.3	−04 43 12	−6.72	−6.74	−7.86	−7.60	−7.78
13 40 40.0	−04 44 52		−6.28	−7.81	−7.82	−8.11
13 40 38.5	−04 45 20		−6.06	−7.26	−6.98	−7.07
13 40 38.0	−04 43 10		−6.02	−7.39	−7.21	−7.35
13 40 38.3	−04 42 45			−6.82	−6.55	−6.65
13 40 40.0	−04 42 53			−6.98	−6.97	−7.30
13 40 41.0	−04 45 09			−6.96	−7.02	−7.25
13 40 41.1	−04 44 39	−6.12		−7.00	−6.69	−6.77
13 40 42.3	−04 43 15				−6.20	
13 40 39.1	−04 44 54			−6.90		
13 40 41.9	−04 44 28			−6.27		
13 40 40.1	−04 44 33					−6.46
13 40 33.6	−04 42 13	−10.84	−10.64	−11.66	−11.27	−11.36
792sf	**University of Hawaii 88″ LM, SJL 1986**					
13 41 28.8	−06 40 24			−15.31		
13 41 30.0	−06 42 58			−14.57		−12.36
13 41 34.2	−06 42 07					−11.38
13 41 36.0	−06 40 11			−13.70	−14.12	−11.80
13 41 27.5	−06 39 38			−13.02	−13.25	−10.78
13 41 26.7	−06 41 26			−10.94	−11.15	−8.63
13 41 33.0	−06 40 51				−9.96	−8.02
13 41 35.1	−06 41 01					−7.90
13 41 26.4	−06 42 27				−10.31	
13 41 26.9	−06 42 26				−10.17	−7.83
13 41 28.4	−06 43 06			−11.55	−12.30	−10.54
13 41 30.7	−06 43 09				−10.99	−8.85
13 41 34.2	−06 42 07			−13.37	−13.70	

Table B1: (continued) CCD photometry results.

α(1950)	δ(1950)	U	B	V	R	I
13 41 30.5	−06 42 13			−12.27	−12.43	−12.08
13 41 30.4	−06 39 24			−9.25		
13 41 44.6	−06 40 17			−9.66	−9.94	−9.69
13 41 36.7	−06 40 43			−8.88	−9.08	−9.01
13 41 35.1	−06 41 01			−10.04	−10.20	−9.88
13 41 32.3	−06 42 04			−8.64	−8.84	
13 41 43.2	−06 42 12			−8.28	−8.50	
13 41 43.6	−06 41 31			−11.92	−11.87	−11.41
13 41 37.5	−06 43 18					−12.84
13 41 38.8	−06 42 40			−10.24	−10.52	−10.29
13 41 46.1	−06 40 16			−8.13	−8.36	
13 41 45.0	−06 40 26			−8.03	−8.15	
13 41 48.8	−06 40 32				−8.18	−8.59
13 41 50.1	−06 40 48				−8.30	
13 41 48.7	−06 41 10			−8.57	−9.42	−10.16
13 41 45.4	−06 41 17			−9.29	−9.62	−9.45
13 41 45.2	−06 42 34				−7.79	
13 41 48.3	−06 42 24			−9.14	−9.43	−9.35
13 41 48.3	−06 42 48				−8.16	−8.58
13 41 48.2	−06 43 02			−11.25	−11.50	−11.54
13 41 48.2	−06 43 20			−8.24	−8.51	−8.63
13 41 49.8	−06 43 00			−8.18	−8.36	−8.38
13 41 49.9	−06 43 22			−9.93	−10.33	−10.51
13 41 43.2	−06 43 20					−8.05
13 41 43.0	−06 43 30			−10.17	−10.57	−10.53
13 41 42.8	−06 43 46			−9.75	−10.51	−11.12
13 41 38.4	−06 43 50			−10.40	−10.68	−10.56
13 41 37.5	−06 43 52			−8.72	−9.01	−8.90

Table B1: (continued) CCD photometry results.

α(1950)	δ(1950)	U	B	V	R	I
793nf	**University of Hawaii 88″ LM, SJL 1986**					
13 53 11.7	−03 10 03				−15.55	−15.01
13 53 10.8	−03 09 03				−12.93	−12.50
13 53 16.1	−03 10 09					−10.82
13 53 10.3	−03 11 06				−12.46	−12.09
13 53 12.7	−03 11 30				−12.70	−12.44
13 53 13.6	−03 11 21				−11.83	−11.43
13 53 06.5	−03 10 38				−13.65	−12.96
13 53 09.3	−03 08 19			−12.00	−12.53	−12.39
13 53 08.5	−03 09 04			−12.15	−12.10	−11.42
13 53 00.9	−03 09 03			−11.41	−11.60	−10.78
13 53 10.3	−03 11 06			−12.26	−12.44	−12.10
13 53 01.3	−03 08 05					−8.27
13 53 09.7	−03 08 04				−8.15	−8.79
13 52 59.8	−03 09 34			−9.60	−9.50	−8.47
13 53 01.5	−03 09 32			−10.44	−10.79	−10.31
13 53 01.9	−03 09 51			−8.86	−9.08	−8.39
13 53 06.7	−03 09 40			−10.78	−10.81	−10.12
13 53 03.2	−03 10 08			−9.37	−9.00	
13 53 00.4	−03 10 42				−7.95	
13 52 55.6	−03 10 14				−8.12	
793nf	**Isaac Newton Telescope INR 1986**					
13 53 11.7	−03 10 03	−12.23	−14.40	−15.74		
13 53 06.6	−03 10 39	−10.18	−12.46	−13.84		
13 53 10.7	−03 09 04	−8.65	−11.40	−12.94		
13 53 08.5	−03 09 05	−8.77	−10.95	−12.26		
13 53 09.2	−03 08 21		−10.23	−12.18		
13 53 10.4	−03 11 06	−7.95	−10.87	−12.49		

Table B1: (continued) CCD photometry results.

α(1950)	δ(1950)	U	B	V	R	I
13 52 51.1	−03 10 26	−9.51	−12.05	−13.45		
13 53 00.9	−03 09 05		−9.74	−11.44		
13 53 06.7	−03 09 42		−9.34	−10.86		
13 53 01.6	−03 09 34		−8.61	−10.47		
13 52 59.8	−03 09 38			−9.64		
13 53 03.3	−03 10 10		−8.63	−9.50		
13 52 51.0	−03 09 55		−9.09	−11.03		
13 52 54.4	−03 08 47			−8.55		
13 52 54.2	−03 07 40			−9.26		
13 53 10.6	−03 08 23			−8.40		
13 53 02.0	−03 09 53			−9.01		
794np	**University of Hawaii 88″ LM, SJL 1986**					
14 14 45.1	−03 52 39				−17.56	−16.97
14 14 42.4	−03 53 56				−16.69	−16.08
14 14 37.8	−03 50 36				−13.59	−12.88
14 14 39.3	−03 50 41				−15.52	−14.73
14 14 47.0	−03 52 49					−12.14
14 14 44.4	−03 53 20				−14.07	−13.55
14 14 36.4	−03 53 47				−12.75	−12.17
14 14 45.2	−03 51 31				−13.49	−12.94
14 14 45.1	−03 50 34				−14.02	−13.50
14 14 46.1	−03 50 38				−14.76	−14.23
14 14 41.2	−03 49 15					−11.01
14 14 49.4	−03 49 13				−9.89	
14 14 51.2	−03 49 28				−10.56	−10.11
14 14 47.4	−03 51 23				−9.99	−9.52
14 14 44.1	−03 52 24				−10.10	−9.70
14 14 41.1	−03 52 22				−13.90	−13.42
14 14 50.0	−03 50 07				−12.11	−11.74

Table B1: (continued) CCD photometry results.

α(1950)	δ(1950)	U	B	V	R	I
14 14 50.5	−03 51 02				−12.52	−12.08
14 14 51.9	−03 51 22				−11.84	−12.15
14 14 57.7	−03 50 33				−12.97	−12.68
14 14 48.9	−03 48 53				−12.05	−11.51
14 14 49.4	−03 48 51				−9.95	−9.47
14 14 55.3	−03 49 03				−9.66	−9.50
14 14 58.6	−03 49 04				−9.36	−9.00
14 15 01.0	−03 49 31				−9.63	−10.24
14 14 57.5	−03 50 12				−9.39	−9.27
14 14 53.1	−03 50 36				−11.51	−11.53
14 14 52.9	−03 51 01				−10.33	−10.25
14 14 53.0	−03 51 26				−9.59	−9.13
14 14 50.8	−03 52 13				−9.55	−10.08
14 14 51.3	−03 52 16				−9.00	−10.01
14 14 54.5	−03 52 02				−10.71	−10.18
14 14 56.3	−03 52 26					−8.79
14 14 58.1	−03 52 27					−9.00
794sp	**University of Hawaii 88″ LM, SJL 1986**					
14 13 52.9	−06 57 26			−15.04	−14.73	−14.59
14 13 52.2	−06 56 49			−12.27	−11.91	−11.77
14 13 56.2	−06 55 51			−11.04	−10.74	−10.59
14 13 57.5	−06 56 03			−11.35	−11.11	−11.07
14 13 58.8	−06 55 50			−12.85	−12.64	−12.53
14 13 59.4	−06 56 11			−12.04	−11.80	−11.73
14 14 02.2	−06 56 05			−11.17	−10.91	−10.91
14 13 51.0	−06 53 48			−8.55	−8.73	−9.04
14 13 55.3	−06 54 29				−7.63	
14 14 02.3	−06 54 22					−8.03
14 13 54.2	−06 55 11					−8.32

Table B1: (continued) CCD photometry results.

α(1950)	δ(1950)	U	B	V	R	I
14 14 04.2	−06 55 34				−7.63	−7.92
14 13 54.8	−06 56 49			−9.57	−9.47	−9.56
14 13 52.9	−06 57 26			−15.76	−14.49	
14 13 46.8	−06 58 31			−14.09	−13.04	
14 13 48.4	−06 59 44			−13.30	−12.12	−11.75
14 13 49.3	−07 00 28			−13.35	−12.19	−11.95
14 13 40.8	−06 58 03			−9.23	−8.34	−8.07
14 13 46.2	−06 57 55					−7.62
14 13 47.7	−06 58 07			−9.10	−7.80	
14 13 44.1	−06 58 59			−9.63	−8.37	−7.94
14 13 51.8	−06 59 31			−10.80	−9.69	−9.40
14 13 52.3	−06 59 38			−8.51		−8.01
14 13 42.0	−06 59 42			−9.95	−8.91	−8.32
14 13 41.2	−06 59 54			−9.29	−7.96	
14 13 42.4	−07 00 23			−10.55	−9.39	−8.99
14 13 44.4	−07 00 21			−8.16		
14 13 42.3	−07 00 58			−10.18	−8.95	−8.55
14 13 42.2	−07 01 02			−9.73	−8.52	−8.20
14 13 44.7	−07 00 54			−10.85	−9.64	−9.14
14 13 48.9	−07 00 43			−9.13	−8.17	−8.17

Categorised by field, followed by telescope, observers and year of observations.
Initials are as follows:
PSM: Mitchell, P.S.; LM: Miller, L.;
SJL: Lilly, S.J.; INR: Reid, I.N.;
RSS: Stobie, R.S.; WKG: Griffiths, W.K.;
RDC: Cannon,R.D.

Table B2: CCD photometry results for the $\delta = 0$ strip.

α(1950)	δ(1950)	U	B	V	R	I
861sp	**University of Arizona 90″ PSM, RMP 1986**					
12 33 21.8	−00 43 52	−12.59	−15.22	−15.64	−15.10	−14.97
12 33 20.6	−00 44 55	−11.72	−13.52	−13.91	−13.34	−13.18
12 33 19.4	−00 45 00	−6.93	−10.13	−11.13	−11.05	−11.63
12 33 20.3	−00 44 11	−9.29	−11.27	−11.54	−10.92	−10.74
12 33 22.4	−00 45 41	−6.16	−8.78	−9.97	−9.51	−9.63
12 33 21.1	−00 44 53		−7.82	−8.84	−8.61	−8.80
12 33 21.0	−00 44 37		−7.97	−8.94	−8.52	−8.73
12 33 19.2	−00 44 08		−7.41	−8.08	−8.25	−9.03
861sc	**Isaac Newton Telescope RSS, RDC, WKG 1986**					
12 40 51.4	−00 55 08	−12.81	−14.13	−14.12	−14.61	−13.81
12 40 57.2	−00 54 13	−11.25	−13.14	−13.33	−13.99	−13.36
12 40 57.4	−00 56 05	−11.51	−12.76	−12.77	−13.34	−12.59
12 40 59.1	−00 55 14	−10.60	−11.90	−11.91	−12.49	−11.76
12 40 57.8	−00 54 35	−8.36	−10.44	−11.25	−12.43	−13.19
12 41 11.9	−00 54 59	−11.17	−12.76	−12.88	−13.51	−12.84
12 41 10.5	−00 54 24	−10.89	−12.14	−12.14	−12.69	−11.94
12 41 03.4	−00 54 27	−10.00	−11.45	−11.51	−12.10	−11.39
12 40 54.0	−00 56 27	−10.40	−11.45	−11.38	−11.89	−11.06
12 41 11.1	−00 56 28	−7.32	−8.86	−8.99	−9.60	−8.97
12 41 04.3	−00 55 41	−6.69	−7.94	−7.73	−8.40	−7.41
12 40 59.2	−00 55 33		−7.00	−8.02	−9.26	−9.68
12 40 51.7	−00 55 43		−7.62	−8.31	−9.21	−8.80
12 40 52.8	−00 55 34		−7.26	−8.14	−8.97	−8.62
12 40 49.5	−00 56 51		−7.35	−7.82	−9.06	−9.16
12 40 51.7	−00 56 51			−7.48	−8.42	−8.05

Table B2: (continued) CCD photometry results.

α(1950)	δ(1950)	U	B	V	R	I
861sc	**ESO-Danish 1.5m PSM, LM 1986**					
12 40 57.2	−00 54 13	−9.58	−9.96	−11.11	−10.55	−10.58
12 40 51.5	−00 55 07	−11.22	−10.92	−11.82	−11.13	−11.06
12 40 54.1	−00 52 45	−7.92	−9.21	−10.71	−10.34	−10.48
12 41 00.3	−00 52 29	−9.04	−8.97	−9.90	−9.24	−9.21
12 40 59.2	−00 55 13	−8.90	−8.69	−9.63	−8.98	−8.92
12 40 57.8	−00 54 34	−6.39	−7.25	−9.03	−9.24	−10.33
12 40 52.0	−00 54 11		−3.98	−6.30	−5.94	−6.11
12 40 59.2	−00 55 33			−5.69	−5.82	−6.70
861sf	**ESO-Danish 1.5m PSM, LM 1986**					
12 43 49.3	−01 14 03		−12.00	−11.56	−11.33	−11.51
12 43 50.2	−01 14 02		−10.92	−10.96	−11.09	−11.41
12 43 52.5	−01 13 48		−10.72	−10.67	−10.74	−11.07
12 43 53.8	−01 13 53		−15.03	−14.52	−14.28	−14.43
12 43 56.9	−01 13 54		−13.83	−13.47	−13.26	−13.42
12 43 53.5	−01 13 04		−9.23	−8.92	−8.79	−8.98
12 43 53.6	−01 12 40		−8.28	−8.51	−8.66	−9.11
12 43 52.6	−01 12 37		−9.56	−9.27	−9.33	−9.56
12 43 51.6	−01 12 49		−7.90	−7.43	−8.02	−8.54
12 43 50.4	−01 12 54		−10.54	−9.97	−9.65	−9.83
12 43 55.8	−01 14 53		−8.46	−8.52	−8.79	−9.19
12 43 49.1	−01 12 45			−7.55	−8.11	−9.17
12 43 48.8	−01 14 34			−6.34	−6.48	−6.55
12 43 51.6	−01 14 35			−5.60	−7.36	−7.58
12 43 50.8	−01 14 16			−6.51	−6.93	−8.05
12 43 56.8	−01 14 54			−6.23	−5.47	−6.09
12 43 55.1	−01 12 23			−7.05	−7.04	−7.57
12 43 56.2	−01 12 08			−6.66	−7.08	−7.52

Table B2: (continued) CCD photometry results.

α(1950)	δ(1950)	U	B	V	R	I
862c	**Isaac Newton Telescope RSS, RDC, WKG 1986**					
13 00 00.1	−00 12 32	−11.20	−14.71	−14.90	−15.45	−14.99
13 00 09.2	−00 12 34	−11.74	−14.88	−14.88	−15.30	−14.69
12 59 57.2	−00 10 35	−10.97	−13.94	−13.89	−14.32	−13.69
12 59 53.2	−00 11 16	−9.89	−12.96	−12.94	−13.40	−12.79
12 59 57.2	−00 11 17	−9.08	−12.44	−12.65	−13.22	−12.73
12 59 55.2	−00 10 18	−8.24	−12.09	−12.39	−13.04	−12.61
12 59 56.9	−00 12 33	−7.36	−11.94	−12.34	−13.07	−12.69
13 00 00.5	−00 11 12	−7.25	−10.80	−11.05	−11.54	−11.23
12 59 53.0	−00 09 23	−7.64	−11.03	−11.09	−11.49	−11.01
12 59 47.8	−00 11 01	−7.35	−10.66	−10.70	−11.07	−10.60
12 59 52.3	−00 12 36		−9.89	−9.92	−10.29	−9.87
12 59 52.3	−00 12 10			−8.77	−9.75	−11.05
13 00 00.5	−00 10 08			−8.91	−9.60	−9.51
13 00 01.0	−00 09 17		−11.45	−11.44	−11.77	−11.27
12 59 59.0	−00 12 28			−8.63	−9.52	−9.80
13 00 03.7	−00 12 32		−9.73	−9.94	−10.44	−10.12
13 00 10.1	−00 11 20		−9.27	−9.26	−9.56	−9.10
12 59 58.6	−00 12 02				−8.51	−8.72
12 59 54.9	−00 12 23		−8.69	−8.78	−9.13	−8.75
862sp	**University of Hawaii 88″ LM, SJL 1986**					
12 56 07.6	−01 20 11			−15.15		−12.62
12 55 59.3	−01 21 34	−12.64	−14.01	−14.02	−13.60	−11.89
12 56 01.5	−01 21 42	−11.02	−12.50	−12.53	−12.19	−10.63
12 56 05.0	−01 21 51	−10.42	−11.77	−11.66	−11.25	−9.64
12 56 06.7	−01 23 03	−11.02	−12.37	−12.20	−11.83	−10.25
12 56 01.1	−01 22 57	−9.51	−10.56	−10.32	−9.93	−8.25
12 56 02.1	−01 21 53	−9.53	−10.71	−10.52	−10.05	−8.46

Table B2: (continued) CCD photometry results.

α(1950)	δ(1950)	U	B	V	R	I
12 56 07.6	−01 21 54				−8.86	−7.22
12 56 07.8	−01 24 22	−12.84	−14.40	−14.15	−13.60	
12 56 04.6	−01 25 10			−11.84	−11.59	−10.19
12 56 06.7	−01 25 40			−11.04	−10.70	−9.17
12 56 04.2	−01 24 27			−9.23	−8.87	−7.37
12 56 02.2	−01 26 13			−9.26	−9.19	−7.94
12 55 57.4	−01 25 41			−9.22	−9.21	−7.83
12 56 11.1	−01 25 24			−10.84	−10.92	−9.64
12 56 12.6	−01 25 32			−12.14		
12 56 14.2	−01 25 42			−9.38	−9.71	−9.43
12 56 12.9	−01 26 24			−11.75	−11.83	−10.63
12 56 06.3	−01 26 02			−9.09	−9.04	−7.83
12 56 16.3	−01 26 53			−10.65	−10.53	−9.26
12 56 15.7	−01 26 55			−11.25	−10.77	−9.19
12 56 18.4	−01 25 08			−8.70	−8.89	−7.85
12 55 58.3	−01 21 43	−8.10	−10.07			
12 56 07.8	−01 23 26	−7.78	−10.60			
863np	**ESO-Danish 1.5m PSM, LM 1986**					
13 15 27.4	+01 30 31		−15.00	−15.00	−15.00	−15.00
13 15 23.1	+01 29 56		−13.91	−14.13	−14.25	−14.34
13 15 22.3	+01 28 22		−15.28	−15.57	−15.75	−15.84
13 15 23.7	+01 31 07		−12.89	−13.35	−13.66	−13.84
13 15 22.0	+01 31 00		−12.28	−12.36	−12.35	−12.38
13 15 25.0	+01 30 47		−11.11	−11.37	−11.55	−11.63
13 15 27.0	+01 30 00		−10.77	−11.12	−11.32	−11.42
13 15 26.7	+01 29 41		−8.71	−9.61	−10.40	−11.30
13 15 26.0	+01 28 44		−9.87	−10.25	−10.49	−10.65
13 15 28.2	+01 28 24		−10.82	−10.94	−11.01	−11.06
13 15 26.8	+01 28 03		−9.82	−10.58	−11.18	−11.64
13 15 29.7	+01 28 27		−9.66	−9.74	−9.74	−9.70

Table B2: (continued) CCD photometry results.

α(1950)	δ(1950)	U	B	V	R	I
863nf	**University of Arizona 90″ PSM, RMP 1986**					
13 19 02.9	+01 50 53	−15.37	−15.83	−16.68	−17.19	−17.65
13 19 05.0	+01 50 30	−11.38	−12.57	−13.81	−14.63	−15.49
13 19 03.6	+01 49 48	−12.57	−12.38	−12.78	−13.00	−13.26
13 19 01.4	+01 50 48	−9.90	−8.38		−9.94	
863c	**ESO-Danish 1.5m PSM, LM 1986**					
13 19 59.1	−00 12 10	−15.16	−15.50	−16.29	−16.74	−17.16
13 20 05.6	−00 11 50	−14.51	−14.60	−15.15	−15.48	−15.81
13 20 03.6	−00 13 29		−13.49	−14.24	−14.65	−15.00
13 20 00.3	−00 13 19		−10.09	−11.34	−12.18	−12.82
13 20 01.5	−00 11 07	−10.82	−11.43	−12.28	−12.80	−13.23
13 20 04.1	−00 11 28	−11.31	−11.29	−11.78	−12.06	−12.41
13 20 02.8	−00 10 56	−10.09	−10.12	−10.77	−11.14	−11.54
13 20 03.1	−00 10 27	−10.34	−10.31	−10.97	−11.38	−11.79
13 20 04.9	−00 10 44	−10.85	−11.16	−11.86	−12.28	−12.65
863sp	**University of Arizona 90″ PSM, RMP 1986**					
13 16 05.7	−00 56 26		−18.00	−18.00	−18.00	−18.00
13 16 05.4	−00 56 08		−12.09	−12.38	−12.71	
13 16 05.4	−00 55 49		−13.93	−14.59	−15.01	−15.85
13 16 02.9	−00 55 55		−13.33	−13.92	−14.44	−15.53
13 16 01.3	−00 55 47		−12.42	−12.78	−13.15	−13.36
13 16 01.0	−00 57 09		−17.19	−16.97	−16.83	−16.75
13 16 04.2	−00 57 30		−14.30	−14.23	−14.21	−14.17
13 16 03.9	−00 57 19				−12.13	−12.13

Table B2: (continued) CCD photometry results.

α(1950)	δ(1950)	U	B	V	R	I
863sf	**University of Arizona 90″ PSM, RMP 1986**					
13 25 53.4	−01 12 22	−15.26	−15.42	−16.08	−16.46	−16.81
13 25 58.7	−01 11 34	−13.01	−13.17	−13.90	−14.35	−14.76
13 25 58.8	−01 10 29	−13.86	−13.90	−14.56	−14.95	−15.34
13 25 58.1	−01 11 00	−11.98	−11.74	−12.23	−12.52	−12.87
13 25 57.3	−01 11 35			−10.93	−11.58	−12.17
13 25 55.2	−01 10 53	−10.39		−10.82	−11.12	−11.49
864c	**Isaac Newton Telescope RSS, RDC, WKG 1986**					
13 37 26.9	+00 15 51	−12.18	−15.20	−15.30	−15.78	−15.19
13 37 34.8	+00 18 45	−11.19	−14.19	−14.36	−14.80	−14.38
13 37 37.0	+00 18 35	−9.57	−12.74	−12.92	−13.59	−13.27
13 37 38.0	+00 17 29	−11.48	−13.90	−13.77	−14.14	−13.62
13 37 25.6	+00 16 31	−10.44	−13.18	−13.24	−13.67	−13.28
13 37 31.7	+00 17 30	−9.45	−11.91	−11.84	−12.25	−11.82
13 37 23.9	+00 18 04	−9.56	−12.02	−11.90	−12.28	−11.81
13 37 38.6	+00 18 03		−8.30	−8.95	−9.72	−9.63
13 37 45.4	+00 16 14		−8.02	−8.82	−9.49	−9.41
13 37 33.1	+00 16 46	−7.68	−10.91	−11.13	−11.80	−11.54
13 37 43.9	+00 16 28			−8.25	−8.91	−8.82
13 37 34.7	+00 17 07	−9.74	−12.20	−11.76	−11.90	−11.17
13 37 32.6	+00 16 32	−7.64	−10.33	−10.37	−10.85	−10.48
13 37 43.1	+00 17 37	−7.72	−10.53	−10.68	−11.22	−10.92
13 37 25.8	+00 18 39		−8.07	−8.84	−9.85	−10.37
13 37 33.6	+00 16 17		−8.26	−8.54	−9.16	−8.96
13 37 29.8	+00 15 42					−9.24
13 37 37.6	+00 16 38		−8.43	−8.89	−9.66	−9.54
13 37 31.6	+00 17 07	−6.68	−8.82	−8.84	−9.25	−8.76
13 37 41.4	+00 16 56	−6.56	−8.88	−8.95	−9.45	−9.16

Table B2: (continued) CCD photometry results.

α(1950)	δ(1950)	U	B	V	R	I
864sf	**University of Hawaii 88″ LM, SJL 1986**					
13 45 44.2	−01 50 35	−11.53	−12.70	−14.38		−14.98
13 45 43.7	−01 50 24	−8.50	−10.03	−11.87	−12.44	−12.72
13 45 44.6	−01 52 32	−11.78	−12.05	−13.49	−13.70	−13.66
13 45 46.5	−01 51 21	−9.19	−10.98	−12.93	−13.70	−14.24
13 45 45.6	−01 51 43	−11.46	−11.97	−12.94	−13.01	−12.84
13 45 42.6	−01 52 07	−10.42	−11.04	−12.47	−12.87	−12.90
13 45 48.4	−01 53 14	−10.49	−11.71	−13.30	−13.81	−14.10
13 45 43.3	−01 53 37	−11.11		−13.06	−13.47	−13.57
13 45 36.5	−01 51 50			−10.80	−11.14	−11.17
13 45 38.1	−01 53 42			−9.99	−10.66	−11.02
13 45 46.3	−01 53 09	−9.77	−9.89	−11.13	−11.48	−11.58
13 45 50.4	−01 51 59	−8.74	−9.05	−10.28	−10.71	−10.95
13 45 45.9	−01 54 26	−8.86	−9.91	−11.45	−12.01	−12.28
13 45 38.1	−01 53 04			−9.29	−9.55	−9.67
13 45 43.1	−01 53 57		−6.64	−6.56		
13 45 40.7	−01 52 21			−8.13		
865cf	**Isaac Newton Telescope RSS, RDC, WKG 1986**					
14 00 43.5	−00 09 58	−11.29	−14.27	−14.52	−15.12	
14 00 37.6	−00 08 08	−11.26	−13.58	−13.55	−14.07	−13.74
14 00 39.4	−00 09 59	−8.96	−11.35	−11.35	−11.83	−11.51
14 00 49.0	−00 09 55	−7.32	−11.05	−11.68	−12.70	−12.70
14 00 48.0	−00 08 45	−7.79	−10.56	−10.68	−11.29	−10.79
14 00 54.9	−00 07 21	−8.92	−11.74	−11.89	−12.51	−12.03
14 00 52.8	−00 07 29	−8.08	−11.08	−11.39	−11.84	−11.66
14 00 51.0	−00 06 41	−8.03	−10.32	−10.33	−10.69	−10.31
14 00 47.4	−00 08 01		−9.23	−9.77	−10.60	−10.49
14 00 43.4	−00 06 58		−8.40	−8.34	−8.85	−8.25

Table B2: (continued) CCD photometry results.

α(1950)	δ(1950)	U	B	V	R	I
14 00 50.7	−00 09 45		−8.26	−7.88	−8.01	−7.44
14 00 48.4	−00 09 30		−8.01	−7.90	−8.38	−7.91
14 00 43.1	−00 08 49		−8.10	−8.23	−8.69	−8.38
865sp	**University of Hawaii 88″ LM, SJL 1986** & Isaac Newton Telescope INR 1986					
13 57 47.5	−01 08 26	−10.94	−15.57	−15.33		−15.49
13 57 46.8	−01 07 35			−14.77	−14.94	−14.48
13 57 50.2	−01 08 27	−7.60	−12.30	−12.16	−12.92	−12.48
13 57 42.8	−01 08 37	−6.42	−11.48	−11.19	−12.10	−11.68
13 57 41.0	−01 07 46				−11.37	
13 57 40.7	−01 09 42	−9.10	−13.76	−13.57	−14.26	−13.70
13 57 39.9	−01 10 42	−7.03	−12.53	−12.61	−13.59	−13.25
13 57 48.5	−01 11 39		−11.44	−11.79	−13.05	−13.19
13 57 44.7	−01 12 00			−12.16	−13.01	−12.52
13 57 39.4	−01 11 58			−11.90	−12.56	−11.90
13 57 37.5	−01 09 56		−10.39	−10.81	−12.01	−11.96
13 57 49.1	−01 11 23		−9.98	−10.16	−11.24	−11.06
13 57 48.6	−01 10 49		−8.65	−8.63	−9.51	−9.47
13 57 42.1	−01 12 13			−8.95	−9.77	−9.29
13 57 38.9	−01 12 30			−8.71	−9.62	−9.22
13 57 37.6	−01 10 46			−7.99	−9.02	−8.74
13 57 39.6	−01 09 51		−9.70	−9.34	−9.94	−9.35
13 57 42.0	−01 11 21				−8.30	−8.86
13 57 37.0	−01 08 16		−11.28			
13 57 40.7	−01 11 17		−10.17			
13 57 34.1	−01 08 54		−10.15			
13 57 43.1	−01 08 56		−8.65			
13 57 34.5	−01 09 52		−8.38			
13 57 52.0	−01 08 30		−8.41			

Table B2: (continued) CCD photometry results.

α(1950)	δ(1950)	U	B	V	R	I
866cf	**ESO-Danish 1.5m PSM, LM 1986**					
14 22 55.2	+00 07 37	−12.61	−12.82	−13.83	−13.57	−13.75
14 23 03.8	+00 07 42	−11.54	−11.63	−12.50	−12.18	−12.34
14 23 01.8	+00 06 24	−10.63	−11.27	−12.42	−12.27	−12.51
14 23 03.6	+00 07 08	−10.49	−10.53	−11.39	−11.10	−11.29
14 23 00.3	+00 05 59	−9.93	−10.06	−10.98	−10.72	−10.92
14 22 56.8	+00 05 07	−10.48	−10.71	−11.65	−11.34	−11.55
14 23 00.7	+00 06 43	−7.57	−8.66	−10.00	−10.02	−10.36
14 22 57.6	+00 06 11	−6.96	−7.41	−8.47	−8.28	−8.52
14 22 57.9	+00 04 52		−8.07	−8.95	−8.66	−8.84
14 22 59.3	+00 04 51		−7.90	−8.86	−8.62	−8.86
14 23 01.7	+00 04 48		−7.63	−8.55	−8.28	−8.45
14 23 02.2	+00 06 10	−6.49	−6.58	−7.57	−7.37	−7.06
14 23 01.2	+00 07 50			−6.97	−7.56	−8.61
14 23 01.1	+00 07 44			−7.00	−7.41	−8.18
14 23 00.9	+00 07 30					−6.77
14 23 02.2	+00 05 12			−6.28		−6.47
14 23 01.8	+00 04 29			−6.34	−6.65	−7.29
14 22 57.0	+00 08 35	−7.55		−9.81	−9.66	−10.08
866sp	**University of Hawaii 88″ LM, SJL 1986**					
14 19 52.7	−00 44 09	−12.08	−15.11		−17.23	−17.31
14 19 51.8	−00 41 46				−15.08	−15.18
14 19 48.0	−00 44 27	−10.44	−12.45	−12.60	−14.18	−14.12
14 19 51.2	−00 43 42	−8.79	−11.31	−11.58	−13.40	−13.14
14 19 42.6	−00 43 24	−10.60	−11.33	−11.45	−13.22	−13.06
14 19 43.8	−00 43 18	−9.53	−10.49	−10.72	−12.50	−12.45
14 19 45.0	−00 43 53		−9.29	−9.93	−12.10	−12.48
14 19 36.5	−00 44 47		−12.28			−13.84

Table B2: (continued) CCD photometry results.

α(1950)	δ(1950)	U	B	V	R	I
14 19 49.7	−00 44 37			−8.90	−10.51	−10.59
14 19 50.4	−00 44 43				−9.97	−10.88
14 19 41.1	−00 44 13		−7.42	−8.11	−10.47	−11.28
14 19 43.3	−00 42 51		−8.76	−8.92	−10.67	
14 19 45.1	−00 42 57		−7.83	−8.02	−9.74	−9.61
14 19 42.0	−00 41 42				−11.08	−10.93
14 19 40.8	−00 41 41				−10.22	−10.77
14 19 51.7	−00 42 34				−9.09	−9.27
14 19 44.2	−00 42 11				−9.66	−9.60
14 19 39.7	−00 41 59				−9.17	−8.96
14 19 48.4	−00 43 48		−7.59	−7.51	−9.04	−8.88
14 19 33.2	−00 45 17		−8.15	−8.47		
14 19 33.9	−00 44 49		−8.27	−8.38		
867np	**University of Arizona 90″ PSM, RMP 1986**					
14 33 37.7	+01 36 40		−15.61	−15.64	−15.65	−15.64
14 33 32.5	+01 36 12		−15.00	−15.00	−15.00	−15.00
14 33 33.3	+01 35 40		−11.80	−11.72	−11.66	−11.60
14 33 34.4	+01 35 31		−10.98	−10.83	−10.81	−10.73
14 33 35.1	+01 36 10		−10.99	−11.07	−11.15	−11.32
14 33 36.9	+01 36 32		−10.27	−10.59	−10.78	−10.72
14 33 36.3	+01 35 11		−9.44	−9.73	−9.97	−10.42
14 33 36.6	+01 35 38			−9.06	−9.62	−9.90
14 33 33.1	+01 36 29		−8.74	−9.00	−10.48	−9.08
867s	**ESO-Danish 1.5m PSM, LM 1986**					
14 38 11.6	−01 34 09	−17.00	−16.98	−17.56	−17.91	−18.24
14 38 13.7	−01 35 11		−14.60	−15.28	−15.71	−15.95
14 38 15.8	−01 33 15	−12.02	−12.61	−13.34	−13.99	−14.41

Table B2: (continued) CCD photometry results.

α(1950)	δ(1950)	U	B	V	R	I
14 38 16.8	−01 33 44	−12.76	−12.82	−13.38	−13.74	−14.04
14 38 11.2	−01 34 40		−12.42	−13.01	−13.40	−13.69
14 38 12.8	−01 34 48		−11.09	−11.79	−12.18	−12.54
14 38 11.3	−01 33 46	−13.77	−14.25	−15.04	−15.55	−15.90
14 38 12.3	−01 31 37	−11.80	−12.24	−13.04	−13.55	−13.89
14 38 11.2	−01 32 23	−13.89	−14.36	−15.16	−15.68	−16.04
14 38 14.9	−01 32 01	−13.04	−13.51	−14.26	−14.70	−15.04
867cp	**University of Arizona 90″ PSM, RMP 1986**					
14 38 09.4	−00 18 47		−15.00	−15.00	−15.00	−15.00
14 38 10.7	−00 18 58		−12.05	−12.74	−13.29	−14.16
14 38 08.7	−00 19 08		−10.64	−10.48	−10.50	−10.55
14 38 08.1	−00 19 20		−12.75	−12.57	−12.50	−12.47
14 38 08.5	−00 19 29		−10.95	−10.97	−10.98	−11.09
14 38 10.6	−00 17 58		−10.11	−9.96	−9.93	−9.76
14 38 07.0	−00 19 09		−7.40	−7.98	−9.02	−9.64
867cf	**Isaac Newton Telescope INR 1986**					
14 45 41.2	−00 38 18	−15.26	−16.34	−17.49		
14 45 29.8	−00 37 05	−14.21		−17.81		
14 45 32.8	−00 36 39	−12.44	−14.52	−15.94		
14 45 30.7	−00 37 18		−12.34	−13.34		
14 45 32.4	−00 37 24		−11.23	−12.50		
14 45 33.8	−00 36 26		−11.84	−13.49		
14 45 33.7	−00 35 28		−11.10	−11.94		
14 45 49.2	−00 36 54	−12.93	−14.32	−15.65		
14 45 44.9	−00 37 02		−11.43	−12.64		

Table B2: (continued) CCD photometry results.

α(1950)	δ(1950)	U	B	V	R	I
14 45 42.0	−00 35 46		−12.48	−13.77		
14 45 41.1	−00 36 05		−11.21	−12.42		
867cf	**ESO-Danish 1.5m PSM, LM 1986**					
14 45 29.9	−00 37 04				−18.08	
14 45 32.8	−00 34 57				−15.94	
14 45 37.0	−00 34 24				−16.17	
14 45 29.1	−00 33 53				−15.15	
14 45 32.8	−00 36 37				−16.18	
14 45 29.8	−00 34 10				−12.38	
14 45 33.1	−00 33 56				−10.91	
14 45 30.8	−00 34 52				−11.17	
14 45 33.7	−00 35 27				−11.77	
14 45 33.8	−00 36 25				−14.02	
14 45 28.2	−00 34 00				−11.47	
14 45 27.6	−00 34 11				−10.92	
14 45 32.1	−00 35 06				−13.49	
14 45 28.3	−00 34 22				−10.71	

Categorised by field, followed by telescope, observers and year of observations.
Initials are as follows:
PSM: Mitchell, P.S.; LM: Miller, L.;
SJL: Lilly, S.J.; INR: Reid, I.N.;
RSS: Stobie, R.S.; WKG: Griffiths, W.K.;
RDC: Cannon,R.D.

Appendix C

Photoelectric Photometry Results

This appendix contains photoelectric photometry results for the Edinburgh Multicolour Survey. Fields are listed in RA order, and measured star coordinates are given, followed by derived *UBVRI* colours, as described in Chapter 3. Abbreviations used in the tables and the sources for external calibrations are listed at the end of the appendix.

Table C1: Photoelectric photometry results for the $\delta = -5$ strip.

α(1950)	δ(1950)	V	$U-B$	$B-V$	$V-R$	$R-I$	Night#
789	**Steward Observatory 60″ PSM, RMP 1986**						
12 33 31.2	−05 08 40	12.54	0.01	0.60	0.36	0.36	10, 14
12 33 37.1	−05 06 44	12.28	0.02	0.57	0.35	0.35	10
12 39 07.2	−05 12 33	12.43	0.90	1.11	0.58	0.55	14
790	**Steward Observatory 60″ PSM, RMP 1986**						
12 57 06.0	−05 40 39	11.92	1.26	1.14	0.61	0.51	13
12 57 04.2	−05 40 52	13.54	0.33	0.76	0.40	0.37	14
791	**Steward Observatory 60″ PSM, RMP 1986**						
13 20 04.2	−04 45 17	13.51	−0.11	0.59	0.22	0.33	9
13 20 06.2	−04 47 51	13.29	0.30	0.76	0.43	0.40	12
13 20 10.1	−04 46 09	14.20	0.25	0.82	0.36	0.61	9
792	**Steward Observatory 60″ PSM, RMP 1986**						
13 40 40.7	−04 42 47	13.15	0.47	−0.02	0.29	0.28	12, 13
793	**Steward Observatory 60″ PSM, RMP 1986**						
14 03 03.0	−04 36 13	12.05	0.07	0.52	0.29	0.30	12
14 03 02.3	−04 35 41	13.74	0.60	0.87	0.52	0.44	9
794	**Steward Observatory 60″ PSM, RMP 1986**						
14 19 12.4	−05 18 34	12.94	0.28	0.71	0.40	0.35	12, 13
14 19 03.8	−05 19 58	14.27	0.68	0.88	0.52	0.48	12, 13

Table C2: Photoelectric photometry results for the $\delta = 0$ strip.

α(1950)	δ(1950)	V	$U-B$	$B-V$	$V-R$	$R-I$	Night#
861	**Steward Observatory 60″ PSM, RMP 1986**						
12 40 51.4	−00 55 08	12.91	0.62	0.07	0.35	0.35	10, 13
12 40 57.2	−00 54 13	13.71	0.87	0.59	0.51	0.43	10, 14
12 43 53.9	−01 13 53	12.43	0.58	0.02	0.34	0.32	14
862	**Steward Observatory 60″ PSM, RMP 1986**						
12 56 07.6	−01 20 11	13.58	0.03	0.13	0.08	0.10	10
12 56 07.8	−01 24 22	14.50	0.03	0.58	0.37	0.39	10
12 59 57.2	−00 10 35	14.11	−0.07	0.54	0.34	0.35	10
13 00 00.1	−00 12 32	13.08	0.43	0.85	0.48	0.46	10, 13
863	**Steward Observatory 60″ RMP 1985**						
13 18 15.2	+00 01 09	13.01	0.42	0.80	0.72	0.38	-
13 18 20.7	+00 04 13	14.11	0.18	0.58	0.59	0.32	-
13 18 34.8	+00 01 00	14.19	0.33	0.74	0.61	0.29	-
13 18 02.0	+00 02 16	12.85	0.00	0.52	0.40	0.30	-
13 18 19.1	+00 05 03	13.44	0.26	0.70	0.48	0.34	-
13 18 26.4	+00 01 20	16.05	−0.19	0.62	0.49	0.22	-
863	**Steward Observatory 60″ PSM, RMP 1986**						
13 19 59.1	−00 12 10	12.71	0.36	0.78	0.45	0.42	13
13 15 22.2	+01 28 23	14.02	0.48	0.88	0.48	0.47	13
13 25 53.4	−01 12 22	12.92	0.16	0.66	0.38	0.35	13
13 16 12.9	−00 59 52	13.16	0.03	0.66	0.38	0.38	13
13 19 03.0	+01 50 54	12.32	0.46	0.85	0.50	0.46	13

Table C2: (continued) Photoelectric photometry results.

α(1950)	δ(1950)	V	$U-B$	$B-V$	$V-R$	$R-I$	Night#
864	**Steward Observatory 60″ PSM, RMP 1986**						
13 37 37.9	+00 17 29	13.99	−0.06	0.40	0.33	0.36	8
13 37 34.8	+00 18 45	13.48	0.39	0.77	0.43	0.39	13
13 45 53.9	−01 55 11	14.61	0.09	0.64	0.39	0.36	10
13 45 44.2	−01 50 35	14.23	0.62	0.94	0.44	0.45	10
13 45 54.5	−01 52 30	13.69	0.30	0.74	0.41	0.34	10
865	**Steward Observatory 60″ PSM, RMP 1986**						
14 00 43.5	−00 09 58	12.89	0.53	0.88	0.51	0.46	12, 13
14 00 37.5	−00 08 08	13.82	−0.06	0.56	0.34	0.38	13
866	**Steward Observatory 60″ PSM, RMP 1986**						
14 19 52.6	−00 44 07	11.94	1.00	1.09	0.57	0.52	10
14 19 49.2	−00 40 55	13.66	0.19	0.72	0.42	0.34	10
14 22 55.2	+00 07 37	12.78	0.26	0.69	0.38	0.35	7, 13
14 23 01.7	+00 06 24	14.27	0.52	0.83	0.50	0.45	7
14 23 03.8	+00 07 42	14.13	−0.04	0.52	0.23	0.35	7
14 19 42.7	−00 41 23	13.72	0.65	0.94	0.50	0.44	10
867	**— RSS, GG, INR, RS 1982/83; see text.**						

Categorised by field, followed by telescope, observers and year of observations.
Initials are as follows:
PSM: Mitchell, P.S.; RMP: Prestage, R.M.;
RSS: Stobie, R.S.; GG: Gilmore, G.;
INR: Reid, I.N.; RS: Sagar, R.

Photometry for field 867 is largely taken from photoelectric and CCD sequences in:
Stobie, R.S., Gilmore, G. & Reid, N. 1985. *Astron. Astrophys. Suppl. Ser.*, **60**, 495.
Stobie, R.S., Sagar, R. & Gilmore, G. 1985. *Astron. Astrophys. Suppl. Ser.*, **60**, 503.

Appendix D

Colour-space projections

The following pages show two-colour plots for each survey field. Objects with $17 \leq R \leq 18.5$ present in all wavebands are plotted in four projections covering all the colour information available in the Edinburgh Multicolour Survey. Note that no two-colour plots maximise the information available and a multi-dimensional nearest-neighbour search may detect many objects inaccessible by visual inspection of such plots.

Figure D1: Two-colour diagrams for Schmidt field 789. Various colour indices are shown, derived in the Schmidt photographic system as described in earlier chapters. Objects present in all wavebands are plotted with $17 \leq R \leq 18.5$.

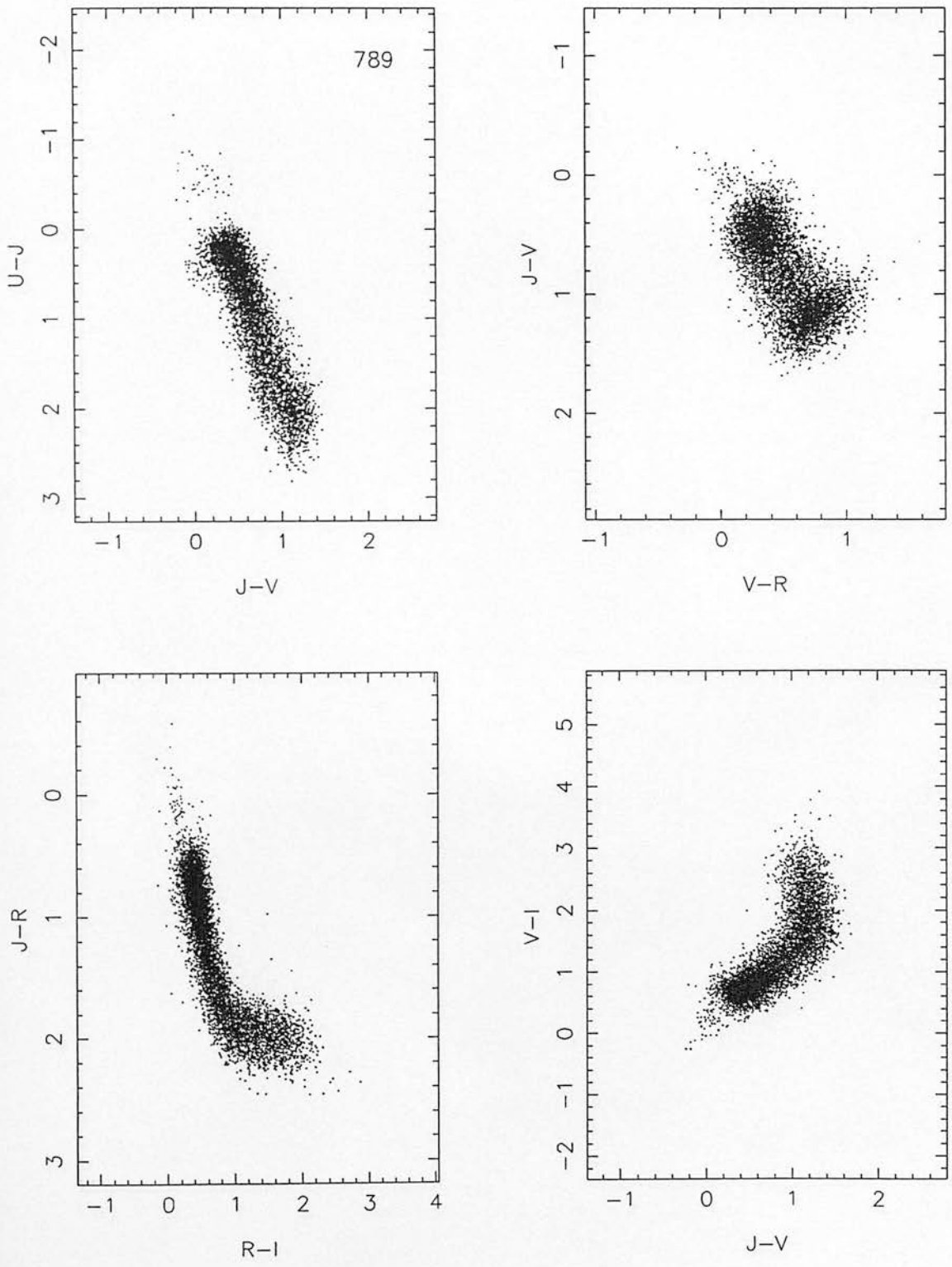

Figure D2: Two-colour diagrams for Schmidt field 790.

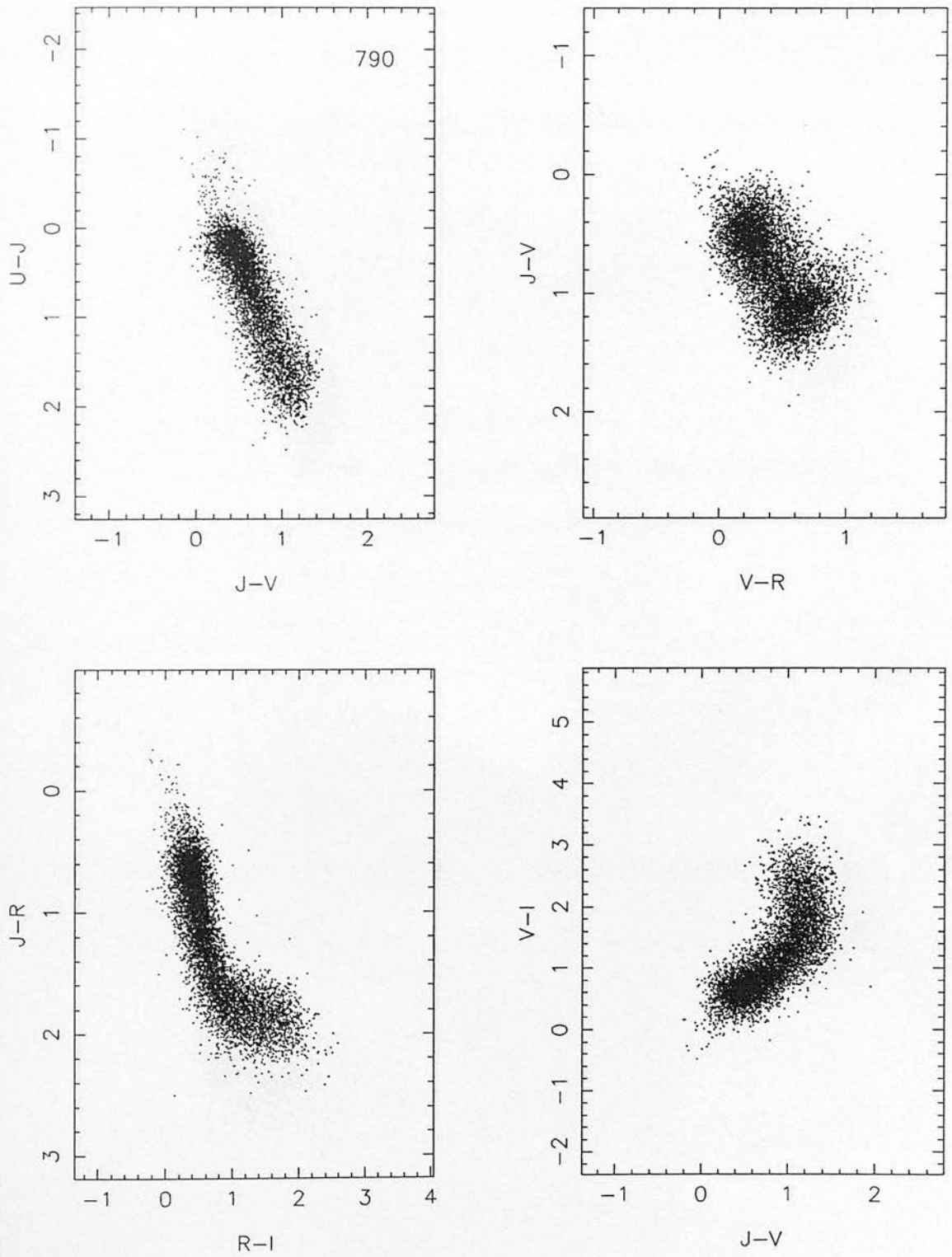

Figure D3: Two-colour diagrams for Schmidt field 791.

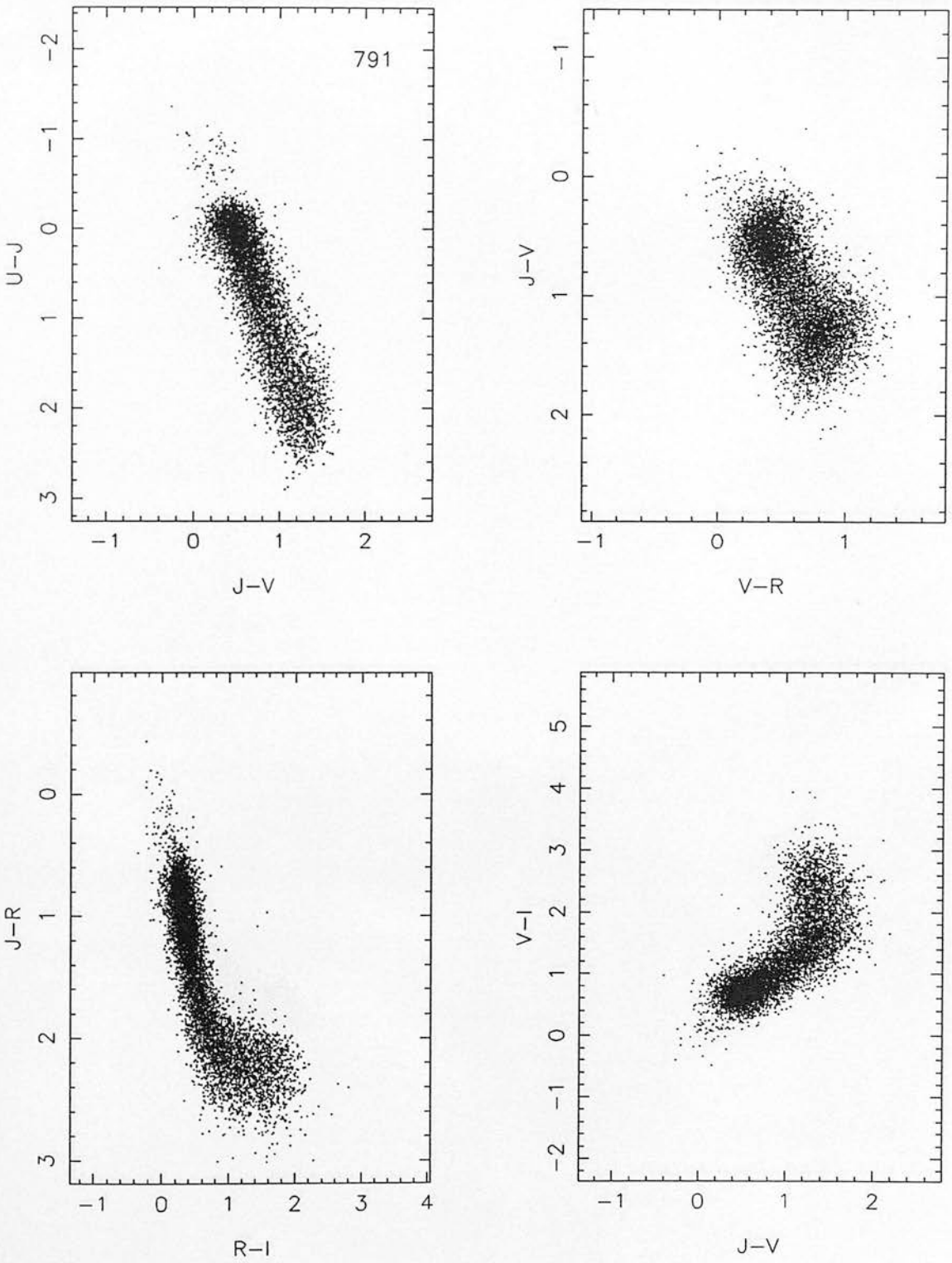

Figure D4: Two-colour diagrams for Schmidt field 792.

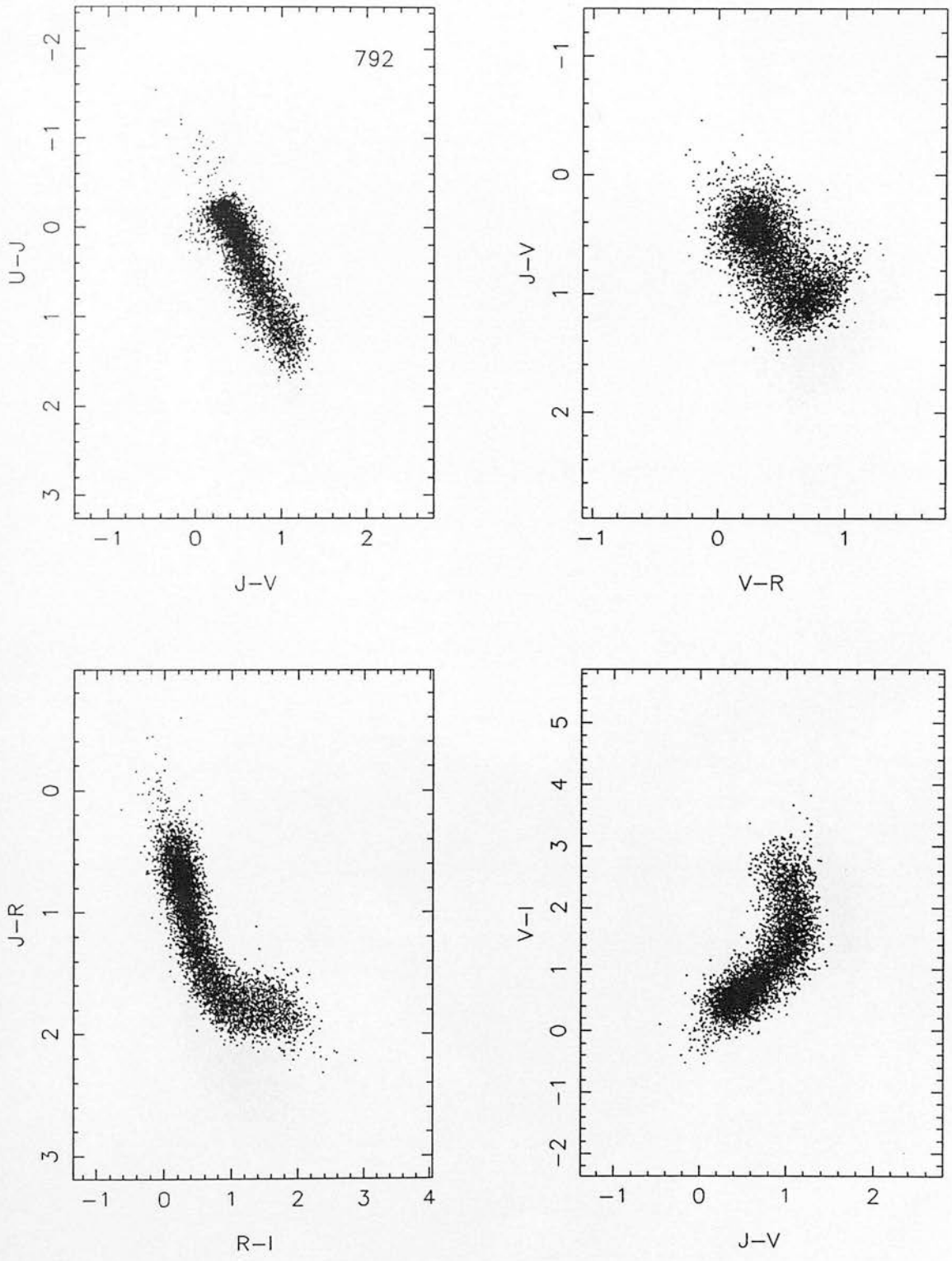

Figure D5: Two-colour diagrams for Schmidt field 861.

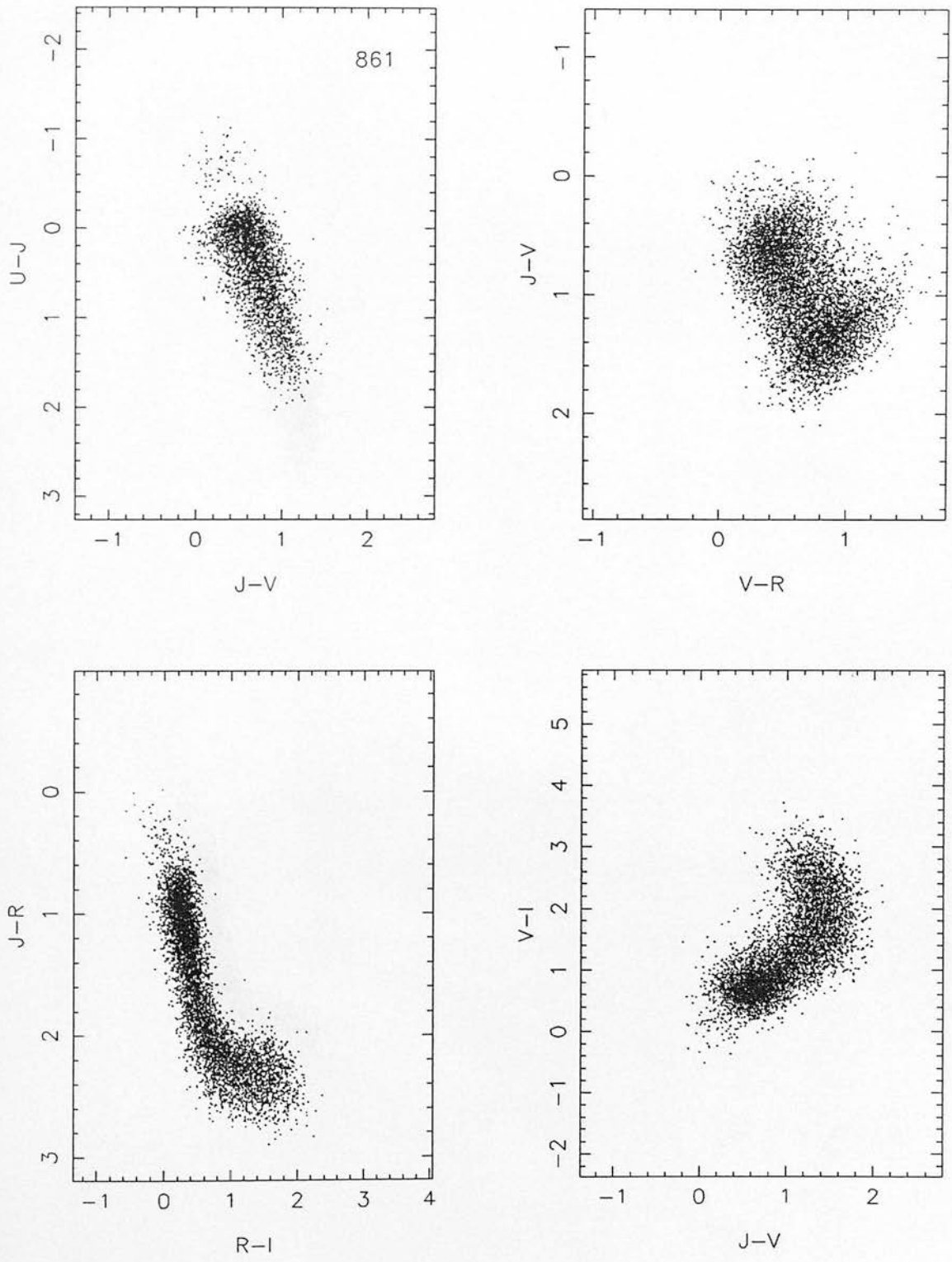

Figure D6: Two-colour diagrams for Schmidt field 862.

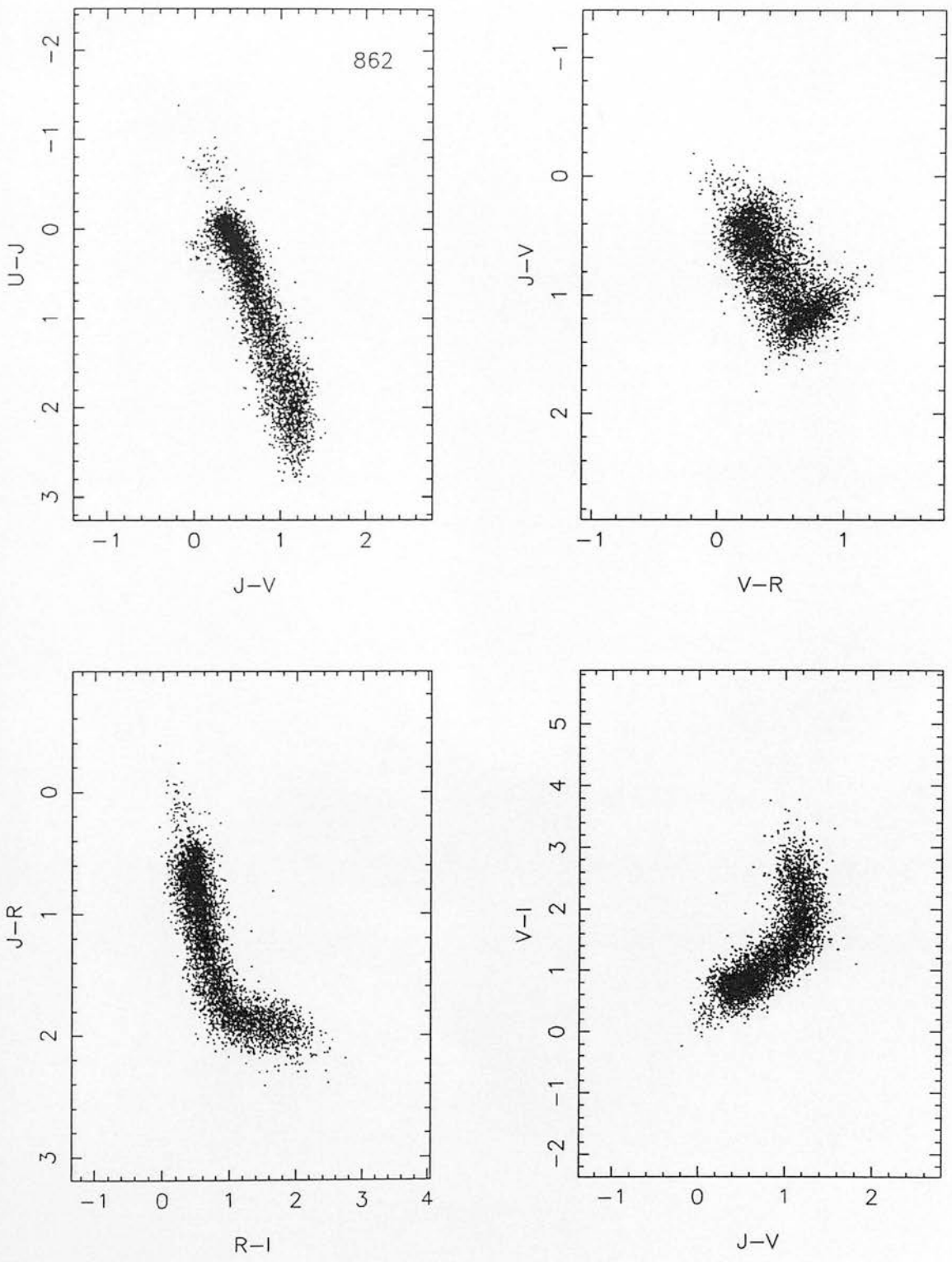

Figure D7: Two-colour diagrams for Schmidt field 863.

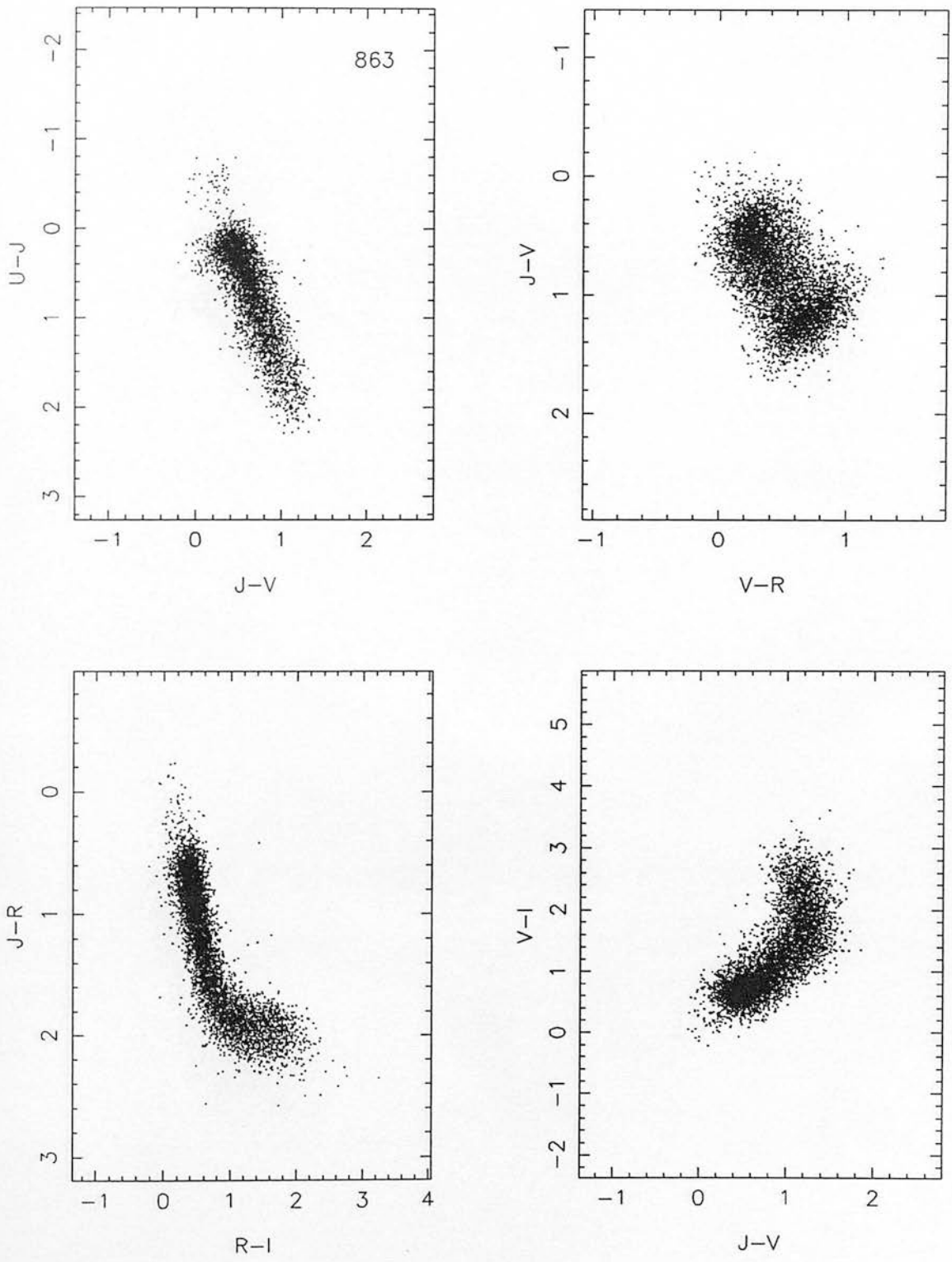

Figure D8: Two-colour diagrams for Schmidt field 864.

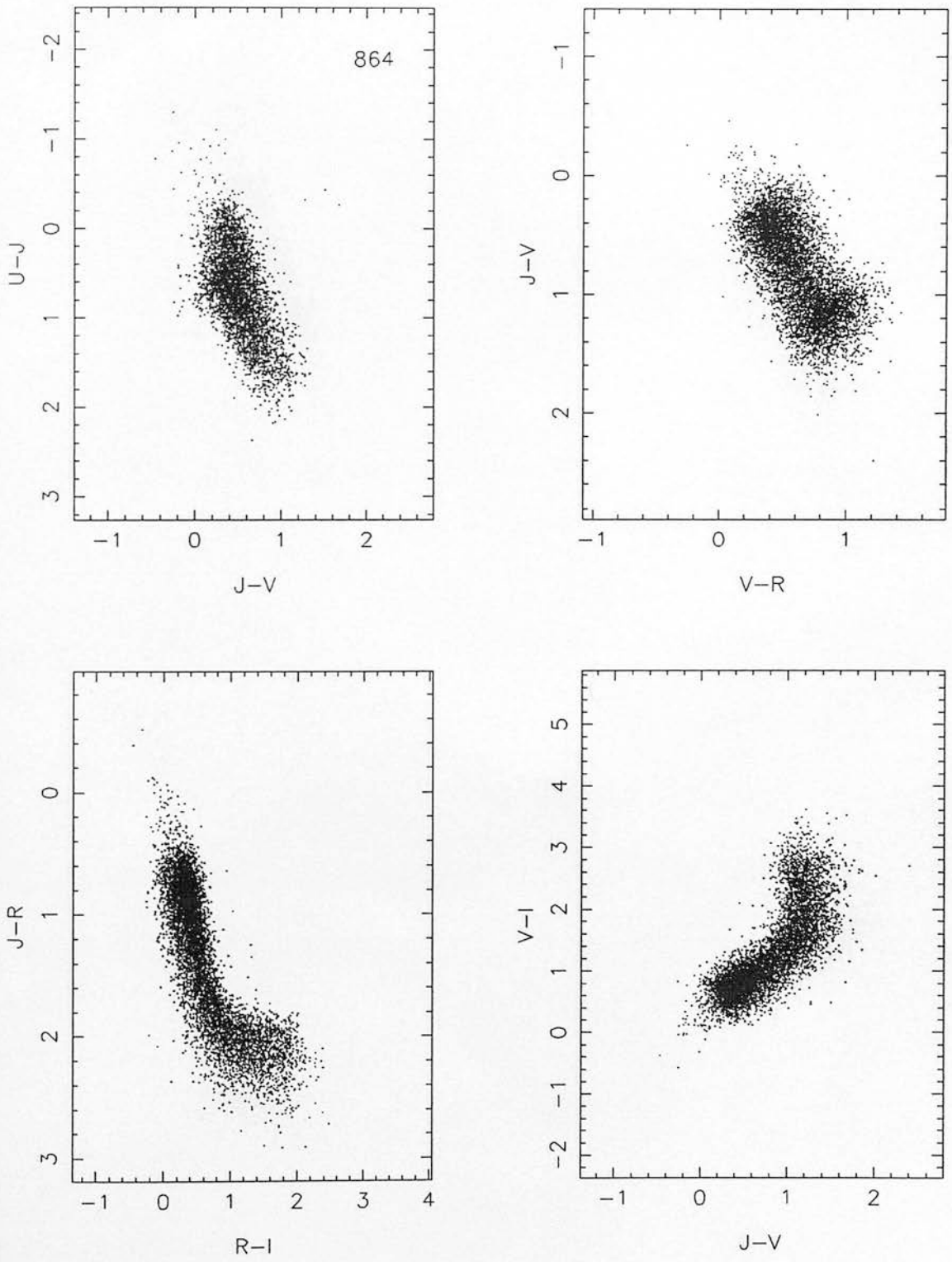

Figure D9: Two-colour diagrams for Schmidt field 865.

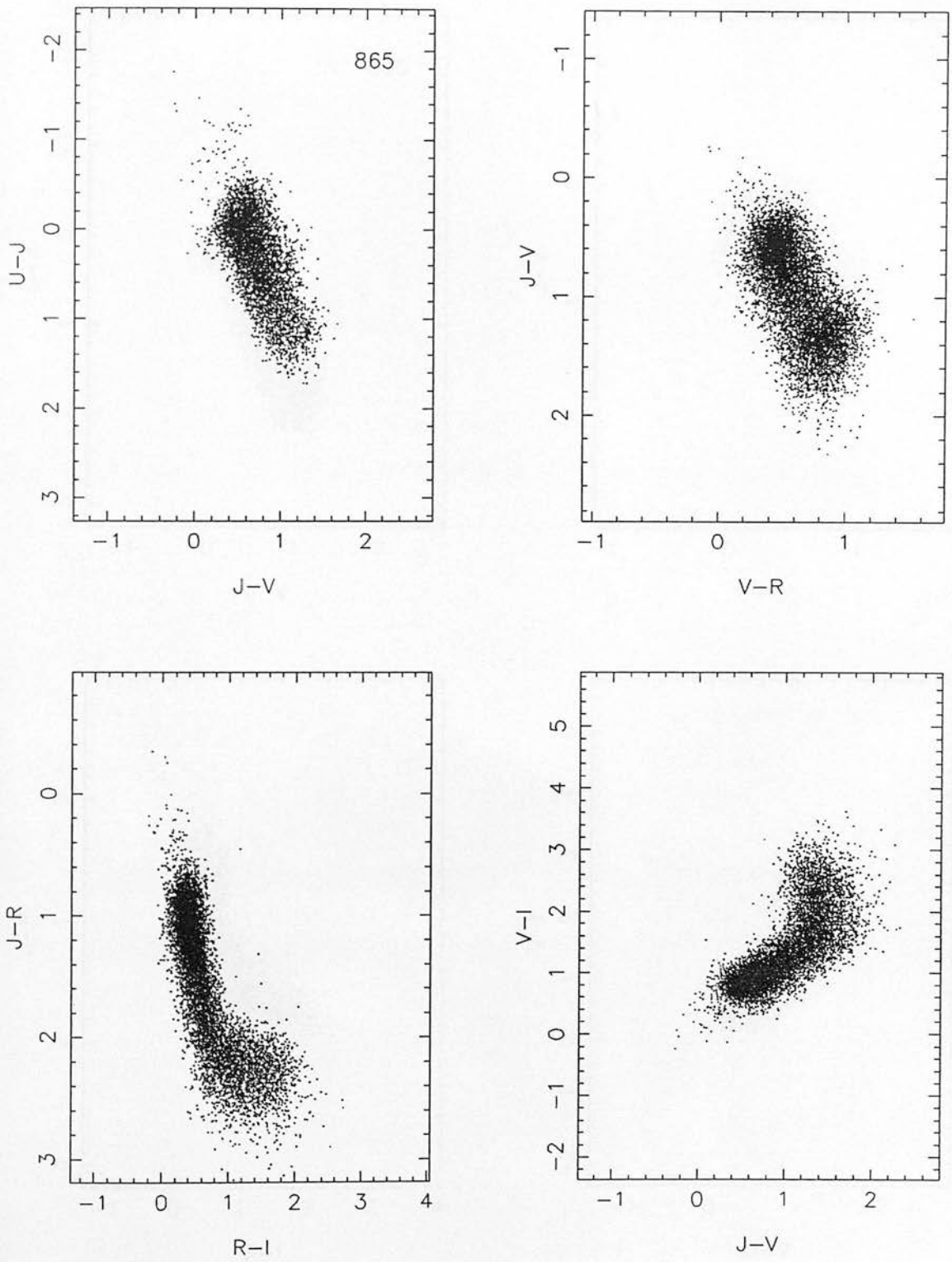

Figure D10: Two-colour diagrams for Schmidt field 866.

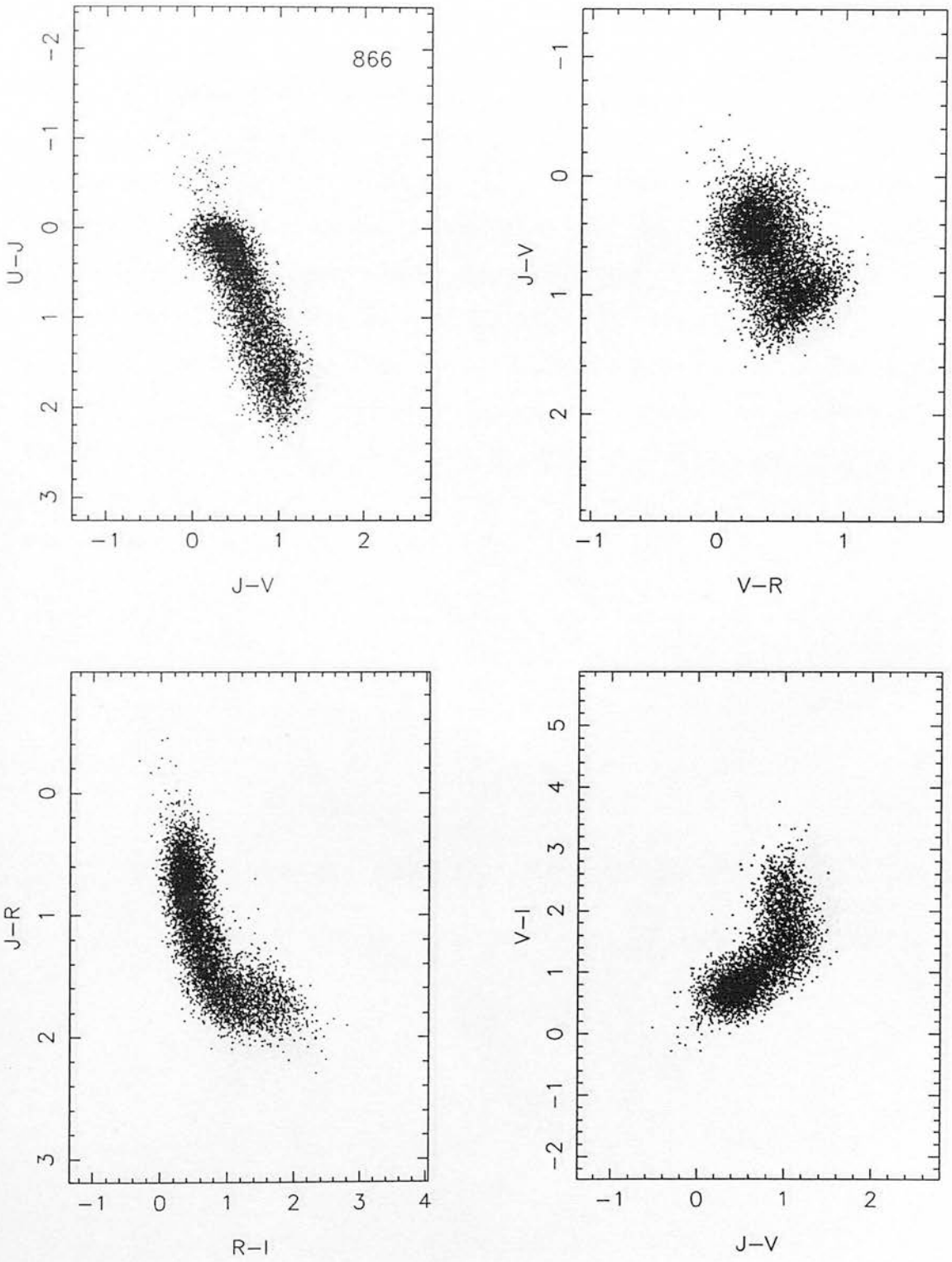

Figure D11: Two-colour diagrams for Schmidt field 867.

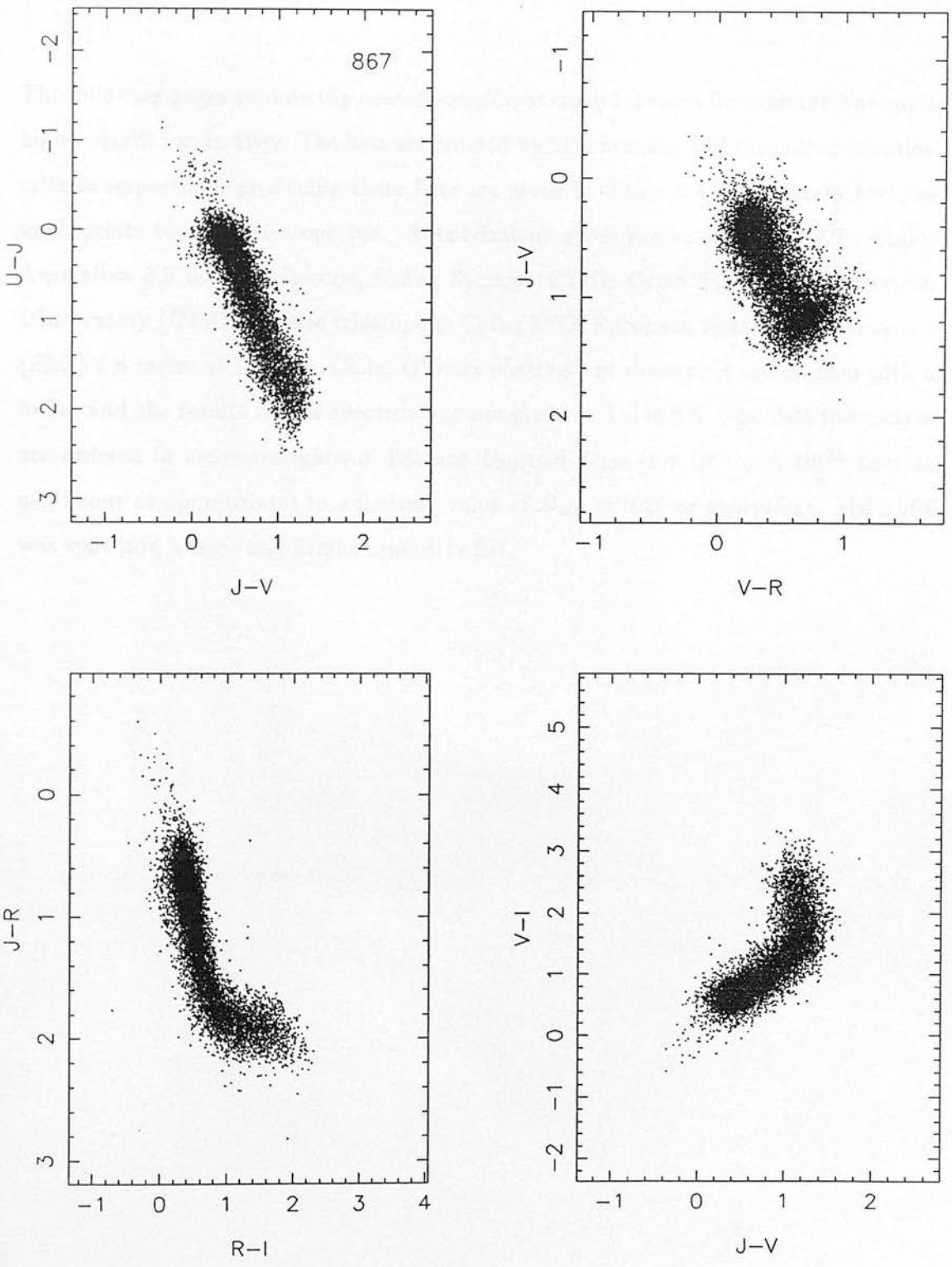

Appendix E

High-redshift candidate lists

The following pages contain top nearest-neighbour candidate lists for each spectroscopic high-redshift run in 1989. The lists are ordered by field number and the colour selection criteria imposed in producing these lists are given in Table 6.4 in the main text, as appropriate to each telescope run. Abbreviations given are as follows: AAT: Anglo-Australian 3.9 metre Telescope, Siding Springs; CTIO: Cerro Tololo Inter-American Observatory (CTIO) 4 metre telescope in Chile; ESO: European Southern Observatory (ESO) 3.6 metre at La Silla, Chile. Objects observed on these runs are marked with a bullet and the results of this spectroscopy are given in Table 6.5. The lists themselves are ordered in nearest-neighbour distance D_{10} and D_{100} (for 10^{th} and 100^{th} nearest neighbour as appropriate) to a limiting value of $D_{100} = 0.25$ or equivalent. Field 867 was split into a faint and bright candidate list.

Table E1: Top candidates in field 789 in 100th nearest-neighbour distance. D_{10} and D_{100} give distances for 10th and 100th neighbours in the catalogue, and observed objects are marked with a bullet. The selection colour criterion imposed were those for the AAT spectroscopic run.

Object	R	U-B	B-V	V-R	R-I	B-R	B-I	α(1950)	δ(1950)	D_{10}	D_{100}
3617 •	18.41	1.20	1.20	0.53	0.97	1.73	2.70	12 34 28.20	−05 07 55.4	0.28	0.39
4362	18.19	1.38	0.97	0.76	0.98	1.72	2.70	12 35 42.62	−03 57 39.7	0.26	0.37
1195	18.09	1.29	1.05	0.70	0.94	1.75	2.68	12 30 21.45	−07 36 10.6	0.27	0.36
1208 •	18.37		1.48	0.45	0.46	1.93	2.39	12 30 27.88	−03 35 05.1	0.23	0.34
4552 •	17.05	0.92	0.71	0.36	-0.01	1.07	1.05	12 36 02.33	−04 08 33.9	0.26	0.34
1535	17.63	2.64	1.16	0.44	0.87	1.60	2.47	12 30 58.91	−05 29 51.4	0.19	0.33
539	17.80	2.46	0.81	0.58	0.62	1.38	2.00	12 29 18.90	−02 36 33.4	0.20	0.33
9342 •	18.33	0.77	1.11	0.06	0.34	1.17	1.51	12 43 43.77	−06 06 33.6	0.24	0.32
12110	17.16	2.68	1.18	0.74	0.92	1.93	2.84	12 48 15.93	−05 34 46.9	0.21	0.31
10820	17.39	2.70	0.86	0.67	0.86	1.53	2.39	12 46 05.65	−07 03 02.3	0.21	0.31
7732 •	18.42	1.50	0.77	0.47	0.16	1.24	1.40	12 41 03.21	−07 13 39.4	0.20	0.30
2122 •	18.30	1.30	1.23	0.14	0.88	1.37	2.25	12 32 02.95	−03 48 27.4	0.23	0.30
1229	18.36	0.93	0.60	0.58	0.81	1.18	1.99	12 30 30.11	−04 56 00.3	0.21	0.30
455 •	18.40	1.88	0.89	0.31	0.42	1.20	1.62	12 28 56.69	−07 04 45.1	0.20	0.29
9957 •	17.74	1.01	0.77	0.30	0.12	1.07	1.20	12 44 45.99	−04 24 10.5	0.20	0.28
413 •	18.29	1.30	0.64	0.44	0.16	1.08	1.24	12 28 58.27	−04 50 37.0	0.20	0.28
2538	18.35	1.21	0.76	0.73	0.74	1.49	2.23	12 32 41.67	−05 06 27.2	0.18	0.28
10710	17.88	2.35	0.93	0.53	0.57	1.46	2.03	12 46 00.83	−05 53 07.2	0.18	0.28
11362	18.39	0.52	0.52	0.69	0.54	1.21	1.75	12 47 02.29	−06 40 13.3	0.19	0.28
10267	17.43	2.63	1.06	0.74	0.81	1.80	2.61	12 45 15.14	−06 44 36.8	0.15	0.28
3259 •	18.20	1.64	0.86	0.40	0.30	1.26	1.55	12 33 52.68	−02 58 17.5	0.18	0.27
1301	17.82	2.35	1.00	0.47	0.65	1.46	2.11	12 30 40.23	−02 45 21.6	0.16	0.27
1765	17.28	1.26	0.84	0.65	0.81	1.49	2.30	12 31 26.59	−03 24 27.6	0.18	0.27
5265 •	18.24	1.44	1.32	0.35	0.50	1.67	2.17	12 37 05.77	−06 42 54.1	0.18	0.27
3881 •	17.88	2.18	1.20	0.39	0.59	1.59	2.18	12 34 56.12	−03 37 04.6	0.16	0.27
3549	18.00	1.05	0.56	0.79	0.54	1.35	1.89	12 34 16.95	−05 44 45.0	0.19	0.27
8359 •	18.39	2.08	0.92	0.32	0.63	1.23	1.86	12 42 11.11	−05 41 43.8	0.17	0.27
7433 •	18.36	2.04	1.03	0.40	0.47	1.43	1.91	12 40 35.51	−06 05 06.9	0.18	0.26
9277 •	18.21	1.83	0.69	0.31	0.63	1.00	1.63	12 43 28.70	−07 32 18.4	0.20	0.26
6684 •	18.38	1.54	0.85	0.20	0.46	1.05	1.51	12 39 27.64	−05 45 19.4	0.17	0.26
11839	17.80	1.27	0.76	0.64	0.81	1.40	2.21	12 47 54.60	−06 49 22.3	0.15	0.26
7350	17.64	2.63	0.95	0.72	0.85	1.67	2.52	12 40 28.95	−06 16 05.8	0.14	0.26
11364	18.37	1.52	1.31	0.74	0.94	2.05	2.99	12 47 03.34	−06 46 27.8	0.19	0.26
720 •	18.16	1.33	0.87	0.40	0.21	1.27	1.48	12 29 19.23	−07 31 25.2	0.18	0.26
3946 •	18.30	1.19	1.13	0.18	0.46	1.32	1.78	12 35 12.85	−02 38 35.9	0.18	0.26
9195 •	18.24	2.09	0.78	0.51	0.48	1.30	1.78	12 43 34.88	−03 36 51.1	0.15	0.25
2604 •	18.21	1.31	1.05	0.07	0.70	1.12	1.82	12 32 50.50	−03 37 31.3	0.18	0.25
3764	18.41		0.77	0.78	0.84	1.55	2.39	12 34 39.00	−07 40 58.5	0.14	0.25
8871	18.39		1.08	0.59	0.70	1.66	2.37	12 42 58.26	−06 28 38.3	0.15	0.25
105 •	18.37	1.61	1.03	0.24	0.48	1.27	1.75	12 28 17.67	−06 05 25.5	0.14	0.25
9936 •	18.18		1.27	0.22	0.64	1.50	2.14	12 44 46.42	−03 14 50.4	0.16	0.25
11290	18.38		1.59	0.39	0.97	1.99	2.96	12 47 04.25	−02 47 18.9	0.17	0.25
4610 •	18.46	1.85	1.04	0.24	0.59	1.29	1.88	12 36 01.46	−07 00 51.8	0.14	0.25
390	18.41	2.11	0.69	0.65	0.49	1.34	1.83	12 28 59.16	−03 23 16.7	0.14	0.25

Table E2: Top candidates in field 789 in 100th nearest-neighbour distance. This selection is for the ESO criterion.

Object	R	U-B	B-V	V-R	R-I	B-R	V-I	α(1950)	δ(1950)	D_{10}	D_{100}
3189 •	17.47	-0.12	-0.04	-0.12	0.09	-0.16	-0.03	12 33 45.06	−04 28 06.3	0.50	0.86
9269 •	18.35	-0.84	0.30	0.52	0.07	0.83	0.60	12 43 28.79	−07 14 23.8	0.38	0.78
10074 •	17.68		0.45	0.25	0.36	0.70	0.61	12 44 58.16	−05 09 54.4	0.63	0.77
12161 •	18.33	-0.33	-0.21	0.26	0.52	0.06	0.78	12 48 28.58	−03 34 21.6	0.33	0.73
7453 •	18.49		0.24	0.12	0.58	0.36	0.70	12 40 38.54	−07 06 33.8	0.62	0.72
2294 •	18.19	0.05	0.05	0.08	-0.12	0.13	-0.04	12 32 04.35	−07 31 09.8	0.37	0.64
11414	18.33	-0.31	-0.08	0.43	0.07	0.36	0.51	12 47 16.24	−04 24 02.9	0.33	0.64
144	17.96	0.18	-0.05	0.04	0.06	-0.01	0.10	12 28 32.00	−03 36 45.7	0.27	0.59
2490	17.34	0.35	-0.06	0.00	0.10	-0.06	0.09	12 32 44.59	−02 40 27.4	0.20	0.56
8697	18.12	0.52	0.12	-0.19	0.14	-0.07	-0.04	12 42 47.56	−02 53 05.0	0.22	0.54
8167	17.87	0.56	-0.06	-0.06	0.17	-0.12	0.11	12 41 46.52	−06 36 27.4	0.18	0.53
3303 •	18.46	-0.39	0.06	0.46	0.39	0.51	0.85	12 33 50.43	−05 53 29.1	0.28	0.51
4536	17.95	0.47	-0.08	0.04	0.13	-0.05	0.16	12 36 00.43	−03 21 07.9	0.15	0.50
5353	17.77	0.36	-0.10	0.04	0.21	-0.06	0.25	12 37 16.71	−06 38 54.9	0.18	0.50
2978	17.29	0.28	0.04	0.01	0.10	0.05	0.11	12 33 28.41	−03 39 42.0	0.16	0.48
4797	17.75	0.69	0.14	-0.05	0.08	0.09	0.03	12 36 21.03	−06 48 15.4	0.25	0.47
11584	18.18	0.43	-0.07	0.14	0.04	0.07	0.18	12 47 33.18	−02 53 03.1	0.15	0.46
4159	17.39	0.30	0.14	-0.03	0.07	0.11	0.04	12 35 24.50	−03 47 45.8	0.17	0.45
8200 •	17.62	-0.36	0.24	0.22	0.37	0.46	0.59	12 42 00.93	−03 11 47.4	0.24	0.43
148	17.04	0.07	0.08	0.06	0.20	0.15	0.26	12 28 35.49	−03 53 45.6	0.23	0.43
11983	17.80	0.63	-0.01	0.06	0.11	0.06	0.17	12 48 04.63	−04 00 11.2	0.17	0.43
5566	17.83	0.40	-0.06	0.11	0.15	0.05	0.26	12 37 30.33	−07 35 40.4	0.14	0.42
4811	17.03	0.48	-0.01	0.02	0.20	0.01	0.21	12 36 32.37	−02 35 51.3	0.12	0.41
1847	17.09	0.35	0.07	0.01	0.15	0.07	0.16	12 31 35.83	−03 44 48.7	0.12	0.41
3257	18.47	0.67	0.10	0.02	0.12	0.12	0.15	12 33 56.42	−02 47 18.2	0.21	0.41
2532	17.86	0.51	0.07	0.02	0.12	0.09	0.14	12 32 40.83	−04 54 34.8	0.13	0.40
9724	18.08	0.49	0.04	-0.01	0.21	0.03	0.20	12 44 21.85	−07 15 14.4	0.13	0.40
3295 •	18.47	-0.38	0.40	0.55	0.34	0.94	0.89	12 33 51.21	−05 36 12.3	0.32	0.39
4530	17.43	0.40	-0.10	0.34	-0.02	0.24	0.32	12 36 03.52	−03 03 00.1	0.22	0.39
10125	17.52	0.57	0.08	-0.02	0.21	0.06	0.20	12 45 00.54	−03 05 34.4	0.14	0.38
7414	17.33	0.55	-0.02	0.15	0.10	0.14	0.25	12 40 35.75	−04 48 28.9	0.14	0.38
2014	17.18	0.21	0.02	0.06	0.32	0.07	0.38	12 31 51.81	−02 55 05.9	0.20	0.37
9558	17.69	0.00	0.04	0.24	0.22	0.28	0.46	12 44 11.44	−03 48 29.4	0.24	0.37
4754 •	18.38		0.75	0.88	0.05	1.62	0.93	12 36 18.96	−04 08 14.5	0.27	0.37
4492	17.41	0.27	0.19	-0.01	0.14	0.18	0.12	12 35 48.11	−06 15 23.4	0.16	0.36
8220	17.78	0.47	0.02	0.07	0.18	0.09	0.24	12 42 04.21	−04 06 54.6	0.12	0.36
8037 •	18.01	0.41	0.23	-0.06	0.16	0.17	0.10	12 41 38.70	−03 58 16.2	0.16	0.35
1208 •	18.37		1.48	0.45	0.46	1.93	0.91	12 30 27.88	−03 35 05.1	0.23	0.34
4552 •	17.05	0.92	0.71	0.36	-0.01	1.07	0.34	12 36 02.33	−04 08 33.9	0.26	0.34
3086	17.63	0.31	0.10	0.03	0.20	0.13	0.23	12 33 33.78	−03 35 37.9	0.13	0.34
2024	18.06	0.21	0.05	0.09	0.25	0.14	0.35	12 31 51.63	−03 23 28.3	0.17	0.34
6107	17.58	0.52	0.04	0.07	0.21	0.11	0.29	12 38 26.50	−04 19 15.8	0.13	0.33
388	18.46	0.34	0.16	0.01	0.18	0.16	0.19	12 28 56.89	−03 20 09.3	0.12	0.33

Table E2: Top candidates in field 789 continued.

Object	R	U-B	B-V	V-R	R-I	B-R	V-I	α(1950)	δ(1950)	D_{10}	D_{100}
539	17.80	2.46	0.81	0.58	0.62	1.38	1.20	12 29 18.90	−02 36 33.4	0.20	0.33
9342 •	18.33	0.77	1.11	0.06	0.34	1.17	0.40	12 43 43.77	−06 06 33.6	0.24	0.32
8800 •	18.04	-0.13	0.27	0.11	0.32	0.38	0.43	12 42 44.23	−07 22 19.2	0.21	0.32
10594 •	18.37	-0.18	0.36	0.47	0.56	0.84	1.03	12 45 52.55	−04 45 39.1	0.25	0.32
6834	17.98	0.57	0.03	0.07	0.38	0.10	0.45	12 39 41.12	−03 13 25.1	0.21	0.31
2227	17.84	0.38	0.00	0.13	0.23	0.14	0.36	12 32 08.94	−03 46 23.5	0.13	0.31
201 •	18.20	0.08	0.40	0.34	-0.14	0.74	0.20	12 28 28.28	−07 03 19.5	0.22	0.30
11659	17.89	0.38	-0.02	0.25	0.12	0.23	0.37	12 47 36.37	−07 02 57.7	0.15	0.30
4225 •	18.30	0.34	0.25	0.08	0.03	0.33	0.12	12 35 25.98	−06 40 24.6	0.17	0.30
7732 •	18.42	1.50	0.77	0.47	0.16	1.24	0.63	12 41 03.21	−07 13 39.4	0.20	0.30
8696	17.52	0.39	0.02	0.19	0.14	0.21	0.33	12 42 46.35	−02 51 08.5	0.13	0.30
455 •	18.40	1.88	0.89	0.31	0.42	1.20	0.73	12 28 56.69	−07 04 45.1	0.20	0.29
9957 •	17.74	1.01	0.77	0.30	0.12	1.07	0.42	12 44 45.99	−04 24 10.5	0.20	0.28
413 •	18.29	1.30	0.64	0.44	0.16	1.08	0.60	12 28 58.27	−04 50 37.0	0.20	0.28
11613	17.06	0.39	0.15	0.09	0.14	0.24	0.24	12 47 33.07	−04 50 46.3	0.12	0.28
9749	17.07	0.38	0.07	0.11	0.22	0.18	0.33	12 44 27.00	−03 22 21.4	0.12	0.28
5996	18.46	1.18	0.43	0.82	0.55	1.26	1.38	12 38 22.64	−03 14 36.9	0.20	0.28
8089	17.76	2.47	0.82	0.81	0.58	1.63	1.39	12 41 38.95	−06 57 14.0	0.19	0.28
10710	17.88	2.35	0.93	0.53	0.57	1.46	1.10	12 46 00.83	−05 53 07.2	0.18	0.28
8222	18.40	1.42	0.99	0.87	0.54	1.86	1.42	12 42 02.09	−04 09 39.2	0.19	0.28
11362	18.39	0.52	0.52	0.69	0.54	1.21	1.23	12 47 02.29	−06 40 13.3	0.19	0.28
11142	18.36	1.68	0.43	0.75	0.69	1.18	1.45	12 46 46.38	−04 35 21.7	0.20	0.28
8154	18.31	0.37	0.06	0.39	-0.02	0.45	0.37	12 41 51.42	−05 50 29.7	0.19	0.28
2880	17.59	0.00	0.07	0.33	0.29	0.40	0.62	12 33 19.58	−03 16 32.4	0.16	0.27
3259 •	18.20	1.64	0.86	0.40	0.30	1.26	0.69	12 33 52.68	−02 58 17.5	0.18	0.27
12025	18.35	0.15	0.07	0.48	0.63	0.55	1.12	12 48 05.75	−06 31 45.8	0.21	0.27
1301	17.82	2.35	1.00	0.47	0.65	1.46	1.12	12 30 40.23	−02 45 21.6	0.16	0.27
5265 •	18.24	1.44	1.32	0.35	0.50	1.67	0.85	12 37 05.77	−06 42 54.1	0.18	0.27
3881 •	17.88	2.18	1.20	0.39	0.59	1.59	0.98	12 34 56.12	−03 37 04.6	0.16	0.27
3549	18.00	1.05	0.56	0.79	0.54	1.35	1.34	12 34 16.95	−05 44 45.0	0.19	0.27
8359 •	18.39	2.08	0.92	0.32	0.63	1.23	0.95	12 42 11.11	−05 41 43.8	0.17	0.27
7433 •	18.36	2.04	1.03	0.40	0.47	1.43	0.87	12 40 35.51	−06 05 06.9	0.18	0.26
9277 •	18.21	1.83	0.69	0.31	0.63	1.00	0.95	12 43 28.70	−07 32 18.4	0.20	0.26
6684 •	18.38	1.54	0.85	0.20	0.46	1.05	0.67	12 39 27.64	−05 45 19.4	0.17	0.26
5225	18.20	0.74	0.17	0.74	0.40	0.91	1.15	12 37 09.05	−04 50 38.2	0.18	0.26
720 •	18.16	1.33	0.87	0.40	0.21	1.27	0.61	12 29 19.23	−07 31 25.2	0.18	0.26
3946 •	18.30	1.19	1.13	0.18	0.46	1.32	0.65	12 35 12.85	−02 38 35.9	0.18	0.26
9195 •	18.24	2.09	0.78	0.51	0.48	1.30	0.99	12 43 34.88	−03 36 51.1	0.15	0.25
8912 •	18.23	1.32	0.37	0.40	0.42	0.77	0.82	12 43 06.67	−03 22 49.0	0.18	0.25
1204 •	18.43	1.03	0.49	0.39	0.17	0.88	0.56	12 30 32.23	−02 51 11.0	0.17	0.25
12492 •	18.42	0.69	0.23	0.49	0.09	0.72	0.58	12 48 55.86	−06 49 30.3	0.18	0.25
105 •	18.37	1.61	1.03	0.24	0.48	1.27	0.72	12 28 17.67	−06 05 25.5	0.14	0.25
11701 •	17.75	0.06	0.23	0.19	0.15	0.43	0.34	12 47 39.63	−03 31 03.5	0.13	0.25
9936 •	18.18		1.27	0.22	0.64	1.50	0.87	12 44 46.42	−03 14 50.4	0.16	0.25
4610 •	18.46	1.85	1.04	0.24	0.59	1.29	0.83	12 36 01.46	−07 00 51.8	0.14	0.25
390	18.41	2.11	0.69	0.65	0.49	1.34	1.14	12 28 59.16	−03 23 16.7	0.14	0.25

Table E3: Top candidates in field 790 in 100th nearest-neighbour distance. AAT criterion.

Object	R	U-B	B-V	V-R	R-I	B-R	B-I	α(1950)	δ(1950)	D_{10}	D_{100}
1144 •	18.45		1.95	0.55	0.14	2.50	2.64	12 50 04.82	−02 39 01.4	0.50	0.65
8876 •	18.43	0.34	1.10	0.49	0.69	1.59	2.28	13 00 14.97	−03 00 54.3	0.34	0.44
4801	18.29			0.35	1.00			12 54 51.59	−02 44 02.3	0.33	0.43
14186	18.45		1.12	0.38	-0.10	1.50	1.40	13 07 12.66	−07 21 58.7	0.28	0.43
8286 •	18.30	-0.47	0.62	0.36	0.54	0.98	1.52	12 59 20.77	−07 08 21.2	0.35	0.42
5328 •	18.22	0.71	1.28	0.61	0.58	1.89	2.47	12 55 28.86	−06 53 18.4	0.32	0.41
2187 •	17.88		0.60	0.21	0.52	0.81	1.33	12 51 23.07	−05 53 19.8	0.24	0.41
2568	18.37	0.20	0.80	0.01	-0.19	0.80	0.61	12 51 48.78	−07 21 37.3	0.28	0.40
12938	18.32	0.43	0.52	0.72	0.70	1.24	1.94	13 05 26.31	−05 40 45.8	0.27	0.39
183	18.47	0.70	1.06	0.68	0.64	1.74	2.37	12 48 26.55	−07 36 44.0	0.25	0.38
2366	18.00	0.97	1.39	0.54	0.94	1.94	2.88	12 51 43.39	−03 29 04.9	0.26	0.36
9029	18.24	0.49	0.79	0.66	0.64	1.45	2.09	13 00 30.45	−03 52 11.4	0.23	0.36
4308 •	18.47		1.72	0.49	0.65	2.21	2.85	12 54 09.59	−06 08 22.9	0.22	0.35
1726 •	18.44	-0.25	0.60	0.56	0.14	1.17	1.31	12 50 44.24	−03 19 36.5	0.29	0.35
14482 •	18.48		1.44	0.34	0.31	1.78	2.10	13 07 36.47	−04 28 54.4	0.24	0.35
7039	18.23	1.99	0.65	0.40	0.44	1.05	1.49	12 57 46.96	−02 33 04.8	0.21	0.35
428	17.43		0.81	0.30	0.61	1.10	1.72	12 48 58.68	−04 52 17.4	0.23	0.34
2345	17.98	1.00	1.34	0.59	0.69	1.93	2.61	12 51 24.94	−07 28 14.4	0.26	0.33
7290 •	18.48	0.77	1.12	0.62	0.50	1.74	2.23	12 58 04.79	−03 28 03.7	0.20	0.32
5586	17.74		0.62	0.34	0.62	0.96	1.57	12 56 01.98	−03 13 06.8	0.20	0.32
4260	18.07	1.91	0.68	0.44	0.38	1.12	1.50	12 54 07.29	−04 06 02.1	0.19	0.32
14021 •	17.42	0.57	1.16	0.42	0.33	1.58	1.91	13 06 59.86	−05 19 14.7	0.24	0.32
13838	18.15	0.30	0.62	0.59	0.62	1.22	1.83	13 06 42.34	−06 34 13.9	0.22	0.32
6659	18.00	0.39	0.75	0.38	0.83	1.12	1.95	12 57 09.76	−07 03 42.0	0.22	0.31
14519	17.94	1.94	0.60	0.66	0.38	1.26	1.65	13 07 35.62	−06 24 12.4	0.21	0.31
14354	18.41	0.54	0.56	0.72	0.54	1.29	1.82	13 07 24.47	−04 42 10.5	0.21	0.31
578	17.02	2.24	1.23	0.69	0.96	1.92	2.88	12 49 03.15	−06 42 29.8	0.21	0.31
14063	18.03	1.68	0.56	0.45	0.31	1.01	1.32	13 06 59.50	−07 26 36.8	0.18	0.30
8259 •	18.38	0.55	1.02	-0.08	0.28	0.94	1.22	12 59 19.52	−05 53 13.8	0.22	0.30
4255	18.43	0.87	0.88	0.74	0.61	1.62	2.23	12 54 11.02	−03 53 49.8	0.19	0.30
12055	18.46		0.61	0.77	0.99	1.38	2.37	13 04 17.74	−07 12 00.6	0.22	0.30
8038	18.11	0.46	0.71	0.53	0.70	1.24	1.94	12 59 03.60	−06 03 37.0	0.20	0.30
91 •	18.41		1.17	0.54	0.21	1.71	1.92	12 48 32.72	−02 35 17.6	0.20	0.29
9680 •	18.17		1.54	0.39	0.60	1.93	2.53	13 01 07.40	−05 20 32.1	0.16	0.29
15176	18.39		0.67	0.68	0.02	1.34	1.36	13 08 34.45	−04 06 38.9	0.21	0.29
3149 •	18.23		1.26	0.53	0.26	1.79	2.05	12 52 49.33	−03 15 42.5	0.19	0.29
7888 •	18.43		1.44	0.28	0.63	1.72	2.35	12 58 50.27	−03 45 50.2	0.15	0.29
7528 •	18.40	0.89	1.24	0.31	0.31	1.55	1.85	12 58 23.13	−03 34 43.1	0.21	0.29
10011	18.40	0.61	0.98	0.55	0.56	1.53	2.09	13 01 43.60	−04 14 33.8	0.20	0.29
14191	17.25	2.18	0.93	0.54	0.53	1.47	2.00	13 07 10.01	−07 32 59.7	0.18	0.29
10690	18.44	0.78	0.88	0.51	0.83	1.39	2.22	13 02 37.23	−04 55 28.4	0.20	0.29
13482	18.45	0.96	0.71	0.68	0.80	1.39	2.19	13 06 12.16	−05 29 06.8	0.20	0.29
14064 •	17.55	0.94	0.54	0.38	0.00	0.92	0.92	13 06 58.22	−07 35 08.2	0.19	0.29
5930	18.26	1.03	1.00	0.46	0.96	1.45	2.42	12 56 19.70	−07 12 46.6	0.21	0.29
4945 •	18.33		1.37	0.16	0.60	1.53	2.13	12 55 04.03	−05 15 24.2	0.17	0.29

Table E3: Top candidates in field 790 continued.

Object	R	U-B	B-V	V-R	R-I	B-R	B-I	α(1950)	δ(1950)	D_{10}	D_{100}
12897	18.25	1.57	0.65	0.40	0.26	1.05	1.31	13 05 29.60	−03 42 43.8	0.17	0.28
1907	18.45		1.45	0.70	0.52	2.15	2.67	12 50 56.36	−06 53 43.3	0.20	0.28
14543	18.34	1.41	0.52	0.40	0.23	0.93	1.16	13 07 36.43	−07 23 00.1	0.19	0.28
7876	17.39		0.77	0.40	0.64	1.17	1.81	12 58 51.68	−02 45 49.1	0.18	0.28
4831	18.30		0.75	0.78	0.95	1.52	2.47	12 54 50.20	−04 42 54.8	0.11	0.28
490 •	18.48		1.21	0.18	0.34	1.40	1.74	12 48 50.81	−07 32 44.5	0.18	0.28
12555	17.16	2.21	1.17	0.46	0.70	1.63	2.33	13 04 59.88	−03 15 42.8	0.19	0.28
483	17.88	0.65	0.73	0.71	0.46	1.44	1.90	12 48 51.78	−07 15 15.6	0.18	0.28
1646	18.37	1.73	0.55	0.54	0.37	1.09	1.46	12 50 39.88	−04 59 11.9	0.17	0.27
7571	18.23	0.80	0.68	0.20	0.05	0.88	0.93	12 58 23.88	−05 19 42.1	0.18	0.27
11724	17.90	2.16	0.79	0.44	0.85	1.23	2.08	13 03 55.59	−02 53 13.6	0.19	0.27
11051	18.49	0.80	1.04	0.55	0.64	1.59	2.23	13 02 59.72	−04 46 27.0	0.16	0.27
4077	18.21	1.17	0.63	0.68	0.84	1.31	2.15	12 53 52.18	−06 16 35.8	0.18	0.27
3843	17.40	1.20	1.18	0.73	0.96	1.91	2.87	12 53 30.88	−07 14 37.8	0.15	0.27
741	18.39	0.78	0.71	0.68	0.62	1.39	2.01	12 49 27.59	−03 15 50.1	0.16	0.27
9231	18.34	1.16	0.50	0.73	0.72	1.23	1.96	13 00 36.79	−07 27 59.6	0.17	0.27
14188	18.26	0.39	0.74	0.12	-0.01	0.87	0.86	13 07 10.93	−07 29 12.0	0.17	0.27
6631	18.48	0.49	0.91	0.04	0.15	0.95	1.10	12 57 09.66	−05 57 14.7	0.19	0.27
12405	18.02	1.43	0.78	0.39	0.19	1.17	1.36	13 04 42.77	−06 25 36.0	0.16	0.27
4419	18.46	0.07	0.78	0.15	-0.02	0.92	0.90	12 54 15.44	−06 25 41.7	0.18	0.26
7389	18.46	0.50	0.96	0.48	0.50	1.43	1.94	12 58 15.63	−03 17 52.6	0.20	0.26
15358	17.95	1.74	0.63	0.41	0.44	1.05	1.48	13 08 44.54	−07 13 15.6	0.13	0.26
7312	18.34	0.28	0.56	0.52	0.62	1.08	1.70	12 58 11.15	−04 24 53.4	0.18	0.26
11960	17.42	2.14	1.04	0.29	0.97	1.33	2.30	13 04 11.32	−02 33 19.9	0.18	0.26
4010	18.49		0.82	0.71	0.85	1.53	2.38	12 53 54.95	−03 38 41.3	0.10	0.26
4699	18.39		1.51	0.25	1.00	1.75	2.75	12 54 42.64	−03 02 47.9	0.13	0.26
11714	17.81	1.74	0.79	0.32	0.45	1.11	1.56	13 04 00.95	−02 38 14.1	0.14	0.25
12352	18.47	1.56	0.59	0.34	0.43	0.93	1.36	13 04 47.31	−04 04 44.1	0.15	0.25
20	18.23		1.24	0.19	0.43	1.42	1.86	12 48 17.07	−03 12 48.4	0.16	0.25
15250	18.02	1.91	0.84	0.41	0.50	1.25	1.75	13 08 36.87	−07 38 08.9	0.14	0.25
7636	17.69	2.06	0.79	0.45	0.65	1.24	1.89	12 58 31.66	−03 01 22.9	0.14	0.25
567	18.11		1.32	0.48	0.46	1.81	2.27	12 49 02.39	−06 17 39.2	0.14	0.25
96	18.38	1.16	0.91	0.19	0.24	1.10	1.33	12 48 32.09	−02 39 37.4	0.15	0.25
13872	17.37	1.52	0.70	0.69	0.24	1.39	1.63	13 06 41.69	−07 33 40.5	0.17	0.25
14384	18.03	1.66	0.61	0.71	0.36	1.32	1.68	13 07 31.14	−05 58 47.1	0.17	0.25
13	18.12	1.26	0.82	0.28	0.21	1.09	1.30	12 48 21.44	−02 35 20.3	0.15	0.25
8501	18.49		1.48	0.71	0.75	2.19	2.94	12 59 36.60	−06 23 44.6	0.12	0.25
15343	18.17	0.91	0.85	0.57	0.77	1.43	2.20	13 08 38.92	−06 48 07.1	0.15	0.25
6077	18.49	0.57	0.97	0.15	0.18	1.12	1.29	12 56 26.77	−07 37 02.4	0.17	0.25
9227	18.03		1.05	0.48	0.92	1.53	2.45	13 00 35.47	−07 10 20.9	0.17	0.25
3617	17.90	1.07	0.78	0.31	0.12	1.10	1.22	12 53 06.28	−07 39 36.6	0.14	0.25
13314	17.51		0.92	0.28	0.76	1.20	1.97	13 06 07.39	−02 34 46.5	0.14	0.25
12579	18.03	1.72	0.78	0.33	0.44	1.11	1.56	13 05 04.05	−04 04 03.5	0.12	0.25
14803	18.42		1.39	0.24	0.81	1.62	2.44	13 08 05.36	−03 17 45.5	0.11	0.25

Table E4: Top candidates in field 791 in 100th nearest-neighbour distance. AAT criterion.

Object	R	U-B	B-V	V-R	R-I	B-R	B-I	α(1950)	δ(1950)	D_{10}	D_{100}
2394 •	18.36			0.52	0.47			13 11 55.96	−03 23 01.9	0.43	0.53
2656	17.64	0.40	0.61	0.67	0.95	1.28	2.23	13 12 10.89	−06 15 16.7	0.37	0.50
4437	17.95	0.62	0.83	0.75	0.88	1.58	2.47	13 14 37.03	−03 30 40.9	0.36	0.48
10569	18.36	1.07	1.47	0.75	0.89	2.22	3.11	13 22 52.57	−04 02 00.2	0.29	0.43
7619 •	18.50		2.03	0.54	0.61	2.56	3.18	13 18 51.86	−05 31 43.0	0.24	0.41
13217	17.68	0.47	0.90	0.57	0.82	1.48	2.30	13 26 11.98	−05 37 47.3	0.29	0.39
2779 •	18.33		1.71	0.64	0.48	2.36	2.83	13 12 15.55	−06 29 11.7	0.20	0.38
7404	17.99	1.14	1.17	0.74	0.90	1.91	2.81	13 18 39.06	−05 34 09.0	0.26	0.37
9707	18.32	0.97	1.34	0.71	0.68	2.04	2.72	13 21 39.41	−05 14 34.4	0.23	0.35
14531	18.25		1.94	0.49	0.86	2.43	3.29	13 27 57.28	−06 23 11.6	0.20	0.34
2795 •	18.39	0.55	0.57	0.46	-0.17	1.03	0.87	13 12 17.82	−07 18 29.8	0.26	0.34
3140 •	18.12	0.55	1.06	0.68	0.53	1.74	2.27	13 13 01.29	−03 04 28.7	0.20	0.33
7286	18.21		1.84	0.73	0.62	2.57	3.19	13 18 29.46	−05 41 56.0	0.14	0.32
9687 •	18.03	2.08	1.41	0.37	0.42	1.78	2.20	13 21 39.56	−04 22 18.9	0.23	0.32
14937	17.31	2.49	1.55	0.56	0.66	2.11	2.77	13 28 38.51	−03 32 16.4	0.13	0.32
1931 •	17.82	2.31	1.26	0.37	0.58	1.63	2.21	13 10 58.80	−07 03 44.7	0.21	0.32
2258 •	17.72	2.06	0.78	0.50	0.46	1.28	1.73	13 11 25.78	−07 14 54.5	0.22	0.32
10933	18.25		1.99	0.59	0.91	2.58	3.49	13 23 21.27	−05 39 20.4	0.17	0.32
7039	18.50	0.33	0.79	0.62	0.66	1.41	2.07	13 18 11.13	−04 28 07.0	0.21	0.32
11077 •	18.28		1.61	0.57	0.61	2.18	2.79	13 23 34.23	−06 39 31.8	0.12	0.31
13450	18.28		1.86	0.67	0.72	2.53	3.25	13 26 30.71	−06 19 32.9	0.12	0.31
6827 •	17.68		1.56	0.43	0.45	1.99	2.45	13 17 54.07	−05 07 51.9	0.17	0.31
3237 •	17.82	2.26	1.11	0.54	0.39	1.66	2.05	13 12 55.52	−07 06 57.6	0.21	0.31
13999	18.30	0.94	1.07	0.74	0.66	1.81	2.48	13 27 16.51	−04 36 39.4	0.18	0.31
14922	17.93	0.90	1.29	0.57	0.63	1.86	2.50	13 28 38.87	−02 43 48.0	0.17	0.31
514	18.42	1.66	0.96	0.21	0.80	1.16	1.96	13 09 01.14	−05 46 32.8	0.19	0.30
11719	17.87	2.37	1.01	0.49	0.65	1.50	2.15	13 24 24.08	−02 56 44.5	0.20	0.30
14648 •	18.22	1.08	1.47	0.37	0.61	1.84	2.45	13 28 03.49	−06 14 56.6	0.20	0.30
15075	18.29	0.92	1.32	0.65	0.39	1.97	2.36	13 28 47.82	−04 57 26.2	0.18	0.30
2584	17.54	2.50	1.17	0.72	0.49	1.89	2.39	13 11 54.48	−07 31 28.6	0.20	0.30
8896 •	18.43		1.50	0.21	0.62	1.71	2.33	13 20 36.51	−03 56 59.4	0.20	0.30
13796	17.14	0.96	1.09	0.67	0.71	1.77	2.47	13 27 02.81	−06 09 36.9	0.17	0.29
5875	18.50	0.57	0.99	0.71	0.46	1.71	2.17	13 16 41.04	−04 57 40.6	0.16	0.29
8815	18.12	1.08	1.09	0.71	0.75	1.80	2.55	13 20 25.62	−05 28 42.5	0.16	0.29
11674	18.40	0.03	0.56	0.49	0.71	1.05	1.76	13 24 17.71	−06 36 56.7	0.21	0.29
5394	18.47		1.96	0.55	0.98	2.51	3.49	13 16 05.25	−02 47 33.2	0.14	0.29
12217	18.14	0.99	1.33	0.63	0.58	1.96	2.54	13 25 01.00	−03 54 31.0	0.17	0.29
375 •	18.44		1.67	0.28	0.83	1.94	2.77	13 08 57.54	−03 42 28.5	0.16	0.29
10226	18.43		1.68	0.45	0.55	2.13	2.68	13 22 24.41	−03 21 18.5	0.14	0.29
14945	18.49		1.79	0.74	0.81	2.53	3.34	13 28 36.75	−03 45 59.4	0.13	0.29
6616	18.49		1.23	0.45	0.17	1.69	1.86	13 17 28.85	−05 50 03.5	0.18	0.29
13198	17.66	2.48	1.35	0.47	0.74	1.82	2.56	13 26 17.05	−04 43 14.8	0.18	0.29
13171	18.45		1.48	0.52	0.37	2.01	2.38	13 26 20.81	−03 32 34.8	0.16	0.29
10558	18.34		1.52	0.78	0.53	2.31	2.83	13 22 51.35	−03 23 42.8	0.14	0.29
11150	17.91		1.55	0.64	0.59	2.19	2.79	13 23 41.27	−04 55 55.2	0.10	0.29
3399	17.83	2.28	0.98	0.58	0.47	1.56	2.03	13 13 11.25	−04 12 25.8	0.17	0.28
9397	18.37		1.43	0.68	0.25	2.11	2.36	13 21 09.60	−05 41 25.5	0.19	0.28
8900	17.53	2.58	1.37	0.61	0.72	1.98	2.69	13 20 40.52	−04 06 35.6	0.15	0.28
11613	18.48	1.37	1.41	0.19	0.71	1.61	2.32	13 24 15.51	−03 29 44.3	0.19	0.28
3057	18.48		1.73	0.53	0.57	2.26	2.83	13 12 47.56	−04 40 10.6	0.16	0.28
1823	18.12	1.44	1.58	0.33	0.72	1.91	2.63	13 11 11.80	−02 55 43.5	0.17	0.28
2734	17.76	1.41	1.01	0.66	0.92	1.67	2.59	13 12 14.89	−04 56 05.5	0.18	0.28

Table E4: Top candidates in field 791 continued.

Object	R	U-B	B-V	V-R	R-I	B-R	B-I	α(1950)	δ(1950)	D_{10}	D_{100}
2075	18.01	0.72	1.26	0.21	0.38	1.48	1.85	13 11 27.08	−03 19 45.4	0.18	0.28
609	17.48	2.16	1.41	0.36	0.60	1.77	2.37	13 09 08.06	−06 15 37.1	0.17	0.28
7377	18.33	0.87	1.34	0.30	0.48	1.64	2.12	13 18 36.29	−04 21 39.1	0.19	0.28
9236	18.41	2.03	0.99	0.47	0.41	1.46	1.87	13 21 00.28	−02 59 48.8	0.17	0.27
5008	18.37	1.75	0.92	0.55	0.22	1.47	1.69	13 15 25.68	−04 25 12.1	0.20	0.27
14959	18.38		1.58	0.41	0.55	1.99	2.54	13 28 38.08	−04 33 41.6	0.12	0.27
13434	18.25		1.90	0.49	0.99	2.40	3.39	13 26 35.51	−05 39 54.6	0.12	0.27
1320	18.41	0.75	0.64	0.44	0.82	1.08	1.90	13 10 16.94	−05 45 25.6	0.19	0.27
6864	18.49	0.30	0.63	0.71	0.53	1.34	1.87	13 17 53.06	−06 27 49.6	0.19	0.27
359	18.20		1.21	0.32	0.38	1.53	1.92	13 08 39.11	−07 34 48.8	0.15	0.27
8740	18.25		1.90	0.63	0.90	2.53	3.43	13 20 13.96	−07 22 30.4	0.14	0.27
1676	18.12	1.91	0.85	0.45	0.49	1.30	1.79	13 10 45.90	−06 32 01.1	0.17	0.27
9373	18.37	-0.31	0.73	0.36	0.55	1.09	1.63	13 21 11.57	−04 53 43.2	0.19	0.27
3248	18.32	1.16	0.91	0.43	0.10	1.34	1.44	13 12 49.21	−07 40 53.5	0.18	0.27
8597	17.78	1.72	0.61	0.55	0.55	1.16	1.72	13 20 08.24	−06 55 31.8	0.17	0.27
791	18.30		1.90	0.60	0.92	2.51	3.43	13 09 31.98	−04 59 59.5	0.11	0.27
2230	18.22	1.18	1.42	0.59	0.45	2.01	2.46	13 11 32.90	−05 47 41.3	0.14	0.26
13416	18.25	1.88	1.39	0.43	0.40	1.82	2.22	13 26 38.38	−04 41 44.3	0.16	0.26
1044	18.14	1.54	1.31	0.28	0.43	1.60	2.03	13 10 00.20	−02 40 30.6	0.14	0.26
1504	17.94	2.49	0.93	0.79	0.67	1.72	2.40	13 10 41.85	−03 18 41.7	0.17	0.26
7599	18.23	1.32	1.51	0.58	0.73	2.09	2.82	13 18 50.52	−04 40 34.6	0.17	0.26
7187	18.13	1.51	1.28	0.53	0.23	1.81	2.04	13 18 12.36	−05 55 41.6	0.17	0.26
8035	18.37	1.72	1.10	0.25	0.60	1.35	1.95	13 19 23.18	−07 03 31.4	0.15	0.26
1895	18.04	0.87	0.75	0.23	0.22	0.97	1.19	13 10 59.34	−05 51 34.8	0.17	0.26
2205	17.85		1.72	0.79	0.79	2.51	3.29	13 11 29.67	−04 38 34.2	0.10	0.26
4563	18.08	2.00	1.15	0.40	0.48	1.55	2.03	13 14 44.40	−03 13 48.5	0.14	0.26
1382	17.69	1.23	0.80	0.47	0.84	1.27	2.11	13 10 34.80	−02 50 07.5	0.17	0.26
9471	18.40		1.78	0.55	0.67	2.33	3.00	13 21 20.15	−03 28 01.3	0.16	0.26
1053	18.16	1.63	0.67	0.44	0.50	1.11	1.61	13 10 00.45	−03 03 57.2	0.16	0.26
5582	18.49		1.53	0.69	0.44	2.23	2.67	13 16 11.34	−06 22 07.7	0.12	0.26
2393	18.17	1.89	0.71	0.58	0.55	1.29	1.84	13 11 56.96	−03 18 03.3	0.16	0.25
8495	18.22	1.85	1.03	0.35	0.51	1.38	1.88	13 20 12.40	−03 01 18.5	0.15	0.25
10505	18.22	1.16	1.18	0.58	0.77	1.76	2.53	13 22 39.64	−05 44 00.5	0.15	0.25
9530	18.17	0.09	0.92	-0.06	0.40	0.86	1.26	13 21 24.84	−06 02 54.2	0.17	0.25
1359	17.86	1.93	0.85	0.64	0.32	1.50	1.82	13 10 17.31	−07 15 54.3	0.15	0.25
8763	17.24	2.55	1.18	0.60	0.82	1.79	2.61	13 20 29.47	−03 23 18.9	0.15	0.25
12211	18.06	2.25	0.98	0.52	0.70	1.50	2.20	13 25 07.62	−03 44 19.8	0.16	0.25
9445	18.11	1.17	1.38	0.39	0.65	1.77	2.42	13 21 11.04	−07 35 46.4	0.15	0.25
4739	18.11		1.72	0.75	0.63	2.47	3.10	13 14 56.12	−06 25 50.4	0.11	0.25
4695	18.43		1.52	0.58	0.40	2.09	2.49	13 14 54.64	−04 31 35.0	0.16	0.25
632	18.29		0.65	0.77	0.70	1.41	2.12	13 09 07.77	−07 13 04.2	0.16	0.25
7032	17.96	0.56	0.90	0.75	0.32	1.65	1.97	13 18 09.35	−04 09 43.2	0.15	0.25
2746	18.42	1.31	0.60	0.56	0.22	1.16	1.38	13 12 15.90	−05 24 59.1	0.15	0.25
8878	18.44	0.36	0.89	0.63	0.43	1.53	1.96	13 20 34.40	−03 06 16.5	0.17	0.25
2721	18.25	1.10	0.66	0.25	0.42	0.91	1.32	13 12 17.04	−04 16 25.5	0.18	0.25
572	17.93	2.01	1.25	0.43	0.46	1.69	2.14	13 09 16.43	−04 28 57.6	0.15	0.25
5038	17.84	1.41	1.33	0.71	0.88	2.04	2.91	13 15 22.02	−05 50 55.3	0.15	0.25
11645	18.36	-0.09	0.70	0.33	-0.12	1.03	0.91	13 24 17.70	−04 57 20.0	0.17	0.25
5594	18.10	1.64	0.56	0.67	0.48	1.23	1.71	13 16 03.99	−06 47 34.2	0.16	0.25
11890	17.99		1.52	0.74	0.48	2.26	2.74	13 24 38.26	−05 29 23.6	0.12	0.25
13981	18.46		1.43	0.56	0.48	1.99	2.47	13 27 16.36	−04 00 04.0	0.13	0.25

Table E5: Top candidates in field 792 in 100^{th} nearest-neighbour distance. AAT criterion.

Object	R	U-B	B-V	V-R	R-I	B-R	B-I	α(1950)	δ(1950)	D_{10}	D_{100}
7083 •	17.78	1.72	0.96	0.48	0.49	1.45	1.94	13 39 07.72	−04 42 36.0	0.29	0.39
4380 •	18.31	1.17	1.01	0.14	0.39	1.15	1.54	13 35 21.32	−04 18 44.6	0.24	0.35
5776	18.42	-0.48	0.50	0.35	0.56	0.85	1.41	13 37 14.91	−04 30 14.8	0.28	0.34
10919 •	18.29	0.66	1.01	0.09	0.17	1.10	1.27	13 44 46.47	−03 10 04.9	0.24	0.33
7211	18.26	0.98	0.67	0.35	0.08	1.02	1.11	13 39 11.88	−05 07 59.8	0.23	0.33
11060	18.30	1.24	0.61	0.62	0.20	1.23	1.43	13 44 57.33	−04 32 22.3	0.20	0.30
9909	18.45	0.95	0.62	0.41	0.12	1.03	1.15	13 43 15.44	−05 32 24.4	0.18	0.29
5987 •	18.47		1.47	0.28	0.78	1.75	2.53	13 37 32.50	−03 30 41.2	0.20	0.28
11152 •	17.71	1.51	0.88	0.53	0.46	1.42	1.88	13 45 07.48	−04 33 02.9	0.20	0.28
9615 •	18.47		1.45	0.28	0.85	1.73	2.58	13 42 44.27	−05 37 53.7	0.20	0.27
10111	18.36	1.25	0.69	0.35	0.52	1.04	1.55	13 43 37.68	−04 14 54.6	0.20	0.27
4517 •	17.49	1.34	1.03	0.55	0.33	1.58	1.92	13 35 24.33	−05 36 36.2	0.17	0.27
21	17.26	0.11	0.62	0.34	0.75	0.95	1.70	13 28 16.21	−06 16 17.6	0.20	0.27
261	18.49	0.43	0.75	0.47	0.78	1.21	1.99	13 28 39.17	−06 40 21.7	0.19	0.27
6665 •	18.31	0.92	0.83	0.25	0.25	1.08	1.33	13 38 33.94	−05 39 50.3	0.18	0.27
11056 •	18.35		0.99	0.49	0.09	1.48	1.57	13 44 55.81	−04 18 36.7	0.18	0.26
3823 •	18.24	0.77	1.11	0.11	0.50	1.21	1.72	13 34 32.79	−02 51 16.6	0.18	0.26
2226	18.30	0.54	0.65	0.45	-0.07	1.09	1.03	13 31 52.45	−06 12 33.8	0.19	0.26
5153	18.14	0.49	0.68	0.33	-0.05	1.01	0.96	13 36 22.65	−06 16 32.8	0.18	0.26
6239 •	18.28	1.19	0.81	0.48	0.25	1.29	1.54	13 37 54.75	−04 34 29.9	0.15	0.26
6154	18.44	1.07	0.65	0.45	0.26	1.10	1.36	13 37 44.19	−06 09 23.1	0.16	0.25
11350	17.13	1.57	1.22	0.68	0.89	1.90	2.79	13 45 25.49	−03 45 39.4	0.15	0.25
9273 •	18.39		1.02	0.31	0.27	1.34	1.61	13 42 18.35	−05 01 41.3	0.16	0.25
565 •	18.41		1.12	0.22	0.80	1.34	2.14	13 29 15.76	−05 21 41.1	0.16	0.25
2598	17.49	0.31	0.64	0.67	0.51	1.31	1.82	13 32 28.13	−04 47 04.7	0.18	0.25
7873	17.14	1.61	1.14	0.66	0.73	1.81	2.53	13 40 24.74	−03 26 53.2	0.15	0.25
11131	18.34	0.07	0.56	0.48	-0.18	1.04	0.86	13 45 09.95	−03 06 39.7	0.18	0.25

Table E6: Top candidates in field 861 in 100^{th} nearest-neighbour distance. AAT criterion.

Object	R	U-B	B-V	V-R	R-I	B-R	B-I	α(1950)	δ(1950)	D_{10}	D_{100}
9510	18.47	-0.87	0.68	0.16	0.76	0.84	1.60	12 44 49.87	−00 34 47.5	0.46	0.63
5942 •	17.44	-0.96	0.55	0.45	0.16	1.01	1.17	12 38 34.76	+00 39 23.9	0.34	0.61
11511 •	18.25	1.75	0.83	0.22	0.37	1.05	1.42	12 47 59.38	−00 22 05.5	0.38	0.48
9244 •	18.20	0.80	0.96	0.20	-0.06	1.16	1.09	12 44 22.10	−01 40 15.3	0.31	0.42
7104 •	18.28	0.12	1.36	0.36	0.48	1.72	2.20	12 40 44.47	+01 43 42.6	0.31	0.40
6533 •	18.44		1.56	0.22	0.45	1.78	2.22	12 39 40.51	+00 49 54.7	0.25	0.40
2997 •	18.30	1.45	0.79	0.28	0.24	1.07	1.32	12 33 42.32	+01 12 56.4	0.28	0.39
4832 •	18.36	-0.63	0.74	0.16	0.46	0.90	1.36	12 36 43.59	+02 03 22.6	0.27	0.38
3080	18.47		1.78	0.22	0.60	1.99	2.59	12 33 54.82	+01 44 16.8	0.18	0.37
3380 •	17.81	0.31	1.10	0.50	0.71	1.59	2.30	12 34 23.12	+00 47 35.4	0.26	0.37
12020 •	18.40	0.39	1.04	0.75	0.52	1.79	2.31	12 48 43.63	−01 58 07.6	0.27	0.36
11621	17.90	-0.22	0.61	0.79	0.37	1.40	1.76	12 48 03.36	−00 38 55.2	0.26	0.35
3332	18.49	0.48	0.69	0.43	-0.21	1.12	0.91	12 34 09.93	−02 11 33.9	0.25	0.34
5677	18.34		1.77	0.41	0.43	2.18	2.61	12 38 14.33	+00 09 34.1	0.17	0.34
8829	17.61	1.07	1.46	0.53	0.91	1.99	2.90	12 43 39.83	+01 20 50.4	0.25	0.34
1646	18.17	-0.51	0.63	0.43	0.47	1.07	1.53	12 31 26.31	+00 19 39.8	0.24	0.33
2900	17.90	0.90	1.52	0.30	0.66	1.82	2.48	12 33 36.66	+01 14 16.0	0.16	0.33
3507	18.49		1.91	0.32	0.80	2.23	3.03	12 34 28.71	−00 18 34.0	0.20	0.32
1620	18.33		1.41	0.39	0.42	1.80	2.22	12 31 24.61	+01 57 43.1	0.14	0.32
12042 •	18.25		1.62	0.39	0.38	2.00	2.39	12 48 52.41	+01 29 10.2	0.20	0.32
1011	17.79	1.33	0.62	0.65	0.09	1.26	1.36	12 30 23.48	+00 57 12.6	0.21	0.32
10958	18.35	0.26	0.51	0.76	0.59	1.27	1.86	12 47 07.46	−02 30 08.2	0.22	0.32
7779	18.03		1.54	0.45	0.47	1.99	2.47	12 41 55.08	−01 32 22.7	0.14	0.32
10911 •	18.43		1.44	0.42	0.20	1.86	2.06	12 47 01.07	+00 13 17.5	0.19	0.32
6207	18.38	0.49	1.01	0.42	0.77	1.43	2.20	12 39 05.84	−00 47 07.3	0.21	0.31
7168 •	17.76	1.29	1.51	0.37	0.35	1.88	2.24	12 40 50.66	−01 29 32.9	0.23	0.31
754 •	18.02	1.03	0.72	0.56	-0.02	1.29	1.26	12 29 55.57	+00 28 59.1	0.21	0.31
1992 •	18.42	0.91	0.99	0.12	0.28	1.11	1.39	12 32 05.26	−00 00 33.0	0.19	0.31
3747	18.24		1.53	0.32	0.57	1.85	2.42	12 34 54.16	+00 40 03.2	0.15	0.31
2839	18.36		1.78	0.43	0.49	2.20	2.70	12 33 30.75	−01 13 21.4	0.14	0.30
6744	18.12		1.90	0.58	0.63	2.48	3.11	12 40 01.21	−02 01 11.9	0.16	0.30
3741	18.36		0.58	0.40	0.07	0.98	1.05	12 34 56.17	+01 11 03.1	0.20	0.30
10464 •	18.06	0.36	1.18	0.12	0.16	1.31	1.47	12 46 20.48	−01 52 29.0	0.21	0.30
5492	18.25	-0.55	0.62	0.38	0.20	1.00	1.20	12 37 55.06	+00 33 33.6	0.20	0.30
3066	18.23		1.37	0.43	0.36	1.79	2.15	12 33 45.96	−02 21 10.5	0.13	0.30
10914	17.92		1.98	0.59	0.78	2.57	3.35	12 47 04.12	+00 05 38.1	0.19	0.30
9684	17.32	1.99	0.93	0.67	0.39	1.61	1.99	12 45 05.26	−00 52 31.2	0.20	0.30
5632	18.23		1.78	0.48	0.47	2.25	2.72	12 38 04.07	−01 47 07.9	0.13	0.30
7925	17.83		1.99	0.59	0.88	2.58	3.46	12 42 11.45	−00 16 57.8	0.16	0.30
11023	18.42	0.17	0.82	0.66	0.51	1.48	1.99	12 47 15.97	−01 07 37.5	0.21	0.29
4929	18.15		1.88	0.56	0.63	2.44	3.07	12 36 56.59	+01 37 55.2	0.15	0.29
3829	18.33		1.83	0.47	0.55	2.30	2.85	12 35 03.73	+00 54 07.9	0.14	0.29
1632	18.38	1.04	0.60	0.31	0.62	0.91	1.53	12 31 28.95	+01 14 01.8	0.20	0.28
4003	18.40		0.69	0.76	-0.14	1.45	1.31	12 35 28.71	+02 08 01.9	0.20	0.28
8732	17.90		0.64	0.72	0.74	1.36	2.10	12 43 36.00	+00 43 55.6	0.17	0.28
4772	18.37		1.56	0.34	0.60	1.90	2.50	12 36 41.59	+00 35 23.9	0.12	0.28
5727 •	18.49	0.71	0.90	0.05	0.41	0.95	1.36	12 38 09.78	−02 22 50.6	0.20	0.28
9178	18.10	0.92	0.52	0.64	0.01	1.16	1.18	12 44 09.89	−02 16 35.9	0.18	0.28
2994	18.06		1.11	0.46	0.77	1.58	2.35	12 33 46.01	+01 28 06.2	0.21	0.28
4314	18.19		1.36	0.62	0.19	1.98	2.16	12 35 55.40	−01 01 47.6	0.17	0.28
5071	18.39		1.35	0.50	0.17	1.85	2.02	12 37 11.06	−01 14 05.3	0.15	0.28
3297	18.42		1.80	0.50	0.52	2.30	2.82	12 34 09.61	+00 03 38.5	0.13	0.28
2482	17.92		1.93	0.64	0.77	2.58	3.34	12 32 55.46	−00 43 46.6	0.16	0.28
5005	17.38	0.80	0.91	0.69	0.67	1.61	2.28	12 37 10.21	+02 13 39.6	0.20	0.28
10820	18.47		1.92	0.42	0.97	2.34	3.31	12 46 49.97	−00 24 03.2	0.17	0.28
493	18.48		0.62	0.73	0.70	1.35	2.05	12 29 30.47	+00 23 23.4	0.17	0.28
766	18.10	0.98	0.71	0.63	-0.01	1.34	1.33	12 29 52.14	−00 16 26.9	0.18	0.27
3219	18.24		1.31	0.34	0.26	1.64	1.91	12 34 07.55	−01 08 16.1	0.16	0.27
5272	18.49	0.69	1.05	0.39	0.76	1.44	2.20	12 37 28.62	−01 45 56.0	0.18	0.27
4362	18.07		1.88	0.57	0.77	2.46	3.23	12 36 02.15	+01 18 31.8	0.17	0.27

Table E6: Top candidates in field 861 continued.

Object	R	U-B	B-V	V-R	R-I	B-R	B-I	α(1950)	δ(1950)	D_{10}	D_{100}
1016	18.38		0.91	0.66	0.90	1.57	2.48	12 30 20.75	+00 41 16.5	0.17	0.27
9444	18.34	0.94	1.10	0.11	0.47	1.20	1.68	12 44 34.24	−02 07 29.6	0.16	0.27
9955	18.46		1.68	0.33	0.66	2.01	2.67	12 45 34.58	−00 20 14.1	0.11	0.27
3788	18.20	1.29	0.62	0.44	0.56	1.06	1.62	12 35 02.97	−02 29 54.1	0.18	0.27
11783	17.77	1.57	0.76	0.69	0.24	1.45	1.69	12 48 23.83	+00 39 47.7	0.16	0.27
9205	18.45		1.32	0.43	0.36	1.75	2.11	12 44 16.87	+00 36 25.0	0.11	0.27
9731	17.96	0.80	1.10	0.23	0.19	1.34	1.53	12 45 15.37	+01 22 15.0	0.17	0.27
4545	18.05		1.32	0.38	0.45	1.70	2.15	12 36 24.02	+01 58 55.2	0.10	0.27
4861	17.75	0.89	0.88	0.77	0.64	1.65	2.28	12 36 44.81	−00 00 12.2	0.18	0.27
4625	18.19		1.74	0.41	0.58	2.14	2.73	12 36 23.19	−02 00 43.1	0.10	0.27
8899	18.11		1.87	0.40	0.92	2.27	3.19	12 43 42.48	−01 48 35.1	0.14	0.27
4043	18.11		1.37	0.23	0.51	1.60	2.11	12 35 25.19	−00 08 01.2	0.18	0.27
1800	17.99	1.44	0.67	0.50	0.43	1.17	1.60	12 31 49.22	+02 08 07.3	0.17	0.27
10383 •	18.28	-0.16	0.85	0.10	-0.04	0.94	0.90	12 46 05.15	−02 28 03.5	0.18	0.27
8251	18.36	-0.21	0.60	0.70	-0.15	1.30	1.15	12 42 42.84	+01 19 28.8	0.20	0.27
2133	17.68		1.41	0.51	0.57	1.93	2.50	12 32 12.24	−01 56 43.1	0.10	0.27
6192	18.12		1.28	0.44	0.20	1.72	1.93	12 39 08.36	+00 33 27.7	0.17	0.27
2945	18.47		1.27	0.19	0.62	1.45	2.07	12 33 32.92	−00 56 59.6	0.18	0.27
8277	18.47	-0.07	0.73	0.18	-0.14	0.91	0.77	12 42 45.33	−00 15 54.0	0.17	0.26
2561	18.08	1.35	1.00	0.38	0.27	1.38	1.65	12 33 02.79	+00 44 57.0	0.17	0.26
9386	18.09	0.40	1.24	0.33	0.28	1.57	1.85	12 44 40.12	+00 42 48.3	0.17	0.26
7934	17.97	0.04	0.90	0.35	0.61	1.25	1.85	12 42 12.06	−00 43 02.9	0.18	0.26
6966	18.27		1.58	0.71	0.34	2.29	2.62	12 40 28.65	−00 01 18.1	0.18	0.26
6838	18.35	-0.05	0.68	0.67	0.41	1.35	1.77	12 40 16.38	−02 20 59.9	0.17	0.26
2508	18.20		1.33	0.29	0.40	1.62	2.03	12 32 48.66	−01 48 32.5	0.14	0.26
4115	18.50		1.68	0.38	0.62	2.05	2.67	12 35 35.91	+00 52 06.5	0.10	0.26
3000 •	18.23	-0.33	0.92	0.11	0.09	1.03	1.12	12 33 46.79	+01 01 27.1	0.19	0.26
6460	17.95		1.56	0.61	0.38	2.17	2.55	12 39 36.51	+00 01 55.6	0.12	0.26
11526	18.11	0.89	1.05	0.18	0.28	1.24	1.52	12 48 02.51	−00 56 06.4	0.15	0.26
6481	18.37		0.67	0.35	0.13	1.01	1.14	12 39 34.64	−01 39 08.8	0.17	0.26
2355	17.80	1.58	1.19	0.41	0.40	1.61	2.01	12 32 41.32	+01 32 46.5	0.16	0.26
4259	17.63	1.30	0.94	0.68	0.08	1.62	1.70	12 35 50.73	+02 13 01.5	0.17	0.26
6598	18.44		1.04	0.71	0.13	1.75	1.88	12 39 49.16	+01 33 50.3	0.18	0.26
4184	18.02	1.07	0.76	0.61	0.04	1.38	1.42	12 35 42.68	+01 39 42.9	0.17	0.26
11449	18.35	0.47	0.95	0.56	0.61	1.51	2.12	12 47 50.10	−02 17 53.2	0.15	0.26
3529	17.96		1.43	0.42	0.63	1.84	2.47	12 34 33.56	−01 14 37.3	0.10	0.26
3500	18.39	0.44	1.22	0.28	0.26	1.50	1.75	12 34 30.55	+00 11 00.4	0.17	0.26
366	17.62	1.72	0.79	0.75	0.34	1.55	1.88	12 29 06.65	−01 31 33.7	0.15	0.26
6950	17.80	1.48	0.68	0.63	0.32	1.30	1.63	12 40 26.74	+00 41 03.2	0.14	0.26
6397	18.47		1.39	0.47	0.27	1.85	2.12	12 39 27.50	−01 51 26.9	0.12	0.26
10855	18.44		1.66	0.47	0.50	2.12	2.63	12 46 55.78	−02 01 49.4	0.11	0.25
1648	18.46		1.29	0.54	0.35	1.83	2.18	12 31 28.77	+00 17 17.0	0.11	0.25
1026	17.99	0.98	0.62	0.48	0.16	1.09	1.25	12 30 21.56	+00 18 39.6	0.16	0.25
11690	17.23	2.04	0.91	0.71	0.63	1.62	2.25	12 48 16.49	+00 00 13.6	0.15	0.25
1612	18.41	0.57	1.20	0.60	0.29	1.79	2.08	12 31 24.25	−02 32 44.1	0.16	0.25
6148	18.34		1.35	0.57	0.33	1.92	2.24	12 39 00.65	−01 58 25.2	0.10	0.25
1765	18.33		1.33	0.73	0.26	2.06	2.31	12 31 37.10	−01 25 22.8	0.14	0.25
5177	17.90	1.29	0.75	0.55	0.20	1.31	1.50	12 37 14.92	−01 57 27.2	0.12	0.25
9088	18.41		1.63	0.34	0.72	1.97	2.70	12 44 04.32	−01 35 12.9	0.10	0.25
3122	18.25		1.70	0.42	0.59	2.12	2.71	12 33 59.59	−00 35 57.7	0.10	0.25
7432	18.31	0.48	0.74	0.77	0.49	1.52	2.00	12 41 14.57	−02 10 12.9	0.16	0.25
1725	18.41	0.89	1.03	0.14	0.41	1.17	1.58	12 31 36.94	+00 35 11.2	0.14	0.25
2124	17.64	1.30	1.26	0.32	0.40	1.58	1.98	12 32 10.46	−01 22 17.5	0.14	0.25
8348	18.21		1.28	0.43	0.39	1.71	2.10	12 42 57.93	+00 21 42.7	0.10	0.25
9029	18.44		1.82	0.59	0.74	2.42	3.16	12 43 56.60	+01 43 46.1	0.14	0.25
6543	18.23	0.80	0.65	0.69	-0.01	1.34	1.33	12 39 39.51	−00 00 57.7	0.15	0.25
2070	17.83	1.06	1.08	0.34	0.22	1.42	1.64	12 32 16.16	+01 08 43.5	0.14	0.25
4110	18.46	0.60	1.11	0.11	0.47	1.22	1.69	12 35 31.09	+00 59 20.4	0.16	0.25
4568	18.12	1.30	0.61	0.61	0.31	1.22	1.53	12 36 25.74	+00 42 04.4	0.14	0.25
2135	18.34	1.17	0.68	0.43	0.30	1.11	1.42	12 32 11.71	−01 57 34.5	0.15	0.25

Table E7: Top candidates in field 862 in 100th nearest-neighbour distance. AAT criterion.

Object	R	U-B	B-V	V-R	R-I	B-R	B-I	α(1950)	δ(1950)	D_{10}	D_{100}
7362	18.29			0.55	0.88			13 01 46.94	−00 41 55.0	0.51	0.72
7190 •	18.46			0.67	0.63			13 01 31.02	−00 44 47.3	0.44	0.53
11682 •	18.47		1.82	0.31	0.79	2.13	2.92	13 08 48.58	+00 43 52.0	0.34	0.45
4473	17.63	2.73	1.17	0.41	0.89	1.59	2.47	12 57 07.12	+01 34 06.6	0.23	0.44
10982	17.80	2.78	1.17	0.44	0.96	1.61	2.57	13 07 36.77	−01 29 05.8	0.25	0.44
10512	17.88	2.82	1.03	0.62	0.84	1.65	2.49	13 06 50.22	−01 41 10.5	0.24	0.44
4088	17.38	2.70	1.14	0.68	0.94	1.82	2.76	12 56 21.69	−00 48 48.4	0.20	0.36
4153 •	18.18	0.22	0.97	0.48	0.59	1.44	2.04	12 56 32.77	+00 34 37.1	0.27	0.35
9079 •	18.03	2.21	0.82	0.58	0.40	1.40	1.80	13 04 39.27	−01 36 02.8	0.20	0.34
8933 •	18.26	0.59	1.16	0.44	0.58	1.60	2.18	13 04 33.33	+01 37 18.7	0.26	0.34
10975 •	18.42		0.81	0.23	0.53	1.05	1.57	13 07 35.26	−01 12 19.5	0.22	0.33
2348	17.74	2.58	1.03	0.65	0.73	1.68	2.40	12 53 18.22	+01 27 09.0	0.17	0.33
1006	18.11	2.48	1.08	0.33	0.93	1.41	2.33	12 50 41.51	+00 51 50.7	0.20	0.33
276	17.70	2.55	1.13	0.61	0.76	1.74	2.50	12 49 00.62	−01 27 16.4	0.14	0.33
2398	17.52	2.51	1.13	0.62	0.69	1.74	2.44	12 53 12.74	−00 56 08.3	0.15	0.33
430	18.31	0.35	0.57	0.43	0.97	1.00	1.96	12 49 24.28	+01 58 36.5	0.20	0.32
763 •	18.48	1.61	0.76	0.44	0.32	1.20	1.52	12 50 11.10	+02 09 13.4	0.19	0.31
9574	18.32	2.02	0.57	0.66	0.90	1.22	2.12	13 05 28.84	−02 03 42.6	0.22	0.31
9482	18.14	0.18	0.50	0.41	0.92	0.91	1.83	13 05 23.72	−01 55 36.0	0.22	0.31
2311	17.86	2.50	1.13	0.59	0.74	1.72	2.46	12 53 05.72	−01 00 34.4	0.14	0.31
2760	17.68	2.45	1.31	0.56	0.86	1.88	2.74	12 53 50.85	−00 09 10.5	0.16	0.31
8001 •	18.44	2.06	0.81	0.34	0.67	1.15	1.83	13 02 56.81	−01 04 18.6	0.18	0.30
5816	18.43	0.26	0.64	0.59	0.70	1.23	1.93	12 59 25.20	+01 46 09.5	0.21	0.30
5196	18.35	2.22	1.04	0.33	0.65	1.37	2.02	12 58 19.95	+02 09 27.0	0.17	0.30
7771	18.50		1.61	0.38	0.95	1.99	2.94	13 02 31.90	+00 54 20.5	0.20	0.30
5485 •	18.42	1.64	1.07	0.20		1.27		12 58 51.19	+01 49 15.9	0.16	0.30
8571	17.68	2.53	1.07	0.67	0.78	1.75	2.53	13 03 44.79	−02 20 15.7	0.12	0.29
51 •	18.14	0.44	0.80	0.22	0.08	1.03	1.11	12 48 32.46	+01 22 02.0	0.17	0.28
7186	18.43	0.40	0.70	0.63	0.61	1.32	1.93	13 01 30.13	−00 27 26.7	0.20	0.28
1476	18.23	0.42	0.77	0.46	0.81	1.23	2.04	12 51 33.71	−00 28 15.6	0.20	0.28
9463	17.64	2.56	1.19	0.61	0.99	1.80	2.79	13 05 21.18	−01 05 00.0	0.15	0.28
6123	17.68	2.57	1.06	0.64	0.91	1.70	2.61	12 59 54.44	−00 14 37.8	0.15	0.28
6530	17.88	2.42	1.18	0.44	0.83	1.62	2.45	13 00 27.32	−01 22 53.1	0.13	0.28
6056	17.31	2.14	1.51	0.60	0.90	2.11	3.01	12 59 42.24	−01 19 12.5	0.20	0.28
4689	17.77	2.56	0.98	0.79	0.95	1.77	2.72	12 57 22.38	+01 00 50.1	0.18	0.28
6706 •	18.47	2.13	1.02	0.39		1.41		13 00 41.06	+00 26 02.1	0.14	0.28
11707 •	18.48	2.11	1.13	0.60	0.44	1.73	2.18	13 08 50.68	−01 24 26.2	0.17	0.28
46 •	18.21	1.85	1.00	0.33	0.50	1.33	1.83	12 48 27.97	+02 11 35.5	0.14	0.28
240	18.08	2.28	1.21	0.49	0.64	1.70	2.35	12 49 02.56	+01 00 20.4	0.14	0.28
2083	17.98	2.47	1.17	0.51	0.87	1.67	2.54	12 52 39.43	−02 38 31.3	0.12	0.27
9679	18.20	1.26	0.61	0.57	0.96	1.18	2.14	13 05 37.08	−02 12 12.4	0.19	0.27
5337 •	18.28	0.89	1.15	0.05	0.69	1.21	1.90	12 58 28.62	−00 12 01.2	0.20	0.27
3642	17.94	2.41	0.87	0.58	0.79	1.45	2.24	12 55 36.70	+01 07 13.7	0.16	0.27
3638	18.03	2.19	1.00	0.42	0.61	1.42	2.03	12 55 35.47	+01 17 36.6	0.14	0.27
10784	18.44	2.39	0.99	0.41	0.98	1.40	2.38	13 07 17.17	−00 46 27.6	0.17	0.27

Table E7: Top candidates in field 862 continued.

Object	R	U-B	B-V	V-R	R-I	B-R	B-I	α(1950)	δ(1950)	D_{10}	D_{100}
879	17.70	2.23	1.21	0.40	0.70	1.61	2.31	12 50 25.83	+00 07 06.0	0.15	0.27
11416	18.16	-0.45	0.54	0.30	0.51	0.83	1.34	13 08 27.75	−00 26 19.2	0.21	0.27
7623	17.61	0.73	0.80	0.60	0.74	1.40	2.14	13 02 16.86	−01 02 16.1	0.16	0.27
1988	18.38	1.15	0.99	0.61	0.89	1.60	2.50	12 52 30.15	−01 26 06.5	0.16	0.27
9205	18.36	1.78	0.57	0.59	0.67	1.16	1.83	13 05 06.30	+01 49 48.2	0.17	0.27
6440	18.19	2.12	1.00	0.49	0.50	1.50	2.00	13 00 16.62	−01 33 09.6	0.13	0.26
3867	17.95	2.21	1.09	0.56	0.54	1.65	2.20	12 56 05.19	+01 51 40.6	0.14	0.26
417	17.80	2.41	1.14	0.67	0.74	1.80	2.54	12 49 12.80	−02 26 35.6	0.12	0.26
8610	18.39	1.97	0.63	0.74	0.70	1.37	2.07	13 04 01.55	+00 40 40.0	0.15	0.26
10829	18.50		1.22	0.76	0.50	1.98	2.48	13 07 26.36	+02 06 19.3	0.16	0.26
582	17.82	2.19	1.01	0.39	0.66	1.40	2.06	12 49 46.10	+01 02 37.4	0.13	0.26
9837 •	18.34	1.44	1.20	0.38		1.58		13 05 56.85	−00 54 32.8	0.15	0.26
5587	18.15	1.67	0.87	0.50	0.36	1.37	1.73	12 58 58.70	+00 21 10.0	0.14	0.26
1049	18.41	2.07	0.85	0.52		1.37		12 50 36.26	−02 06 25.1	0.12	0.26
6866	17.57	2.24	1.00	0.64	0.57	1.64	2.21	13 00 50.01	−02 36 02.8	0.14	0.25
9861	17.87	2.47	1.14	0.57	0.89	1.71	2.59	13 05 59.81	−02 15 46.1	0.11	0.25
288	17.60	2.26	1.16	0.45	0.70	1.62	2.31	12 48 56.62	−02 25 26.7	0.13	0.25
2516	18.48	1.58	0.97	0.41	0.39	1.37	1.76	12 53 23.88	−02 18 47.6	0.13	0.25
5392	18.49	0.90	1.05	0.03	0.68	1.08	1.76	12 58 34.19	+01 59 24.3	0.18	0.25
695	18.37	1.69	0.89	0.22	0.84	1.11	1.95	12 50 06.02	+01 24 00.2	0.17	0.25
6748	18.33	2.01	0.96	0.43	0.52	1.39	1.91	13 00 43.04	−01 27 47.6	0.12	0.25
10273	18.00	2.51	1.10	0.62	0.94	1.73	2.66	13 06 32.73	−00 48 57.1	0.13	0.25
3836	18.23	0.64	0.53	0.73	0.50	1.26	1.76	12 55 47.77	−01 12 07.0	0.18	0.25
2291	18.46	2.04	0.80	0.57	0.51	1.37	1.88	12 53 10.98	+00 34 05.5	0.14	0.25
11158	17.27	2.48	1.06	0.75	0.89	1.82	2.71	13 07 53.49	−01 29 12.7	0.15	0.25
834	17.35	1.68	1.07	0.31	0.51	1.39	1.89	12 50 10.44	−02 27 06.0	0.14	0.25
4438	18.01	2.38	1.11	0.50	0.79	1.61	2.40	12 56 58.68	−01 27 07.0	0.12	0.25
9	17.80	0.90	0.81	0.34	0.20	1.16	1.36	12 48 19.25	+01 21 43.5	0.12	0.25
6144	17.92	1.30	1.02	0.41	0.33	1.43	1.76	12 59 48.97	−01 23 54.1	0.15	0.25
3779	18.12	1.44	0.63	0.80	0.43	1.43	1.86	12 55 54.11	+01 51 37.3	0.17	0.25
2771	17.75	1.43	1.11	0.53	0.36	1.63	1.99	12 53 50.03	−00 37 25.9	0.14	0.25
11667	17.83	0.53	0.79	0.03	0.92	0.82	1.74	13 08 43.79	−02 41 17.3	0.17	0.25
8587	18.30	1.78	0.59	0.75	0.70	1.35	2.05	13 03 56.35	+01 59 21.5	0.17	0.25
3791	18.20	2.27	0.81	0.69	0.75	1.50	2.26	12 55 48.67	+01 15 03.3	0.15	0.25
2923	18.40	1.91	0.95	0.38	0.54	1.34	1.88	12 54 11.73	+01 35 35.3	0.11	0.25
4168	18.13	2.26	1.04	0.43	0.76	1.46	2.22	12 56 30.08	+00 02 19.4	0.12	0.25

Table E8: Top candidates in field 863 in 100^{th} nearest-neighbour distance. AAT criterion.

Object	R	U-B	B-V	V-R	R-I	B-R	B-I	α(1950)	δ(1950)	D_{10}	D_{100}
4431 •	18.22		1.86	0.71	0.64	2.57	3.20	13 15 12.50	+02 21 31.2	0.24	0.47
12965	18.46	0.28	0.67	0.66	0.78	1.33	2.11	13 27 40.85	−00 44 41.5	0.30	0.46
3656 •	18.47	0.55	1.15	0.17	0.88	1.32	2.20	13 13 59.15	−02 29 37.1	0.31	0.37
5703 •	17.93	0.37	0.85	0.62	0.57	1.47	2.04	13 16 56.66	−00 47 31.8	0.25	0.36
3474	18.37			0.66	0.99			13 13 49.85	+00 33 00.2	0.23	0.36
1007	17.37	1.04	1.20	0.49	0.95	1.69	2.64	13 10 03.91	+00 20 39.8	0.24	0.35
2826	17.80	0.49	0.83	0.24	0.93	1.07	2.00	13 12 41.99	−02 21 32.0	0.24	0.33
3585	18.36	0.52	0.55	0.66	0.69	1.21	1.90	13 14 01.61	+00 42 14.9	0.20	0.32
7213 •	18.24		1.25	0.66	0.34	1.91	2.25	13 19 19.30	+00 55 57.2	0.17	0.30
2115	17.87	1.08	1.02	0.45	0.98	1.47	2.45	13 11 39.56	−01 05 31.8	0.22	0.30
5007	18.47	1.08	0.57	0.63	0.84	1.20	2.04	13 15 59.45	−02 11 09.1	0.18	0.30
4752 •	18.47		1.45	0.19	0.64	1.64	2.28	13 15 41.91	+00 22 32.0	0.20	0.30
6600	18.26	0.53	0.75	0.57	0.67	1.33	2.00	13 18 20.86	−00 04 38.6	0.18	0.29
7154 •	18.48		1.56	0.31	0.91	1.86	2.77	13 19 10.47	−00 39 12.5	0.20	0.29
12571 •	18.43	1.51	0.90	0.18	0.39	1.08	1.47	13 27 17.01	+02 15 59.7	0.19	0.29
582	18.32		1.19	0.55	0.25	1.74	1.99	13 09 17.00	−01 22 14.2	0.22	0.29
13688	17.96		1.64	0.37	0.97	2.00	2.98	13 28 48.30	+00 53 23.9	0.19	0.29
4332	18.44		1.67	0.62	0.89	2.29	3.18	13 15 05.88	+01 57 18.6	0.17	0.29
11850 •	17.15	2.17	1.07	0.38	0.64	1.46	2.09	13 26 13.14	+02 03 22.7	0.14	0.28
8251 •	18.45		1.58	0.26	0.73	1.84	2.56	13 20 48.04	+00 31 22.9	0.16	0.28
10176	18.17		1.72	0.42	0.91	2.14	3.05	13 23 31.98	−01 00 11.5	0.16	0.28
2005 •	17.71		1.58	0.23	0.88	1.80	2.68	13 11 28.32	−00 29 18.5	0.16	0.28
12025	18.23	1.13	0.50	0.66	0.80	1.16	1.96	13 26 23.37	−02 13 49.0	0.16	0.28
8247	17.83	0.37	0.75	0.32	0.80	1.07	1.87	13 20 53.31	+00 52 47.7	0.19	0.28
755	18.43		0.64	0.78	0.98	1.42	2.40	13 09 35.23	−00 32 06.4	0.18	0.28
3889	18.32				0.37	1.80	2.17	13 14 24.42	+02 23 15.9	0.14	0.28
7648 •	17.99	-0.09	0.53	0.41	0.55	0.95	1.50	13 19 57.28	+00 04 15.0	0.20	0.27
3676	18.41				0.59	2.09	2.68	13 14 08.68	+02 03 24.0	0.16	0.27
11097 •	17.40		0.72	0.39	0.42	1.11	1.53	13 24 59.00	−02 16 59.5	0.19	0.26
3641	18.48	0.61			0.67	1.18	1.84	13 14 00.68	−01 51 43.9	0.16	0.26
7201	18.25	0.97	1.06	0.61	0.59	1.67	2.26	13 19 17.02	+01 44 34.3	0.20	0.26
7736	18.26		1.55	0.37	0.99	1.91	2.91	13 20 02.45	+00 01 18.9	0.14	0.26
13256	18.49		1.30	0.77	0.59	2.08	2.67	13 28 11.73	+02 14 36.8	0.15	0.26
4729	18.13	0.43	0.58	0.50	0.71	1.08	1.79	13 15 40.39	+01 19 13.3	0.16	0.26
12762 •	18.45	1.46	0.63	0.29	0.44	0.92	1.36	13 27 22.00	−00 50 37.5	0.17	0.26
6987 •	18.27	1.06	1.02	0.13	0.32	1.15	1.47	13 18 47.36	−02 16 48.3	0.16	0.26
5774 •	18.13	1.47	0.96	0.14	0.47	1.10	1.57	13 17 13.74	+01 23 17.0	0.16	0.26
13675	18.42		1.66	0.41	0.92	2.07	3.00	13 28 44.95	+01 35 37.6	0.13	0.25
704	17.90	1.80	0.60	0.55	0.55	1.15	1.70	13 09 22.64	−02 36 05.4	0.17	0.25
12529 •	17.05	2.28	1.13	0.46	0.68	1.59	2.27	13 27 06.53	−00 54 54.2	0.15	0.25
8584	18.32	0.91	0.71	0.17	0.20	0.88	1.09	13 21 17.70	+00 43 28.5	0.16	0.25
6788 •	18.32	1.45	0.69	0.38	0.32	1.07	1.39	13 18 45.72	+02 05 20.4	0.16	0.25
12974 •	17.58	1.95	0.96	0.41	0.52	1.37	1.89	13 27 40.93	−01 04 09.7	0.13	0.25
6024 •	17.81	1.88	0.98	0.33	0.54	1.32	1.86	13 17 32.34	−00 18 20.3	0.13	0.25
2992 •	17.86	1.68	0.73	0.58	0.33	1.31	1.63	13 13 02.80	−00 19 06.1	0.17	0.25
4898 •	17.98	1.74	1.07	0.18	0.61	1.25	1.86	13 15 49.69	−01 42 03.6	0.15	0.25
11420	18.21		1.50	0.23	0.92	1.73	2.65	13 25 25.69	−02 20 46.8	0.14	0.25
12428 •	18.25		1.18	0.21	0.84	1.39	2.23	13 27 01.19	−01 26 14.9	0.16	0.25

Table E9: Top candidates in field 864 in 10th nearest-neighbour distance. CTIO criterion.

Object	R	U-B	B-V	V-R	R-I	B-R	B-I	α(1950)	δ(1950)	D_{10}	D_{100}
12315 •	18.49	-0.15	-0.01	-0.09	-0.24	-0.10	-0.34	13 43 45.90	−00 39 10.3	0.56	0.88
1042 •	18.35			1.06				13 29 47.20	+01 07 56.5	0.53	0.88
13954 •	17.60		0.37	0.25	0.26	0.62	0.88	13 45 57.94	+01 56 52.1	0.51	0.60
14890 •	18.18		1.25	0.74		1.99		13 47 03.80	+02 20 56.0	0.51	0.75
2779 •	18.38	-0.32	1.27	0.71	-0.22	1.99	1.77	13 31 49.67	−00 18 44.9	0.50	0.70
11177	17.78	0.68	0.73	0.98	0.77	1.71	2.48	13 42 20.23	+00 09 15.2	0.43	0.56
5560	18.00	0.08	-0.16	0.07	-0.10	-0.09	-0.19	13 35 23.21	−00 41 32.9	0.42	0.69
7557	17.51	0.62	0.62	0.79	0.90	1.41	2.32	13 37 56.20	+00 26 32.6	0.41	0.51
10982 •	17.66		0.40	0.26	0.39	0.65	1.04	13 42 02.05	−02 34 53.7	0.40	0.50
5944	18.48	0.56	0.48	0.91	0.64	1.40	2.04	13 35 46.93	−00 31 26.2	0.37	0.44
2231 •	18.20			0.64	0.33			13 31 05.05	−02 46 14.7	0.37	0.75
12700	18.44	0.99	0.64	0.58		1.21		13 44 12.57	−01 02 10.4	0.36	0.46
14553 •	18.39			0.80	0.72			13 46 43.18	+01 27 17.2	0.35	0.49
9727	18.29	0.43	0.12	0.55		0.67		13 40 29.30	−00 55 44.5	0.35	0.48
15805	18.38	1.00	0.60	0.73	0.97	1.34	2.30	13 48 11.06	+00 49 32.2	0.33	0.43
5960	18.05	-0.27	0.05	0.07	-0.03	0.11	0.08	13 35 50.59	−01 15 02.7	0.32	0.63
1333	18.35	0.55	0.20	0.44		0.64		13 29 56.79	−02 19 14.0	0.31	0.45
13502	18.12	-0.34	0.00	0.03	0.20	0.03	0.23	13 45 17.84	−00 00 22.9	0.31	0.63
329	18.41	0.31	0.18	0.34		0.52		13 28 42.20	−02 13 03.1	0.30	0.44
12404 •	18.49	0.34	0.93	0.64	0.40	1.57	1.97	13 43 54.88	+00 23 46.8	0.28	0.36
9400	18.33	0.09	0.02	0.03	0.06	0.05	0.11	13 40 19.76	+01 25 47.4	0.28	0.48
3775	18.13	0.74	0.06	0.14	-0.26	0.20	-0.06	13 33 01.97	−02 34 29.1	0.28	0.55
16265 •	18.25	-0.31	-0.09	0.62	0.00	0.54	0.53	13 48 48.21	+00 31 37.0	0.27	0.44
15132	17.98	0.44	-0.20	0.17	-0.05	-0.02	-0.08	13 47 13.09	−02 31 46.8	0.27	0.55
13267	17.89	0.54	-0.17	0.11	0.04	-0.06	-0.02	13 44 57.86	−00 14 04.2	0.27	0.53
1475 •	18.17		1.02	0.03	0.36	1.04	1.41	13 30 21.15	+01 08 14.0	0.27	0.35
14870	18.23			0.97	0.95			13 46 54.54	−02 12 38.1	0.27	0.32
337 •	18.48	0.01	0.40	0.82	0.22	1.23	1.44	13 28 35.71	−02 31 28.9	0.27	0.34
14766 •	18.46		0.20	1.02	-0.10	1.22	1.12	13 46 57.27	+01 48 17.2	0.26	0.35
1940	18.47	0.40	0.19	0.42		0.61		13 30 43.76	−01 35 39.7	0.26	0.37
11992	18.21	0.83	-0.24	0.24	-0.14	0.00	-0.14	13 43 14.25	−01 49 10.5	0.26	0.60
343 •	17.96		0.81	0.21	0.18	1.02	1.20	13 28 45.12	+02 18 36.5	0.26	0.34
16133	18.26	0.53	-0.17	0.40	0.11	0.24	0.35	13 48 43.14	+01 46 35.2	0.25	0.36
2599 •	18.27		1.27	0.24	0.22	1.51	1.73	13 31 42.90	+02 21 15.6	0.25	0.36
3129	17.88	0.85	1.04	0.79	0.51	1.83	2.34	13 32 20.89	−00 27 41.8	0.25	0.36
16197	18.02	1.16	0.83	0.86	0.79	1.69	2.47	13 48 36.06	−00 59 52.9	0.24	0.36
12535	18.04	0.67	-0.17	0.15	0.06	-0.02	0.04	13 44 06.83	+00 14 26.6	0.24	0.51
7102	17.90	0.59	-0.07	0.21	-0.10	0.14	0.04	13 37 25.19	−00 20 43.4	0.24	0.47
3248 •	18.22	-0.26	1.67	0.69	0.12	2.37	2.49	13 32 23.18	−00 18 39.8	0.24	0.83
6930	18.46		1.86	0.72	0.61	2.59	3.20	13 37 12.66	+02 24 40.6	0.24	0.39
1440	18.50	0.79	0.31	0.58	-0.26	0.89	0.63	13 30 07.61	−02 20 15.0	0.24	0.33
10641	18.45	0.08	0.12	0.65		0.77		13 41 51.27	+00 55 06.4	0.24	0.36
11167	18.15	0.41	0.10	0.10	-0.05	0.20	0.15	13 42 23.42	+00 36 48.1	0.24	0.41
5706	17.66	0.80	0.06	0.03	0.31	0.09	0.40	13 35 34.86	−01 37 24.1	0.24	0.40
8275	18.24	1.14	0.43	0.37	0.04	0.80	0.84	13 38 40.02	−02 19 57.6	0.23	0.31
14814	17.51	-0.16	-0.05	0.20	0.29	0.16	0.45	13 47 00.21	−00 26 10.8	0.23	0.42
4198	17.52	0.76	0.09	0.01	0.22	0.10	0.32	13 33 43.79	−01 04 09.0	0.23	0.41
2314	18.20	1.07	0.72	0.92	0.57	1.64	2.21	13 31 13.21	−00 44 04.2	0.23	0.31
14113	18.26	0.52	-0.10	0.43	0.00	0.33	0.33	13 46 03.53	+00 14 58.0	0.22	0.33
463	17.94	0.29	0.56	0.38	-0.25	0.94	0.68	13 29 00.16	+01 18 06.6	0.22	0.32
12764	17.87	0.13	0.33	0.77	0.30	1.10	1.39	13 44 19.82	+01 08 43.2	0.22	0.29
13626	17.54	1.41	1.03	0.84	0.99	1.88	2.87	13 45 29.04	+00 03 15.5	0.22	0.30
14928	17.73	0.52	-0.06	0.14	0.03	0.08	0.11	13 47 08.37	+00 21 51.6	0.22	0.44
14869	18.23	0.84	0.08	0.20	-0.19	0.28	0.09	13 47 00.04	−02 12 19.2	0.22	0.47
11516	17.71	0.19	0.05	0.13	0.07	0.18	0.25	13 42 49.45	+01 53 56.6	0.22	0.36
9873	18.20	0.93	-0.18	0.28	0.05	0.10	0.15	13 40 46.38	−01 56 14.6	0.22	0.46
7766	18.09	0.07	0.11	0.12	-0.05	0.23	0.18	13 38 15.34	+02 04 21.4	0.22	0.39
5132	17.85	0.28	0.03	0.16	0.17	0.19	0.37	13 34 51.88	+00 04 00.7	0.22	0.31
2833	17.63	0.62	0.03	0.01	0.10	0.04	0.15	13 31 52.06	−02 17 23.9	0.22	0.47
2126 •	18.42		1.15	0.49	0.20	1.64	1.84	13 31 02.82	+01 46 13.8	0.22	0.32
9331	18.27	1.09	1.20	0.68	0.73	1.87	2.60	13 40 03.37	−00 52 46.2	0.21	0.31

Table E9: Top candidates in field 864 continued.

Object	R	U-B	B-V	V-R	R-I	B-R	B-I	α(1950)	δ(1950)	D_{10}	D_{100}
3027	18.10	0.79	0.76	0.81	0.51	1.58	2.08	13 32 11.29	−00 30 52.4	0.21	0.30
10800	18.27	-0.39	0.13	0.58	0.03	0.71	0.74	13 41 53.90	−00 15 26.5	0.21	0.35
3363	17.85	0.79	1.02	0.56	0.60	1.58	2.18	13 32 38.73	−00 29 55.2	0.21	0.28
1118	18.45	-0.32	0.14	0.22	0.05	0.36	0.42	13 29 43.03	−02 25 26.7	0.21	0.40
8421	17.82	0.96	0.11	0.22	0.09	0.33	0.42	13 38 56.50	−02 44 09.0	0.21	0.34
6218	18.45		0.97	1.06	0.15	2.03	2.18	13 36 18.21	+02 08 50.5	0.21	0.30
8067	18.50		0.77	0.83	-0.04	1.59	1.55	13 38 38.26	+01 29 34.9	0.20	0.28
4463	17.66	1.31	0.96	0.92	0.72	1.89	2.61	13 33 55.51	−01 40 56.0	0.20	0.28
2670	18.09	0.11	-0.05	0.32	0.25	0.27	0.52	13 31 46.30	−00 52 24.3	0.20	0.28
12205	17.54	0.81	-0.14	0.17	-0.05	0.04	-0.02	13 43 40.16	−01 02 23.8	0.20	0.53
9513	18.49		1.72	0.59	0.56	2.31	2.87	13 40 22.27	+02 17 04.3	0.20	0.34
3462	18.41	0.26	0.13	0.32	-0.13	0.45	0.31	13 32 50.55	+00 22 02.4	0.20	0.30
3442	18.22	0.02	0.11	0.17	-0.07	0.27	0.20	13 32 50.16	+01 29 26.3	0.20	0.38
7299	17.88	0.11	-0.03	0.28	0.01	0.25	0.26	13 37 40.59	+01 14 58.0	0.20	0.35
3246	18.21	0.22	0.92	0.50	0.21	1.41	1.62	13 32 28.42	−00 15 49.6	0.20	0.30
8975	18.02	0.45	0.19	0.15	0.03	0.34	0.37	13 39 42.81	−00 05 15.9	0.20	0.30
13285	18.22	0.62	0.37	0.85	0.40	1.21	1.62	13 44 59.42	−01 02 50.5	0.20	0.27
12737	17.98	1.89	0.75	0.53	0.41	1.28	1.68	13 44 23.06	+01 57 35.6	0.20	0.27
9762	17.72	0.88	0.01	0.28	0.18	0.28	0.46	13 40 35.30	−01 57 13.7	0.20	0.30
9613	17.71	1.39	1.03	0.88	0.88	1.91	2.79	13 40 27.88	−01 43 42.4	0.20	0.29
5345	18.05	0.21	0.07	0.21	0.56	0.28	0.83	13 35 01.61	−02 41 53.6	0.20	0.28
1662	18.12	0.74	0.10	0.21	-0.16	0.32	0.15	13 30 24.17	−01 28 54.5	0.20	0.42
1436	17.61	1.26	0.95	0.85	0.76	1.80	2.56	13 30 09.76	−02 07 01.6	0.20	0.29
6872	18.02	0.51	0.08	0.24	0.01	0.32	0.33	13 36 59.81	−00 16 27.0	0.19	0.31
4359	18.47	-0.21	0.37	0.62	-0.04	0.99	0.95	13 33 55.87	+02 21 01.0	0.19	0.26
2912	18.01	0.60	1.10	0.50	0.45	1.60	2.05	13 32 04.55	−00 27 53.6	0.19	0.31
2778	18.45	0.50	0.96	0.62	0.35	1.59	1.93	13 31 53.57	−00 12 57.6	0.19	0.31
2461	17.91	1.13	0.58	0.54	0.88	1.12	2.00	13 31 27.31	−01 52 49.7	0.19	0.28
1837	18.29	0.08	0.67	0.33	-0.13	1.00	0.86	13 30 51.15	+02 21 40.5	0.19	0.27
14073	18.37	1.79	0.76	0.61	0.30	1.37	1.67	13 46 01.22	+02 00 30.7	0.19	0.26
15746	17.68	0.83	0.05	0.26	-0.09	0.31	0.22	13 48 01.49	−02 04 42.3	0.19	0.39
11892	18.29	0.49	0.36	0.45	-0.24	0.81	0.57	13 43 15.03	+01 53 20.7	0.19	0.29
9366	18.24	0.90	0.05	0.14	0.04	0.19	0.24	13 40 06.42	−02 04 06.2	0.19	0.41
6541	18.38	0.80	0.00	0.82	0.00	0.82	0.82	13 36 30.64	−01 55 36.1	0.19	0.28
5428	18.50	0.76	0.26	0.87	0.38	1.13	1.52	13 35 13.03	−00 53 59.0	0.19	0.26
581	18.02	-0.27	0.14	0.16	0.16	0.30	0.47	13 29 05.05	+00 57 46.8	0.18	0.37
16102	17.60	0.84	-0.02	0.10	0.00	0.08	0.08	13 48 32.34	−01 52 48.5	0.18	0.50
7365	17.64	0.91	0.09	0.23	0.00	0.32	0.32	13 37 41.22	−01 28 20.2	0.18	0.37
7057 •	18.47		1.26	0.52	0.20	1.78	1.98	13 37 22.82	+01 48 42.1	0.18	0.30
5710	17.86	0.89	0.06	0.17	-0.07	0.23	0.17	13 35 31.28	−01 55 46.7	0.18	0.43
4325	18.08	1.15	0.67	0.82	0.67	1.50	2.16	13 33 46.35	−01 36 01.7	0.18	0.26
3310	18.49	-0.16	0.60	0.26	-0.14	0.86	0.72	13 32 38.76	+02 10 14.5	0.18	0.28
1424	18.49	0.79	-0.06	0.32	-0.11	0.25	0.14	13 30 08.75	−01 27 58.9	0.18	0.42
673 •	18.03		0.57	0.58	-0.05	1.15	1.11	13 29 18.11	+02 26 31.6	0.18	0.26
2781	18.44		1.80	0.72	0.74	2.52	3.26	13 31 51.09	−00 24 52.2	0.18	0.32
12818	18.37	-0.04	-0.03	0.33	0.19	0.30	0.49	13 44 23.42	−01 06 21.8	0.18	0.30
9676	18.36		1.39	0.97	0.45	2.37	2.81	13 40 34.76	+01 11 09.0	0.18	0.28
3244	18.21	0.22	0.79	0.55	0.23	1.35	1.58	13 32 24.62	−00 12 23.3	0.18	0.26
2216	18.46		0.33	0.95	0.07	1.28	1.35	13 31 04.96	−02 02 08.1	0.18	0.27
6586	18.50	0.50	1.03	0.36	0.27	1.39	1.67	13 36 46.37	+01 19 48.2	0.18	0.27
3667 •	18.35		0.97	0.44	0.04	1.42	1.45	13 33 04.16	+01 46 19.7	0.18	0.30
330	18.32	1.16	0.79	0.74	0.75	1.53	2.28	13 28 33.80	−02 15 23.5	0.18	0.27
9824	18.21	0.78	0.82	0.22	0.12	1.04	1.16	13 40 43.23	+00 33 34.7	0.18	0.27
2124	18.17		1.54	0.66	0.52	2.20	2.72	13 31 04.56	+01 49 12.1	0.18	0.27
4905	17.96	1.15	1.13	0.69	0.40	1.82	2.21	13 34 40.13	+00 01 18.3	0.18	0.26
16241	17.78	1.62	0.45	0.44	0.51	0.89	1.40	13 48 45.72	+01 50 42.4	0.18	0.25
1128	18.32	0.48	0.81	0.30	-0.01	1.11	1.10	13 29 50.87	+02 23 06.7	0.17	0.27
11866	18.10	0.89	0.13	0.90	0.15	1.02	1.17	13 43 11.64	−02 12 23.4	0.17	0.26
4251	18.19	0.08	0.34	0.70	-0.11	1.03	0.92	13 33 53.88	+02 03 51.8	0.17	0.26

Table E10: Top candidates in field 865 in 10^{th} nearest-neighbour distance. CTIO criterion.

Object	R	U-B	B-V	V-R	R-I	B-R	B-I	α(1950)	δ(1950)	D_{10}	D_{100}
12460	17.23		0.50	0.43	0.42	0.93	1.34	14 02 54.12	−02 33 20.9	0.57	0.69
12571	17.08		0.46	0.57	0.39	1.02	1.42	14 03 03.28	−01 55 02.4	0.55	0.67
17030	18.05	0.41	0.73	0.58		1.31		14 08 02.75	−01 07 35.7	0.48	0.75
13022	17.14		0.58	0.52	0.38	1.10	1.49	14 03 30.17	−02 35 24.5	0.47	0.59
4352 •	18.18	0.32	1.00	0.47		1.47		13 53 48.65	+02 17 55.0	0.43	0.69
2274 •	18.32	-0.37	0.92	0.51		1.43		13 51 23.54	+01 51 21.5	0.43	0.53
868	17.77			0.63	0.64			13 49 34.31	−00 17 49.6	0.43	0.74
7096	17.57	0.12	1.18	0.85	0.88	2.03	2.90	13 56 48.66	−00 05 44.6	0.41	0.56
16530	18.44			0.94				14 07 35.60	+02 17 24.2	0.40	0.49
14377 •	17.08			0.53	0.43			14 05 07.18	−01 14 45.0	0.40	0.71
12129 •	18.40	-0.06	0.78	0.38		1.15		14 02 38.13	−00 31 10.6	0.39	0.48
377	18.13	-0.20	0.93	0.76	0.83	1.69	2.53	13 48 56.85	+00 40 27.4	0.38	0.51
10636	18.49			1.00				14 00 57.54	−00 22 18.9	0.37	0.45
9632	17.69	-0.18	-0.05	0.14	0.05	0.09	0.14	13 59 44.75	−02 35 24.4	0.37	0.73
9721	17.51		0.62	0.51	0.31	1.13	1.44	13 59 55.26	−00 30 12.4	0.36	0.46
9901	18.13		1.09	0.79		1.89		14 00 05.62	−02 40 35.6	0.35	0.69
514	18.07	-0.08	1.02	0.61	0.92	1.63	2.55	13 49 01.07	−01 00 33.2	0.34	0.47
4170	18.48		0.17	0.53	0.59	0.69	1.28	13 53 29.15	−00 49 43.1	0.33	0.40
6747 •	18.46	-0.29	0.72	0.59		1.32		13 56 32.71	+02 12 20.4	0.31	0.40
6973	18.13	0.13	0.15	0.11	-0.08	0.26	0.19	13 56 46.31	−00 48 28.8	0.30	0.59
3788	18.49		2.33	0.86	0.87	3.19	4.06	13 53 05.62	−00 46 37.5	0.29	0.52
223	17.70	0.00	0.02	0.10	0.06	0.12	0.18	13 48 32.40	−01 52 49.7	0.29	0.64
11759	17.10	0.28	0.10	0.22	-0.12	0.32	0.20	14 02 10.27	−01 21 28.8	0.28	0.55
3141	18.33	-0.33	0.08	0.26	0.11	0.34	0.46	13 52 19.63	+00 47 06.2	0.28	0.54
17209	17.36	0.09	0.08	0.13	-0.03	0.21	0.18	14 08 06.76	−02 20 10.5	0.28	0.61
16987	17.76	0.20	0.04	0.27	-0.13	0.31	0.18	14 08 00.33	+00 25 24.6	0.28	0.56
3332	17.11	-0.03	-0.03	0.16	0.23	0.13	0.36	13 52 24.83	−02 14 48.3	0.27	0.55
3242 •	17.64	-0.02	1.35	0.66	0.29	2.01	2.30	13 52 26.55	+01 32 47.6	0.27	0.39
14716	18.29	0.11	1.10	0.71	0.74	1.80	2.55	14 05 32.43	+00 53 14.0	0.26	0.38
4844	17.35		0.79	0.53	0.38	1.32	1.70	13 54 15.94	−00 49 24.8	0.26	0.36
16117	18.16	0.32	1.24	0.79	0.61	2.04	2.65	14 07 09.51	+00 43 36.2	0.25	0.38
5943	18.35		2.28	0.80	0.91	3.08	3.99	13 55 37.41	+01 52 57.5	0.25	0.47
8030	18.19	0.27	-0.09	0.31	0.16	0.22	0.37	13 57 58.68	−01 12 05.8	0.25	0.46
2491 •	17.42	-0.27	0.15	0.16	0.25	0.31	0.56	13 51 27.76	−01 16 16.6	0.25	0.47
12632	18.42	0.26	0.11	0.05	0.37	0.16	0.53	14 03 21.00	+00 47 29.6	0.24	0.43
4504	18.13	0.06	0.87	0.77	0.71	1.64	2.35	13 54 01.87	+02 11 17.9	0.24	0.36
10405	17.31	0.24	0.97	0.73	0.82	1.70	2.52	14 00 42.87	−02 30 50.7	0.24	0.37
7712	18.38	0.55	1.42	0.74	0.68	2.16	2.84	13 57 42.60	+01 14 31.7	0.24	0.35
17223	18.49	0.33	1.43	0.54	0.42	1.97	2.39	14 08 25.85	+02 12 19.4	0.22	0.33
11756	17.91	-0.31	0.16	0.34	0.30	0.49	0.79	14 02 11.24	−01 16 02.0	0.22	0.34
17227	18.11	-0.13	0.52	0.17	-0.01	0.68	0.68	14 08 25.91	+02 09 41.1	0.22	0.33
10200 •	18.47	0.52	0.93	0.26	0.11	1.20	1.31	14 00 31.50	+00 58 52.2	0.22	0.30
14386	18.49	-0.08	0.82	0.75	0.57	1.57	2.13	14 05 07.79	−01 24 50.9	0.22	0.30
14843	18.10	0.40	0.60	0.42	-0.04	1.02	0.98	14 05 48.43	+00 41 01.9	0.22	0.30
8913	17.08	0.78	0.64	0.90	0.72	1.54	2.27	13 58 55.85	−00 32 52.4	0.22	0.30
12162	18.14	0.17	0.02	0.32	0.36	0.34	0.70	14 02 36.09	−01 50 50.6	0.21	0.31
16058	17.54		0.67	0.53	0.58	1.20	1.78	14 06 53.60	−02 27 52.9	0.21	0.30
13146	17.09	0.05	0.01	0.20	0.19	0.21	0.40	14 03 43.07	−01 49 16.2	0.21	0.48
12116	18.33	0.82	1.18	0.99	0.32	2.17	2.48	14 02 40.20	+00 02 42.4	0.21	0.29
5677	18.25	-0.21	0.23	0.15	0.17	0.38	0.55	13 55 04.88	−02 35 07.3	0.21	0.43
11084	18.42	0.10	0.66	0.93	0.36	1.59	1.95	14 01 29.01	−02 14 02.0	0.21	0.29
16279	17.72	0.33	0.20	0.12	0.15	0.32	0.47	14 07 17.09	−00 08 51.8	0.21	0.41
8651	17.66	0.93	0.95	0.17	0.63	1.12	1.75	13 58 42.82	−01 07 49.9	0.21	0.27
372	17.32	-0.36	0.43	0.17	0.16	0.60	0.76	13 48 55.45	+00 53 13.8	0.21	0.33
15970	17.72	0.19	0.26	0.19	-0.01	0.45	0.44	14 06 59.22	+01 04 32.2	0.21	0.40
3392	18.07	0.60	1.20	0.86	0.53	2.06	2.59	13 52 32.64	+00 33 41.6	0.20	0.30
17508	17.66	1.29	0.88	0.33	0.77	1.21	1.98	14 08 30.48	−02 40 21.6	0.20	0.27
8840	18.23	-0.05	0.37	0.25	-0.06	0.62	0.56	13 59 01.95	+01 39 55.5	0.20	0.35
3236	18.41		1.69	0.97	0.44	2.66	3.10	13 52 29.10	+01 50 06.8	0.20	0.31
16756 •	18.46		2.13	0.64	0.70	2.77	3.48	14 07 40.86	−00 57 44.9	0.20	0.37
15681 •	18.48	-0.23	0.92	0.02	0.23	0.93	1.16	14 06 37.91	+02 08 30.9	0.20	0.28

Table E10: Top candidates in field 865 continued.

Object	R	U-B	B-V	V-R	R-I	B-R	B-I	α(1950)	δ(1950)	D_{10}	D_{100}
8043	18.10	0.38	0.84	0.59	0.87	1.43	2.30	13 57 58.33	−01 41 38.0	0.20	0.28
649	18.30		0.64	0.28	0.66	0.93	1.59	13 49 11.68	−01 43 56.2	0.20	0.27
13295	18.47			0.38	0.72			14 03 49.99	−02 02 40.5	0.20	0.30
7542 •	18.23		1.16	0.12	0.63	1.29	1.92	13 57 13.60	−02 31 31.4	0.20	0.27
962	18.23		2.01	0.90	0.80	2.91	3.72	13 49 44.10	+00 27 40.1	0.20	0.33
12471	17.88	0.09	0.30	0.04	0.32	0.34	0.66	14 03 12.93	+02 06 33.9	0.19	0.33
4811	18.06	0.04	0.46	0.00	0.28	0.46	0.74	13 54 17.60	+00 49 09.7	0.19	0.31
11654	17.91	-0.18	0.28	0.25	0.06	0.53	0.59	14 01 59.89	−02 15 22.1	0.19	0.36
11130	18.45	0.04	0.23	0.12	0.14	0.35	0.49	14 01 33.42	+01 33 14.3	0.19	0.41
16356	18.42	0.57	0.75	0.13	0.48	0.88	1.36	14 07 16.37	−02 29 26.5	0.19	0.26
14280	17.65	0.28	0.65	0.74	-0.05	1.39	1.34	14 05 12.58	+01 36 11.4	0.19	0.26
1270	17.96	0.86	1.41	0.78	0.98	2.18	3.16	13 50 01.18	−02 28 27.0	0.19	0.29
4631	17.64	0.81	1.39	0.85	0.68	2.24	2.92	13 54 08.18	+01 57 56.4	0.19	0.27
8182	17.05	-0.17	0.24	0.16	0.19	0.40	0.59	13 58 00.71	−02 33 37.7	0.18	0.39
5037	18.41		1.64	0.96	0.40	2.60	3.00	13 54 37.57	+02 22 37.9	0.18	0.29
4368 •	18.37	0.02	1.19	0.26	0.28	1.45	1.74	13 53 50.98	+01 51 32.1	0.18	0.27
3306	17.04	-0.27	0.41	0.83	0.29	1.24	1.53	13 52 25.20	−00 45 29.5	0.18	0.25
2164 •	18.47	-0.10	1.13	0.18	0.47	1.31	1.78	13 51 17.96	+01 17 24.5	0.18	0.25
13773	18.26	0.26	0.12	0.68	0.09	0.80	0.89	14 04 26.87	−00 45 01.7	0.18	0.24
16146	18.48		0.96	0.89	0.17	1.85	2.02	14 07 06.41	−00 23 27.1	0.18	0.27
2328	18.45	0.36	0.89	0.91	0.32	1.80	2.12	13 51 25.77	−00 01 51.8	0.18	0.26
9750	17.35	1.73	1.30	0.71	0.89	2.01	2.90	13 59 58.25	−01 45 48.8	0.18	0.23
16365	17.74	-0.11	0.69	0.58	0.73	1.27	2.00	14 07 26.48	+02 22 22.8	0.18	0.27
5654	17.97	0.71	1.05	0.89	0.54	1.94	2.48	13 55 12.16	−01 44 42.4	0.18	0.25
13530	17.11	0.00	0.07	0.43	0.22	0.50	0.72	14 04 07.71	−01 46 35.7	0.18	0.27
4007	18.46	-0.14	0.96	0.56	0.57	1.52	2.09	13 53 23.46	+00 59 55.2	0.18	0.26
17424	18.17	0.30	0.25	0.19	0.24	0.44	0.67	14 08 25.50	+00 38 40.9	0.17	0.30
3579	18.48	-0.05	1.18	0.38	0.52	1.56	2.08	13 52 56.22	+02 13 30.0	0.17	0.26
4139	17.74	0.06	0.24	0.12	0.21	0.37	0.58	13 53 30.53	+00 35 47.4	0.17	0.35
4349	18.19	-0.26	0.85	0.51	-0.02	1.36	1.34	13 53 49.43	+02 21 07.7	0.17	0.25
12883	17.63	-0.04	0.19	0.18	0.25	0.37	0.62	14 03 41.00	+02 05 01.3	0.17	0.33
1785	18.35	0.00	1.20	0.38	0.39	1.58	1.98	13 50 43.04	+01 30 21.1	0.17	0.24
7584	17.77	0.76	1.40	0.63	0.76	2.03	2.80	13 57 31.78	+00 54 15.5	0.17	0.24
17294	18.39	0.17	0.53	0.25	0.04	0.78	0.82	14 08 20.16	−00 14 11.6	0.17	0.26
15191	18.06	0.40	0.31	0.83	0.48	1.14	1.62	14 06 04.52	−00 39 35.7	0.17	0.24
14393	17.20	0.27	0.16	0.35	0.15	0.51	0.66	14 05 09.25	−01 43 41.1	0.17	0.27
12514	18.45		1.74	0.85	0.54	2.59	3.13	14 03 04.10	+00 21 34.8	0.17	0.26
6490	17.69	0.51	1.14	0.81	0.41	1.95	2.37	13 56 13.13	+01 51 49.5	0.17	0.26
1062	18.44		2.04	0.64	0.75	2.69	3.44	13 49 46.86	+01 38 56.0	0.17	0.31
747	17.70	0.14	0.93	0.42	0.79	1.35	2.15	13 49 21.51	−00 45 40.0	0.17	0.25
218	18.27	-0.15	0.23	0.23	0.34	0.45	0.79	13 48 33.09	−01 42 53.5	0.17	0.27
12707	17.30	0.80	0.77	0.59	0.90	1.36	2.26	14 03 15.65	−02 07 18.5	0.17	0.25
11785	18.20	0.14	0.17	0.37	0.64	0.54	1.18	14 02 07.56	−02 26 00.5	0.17	0.23
14286	17.27	0.09	0.12	0.34	0.10	0.46	0.56	14 05 10.71	+01 31 01.6	0.16	0.32
10860	17.83	-0.09	0.31	0.60	-0.06	0.91	0.85	14 01 21.03	+01 39 47.2	0.16	0.23
892	18.39	0.19	0.64	0.76	0.61	1.40	2.00	13 49 30.12	−01 23 04.0	0.16	0.24
15224	18.47	0.47	0.47	0.23	0.67	0.70	1.37	14 06 04.80	−01 44 32.1	0.16	0.24
17367	18.31	0.60	0.79	0.13	0.70	0.91	1.61	14 08 15.07	−02 35 13.0	0.16	0.24
9847	18.02	0.02	0.69	0.34	-0.02	1.03	1.00	14 00 02.69	−00 34 25.5	0.16	0.24
8780	18.25	0.23	0.98	0.69	0.67	1.66	2.33	13 58 50.16	−01 13 18.1	0.16	0.27
2718	18.03	-0.02	0.98	0.56	0.14	1.54	1.68	13 51 48.89	+00 53 03.1	0.16	0.22
1475	17.50		1.03	0.39	0.65	1.41	2.06	13 50 13.04	−02 31 15.8	0.16	0.25
4919	18.15	0.48	1.19	0.74	0.54	1.93	2.47	13 54 23.26	+01 31 12.8	0.16	0.26
15480	18.07		0.56	0.91	0.58	1.48	2.06	14 06 18.31	−00 12 03.1	0.16	0.25
2170	17.46	0.93	1.36	0.87	0.92	2.23	3.15	13 51 12.08	+01 05 44.9	0.16	0.23
16752	18.29		1.39	0.72	0.31	2.10	2.42	14 07 39.32	−00 41 12.6	0.16	0.24
15833	17.61	-0.02	0.24	0.18	0.13	0.42	0.55	14 06 51.36	+01 05 36.2	0.16	0.36
12596	17.87	-0.12	0.35	0.25	0.07	0.60	0.67	14 03 17.97	+02 03 12.6	0.16	0.29
6112	17.04	0.98	1.18	0.97	0.52	2.16	2.67	13 55 45.55	−00 00 03.4	0.16	0.22

Table E11: Top candidates in field 866 in 100th nearest-neighbour distance. AAT criterion.

Object	R	U-B	B-V	V-R	R-I	B-R	B-I	α(1950)	δ(1950)	D_{10}	D_{100}
4404 •	17.92			0.55				14 13 33.49	−00 22 32.3	0.38	1.21
13582 •	18.31			0.26				14 23 54.54	+02 26 48.2	0.52	1.06
518 •	17.06		0.78	0.29	0.43	1.07	1.50	14 08 55.25	−01 50 18.4	0.68	0.79
16552 •	18.28			0.53				14 27 11.51	+00 36 35.4	0.57	0.70
12	18.34							14 08 21.01	+01 32 43.8	0.52	0.64
16048 •	17.43	1.96	0.64	0.41	0.08	1.05	1.14	14 26 28.10	−01 31 57.5	0.34	0.50
11414	18.33				0.54			14 21 32.01	−00 53 36.0	0.31	0.43
18150	18.31	0.62	0.64	0.62	0.98	1.27	2.25	14 28 47.02	−00 21 27.4	0.30	0.41
15844	17.52	0.29	0.66	0.58	0.85	1.24	2.09	14 26 22.06	+00 39 39.2	0.32	0.39
11458	17.88	1.91	1.08	0.61		1.68		14 21 23.89	−02 17 11.2	0.23	0.34
12763	17.96	2.01	0.95	0.44	0.37	1.40	1.77	14 22 45.03	−02 18 51.2	0.22	0.34
17604	18.24	1.78	0.64	0.49	0.22	1.13	1.35	14 28 14.77	+00 31 57.6	0.19	0.33
8550	18.26	2.16	0.88	0.30	0.72	1.18	1.90	14 18 29.81	+02 12 04.0	0.21	0.33
16250	18.47	0.69				1.70		14 26 49.29	+01 28 09.8	0.23	0.32
8271	17.70	2.10	1.34	0.35	0.97	1.69	2.66	14 17 52.85	−01 59 00.7	0.22	0.32
2789	17.98	2.01	0.89	0.46		1.35		14 11 42.94	−00 48 28.0	0.22	0.32
5008	17.69	2.30	1.02	0.54	0.84	1.56	2.40	14 14 20.89	−00 04 40.0	0.22	0.32
9899 •	18.42		1.38	0.20		1.57		14 19 43.23	−01 22 54.4	0.15	0.32
6569	17.44	2.32	0.91	0.68	0.92	1.59	2.51	14 16 09.15	+00 45 53.8	0.19	0.32
18098 •	18.46		1.38	0.19		1.57		14 28 51.71	+02 21 51.7	0.14	0.31
14402	18.46	0.10			0.60	1.20	1.80	14 24 36.94	−01 33 42.3	0.20	0.31
15813 •	18.12	1.58	1.09	0.30	0.27	1.39	1.66	14 26 25.34	+01 45 28.6	0.20	0.30
9872	18.48	1.47	1.38	0.06	0.85	1.44	2.29	14 19 44.12	−00 10 56.0	0.23	0.30
4485	17.68	0.22	0.56	0.53	0.75	1.10	1.85	14 13 38.23	+01 58 55.1	0.21	0.30
9331	18.47	1.90	0.65	0.50	0.35	1.15	1.50	14 19 11.10	+01 10 28.1	0.17	0.30
17929	17.79	2.26	1.00	0.49	0.84	1.48	2.32	14 28 33.41	−01 09 16.9	0.19	0.30
16452	17.93		1.11	0.60	0.45	1.71	2.16	14 26 53.25	−00 56 22.6	0.16	0.30
5237	18.20		1.53	0.35	0.78	1.89	2.66	14 14 36.44	+00 58 35.5	0.18	0.30
14707	17.72	1.26	0.70	0.47	0.08	1.17	1.25	14 25 11.85	+02 01 08.0	0.20	0.29
495	17.40	2.19	1.03	0.76	0.86	1.78	2.64	14 08 57.15	−00 49 07.3	0.15	0.29
7983	18.44					0.84		14 17 41.58	−01 31 09.7	0.19	0.29
13388 •	18.49	0.40	0.98	-0.10		0.87		14 23 33.17	−00 20 27.8	0.20	0.29
5047	17.79	0.96	1.04	0.26		1.30		14 14 19.92	−01 54 52.7	0.18	0.29
13792	18.18	1.89	1.29	0.16	0.91	1.45	2.36	14 24 05.05	+00 01 10.5	0.15	0.29
13810	18.49	0.94	1.27	0.23		1.49		14 24 01.73	−00 24 48.6	0.21	0.28
14647	18.13		1.22	0.54		1.76		14 24 54.16	−01 07 12.4	0.18	0.28
4393	17.69	1.24	0.60	0.66	0.97	1.27	2.23	14 13 33.40	+00 13 55.8	0.20	0.28
8420	18.18		1.22	0.59		1.81		14 18 16.73	+02 16 09.0	0.17	0.28
17350	18.22	2.08				1.19		14 27 57.10	−01 12 37.3	0.17	0.27
14322	18.05	2.06	0.66	0.67	0.50	1.33	1.83	14 24 41.79	+01 01 42.1	0.17	0.27
14895	18.30		1.52	0.29	0.93	1.81	2.74	14 25 13.55	+00 11 08.9	0.13	0.27
6660	17.79	1.77	0.80	0.34	0.40	1.14	1.54	14 16 15.42	+02 13 54.7	0.15	0.27
16440	18.08	2.02	0.99	0.41	0.57	1.39	1.96	14 26 58.26	−00 24 13.4	0.15	0.27
5442	17.60	2.13	0.89	0.69	0.60	1.58	2.19	14 14 46.83	−01 41 06.4	0.15	0.27
15650	18.03		1.33	0.26	0.90	1.59	2.49	14 26 04.05	−02 37 44.0	0.12	0.26

Table E11: Top candidates in field 866 continued.

Object	R	U-B	B-V	V-R	R-I	B-R	B-I	α(1950)	δ(1950)	D_{10}	D_{100}
6399	18.21	1.98	0.57	0.66	0.51	1.23	1.75	14 16 01.42	+02 20 55.3	0.17	0.26
15187	18.33	0.73			0.23	1.51	1.74	14 25 34.25	−00 37 29.7	0.20	0.26
13258	18.26	1.45	0.53	0.37	0.37	0.90	1.27	14 23 30.04	−00 18 11.6	0.14	0.26
12255	18.32	0.69	1.06	0.49		1.55		14 22 21.62	−00 23 06.8	0.17	0.26
16439	18.24	0.38	0.96	0.09		1.05		14 26 54.42	−00 23 31.8	0.17	0.26
15554	18.18	1.86	0.64	0.56	0.40	1.20	1.60	14 26 00.80	+00 59 53.4	0.15	0.26
215	18.34	1.34	0.83	0.08	0.54	0.91	1.45	14 08 35.95	+00 56 20.4	0.16	0.26
9792	18.28	0.26				1.22		14 19 35.50	−01 44 42.3	0.16	0.26
6744	18.18		0.53	0.50	0.44	1.03	1.48	14 16 14.57	−00 51 52.6	0.15	0.26
12243	18.20	0.94	0.70	0.51	0.03	1.21	1.24	14 22 25.01	+00 01 20.5	0.17	0.26
15256	17.97	1.67	0.71	0.62	0.23	1.33	1.56	14 25 44.30	+02 06 40.0	0.17	0.26
199	18.35				0.37	1.86	2.23	14 08 42.98	+01 36 41.7	0.17	0.26
8556	18.42		1.31	0.26	0.93	1.57	2.49	14 18 23.55	+01 53 34.1	0.12	0.26
3255	18.23	1.98	1.05	0.35	0.64	1.39	2.03	14 12 18.83	+01 59 51.4	0.14	0.25
966	18.27	-0.21	0.77	0.18		0.95		14 09 34.20	+00 17 28.1	0.20	0.25
13782	18.20	1.38	0.77	0.39	0.24	1.16	1.39	14 24 01.81	+00 19 46.5	0.16	0.25
10241	18.21		1.39	0.47	0.64	1.86	2.50	14 20 17.86	+01 37 45.9	0.16	0.25
2579	18.13	2.02	0.59	0.69	0.62	1.28	1.91	14 11 37.82	+02 14 14.3	0.15	0.25
1280	18.20		1.32	0.18	0.67	1.51	2.17	14 09 57.86	+02 16 54.6	0.16	0.25
16504	18.30	1.62	0.56	0.30	0.64	0.86	1.49	14 27 05.60	+02 14 55.0	0.15	0.25
6397	17.85	1.84	1.11	0.26	0.64	1.37	2.01	14 15 55.88	+02 26 53.1	0.15	0.25
1474	17.23	1.94	1.13	0.58	0.56	1.71	2.26	14 10 14.20	−00 25 48.3	0.12	0.25
16466	17.44	1.19	0.61	0.73	0.84	1.34	2.18	14 26 58.29	−01 37 00.0	0.17	0.25
17971	17.87	1.86	1.04	0.23	0.70	1.27	1.98	14 28 37.27	+02 21 36.9	0.15	0.25
3598	18.36		1.23	0.33	0.46	1.55	2.02	14 12 32.24	−00 42 15.9	0.17	0.25
1468	18.44	1.40	0.67	0.16	0.58	0.82	1.41	14 10 12.75	−00 11 07.7	0.15	0.25
1628	18.48	1.44	1.13	0.09		1.22		14 10 21.57	−00 23 18.6	0.17	0.25
16356	17.96	2.04	0.75	0.42	0.76	1.18	1.94	14 27 02.35	+02 25 12.9	0.15	0.25

Table E12: Top candidates in field 867 in 10^{th} nearest-neighbour distance. Bright list, CTIO criterion.

Object	R	U-B	B-V	V-R	R-I	B-R	B-I	α(1950)	δ(1950)	D_{10}	D_{100}
4698	17.59	0.04	-0.10	-0.15	0.10	-0.26	-0.16	14 32 41.78	−02 18 23.2	0.41	0.64
16279	17.28	-0.25	-0.22	-0.11	0.04	-0.33	-0.30	14 42 40.75	+01 13 49.5	0.40	0.86
10414	17.38		0.50	0.23	0.55	0.73	1.27	14 37 42.95	+01 53 31.5	0.37	0.75
14761 •	17.94	1.23	0.79	0.38		1.17		14 41 13.36	−02 38 18.9	0.36	0.54
23048	17.95	0.37	0.57	0.08		0.65		14 48 17.42	+01 24 12.1	0.31	0.44
23318 •	17.99	0.92	0.63	0.48		1.11		14 48 20.50	−00 54 03.2	0.30	0.42
5325	17.96	0.21	-0.16	0.11	-0.08	-0.05	-0.13	14 33 16.06	−01 18 58.7	0.28	0.53
9503	17.43	0.28	-0.16	0.05	-0.01	-0.12	-0.12	14 36 58.58	+02 15 53.6	0.27	0.53
14540	17.89	0.10	0.24	0.20		0.44		14 41 00.28	−01 37 00.0	0.24	0.40
1825 •	17.73	1.90	1.14	0.30	0.37	1.45	1.81	14 29 56.40	−02 38 01.9	0.24	0.33
70	17.23	2.46	1.08	0.61	0.77	1.69	2.46	14 28 17.46	−00 16 40.9	0.24	0.41
4962	17.58	2.34	0.82	0.72	0.73	1.55	2.28	14 32 54.32	−00 32 39.1	0.24	0.33
671	17.14	2.49	1.04	0.53	0.99	1.57	2.56	14 28 50.34	−00 55 58.7	0.23	0.39
20624	17.29	2.45	1.09	0.74	0.94	1.84	2.77	14 46 14.96	+01 59 17.8	0.22	0.40
930	17.94	0.75	0.87	0.59	0.73	1.46	2.19	14 29 06.61	+00 16 34.9	0.19	0.28
3451	17.18	0.24	-0.04	-0.04	0.18	-0.09	0.09	14 31 38.33	+00 38 25.1	0.19	0.41
759	17.71	-0.03	0.05	0.13	0.08	0.18	0.27	14 29 04.97	+01 01 47.7	0.19	0.30
17656	17.28	0.32	-0.08	0.00	0.16	-0.07	0.08	14 43 35.23	−01 58 05.6	0.18	0.40
1064	17.24	2.26	1.02	0.69	0.69	1.71	2.40	14 29 17.03	+01 19 25.7	0.18	0.28
9499	17.17	0.28	-0.07	0.10	0.20	0.03	0.23	14 36 57.76	+02 25 27.7	0.18	0.31
10692	17.72	0.39	0.15	-0.01	0.08	0.14	0.22	14 37 55.01	−00 31 21.4	0.18	0.34
20154	17.51	0.40	-0.05	0.02	0.15	-0.03	0.12	14 45 52.38	−00 15 55.9	0.18	0.39
18710	17.19	0.19	0.29	0.36	0.76	0.65	1.41	14 44 33.17	−01 54 20.3	0.18	0.24
213	17.07	2.32	1.14	0.61	0.80	1.75	2.55	14 28 21.80	−00 29 30.0	0.18	0.32
23182 •	17.86	0.27	-0.07	0.01	0.15	-0.06	0.10	14 48 17.95	−02 16 00.9	0.17	0.39
14602	17.61	0.47	0.90	0.47	0.55	1.37	1.93	14 41 19.12	+01 53 06.7	0.17	0.24
16796 •	17.96	0.41	0.71	0.60	0.28	1.31	1.59	14 43 09.31	+02 21 14.7	0.17	0.22
10284	17.10	0.42	0.09	0.04	0.07	0.13	0.20	14 37 34.96	+00 53 03.6	0.17	0.34
4190	17.92	0.02	0.02	0.11	0.21	0.12	0.33	14 32 26.86	+02 04 05.1	0.17	0.27
19688	17.62	2.08	1.20	0.40	0.63	1.60	2.24	14 45 31.41	+01 44 37.3	0.17	0.26
17168	17.71	1.22	1.24	0.66	0.74	1.90	2.64	14 43 28.59	+02 14 38.7	0.17	0.24
21765	17.51	1.12	1.24	0.53	0.82	1.78	2.59	14 47 12.63	+00 30 06.5	0.17	0.26
7520	17.08	0.16	-0.03	0.16	0.14	0.13	0.27	14 35 16.89	+02 19 21.6	0.17	0.27
17685	17.80	1.01	1.23	0.45	0.52	1.68	2.20	14 43 51.74	+01 55 17.2	0.16	0.23
19907	17.34	0.23	0.26	-0.07	0.14	0.19	0.33	14 45 42.68	+01 01 37.3	0.16	0.28
13826	17.52	1.21	0.95	0.67	0.86	1.62	2.47	14 40 28.49	−01 35 11.2	0.16	0.24
539	17.35	0.00	-0.01	0.10	0.36	0.09	0.45	14 28 44.29	−01 14 05.9	0.16	0.25
22486	17.65	2.15	1.16	0.34	0.86	1.50	2.36	14 47 46.53	+01 35 30.0	0.16	0.25
12146	17.98	1.10	1.12	0.60	0.79	1.72	2.51	14 39 06.49	−00 46 46.2	0.16	0.25
3690	17.61	0.15	0.19	0.03	0.04	0.22	0.27	14 31 47.84	−02 12 48.6	0.16	0.27
10000	17.93	1.06	0.94	0.75	0.53	1.69	2.22	14 37 12.03	−01 11 06.7	0.16	0.23
21910	17.44	0.28	-0.02	0.03	0.17	0.01	0.18	14 47 20.06	+01 42 09.6	0.15	0.33
19483	17.30	0.22	0.06	0.12	0.04	0.18	0.22	14 45 11.36	−02 35 11.2	0.15	0.28
428	17.88	0.62	0.54	0.10	0.24	0.65	0.89	14 28 30.31	−02 36 44.6	0.15	0.21
3923	17.70	2.19	0.98	0.53	0.93	1.50	2.43	14 32 00.82	+00 13 54.7	0.15	0.23
19296	17.99	1.96	1.09	0.43	0.50	1.51	2.02	14 45 04.53	−02 11 40.1	0.15	0.23
1211 •	17.99	1.87	1.01	0.39	0.46	1.40	1.86	14 29 29.88	+02 01 54.1	0.15	0.24
16187	17.30	2.28	1.15	0.70	0.93	1.85	2.78	14 42 25.56	−01 04 11.7	0.15	0.28
6076	17.53	1.22	1.05	0.69	0.84	1.74	2.57	14 34 05.34	+02 02 22.4	0.14	0.24
4857	17.03	0.28	0.03	0.06	0.09	0.09	0.18	14 32 46.48	−02 04 44.1	0.14	0.32
734	17.06	-0.21	0.11	0.11	0.32	0.22	0.54	14 29 01.35	+02 05 28.9	0.14	0.25
1055	17.29	2.16	1.16	0.54	0.72	1.70	2.43	14 29 17.17	+01 29 24.2	0.14	0.23

Table E13: Top candidates in field 867 in 10^{th} nearest-neighbour distance. Faint list, CTIO criterion.

Object	*R*	*U-B*	*B-V*	*V-R*	*R-I*	*B-R*	*B-I*	α(1950)	δ(1950)	D_{10}	D_{100}
13790 •	18.49	0.21	0.53	1.23	-0.71	1.76	1.06	14 40 27.94	−00 31 19.7	0.67	0.77
15521	18.20	0.08	0.60	0.85	0.66	1.46	2.12	14 41 56.63	+01 23 36.8	0.45	0.55
3413	18.46	0.00	0.25	0.81	0.65	1.06	1.72	14 31 34.67	+01 51 40.6	0.38	0.48
7959	18.07	0.43	0.66	0.53	0.99	1.19	2.18	14 35 38.71	−00 30 41.6	0.35	0.45
274 •	18.47	-0.08	0.22	0.17	-0.47	0.39	-0.08	14 28 19.54	−02 36 24.8	0.34	0.59
225 •	18.23		0.91	0.53		1.44		14 28 27.29	−00 52 40.5	0.31	0.42
4644 •	18.43	0.12	0.34	0.88		1.22		14 32 42.81	−01 11 54.6	0.29	0.36
21614 •	18.34	0.95	0.15	0.89	0.44	1.04	1.48	14 46 57.83	−00 30 04.9	0.28	0.35
17169 •	18.30	0.92	1.37	0.55	0.65	1.93	2.57	14 43 21.72	+02 11 57.0	0.27	0.36
6941	18.43	0.62	0.88	0.69	0.72	1.58	2.30	14 34 35.93	−01 39 58.9	0.27	0.39
6434	18.48	-0.21	0.47	0.45	0.63	0.91	1.54	14 34 13.36	−02 36 04.8	0.26	0.31
3788	18.44	-0.25	-0.11	0.47	0.10	0.36	0.46	14 31 54.28	−00 13 58.3	0.26	0.36
1003 •	18.31		1.00	0.49		1.50		14 29 10.38	−01 52 09.5	0.25	0.36
10305	18.19	0.80	0.87	0.66	0.82	1.54	2.35	14 37 35.61	−00 08 40.7	0.25	0.35
7053	18.30	0.98	1.30	0.66	0.63	1.95	2.58	14 34 50.53	+00 02 11.2	0.25	0.34
20696	18.32	-0.03	0.77	0.38	0.61	1.15	1.76	14 46 14.09	−00 20 21.0	0.25	0.31
10131	18.36	0.54	0.77	0.69	0.61	1.46	2.07	14 37 24.94	+00 11 08.0	0.25	0.33
16373	18.37	0.16	0.16	0.25	-0.30	0.41	0.11	14 42 40.08	−01 15 36.9	0.24	0.39
18229 •	18.19	0.25	0.12	0.02	-0.13	0.14	0.01	14 44 03.40	−02 30 22.5	0.24	0.43
21718	18.03	0.28	0.64	0.35	0.89	0.99	1.88	14 47 16.90	+01 53 25.0	0.23	0.32
16167 •	18.27	1.46	1.27	0.27	0.29	1.54	1.83	14 42 28.80	−00 15 54.6	0.23	0.32
18879	18.05	0.57	0.74	0.66	0.67	1.40	2.07	14 44 48.04	−01 02 01.7	0.23	0.31
21540 •	18.29	0.22	0.33	-0.04	-0.09	0.29	0.21	14 47 02.16	+01 37 18.9	0.23	0.36
17173 •	18.38	0.01	1.01	0.13	0.38	1.15	1.53	14 43 19.65	+01 56 53.5	0.23	0.30
1496	18.28	0.00	0.06	0.28	-0.17	0.34	0.17	14 29 38.57	−01 58 18.8	0.23	0.36
3897	18.48	0.13	-0.17	0.46	0.03	0.29	0.32	14 32 03.31	+00 57 11.2	0.23	0.31
1826	18.39	0.06	0.06	0.30	-0.21	0.36	0.15	14 29 51.28	−02 38 57.9	0.22	0.35
4519	18.34	1.11	0.26	0.55	0.22	0.81	1.03	14 32 33.58	−02 36 55.1	0.22	0.28
22659	18.41	0.46	0.17	0.79	0.29	0.96	1.25	14 47 58.08	+01 55 36.1	0.22	0.28
19814 •	18.41	0.33	-0.14	0.01	0.09	-0.13	-0.04	14 45 28.82	−01 19 40.8	0.22	0.48
14731	18.42	0.40	0.59	0.74	0.39	1.33	1.71	14 41 12.04	−01 37 41.9	0.22	0.28
2257	18.44	0.77	0.87	0.59	0.80	1.46	2.27	14 30 19.37	−01 14 53.7	0.22	0.32
17170	18.08		1.55	0.84	0.98	2.38	3.36	14 43 20.87	+02 01 34.0	0.22	0.30
12401 •	18.12	0.42	0.63	0.29	-0.14	0.92	0.78	14 39 29.29	+01 51 21.8	0.22	0.31
8559 •	18.01	1.36	0.86	0.07	0.46	0.94	1.40	14 36 01.25	−02 34 32.0	0.21	0.29
316 •	18.33	1.65	0.68	0.19	0.57	0.87	1.44	14 28 37.38	+01 16 25.0	0.21	0.31
16800	18.23	0.57	1.06	0.48	0.55	1.53	2.08	14 43 04.08	+01 59 28.4	0.21	0.29
17211	18.47	0.38	0.36	0.19	-0.14	0.55	0.41	14 43 21.34	+00 53 36.2	0.21	0.32
23402 •	18.29	1.62	0.97	0.43	0.19	1.40	1.59	14 48 35.69	+01 56 30.7	0.20	0.30
17350	18.49	0.33	0.91	0.49	0.44	1.41	1.85	14 43 34.35	+02 13 57.4	0.20	0.28
17172 •	18.11	0.68	1.11	0.40	0.31	1.52	1.83	14 43 26.93	+01 58 42.8	0.20	0.27

Table E13: Top candidates in field 867 continued.

Object	R	U-B	B-V	V-R	R-I	B-R	B-I	α(1950)	δ(1950)	D_{10}	D_{100}
9261 •	18.16	0.28	0.02	0.04	-0.08	0.06	-0.02	14 36 42.31	−02 04 45.8	0.20	0.44
1991 •	18.15	1.23	1.17	0.13	0.39	1.29	1.69	14 30 15.14	+02 25 36.8	0.20	0.28
5363	18.41	-0.06	0.51	0.00	-0.05	0.52	0.47	14 33 20.05	−02 29 23.7	0.20	0.29
1505 •	18.35	1.04	0.71	0.09	0.37	0.80	1.17	14 29 37.16	−02 27 41.6	0.20	0.26
11034	18.04	1.17	0.80	0.85	0.65	1.65	2.30	14 38 12.59	−00 29 05.6	0.19	0.27
1368	18.40	0.07	0.15	-0.09	0.25	0.06	0.31	14 29 34.82	+01 25 53.1	0.19	0.30
10911	18.28	1.04	0.41	0.64	0.08	1.05	1.12	14 38 01.72	−02 16 32.2	0.19	0.27
2632	18.15	0.84	1.21	0.36	0.51	1.57	2.08	14 30 40.09	−02 10 12.4	0.19	0.25
2446 •	18.39	0.95	0.78	0.49	0.00	1.28	1.28	14 30 30.46	−01 35 50.7	0.18	0.29
1099	18.44	-0.08	0.07	0.44	0.58	0.51	1.08	14 29 18.77	+00 16 16.9	0.18	0.25
16970	18.27	0.06	0.35	0.58	0.53	0.93	1.46	14 43 13.39	+02 22 06.4	0.18	0.25
12138	18.23	0.15	0.59	0.22	-0.15	0.81	0.65	14 39 02.87	−00 38 13.9	0.18	0.29
1494	18.41	-0.13	0.24	0.12	-0.06	0.37	0.31	14 29 36.34	−01 51 46.7	0.18	0.31
7646	18.27	0.30	0.32	0.66	0.49	0.98	1.48	14 35 13.27	−01 45 52.2	0.18	0.24
406	18.20	1.27	0.55	0.48	0.18	1.04	1.22	14 28 33.98	−01 59 01.9	0.18	0.26
6531	18.32	0.18	0.24	0.57	0.62	0.81	1.42	14 34 24.60	−00 25 48.5	0.18	0.26
7701	18.41	1.47	0.42	0.72	0.41	1.14	1.55	14 35 27.36	+01 28 28.1	0.17	0.25
12511	18.34	0.94	0.59	0.81	0.49	1.40	1.89	14 39 22.56	−01 10 41.7	0.17	0.25
19402	18.04	1.10	1.00	0.72	0.69	1.72	2.41	14 45 15.95	−00 40 28.6	0.17	0.25
16479	18.44	0.02	0.77	0.36	0.13	1.14	1.27	14 42 44.92	+00 54 17.4	0.17	0.24
12605 •	18.49	0.25	0.46	0.38	-0.20	0.84	0.64	14 39 37.30	+01 48 36.0	0.17	0.29
17875	18.43	0.48	0.60	0.37	0.83	0.96	1.79	14 43 58.85	+01 49 56.6	0.17	0.25
16194 •	18.03		1.15	0.84	0.28	1.99	2.27	14 42 29.90	−01 16 01.3	0.17	0.27
16198 •	18.27	0.39	0.57	0.29	-0.09	0.86	0.77	14 42 24.98	−01 30 45.2	0.17	0.27
12458	18.47	1.27	0.40	0.76	0.49	1.17	1.65	14 39 22.35	+00 14 06.9	0.17	0.24
10104	18.50	0.83	1.13	0.49	0.60	1.61	2.21	14 37 25.21	+00 55 08.4	0.17	0.26
4045 •	18.15	1.06	0.79	0.23	0.14	1.02	1.17	14 32 13.18	+01 39 12.6	0.17	0.29
2002	18.34	0.83	0.26	0.51	0.63	0.77	1.40	14 30 13.47	+01 39 37.6	0.17	0.23
958 •	18.29		0.73	0.61		1.33		14 29 11.65	−00 36 45.0	0.17	0.25
1054	18.29	0.34	0.69	0.56	0.49	1.25	1.74	14 29 17.33	+01 30 10.5	0.17	0.23
6327	18.13	0.33	0.12	-0.05	0.06	0.07	0.13	14 34 16.63	+00 15 10.0	0.16	0.37
17553	18.12	0.36	0.81	0.31	0.73	1.11	1.85	14 43 40.99	+00 57 04.2	0.16	0.23
874	18.47		0.58	0.96	0.58	1.54	2.11	14 29 10.21	+02 20 57.3	0.16	0.27
5205	18.03	2.09	1.00	0.37	0.79	1.37	2.16	14 33 14.24	+02 18 52.5	0.16	0.24
163	18.39	-0.03	0.23	0.25	-0.16	0.47	0.32	14 28 28.88	+01 14 54.3	0.16	0.29
20811	18.44	0.95	0.89	0.24	0.14	1.14	1.28	14 46 25.49	+01 15 28.1	0.16	0.27
176 •	18.31		1.28	0.77	0.46	2.05	2.51	14 28 27.16	+00 48 26.3	0.16	0.23
10705	18.38	0.61	0.87	0.54	0.59	1.41	2.01	14 37 48.99	−01 01 02.6	0.15	0.24
22785	18.45	0.75	0.44	0.72	0.55	1.16	1.71	14 47 53.73	−01 37 18.7	0.15	0.23
17555	18.31	1.12	1.04	0.70	0.62	1.75	2.37	14 43 38.67	+00 54 28.0	0.15	0.23
11828	18.07	0.17	0.53	-0.11	0.27	0.42	0.69	14 38 49.69	−01 52 12.3	0.15	0.22
3100	18.23	1.77	0.83	0.42	0.38	1.25	1.63	14 31 08.74	−02 28 44.0	0.15	0.25
23172	18.25	1.14	0.98	0.38	0.18	1.36	1.54	14 48 15.41	−02 02 13.9	0.15	0.24
3102	18.05	1.09	0.71	0.33	0.13	1.04	1.17	14 31 09.62	−02 31 33.5	0.15	0.26